REVIEW OF THE VKI DOCTORAL RESEARCH

2019 - 2020



von Karman Institute for Fluid Dynamics

Front cover: Steady-state velocity distribution and streamlines of a Reynolds 20 compressible flow closed by Van der Waals equation of state around a solid cylinder. The simulation has been performed with the Argo discontinuous Galerkin (DG) solver at fifth order, on conformal (top) and immersed interface (bottom) configurations, on similar unstructured meshes. The immersed interface is handled by a high-order sharp interface extended DG method.
Picture of David Henneaux

©2020 by the von Karman Institute for Fluid Dynamics
Waterloosesteenweg 72, B-1640 Sint-Genesius-Rode
To order: https://www.vki.ac.be

ISBN 978-2-87516-162-8

D/2020/0238/732, T. Magin, Editor-in-Chief

The contents of this book are the property of the von Karman Institute for Fluid Dynamics. No part of this book may be reproduced or distributed in any form of by any means, or stored in a database or retrieval system, without the prior written permission from the Publisher.

PREFACE

The eleventh symposium on the doctoral research of the von Karman Institute for Fluid Dynamics took place online during the period May 18 to 20, 2020. The doctoral students present the progress of their research work carried out in the three departments: Aeronautics and Aerospace, Environmental and Applied Fluid Dynamics, Turbomachinery and Propulsion. The first year students have presented a poster on their research plans and some preliminary results, while the most advanced students have proposed a presentation followed by a session of questions.

This event was attended by the faculty of the von Karman Institute, as well as by colleagues from universities and industrial partners. The Symposium is open to external attendees free of charge. In addition to the presentations of the PhD candidates, we had the pleasure to welcome three prominent keynote lecturers who open each day the Symposium:

- Prof. Isabelle Gallagher, École Normale Supérieure, University Paris-Diderot, Paris, France, *"Deriving fluid mechanics equations from particle systems,"*
- Dr. Jean Rabault, University of Oslo, Oslo, Norway, "*Recent results on Deep Reinforcement Learning applied to flow control and optimal design,"*
- Prof. Koen Hillewaert, University of Liège, Belgium, "*Using DNS and LES to improve understanding of flow phenomena in turbomachinery passages."*

This year, the best presentation award has been attributed to David Henneaux for his research on "Towards a high-fidelity multiphase solver with application to space debris aerothermal ablation modeling" We would like to congratulate him on this achievement. The illustrated cover art of these proceedings is based on his research results. Due to the COVID-19 situation, the symposium had to be organized online and the poster session was replaced by a pitch session.

This proceedings volume contains 43 papers, which are divided into the following topics: Rarefied and Plasma Flows, Aerothermodynamics, Numerical Methods, Aerothermochemistry, Environmental Flows and Safety, Propulsion, Liquid Metal and Industrial Flows, Aeroacoustics, Turbine and Compressor Aerodynamics & Heat Transfer.

We would like to emphasize that this publication serves as a tool for communication and aims to enhance exchange between the doctoral candidates, the faculty and external attendees. The annual publication of their results in proceedings is of crucial importance to the VKI research providing a thorough review of the different activities within the three departments.

As such, the doctoral candidate students play a key role in strengthening the expertise in experimental research, computational methods, and physical modelling. In addition to basic research, works carried out at the von Karman Institute often leads to implementation of real-life industrial applications critical to the fluid dynamics community.

Andrea Fagnani Fabio Pino Phd Representatives	Thierry Magin Professor	Christelle Debeer Organizer / Editor

The contribution of all VKI members who helped with this event is deeply acknowledged in particular the faculty, library and printing office staff.

TABLE OF CONTENTS

Editorial notes i

Table of contents iii

RAREFIED AND PLASMA FLOWS

Simon DEMANGE 3
Effect of property models on heated round jets oscillations

Vincent Fitzgerald GIANGASPERO 13
Modeling strategy for blackout analysis of re-entry phases in space exploration missions

Louis REBOUL (first year PhD) 23
Mathematical modeling and simulation of non-equilibrium plasmas for the prediction of the electric propulsion

AEROTHERMODYNAMICS

Iván PADILLA MONTERO 27
Analysis of the stability of a flat plate high-speed boundary layer with discrete roughness

Ludovico ZANUS 41
Nonlinear parabolized stability analysis of chemically reacting boundary-layers

Dániel Gábor KOVÁCS (first year PhD) 49
Dynamic stability of slender bodies in the transonic regime

AEROTHERMOCHEMISTRY

Michele CAPRIATI (first year PhD) 53
Simulation of a 3D unsteady hypersonic flow under uncertainty

Anable DEL VAL 55
A Bayesian perspective on TPS catalysis phenomena: learning from experiments and proposing new ones

Joffrey COHEUR 71
Gradient-informed sampling of Bayesian posteriors in probabilistic inversion of pyrolysis models

Andrea FAGNANI 83
Development of a robust framework for space debris material testing in the VKI Plasmatron facility

David HENNEAUX 97
Towards a high-fidelity multiphase solver with application to space debris aerothermal ablation modeling

Francisco TORRES HERRADOR 109
Characterization of the thermal degradation of carbon-phenolic materials: an experimental effort on the ZURAMR© ablator

ENVIRONMENTAL FLOWS AND SAFETY

Yoshiyuki NISHIO 121
VMS implementation for CBRN dispersion modeling in the atmosphere

Cem Berk SENEL 131
A new one-dimensional planetary boundary layer (PBL) scheme from large-eddy simulations: VKIPBL-01

Abdelhafidh MOUMEN (first year PhD) 143
Quantitative analysis and visualization of muzzle flow

Loreline FAUGIER (first year PhD) 145
CFD modeling of a contaminant release in a subway station

Tom LAURIKS (first year PhD) 147
Monotone integrated large eddy simulation (MILES) and uncertainty quantifications
for improved CFD modeling of urban environments

Aude LECARDONNEL (first year PhD) 151
Aerothermal characterization of compact heat exchanger elements

Svana ROGALLA (first year PhD) 153
The evolution of darker wings improves flight efficiency in seabirds

PROPULSION

Domenico FIORINI 157
Gas-liquid interface dynamics in non-isothermal sloshing: experimental analysis and simplified modeling

Maria Teresa SCELZO 169
Toward densified propellants for space launchers: the effect of solid particles on the flow convective heat transfer coefficient in slurry pipe flow

Ali Can ISPIR (first year PhD) 179
Multi-dimensional design and optimization of a hypersonic propulsion system

LIQUID METAL AND INDUSTRIAL FLOWS

Zoé JARDON 183
Offline powder-gas nozzle jet characterization for coaxial direct laser deposition

Fabio PINO (first year PhD) 193
Feedback control of liquid metal coating

Maxim VAN CAPPELLEN 195
Modelling of particle-laden flows in two dimensions, an optimization-based multivariable quadrature moment method

Andrea ATTAVINO 203
Numerical investigation of the effect of buoyancy forces on the deflagration of hydrogen in the Thai facility

Mathilde FIORE (first year PhD) 215
Thermal turbulence modelling of liquid metal flows via data analysis and machine learning

David BARREIRO (first year PhD) 217
A numerical study on the jet wiping process using LES and VOF methods

AEROACOUSTICS

Joachim DOMINIQUE 221
Inferring empirical wall pressure spectral models using Gene Expression Programing

Alessandro ZARRI 233
Influence of forward-swept blades on low-order acoustic prediction for low-speed fans

Riccardo ZAMPONI 241
Experimental investigation of the distortion of turbulence interacting with a porous airfoil

NUMERICAL METHODS

Ray VANDENHOECK 255
Massively parallel and robust high-order methods for transitional hypersonic flow modelling on unstructured grids

Firas BEN AMEUR 269
R-adaptive mesh algorithms with high-order flux reconstruction scheme for simulating high-speed flows with uncertainties

SHAPE OPTIMIZATION

Tom DE BRUYN 283
Aero structural optimization using adjoint method: treatment of testcases with several blade rows

Luca ZAMPINI (first year PhD) 291
One-shot and multigrid acceleration for industrial shape optimization

COMPRESSOR AERODYNAMICS & HEAT TRANSFER

Cédric BABIN 295
Numerical characterization of a HP compressor stage equipped with a closed shrouded stator cavity

Riccardo TORACCHIO (first year PhD) 311
Performance and stability analysis of a highly-loaded low-pressure compressor under distorted inflow conditions

TURBINE AERODYNAMICS & HEAT TRANSFER

Gustavo LOPES (first year PhD) 315
Purge and leakage flow effects on the aerodynamics of a high-speed low-pressure turbine cascade

Tânia Sofia CACAO FERREIRA 317
Implicit large eddy simulation of the high-pressure turbine vane LS89

Mizuki OKADA (first year PhD) 327
Advanced PIV measurement in high-speed turbomachinery flows

Antonio Federico Maria TORRE (first year PhD) 329
Experimental investigation of a high-speed low-pressure turbine

INSTRUMENTATION AND MEASUREMENT TECHNIQUES

Mushin Can AKKURT (first year PhD) 333
Aero-thermal investigation of roughened circular channels

Bart BROUWERS (first year PhD) 335
Monitoring of flow mechanics in cohesive sediment layers

RAREFIED AND PLASMA FLOWS

Effect of property models on heated round jets oscillations

Simon Demange

Aeronautics and Aerospace Department, von Karman Institute for Fluid Dynamics, Belgium, simon.demange@vki.ac.be

Supervisor: Olivier Chazot

Head of department, Aeronautics and Aerospace Department, von Karman Institute for Fluid Dynamics, Belgium, chazot@vki.ac.be

University Supervisor: Gérard Degrez

Dean, Aéro-Thermo-Mécanique, Université Libre de Bruxelles, Belgium, gdegrez@ulb.ac.be

Abstract

Absolute instabilities in heated top-hat and coaxial round jets are investigated with the spatio-temporal local Linear Stability Theory and axisymmetric Direct Numerical Simulations. The influence of thermo-transport properties on the stability is quantified by considering models of increasing complexity assuming respectively: constant properties, a calorically perfect gas, and mixture of gases in local thermo-chemical equilibrium. Results are compared against unsteady simulations.

Keywords: Jet instabilities, Absolute Instabilities, Linear Stability Theory

1. Introduction

Understanding the stability features of high-enthalpy jets is a critical point for experiments carried out in plasma wind tunnels, which aim to recreate atmospheric entry conditions while minimizing perturbations in the flow field. However, heated axisymmetric jets are known to support self-sustained oscillations once the ambient-to-jet temperature ratio S is lowered below a critical value. The occurrence of these *global modes* as defined by [1] has been correlated to the absolute nature of local instabilities by [2] using the spatio-temporal Linear Stability Theory (LST), and experimentally confirmed by [3]. Consequently, several studies, among which the work of [4; 5; 6; 7], have used simplified analytical *top-hat* and coaxial jet profiles to study the influence of flow parameters on the convective to absolute transition. The work of [4] identified the baroclinic torque as a source of absolute instabilities in heated round jets, while [8] showed that absolute instabilities could also be caused by strong shears in low velocity regions in the absence of a density gradient.

However, these models are not necessarily representative from real configurations as the flow non-dimensional parameters are varied independently. This was highlighted by the contribution of [9], performing LST analysis on numerically integrated boundary layer equations, which showed different critical parameters than the one found with simplified profiles. This was further investigated by [8], who could obtain absolutely unstable round jets with uniform density by deforming the velocity profile shapes. Therefore, a definition of the base state as physically based as possible is an important factor to consider for this kind of analysis. In the case of heated jets with large temperature ratios, thermo-transport properties are expected to vary significantly from the centerline to the ambient gas. Most models found in the literature neglect this aspect and consider both constant viscosity and thermal conductivity in their models, such as [10; 1]. However, a Sutherland viscosity law indicates a centerline-to-ambient viscosity ratio of 3.33 for a centerline-to-ambient density ratio of $S_1 = 7$, which is expected to influence both the base state and the stability properties of the flow. Furthermore, comparisons of LST against DNS and experimental observations done by [11; 10; 1; 12] have shown that a long enough region of absolute instability (around one absolute wavelength) should exist in order to set off the global modes. Here again, different property models

are expected to change the stream-wise evolution of the base state and thus of the LST results. In turn, this could potentially influence the length of the absolute region. [1] also indicates that the global mode is expected to beat near the absolute frequency found at the upstream boundary of the absolute pocket for jets close to critical parameters.
The objective of the present work is to asses the influence of different thermo-transport properties modeling on the stability of axisymmetric heated jets. To this end, three models of Thermo-Transport Properties (TTP) are defined and implemented in the DNS code developed by [13]:

1. **TTPcst**: considering constant properties, similarly to the original code;
2. **CPG**: considering a Calorically Perfect Gas, with approximations of the TTPs commonly found in literature for low to moderate temperatures;
3. **LTE**: considering a mixture of perfect gases in Local Thermo-chemical Equilibrium, which can be used to describe Inductively Coupled plasma wind tunnel jets as in [14].

Two types of jets are considered by injecting respectively top-hat [15] and coaxial [7] jet profiles in the domain. For each jet, both steady and unsteady results are obtained by turning respectively on and off a Selective Frequency Damping (SFD) method. The stability features of the jets are retrieved by seeking the numerical solutions to the spatio-temporal local Linear Stability Theory (LST) problem on the steady states. Stability equations are adapted to each model and the results are compared against the time evolution of large coherent structures in the DNS fields without SFD. For each case, results from the three TTP models presented in section 2 are compared.

2. Base states

The present cases are described using the cylindrical coordinates $(r,\ \theta,\ x)$, respectively in the radial, azimuthal and stream-wise directions, and the velocity vector is decomposed as $\vec{U} = U\vec{e_r} + V\vec{e_\theta} + W\vec{e_x}$. Base states investigated are obtained by the injection of velocity and temperature profiles in the domain at $x = 0$. Expressions corresponding to the profile number 2 from [15] are used to define the inlet of top-hat jets, while the definition from [7] is used for coaxial jets. In both cases, the profiles are defined by a thickness parameter R/θ, where R is the jet radius and θ the momentum shear layer thickness, a centerline-to-ambient temperature ratio S, and an inlet Reynolds number based on the jet diameter. For coaxial jets, $h = {}^{W_s}/_{W_j}$ is the ratio between the secondary and the primary stream velocities at the inlet. For all cases, a low Mach number is assumed which implies that the temperature profiles take the same shape as the stream-wise velocity ones. Only the primary stream is heated for coaxial jet. A co-flow of 1% of the inlet centerline velocity W_j is also injected in the simulations to improve the convergence.
The motion of the flow after the inlet is described with the low Mach number approximation of the axisymmetric Navier-Stokes equations. The equations and implementation of [13] is directly used for our flow model assuming constant properties, while neglecting buoyancy effects. Furthermore, a single species of gas is considered by ignoring the mixture fraction equation described by [13], and the temperature ratio S is defined as the inverse of the density ratio S_1 of [13]. The flow in the simulations is described in terms of stream-wise and radial velocities, temperature T and density ρ.
For the three models, the reference length is the primary jet diameter D and the reference velocity used to obtain the non-dimensional fields is the inlet centerline one W_j. The non-dimensional temperature is obtained as $T = (T_{dim} - T_\infty)/(T_j - T_\infty)$, where T_∞ is the outer flow temperature set to 350 K, and T_j the inlet centerline temperature. The density is however made non-dimensional with respect to the outer flow value ρ_∞ in all models. The model of [13] assumes a constant viscosity $\mu = \mu_\infty$ and thermal conductivity $\lambda = \lambda_\infty$, as well as a unit Prandtl number $Pr = 1$. In these conditions the Reynolds number is computed from D, the inlet velocity U_j, μ_∞ and the density at the inlet ρ_j.
Results are computed on a mesh of 255×513 nodes along $(r,\ z)$. The boundary conditions and Selective Frequency Damping method used for the current analysis are the same as the ones described by [16]. The numerical domain extends to 20 jet diameters in stream-wise directions and respectively 4 and 6 diameters in the radial direction for top-hat and coaxial jets.

2.1. Modifications for the CPG model

Modifications introduced in the DNS code for the CPG model are limited to the introduction of a variable viscosity and thermal conductivity. The reference viscosity and thermal conductivity are taken at the inlet: μ_j and λ_j. Therefore, the Reynolds number is defined using the inlet centerline viscosity μ_j instead of

μ_∞. The variable viscosity is obtained using a Sutherland law, and the thermal conductivity is obtained by imposing a constant Prandtl $Pr = 0.7$. Finally, modifications have been introduced in the energy and momentum equations to take into account the temperature derivatives of μ and λ.

2.2. Modifications for the LTE model

In order to take into account high temperature effects, the flow is assumed to be a mixture of perfect gases in Local Thermo-chemical Equilibrium. This model is the simplest available to describe accurately high enthalpy flows, as it considers a single temperature and chemical reaction rates much faster than the flow characteristic velocity. In such case, chemistry effects are contained in the variations of the thermodynamic and transport properties due to the (seemingly) instantaneous adaptation of the flow composition with variations of pressure and temperature. In order to approach conditions where the equilibrium assumption has been verified experimental by [14] in the VKI plasma wind tunnel, a static pressure $p_\infty = 100$ mbar is considered. Note that the same pressure is assumed for the models of previous sections when rebuilding dimensional quantities. The current model considers an 11-species air mixture containing: $[N,\ O,\ NO,\ N_2,\ O_2,\ N^+,\ O^+,\ NO^+,\ N_2^+,\ O_2^+,\ e^-]$.
For a flow in LTE, the definition of the Mach number becomes ambiguous, and the Eckert number Ec is generally preferred. Furthermore, expressing the energy equation in terms of static enthalpy is more convenient, and some reference quantities are changed with respect to the CPG case. Details of the implementation of the LTE low-Eckert approximation DNS are available in [17]. For completeness, the non-dimensional equations implemented are given as:

$$\frac{\partial \rho}{\partial t} + \nabla(\rho u) = 0, \tag{1a}$$

$$\nabla p^{(0)} = 0, \tag{1b}$$

$$\frac{\partial(\rho u)}{\partial t} + \nabla(\rho u u) = \nabla p^{(1)} - \frac{1}{S_1 Re}\nabla(\tau), \tag{1c}$$

$$\rho\frac{Dh}{Dt} = \frac{1}{S_1 RePr}\nabla(\lambda \nabla T). \tag{1d}$$

With,

$$S_1 = \frac{\rho_\infty}{\rho_j}, Re = \frac{\rho_j u_j d}{\mu_j}, Pr = \frac{\mu_j}{\lambda_j T_j}\frac{p_\infty}{\rho_\infty}, Ec = \frac{\rho_\infty u_j^2}{p_\infty}. \tag{2}$$

Where τ is the viscous stress tensor defined in [13], h is the static enthalpy, and the indices $^{(0)}$, $^{(1)}$ denote the order of approximation used in the low Eckert expansion for the pressure terms, similarly to [13] in the low Mach number approximation. The coupling of equation (1b) with steady pressure boundary conditions at the far-field imply that $p^{(0)} = cst$. In the current implementation, the constant slow component of the pressure $p^{(0)}$ is used to justify that the thermodynamic and transport properties only depend on temperature due to the low Eckert approximation. Properties are therefore interpolated from pre-computed tables at p_∞ during the DNS routine using a cubic Hermite interpolant method .
Furthermore, an inlet top-hat jet profile is imposed in terms of the static enthalpy for this case, in order to obtain more realistic temperature profiles. To impose this profile, an enthalpy ratio equivalent to the temperature ratio S imposed to the other models is computed and the temperature field is retrieved from the enthalpy one by inverting the interpolation of the LTE table.

3. Stability analysis

The stability analysis is carried out in the VKI Extensible Stability and Transition Analysis toolkit [18]. Stability equations associated with the constant properties and CPG models are automatically derived from the compressible Navier-Stokes equations in the Automatic Derivation and Implementation Tool (ADIT) described in [19], and can be found in [18]. LTE stability equations are also derived in the ADIT and include grouping terms specific to high temperatures defined by [20].
The base state are obtained from the stream-wise velocity and temperature fields extracted from the DNS with SFD. The properties are then reconstructed according to each model hypotheses. The stability equations consider the $(u,\ v,\ w,\ p,\ T)$ variables respectively the components of the velocity along $(r,\ \theta,\ z)$, the pressure and temperature. The classical LST ansatz is used to replace the flow quantities q by:

$$q = \bar{q} + q' = \bar{q} + \tilde{q}(r)e^{i(\alpha z + m\theta - \omega t)} + c.c. \tag{3}$$

With $q' \ll \bar{q}$, α and m respectively the stream-wise and integral azimuthal wavenumbers and ω denotes the angular frequency. In this process, perturbations of the transport properties are considered by expanding them using their derivatives with respect to pressure and temperature, as described by [18]. Stability equations are discretized in the radial direction using a pseudo-spectral Chebyshev collocation method,

stretched by using mapping techniques from [21] for top-hat jets, and from [22] for coaxial jets. Stability equations completed with the boundary conditions described in [17], reduce to a generalized eigenvalue problem solved by imposing a complex α to obtain the corresponding complex ω.

4. Results

The present work investigates four sets of jet parameters summarized in table 1.

Case	Type	Re_D	S	h	R/θ
1	**Top-hat**	400	1/7	-	20
2	**Top-hat**	225	1/15	-	20
3	**Coaxial**	800	1/3	0.5	33
4	**Coaxial**	800	1/6	0.1	33

Table 1: Main parameters of the jet flows investigated.

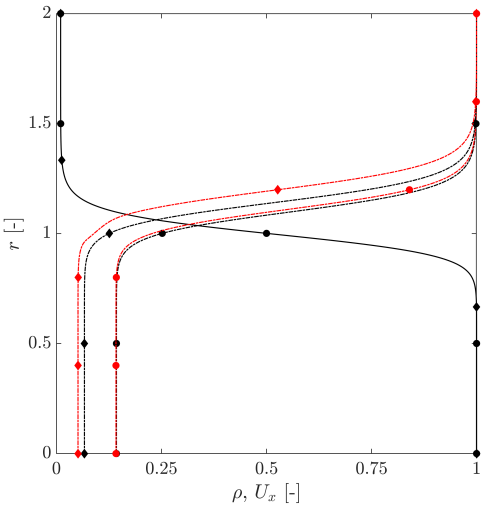

Figure 1: Top-hat jets inlet radial profiles of stream-wise velocity (−) and density (- ·) in CPG (black) and LTE (red). Case 1 (●) and 2 (⧫) are plotted.

For all cases, low Reynolds numbers are imposed in order to approach the conditions found in plasma wind tunnels [17]. However, other non-dimensional parameters are chosen so as to impose absolutely unstable inlet profiles based on results from [4] for top-hat jets and [7] for coaxial jets.
High temperature effects are expected to be particularly important in case 2, while cases 3 and 4 are chosen to excite respectively the outer and inner modes described by [7]. One should be reminded that although the same Reynolds number is imposed for the three models, they correspond to different dimensional inlet velocities.

4.1. Comparison of base states

The stream-wise velocity and temperature profiles injected at the inlet are displayed in figure 1 for the top-hat jets and in figure 2 for coaxial jets. Profiles for the *TTPcst* model are identical to the CPG ones, and are therefore not plotted. As expected for temperatures below 2500 K (cases 1, 3 and 4), the LTE and CPG models give similar results. However, for case 2 the centerline temperature reaches T_c = 5250 K and the resulting LTE density layer is thicker and pushed outwards with respect to the CPG model.

The downstream evolution of each jet is analyzed by plotting profiles at x = 5 and x = 15 in figure 8. At low temperatures (cases 1, 3 and 4), the model with constant properties exhibit thicker density and velocity layers than the CPG and LTE models. According to [8], weaker gradients should lead to a more stable configuration. For all cases, the constant property model also yields faster decreasing centerline quantities, this effect is more predominant as the centerline temperature increases. For the coaxial jets, the CPG and LTE models yield similar results. An offset of the LTE density toward the exterior of the jet is noticeable in case 1.
For the high temperature case (2), results from the LTE model are differ significantly from the CPG model. At x = 15, the LTE shear layer has moved to approximately twice the radius of the CPG one and of the LTE velocity shear, this is particularly important as it is expected to damp the effect of the baroclinic torque and lead to a stable configuration shortly after the inlet. The centerline density decreases faster along x in the CPG and constant property models than in LTE, due to the over-estimation of the thermal conductivity. Additionally, a hump in the LTE density profile caused by the chemical activity is observed.
From these observations, the constant CPG model is expected to yield the most unstable jet for all the configurations studied.

4.2. Stability analysis

A spatio-temporal analysis is carried out on the base states described in the previous section, and is

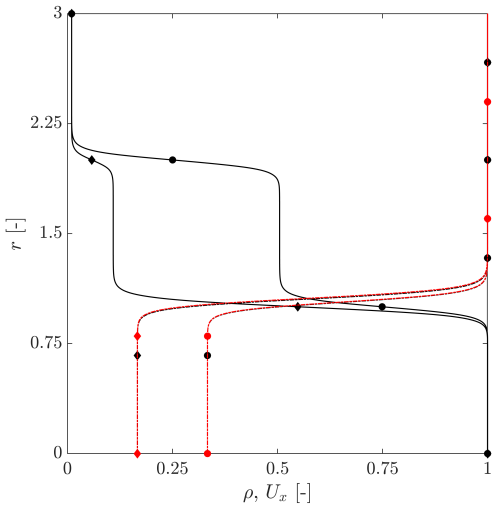

Figure 2: Coaxial jets inlet radial profiles of stream-wise velocity (−) and density (- ·) in CPG (black) and LTE (red). Cases 3 (●) and 4 (⧫) are plotted.

restricted to axisymmetric disturbances by imposing $m = 0$. Contours of the spatio-temporal growth-rate $\mathrm{Im}(\omega) = \omega_i$ are obtained by tracking the least stable mode along the complex wavenumber plane. In the case of coaxial jets, two unstable modes are found in agreement with [7], and only the least stable one is considered.

For all the jets and models studied, the spatio-temporal analysis at the inlet reveals the presence of a saddle point similar to the one displayed in figure 3 for the CPG model and case 1. These saddles are valid from the perspective of the Briggs-Bers criteria and their complex frequencies are given in table 3. Saddles for the top-hat jets display positive growth-rates at the inlet, in agreement with results from [4] at similar parameters. As expected, the LTE assumption has a damping effect at the inlet.

The absolute growth-rate at the inlet of coaxial jets is lower than the one predicted by [7], even reaching a negative value for the case 3 with the TTPcst model. However, this result is coherent with the damping effect associated with viscosity described by [4], while results of [7] were restricted to the inviscid regime ($Re \to \infty$).

Shapes of the perturbations associated with the saddle points at the inlet are displayed in figure 10 for the CPG model. Both top-hat jets display shapes with a strong velocity component at the centerline, similar to the jet-column modes observed by [4]. As anticipated, the coaxial jet with low bypass ratio supports an inner mode with perturbations peaking in the inner shear, while case 4 with $h = 0.5$ supports an outer mode with perturbations in the second shear. Perturbations for other TTP models are similar to the CPG ones, with the exception of the LTE temperature perturbation of case 2, which displays an additional peak around the location of the density hump described in section 4.1.

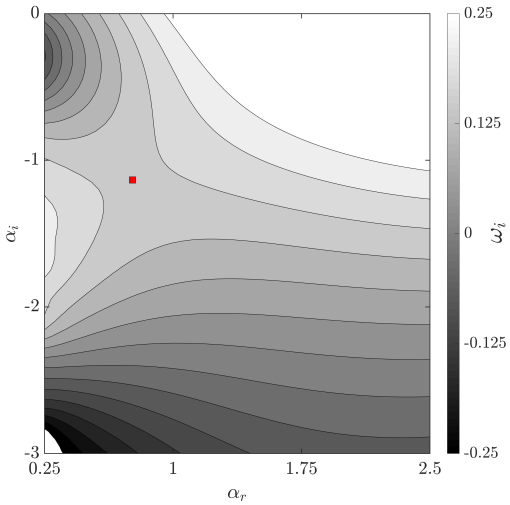

Figure 3: Contours of the spatio-temporal growth-rate obtained at the inlet from the LST for the CPG jet with $Re = 400$ and $R/\theta = 20$ and $S = 1/7$.

The saddle points found at the inlet are then tracked along the stream-wise direction, and the resulting curves of absolute growth-rate are plotted in figure 4 for top-hat jets and figure 5 for coaxial jets. One can note that the stability reference length being the jet radius, the non-dimensional length extends to 40 in these figures. For all cases and models analyzed, a region of absolute instability is found ($\omega_i > 0$). For the top-hat jets studied, the growth-rate decreases monotonically with x, while the one of coaxial jets increases after the inlet towards its maximum value, and decreases. Thus, even for a negative inlet growth-rate, a region of absolute instability may exists for coaxial jets, as in case 3 with the TTPcst model. The length of the absolute regions l_{ac} is reported in table 3.

As suspected, the absolute region depends strongly on the property model used. For all cases, the CPG model predicts the largest region. For cases 1, 3 and 4, the CPG and LTE models yield similar results due to the moderate temperatures. However, in the case

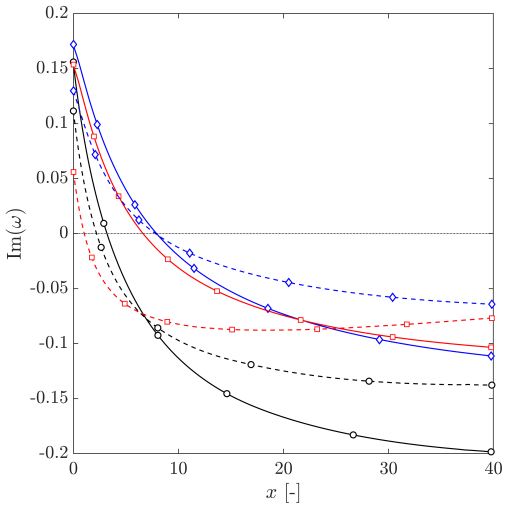

Figure 4: Stream-wise evolution of the absolute growth-rate obtained from the LST for the top-hat jets 1 (−) and 2 (- -) assuming constant properties (*black* ○), CPG (*blue* ◇) and LTE (*red* □).

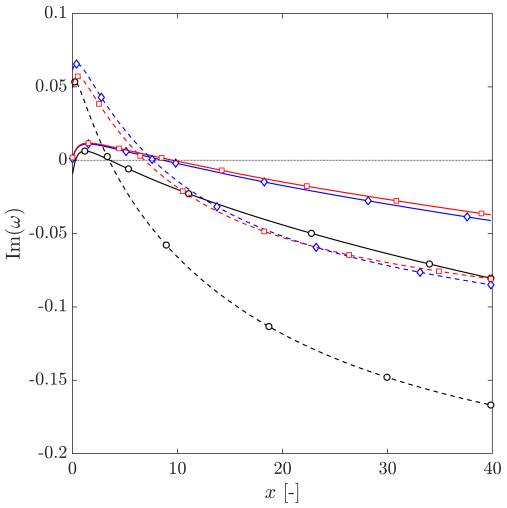

Figure 5: Stream-wise evolution of the absolute growth-rate obtained from the LST of the coaxial jets 3 (−) and 4 (- -) assuming constant properties (*black* ○), CPG (*blue* ◇) and LTE (*red* □).

of extreme heating, the LTE model yields the shortest absolute region, which is most likely due to the fast radial expansion of the density layer.
In order to predict the development of self-sustained oscillations in the jet studied, the absolute length l_{ac} is compared against the inlet absolute wavelength $\lambda_0 = {}^{2\pi}/_{\alpha_{0,r}}$. According to [12], the absolute region length should be of order of the absolute wavelength to trigger a global mode. Furthermore, the dimensional absolute frequency $f = {}^{\omega_r W_c}/_{2\pi R}$ at the beginning of the absolute region is given in table 2 for each case assuming $R = 0.1$ m, as they should be closed to the frequency of the global mode.

4.3. Unsteady simulations

The time evolution of the jets is investigated by setting the gain of the Selective Frequency Damping to zero in the DNS. A non-dimensional time step of $\Delta t = 0.005$ is imposed during the simulations, which again leads to different dimensional times for the different models. Unlike the study of [1], the injection of disturbances was not necessary to trigger the global modes for the present cases. This is believed to be linked to the initialization procedure used in the simulations, which consists in copying the inlet profiles through the whole domain at $t = 0$.
For all the simulations, a transient phase is observed after the initialization, after which an oscillatory state is reached. This later state is characterized by the development of vortices at the shear layers and/or pulses around the centerline depending on the configuration. For some cases, this oscillatory case is only temporary and the oscillations are eventually damped. This is illustrated in figure 6 where the non-dimensional density from simulations is probed at a position on the path of the vortices.

We find that the CPG model allows each of the jet studied to sustain self-sustained oscillations, whereas the LTE jet is only globally stable for extreme heating (case 2). The model with constant properties for its part only allows such oscillations to last in the coaxial jet with small bypass ratio (case 4). These results are in good agreement with the comparison of absolute region length against the initial absolute wavelength for the jets of cases 1, 2 and 3. However, we find that this is no longer the case for the coaxial jet with low bypass ratio for which l_{ac} at most half of the λ_0. To explain such result, an analysis similar to the one of [11] might be necessary, but is however beyond the scope of the present study.
As a side note, [1] already pointed out that axisymmetric simulations allow the growth of strong 2D rolled up vortices that would be highly unstable in a 3D configuration and lead to breakdown. However, even if their long-time development is nonphysical in the present simulations, their initial growth is

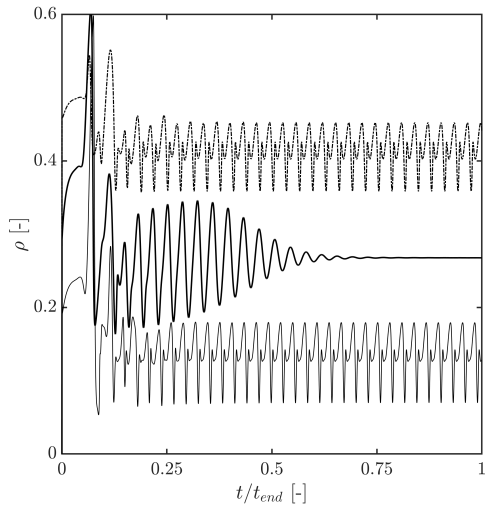

Figure 6: Temporal evolution of the non-dimensional density of case 1 at $(r, x) = (0.5, 4)$ for each model: constant properties (*thick line*), CPG (*thin line*) and LTE (*dashed line*). Times are normalized and density values are shifted up and down for better visibility.

representative of physical phenomena driving the jet instabilities. This is further supported by the predominance of symmetrical absolute modes over their non-symmetric counter-part. Such vortices can be observed in the the instantaneous temperature field contours plotted in figure 9 for each of the cases investigated with the CPG model and at $\Delta t = 100$. Structures in the top-hat jets increase in size when the centerline temperature is raised. For, coaxial jets, the distinction between the structures due to the outer mode (case 3) and inner mode (case 4) can be clearly made. Due to the confinement of the heating to the primary core, the vortices of case 3 have a lower influence on the temperature distribution through the jet.

Although the present flows are two-dimensional, the mode shapes retrieved by the 1D-LST at the inlet are in good qualitative agreement with the variance of the unsteady simulation profiles at $r = 1 \times D$ plotted in figure 10. For this comparison, the variance is computed excluding the time steps during which the flow is in the transient state.

Finally, a Fourier analysis of the unsteady density evolution was carried out for each model using the MATLAB *fft* routine. Dimensional frequencies are obtained by considering a jet diameter of $D = 0.2$ m, in agreement with the dimensional radius imposed for the LST. An example of resulting normalized power spectra is displayed in figure 7 for the case 4 and each model of properties. Results of the FFT analysis show a clear peak close to the value of absolute frequency at the inlet for each model. The presence of a harmonics is found for the jets sustaining global modes, but is not observed for jets unable to sustain global oscillations. Results for the cases where a clear frequency is identified are summarized in table 2. The agreement between the absolute frequency from the LST and the one retrieved from the FFT analysis is highly dependent on the jets and models studied. Increasing the centerline temperature seem to increase the error between the frequencies, which is contained between 20% and 30% for the cases 1, 2 and 4 in CPG and LTE. However, the Cst model achieves a remarkable precision below 1% for the case 1, while the CPG and LTE models retrieve the frequency of case 3 with a 3% accuracy. Similar observations on the discrepancy between the LST frequency and observed ones were already observed by [1] for super-critical jets.

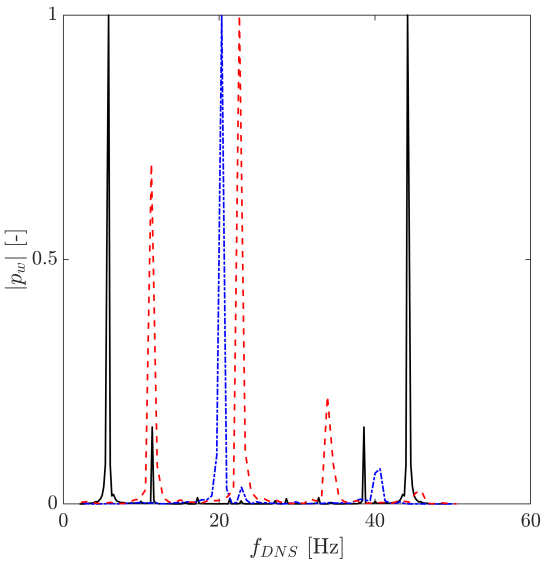

Figure 7: FFT normalized power spectrum of the non dimensional density obtained for the case 4, using each TTP model: constant properties (black −), CPG (blue - ·) and LTE (red - -).

5. Conclusions

The effects of different property models on the stability of heated top-hat and coaxial axisymmetric jets have been investigated using the spatio-temporal

LST on steady states and a Fourier analysis on unsteady simulations. Three property models of increasing complexity have been implemented in a literature DNS code assuming respectively: constant properties, a calorically perfect gas and a mixture of gases in LTE. Results show that even for moderate temperature ratio through the jet, considering a variable viscosity and thermal conductivity has a non-negligible destabilizing effect on the stability properties by extending the length of the absolute region. At moderate temperatures, the CPG and LTE models yield similar results. At higher temperatures (case 2), the CPG models largely over-predicts the growth-rate of absolute instabilities, and the LTE model becomes the most stable one.

By changing the length of the absolute region in the jet, the choice of model has a non-negligible influence on the development of self-sustained oscillations observed in the unsteady simulations. We find that the 1D LST is particularly relevant at predicting the shape of perturbations near the inlet of globally unstable jets. However, its accuracy when predicting the global mode frequency ranges between 1% and 35% depending on the flow parameters studied, in agreement with observations of [1] for super-critical jets.

Appendix

Test	f_{LST} [Hz]			f_{FFT} [Hz]		
	Cst	CPG	LTE	Cst	CPG	LTE
1	2.61	8.44	15.55	2.62	11.29	12.76
2	1.88	8.86	11.26	-	6.55	-
3	1.70	3.54	3.92	-	3.64	4.03
4	4.69	13.98	16.16	5.81	20.33	22.6

Table 2: Comparison of the dimensional frequencies obtained from the LST and FFT analysis assuming a diameter of $D = 0.2$ m. A symbol "-" is used when no distinct frequency can be identified in the FFT power spectrum.

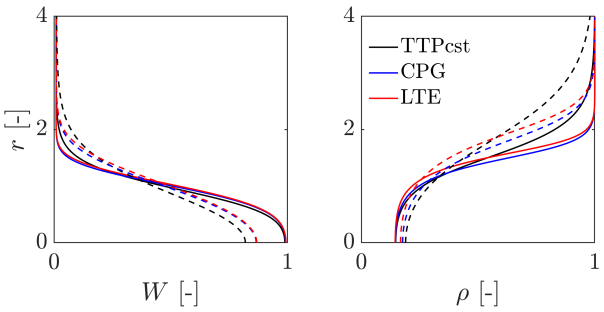

(a) Top-hat jet with $S = 1/7$.

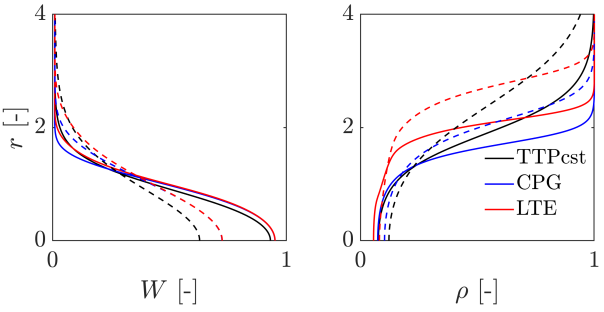

(b) Top-hat jet with $S = 1/15$.

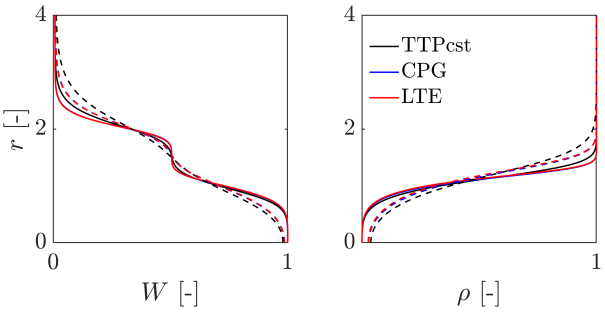

(c) Coaxial jet with $S = 1/3$ and $h = 0.5$.

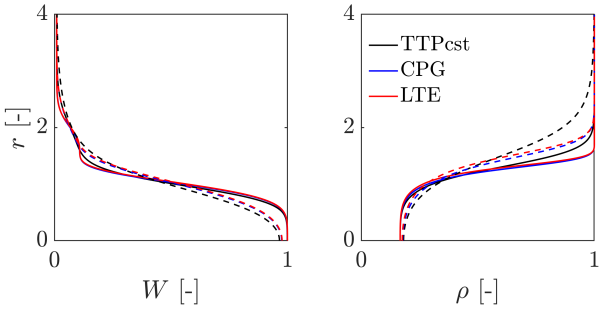

(d) Coaxial jet with $S = 1/6$ and $h = 0.1$.

Figure 8: Non-dimensional velocity and temperature profiles for each case at $x = 5$ (−) and $x = 15$ (- -) with the *TTPcst* (black), CPG (blue) and LTE (red) models.

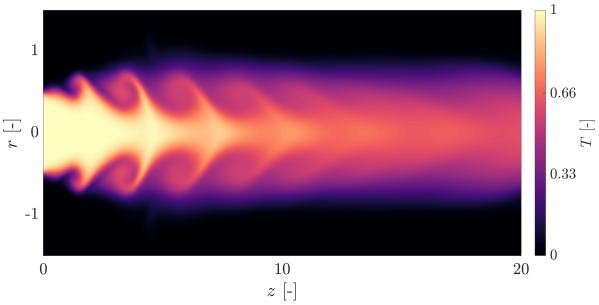

(a) Top-hat jet with $S = 1/7$.

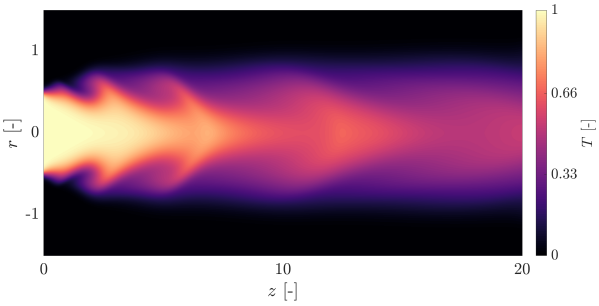

(b) Top-hat jet with $S = 1/15$.

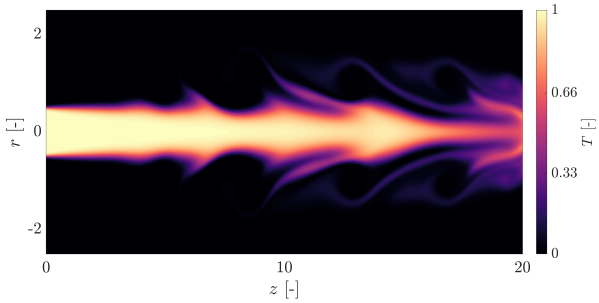

(c) Coaxial jet with $S = 1/3$ and $h = 0.5$.

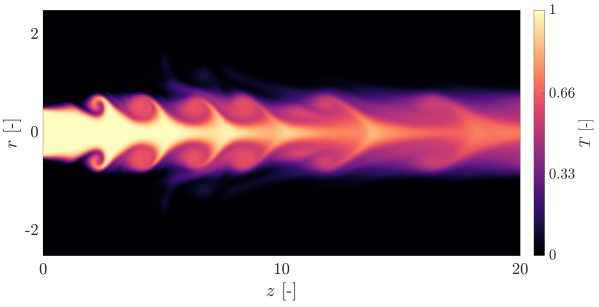

(d) Coaxial jet with $S = 1/6$ and $h = 0.1$.

Figure 9: Contour of constant non-dimensional temperature from the CPG unsteady simulations at $t = 100$ for the four cases investigated.

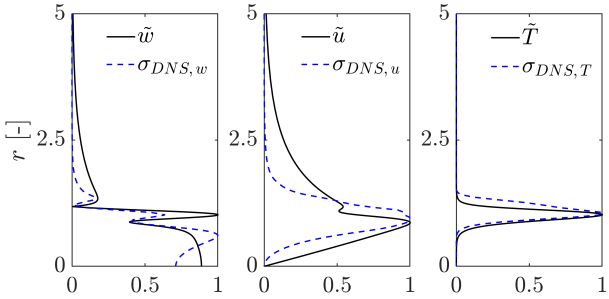

(a) Top-hat jet with $S = 1/7$.

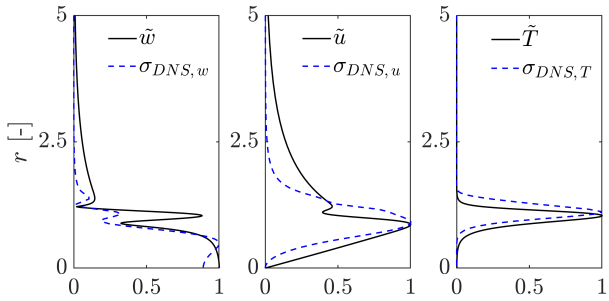

(b) Top-hat jet with $S = 1/15$.

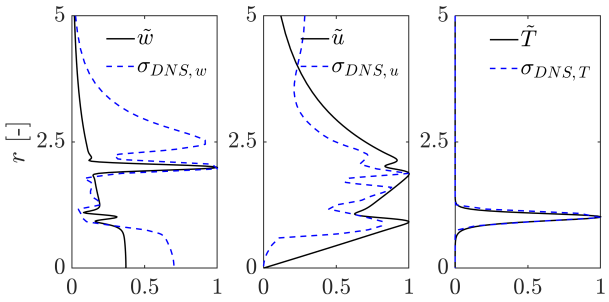

(c) Coaxial jet with $S = 1/3$ and $h = 0.5$.

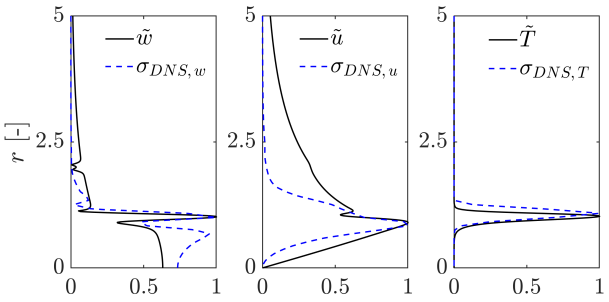

(d) Coaxial jet with $S = 1/6$ and $h = 0.1$.

Figure 10: Comparison between the absolute mode eigenfunctions at the inlet against the variance of unsteady simulation fields at $x = 1$ for the case 1.

Test	ω_0			λ_0 [-]			l_{ac} [-]		
	TTPcst	CPG	LTE	TTPcst	CPG	LTE	TTPcst	CPG	LTE
1	0.562 + 0.156i	0.546 + 0.172i	0.529 + 0.154i	8.16	8.24	8.32	3.19	7.91	6.63
2	0.335 + 0.111i	0.317 + 0.13i	0.215 + 0.056i	9.8	10.18	12.26	2.20	7.81	1.03
3	0.4258	0.432 + 0.001i	0.431 + 0.002i	11.04	11.41	11.47	3.26	8.62	9.54
4	0.59 + 0.05i	0.574 + 0.061i	0.56 + 0.052i	13.73	13.82	14.19	3.49	7.66	6.87

Table 3: Main spatio-temporal stability analysis results for the top-hat and coaxial jets. Results are taken at the first absolutely unstable position in the jet.

Acknowledgments

The author would like to thank M. Juniper and U. Ali Qadri from Cambridge University for their collaboration. This work was further supported by the Fonds de la Recherche Scientifique - FNRS under the FRIA Grant.

References

[1] L. Lesshafft, P. Huerre, P. Sagaut, Frequency selection in globally unstable round jets, Physics of Fluids 19 (2007) 054108.

[2] P. Monkewitz, K. Sohn, Absolute instability in hot jets, AIAA Journal 26 (8).

[3] P. Monkewitz, D. Bechert, B. Barsikow, B. Lehmann, Self-excited oscillations and mixing in a heated round jet, Journal of Fluid Mechanics 213 (1990) 611–639.

[4] L. Lesshafft, P. Huerre, Linear impulse response in hot round jets, Physics of Fluids 19 (2) (2007) 024102.

[5] M. J. Juniper, The effect of confinement on the stability of two-dimensional shear flows, Journal of Fluid Mechanics 565 (2006) 171–195.

[6] M. J. Juniper, The effect of confinement on the stability of non-swirling round jet/wake flows, Journal of Fluid Mechanics 605 (2008) 227–252.

[7] G. Balestra, M. Gloor, L. Kleiser, Absolute and convective instabilities of heated coaxial jet flow, Physics of Fluids 27 (5) (2015) 054101.

[8] L. Lesshafft, O. Marquet, Optimal velocity and density profiles for the onset of absolute instability in jets, Journal of Fluid Mechanics 662 (2010) 398408.

[9] W. Coenen, A. Sevilla, A. L. Sanchez, Absolute instability of light jets emerging from circular injector tubes, Physics of Fluids 20.

[10] J. Nichols, P. Schmid, J. Riley, Self-sustained oscillations in variable-density round jets, Journal of Fluid Mechanics 582 (2007) 341–376.

[11] W. Coenen, A. Sevilla, The structure of the absolutely unstable regions in the near field of low-density jets, Journal of Fluid Mechanics 713 (2012) 123–149.

[12] L. Lesshafft, P. Huerre, P. Sagaut, M. Terracol, Nonlinear global modes in hot jets, Journal of Fluid Mechanics 554 (2006) 393409. doi:10.1017/S0022112006008974.

[13] J. Nichols, Simulation and stability analysis of jet diffusion flames, Ph.D. thesis, University of Washington (2005).

[14] A. Cipullo, B. Helber, F. Panerai, F. Zeni, O. Chazot, Investigation of freestream plasma flow produced by inductively coupled plasma wind tunnel, Journal of Thermophysics and Heat Transfer 28 (3) (2014) 381–393.

[15] A. Michalke, Survey on jet instability theory, Progress in Aerospace Sciences 21 (1984) 159–199.

[16] U. Qadri, G. Chandler, M. Juniper, Passive control of global instability in low-density jets, European Journal of Mechanics / B Fluids 72 (2018) 311–319.

[17] S. Demange, U. A. Qadri, F. Pinna, Linear impulse response of a plasma jet, Proceedings of the IUTAM Symposium on Laminar Turbulent Transition (to be published).

[18] F. Pinna, Numerical study of stability for flows from low to high mach number, Ph.D. thesis, Universita La Sapienza di Roma/von Karman Institute (2012).

[19] F. Pinna, K. Groot, Automatic derivation of stability equations in arbitrary coordinates and for different flow regimes, in: 44th AIAA Fluid Dynamics Conference, AIAA AVIATION Forum, American Institute of Aeronautics and Astronautics, 2014. doi:10.2514/6.2014-2634.

[20] M. R. Malik, E. C. Anderson, Real gas effects on hypersonic boundarylayer stability, Physics of Fluids 3.

[21] A. Bayliss, E. Turkel, Mappings and accuracy for chebyshev pseudo-spectral approximations, Journal of Computational Physics 101 (2) (1992) 349–359.

[22] A. Bayliss, A.Class, B. J.Matkowsky, Adaptive approximation of solutions to problems with multiple layers by chebyshev pseudo-spectral methods, Journal of Computational Physics 116 (1995) 160–172.

Modeling strategy for blackout analysis of re-entry phases in space exploration missions

Vincent Fitzgerald Giangaspero

Aeronautics and Aerospace Department, von Karman Institute for Fluid Dynamics, Belgium, vincent.giangaspero@vki.ac.be

Supervisor: Thierry Magin

Professor, Aeronautics and Aerospace Department, von Karman Institute for Fluid Dynamics, Belgium, magin@vki.ac.be

Advisor: Andrea Lani

Research Expert, Aeronautics and Aerospace Department, von Karman Institute for Fluid Dynamics, Belgium, lani@vki.ac.be

University Supervisor: Stefaan Poedts

Professor, Department of Mathematics, KU Leuven, Belgium, stefaan.poedts@kuleuven.be

Abstract

During the re-entry phase of a spacecraft into a planetary atmosphere, high temperatures result in the formation of a plasma layer around the vehicle. Plasma interacts with electromagnetic waves disrupting all communication, navigation and telemetry signals, leading to the well known radio blackout problem. Communication or radio blackout problem is an important issue for hypersonic vehicles and it is extremely important to develop strategies for propagating telemetry during hypersonic flight. With future space missions aimed towards Mars, including NASAs Mars 2020 and ESAs Exo-Mars 2020, there is a strong motivation to improve the understanding of the physics regarding the communication blackout. In this paper, the methodology already developed at the von Karman Institute for blackout analysis has been enhanced by the development of state-of-the-art methods for full wake ionized flow CFD solutions, allowing a better characterization of the blackout phenomena. Hypersonic CFD simulations are performed over the ExoMars Schiaparelli module with the COOLFluiD aerothermodynamics Finite Volume solver and subsequently a raytracing algorithm is applied to examine the propagation of electromagnetic waves in the wake flow of the ExoMars re-entry vehicle.

Keywords: High-speed flow, gas dynamics, computational methods, plasmas, laminar reacting flows, CFD

1. Introduction

The re-entry phase is one of the most challenging aspects to be considered for the design of a space missions. The severe conditions experienced during hypersonic re-entry flights pose specific spacecraft design constraints and the characterization of the corresponding flows requires advanced theoretical, experimental and numerical investigation, which are all part of ongoing research efforts. Performing experimental work to replicate flight scenarios can be difficult and expensive, thus Computational Fluid Dynamics (CFD) codes that are capable of simulating hypersonic flows, by including all the relevant effects, are of paramount importance for the development of new technologies. Among the open challenges in the aerospace sector, communication blackout is an important issue for space exploration missions and it is extremely important to develop strategies for ensuring the propagation of telemetry during entry flights.

Communications blackout is a well-known phenomenon since the early days of the space era and jumped to the forefront of the public eye during the infamous Apollo 13s mission, with its failed attempt at a moon landing. During the re-entry phase in the Earth atmosphere, due to uncertainties on the re-entry angle of the spacecraft, there was a serious risk of crash

landing. A longer blackout than predicted (around 6 minutes) left NASA engineers and the world without information on what was happening on board the capsule or the status of the crew. After almost 50 years, hypersonic vehicles still experience radio blackout during re-entry, as the Soyuz TMA (Transport Modified Anthropometric) capsule that experience about 10 minutes of radio blackout. Communications blackouts for re-entry are not solely confined to entry into Earth atmosphere but they apply to entry into any atmosphere whenever ionization occurs within the flow surrounding the spacecraft. For instance, Mars Pathfinder endured a 30 second communication blackout as it entered Mars atmosphere while the Huygens probe experienced it while flying through Titan atmosphere. During blackout, vehicles cannot receive useful guidance or maneuvering information from a control center and can travel for hundreds of miles, possibly endangering the whole mission and deeply affecting crew or payload safety. Clearly a way to minimize or remove this disruption would provide a significant advantage for future missions, allowing the transmission of more data and a safer control of the vehicle during the delicate re-entry phase.

The present paper presents a novel methodology to analyze Blackout occurring during atmospheric re-entry based on raytracing techniques. It is based on previous research carried on the von Karman Institute over the past years and already reported in [1]. In this work, the existing tools have been enhanced with the capability of simulating the spacecraft entire ionized wake flow allowing a complete raytracing analysis of the domain. After giving an overview of the re-entry Blackout from a physical point of view in section 2, the proposed methodology is presented in section 3. Subsequently the implementation of the raytracing technique is discussed in section 4. Finally, section 5 presents a the preliminay results achieved with the improvements developed so far to the method.

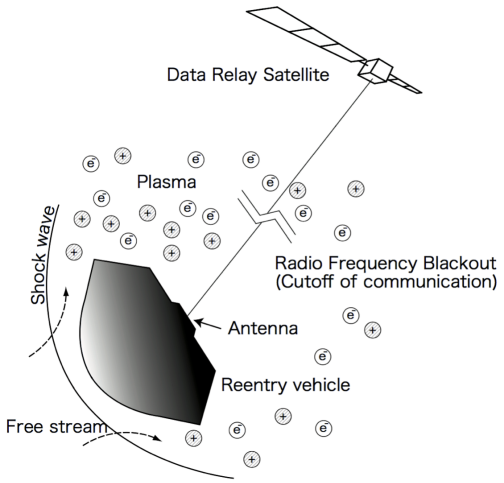

Figure 1: Sketch representation of plasma flow formation during re-entry

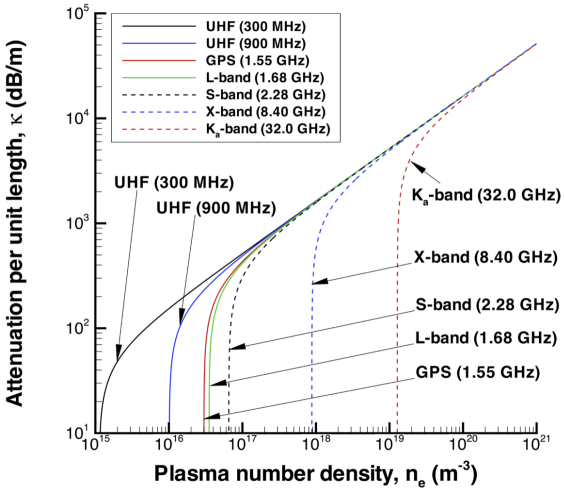

Figure 2: Signal attenuation along with plasma density for different radio wave band

2. The Blackout Phenomena

When a spacecraft enters a planetary atmosphere at hypersonic speed, high velocities (typically around or higher than 10 km/s) will generate strong shock waves and extreme aerodynamic heating of the vehicle. High post-shock temperatures result in dissociation and ionization of the hot gas, generating an ionized flow, a.k.a. plasma, around the vehicle, as shown in Figure 1.

Due to the presence of free charge carriers, plasma reacts to electromagnetic fields and interacts with the onboard transmission systems of the spacecraft. Plasma attenuates the radio frequency (RF) signal from the spacecraft, and transmission is possible only at RF frequencies greater than the characteristic plasma frequency [2]. The plasma frequency is directly related to the electron number density around the vehicle, which represents the ionization degree of the gas. At different signal transmission frequencies correspond different electron number densities that disrupt the signal propagation, as shown in Figure 2.

The ionization degree of the flow depends on the vehicles geometry, flight conditions, and altitude [3]. In order to minimize the risk of blackout, missions such as MSL, Mars Pathfinder, and ExoMars Schiaparelli have placed an antenna in the vicinity of the vehicle aft, where the flow is less ionized, as shown in Figure 3. Communication is restored when the plasma frequencies decrease, which is due primarily to the deceleration of the re-entry vehicle.

sketch.png

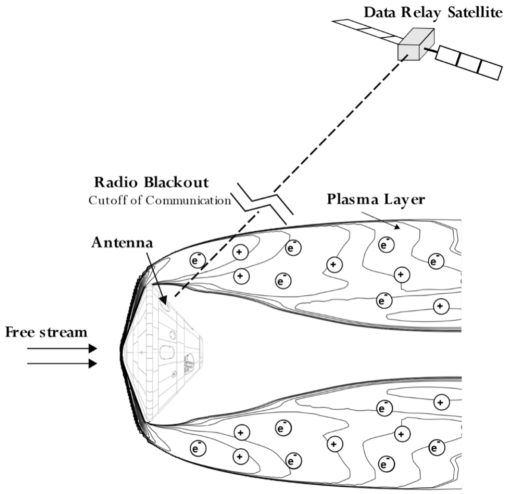

Figure 3: Schematic of wake flow ionization over re-entry capsule

3. The Blackout Numerical Analysis

Blackout prediction is far from trivial, involving simplified empirical models as well as advanced numerical simulations able to estimate the electron density field in the plasma surrounding the spacecraft. CFD simulations can be computationally expensive due to the large number of unknowns (and corresponding equations to be solved), including multiple species (neutral and ionized), at least two temperatures and the dozens of chemical reactions (e.g. associative ionization, charge exchange, electron-impact ionization) to be considered. In general, blackout analysis is composed by two different steps. The first step consist in obtaining plasma density profiles and collision frequencies around the space re-entry vehicle from non-equilibrium hypersonic CFD simulations. Subsequently various methods can be applied to examine the blackout period simulating electromagnetic waves, as the plasma frequency approach, geometrical optics (raytracing), or using a frequency-dependent finite-difference-time domain (FD2TD) method [1]. Fundamental theoretical background for radio-frequency (RF) blackout during re-entry was provided by the works of Dunn [4] and Evans [5]. Communications blackout have been examined by several authors for various re-entry missions. Reference works regarding Earth re-entry missions are [6], who performed CFD simulations of small cone-shaped re-entry vehicles, and [7] who examined the blackout of ESAs Atmospheric Re-entry Demonstrator (ARD). For Mars re-entry missions, limited work has been published, where the plasma frequency approach has been primarily used. Morabito involved 3D CFD simulations of the Mars Science Laboratory (MSL) in thermochemical non-equilibrium for the Martian atmosphere [8]. The first step for blackout analysis is the numerical simulations of different trajectory points during re-entry missions. The CFD solver needs to be capable to deliver accurate electron density fields, which are needed for the analysis of interaction between electromagnetic waves and plasma, both for air and CO_2 mixtures. The methodology and approach used in examining the blackout period for this work is applied on 2D axisymmetric simulations performed on the ExoMars Schiaparelli re-entry trajectory. In the previous approach, presented in [1], the electron density field were extracted using a Lagrangian solver [9] from a neutral mixture solution, capable of reconstructing the ionized solution along streamlines . This approach had the advantage of reducing the computational cost of a full ionized flow solution, allowing preliminary results to assess the accuracy and viability of the specific proposed raytracing technique. The drawback of this decoupled approach between CFD simulations and electron densities field reconstruction lies in the impossibility of extracting flow information coming from the stagnation zone of the spacecraft, that generally travels in the wake region of the flow. The inaccuracy associated with this approach is that for regions where the ionization is appreciable, the density and velocity fields might experience strong deviations from the previous neutral computation, leading to errors in the non-equilibrium region. For this work, the first step to enhance the accuracy of the overall methodology has been the implementation of the implementation of accurate thermochemical non-equilibrium models into the COOLFluiD ATD solver [10]. This has been possible by developing and upgrading the interface of COOLFluiD to the thermo-

cemical library solver PLATO, developed at the University of Illinois at Urbana-Champaign (UIUC). In section 5 will be presented the CFD solution obtained for this test-case.

4. Propagation of Electromagnetic Waves in Plasma

This work employs raytracing to follow field propagation from the antenna in the inhomogeneous region until it has emerged from the plasma. Ray tracing theory is founded on geometrical optics, and provides a reliable method to estimate the dominant path of energy flow in propagating EM waves.

4.1. Optical description of the flow

The propagation of electromagnetic waves in a medium is described by the Appleton equation which Davies presents in various forms [11]. In general, the propagation is governed by the complex refractive index of the plasma n; which consists of a real part, μ, and an imaginary part, χ. The real part μ represents the real refractive index while the imaginary part χ represents the attenuation factor. Davies [11] derives the Appleton equation based on the Maxwell equations and the conservation of momentum of free electrons. Regarding the properties of the wave, Davies assumes that the wave is a simple harmonic progressive wave, steady-state solution, and plane waves with a given polarization. For the medium, Davies assumes electrically neutral charges distributed with statistical uniformity, uniform external magnetic field, electrons only are effective, electronic collisions are independent of electron energy, and the thermal motions of the electrons can be neglected.

The Appleton equation reads:

$$n^2 = (\mu - \chi i)^2 = 1 - \\ - \frac{X}{1 - Zi - \frac{{Y_T}^2}{2\,(1 - X - Zi)} \pm \sqrt{\frac{{Y_T}^4}{4\,(1 - X - Zi)^2} + {Y_L}^2}} \tag{1}$$

where

$$\begin{aligned} X &= e^2 N_e / \left(\epsilon_0 m \omega^2\right) \\ Y_L &= eB_L / \left(m\omega\right) \\ Y_T &= eB_T / \left(m\omega\right) \\ Z &= \nu / \omega \\ \omega &= 2\pi f \end{aligned} \tag{2}$$

Here, N_e is the electron number density, e is the electron charge, ϵ_0 is the vacuum permittivity, ν is the electron-heavy particle collision frequency, B_L and B_T are longitudinal and transversal magnetic fields, and f is the transmission frequency. In this work, no magnetic field is assumed since Mars has a weak magnetic field $50\,nT$ [12] and hence $Y_T = Y_L = 0$. The resulting Appleton equation then becomes a function of X, which is a function of the electron number density, and which is a function of the collision frequency ν. Thus, the parameter X shows the effect of the electron density in the medium on the transmission while the parameter Z describes the effect of the collision frequency on the transmission. The effect of neglecting or considering collisions on the Appleton formula has been already studied in [1] for CO_2 atmospheric entry, were it was seen to have a negligible effect. For this reason, in this work has been used the simplest form of the Appleton Equation where all complex terms vanish. It reads as follow:

$$n = \mu = \sqrt{1 - X} = \sqrt{1 - \left(\frac{f_p}{f}\right)^2} \tag{3}$$

$$f_p = \sqrt{kN_e} \tag{4}$$

$$k = e^2 / \left(4\pi^2 \epsilon_0 m\right) \tag{5}$$

The refractive index of the plasma thus becomes a function of the electron plasma frequency f_p and a given frequency f in Hz. Here f_p is the measure of the oscillatory movement of the electrons within the plasma and depends on the electron number density and constant k. This equation illustrates that the refractive index must be equal to or be less than unity. Furthermore, to have propagation of the EM wave, μ must be real. For a given wave frequency f, the refractive index decreases with an increase of electron density N_e, and for a given electron density the refractive index increases with an increase of wave frequency. Thus, as the EM wave penetrates into levels of increasing electron concentration, μ becomes lower and lower.

Figure 4 describes the distinctive flow structure within the wake flow of the ExoMars Schiaparelli reentry module. The flow is first turned as it passes over the shoulder of the capsule resulting in an expansion fan, which curves the bow shock. The expansion region is followed by a recompression shock that is created as the flow realigns with the axis due to the axisymmetric boundary condition. An excess of electrons is available in the hot regions of the flow, i.e.

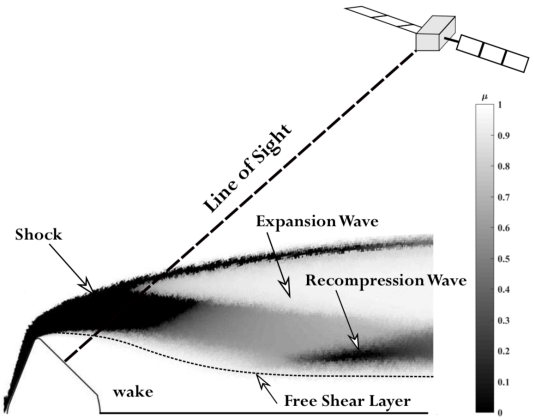

Figure 4: Wake flow structure with refractive index

behind the shock near the stagnation region and the recompression shock. Their occurrence significantly changes the optical properties of the gas. For example, a relatively cold gas has a refractive index around unity and approaches zero where electrons are abundant.

4.2. Raytracing

It has been demonstrated that the actual path of the radio signal rays needs to be modeled to understand if they reach a receiver [13]. As no analytical method is known, an iterative marching technique similar to the one of Vecchi et al. [13] is employed in this work. It assumes discrete, straight wave propagation over small distances. To clarify the algorithm process, at the vehicles aft position, the signal emerges from the antenna location where the antenna is assumed to be half-omnidirectional, i.e. the signal is equally strong in each direction away from the surface. At each step, the direction of the ray is determined using the laws of geometrical optics. Ling et al. describes in detail how a raytracing method works [14]. In this work, the raytracer is not used to compute the attenuation of the signal, which will be done in future work. Rather it is used as a tool to trace the propagation of the rays in the plasma. We model the deviation of a rays path from a straight line by the use of Snells law, as illustrated in Figure 5:

$$\mu_1 \sin\alpha_1 = \mu_2 \sin\alpha_2 \tag{6}$$

In a typical re-entry application case, the rays, emerging from an antenna at the vehicles surface move from a relatively cold region with a refractive index of around 1 towards a hot region where the refractive index is low, or very close to zero. The situation corresponds to light transitioning from water into air, i.e. a medium of that is optically dense to a medium that is less dense. Therefore, rays are initially bend away from a normal of an electron density isosurface.

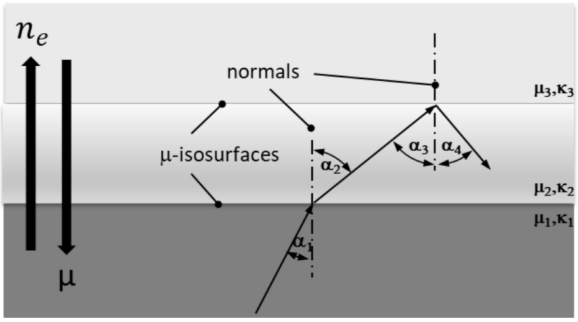

Figure 5: Snells Law

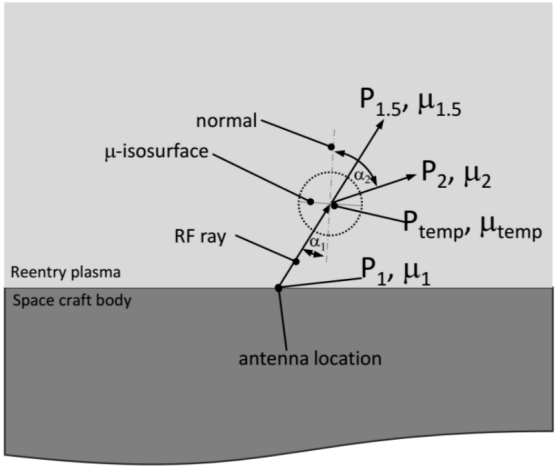

Figure 6: Marching Technique

The ray-tracing algorithm is a marching-in-space method and thus the signal is modeled as a ray that advances for a chosen finite distance called the step size as shown in 6. A chosen step size in the domain represents a region of constant refractive index which is called an isosurface. Snells Law is then applied at the boundaries of the isosurfaces. To clarify the algorithm process, at the vehicles aft position, the signal emerges from the antenna location where the antenna is assumed to be half-omnidirectional, i.e. the signal is equally strong in each direction away from the sur-

face and can be modeled through a number of rays emerging out of the half-sphere. The marching technique as shown in figure 5, starts by advancing one step size from P_1 to $P_{1.5}$. The refractive index is determined at $P_{1.5}$ and the algorithm then goes back to P_{temp} by advancing backwards at half the step size. The radius of the isosurface and its associated normal is found. Snells Law is then applied between P_1 and $P_{1.5}$ to find α_2. The algorithm then advances to P_2 by advancing half the value of the step size from P_{temp} at an angle α_2. The process is repeated until a border of the domain is reached or the attenuation of the signal reaches a threshold. The described methodology is implemented in a Matlab based script called Black-Out-RAy-Tracer (BORAT) of which version 1.1 is used here. More details on the raytracing algorithm implementation can be found in [1].

5. Results

In this section results from the application of the combined CFD simulations of the flow-field and raytracing analysis will be presented. The computational domain is shown in figure 7. The ExoMars Schiaparelli geometry is a 71-deg sphere cone front shield with a nose radius of 0.6 m and an overall vehicle diameter of 2.4 m [15]. A 0.06 m radius shoulder connects the forebody to a 47-deg conical back shield. ANSYS ICEM CFD, Release 18.1, has been used to create a single block grid where the grid is made orthogonal to the body at its surface.

The grid extends 5 vehicle radii downstream and in this way it is ensured that the mesh has a sufficient resolution to capture the temperature field in the shock and over the shoulder. Since the ExoMars Schiaparelli was a ballistic entry with a maximum angle of attack of 6 deg, a 2D axis-symmetric boundary condition is used. For the CFD simulations, the governing equations include continuity equations for 14 species, two momentum equations, and one energy equation. The 14 species mixture used for the CFD computations is referred to hereafter as Mars14 (CO_2 , CO, CO^+, NO, NO^+, N_2 , O_2 , ${O_2}^+$, N, C, C^+, O, O^+, e^-) The freestream composition is assumed to be 96% CO_2 and 4% N_2. The flowfield is assumed to be in thermal equilibrium and chemical non-equilibrium. Moreover, Park et al confirmed that most chemical equililbration processes in a Martian gas mixture indeed proceeds under a one-temperature environment [16], therefore, as already done in [1], a one-temperature model is deemed sufficient for the CFD computations. An isothermal wall of 1500 K

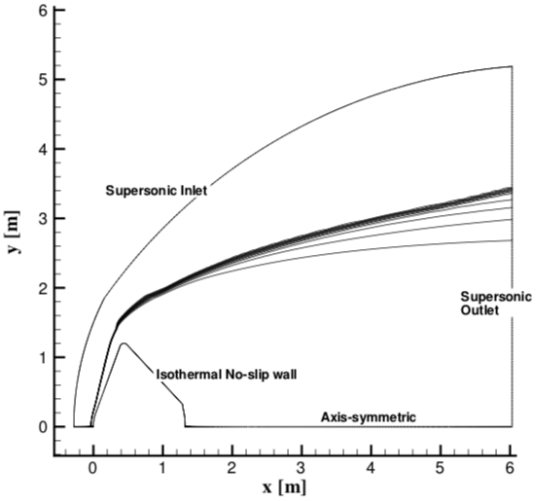

Figure 7: ExoMars Schiaparelli Geometry with boundary conditions

is used over the entire front and aft body along with a supersonic inlet and outlet. The nonslip condition for the velocity and the non-catalytic condition for the mass concentration are imposed at the wall surfaces. The flowfield is assumed to be steady and laminar. Unsteady effects are small at these high speeds but transition to turbulence could occur, particularly at the maximum-deceleration trajectory point. Additionally, no available turbulence models have been shown to be valid in the wake regions of blunt bodies [17]. The flow conditions investigated in this study is detailed in Table I, that reproduces three different re-entry conditions, the one with maximum blackout conditions during the re-entry trajectory (38 seconds after the atmospheric entry), and two brownout phases.

Table 1: Free stream values

$Alt[km]$	$t[s]$	$\rho_\infty\ [kg/m^3]$	$V_\infty\ [m/s]$	$T_\infty\ [K]$
91	27	1.29 e-05	5859	155
80	38	3.72 e-05	5856	175
71	50	1.10 e-04	5736	169

5.1. CFD solutions

The main purpose of this work is to assess the enhanced capabilities of the coupling between the COOLFluiD CFD solver and the thermo-chemical PLATO library for a fully ionized re-entry flow. In this way, raytracing analysis can be carried on in the whole domain without any limitations in the wake re-

gion. This, besides improving the overall blackout prediction analysis, will allow in the future to reproduce more complex scenarios, such as 3D configurations and non-zero angle of attacks re-entry trajectory, that generally result in much more complex flow structures in the wake region. In the next plots the CFD flow-field solution is shown, respectively Mach number field (fig. 8), pressure (fig. 10), temperature (fig. 9) and electron number densities (fig. 11), for the solution at 71 km, during the brownout phase.

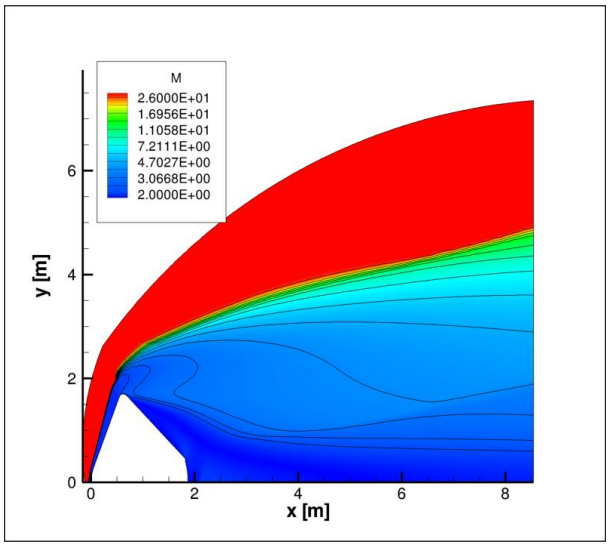

Figure 8: Mach number contour

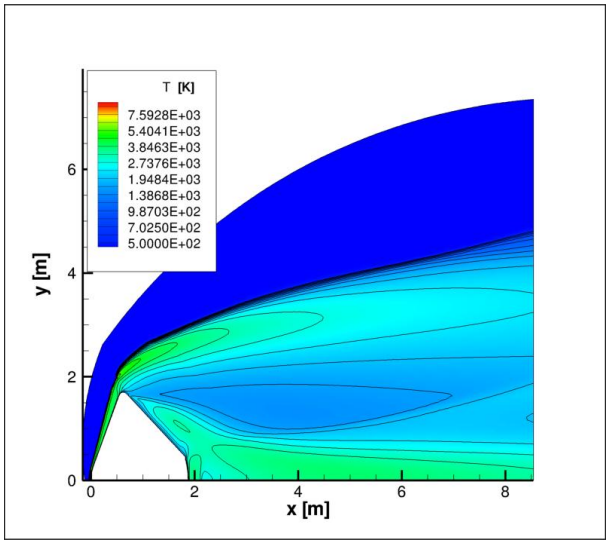

Figure 9: Temperature contour

The main flow feature is the strong shock generated

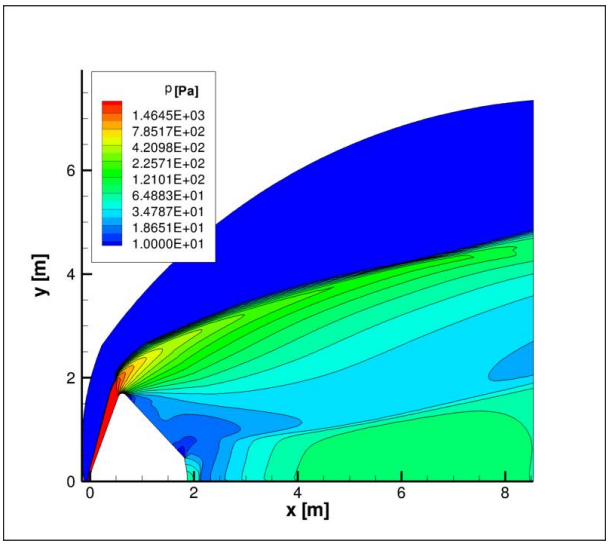

Figure 10: Pressure contour

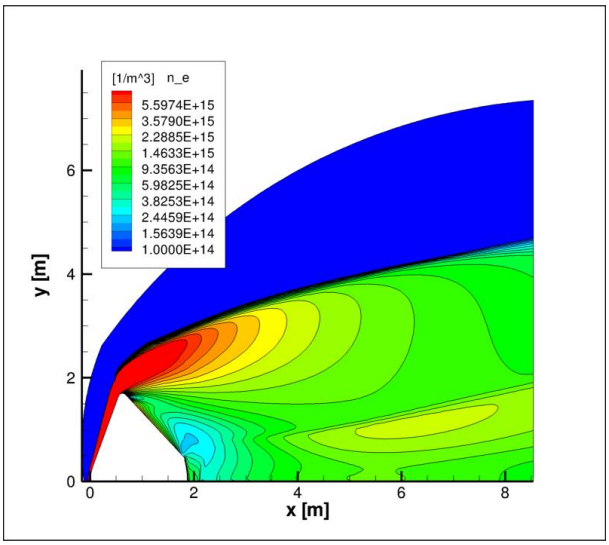

Figure 11: Electron number density contour

in front of the spacecraft, with high peaks of temperature, pressure and electron densities in the stagnation zone. Subsequently, the flow is cooled down and accelerated over the vehicle shoulder by an expansion fan, that lowers the ionization levels of the flow. Generally, this is the region where spacecrafts mount communications antennas to partially overcome blackout conditions during the re-entry. The wake region is characterized by a recirculation region and a recompression zone, that highers electron densities in the wake. Despite the low ionization level of this region, that was impossible to compute with the pre-

vious methodology approach and thus neglected, with the improved capabilities of the solver is now possible to extract important informations for the optical description of the flow needed for the raytracing analysis, as reported in the next section.

5.2. Raytracing analysis

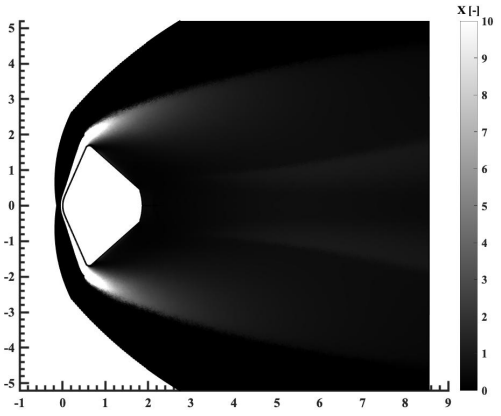

Figure 12: ExoMars Optical Properties at 71 km : ratio of electron plasma frequency over transmission frequency X

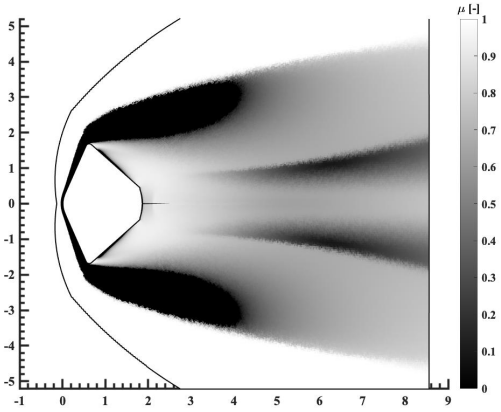

Figure 13: ExoMars Optical Properties at 71 km : refractive index μ

The parameters describing the propagation of an EM wave in a plasma previously described are now computed and plotted for the selected ExoMars trajectory point. An important aspect of the present work is the use of a non-axisymmetric flowfield solution for the raytracing analysis. Due to the specific low angle of attack conditions of the present test-case, to reduce computational costs of the CFD simulations it is possible to solve a reduced domain with a 2D axisymmetrical boundary condition on the symmetry line of the spacecraft. Then, for this specific test-case, the flowfield solution is mirrored on the symmetry axis to retrieve a full bidimensional domain for the extended raytracing analysis. The flow field CFD solution is then used to compute X and μ as described in Eq. (4). The results are computed using the ExoMars transmission frequency of f = 400Mhz. It can be seen that X, in figure 13, a measure for the ratio of the electron plasma frequency over the transmission frequency, exceeds unity and can be as high as 10 in the stagnation region.

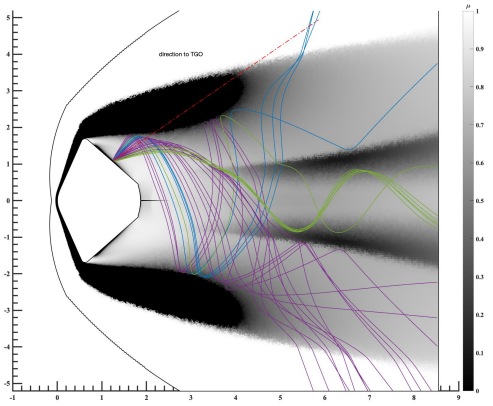

Figure 14: Ray-tracing at 71 km (t=50 s)

In figure 14 the application of the raytracing marching technique is shown. The emitting antenna is located on the upper side of the spacecraft, and for visualization purposes the emitted rays, despite simplified as omni-directional, are limited to a specific angular range [-40:130 degrees] from the normal direction to the antenna. The results show how the emitted rays beam is divided in 3 different regions. Despite some rays (in blue) escape the plasma flow surrounded the capsule, the vast majority is either confined in the wake region (in green) or either deflected into the opposite direction (in purple).

In figure 15 the raytracing solution for the re-entry trajectory point at 91 km is shown, 27 seconds after the beginning of the re-entry phase. Due to the high altitude, atmosphere density is not high enough to create complete blackout conditions, thus this is a brownout phase. As for the re-entry solution at 71 km,

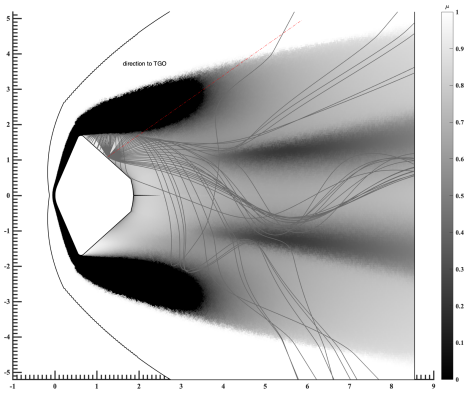

Figure 15: Ray-tracing at 91 km (t = 27s)

rays emitted from the antenna are partially shielded and canalized in the wake region. However, two distinct channels with lower ionization degrees are visible on the sides of the wake, and thus permit communications in these directions.

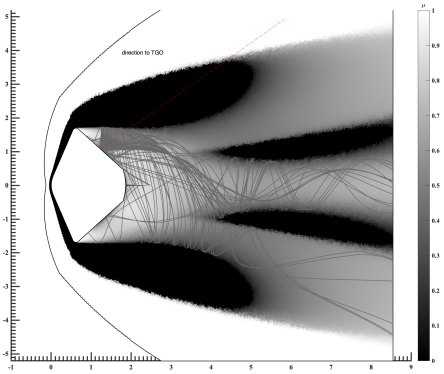

Figure 16: Ray-tracing at 80 km (t = 38s)

In figure 16 instead, the solution for the maximum blackout conditions are shown (38 s). These conditions reproduce the higher level of ionization during the re-entry, thus the whole communication system is shielded by the plasma surrounding the vehicle. This typically occurs at the maximum blackout point in the trajectory, and in these conditions the LOS prediction method will likely be accurate in predicting the blackout.

In conclusion, at the onset and end of the blackout phase it is not likely that all EM waves are fully contained within the plasma envelope resulting in an inaccurate blackout duration prediction using the LOS method. Furthermore, the use of raytracing allows to gather information on possible alternative communication directions during these flight phases, since the accurate EM waves path can be fully reproduced with this method. This analysis is extremely important for both characterizing accurately enough the blackout physical phenomena and to gather important information for possible mitigation solutions.

6. Conclusion

This work implemented and applied blackout prediction tools with a focus on the ExoMars Schiaparelli mission. Numerical CFD simulation was performed at 3 different re-entry trajectory point (91 km, 80 km, 71 km) assuming chemical non-equilibrium and thermal equilibrium. This analysis was carried on to assess the capability of the coupling between the CFD solver COOLFLuiD and the thermochemical library PLATO. The newly updated solver showed accurate results, capable of reproducing ionizing flow during re-entry trajectory for a 14 species Mars re-entry. Respect the previous approach, where the ionized flow numerical solution was computed with a Lagrangian solver with a post-processing step, the implementation of ionized chemical models into the COOLFluiD platform and the capability of computing accurate ionized solutions in the wake region of the spacecraft is of paramount importance for the overall validity of the proposed methodology. First, because it characterizes better the flow features in this region, since the previous approach was unable to extract streamlines information coming from the stagnation region, thus allowing a more accurate path prediction for the traveling EM waves. Second, because the hypothesis of non ionized flow in the wake can be considered valid just in case of zero or low angles of attack flight phases. In any other flight configuration, that is almost the standard in re-entry trajectories, a full 2D or 3D flowfield solution is required to be able to carry on a raytracing analysis. In general, the raytracing results from this study show that the LOS method might yield inaccurate results at the onset and end of the blackout period or when all the EM waves are not fully contained within the plasma sheath. Thus, accurate prediction of the blackout duration requires raytracing in the plasma layer. Using the LOS method might be sufficient for contemporary Mars missions. However, with future missions having higher mass requiring increased landing performance, precise characterization of the blackout duration will be important. Future

work will be focused on reproducing the raytracing blackout analysis at different trajectory points of the ExoMars Schiaparelli mission to be verified with literature and in-flight data. Furthermore, the raytracing algorithm will be upgraded by the implementation of signal attenuation models and 3D features to reproduce more complex flows configurations, with different angles of attacks and different vehicles geometries.

Acknowledgments

The research of Vincent Giangaspero is supported by SB PhD fellowship 1SA8219N of the FWO.

References

[1] S. Ramjatan, A. Lani, S. Boccelli, T. Magin, J. Thoemel, Blackout analysis of reentry vehicles for martian missions, IPPW 15th International Planetary Probe Workshop.

[2] R. Hartunian, et al, Causes and mitigation of radio frequency (rf) blackout during reentry of reusable launch vehicles, AEROSPACE REPORT NO. ATR-2007(5309)-1.

[3] R. Savino, et al, Plasma-radiofrequency interactions around atmospheric re-entry vehicles: Modelling and arc-jet simulation, The Open Aerospace Engineering Journal 3 76–85.

[4] M. Dunn, Theoretical and experimental studies of reentry plasmas, NASA CR-2232 (1973) 1–44.

[5] J. Evans, Boundary-layer profiles for a entry of a blunt slender body at high altitude, NASA TN D-7332 (1973) 1–38.

[6] S. Ramjatan, Blackout analysis of small cone-shaped reentry vehicles, Journal of Thermophysics and Heat Transfer 31 (2016) 269 282.

[7] Y.Takahashi, Prediction performance of blackout and plasma attenuation in atmospheric reentry demonstrator mission, Journal of Spacecraft and Rockets 51 (2014) 1954–1964.

[8] D.Morabito, The mars science laboratory edl communications brownout and blackout at uhf, IPN Prog. Rep. (2014) 42197.

[9] S. Boccelli, Development of a lagrangian solver for thermochemical nonequilibrium flows, Masters thesis, Politecnico di Milano.

[10] A. Lani, An object oriented and high performance platform for aerothermodynamics simulation, Ph.D. thesis, Université Libre de Bruxelles (2008).

[11] K.Davies, Ionospheric radio propagation, US Department of Commerce, National Bureau of Standards.

[12] C. Ho, N. Golshan, A. Kliore, Radio wave propagation handbook for communication on and around mars.

[13] C. Vecchi, Modelling of antenna radiation pattern of a re-entry vehicle in presence of plasma, Antennas and Propagation Society International Symposium.

[14] Ling, Hao, Chou, R. Lee, Shooting and bouncing rays: Calculating the rcs of an arbitrarily shaped cavity, IEEE Transactions on Antennas and Propagation (1989) 194205.

[15] S. Portigliotti, M. Dumontel, M. Capuano, L. Lorenzoni, Landing site targeting and constraints for exomars 2016 mission, International Planetary Probe Workshop.

[16] C. Park, J. T. Howe, R. L. Jaffe, G. V. Candler, Review of chemical-kinetic problems of future nasa missions, ii: Mars entries, Journal of Thermophysics and Heat transfer 8 (1994) 923.

[17] R. A. Mitcheltree, P. A. Gnoffo, Wake flow about the mars pathfinder entry vehicle, Journal of Spacecraft and Rockets 32 (1995) 771776.

Mathematical modeling and simulation of non-equilibrium plasmas with application to electric propulsion systems

Louis Reboul

Centre de Mathématiques Appliquées (CMAP), Ecole polytechnique, France, louis.reboul@polytechnique.edu

Supervisor: Thierry Magin

Professor, Aeronautics and Aerospace Department, von Karman Institute for Fluid Dynamics, Belgium, magin@vki.ac.be

University supervisor: Marc Massot

Professor, Centre de Mathématiques Appliquées (CMAP), Ecole polytechnique, France, marc.massot@polytechnique.edu

University supervisor: Anne Bourdon

Director of research at CNRS (DR2), Laboratoire de Physique des Plasmas (LPP), Ecole polytechnique, France, anne.bourdon@lpp.polytechnique.fr

Abstract

In a society that increasingly relies on the operation of satellites, electric propulsion is a technology that largely reduces the launch costs and provides reliable orbit control capabilities. Nevertheless, the design and development of the thrusters is still semi-empirical, which involves long and expensive life tests. We propose an ambitious project aimed at improving the current mathematical and computational models for electric propulsion. The overarching objective is to assess the limitations and potential of fluid-based simulations compared to particle-in-cell/Monte-Carlo approaches. Towards this goal, the thesis will focus on four main subjects. First, we wish to develop adequate numerical methods by properly addressing the challenges raised by multiscale physics and notably by the presence of very small parameters in our problem, such as the Debye length or the mass ratio between electrons and ions. To that end, we consider asymptotic preserving schemes that allow not to resolve the smallest scales in contexts and areas where they are not needed (see [1],[2],[3],[4]). Our second objective is the implementation of these numerical schemes into canoP, a state-of-the-art high-performance computing (HPC) community code open source developed by the MdlS, CMAP, LPP and IFPEN. As of now, we successfully implemented into canoP a standard first order discretization of two-fluid Euler-Poisson equations, with possibility to incorporate a magnetic field into our model (see figure 1), leading to promising results (qualitatively similar to PIC). We are currently conducting extensive validation tests as well as developing a second order scheme and considering ways to implement the scheme developed in [1]. A third objective of this thesis will be the derivation of a self-consistent fluid model from the kinetic theory, aimed at fixing many ad-hoc terms present in the heuristic fluid models currently used by the industry. The fourth goal is the mathematical analysis of the resulting set of equations to ensure we correctly solve the obtained system of equations. In the end we wish to combine those four goals and discretize the obtained model thanks to the numerical methods currently being developed and implement it into canoP, allowing for accurate numerical simulations of electric propulsion systems.

Keywords: Electric propulsion, low-temperature magnetized plasmas out of equilibrium, kinetic theory of gases, transport coefficients, adaptive mesh refinement, massively parallel computing, Direct Numerical Simulation, high performance computing

Figures

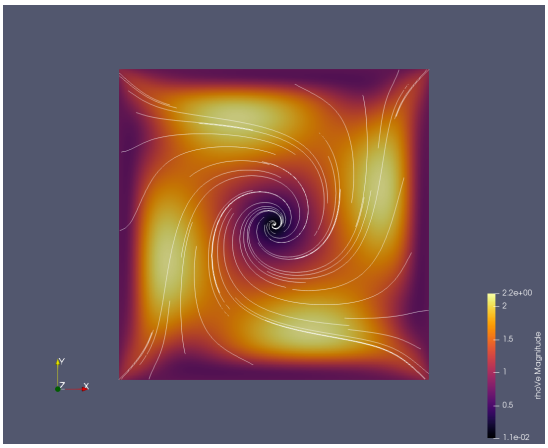

Figure 1: Simulation of a the fluxes of electrons for a magnetized plasma discharge in a 2D square domain, using canoP

Acknowledgments

This work is supported by a joint grant from Région Île-de-France and Agence Innovation Défense

References

[1] A. A. Laguna, T. Pichard, T. Magin, P. Chabert, A. Bourdon, M. Massot, An asymptotic preserving well-balanced scheme for the isothermal fluid equations in low-temperature plasma applications, arXiv preprint arXiv:1904.13092.

[2] P. Crispel, P. Degond, M.-H. Vignal, An asymptotic preserving scheme for the two-fluid Euler–Poisson model in the quasineutral limit, Journal of Computational Physics 223 (1) (2007) 208–234.

[3] P. Degond, J.-G. Liu, M.-H. Vignal, Analysis of an asymptotic preserving scheme for the Euler–Poisson system in the quasineutral limit, SIAM Journal on Numerical Analysis 46 (3) (2008) 1298–1322.

[4] G. Dimarco, R. Loubère, M.-H. Vignal, Study of a new asymptotic preserving scheme for the Euler system in the low Mach number limit, SIAM Journal on Scientific Computing 39 (5) (2017) A2099–A2128.

AEROTHERMODYNAMICS

Analysis of the stability of a flat plate high-speed boundary layer with discrete roughness

Iván Padilla Montero

Aeronautics and Aerospace Department, von Karman Institute for Fluid Dynamics, Belgium, ivan.padilla@vki.ac.be

Supervisors: Fabio Pinna and Olivier Chazot

Senior Research Engineer, Aeronautics and Aerospace Department, von Karman Institute for Fluid Dynamics, Belgium, fabio.pinna@vki.ac.be

Head of Department and Professor, Aeronautics and Aerospace Department, von Karman Institute for Fluid Dynamics, Belgium, olivier.chazot@vki.ac.be

University Supervisor: Gérard Degrez

Dean of the Faculty and Professor, Aero-Thermo-Mechanics Department, Université libre de Bruxelles, Belgium, gdegrez@ulb.ac.be

Abstract

Two-dimensional linear stability theory (2D-LST) is used to analyze the instability of the wake behind a cuboidal roughness element mounted on top of a flat plate at cold and hot boundary-layer edge conditions. Spatial stability results are presented for the streamwise evolution of the leading instabilities along the wake behind the elements, using base flows obtained from steady and laminar Navier-Stokes simulations.

Keywords: boundary layer, stability, transition, hypersonic, roughness, biglobal, high-temperature effects

1. Introduction

Boundary-layer transition from a laminar to a turbulent regime is a critical driver in the design of high-speed vehicles. Turbulent hypersonic boundary layers are usually characterized by large heat transfer rates that lead to strong aerothermodynamic loads. Despite being an active research topic for decades, the physical mechanisms governing hypersonic boundary layer transition are not well understood yet, and the existing transition prediction tools for practical applications still rely heavily on empirical correlations and extensive wind tunnel testing [1; 2]. During the design process, this fact implies the need to account for large safety factors that lead to an oversize of the thermal protection systems, with the consequent reduction in payload capacity.

The natural boundary-layer transition process at hypersonic speeds is known to be strongly influenced by the presence of isolated roughness elements on the surface of a body. Typical examples include damaged heat-shield tiles, rivets or gap fillers, among many others. The perturbations generated by these elements can accelerate the growth of incoming disturbances and introduce additional instability mechanisms in the boundary layer, eventually leading to a premature occurrence of transition. Three-dimensional elements with heights comparable to the local boundary-layer thickness tend to induce counter-rotating streamwise vortices in the wake flow field [3]. These vortices lift-up low-momentum fluid close to the wall and give rise to a low-velocity streak that is surrounded by regions of high streamwise shear, which can support the growth of different instabilities [4; 5; 6; 7; 8]. Since the wake flow field presents a strong inhomogeneity in the wall-normal and spanwise directions, studies focused on boundary-layer stability theory generally employ perturbations with amplitude functions that depend on two spatial directions. This approach, in which the perturbations are inhomogeneous in two spatial directions but homogeneous in the third one and in time, is hereby referred to as two-dimensional linear stability theory (2D-LST), but it is also com-

monly known as BiGlobal stability theory [9].

Although a physics-based prediction of roughness-induced transition is still not available nowadays, several experimental and numerical investigations for calorically perfect gas conditions have considerably increased our knowledge, see for example [4; 10; 5; 11; 6; 7; 8; 12; 13]. Groskopf et al. [4] performed temporal analyses of the instability of the wake behind isolated 3D cuboidal roughness elements in a Mach 4.8 boundary layer, and compared the results against direct numerical simulation (DNS), reporting a very good agreement in the disturbance amplitude shapes. Similar analyses were conducted by De Tullio and coauthors [6] at Mach 2.5 and by Paredes [14] and De Tullio & Sandham [15; 7] at Mach 6 for the same geometry, in both cases comparing DNS results against spatial BiGlobal stability theory and three-dimensional parabolized stability equations (PSE-3D). For the two cases investigated, the two-dimensional eigenfunctions obtained from the 2D stability computations and the growth rates extracted from the PSE-3D simulations were both found to be in close agreement with the DNS data. On the experimental side, Kegerise et al. [10] carried out measurements of the disturbance amplitude shapes behind a diamond element in a flat plate at Mach 3.5, and compared them against the spatial stability analyses of Choudhari and coworkers [5; 11] with satisfactory results. In all the cases analyzed, the dominant wake instability modes were found to be varicose (even) and sinuous (odd) deformations of the low-velocity streak that characterizes the wake flow structure. Whether the leading instability mode has an even or an odd nature appears to be case dependent. Moving to a different configuration, Theiss et al. [12; 16] performed 2D and PSE-3D linear stability computations in the wake behind different roughness geometries located on the heat shield of a reentry capsule in a Mach 5.9 freestream. The varicose wake mode was found to be the disturbance undergoing a higher amplification, with the cylindrical roughness element being the most effective shape.

High-temperature effects on the stability of hypersonic boundary layers were first studied by Malik & Anderson [17], who considered self-similar boundary layer profiles in local thermodynamic equilibrium (LTE). Next, Stuckert & Reed [18] extended this analysis to boundary layers in chemical non-equilibrium and Hudson and coauthors [19] included also thermal non-equilibrium effects. The main findings showed a destabilization of the second Mack mode instability in the presence of internal-energy-mode-excitation and dissociation-driven base-flow cooling, as well as a shift towards lower frequencies. Many authors have since investigated high-enthalpy effects on various configurations and test conditions and with different stability theories [20; 21; 22; 23; 24; 25; 26]. However, the studies were restricted to second-mode instabilities. Regarding the role of isolated roughness elements in boundary-layer transition for high-enthalpy flows, very few studies are available. Groskopf et al. [27] analyzed the instability introduced by a discrete oblique roughness element in cold and hot flow conditions. For the hot case, the base-flow solutions were obtained in chemical non-equilibrium, while a thermally perfect gas model was implemented for the stability computations. The results showed a significant destabilizing influence of high-temperature effects on the stability behavior of the modes developing in the roughness wake. Very recently, Di Giovanni & Stemmer [28] performed direct numerical simulations on a hemispherical capsule-like geometry, finding that the inclusion of chemical non-equilibrium has a destabilizing effect on the evolution of unstable modes in the roughness wake.

In this work, the instability of the wake induced by a cuboidal roughness element located inside a laminar high-speed boundary layer is investigated by means of two-dimensional linear stability theory (2D-LST). Two different configurations are considered, both of them subject to cold hypersonic freestream conditions. In the first case the roughness element is mounted on top of a sharp flat plate, resulting in a low temperature field that can be modeled under the assumption of a calorically perfect gas. The second setup considers the roughness element mounted on top of a 20 degree sharp wedge. The strong shock wave induced at the leading edge of the wedge results in a high boundary-layer edge temperature, requiring the appropriate modeling of the effects of vibrational excitation and molecular dissociation in the flow. For each case, the most unstable disturbances growing in the roughness wake are identified and their evolution along the roughness wake is analyzed.

2. Theoretical framework

The governing equations considered in this analysis are the Navier-Stokes equations for a compressible Newtonian fluid without body forces. For the flat plate configuration under cold boundary-layer edge conditions, a calorically perfect gas is assumed and Sutherland's law is used to model the variation of the dynamic viscosity and thermal conductivity with tem-

perature, yielding a non-constant Prandtl number. The Sutherland temperature constants employed are, respectively, $S_\mu = 111$ K and $S_k = 194$ K, together with a reference viscosity of $\mu_{ref} = 1.716 \times 10^{-5}$ kg/(m·s) and a reference thermal conductivity of $k_{ref} = 2.41 \times 10^{-2}$ W/(m·K), both corresponding to a reference temperature of $T_{ref} = 273.15$ K.

For the wedge case, the accurate reproduction of the physical features of the resulting high-enthalpy bonudary-layer flow requires appropriate sets of modeling hypotheses. The excitation of internal energy modes and the subsequent departure of the gas' thermal law from a linear one (constant specific heat), as well as the dissociation of molecules, must be accounted for. To that end, three different flow assumptions are considered [29]. The first is a mixture of perfect gases in chemical non-equilibrium (CNE) with five species, N, O, NO, N_2 and O_2, in which reactions are allowed to occur at a finite rate (see Park et al. [30]). The second is a thermally perfect gas (TPG) with frozen chemistry, in which the excitation of internal energy modes is considered but the flow time scale is assumed to be much smaller than that of chemical reactions. The third is a calorically perfect gas (CPG), which establishes a constant value of the heat capacity, thus assuming the enthalpy to be a linear function of temperature.

For the CNE and TPG assumptions, the thermal properties of the mixture are obtained employing the polynomial expressions for each species provided by Thompson et al. [31]. Regarding the transport properties, two different sets of models are compared for the CPG assumption. The first is Sutherland's law (with the coefficients reported by White [32]) to obtain the dynamic viscosity, combined with a constant Prandtl number of 0.7 to retrieve the thermal conductivity. The second employs Gupta et al.'s [33] polynomial-logarithmic curve fits to retrieve the species viscosities and thermal conductivities. These are then mixed with Wilke's mixing rule [34]. It is therefore referred to as the Gupta-Wilke (GW) model, and it is also the one used for the other flow assumptions (TPG and CNE). The use of the CPG assumption, together with the two mentioned sets of transport models is distinguished by denoting them as CPGS (Sutherland) and CPGGW (Gupta-Wilke).

2.1. Formulation of the two-dimensional linear stability problem

The vector of primitive flow variables $\mathbf{q}$ is split into a steady reference state $\bar{\mathbf{q}}$, also known as base flow, and a small unsteady perturbation field $\tilde{\mathbf{q}}$:

$$\mathbf{q} = \bar{\mathbf{q}} + \epsilon\tilde{\mathbf{q}}, \tag{1}$$

with $\epsilon \ll 1$. The base flow is assumed to be locally parallel in the streamwise (x) direction, so that $\bar{\mathbf{q}} = \bar{\mathbf{q}}(y, z)$ at a given x coordinate, and the base flow wall-normal velocity component ($\bar{v}$) is assumed to be zero. The amplitude of the perturbations is considered to be a function of both the wall-normal (y) and the spanwise (z) directions, such that the ansatz of the modal perturbations for this case can be written as

$$\tilde{\mathbf{q}}(x, y, z, t) = \hat{\mathbf{q}}(y, z)\exp[i(\alpha x - \omega t)] + c.c., \tag{2}$$

where $\hat{\mathbf{q}}$ is the two-dimensional amplitude function, α is the wavenumber along the streamwise direction, ω is the angular frequency and $c.c.$ denotes the complex conjugate. In this work, the attention is focused on the spatial growth of the wake instabilities. In the spatial framework, ω is considered to be real and represents the angular frequency of the perturbations. On the contrary, α is complex, with the real part $\alpha_r = \Re\{\alpha\}$ being the streamwise wavenumber of $\tilde{\mathbf{q}}$ and the imaginary part $\alpha_i = \Im\{\alpha\}$ its spatial growth rate. With this definition, a positive value of α_i means a spatial decay of the amplitude function whereas a negative value implies a spatial growth.

The equations governing the linear stability problem are obtained by substituting the splitting given by Eq. (1) together with the ansatz defined by Eq. (2) into the Navier-Stokes system, and then neglecting the resulting non-linear terms, which are of order $O(\epsilon^2)$. In the end, the resulting system of linear partial differential equations can be written in the following compact form

$$\mathbf{A}\hat{\mathbf{q}} = \alpha\mathbf{B}\hat{\mathbf{q}} + \alpha^2\mathbf{C}\hat{\mathbf{q}}, \tag{3}$$

where $\mathbf{A}$, $\mathbf{B}$ and $\mathbf{C}$ are complex and nonsymmetric differential matrix operators.

The stability equations are made non-dimensional using the boundary-layer edge properties, denoted by the subscript e. The reference length employed for non-dimensionalization is denoted by l_e, which corresponds to the local Blasius length scale at the streamwise location where the stability analysis is performed, given by $l_e = \sqrt{\mu_e x/\rho_e u_e}$.

After discretization of Eq. (3), an algebraic generalized eigenvalue problem (GEVP) is obtained, which is nonlinear in the eigenvalue α. The problem is linearized by means of the companion matrix method [35].

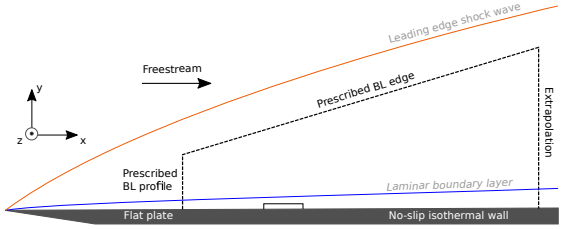

Figure 1: Representation of the geometrical configuration of the problem under study and the computational domain employed for the base flow calculations (not to scale).

3. Numerical methodology

3.1. Computation of the laminar base flow

The geometrical configuration of the problem under investigation is represented in Fig. 1. A sharp-edged cuboidal roughness element is mounted on top of an infinitely sharp flat plate at a given distance behind the leading edge and centered along the spanwise direction at $z = 0$ (roughness symmetry plane). The computational domain, denoted by a dashed line, is located inside the shock layer established between the surface and the weak shock wave induced at the flat plate leading edge. This approach has already been employed in similar studies found in literature (see for example [6; 12]). The top boundary has an angle to avoid roughness-induced shock waves to impinge on it, which would complicate the treatment of boundary conditions at this location. The spanwise symmetry of the geometrical configuration is also exploited by reducing the computational domain to solve only half of the roughness width.

The numerical solution of the base flow is steady and laminar, and is carried out using the software CFD++® on a block-structured grid consisting of hexahedral cells. The spatial discretization is based on a second-order upwind finite volume scheme, which features a limited total variation diminishing (TVD) flux interpolation together with the HLLC Riemann solver to minimize numerical oscillations in the vicinity of discontinuities. Concerning time integration, a point-implicit scheme (backward Euler) with multigrid acceleration and residual smoothing is employed to enhance convergence to the steady state as much as possible.

The boundary conditions considered for the base flow computation are as follows. At the inflow, a self-similar boundary layer profile is imposed. Similarly, at the top boundary, boundary-layer edge quantities are prescribed for all primitive variables. At the center ($z = 0$) and the far side ($z = z_\infty$) spanwise boundaries, symmetry conditions are specified. At the wall, a no-slip isothermal condition is enforced. Lastly, at the outlet boundary a supersonic outflow condition is specified, in which all the primitive flow variables are extrapolated from the interior of the domain.

The computational grids used to obtain the base flow solutions are generated using OpenFOAM's blockMesh utility. The grid is clustered towards the element in all directions as well as towards the flat plate wall to maintain a reasonable computational effort. The transition in cell size between the different blocks is kept as smooth as possible by appropriately adapting the expansion ratios along each edge.

3.2. Solution of the generalized eigenvalue problem

The numerical solution of the stability problem given by Eq. (3) is performed using the von Karman Institute Extensible Stability & Transition Analysis (VESTA) toolkit, originally developed by Pinna [36]. The particular structure of the matrices **A**, **B** and **C** for a given case is automatically derived and implemented in MATLAB® by means of a tool based on the computer algebra system Maxima. The two-dimensional partial differential eigenvalue problem resulting from the linear stability formulation is assembled and discretized by means of a high-order finite difference scheme with uniform error developed by Hermanns & Hernández [37], also known as FD-q. Following a similar philosophy to the Chebyshev collocation method [38], the idea behind the FD-q technique is to construct a finite difference scheme in a structured grid with a specific non-uniform point distribution, based on a piecewise Lagrange polynomial interpolation. For a given degree q of the interpolating polynomials, an optimal grid point distribution is computed which minimizes the interpolation error. In the limit of $q = N_p$, with $N_p + 1$ being the total number of grid points, the Chebyshev-Gauss-Lobatto point distribution is retrieved. The advantage of this scheme lies upon the fact that by reducing the order of the discretization to $q << N_p$, a high degree of sparsity is introduced in the matrices that compose the discrete eigenvalue problem, which can then be exploited to provide a significant reduction of the computational cost at an acceptable decrease in accuracy.

To translate the collocation grid to the physical domain of interest, the mapping originally introduced by Malik [39] is applied in the wall-normal direction, which allows placing half of the grid points below a given coordinate. In the spanwise direction, a Bi-Quadratic mapping [40] is employed, which concentrates one-third of the grid points in a desired region.

In this way, the grid used for solving the stability problem can be clustered towards the boundary layer and the roughness symmetry plane, which is the region where the strongest base flow gradients are encountered. The mapped grid defined by the FD-q point distribution does not coincide with the grid employed to obtain the base flow solution. Before building the eigenvalue problem, the base flow data is interpolated on the FD-q grid by means of a cubic spline interpolation in each spatial direction.

The boundary conditions for the disturbance quantities enforce a homogeneous Dirichlet condition on the velocity and temperature perturbations at the wall and at the wall-normal far-field boundary. The density fluctuation is determined by means of a compatibility condition satisfying the wall-normal momentum equation at both wall-normal boundaries. For the case of CNE, four of the five species are forced to obey the species wall-normal momentum equation (see Miró Miró & Pinna [41]). Regarding the spanwise boundaries, periodic boundary conditions are specified for all the perturbation variables, meaning that the value of each disturbance quantity and its first derivative normal to the boundary must be equal at both spanwise boundaries.

For the cases under study, the discrete matrices of the eigenvalue problem reach a dimension of order $O(10^5)$. Given the large-scale of the problem, the implicitly restarted Arnoldi method [42] is considered in order to compute only a small number of eigenvalues of the stability spectrum. To focus the solution in the region of interest, a shift-invert transformation is applied.

4. Stability analysis of the roughness wake for cold boundary-layer edge conditions

The first case analyzed in this work considers the high-Reynolds test conditions of the von Karman Institute H3 hypersonic wind tunnel (see for instance [43]). The corresponding freestream conditions are $M_\infty = 6$, $T_\infty = 60.98$ K and $p_\infty = 1963.42$ Pa, resulting in a unit Reynolds number of $Re_\infty/l = 2.60 \times 10^7$ m^{-1}, based on Sutherland's law. The wall temperature is fixed to $T_w = 300$ K. Because of the low freestream static temperature (total temperature $T_0 = 500$ K), no significant excitation of the vibrational internal energy mode is expected in the flow field for this configuration, therefore the assumption of a calorically perfect gas is deemed to be acceptable.

The dimensions of the computational domain for this case are the following. The streamwise coordinate and height of the domain inlet are, respectively, $x_{in} = 50$ mm and $y_{in} = 7.69$ mm. The respective outlet coordinates are $x_{out} = 400$ mm and $y_{out} = 88.49$ mm. The spanwise domain size is fixed to $z_\infty = 15$ mm. The roughness element has a height of $h_r = 0.4$ mm and it is located at a streamwise distance of $x_r = 60$ mm from the flat plate leading edge. The planform shape of the obstacle is assumed to be squared with edge length $d = 2.27$ mm. This configuration results in a roughness Reynolds number of $Re_r = u_r h_r/\nu_r = 331$, where u_r and ν_r are respectively the streamwise velocity and kinematic viscosity of the flow evaluated at $y = h_r$ and at the streamwise location of the roughness element in the corresponding self-similar boundary layer. The ratio of roughness height to the local boundary layer thickness is $h_r/\delta_{99} = 0.59$, where δ_{99} is determined by means of the total enthalpy (h_0) criterion $h_0/h_{0,\infty} = 0.995$, once again based on the self-similar boundary-layer profile.

The grid resolution considered for the base flow computation in this case is $N_x \times N_y \times N_z = 841 \times 351 \times 231$, leading to a total number of about 65 million grid points.

4.1. Base flow solution

The main physical features of the base flow solution obtained for this configuration are highlighted in Fig. 2, which depicts Mach number and streamwise velocity contours at different planes. Focusing on the Mach number contours, illustrated on a x-y plane located at $z = 0$, it can be observed that the presence of the roughness element introduces a displacement of the boundary layer upstream of the leading edge, progressively inducing a set of compression waves that eventually merge into an oblique shock wave further downstream. As the flow reaches the trailing edge of the obstacle, it turns and detaches, generating an expansion wave and creating a region of separated flow immediately downstream. Next, as the flow progressively reattaches further downstream, another fan of compression waves is induced, which once again merges into an additional oblique shock. In addition, a region of separated flow is also encountered immediately upstream of the element due to the strong flow blockage imposed by the blunt geometry.

The wake flow structure is represented in the x-z plane by means of the streamwise velocity contour plot in Fig. 2 and the cross-plane plots displayed in Fig. 3. Fig. 3 shows contours of the streamwise shear magnitude, defined as $\bar{u}_s = \sqrt{(\partial\bar{u}/\partial y)^2 + (\partial\bar{u}/\partial z)^2}$, and of the streamwise vorticity, given by $\bar{\xi}_x = \partial\bar{w}/\partial y -$

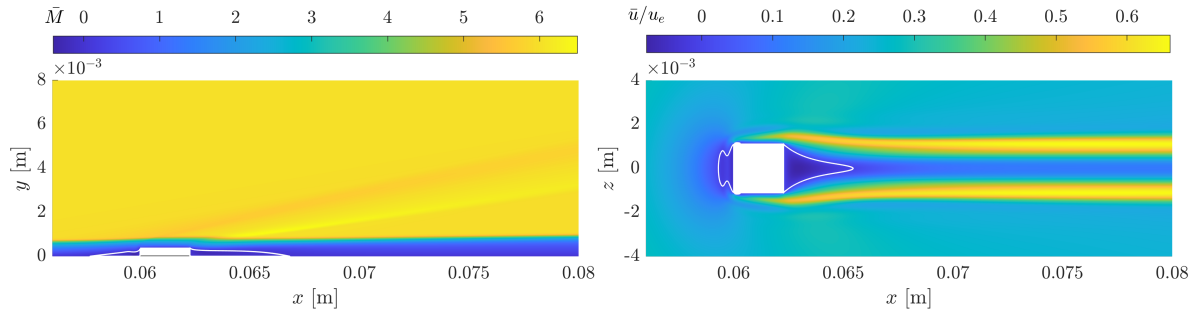

Figure 2: Main features of the base flow solution obtained for cold boundary-layer edge conditions: (left) Mach number contours at the roughness symmetry plane (z = 0 m); (bottom) Non-dimensional streamwise velocity contours on a plane located at $y = 0.5h_r$. The white solid lines represent isolines of $\bar{u} = 0$, delimiting regions of separated flow.

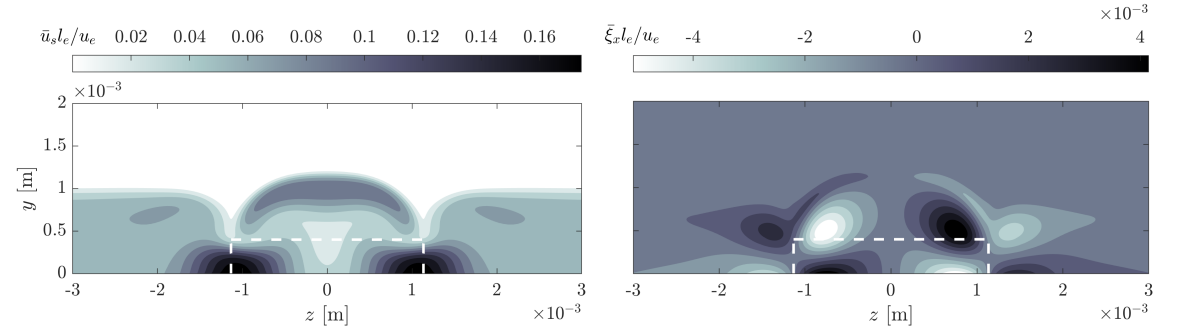

Figure 3: Contours of non-dimensional streamwise shear magnitude (left) and of non-dimensional streamwise vorticity (right) on a y-z plane located at a distance of x = 0.1 m from the flat plate leading edge, for cold boundary-layer edge conditions. The white dashed lines represent a projection of the roughness element cross-section.

$\partial\bar{v}/\partial z$, on a y-z plane located behind the roughness element at a distance of x = 0.1 m with respect to the flat plate leading edge. A pair of strong streamwise counter-rotating vortices can be identified, which form at the edges of the roughness element due to a small pressure gradient between the side and the top surfaces. These streamwise structures lift-up low-momentum fluid adjacent to the flat plate wall and give rise to a mushroom-shaped low-velocity streak located at the center of the wake. At the same time, high-velocity fluid located above the boundary-layer edge is pulled down towards the sides of the wake, leading to the appearance of two high-velocity streaks respectively at each side of the low-velocity streak. This flow structure results in a three-dimensional shear layer featuring regions of large streamwise shear magnitude.

4.2. Stability analysis

Spatial two-dimensional linear stability analyses have been performed at y-z planes in the wake behind the roughness element. The discretization employed to solve the partial differential eigenvalue problem considers interpolating polynomials of order q = 8 in both spatial directions, with a grid resolution of $N_y \times N_z = 101 \times 121$ points.

The wake flow structure induced behind the roughness element supports the growth of different instability modes. A discussion of different unstable modes appearing in the spatial stability spectrum for a particular streamwise position and frequency can be found in reference [44]. The most amplified wake modes are found to be varicose and sinuous instabilities developing in different regions around and inside the low-velocity streak induced by the roughness element. In this work, different streamwise locations and frequencies have been analyzed in order to find the most relevant instability mode. The results of the stability calculations are summarized in Figs. 4 and 5. Fig. 4 displays the magnitude of the two-dimensional streamwise velocity amplitude function associated to the most amplified instability at three different streamwise locations behind the roughness element, for a fre-

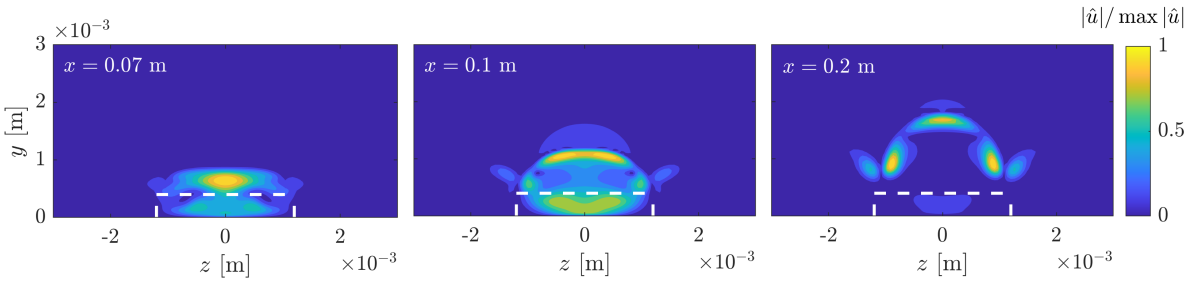

Figure 4: Contours of the normalized magnitude of the streamwise velocity eigenfunction of the most amplified instability mode for cold boundary-layer edge conditions at three different streamwise locations. Frequency f = 280 kHz.

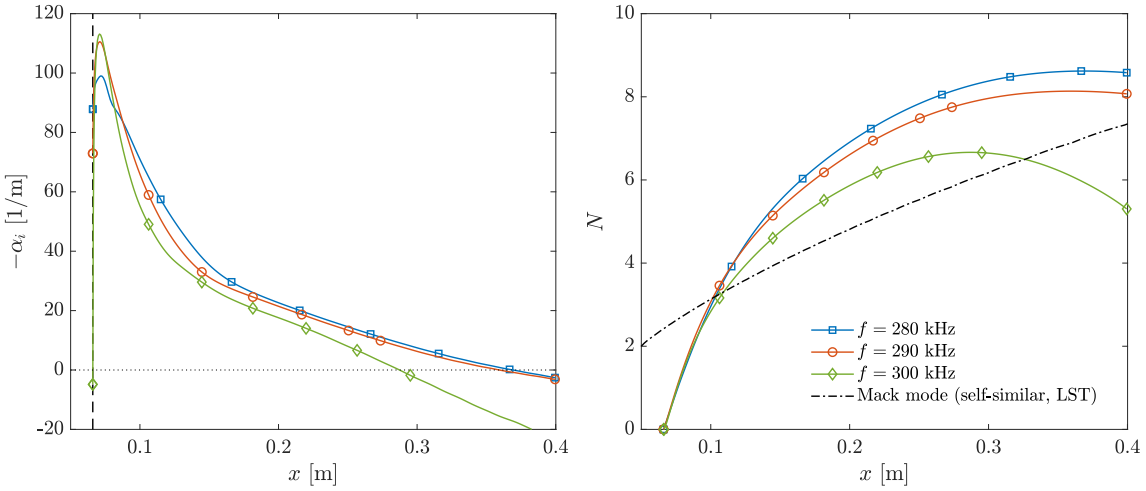

Figure 5: Streamwise evolution of the growth rate (left) and the integrated amplification factor (right) of the most unstable mode for cold boundary-layer edge conditions at three different frequencies. The dashed line denotes the location of the end of the separation bubble generated at the trailing of the roughness element ($x_{b,TE}$).

quency of 280 kHz. The most unstable disturbance developing in the roughness wake is a varicose deformation of the low-velocity streak that characterizes the wake flow structure, as it can be determined from its symmetric amplitude function with respect to the roughness symmetry plane. The regions of development of the instability mode change significantly as the low-velocity streak evolves downstream. At x = 0.07 m, a location shortly after the trailing edge of the roughness geometry, the mode is developing in the central region of the low-velocity streak. At this position, the wake flow structure is not yet fully developed and the lift-up effect features its maximum strength. Further downstream, at x = 0.1 m, the disturbance amplitude is mainly concentrated in the top part of the streak, coinciding with the location of highest shear magnitude in the three-dimensional shear layer surrounding the streak (see Fig. 3). In addition, a region of development near the flat plate wall can also be observed. For longer distances downstream, such as at x = 0.2 m, the amplitude of the instability is completely distributed around the shear layer that separates the low-velocity streak from the outer inviscid flow.

The left plot in Fig. 5 presents the streamwise evolution of the growth rate of the most unstable mode at three different frequencies. Due to the parallel flow assumption inherent to linear stability theory, the analysis is started at the end of the separation bubble generated at the trailing edge of the roughness elements, denoted by $x_{b,TE}$. The instability mode features its maximum amplification rate immediately after the trailing edge separation bubble and then progressively decays downstream. This is in accordance with the dissipation of the counter-rotating vortex pair as the flow evolves downstream. It is worth noting that the mode

remains unstable almost until the end of the domain, except for a frequency of $f = 300$ kHz, for which it becomes stable approximately for $x > 0.3$ m. This reflects the fact that the effect of the counter-rotating vortex pair persists a long distance downstream.

The right graph in Fig. 5 shows the corresponding integrated logarithmic amplification factors, given by

$$N = \int_{x_0}^{x} -\alpha_i \, \mathrm{d}x, \tag{4}$$

where x_0 is the streamwise location at which the perturbation becomes unstable. An important note must be made here regarding the definition of x_0 in this study. As it can be observed in the growth rate evolution plots, the wake instability mode is already unstable almost at the first streamwise location in which it is evaluated, namely, at the end of the downstream separation bubble. In this situation, the N-factor is assumed to be equal to zero at this location and the integration is carried out from this point onwards. This is the same approach followed by similar studies in literature, see for instance [11; 12]. For comparison purposes, the dash-dot line corresponds to the N-factor envelope of the Mack mode developing in the smooth flat plate boundary layer. For $f = 280$ and 290 kHz, the varicose instability reaches a N-factor above 8 within the studied domain length. This value is one unit higher than the one attained by the Mack mode disturbance. In addition, the growth in N is much faster for the wake instability mode. This reflects how the presence of the roughness element has a significant potential to move forward the transition onset location.

5. Influence of high-temperature effects on the roughness wake instability

To investigate the influence of modeling some high-temperature effects on the instabilities induced by the roughness element, another test case has been set up that leads to hot boundary-layer edge conditions. In this configuration, the roughness element is mounted on top of a sharp wedge with a half-angle of 20 degrees. The freestream conditions are $M_\infty = 18$, $T_\infty = 231.45$ K and $p_\infty = 10$ Pa, representative of a point in the reentry trajectory of the Space Shuttle Orbiter. This setup leads to boundary-layer edge temperatures in the order of $T_e = 2500$ K, as given by the Rankine-Hugoniot relationships after the shock wave induced at the wedge leading edge. The wall temperature is fixed to $T_w = 1900$ K, similar to the thermal limit of the Space Shuttle's thermal protection system.

For this case, the stability analysis is performed for each of the four different flow assumptions introduced in § 2. It is important to emphasize that an appropriate evaluation of internal-energy-excitation and dissociation effects on the wake instabilities can only be performed between flow assumptions with an equivalent set of transport models, that is, CPGGW, TPG and CNE. Nevertheless, a comparison of the results between the CPGS and the CPGGW flow assumptions provides a measure of the error purely associated to an inaccurate modeling of the transport properties.

The setup of the computational domain is the same as for cold boundary-layer edge conditions, except that in this configuration the boundary-layer edge properties imposed at the top boundary of the domain correspond to the wedge post-shock conditions obtained for each flow assumption. The dimensions of the domain for this case are: $x_{in} = 0.5$ m, $y_{in} = 0.49$ m, $x_{out} = 60$ m, $y_{out} = 1.87$ m and $z_\infty = 0.65$ m. The roughness is located at $x_r = 1.2$ m, has a height of $h_r = 1.62$ cm and its edge length is equal to $6h_r$, resulting in $Re_r \approx 400$ and $h_r/\delta_{99} \approx 0.6$ (the exact value is dependent on the flow assumption considered). The grid resolution considered for these conditions is $N_x \times N_y \times N_z = 831 \times 321 \times 191$.

5.1. Base flow solution

A comparison of some of the base-flow solutions obtained for the wedge configuration is presented in Fig. 6, which displays the temperature contours obtained for the CPGGW and the CNE flow assumptions on a x-z plane located at half of the roughness element height. There is a significant difference between the temperature values obtained for each of the two assumptions. The excitation of the vibrational energy mode, the presence of chemical reactions and the molecular diffusion accounted for in the CNE case yield a significantly lower temperature field than for the CPG assumption. Such a lower temperature, in turn, leads to a decrease in the boundary layer thickness. The TPG temperature field, although not shown here, is very similar to the CNE one, which implies that only a low level of dissociation is present at the streamwise location of the roughness element.

5.2. Stability analysis

Spatial 2D-LST computations have been performed in the wake behind the roughness element for the four different flow assumptions under study for this second configuration. All the calculations have been carried out using an order of $q = 8$ and a grid resolution of

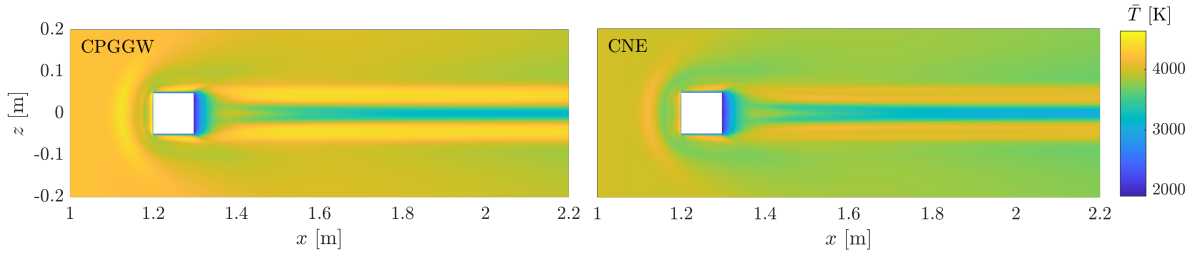

Figure 6: Contours of the base-flow temperature field obtained for the CPGGW and the CNE flow assumptions on a x-z plane located at half of the roughness element height, for the case of hot boundary-layer edge conditions.

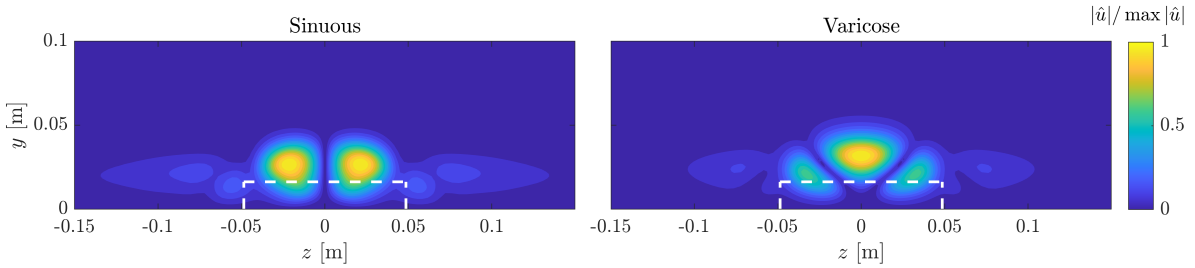

Figure 7: Normalized magnitude of the streamwise velocity amplitude function of the two most unstable modes for CNE at hot boundary-layer edge conditions, at a frequency $f = 3$ kHz and $x = 2$ m.

$N_y \times N_z = 121 \times 121$. Fig. 7 displays contour plots of the streamwise velocity amplitude function of the two most unstable modes obtained for CNE at $x = 2$ m downstream of the wedge leading edge. These two instabilities are, respectively, the sinuous (odd) and varicose (even) modes that develop in the wake behind the roughness element. Their regions of development are concentrated inside and around the low-velocity streak that characterizes the wake flow structure. The sinuous mode features a zero amplitude at the spanwise symmetry plane, which reflects its antisymmetric character. These modes are found to dominate the wake instability for all the various flow assumptions investigated.

Fig. 8 represents the evolution of the growth rate of the two most unstable wake modes as a function of frequency for each flow assumption at $x = 2$ m. At their unstable frequency range, the sinuous and varicose instabilities follow opposite trends when the excitation of the vibrational energy mode is taken into account. While the sinuous mode is more stable for TPG/CNE than for CPGGW, the varicose mode is strongly destabilized. The maximum growth rate of the sinuous mode is larger than that of the varicose disturbance. It can also be observed that the growth rate of both the sinuous and varicose instabilities is significantly different between CPGS and CPGGW for all the frequencies analyzed. The evolution of the varicose mode growth rate with frequency for CPGS happens to be in agreement with that of the TPG and CNE cases. Nevertheless, this is a coincidence rather than a behavior attributed to a correct modeling of the vibrational excitation.

Fig. 9 displays the streamwise evolution of the sinuous and varicose instabilities for the different flow assumptions, both in terms of growth rate and N-factor. The frequency associated to each curve corresponds to the respective most unstable frequency retrieved from the results shown in Fig. 8. The vertical dashed line once again denotes the streamwise coordinate of the end of the separation bubble induced at the trailing edge of the roughness element. Close to the obstacle, the growth rate of the sinuous mode is smaller for CNE than for TPG, which is likewise smaller than for CPGGW. However, this trend is inverted further downstream, and the mode is destabilized for approximately $x > 2.5$ m. This is strongly reflected in the N-factor evolution for each of these cases. The varicose mode features an opposed behavior, as it is destabilized near the roughness element for the TPG or the CNE assumptions. When accounting for vibrational excitation, the varicose mode appears to follow a similar trend to the second Mack mode, which is known to be destabilized in the presence of boundary-layer

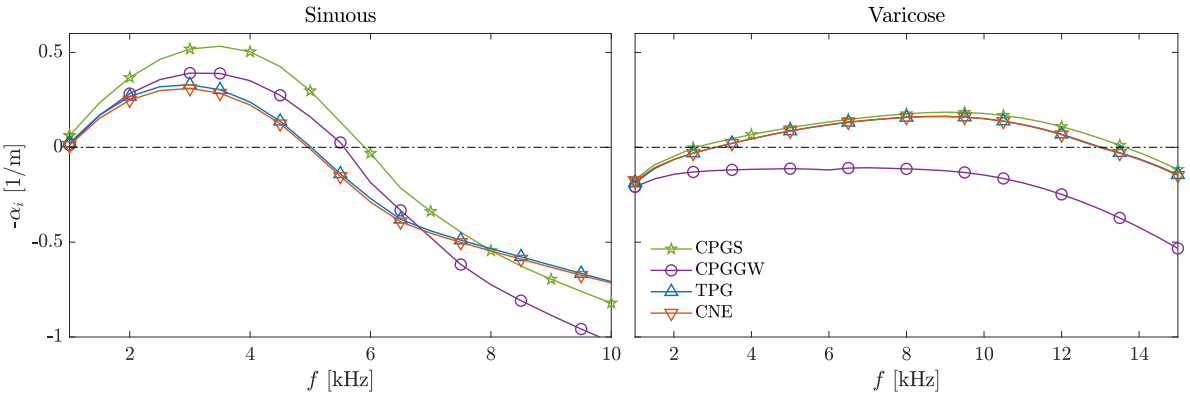

Figure 8: Evolution of the growth rate of the most unstable sinuous and varicose instabilities as a function of frequency for the various flow assumptions under hot boundary-layer edge conditions, at $x = 2$ m.

cooling [17; 18; 19]. Similarities between the second Mack mode and the varicose mode instabilities have been already recognized by previous authors. For the wake behind a cuboidal roughness element in CPG at Mach 6, De Tullio & Sandham [7] found a varicose instability (mode VC) tuned with the boundary-layer thickness, in a similar way to what is observed for the second Mack mode with LST. Nevertheless, in their case they found this varicose disturbance to be stabilized by wall cooling, as opposed to what is retrieved in this analysis for boundary-layer cooling. According to the N-factor values achieved for both disturbances, the sinuous mode is clearly the dominant instability for this configuration, reaching values of N that are almost one order of magnitude higher than for the varicose perturbation. Nevertheless, it is important to note that the maximum N-factor values obtained are still much smaller than for the flat plate configuration analyzed before.

Since the wedge geometry does not feature a stagnation point, no chemical reactions take place at the wedge leading edge. The dissociation of O_2, for instance, which is the most relevant reaction at the temperature range obtained for the CNE case [29], starts to occur downstream of the leading edge. Because of this configuration, the flow did not have enough time to undergo a sufficient amount of dissociation at the location of the roughness element. For this reason, the wake instability results obtained for TPG and CNE are very close to each other. Chemistry effects are expected to be more noticeable for instabilities developing further downstream.

6. Conclusions

The stability characteristics of the wake induced by a cuboidal roughness element located inside a laminar high-speed boundary layer have been investigated using two-dimensional linear stability theory (2D-LST). Two different configurations have been studied, respectively corresponding to cold hypersonic freestream conditions over a flat plate ($M_\infty = 6$, $T_\infty = 60.98$ K and $p_\infty = 1963.42$ Pa) and over a sharp 20 degree wedge ($M_\infty = 18$, $T_\infty = 231.45$ K and $p_\infty = 10$ Pa). For the flat plate case, the flow is assumed to behave as a calorically perfect gas. For the wedge geometry, the strong shock wave induced at the wedge leading edge leads to boundary-layer edge temperatures in the order of 2500 K. In this case, vibrational excitation and molecular dissociation need to be accounted for, so the roughness instability is studied by means of different flow assumptions: a calorically perfect gas, a thermally perfect gas and a mixture of perfect gases in chemical non-equilibrium.

The base flows needed for the stability analysis were obtained by means of laminar and steady Navier-Stokes simulations employing a second-order finite volume solver. The roughness element induces a pair of strong streamwise counter-rotating vortices that give rise to a low-velocity streak through the lift-up of low-momentum fluid from the surface. This structure is surrounded by a three-dimensional shear layer featuring a large streamwise shear magnitude, which supports the growth of different instabilities.

Spatial stability analyses were conducted at different streamwise locations and frequencies along the wake behind the roughness element. For the flat plate geometry, the most unstable disturbance growing in

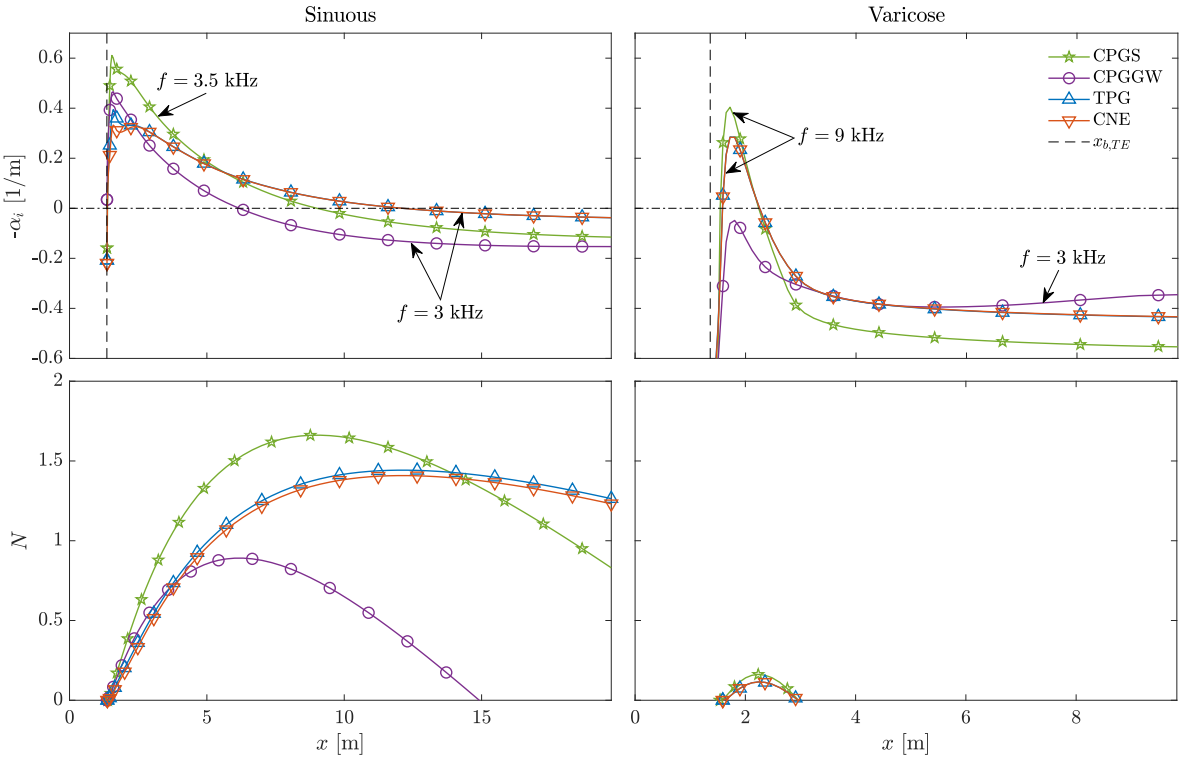

Figure 9: Evolution of the growth rate and associated N-factor curves of the most unstable sinuous and varicose instabilities as a function of the streamwise coordinate for the different flow assumptions under hot boundary-layer edge conditions. The dashed vertical line indicates the streamwise coordinate at the end of the trailing edge recirculation region ($x_{b,TE}$).

the wake has a varicose character, and shows regions of development that are confined inside and around the low-velocity streak. The perturbation has its maximum amplification rate immediately behind the trailing edge recirculation bubble, and remains unstable for a long distance downstream. The N-factor values reached by the instability are significantly higher than the ones found for the development of the Mack mode disturbance in a smooth flat plate boundary layer, giving evidence of the potential of the roughness element to accelerate the transition process.

For the wedge configuration, stability computations have allowed the identification of the varicose and sinuous instabilities also in the presence of vibrational-energy-mode excitation and chemical reactions. The investigation has shown that, in the vicinity of the roughness element, the two types of disturbances feature an opposite behavior. While the sinuous mode is stabilized when vibrational excitation and molecular dissociation are taken into account, the varicose perturbation undergoes a significant destabilization. The varicose mode is then found to behave in the same way as the second Mack mode in the presence of base-flow cooling. Further away from the roughness element, however, the sinuous instability decays at a slower rate when modeling the excitation of the vibrational energy mode and molecular dissociation, reaching a higher integrated amplification factor for the TPG and CNE flow assumptions than for CPGGW. Despite the sinuous disturbance undergoing a much higher amplification than the varicose one, both modes are still far from reaching N-factor values that are comparable to the case of cold boundary-layer edge conditions.

On the other hand, only small differences in the instability of the wake modes have been obtained between the TPG and the CNE flow assumptions, revealing that the influence of chemical reactions is not yet relevant at the conditions investigated. This is due to the lack of a stagnation point in the problem geometry, such that chemical reactions are not active at the wedge leading edge. At the streamwise position of the roughness element, the flow has not yet undergone sufficient dissociation so as to affect the propagation of the instabilities.

Acknowledgments

This work is part of a project that has received funding from the European Union's Horizon 2020 research and innovation programme under the Marie Skłodowska-Curie grant agreement No 675008.

References

[1] D. C. Reda, Review and Synthesis of Roughness-Dominated Transition Correlations for Reentry Applications, Journal of Spacecraft and Rockets 39 (2) (2002) 161–167.

[2] S. P. Schneider, Effects of Roughness on Hypersonic Boundary-Layer Transition, Journal of Spacecraft and Rockets 45 (2) (2008) 193–209.

[3] A. I. Ruban, M. A. Kravtsova, Generation of steady longitudinal vortices in hypersonic boundary layer, Journal of Fluid Mechanics 729 (August 2013) (2013) 702–731.

[4] G. Groskopf, M. J. Kloker, O. Marxen, Bi-global crossplane stability analysis of high-speed boundary-layer flows with discrete roughness, IUTAM Bookseries 18 (2010) 171–176.

[5] M. M. Choudhari, F. Li, C.-L. Chang, J. Edwards, M. Kegerise, R. King, Laminar-Turbulent Transition behind Discrete Roughness Elements in a High-Speed Boundary Layer, AIAA paper 2010-1575.

[6] N. De Tullio, P. Paredes, N. D. Sandham, V. Theofilis, Laminar-turbulent transition induced by a discrete roughness element in a supersonic boundary layer, Journal of Fluid Mechanics 735 (2013) 613–646.

[7] N. De Tullio, N. D. Sandham, Influence of boundary-layer disturbances on the instability of a roughness wake in a high-speed boundary layer, Journal of Fluid Mechanics 763 (2015) 136–145.

[8] G. Groskopf, M. J. Kloker, Instability and transition mechanisms induced by skewed roughness elements in a high-speed laminar boundary layer, Journal of Fluid Mechanics 805 (2016) 262–302.

[9] V. Theofilis, Advances in global linear instability analysis of nonparallel and three-dimensional flows, Progress in Aerospace Sciences 39 (4) (2003) 249–315.

[10] M. Kegerise, R. King, L. Owens, M. Choudhari, A. Norris, F. Li, C.-L. Chang, An experimental and numerical study of roughness-induced instabilities in a Mach 3.5 boundary layer, RTO-AVT-200/RSM-030 29, NATO (2012).

[11] M. Choudhari, F. Li, C. L. Chang, A. Norris, J. Edwards, Wake instabilities behind discrete roughness elements in high speed boundary layers, 51st AIAA Aerospace Sciences Meeting including the New Horizons Forum and Aerospace Exposition 2013 2013-0081.

[12] A. Theiss, S. Hein, S. R. C. Ali, R. Radespiel, Wake flow instability studies behind discrete roughness elements on a generic re-entry capsule, AIAA paper 2016-4382.

[13] A. Di Giovanni, C. Stemmer, Cross-flow-type breakdown induced by distributed roughness in the boundary layer of a hypersonic capsule configuration, Journal of Fluid Mechanics 856 (2018) 470–503.

[14] P. Paredes, N. De Tullio, N. D. Sandham, V. Theofilis, Instability Study of the Wake Behind a Discrete Roughness Element in a Hypersonic Boundary-Layer, in: Instability and Control of Massively Separated Flows, Vol. 107, 2015, pp. 91–96.

[15] N. De Tullio, N. D. Sandham, Direct numerical simulations of roughness receptivity and transitional shock-wave/boundary-layer interactions, RTO-MP-AVT-200 22, NATO (2012).

[16] A. Theiss, S. J. Hein, Investigation on the wake flow instability behind isolated roughness elements on the forebody of a blunt generic reentry capsule, Progress in Flight Physics 9 (2017) 451–480.

[17] M. R. Malik, E. C. Anderson, Real gas effects on hypersonic boundary-layer stability, Physics of Fluids 803 (3) (1991) 803–821.

[18] G. Stuckert, H. L. Reed, Linear Disturbances in Hypersonic, Chemically Reacting Shock Layers, AIAA Journal 32 (7) (1994) 1384–1393.

[19] M. L. Hudson, N. Chokani, G. V. Candler, Linear stability of hypersonic flow in thermochemical nonequilibrium, AIAA Journal 35 (6) (1997) 958–964.

[20] H. B. Johnson, T. G. Seipp, G. V. Candler, Numerical study of hypersonic reacting boundary layer transition on cones, Physics of Fluids 10 (10) (1998) 2676–2685.

[21] M. R. Malik, Hypersonic Flight Transition Data Analysis Using Parabolized Stability Equations with Chemistry Effects, Journal of Spacecraft and Rockets 40 (3) (2003) 332–344.

[22] O. Marxen, G. Iaccarino, T. E. Magin, Direct numerical simulations of hypersonic boundary-layer transition with finite-rate chemistry, Journal of Fluid Mechanics 755 (2014) 35–49.

[23] N. P. Bitter, J. E. Shepherd, Stability of highly cooled hypervelocity boundary layers, Journal of Fluid Mechanics 778 (2015) 586–620.

[24] C. Mortensen, X. Zhong, Real-Gas and Surface-Ablation Effects on Hypersonic Boundary-Layer Instability over a Blunt Cone, AIAA Journal 54 (3) (2016) 980–998.

[25] F. Miró Miró, E. S. Beyak, D. Mullen, F. Pinna, H. L. Reed, Ionization and Dissociation Effects on Hypersonic Boundary-Layer Stability, in: 31st Congress of the International Council of the Aeronautical Sciences, Belo Horizonte, Brazil, 2018.

[26] F. Miró Miró, E. S. Beyak, F. Pinna, H. L. Reed, High-enthalpy models for boundary-layer stability and transition, Physics of Fluids 31 (044101).

[27] G. Groskopf, M. J. Kloker, K. A. Stephani, O. Marxen, G. Iaccarino, Hypersonic flows with discrete oblique surface roughness and their stability properties, in: Center of Turbulence Research, Proceedings of the Summer Program, 2010, pp. 405–422.

[28] A. Di Giovanni, C. Stemmer, Roughness-Induced Boundary-Layer Transition on a Hypersonic Capsule-Like Forebody Including Nonequilibrium, Journal of Spacecraft and Rockets (2019) 1–14.

[29] J. D. Anderson Jr., Hypersonic and High Temperature Gas Dynamics, 2nd Edition, American Institute of Aeronautics and Astronautics, Reston VA, 2006.

[30] C. Park, R. L. Jaffe, H. Partridge, Chemical-Kinetic Parameters of Hyperbolic Earth Entry, Journal of Thermophysics and Heat Transfer 15 (1) (2001) 76–90.

[31] R. A. Thompson, K.-P. Lee, R. N. Gupta, Computer Codes For The Evaluation Of Thermodynamic Properties, Transport Properties, And Equilibrium Constants Of An 11-Species Air Model, Tech. Rep. TM-102602, NASA (1990).

[32] F. White, Viscous Fluid Flow, McGraw-Hill series in mechanical engineering, McGraw-Hill, 1991.

[33] R. N. Gupta, J. M. Yos, R. A. Thompson, K.-P. Lee, A review of Reaction Rates and Thermodynamic and Transport Properties for an 11-Species Air Model for Chemical and Thermal Nonequilibrium Calculations to 30000K, Tech. Rep. RP-1232, NASA (1990).

[34] C. R. Wilke, A Viscosity Equation for Gas Mixtures, The Journal of Chemical Physics 18 (4) (1950) 517–519.

[35] T. J. Bridges, P. J. Morris, Differential eigenvalue problems in which the parameter appears nonlinearly, Journal of Compu-

tational Physics 55 (3) (1984) 437–460.
[36] F. Pinna, VESTA toolkit: a Software to Compute Transition and Stability of Boundary Layers, AIAA paper 2013-2616.
[37] M. Hermanns, J. A. Hernández, Stable high-order finite-difference methods based on non-uniform grid point distributions, International Journal for Numerical Methods in Fluids 56 (2008) 233–255. arXiv:fld.1.
[38] L. N. Trefethen, Spectral Methods in MATLAB, SIAM, 2000.
[39] M. R. Malik, Numerical methods for hypersonic boundary layer stability, Journal of Computational Physics 86 (2) (1990) 376–413.
[40] A. Esposito, Development and analysis of mapping and domain decomposition techniques for compressible shear flow stability calculations, Tech. Rep. VKI SR 2016-16, von Karman Institute for Fluid Dynamics (2016).
[41] F. Miró Miró, F. Pinna, Linear Stability Analysis of a Hypersonic Boundary Layer in Equilibrium and Non-Equilibrium, AIAA paper 2017-4518.
[42] R. B. Lehoucq, D. C. Sorensen, Deflation techniques for an implicitly restarted Arnoldi iteration, SIAM Journal on Matrix Analysis and Applications 17 (4) (1996) 789–821.
[43] S. C. Tirtey, Characterization of a transitional hypersonic boundary layer in wind tunnel and flight conditions, Ph.D. thesis, Université Libre de Bruxelles and von Karman Institute for Fluid Dynamics (2009).
[44] I. Padilla Montero, F. Pinna, BiGlobal stability analysis of the wake behind an isolated roughness element in hypersonic flow, Proceedings of the Institution of Mechanical Engineers, Part G: Journal of Aerospace Engineering 234 (1) (2020) 5–19.

Nonlinear parabolized stability analysis of chemically reacting boundary-layers

Ludovico Zanus

Aeronautics and Aerospace Department, von Karman Institute for Fluid Dynamics, Belgium, ludovico.zanus@vki.ac.be

Supervisor: Fabio Pinna

Senior Research Engineer, Aeronautics and Aerospace Department, von Karman Institute for Fluid Dynamics, Belgium, fabio.pinna@vki.ac.be

Supervisor: Olivier Chazot

Professor and Head of the Aeronautics and Aerospace Department, von Karman Institute for Fluid Dynamics, Belgium, chazot@vki.ac.be

University Supervisor: Gérard Degrez

Professor and Head of the École Polytechnique de Bruxelles, Université Libre de Bruxelles, Belgium, gdegrez@ulb.ac.be

Abstract

Transition on a Mach 10 adiabatic flat-plate boundary layer in both chemically frozen and nonequilibrium conditions is studied. Particularly, a fundamental breakdown transition mechanism is simulated, by means of nonlinear parabolized stability equations (NPSE). Depending on the chosen flow assumption, different types of disturbance harmonics are excited, as well as different perturbation-amplitude levels are reached. This results in an earlier predicted transition onset in the case of a chemically-reacting flow, and to the appearance of a second distortion region of the boundary-layer temperature field, localized close the wall.

Keywords: Transition, stability, PSE, nonlinearities, hypersonic, boundary-layer

1. Introduction

Laminar-to-turbulent boundary-layer transition is a critical aspect to deal with during the design phase of a hypersonic vehicle [1]. In a turbulent flow, surface drag and heat transfer can increase several times, compared to the laminar values [2], with the risk of compromising not only spacecraft Thermal Protection Systems (TPS), but the whole vehicle integrity. On the other hand, low turbulence levels can prevent adequate air-fuel mixing at scramjets inlet, with consequent engines failure [3]. For these reasons, boundary-layer transition is often referred as a potential *aerospace mission killer*, if not properly taken into account.

Whether the interest is in delaying or promoting transition, it is a fundamental requirement to understand the physical mechanisms involved in the entire process. Only then can one provide reliable transition-location predictions and eventually implement effective control strategies. In hypersonic regime, the description of the phenomenon increases in complexity compared to lower-speed flows, due to the amount of effects influencing it (see [4], Ch. 6). Moreover, experimental data are difficult to collect, because of the measurement techniques required and the infeasibility in reproducing simultaneously the whole flight-conditions in ground-test facilities. Hence, for these applications, numerical studies become a fundamental tool for investigation and validation purposes.

During the past thirty years, there have been continuous improvements to the modeling complexity deployed on both the thermophysical gas properties and the perturbation characteristics. Linear stability theory (LST) has been applied to flows in chemical nonequilibrium (CNE) [5], thermo-chemical nonequilibrium (TCNE) [6] and local thermodynamic equi-

librium (LTE) [7] conditions. The same flow assumptions were also investigated by means of linear parabolized stability equations (LPSE), which include in the analysis also nonparallel effects. Examples are the works of Chang et al. [8], Kline et al. [9], Zanus et al. [10] and Johnson et al. [11]. Transition location prediction based on these linear tools can be performed only through the correlations provided by the e^N method. Despite its successful application also to hypersonic flows [12; 13], no knowledge about the physical mechanisms developing in the transition nonlinear stages can be obtained from its employment.

Direct numerical simulations (DNS) can be used to investigate this transition region. Nevertheless, for hypersonic applications, especially in reacting flow regimes, the literature is very scarce, due to the computational effort in solving the size-increased system of equations and the grid resolution to capture the higher disturbance harmonics that generate from the perturbations nonlinear interactions. To authors' knowledge the only studies dealing with this type of analysis are the recent works of Marxen et al. [14] on a flat plate with finite-rate chemical reactions and Di Giovanni et al. [15] on a spherical forebody in TCNE conditions. Both investigations concluded about the importance in taking into account nonequilibrium phenomena when predicting transition in high-Mach scenarios.

Nonlinear PSE are a well-established tool to capture the relevant physics of perturbations evolution within a boundary layer [16; 17]. However, its application to hypersonic flows has been only restricted to frozen chemistry conditions, because of the difficulties in deriving the stability equations, handling the generated enormous amount of terms. To authors' knowledge, the only NPSE analyses of reacting flows are the preliminary simulations of Zanus et al. [18] for flows in equilibrium conditions, while they have never been applied to finite-rate chemically-reacting flows.

In the present work, a Mach 10 boundary layer over an adiabatic flat plate is investigated by means of NPSE, both in frozen and chemical nonequilibrium conditions, simulating a fundamental breakdown mechanism. A very hot flow with an edge-temperature of 600 K is chosen, in order to highlight the presence of chemical reactions. These flow conditions are not representative of any realistic application, but they define an ideal academic problem to test the new NPSE solver for reacting flows. Moreover, avoiding low T_w/T_{ad} ratios, usually encountered at these Mach conditions, allows to suppress the appearance of eventual supersonic modes, whose correct treatment in the PSE framework is still not clear [8; 19].

2. Problem formulation

Stability equations are derived starting from the multi-species Navier-Stokes equations, here expressed in their dimensional invariant form. Superscripts q^i denote vectorial contravariant variables, whereas subscripts q_i denote vectorial covariant variables (see Pinna et al. [20]). Also, indices following a comma denote spatial derivatives (e.g. $u^i_{,j} = \partial u^i/\partial x^j$).

$$\frac{\partial \rho_s}{\partial t} + (u^j \rho_s)_{,j} = -J^j_{s,j} + \dot{\omega}_s \,, \tag{1a}$$

$$\rho \frac{\partial u^i}{\partial t} + \rho u^j u^i_{,j} = -g^{ij} p_{,j} + \mathbb{T}^{ij}_{,j} \,, \tag{1b}$$

$$\rho \frac{\partial h}{\partial t} + \rho u^j h_{,j} = \frac{\partial p}{\partial t} + u^j p_{,j} + (\kappa g^{ij} T_{,i})_{,j} - \mathcal{J}^j_{,j} + g_{ik} \mathbb{T}^{kj} u^i_{,j}, \tag{1c}$$

where g^{ij} is the metric tensor [21], u^j is the velocity, ρ_s the species density, $\dot{\omega}_s$ the chemical production term for the s-species, p the pressure, T temperature, h enthalpy and κ the thermal conductivity. J^j_s are the diffusion mass fluxes of each species, while the energy diffusion fluxes $\mathcal{J}^j$ read:

$$\mathcal{J}^j = \sum_{s \in \mathcal{S}} h_s J^j_s \,. \tag{2}$$

The viscous stress tensor $\mathbb{T}^{ij}$ is defined as:

$$\mathbb{T}^{ij} = \lambda g^{ij} u^k_{,k} + \mu \left(g^{jk} u^i_{,k} + g^{ik} u^j_{,k} \right), \tag{3}$$

where μ and λ are respectively the first and second viscosity coefficients. The numerical algorithm, on the other hand, solves the nondimensional version of the stability equations; details about how the nondimensionalization is performed can be found in Zanus et al. [10].

In perturbation theory, every flow quantity is decomposed into a base flow and a perturbation component (i.e. $q = \bar{q} + \epsilon q'$, with $\epsilon \ll 1$). Inserting this decomposition into Eq.(1) and subtracting the equations satisfied by the laminar base flow, equations governing the physical perturbations evolution are obtained. From here, nonlinear PSE can be derived by assuming every physical perturbation taking the form:

$$q'(x, y, z, t) = \sum_{n=-N}^{N} \sum_{m=-M}^{M} \tilde{q}_{(n,m)}(x, y) \exp(i\Theta) \; + \; c.c. \,, \tag{4}$$

with the exponential argument reading:

$$\Theta = \int_{x_0}^{x} \alpha_{(n,m)}(\xi)\, d\xi + m\beta_0\, z - n\,\omega_0\, t\,, \qquad (5)$$

where $\alpha_{(n,m)}$ is the streamwise wavenumber of mode (n, m), while β_0 and ω_0 are respectively the spanwise wavenumbers and frequency of the fundamental harmonic.

Equation(4) states that every physical disturbance is considered as a sum of multiple wave-like harmonics, defined by the couple of coefficients (n, m), indicating respectively the frequency and spanwise wavenumber indices in the double Fourier expansion. Each mode[1] (n, m) has to satisfy the following equation, written in matrix form:

$$L\,\vec{\tilde{q}} + M\,\frac{\partial \vec{\tilde{q}}}{\partial x} + \frac{\partial \alpha}{\partial x} Na\,\vec{\tilde{q}}\,\Big|_{(n,m)} = \vec{F}_{(n,m)}\,, \qquad (6)$$

where $\vec{\tilde{q}} = [\tilde{u}^i, \tilde{T}, \tilde{\rho_s}]$ is the vector of the perturbation variables, the L, M and Na matrices are functions of the mean-flow quantities and the stability parameters, and $\vec{F}_{(n,m)}$ is the forcing vector for mode (n, m). The forcing vector includes the nonlinear terms in the perturbation equations, associated to the interactions between the different harmonics. It is important to mention that the results presented in this work were obtained considering only quadratic nonlinearities (i.e. after variables decomposition, terms of order ϵ^3 and higher were dropped). This represents an approximation to the more correct derivation of NPSE for chemically-reacting flows, since in principle all orders of perturbations nonlinearities present in the equations should be kept.

Moreover, perturbations of the thermophysical gas properties are obtained by Taylor-expanding them, based on their functional dependency to the state quantities (ρ_s and T). For example perturbation viscosity is defined as:

$$\mu' = \sum_{s\in\mathcal{S}} \frac{\partial \overline{\mu}}{\partial \overline{\rho}_s}\rho'_s + \frac{\partial \overline{\mu}}{\partial \overline{T}}T' + \dots\,. \qquad (7)$$

Only linear terms were retained in this work, even if, to be theoretically consistent, the expansion should include terms up to the maximum perturbation equation nonlinear order kept (in this case second order).

[1] Throughout this article the word *mode* is not used in its mathematical meaning, but as synonym of disturbance harmonic, as defined by Eq.(4).

These choices were made considering the large amount of equations terms already achieved despite these simplifications and the relative computational effort in building the forcing at every algorithm iteration. For this first attempt in applying NPSE to flows in CNE conditions, these decisions were found reasonable, but the effect of including higher-order nonlinearities in the perturbation dependent quantities description and in the governing equations themselves must be verified in the future.

State-of-the-art models are used to described thermal-transport properties, mixture and chemical reactions. Air is modeled with five species (N, O, NO, N_2 and O_2), and with the set of reactions and reaction-rate constants proposed by Park et al. [22]. The thermal state of the mixture is retrieved from assuming the particles behave like a rigid rotor and a harmonic oscillator (RRHO) [23]. The transport properties (μ and κ) are provided by Yos' approximation to Chapman & Enskog's theory [24; 25], and the diffusion fluxes by solving the Stefan-Maxwell equations [26; 27]. The collisional data required for these is obtained from fitting a polynomial-logarithmic expression [28] to Wright et al.'s data [29]. For a more detailed explanation of the models and relative references please refer to the work of Miró Miró et al. [28].

3. Numerical tools

The NPSE solver is developed within the VKI Extensible Stability and Transition Analysis (VESTA) toolkit [30]. Stability equations are derived and implemented into matrix formulations in an automatic manner thanks to the VESTA Automatic Derivation and Implementation Toolkit (AD&IT) [20]. Within the NPSE theory, this approach allows, with a minimum effort, to generate equations by choosing the desired maximum order of nonlinearities to retain or the maximum Taylor-expansion order of the thermophysical gas properties perturbations. The VESTA PSE solver has been extensively verified to include flows in CNE conditions, in its linear version [19; 10] and flows in equilibrium conditions in its nonlinear one [18]. The present work is an extension of the solver to include nonlinearities in the analysis of CNE flows. Details about the general equations implementation, algorithm and numerical methods used can be found in Zanus et al. [19; 18]. Concerning the computation of the considered laminar base flows, the DEKAF [31; 32] boundary-layer code is used.

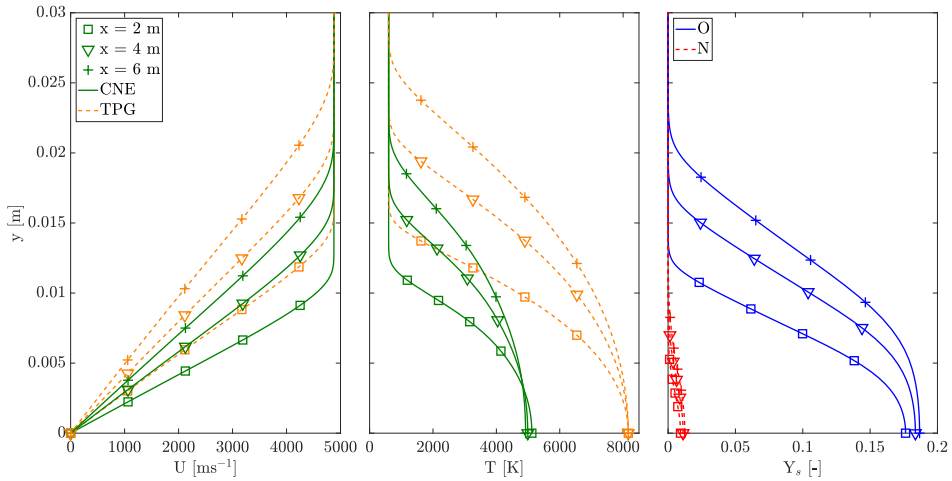

Figure 1: Streamwise velocity, temperature and atomic species mass-fractions profiles at three different locations along the flat plate: comparison between TPG and CNE flow conditions.

4. Results

The laminar base flow considered is a Mach 10 flat-plate boundary layer with a freestream temperature of 600 K and a unit-Reynolds number equal to 6.6×10^6 m^{-1}. The freestream composition is 76.7% N_2 and 23.3% O_2 in mass. Two flow assumptions are taken into account: a thermally perfect gas (TPG) with frozen mixture composition and a gas in chemical nonequilibrium (CNE). Figure 1 displays the streamwise velocity, temperature and atomic species mass-fractions profiles at three different locations along the flat plate. The chemical activity cools down considerably the boundary layer, shrinking its size. Atomic oxygen is present with a relevant concentration, while the atomic nitrogen mass fraction is very small, because of the temperature-levels reached.

A fundamental breakdown transition mechanism is simulated, since for hypersonic Mack's second-mode instability it was found to be one of the most likely scenarios [33]. Within the NPSE framework, this type of breakdown is obtained by initializing the computation with a two-dimensional primary disturbance (i.e. mode (1,0)) and a pair of oblique waves at the same frequency (i.e. modes (1,±1)). An initial amplitude $A_{(1,0)} = 1\%$ of the freestream temperature was chosen for mode (1,0), while for mode (1,1) it was equal to $A_{(1,1)} = 0.01\%$. Results are displayed in terms of maximum physical perturbation amplitude. Hence,

$$A_{(n,m)} = r_n\, r_m\, |\tilde{q}_{(n,m)}|_{max}\, \exp\left(- \int_{x_0}^{x} \alpha_{\Im(n,m)} d\xi \right), \quad \text{with} \quad r_a = \begin{cases} 1 & \text{if } a = 0 \\ 2 & \text{if } a \neq 0 \end{cases}, \tag{8}$$

where $\alpha_\Im$ is the imaginary part of the stramwise wavenumber α. The most critical transition conditions are chosen for both flow assumptions. The frequency of the perturbations initially inserted into the boundary layer were obtained by performing e^N analyses by means of LST, selecting the disturbances expected to promote transition according to a certain N-factor value (in this case equal to 9). Figure 4 shows the N-factors envelopes and it highlights the N curves relative to the chosen frequencies. For the flow in CNE conditions a frequency around $f = 75$ kHz was found, while for a TPG assumption a frequency around $f = 56$ kHz was retrieved. As expected, the boundary-layer cooling, in this case associated with the chemical activity, destabilizes the Mack's second mode, anticipating the predicted transition location.

The fundamental spanwise wavenumber, characterizing the initial conditions of the oblique modes, was chosen by taking the three-dimensional disturbance whose amplitude is mostly excited by the interaction with the primary two-dimensional mode. In order to select it, a series of low-resolved NPSE (i.e. N=M=1 in the Eq.(4) Fourier decomposition) with different β were run. Figure 3 displays the modes amplitude evolutions for the tested spanwise wavenumbers. The

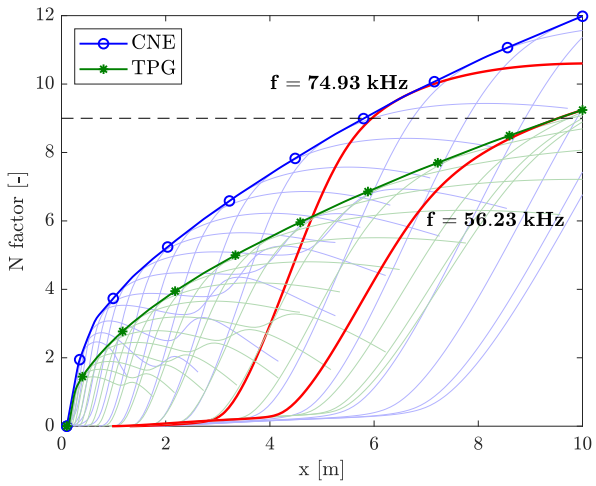

Figure 2: N-factor evolution along the flat plate for TPG and CNE flow conditions, obtained from LST. N-factor curves of the selected instability frequencies used as initial conditions in the NPSE simulations are highlighted.

oblique mode depending on β behaves quite differently according to the flow assumption considered. In particular, in CNE conditions it reaches the highest amplitude for the smallest β value (i.e. $\beta = 43.12$ m^{-1}), while in TPG conditions the highest excitation is obtained for $\beta = 129.97$ m^{-1}, which lies in between the tested β range. It has to be highlighted, that the interaction between the inserted modes is generally weak, only appreciable towards the end of the simulation, where the curves depart form their respective linear solutions. Increasing the initial amplitude of the three-dimensional disturbance would anticipate the appearance of the nonlinear interaction, but qualitatively the result is not expected to change.

With the defined initial conditions, NPSE were run with a maximum of N=6 harmonics in frequency and M=4 in spanwise wavenumber. Figure 4 shows the mode amplitudes evolutions for both flow assumptions considered, highlighting the most relevant modes. Depending on the aerothermodynamic model used, perturbations evolve relative to each other in different ways. Particularly, in CNE conditions the high harmonics of the Mack's mode reach higher amplitude levels at the end of the simulations, as well as the mean-flow distortion (MFD, i.e. mode (0,0)). On the contrary, in frozen conditions the harmonics of the three-dimensional mode and the ones of the longitudinal vortex (0,1) are more excited. Especially the latter shows a significant amplitude difference. As expected, the NPSE simulation stops earlier in CNE conditions, because of the high perturbations amplitude reached farther upstream than assuming TPG conditions.

Finally, the distortion of the boundary layer produced by the nonlinearities is compared for different quantities and flow assumptions. Figure 5 depicts the streamwise velocity, temperature and pressure amplitude profiles of mode (0,0), for TPG and CNE conditions. A position closer to the computational domain end is chosen, respectively at $x = 6$ m in case of TPG flow, and at $x = 4.6$ m for CNE conditions. Disturbance amplitudes are nondimensionalized dividing them by the local respective base-flow quantity, while the wall-normal spatial coordinate is made nondimensional using the local boundary-layer height δ, defined as the 99% of the streamwise velocity. Temperature and streamwise velocity deformations show overall the same qualitative features, regardless the flow assumption. The predominant distortion of the temperature field takes place at the boundary-layer edge. Nevertheless, when chemical reactions are taken into account a second deformation region starts to be noticed close to the wall. Generally, considering a CNE flow assumption leads to the biggest distortion of the boundary layer. The deformation of the pressure field, on the other hand, is predominant and localized at the boundary-layer edge in the case of a frozen flow, while it is closer to the wall and smaller in amplitude, when reactions are introduced in the base flow.

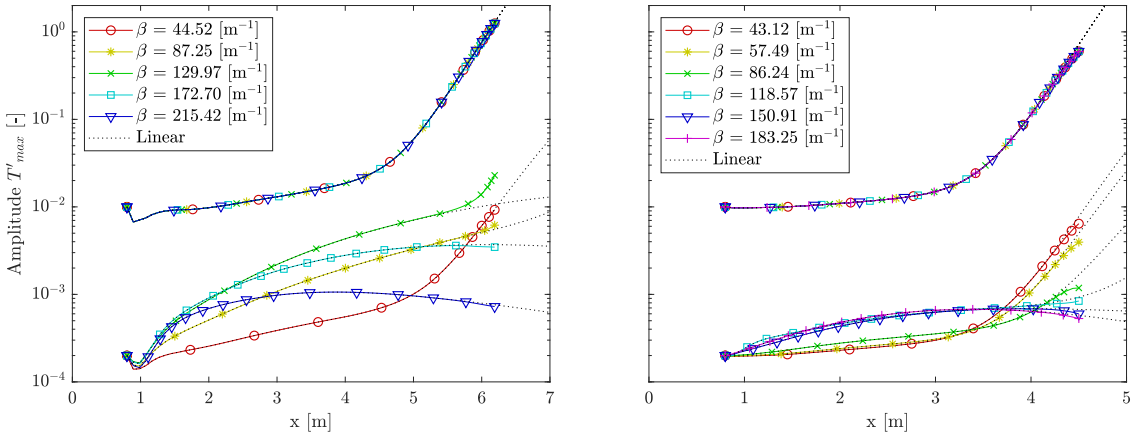

Figure 3: Evolution of maximum temperature perturbation amplitude of modes (1,0) and (1,1), for different initial spanwise wavenumbers: comparison between TPG (left) and CNE (right) flow assumptions.

5. Conclusions

A fundamental breakdown transition mechanism is simulated by means of NPSE on an adiabatic Mach 10 flat-plate boundary layer. Two flow assumptions are investigated: a frozen and a chemical nonequilibrium one, with gas properties described by state-of-the-art models. After selection of initial conditions leading to the most critical transition scenarios, NPSE analyses revealed significant differences in the perturbation-amplitude evolution, both in terms of the magnitude and the type of harmonics excited. In particular, in frozen conditions these were the harmonics of the three-dimensional fundamental disturbance and the ones related to streamwise vortices, while in CNE conditions they were the higher-harmonics of the fundamental two-dimensional Mack's second mode. The distortion of the boundary-layer streamwise velocity and temperature fields show qualitatively the same features, regardless the flow assumption considered. The biggest temperature deformation is localized at the boundary-layer edge. However, perturbations chemical reactions lead to the appearance of a second evident deformation region also close to the wall. Generally, chemical activity produces higher perturbation amplitudes. The pressure field distortion highlights differences in the perturbation-amplitude shape: it is predominant at the boundary-layer edge in case of a frozen flow, while concentrated closer to the wall in CNE conditions. The success in deriving and implementing nonlinear PSE for nonequilibrium chemically-reacting flows is an important step for the development of a tool able to investigate the transition physics in hypersonic regime, with major computational savings with respect to DNS.

Acknowledgments

This research is made possible thanks to the financial support provided by the Fonds de la Recherche Scientifique through their FRIA fellowship program.

References

[1] R. L. Kimmel, Aspects of hypersonic boundary-layer transition control, 41st Aerospace Sciences Meeting and Exhibit 2003-772.

[2] H. L. Reed, R. L. Kimmel, S. P. Schneider, D. Arnal, Drag prediction and transition in hypersonic flow, AIAA paper 1997-1818.

[3] M. K. Lockwood, D. H. Petley, J. G. Martin, J. L. Hunt, Air-breathing hypersonic vehicle design and analysis methods and interactions, Progress in Aerospace Sciences 35.

[4] J. D. Anderson Jr., Hypersonic and High Temperature Gas Dynamics, 2nd Edition, American Institute of Aeronautics and Astronautics, Reston VA, 2006.

[5] G. Stuckert, H. L. Reed, Linear Disturbances in Hypersonic, Chemically Reacting Shock Layers, AIAA Journal 32 (7) (1994) 1384–1393.

[6] M. L. Hudson, N. Chokani, G. V. Candler, Linear stability of hypersonic flow in thermochemical nonequilibrium, AIAA Journal 35 (6) (1997) 958–964.

[7] M. R. Malik, E. C. Anderson, Real gas effects on hypersonic boundary-layer stability, Physics of Fluids 803 (3) (1991) 803–821.

[8] C.-L. Chang, H. Vinh, M. R. Malik, Hypersonic boundary-layer stability with chemical reactions using PSE, AIAA paper 1997-2012.

[9] H. L. Kline, C.-L. Chang, F. Li, Hypersonic Chemically Reacting Boundary-Layer Stability using LASTRAC, AIAA paper 2018-3699.

[10] L. Zanus, F. Miró Miró, F. Pinna, Weak Non-Parallel Effects on Chemically Reacting Hypersonic Boundary Layer Stability, AIAA paper 2019-2853.
[11] H. B. Johnson, G. V. Candler, PSE Analysis of Reacting Hypersonic Boundary Layer Transition, AIAA paper 99-3793.
[12] H. B. Johnson, T. G. Seipp, G. V. Candler, Numerical study of hypersonic reacting boundary layer transition on cones, Physics of Fluids 10 (10) (1998) 2676–2685.
[13] H. B. Johnson, G. V. Candler, Analysis of Laminar-Turbulent Transition in Hypersonic Flight Using PSE-Chem, AIAA paper 2006-3057.
[14] O. Marxen, G. Iaccarino, T. E. Magin, Direct numerical simulations of hypersonic boundary-layer transition with finite-rate chemistry, Journal of Fluid Mechanics 755 (2014) 35–49.
[15] A. Di Giovanni, C. Stemmer, Roughness-Induced Boundary-Layer Transition on a Hypersonic Capsule-Like Forebody Including Nonequilibrium, Journal of Spacecraft and Rockets (2019) 1–14.
[16] T. Herbert, Parabolized Stability Equations, in: AGARD 793 Progress in Transition Modelling, 1993, pp. 4.1–4.34.
[17] R. D. Joslin, C. L. Streett, C. L. Chang, Spatial direct numerical simulation of boundary-layer transition mechanisms: Validation of PSE theory, Theoretical and Computational Fluid Dynamics 4 (6) (1993) 271–288.
[18] L. Zanus, F. Pinna, Stability Analysis of Hypersonic Flows in Local Thermodynamic Equilibrium Conditions by Means of Nonlinear PSE, AIAA paper 2018-3696.
[19] L. Zanus, F. Miró Miró, F. Pinna, Parabolized stability analysis of chemically reacting boundary layer flows in equilibrium conditions, Proceedings of the Institution of Mechanical Engineers, Part G: Journal of Aerospace Engineering 234 (1) (2020) 79–95.
[20] F. Pinna, K. J. Groot, Automatic derivation of stability equations in arbitrary coordinates and different flow regimes, AIAA paper 2014-2634.
[21] R. Aris, Vectors, Tensors and the Basic Equations of Fluid Mechanics, Dover - Prentice Hall, 1962.
[22] C. Park, R. L. Jaffe, H. Partridge, Chemical-Kinetic Parameters of Hyperbolic Earth Entry, Journal of Thermophysics and Heat Transfer 15 (1) (2001) 76–90.
[23] J. B. Scoggins, T. E. Magin, Development of Mutation++: MUlticomponent Thermodynamics And Transport properties for IONized gases library in C++, AIAA paper 2014-2966.
[24] J. M. Yos, Approximate equations for the viscosity and translational thermal conductivity of gas mixtures, Tech. Rep. AVSSD-0112-67-RM, Avco Corporation (1967).
[25] R. N. Gupta, J. M. Yos, R. A. Thompson, K.-P. Lee, A review of Reaction Rates and Thermodynamic and Transport Properties for an 11-Species Air Model for Chemical and Thermal Nonequilibrium Calculations to 30000K, Tech. Rep. RP-1232, NASA (1990).
[26] J. O. Hirschfelder, C. F. Curtiss, R. B. Bird, Molecular theory of gases and liquids, 2nd Edition, Wiley, New York, 1954.
[27] T. E. Magin, G. Degrez, Transport algorithms for partially ionized and unmagnetized plasmas, Journal of Computational Physics 198 (2) (2004) 424–449.
[28] F. Miró Miró, E. S. Beyak, F. Pinna, H. L. Reed, High-enthalpy models for boundary-layer stability and transition, Physics of Fluids 31 (044101).
[29] M. J. Wright, D. Bose, G. E. Palmer, E. Levin, Recommended Collision Integrals for Transport Property Computations Part I: Air Species, AIAA Journal 43 (12) (2005) 2558–2564.
[30] F. Pinna, Numerical study of stability of flows from low to high Mach number, Ph.D. thesis, Università degli Studi di Roma La Sapienza (2012).
[31] K. J. Groot, F. Miró Miró, E. S. Beyak, A. J. Moyes, F. Pinna, H. L. Reed, DEKAF: spectral multi-regime basic-state solver for boundary layer stability, AIAA paper 2018-3380.
[32] F. Miró Miró, E. S. Beyak, D. Mullen, F. Pinna, H. L. Reed, Ionization and Dissociation Effects on Hypersonic Boundary-Layer Stability, in: 31st Congress of the International Council of the Aeronautical Sciences, Belo Horizonte, Brazil, 2018.
[33] C. Hader, H. F. Fasel, Towards simulating natural transition in hypersonic boundary layers via random inflow disturbances, Journal of Fluid Mechanics 847 (July).

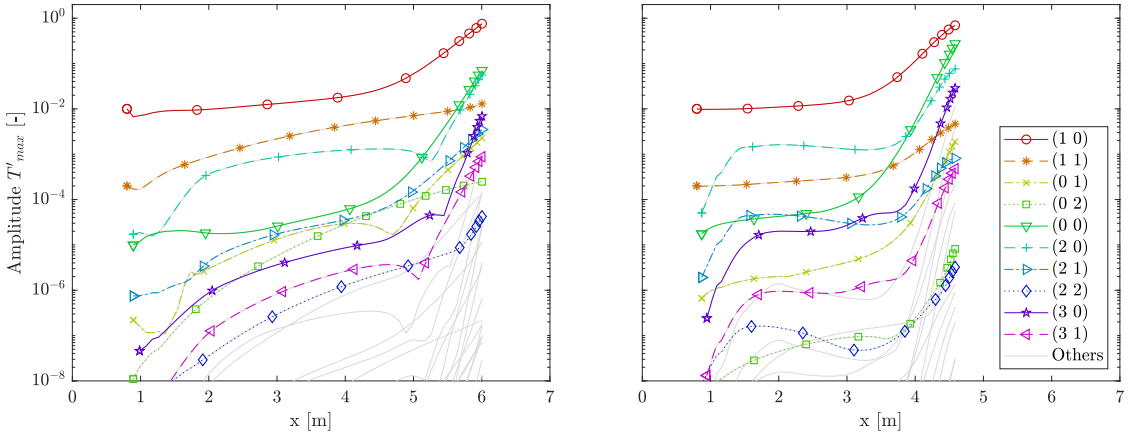

Figure 4: Evolution of maximum temperature perturbation amplitude for different modes: comparison between TPG (left) and CNE (right) flow assumptions.

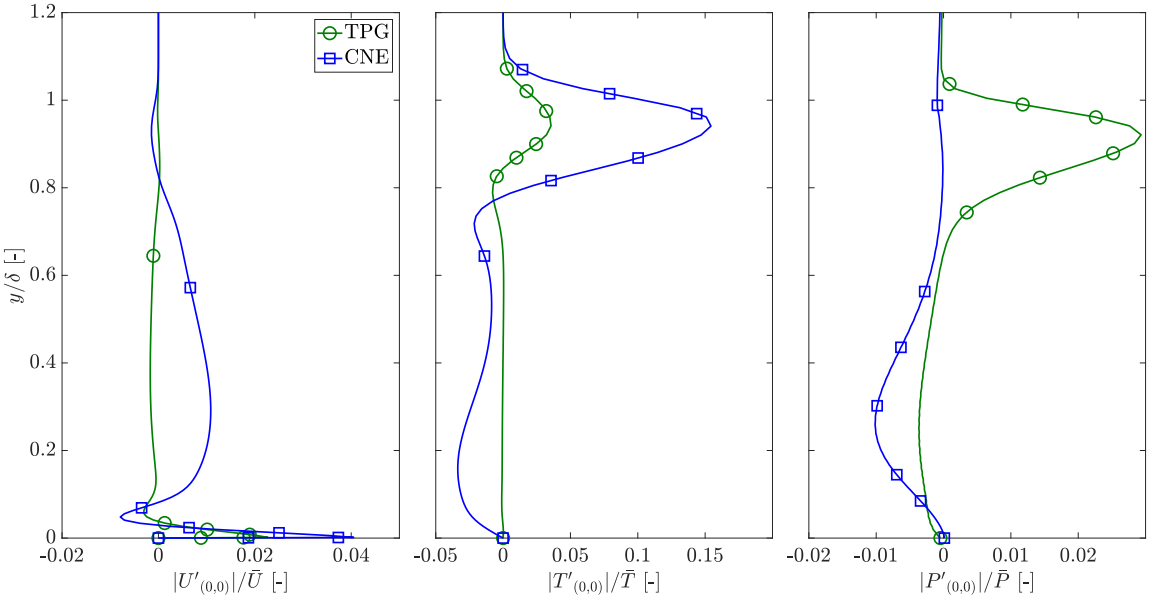

Figure 5: Mean flow distortion, mode (0,0), nondimensional profiles of streamwise velocity, temperature and pressure: comparison between TPG, CNETPG and CNE flow assumptions.

Dynamic stability of slender bodies in the transonic regime

Dániel Gábor Kovács

Aeronautics and Aerospace Department, von Karman Institute for Fluid Dynamics, Belgium, kovacs@vki.ac.be

Supervisor: Christophe Schram

Professor, Aeronautics and Aerospace Department, von Karman Institute for Fluid Dynamics, Belgium, christophe.schram@vki.ac.be

Abstract

The dynamic stability of slender bodies is an essential property to be decomposed in the transonic regime. A semi-free oscillation approach combined with a cable suspension system was designed to determine the pitch damping coefficient. The non-dimensionalized oscillation frequency is preserved between the flight vehicle and the wind tunnel model by the support system enabling the adjustment of the natural frequency.

Keywords: dynamic stability, fluid-structure interaction, aerodynamic damping, transonic flows, supersonic flows, semi-free oscillation

1. Introduction

The control parameters, i.e. stability derivatives, are the derivatives of the aerodynamic coefficients with respect to the angle of attack, which describe the behavior of the object under steady and unsteady conditions. While static stability is characterizing the initial tendency of a vehicle to a small perturbation, dynamic stability includes the inertial effects describing the attributes of the response, e.g. the presence of oscillations. Even though the numerical investigation of transient fluid-solid interaction phenomena has become feasible using Computational Fluid Dynamics (CFD), it requires significant computational power and the results have to be validated by wind tunnel experiments or flight tests.

2. Methodologies

Concerning the enhanced instrumentation requirements of the forced oscillation method, the implementation of a semi-free technique seems to be an adequate solution. A support system consisting of steel wires such as the one applied in [1; 2] can be considered a moderately intrusive solution which allows the oscillation of slender models. The designed experimental rig is presented in Fig. 1. A bearing system is located in the center of gravity to maintain the motion of the object to pure pitching. A non-intrusive optical technique is used to record the variation of the pitch angle by time to moderate the induced perturbations.

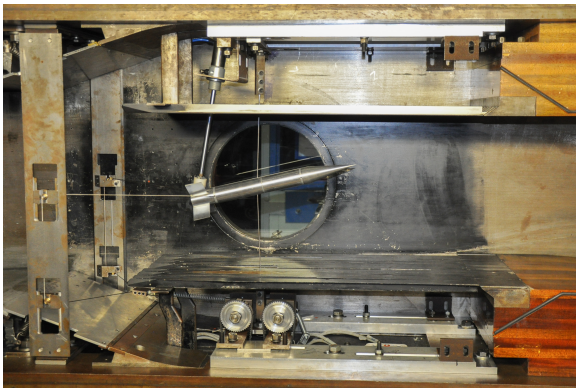

Figure 1: The semi-free oscillation test bench.

Equation (1) [3; 4] describes the motion of a body exposed to flow performing harmonic pitching oscillations:

$$I_y \cdot \ddot{\theta} - \left(C_{mq} + C_{m\dot{\alpha}}\right) \cdot \frac{q_\infty \cdot S \cdot D^2}{2 \cdot U_\infty} \cdot \dot{\theta} + - q_\infty \cdot S \cdot D \cdot \frac{\partial C_m}{\partial \theta} \cdot \theta = \mathcal{M}(t) \,. \quad (1)$$

The aerodynamic pitch damping coefficient may be described by the sum of two distinct terms $\left(C_{mq} + C_{m\dot{\alpha}}\right)$ [3; 4], one relates to the variation in the

pitch angle ($C_{mq} = \partial C_m / \partial \left(\dot{\theta} \cdot D / U_\infty \right)$) and the other corresponds to the variation in the angle of attack ($C_{m\dot{\alpha}} = \partial C_m / \partial (\dot{\alpha} \cdot D / U_\infty)$). Considering wind tunnel measurements these incidences are equal, given that the two coefficients are the same [3; 5], and accounting for short-period damping, the knowledge of the sum of them suffices for determining the stability characteristic [3].

3. Similarity Parameters

The Mach number (M) and the Strouhal number (St) have to be respected [5] in order to preserve the similarity between the dynamic behaviour of the flight vehicle and the wind tunnel model. Oscillations in flight occur about the natural frequency of the vehicle, which in non-dimensional form can be expressed as a Strouhal number. In addition to that, it is advisable to match also the Reynolds number (Re), but in most wind tunnels this can not be fulfilled.

4. Data Reduction

A high-speed camera is used with a shadowgraphy setup to monitor the instantaneous angle of attack, providing the variation of the oscillations in time. In the post-processing of the video recordings, a Gaussian image filtering is applied, and the model boundaries are detected by examining the intensity values of the pixels. As seen in Fig. 2, finding the top and bottom boundaries at two streamwise locations allow the calculation of the angle of attack.

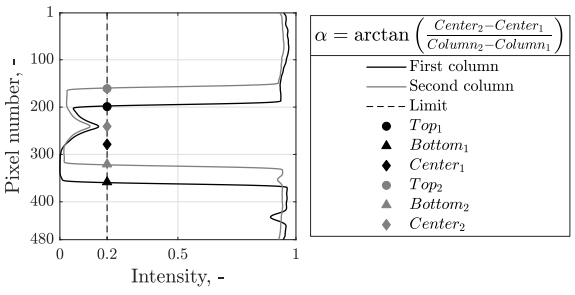

Figure 2: Sketch of the boundary identification technique.

After determining the harmonic motion in time, the maxima and minima of the oscillations must be localized. Figure 3 presents that an exponential curve, depending on the initial angle of attack, the damping and the inertia, can theoretically envelope the peaks. Finding the exponential decay of the oscillations yields the damping coefficient. Performing tare measurements without flow, the aerodynamic contribution can be distinguished from the total damping.

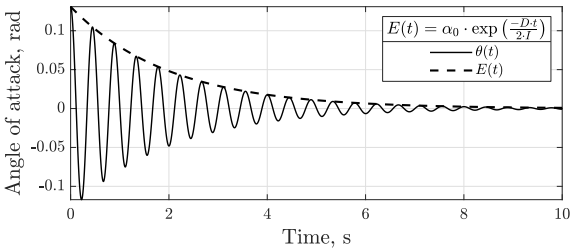

Figure 3: Example of a damped oscillation and its envelope curve.

5. Preliminary Tests

A measurement campaign was performed on two geometries, the Army-Navy Finner (ANF) model and its cone-cylinder basis. Tests were conducted in the VKI-S1 transonic-supersonic wind tunnel at $M = 0.7, 0.8$ and 0.9, at zero angle of attack and at incidence, and applying different cable tensions to vary the natural frequency, thus the Strouhal number.

6. Conclusion

According to the first wind tunnel tests, the setup worked adequately for the ANF model, which has a large aerodynamic damping. In case of the Cone-Cylinder, the mechanical damping of the system was too large giving a low signal-to-noise ratio. This effect must be reduced to enhance the aerodynamic contribution and to decrease the uncertainty.

References

[1] R. Bennett, M. Farmer, R. Mohr, W. Hall Jr., Wind-Tunnel Technique for Determining Stability Derivatives from Cable-Mounted Models, Journal of Aircraft 15 (5) (1977) 304–310. doi:10.2514/3.58360.

[2] C. Franzmann, F. Leopold, Measurement of Pitch Damping Coefficients Using a Wire Suspension, french German Research Institute of Saint-Louis (ISL), Presentation at the 19th STAB-Workshop, November 5-6, Göttingen, Germany (2019).

[3] C. Schueler, L. Ward, A. Hodapp, Techniques for Measurement of Dynamic Stability Derivatives in Ground Test Facilities, in: AGARDograph 121, no. October, AGARD, Paris, 1967, pp. 24–47.

[4] K. J. Orlik-Rückemann, Dynamic Stability Parameters, in: AGARD Lecture Series No.114, AGARD, Neuilly Sur Seine, 1981, pp. 1.1–1.32.

[5] S. Paris, Ö. Karatekin, Experimental Determination of the Dynamic Derivatives of a Reentry Capsule in Transonic Supersonic Regime, in: 8th International Planetary Probe Workshop, Portsmouth, Virginia, no. January, 2011, pp. 1–11.

AEROTHERMOCHEMISTRY

Simulation of a 3D unsteady hypersonic flow under uncertainty

Michele Capriati

Aeronautics and Aerospace Department, von Karman Institute for Fluid Dynamics, Belgium, michele.capriati@vki.ac.be

Supervisor: Thierry Magin

Professor, Aeronautics and Aerospace Department, von Karman Institute for Fluid Dynamics, Belgium, magin@vki.ac.be

University Supervisor: Pietro Congedo

Research Scientist, Inria, CMAP, Ecole Polytechnique, IPP, pietro.congedo@inria.fr

Abstract

In the hypersonic regime occurring during spacecraft atmospheric entry a shock is generated; across it the gas dissociates into reactive atoms, which diffuse through the boundary layer and interact with the surface. Products of the interaction, generally carbon based, are transported in the wake of the spacecraft where they affect the heat flux on the back-shell by radiating energy. Characterizing this radiative heat flux is mandatory to well design the back-shell protection system. Challenges arise by the wake unsteadiness, due to recirculation phenomena, that may significantly alter the species composition in space and time.

We propose to develop an uncertainty quantification tool able to capture the variability on a general output due to unsteady phenomena. In particular, it will be applied to an entry capsule flow to characterize the radiative heat flux from the wake. Beside unsteadiness effects, the flow is also characterized by epistemic uncertainties that needs to be propagated; in the present work we will investigate the effects of gas-surface interactions models, edge expansion fan physic and free-stream condition variability. Their uncertainty will be characterized against the unsteadiness one, that may smooth their effects on the solution, decreasing their overall importance. Given the high number of uncertanty parameters, surrogate models[1] will be used.
From a numerical standpoint, 3D unsteady simulations will be performed by using the CFD software US3D[2] with a thermodynamic closure provided by MUTATION++[3]; radiative heat flux on the surface will be obtained by post-processing the solution using an in-house software. In such a framework also the error given by the numerical grid resolution will be investigated and the most time-efficient mesh dimension will be accessed.

Keywords: Uncertainty Quantification, Unsteady Flows, Hypersonic Flows, Entry Flows

References

[1] A. F. Cortesi, Predictive numerical simulations for rebuilding freestream conditions in atmospheric entry flows, Ph.D. thesis, Universit de Bordeaux (2018).

[2] G. V. Candler, H. B. Johnson, I. Nompelis, V. M. Gidzak, P. K. Subbareddy, M. Barnhardt, Development of the US3D Code for Advanced Compressible and Reacting Flow Simulations. arXiv:https://arc.aiaa.org/doi/pdf/10.2514/6.2015-1893, doi:10.2514/6.2015-1893.
URL https://arc.aiaa.org/doi/abs/10.2514/6.2015-1893

[3] J. B. Scoggins, T. E. Magin, Development of Mutation++: Multicomponent Thermodynamic and Transport Properties for Ionized Plasmas written in C++. arXiv:https://arc.aiaa.org/doi/pdf/10.2514/6.2014-2966, doi:10.2514/6.2014-2966.
URL https://arc.aiaa.org/doi/abs/10.2514/6.2014-2966

A Bayesian perspective on TPS catalysis phenomena: learning from experiments and proposing new ones

Anabel del Val

Aeronautics and Aerospace Department, von Karman Institute for Fluid Dynamics, Belgium, ana.isabel.del.val.benitez@vki.ac.be

Supervisors: Olivier Chazot and Thierry Magin

Head of Department and Professor, Aeronautics and Aerospace Department, von Karman Institute for Fluid Dynamics, Belgium, chazot@vki.ac.be

Professor, Aeronautics and Aerospace Department, von Karman Institute for Fluid Dynamics, Belgium, magin@vki.ac.be

University Supervisor: Pietro Congedo

Research Scientist, DeFI Team (INRIA Saclay Île-de-France, École Polytechnique). Centre de Mathématiques Appliquées (CMAP), École Polytechnique, France, pietro.congedo@inria.fr

Abstract

In this work, state-of-the-art uncertainty quantification techniques are applied to the characterization of the catalytic behavior of thermal protection systems using plasma wind tunnel experiments. A dedicated Bayesian inference framework, derived in a previous work, is here extended to other testing methodologies and testing conditions. The catalysis phenomena affecting re-usable heat shield materials is considered in the physical model through a parameter that represents the exothermic recombination of atoms taking place at the material surface. Posterior uncertainty distributions of this recombination parameter are obtained from experimental data. The testing methodology developed confirms to be a reliable experimental approach for characterizing this phenomena as well as the enthalpy of the flow. This contribution offers a deeper insight to the experiments performed in this domain and how to improve our model upon experimental evidence.

Keywords: Uncertainty Quantification, Bayesian Inference, Plasma Flow Experiments, Catalysis, Thermal Protection Systems

1. Introduction

Space travel, since its beginnings in Low Earth Orbit (LEO) to the exploration of our Solar System, has led to countless scientific advancements in what it is one of the most challenging undertakings of humankind.

From travelling to LEO, to the Moon landings and the exploration of Mars and distant asteroids, traveling around and beyond the orbit of our planet requires large amounts of energy, reaching velocities of the order of 7-11 km/s. All this amount of kinetic and potential energy, dictated by orbital mechanics, is dissipated when a space vehicle enters dense planetary atmospheres. The bulk of this energy is exchanged during the entry phase by converting the kinetic energy of the vehicle into thermal energy in the surrounding atmosphere through the formation of a strong bow shock ahead of the vehicle. In general, a large fraction of the energy dissipated to the atmosphere is carried away from the vehicle through convection and radiation, leaving a small percentage to be absorbed back into the vehicle as thermal energy. A Thermal Protection System (TPS) is used to mitigate this heat load and ensure that the temperature limits of critical components on board are not exceeded during the entry phase. Prediction of the heating rate which is experienced by the TPS remains an imperfect art, leading to very large safety margins for the vehicle design. Failing to correctly predict the heat loads and associated material response of the TPS during the design phase can lead to catastrophic mission failure. To address this prob-

lem, experimental facilities capable of generating high speed and plasma flows are developed to study different aspects of atmospheric entry flows [1], together with physico-chemical models used to describe the state of the flow at a given time and conditions [2]. The delicate interplay between experiments and models represents the main source of knowledge about the physical phenomena and their coupling mechanisms.

Reusable heat shields are used for moderate entry velocity vehicles to dissipate heat by re-radiating the energy back into the flow, and are designed to withstand multiple uses without need for replacement or repair [3]. They are typically constructed from carbon or silicon carbide materials which have high emissivities at high temperatures to promote re-radiation. The interaction between the dissociated gas and the protection system is governed by the material behavior which acts as a catalyst for exothermic recombination reactions of the atomic species in the surrounding gas mixture [4]. The determination of the catalytic properties of thermal protection materials is a difficult task subjected to experimental and model uncertainties, and the design and performance of reusable atmospheric entry vehicles must account for these uncertain characterizations.

The catalytic behavior of these materials cannot be assessed just experimentally. The experiments are coupled with numerical simulations to rebuild from the measurements the free stream enthalpy and the recombination parameters [5]. The logic of the rebuilding consists on measuring certain quantities of interest under relevant testing conditions in the VKI Plasmatron, namely wall heat fluxes, temperatures and pressures, and use them as input conditions for a numerical solver that reproduces the boundary layer in front of the probe. The information needed to reproduce this chemically reacting boundary layer comes from the outer layer conditions and the wall conditions, namely, the material catalytic properties and surface temperature. In the absence of knowledge about the outer edge conditions or the material conditions, whichever can be rebuilt from the information of the other through iterative methods for the computed boundary layer when targetting to fit the available measurements. In this work, the outer edge conditions are represented by the enthalpy of the flow at the boundary layer edge while the wall conditions are defined by a catalytic parameter for each material.

Traditionally, the experimental testing of such catalytic thermal protection materials is carried out using two different probes holding two different materials: a designated reference (or auxiliary) material and the TPS material in question. Both materials are tested under the same flow conditions at a time. The rebuilding of such properties is heavily based on the choice of the auxiliary material, whose catalytic properties are considered well-known. The reasoning behind this is that the catalytic behavior of the TPS material can be determined by performing a two-step rebuilding. The wall conditions for the reference material are well-known so the outer edge conditions are rebuilt. As both materials are tested under the same outer edge conditions (during the same run of the plasma wind tunnel), the wall conditions for the material under study can be rebuilt from the knowledge of the outer edge conditions. This experimental approach comprises the state-of-the-art for catalytic thermal protection systems characterization at VKI [5]. Viladegut [6] took this exercise further by characterizing the catalytic properties of the most common reference material used in the experiments, copper. Through his work, Viladegut developed a 3-probes testing methodology aimed at characterizing well copper catalytic properties for future uses on experiments with TPS materials.

Building on the works of Panerai [5] and Viladegut, this contribution designs a new experimental setup, aimed at characterizing TPS materials very accurately without making any assumptions on the flow outer edge properties or the reference materials catalytic properties. This new experimental setup combines the advantages of the 3-probes methodology developed by Viladegut with the testing of actual TPS materials and not just reference probes as done by Panerai.

As shown by Sanson et al. [7], a fully Bayesian approach combining all set of available measurements can be used to infer the catalytic properties of different materials, while treating them as equal in the priori knowledge. For this work, the new experimental setup is used to get the mesurements and a more accurate Bayesian inference framework is used to infer the catalytic parameters for a full characterization including uncertainties in the measurements and in the knowledge of the reference probes. This way of treating and learning model parameters from the data proves to be very reliable from the fact that gets rid of problematic assumptions and leads the way of improving future characterizations by designing informative experiments in the most relevant conditions as shown in this work. Overall this effort represents a cornerstone in the study and analysis of this parameter from an experimental and mathematical perspective.

2. Experimental facility, measurement techniques and methods

The experimental setup installed at the Plasmatron facility offers intrusive and non-intrusive (optical) measurement techniques. The instrumentation equipment for this work consisted of a 2-color pyrometer, a broad-band radiometer and probes for heat flux and pressure measurements. The main data of interest during this investigation were heat fluxes for the three different materials and surface temperature for the TPS material.

2.1. Plasmatron facility description

The Plasmatron at von Karman Institute (VKI) is an inductively-coupled plasma (ICP) wind tunnel [8], that offers an ideal environment for catalytic studies due to the production of plasma jets of very high chemical purity [5]. This facility has been extensively studied by Bottin [9] and Bottin et al. [8] and a detailed description may be found in their works. Its basic concept consists of a quartz tube surrounded by a coil, which is connected to a generator that provides high voltage (1.2 MW) and high frequency (400 kHz) current. This induces an electromagnetic (EM) field inside the tube, that forces residual charged particles in the flow to form eddy currents which heats up the gas by Joule effect. The injection of gas is done through a ring-shaped inlet at the outer edge of the torch. Due to the induced EM field, the gas ionizes into plasma flow, which exits at subsonic speed into a low pressure test chamber that hosts material probes. Argon is employed as starting gas, facilitating the initial electric discharge, due to the longer lifetime of the free electrons at low pressure compared to the air plasma case. Complementary systems are responsible for the gas circulation, probes, cooling, and diagnostics. TPS material and two reference probes (copper and quartz) are mounted onto holders which are remotely activated to be injected and retracted from the plasma jet. Suitable windows provide the necessary optical access to the testing chamber for the flow and sample diagnostics: the lateral windows (on both sides of the wind tunnel) allow perpendicular side views of the plasma jet and probes, and the the torch-side windows allow a frontal oblique view of the TPS surface.

2.2. Experimental setup and methods

To characterize a TPS material in a ground facility, the environment under which the probe is hosted needs to be known. To calibrate the plasma flow conditions, two water-cooled probes are used. Two 14 mm (sensing area) copper and quartz calorimeters measure the cold wall ($\approx$ 350K and $\approx$ 750K, respectively) heat flux at the stagnation point. These heat fluxes are determined by the water mass flow ($\dot{m}$), which is controlled by a calibrated rotameter, and the temperature difference ($T_{out} - T_{in}$) in the cooling water supply. Thus, the heat flux for the cold wall (q_{cw}) probes is given by

$$q_{cw} = \frac{\dot{m} c_p (T_{out} - T_{in})}{A} \tag{1}$$

where c_p is the water specific heat and A the area of the surface of the probe. The heat flux probe is injected into the plasma flow once the air mass flow and chamber pressure are stabilized. The total pressure (P_T) is measured using a Valydine differential pressure transducer and the static pressure (P_s) in the Plasmatron chamber is measured by an absolute pressure transducer (Memberanovac DM 12, Leybold Vacuum, OC Oerlikon Corporation AG). Then, based on this measurements, the dynamic pressure ($P_{dyn} = P_T - P_s$) is recorded. As the Plasmatron only has three probe holders, the dynamic pressure is recorded during a different test case, where the copper heat flux and pressures of the first experimental run are duplicated.

Figure 1 presents the experimental setup adopted for this study. Copper, TPS and quartz samples are mounted on probe holders. In this work,"standard" ESA geometry probes (also known as Euromodel) for typical non-equilibrium boundary layers, with a radius of 25 mm, are used. To analyse the surface temperature and emissivity of the TPS material, a two-colour pyrometer and an infrared radiometer are used. As previously mentioned, heat flux and pressure probes are used for jet calibration.

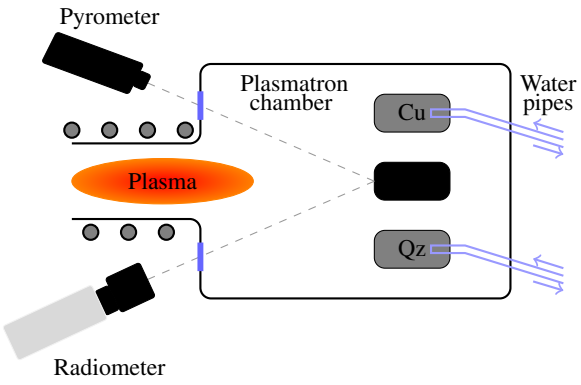

Figure 1: Schematic of experimental setup (seen from top, not to scale) with pyrometer and radiometer optical path in front of the TPS material sample.

The optical instruments as the pyrometer and radiometer are calibrated with the aid of a black-body (BB) source (LANDCAL R1500T, LAND Instruments International), which provides a reference temperature spot with an emissivity value close to 1. The calibration curves presented in this report were provided by Helber [10]. A two-colour Raytek Marathon Series MR1S-C infrared pyrometer with an operating range between 1000 and 3000 is used. Optical access to the testing chamber is offered through a 1 cm thick quartz window, placed at $\sim$ 1 m distance to the probe, with an orientation of $\sim$ 35 with respect to the stagnation line.

To record the surface radiance, a broadband infrared radiometer (KT19, HEITRON-ICS Infrarot Messtechnik GmbH) is used. This instrument is located at $\sim$ 47 angle relative to the surface normal in front of a 1.8 cm thick KRS-5 window, which offers $\sim$ 70 % optical transparency [5] in the whole infrared range of the instrument ($0.6 - 0.39\mu$m). Its temperature range is between 0 and 3000 and the acquisition frequency is set to 1 Hz. The output provided is the integrated thermal radiation over the spectral range, converted into equivalent temperature through an adjustable emissivity value which, in the context of the Plasmatron facility, is set to one.

As the range between $0.6 - 0.39\mu$m contains the highest percentage of thermal radiation at the operation temperatures of the Plasmatron [5], the actual radiance and emissivity can be computed with the Stefann-Boltzmann law. Being T_w^{pyro} the real surface temperature acquired by the pyrometer and T_w^{radio} the equivalent temperature measured by the radiometer, the total emissivity can be determined as

$$\varepsilon = \frac{(T_w^{radio})^4}{(T_w^{pyro})^4}. \tag{2}$$

Among the experimental testing, there are uncertainties associated to the measured flow parameters as the static pressure, P_s, dynamic pressure, P_{dyn}, and cold wall heat fluxes, q_{cw}^{Cu} and q_{cw}^{Qz}; to the measured surface parameters as the surface temperature, T_w^{TPS}, and emissivity, ε; and to the cold wall temperatures assumptions, T_{cw}^{Cu} and T_{cw}^{Qz}. For Uncertainty Quantification (UQ), these are the uncertainties that are treated as aleatory variables with Gaussian distributions.

2.3. On the differential pressure transducer measurements

As previously mentioned, the experiments are performed with three sample probes (copper, TPS and quartz). Therefore, there is no place available for the pressure transducer and, consequently, the measurement of the dynamic pressure cannot be obtained simultaneously. Hence, a second experimental run is performed with the water-cooled copper probe, to perform again the calibration of the plasma flow and to try to duplicate the testing conditions obtained in the first experimental run. Simultaneously, a pressure transducer is mounted on another holder.

As the copper heat fluxes cannot be exactly duplicated in both experimental runs, a correction factor must be applied to obtain the real dynamic pressure. As the dynamic pressure is linearly proportional to the heat flux [6], for static pressures of 15 and 100 mbar, linear regressions are obtained with the values measured in the second experimental run. Once the copper heat fluxes are obtained in the first experimental run, the real values of the dynamic pressure are computed. For a static pressure of 50 mbar, as there is just one point measured, the dynamic pressure is corrected multiplying the measured pressure by the ratio between the heat fluxes of the first and the second experimental runs.

3. Numerical Solvers and Uncertainty Quantification Methodology

The characterization of reusable thermal protection materials by estimation of the catalytic parameter requires performing tests in a relevant and similar environment. These experiments are then coupled with numerical simulations to rebuild from the measurements the enthalpy and recombination parameters. As experiments and models have associated uncertainties, these must be integrated into the numerical framework as well.

3.1. Numerical solvers for catalysis and enthalpy rebuilding

The logic of the rebuilding consists on measuring certain quantities of interest under certain testing conditions in the Plasmatron, and using them as input conditions for two numerical solvers that reproduce the flow around the probe. The rebuilding method provides a simulation of the chemically reacting boundary layer at the stagnation line, together with all the thermodynamic properties, from the outer edge to the wall.

The first software is an in-house Inductively-Coupled Plasma (ICP) solver available within the CoolFluid [11] platform. This solver helps to define

the framework of the problem to be solved around the probe by simulating the interaction between the electromagnetic field around the coil and the gas passing through, with the aim of reproducing the whole Plasmatron chamber. ICP simulations are in Local Thermodynamic Equilibrium (LTE) conditions, which is reasonable away from both the torch exit and the probe [12]. The purpose of the LTE viscous flow computation is to compute the values of non-dimensional parameters (NDPs), Π_i, which characterize the flow near the stagnation point of the heat flux probe in the plasma jet for a selected mass flow rate [13].

The operating conditions of the Plasmatron are defined by the gas mass flow, $\dot{m}$, static pressure, P_s, and power, P_w. These quantities together with the probe configuration (or the probe radius r_p) are used as input for the ICP simulations. Their outputs are then used as inputs for CERBOULA in the form of the NDPs obtained from the LTE viscous flow simulation [13]. In the context of this work, however, the ICP code is not used and the correlation provided by Panerai [5] is implemented for this purpose.

The second software intervening in the rebuilding process is the so-called CERBOULA, a coupling between the NEBOULA (Non-Equilibrium BOUndary LAyer) solver and the CERBERE (Catalycity and Enthalpy ReBuilding on a REference probe) routine. The first was developed by Barbante [14] at VKI and assumes thermal equilibrium and chemical nonequilibrium to compute both the gas thermodynamic and transport properties along the stagnation line in different flow configurations. The condition of LTE is imposed at the boundary layer edge while the surface temperature and the catalytic parameter are introduced as wall boundary conditions. NEBOULA is then plugged into CERBERE routine to be used as a tool for Plasmatron data rebuilding. The input variables of the ensemble CERBOULA are a combination of measured quantities in the Plasmatron and some hydrodynamic outputs from the ICP simulation. CERBOULA ultimately computes the boundary layer edge conditions in front of the probe.

To compute a relationship between the boundary layer edge enthalpy and the catalytic parameter, the static and dynamic pressures, wall temperatures and heat fluxes measurements together with the NDPs are used as variables for the Boundary Layer code. In this scenario, the heat flux can be expressed as function of the input parameters

$$q_w = q_w(H_e, T_w, P_s, \Pi_i, ..., \gamma_i) \tag{3}$$

and either the enthalpy nor the catalytic parameter have to be assumed to have a complete rebuilding characterization. As the heat flux is a measured quantity, the solver iterates until the numerical heat flux coincides with the experimental heat flux, as illustrated in Fig. 2.

3.2. Uncertainty Quantification methodology

The determination of catalytic properties is affected by the noise present in the experimental data, even for well-characterized facilities, together with theoretical assumptions that must be also evaluated. Hence, the uncertainties associated with the experiments and rebuilding methodology must be integrated into the numerical framework, to obtain a more reliable prediction of the catalytic parameter.

In most of the experimental approaches, the authors rely on the knowledge of the reference calorimeter catalytic property which is not an adequate assumption [15]. Therefore, the catalytic property for copper and quartz should also be included as unknowns in the rebuilding process. In this Bayesian inference approach, references and TPS material catalytic properties play the same role in the inference process, being all inferred at the same time.

3.2.1. Prior distribution and likelihood function

According to the Bayes rule, the posterior distribution of any quantity of interest can be divided into a ratio of probabilities. In the case of this work, this ratio reads

$$P(\gamma_{Qz}, \gamma_{TPS}, \gamma_{Cu}|M) = \frac{L(M|\gamma_{Qz}, \gamma_{TPS}, \gamma_{Cu})\, P(\gamma_{Qz}, \gamma_{TPS}, \gamma_{Cu})}{P(M)}, \tag{4}$$

where $M = (q_{cw}^{Qz}, q_{cw}^{Cu}, T_{cw}^{Qz}, T_{cw}^{Cu}, q_w^{TPS}, T_w^{TPS}, P_s, P_{dyn})$ is the set of available measurements and $\gamma_{Qz}, \gamma_{TPS}, \gamma_{Cu}$ are the recombination parameters to be inferred; $L(M|\gamma_{Qz}, \gamma_{TPS}, \gamma_{Cu})$ refers to the likelihood of the data measured M, given the model parameters $\gamma_{Qz}, \gamma_{TPS}$ and γ_{Cu}; $P(\gamma_{Qz}, \gamma_{TPS}, \gamma_{Cu})$ is the prior probability distributions of the model parameters and P(M) is the marginal likelihood, that is, the probability that the considered measurements are obtained. All prior probability distributions are taken as log-uniform in within selected intervals, with constraints on the normalization factor (integral of the distribution is equal to one). In this way, no assumptions are made about the catalytic behavior of the reference probes compared to the one of the material under study. This choice of priors also ensures compliance with the maximum entropy principle [16].

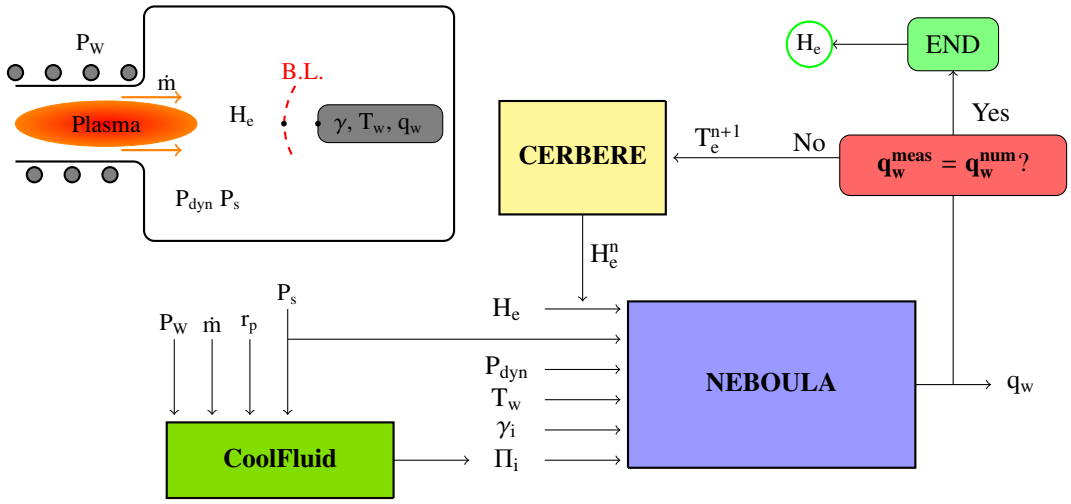

Figure 2: Conventional enthalpy rebuilding workflow for the plasma jet characterization in the Plasmatron. The same workflow applies to the case when we want to estimate γ_i instead of H_e, being the latter known or assumed.

As both materials should play the same role in the inference problem, a likelihood function accounting for the whole set of available measurements was designed, including reference probes and TPS material catalytic properties. This likelihood function quantifies the amount of information carried by the measurements to the Quantities of Interest (QoI) and it measures the compatibility between the measurements and the value of unknown model parameters, such as the recombination parameters. Nevertheless, this likelihood function has two problems. First, the model predictions of q_{wi} do no solely depend on $\gamma_{Qz}, \gamma_{TPS}$ and γ_{Cu} but also on the boundary layer edge enthalpy, H_e. Second, H_e is not predicted by the model, i.e., is not one of its outputs, but instead is an input of the model (as represented in Fig. 2). To tackle these issues, the model inputs that maximize the likelihood function were determined. Assuming that the available measurements are independent unbiased Gaussian, the likelihood function developed takes the form

$$L^{opt}(M|\gamma_{Qz},\gamma_{TPS},\gamma_{Cu}) \propto \exp\left[-\frac{|P_s^{meas}-P_s^{opt}|^2}{2\sigma_{P_s}^2}\right]\exp\left[-\frac{|P_{dyn}^{meas}-P_{dyn}^{opt}|^2}{2\sigma_{P_{dyn}}^2}\right] \prod_{i\in Qz,TPS,Cu}\exp\left[-\frac{|q_{wi}^{meas}-q_{wi}^{opt}|^2}{2\sigma_{q_w}^2}-\frac{|T_{wi}^{meas}-T_{wi}^{opt}|^2}{2\sigma_{T_w}^2}\right] \tag{5}$$

where $H_e^{opt}, P_s^{opt}, P_{dyn}^{opt}, T_{wi}$ are the quantities that maximize the likelihood function and q_{wi}^{opt} the corresponding predictions of the heat fluxes for the three material samples. These optimal quantities are only function of the three material properties $\gamma_{Qz}, \gamma_{TPS}$ and γ_{Cu}.

The optimization process for this task is the Nelder-Mead algorithm [17]. However, applying an optimization method prevents from using directly this approach to sample the posterior distribution due to high computational time. Each point of the sampling space is the result of an optimization procedure which takes in of the order of hundred realizations of the numerical solver. To overcome this limitation, a surrogate model for the log-likelihood of the problem was built.

3.2.2. *Surrogate modeling and sampling of the posterior distribution*

The surrogate model is built by considering the log-likelihood as a function of the log-variables, $\log_{10}\gamma_{Qz}$, $\log_{10}\gamma_{TPS}$ and $\log_{10}\gamma_{Cu}$, using Gaussian Processes (GP). It is considered this way due to smoothness of the approximated function (log-likelihood as function of the log-variables) while sharing the behavior and optimal values as the original likelihood function. Due to their statistical nature, GP provide both a prediction of the approximated function and a measure of the uncertainty (variance) in the prediction. To this end, three dimensional grid in the plane of the log-variables is considered and the corresponding values of the log-likelihood evaluated. In this case, the choice of sampling the QoIs space is by using Latin Hypercube Sampling (LHS) techniques [18], together with a sequential approach to the posterior sampling. This approach starts with a LHS sparse grid upon which the first GP surrogate is built [19]. The GP surrogate is used in place of the exact likelihood function to sample the posterior distribution by means of

the Metropolis-Hastings algorithm [20]., a flavour of Markov Chain Monte Carlo (MCMC) [20]. In subsequent iterations of this procedure, the additional sampling domain can become smaller, focusing only on the part of the 3D domain where MCMC is drawing samples from, refining the accuracy of the GP in that part. The stopping criteria is chosen when the standard deviation of the GP, used as a measurement of its error, is less than 1% the mean value. It was concluded that GP yield good results with low standard deviations on the chain samples. Moreover, the approach is robust, meaning that the MCMC sampling method works smoothly for any given conditions.

4. Results and discussion

In this section, the methodology previously discussed is applied for experimental cases performed at the VKI Plasmatron. All these cases are analyzed under the Bayesian framework to characterize the catalysis behavior of the CMC material with the experimental results obtained in this work.

4.1. Test conditions

To proceed with the experiments, the Plasmatron is switched on and the air mass flow is set with a calibrated rotameter. The vacuum pumps are then regulated until the target static pressure is reached inside the chamber. After that, the probe with the copper calorimeter is injected into the plasma and power is regulated according to the target heat flux being measured, displayed and recorded in real-time. Once the calorimeter reaches a steady-state signal under the imposed conditions, the probe is removed from the plasma jet and that holding the quartz calorimeter is introduced. The heat flux is measured and the injection/ejection process is repeated for the TPS sample. Tables 1 and 2 summarize the experimental testing conditions and associated uncertainties based on the tests carried out with the setup depicted in Sec. **??**.

These experimental test cases are chosen to study the impact of changing the heat flux for the same pressure. Hence, heat fluxes of 500, 700 and 900 kW/m^2 are tested. Additionally, a higher static pressure (100 mbar) is tested for the same heat fluxes. Thereafter, the impact of changing heat fluxes and pressures can be compared in the posterior analysis. These cases are representative of material behaviors of copper, quartz and TPS yielding good posterior distributions for the TPS material. Therefore, they are chosen along with additional conditions for a comprehensive study of the catalysis phenomena.

In the tests performed for this work, the static pressure was not recorded. Hence, a ±10% uncertainty is considered, due to the stability of the pump regulating the vacuum conditions. This assumption was previously applied by different authors working on the Plasmatron as Panerai [5], Viladegut [6] and Fagnani [21]. Uncertainties estimates for the wall temperature are also taken from Helber [22].

For the cold wall heat fluxes, there are experimental uncertainties associated with the measurement chain (MC) used in the Plasmatron. According to Bottin [8], for the cold wall heat flux, the uncertainty estimate due to this chain is given by

$$\delta q_{(i)}^{MC} = \frac{0.089}{2} q^{(i)}, \tag{6}$$

where (i) are both copper and quartz and $q_{(i)}$ the corresponding final heat flux. However, these measurements are performed for a given time with a given frequency and then averaged over the selected points that are considered as relevant. Due to this procedure, there is an associated uncertainty associated to the fluctuations of measurements over time. These type of uncertainties are computed as

$$\delta q_{(i)}^{fluct} = \frac{\sigma_{q_{(i)}}}{\sqrt{N}}, \tag{7}$$

where $\sigma_{q_{(i)}}$ is the standard deviation of the finite number of selected points to average the heat flux and N the number of those selected points. As the number of points is not infinite, a normal distribution cannot be assumed. Thereafter, a t-Student distribution should be taken into consideration when computing the confidence interval. The final uncertainty for the heat flux is computed as

$$\delta q_{total} = \sqrt{\left(q_{(i)}^{MC}\right)^2 + \left(q_{(i)}^{fluct}\right)^2} \times t_{factor}, \tag{8}$$

where t_{factor} is the t-Student factor considering a 95% confidence interval for the number of degrees of freedom of the measurement (N-1).

The same procedure is followed for the dynamic pressure yielding the results depicted in Table 2. Hot wall measurement uncertainties are computed as a results of applying Taylor expansions to the radiative equilibrium condition $q_w^{TPS} = \sigma_B \varepsilon (T_w^{TPS})^4$, where the uncertainties associated with the emissivity are computed through Taylor expansions applied to Eq. 2.

4.2. Experimental and numerical results

From all the experimental conditions, three of them, MTAt1, MTAt2 and MTAt4, are chosen to be high-

Table 1: Plasmatron test conditions (15, 50 and 100 hPa, atmospheric air): targetted cold wall heat flux $q_{cw}^{Cu,ref}$, dynamic pressure P_{dyn}, mean cold wall heat fluxes q_{cw}^{i}, mean surface temperature T_w^{TPS}

Test case	P_s (mbar)	$q_{cw}^{Cu,ref}$ (kW/m^2)	P_{dyn} (Pa)	q_{cw}^{Cu} (kW/m^2)	q_{cw}^{Qz} (kW/m^2)	q_w^{TPS} (kW/m^2)	T_w^{TPS} (K)
MTAt1	15	500	121.48	493.57	219.35	227.79	1462.9
MTAt2	15	700	160.31	702.76	317.90	346.48	1631.0
MTAt3	15	900	196.6	898.39	374.13	417.23	1698.4
MTAt4	50	700	37.40	694.22	258.18	324.75	1585.6
MTAt5	100	500	13.60	492.56	251.00	302.49	1566.5
MTAt6	100	700	16.60	691.56	277.38	381.94	2655.8
MTAt7	100	900	19.62	892.48	337.04	470.45	1741.4

Table 2: Experimental conditions uncertainties

Test case	P_s (mbar)	δP_s (mbar)	δP_{dyn} (Pa)	δq_{cw}^{Cu} (kW/m^2)	δq_{cw}^{Qz} (kW/m^2)	δq_w^{TPS} (kW/m^2)	δT_w^{TPS} (K)
MTAt1	15	0.15	2.31	43.87	19.43	21.37	21.94
MTAt2	15	0.15	2.52	62.60	28.43	32.55	24.46
MTAt3	15	0.15	2.39	79.76	33.29	39.14	25.47
MTAt4	50	0.50	2.64	61.19	22.86	30.50	23.78
MTAt5	100	1.00	2.50	43.54	22.20	28.37	23.49
MTAt6	100	1.00	2.54	61.02	24.58	35.83	24.83
MTAt7	100	1.00	2.58	79.10	29.90	44.13	26.12

light. These three conditions present different tendencies and quality of the results that make them worth exploring in more detail. The analysis of the other cases tested in the context of this work fit well within any of these three tendencies.

4.2.1. MTAt1 results and analysis

Starting with MTAt1, Fig. 3 illustrates the S-curves for this experimental condition. As previously explained, for a 3-probes methodology, the possible enthalpy range varies between the maximum enthalpy for quartz and the minimum enthalpy for copper. In this case, this range is narrow, defining, consequently, a narrow range of the TPS catalytic parameter.

The samples that maximize the likelihood function and, consequently, used for the construction of the posterior distributions are represented in Fig. 4, together with the S-curves and respective 2σ uncertainties limits. As the majority of the samples belong inside these limits, the inference is successful.

The TPS posterior distribution (Fig. 5) presents a peak at around 0.015, with a wide range of possible values, varying between 0.001 and 0.06. Simultaneously, the other two parameters present a flat distribution for low catalysis and high catalysis, respectively, for quartz and copper. This flatness is due to the part of the S-curves where the computed samples lay on. Catalysis values higher than 0.007 are excluded for quartz and values lower than 0.01 excluded for copper.

The enthalpy distribution (Fig. 6) also presents a very wide range of possible values as the information of the free stream is not captured well enough.

4.2.2. MTAt2 results and analysis

Following the detailed analysis, the S-curves presented in Fig. 7 are very closed together, yielding a very similar behavior of copper and quartz and, consequently, a very wide range of values for the enthalpy. For this case, 95% of the MCMC samples computed fit inside the 2σ uncertainty limits (Fig. 8).

Due to the wide range of possible values for the enthalpy, the values that maximize the likelihood function are spread around the sampling space and, consequently, the TPS marginal distribution presents a bimodal distribution with two peaks (Fig. 9), as well as the enthalpy distribution (Fig. 10). From the shape of these distributions, the points with higher probability of occurring fall into two different groups, decreasing the probability density among them. For this case, the TPS material admits recombination parameters between 0.001 and 0.05, with two peaks at 0.007

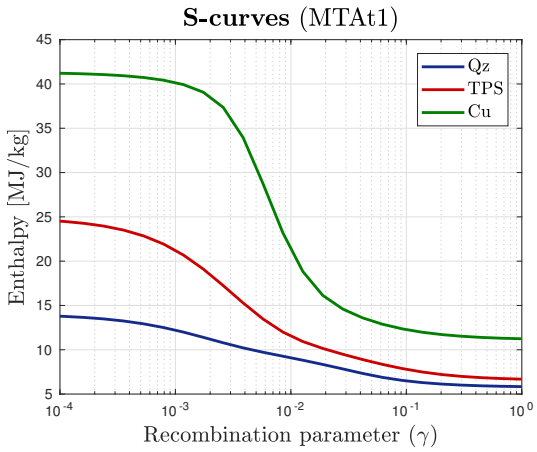

Figure 3: S-curves computed by the boundary layer solver as a relationship between the two unknowns of the rebuilding: H_e and γ

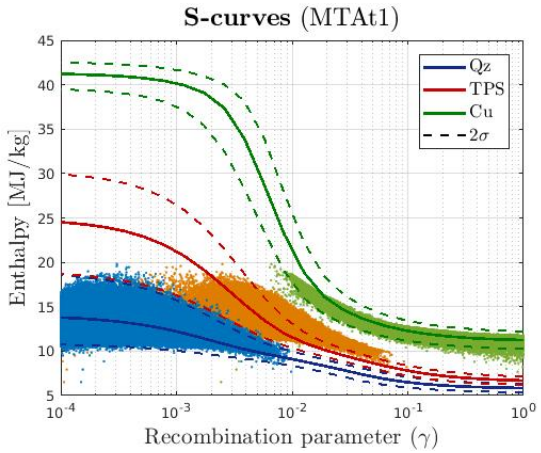

Figure 4: S-curves variability due to measurement uncertainties

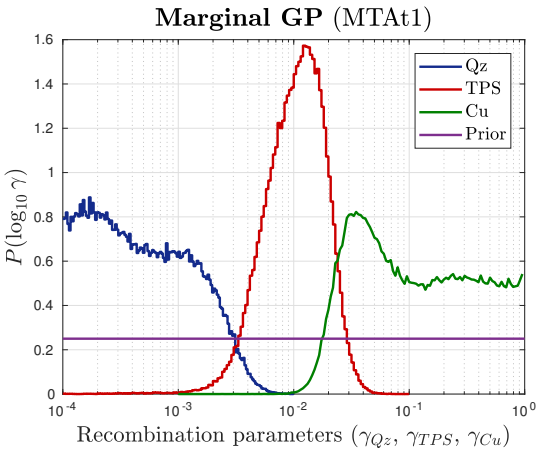

Figure 5: Marginal posterior distributions for the recombination parameters of the three probe materials

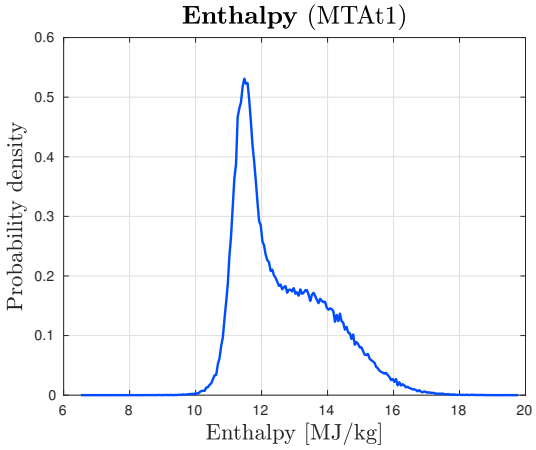

Figure 6: Resulting enthalpy distribution for the free stream flow

and 0.02, the latest having higher probability. Due to the increased overlapping, the points of the reference materials are shifted towards the steep part of the S-curves, translating into a more peaky behavior in the posteriors. The peaks are found at $\gamma_{Cu} \approx 0.015$ and $\gamma_{Qz} \approx 0.005$. Catalysis parameters lower than 0.006 and higher than 0.02 are excluded, respectively, for copper and quartz.

The results concerning the test case of MTAt3 are qualitatively similar to the case of MTAt2. Marginal posterior distributions are yielded for the three catalytic parameters as seen in Fig. 11, with a similar spread in the enthalpy distribution (Fig. 12). This is due to the overlap of the S-curves in the enthalpy sense. MTAt2 and MTAt3 share the order of magnitude of this overlap, yielding the same qualitative inference results.

4.2.3. MTAt4 results and analysis

Figure 13 presents the S-curves for the fourth experimental case and, apparently there is no solution for the enthalpy. The uncertainties associated with the measurements can account for these discrepancies.

To analyse the viability of the results, the samples that maximize the likelihood function and that are used for the construction of the posterior distribution are plotted together with the S-curves and the 3σ uncertainty limits (Fig. 14). For this 99% confidence interval, less than 1% of the points are outside of the limits and, hence, the inference is successful and the uncertainty measurements can account for these discrepancies.

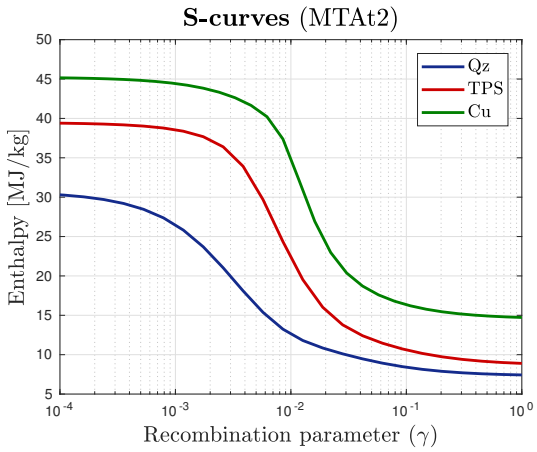

Figure 7: S-curves computed by the boundary layer solver as a relationship between the two unknowns of the rebuilding: H_e and γ

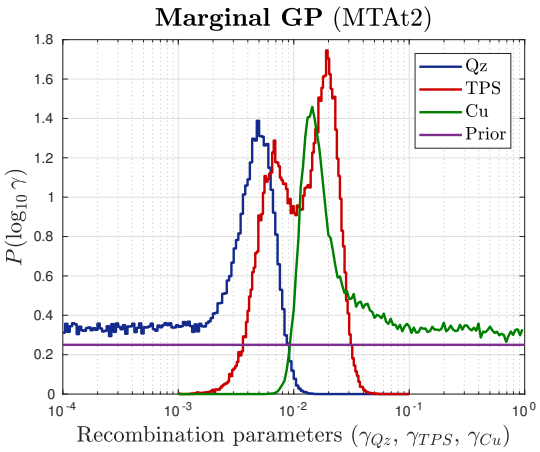

Figure 9: Marginal posterior distributions for the recombination parameters of the three probe materials

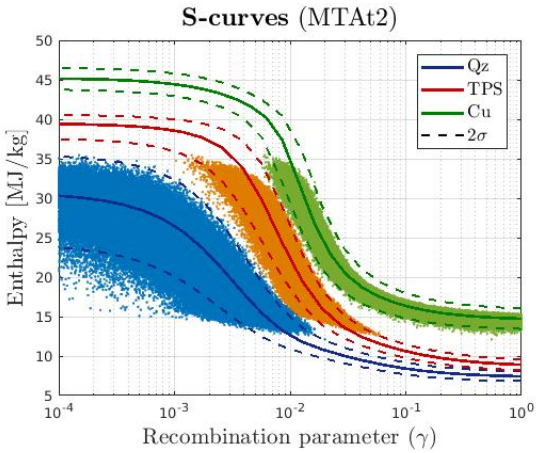

Figure 8: S-curves variability due to measurement uncertainties

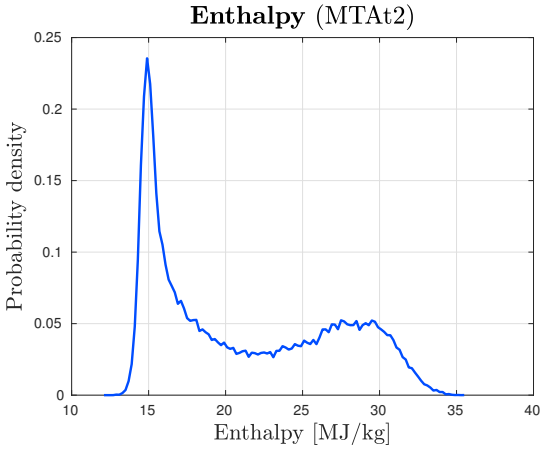

Figure 10: Resulting enthalpy distribution for the free stream flow

From the chain samples (Fig. 14) and the posterior distribution (Fig. 15), the range of values for γ_{TPS} varies between 0.002 and 0.01, with a very well-defined peak at $\gamma_{TPS} = 0.005$.

For the reference materials, the possible values for γ are also contained in a narrow region, being values higher than 0.001 and lower than 0.02 excluded, respectively, for quartz and copper. As the samples for these materials lay in the flat part of the respective S-curve, the most peaky part of the posterior distribution occurs at the lowest and highest extremes, respectively, for quartz and copper.

As the posterior distribution for the TPS is very well-defined, the enthalpy distribution (Fig. 16) resembles a Gaussian distribution with possible values varying between a narrow range.

The results concerning the test case of MTAt5 are qualitatively similar to the ones from case MTAt4. The marginal posterior distributions for the three catalytic parameters are represented in Fig. 17 with a similar spread in the enthalpy distribution (Fig. 18) as in case MTAt4.

Taking this overlap a little further apart is where MTAt6 and MTAt7 lay. For these two cases the inference is not reliable and results are not physical as the points fall out of the limits for the measurement uncertainties. For this reasons these test cases are not analysed here.

4.3. Discussion of obtained distributions

The study of the recombination parameter of a TPS material in the VKI Plasmatron facility requires the

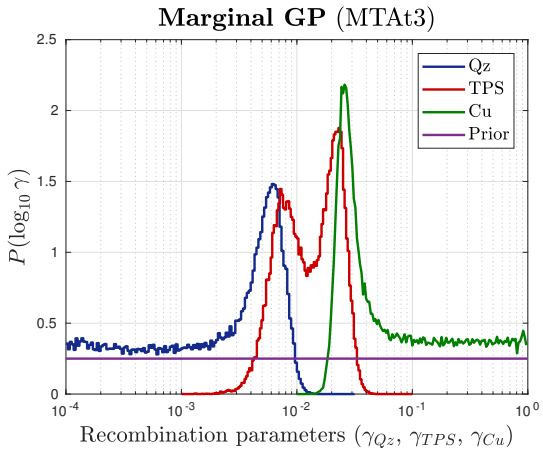

Figure 11: Marginal posterior distributions for the recombination parameters of the three probe materials

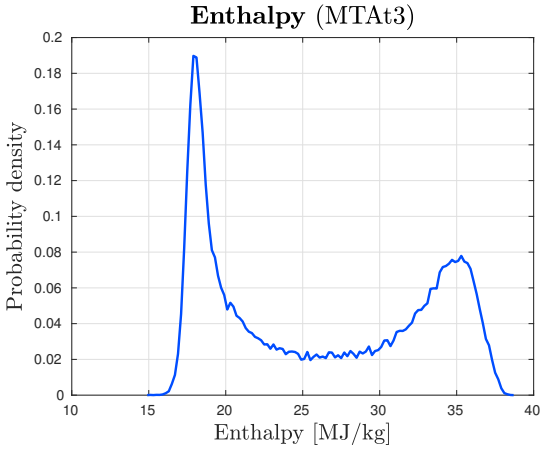

Figure 12: Resulting enthalpy distribution for the free stream flow

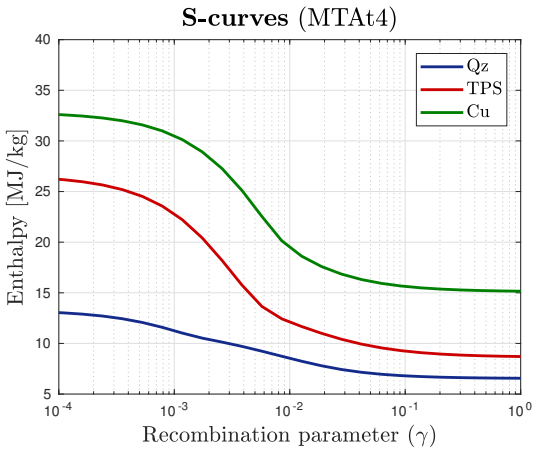

Figure 13: S-curves computed by the boundary layer solver as a relationship between the two unknowns of the rebuilding: H_e and γ

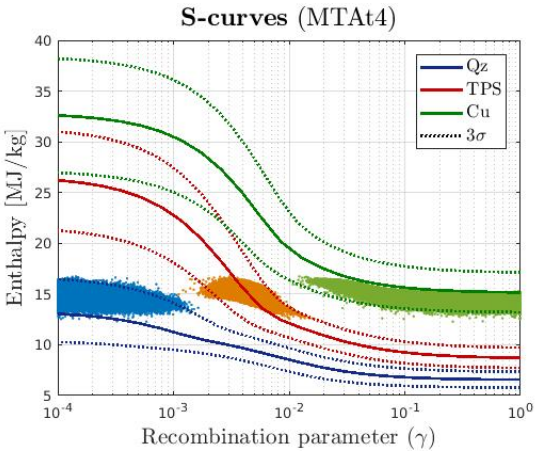

Figure 14: S-curves variability due to measurement uncertainties

use reference probes (two, according to the methodology followed) which, together with the sample material of interest, are subjected to the same plasma flow. Hence, the enthalpy of the flow is the same for all the probes. This represents the cornerstone of this study, where assumptions can be relaxed based on the fact that the enthalpy seen by all the probes are the same for the given conditions.

To compute the relationship between the boundary layer edge enthalpy and the catalytic parameter, the measurements obtained during the experiments are used as variables for the boundary layer code depicted before. This relationship presents a S-shape, since higher catalysis parameters lead to a lower enthalpy due to the higher effective atoms recombination implying lower energy content on the free stream. From these S-curves, the range of values possible for the enthalpy can be estimated: the minimum enthalpy corresponds to the maximum enthalpy possible for the material with lower catalytic properties and the maximum enthalpy corresponds to the minimum enthalpy of the material with higher catalytic properties.

As there are uncertainties associated with the measurements and model parameters, the S-curves also have uncertainty limits where the actual curve is contained within. These limits are computed considering the uncertainty of the heat fluxes and wall temperatures. The influence of the static and dynamic pressures uncertainties is not considered since these pressures play a minor role due to their small uncertainties. Moreover, they are common quantities to the

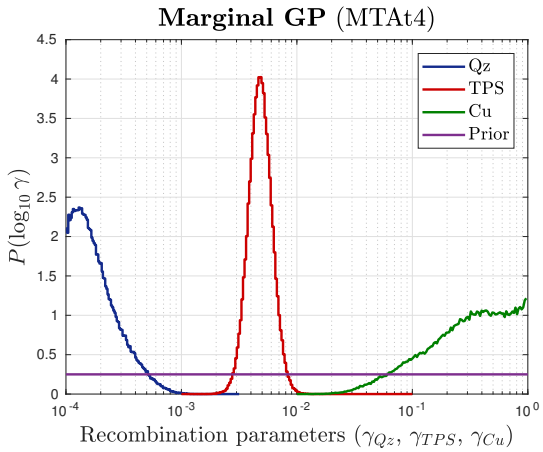

Figure 15: Marginal posterior distributions for the recombination parameters of the three probe materials

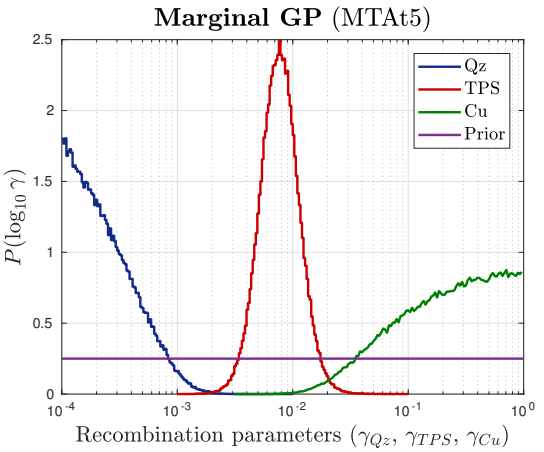

Figure 17: Marginal posterior distributions for the recombination parameters of the three probe materials

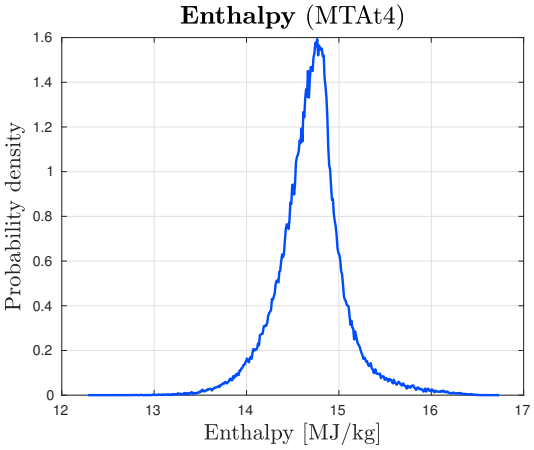

Figure 16: Resulting enthalpy distribution for the free stream flow

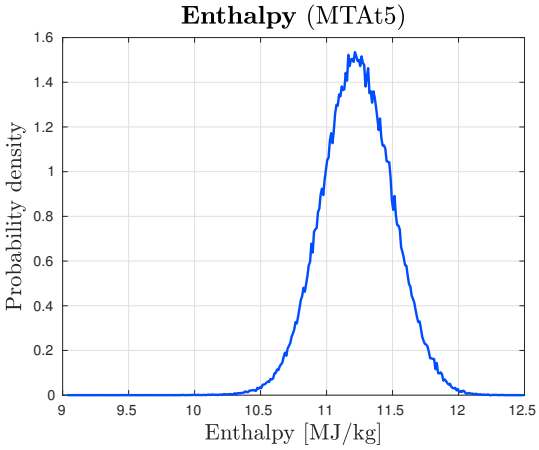

Figure 18: Resulting enthalpy distribution for the free stream flow

three materials, thus, when they change, all curves move together, leaving the problem of the inference unchanged. Thereafter, the upper limit of the S-curve is computed with the maximum wall heat flux and wall temperature estimated considering their uncertainties and the lower limit computed with their minimum values.

The uncertainties from Table 2 correspond to a 2σ uncertainty level, meaning that are computed with a 95% confidence interval, being only the 5% of the samples outside of this range. When this interval is small for the solution to lay on, 3σ uncertainty limits are also computed, i.e., a 99% confidence interval.

To study the influence of pressure and heat flux on the TPS recombination parameter, reference heat fluxes for copper of 500, 700 and 900 kW/m^2 for static pressures of 15 and 100 mbar, and also 700 kW/m^2 for 50 mbar are analysed, relying on the values measured at the Plasmatron facility. The mean value for the recombination parameters of the TPS material and enthalpy, and extremes for a 95% confidence interval are summarized in Tables 3 and 4. These extremes are the results of the k th percentile: the lower piece of the distribution contains k% of the data and the upper piece contains (100-k)%. Hence, for a 95% confidence interval, the 2.5th and 97.5th percentiles leave, respectively, 2.5% of the data below and 2.5% beyond the respective point.

For the lowest pressure (P_s = 15mbar) and higher reference heat fluxes (700 and 900 kW/m^2), these cases depict a bimodal posterior distributions for the TPS material. In each case, both peaks match best the

Table 3: TPS material posterior distribution mean values and respective 2.5th and 97.5th percentiles.

Test case	2.5th γ_{TPS}	Mean γ_{TPS}	97.5th γ_{TPS}
MTAt1	0.0029	0.0120	0.0276
MTAt2	0.0036	0.0134	0.0289
MTAt3	0.0044	0.0147	0.0303
MTAt4	0.0030	0.0049	0.0076
MTAt5	0.0035	0.0083	0.0167

Table 4: Enthalpy distribution mean values and respective 2.5th and 97.5th percentiles (in MJ/kg).

Test case	2.5th H_e	Mean H_e	97.5th H_e
MTAt1	10.8492	12.5977	15.6939
MTAt2	14.3012	21.0952	31.6738
MTAt3	17.3042	26.0089	36.6972
MTAt4	13.9420	14.6995	15.5160
MTAt5	10.7070	11.2314	11.7568

numerical equations, obeying the rebuilding condition $q_{meas} = q_{num}$. This phenomena is caused by the wide range of values possible for the enthalpy and can be caused by epistemic uncertainties. To improve the results under these testing conditions, a better prior distribution for copper and quartz can be used, based on knowledge from previous works.

Due to these bimodal distributions, the samples with higher probability fall into two different groups, decreasing the probability density among them. Consequently, they also present a wide standard deviation for TPS and enthalpy distributions. This phenomena can be analysed in Fig. 19, where the enthalpy for the three first test cases are represented. From this figure, as the range of possible enthalpy becomes wider (for higher heat fluxes), the maximum probability peak decreases and the second peak increases. Moreover, as expected, when the reference heat flux increases, also the mean enthalpy of the flow increases (as also concluded from Table 4).

Figure 20 illustrates the variation of the TPS distribution when the reference heat flux is increased, for the lowest static pressure tested (P_s = 15mbar). Under this condition, all three distributions present a similar range of possible values for the recombination parameter and a very similar mean (see Table 3). Hence, one can conclude that for low pressures, the TPS catalytic parameter is not influenced by the enthalpy of the flow.

For the last three experimental cases, the static pressure corresponds to 100 mbar. Under this condition, the separation between the S-curves is higher. In fact, even with a 99% confidence interval, only for the lowest heat flux (q_{ref} = 500kW/m^2) there is a range of enthalpy possible. For this case, the TPS posterior distribution presents a well-defined peak as the samples lay on a high gradient zone of the S-curve. As the posterior distribution is well-defined also the enthalpy distribution presents a well-defined peak, with low standard deviation.

Even though the first three test cases present a solution, for low pressure the LTE assumption for the boundary layer edge is questionable. At low pressure, there is a small amount of chemical reactions occurring, hence, the number of collisions may not be enough to reach equilibrium. Nevertheless, in each

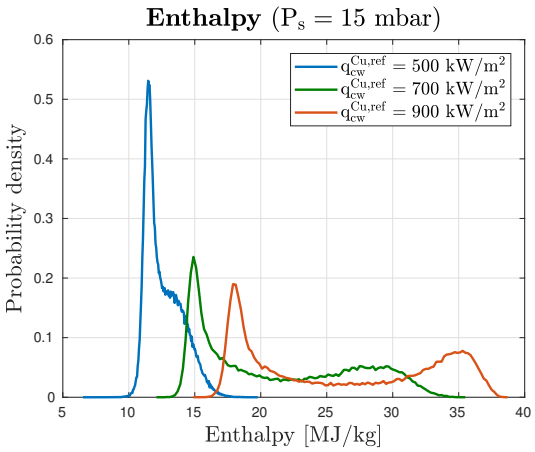

Figure 19: Variation of enthalpy distribution with reference heat flux, for P_s = 15 mbar.

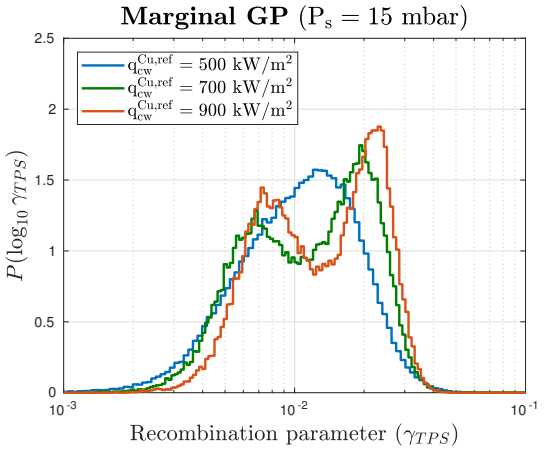

Figure 20: Variation of TPS distribution with reference heat flux, for P_s = 15 mbar.

experimental test, the three probes are under the same flow being the error committed by this assumption similar in order of magnitude for all the results and, therefore, does not affect much the result for γ.

When comparing the evolution of the TPS distribution with the pressure for the same reference heat flux (Figs. 21 and 22), and even though enthalpies are different, as a first conclusion, one can see that the mean value for the recombination parameter decreases as the pressure increases. This increase of pressure causes more recombinations in the gas and influences the diffusion process, consequently diminishing the recombination at the wall and, thereafter, decreasing the mean value of the recombination parameter that explains the experimental data.

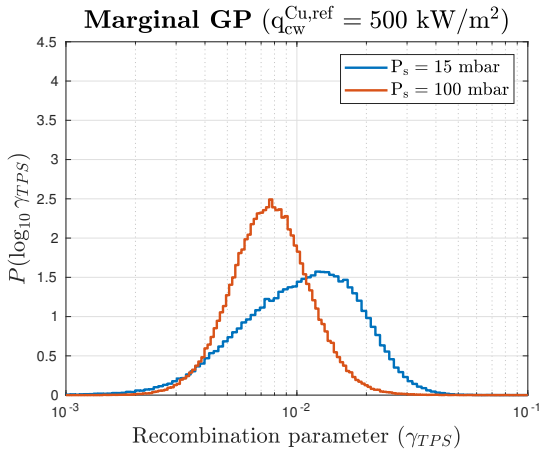

Figure 21: Variation of TPS distribution with static pressure for $q_{cw}^{Cu,ref} = 500$ kW/m^2.

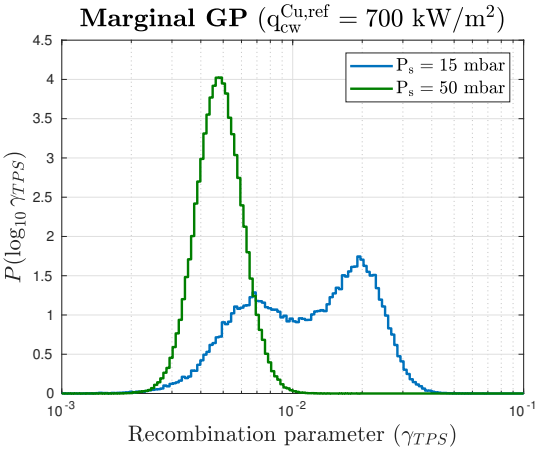

Figure 22: Variation of TPS distribution with static pressure for $q_{cw}^{Cu,ref} = 700$ kW/m^2.

For the cases where there is no apparent solution for the enthalpies, the majority of the samples for the reference materials lay outside of the uncertainty limits, hence the solutions violate the variability of the measurements. For each of these cases, the distributions for q_{meas} and q_{num}, for both copper and quartz, do not match. Even though the TPS distributions match, i.e $q_{meas} = q_{num}$, the reference materials do not have a successful inference, hence the overall inference cannot be trusted.

In the event of non-existence of a solution for the enthalpy, the likelihood algorithm tries to fit the measurements with the points with lowest error, even though further apart than what is expected from the uncertainties. Although the samples computed are the best fit for the numerical models, they are not good enough to match the heat flux distributions and the results are not physical. In these cases (at high static pressures), there is a plentiful of chemical reactions occurring in the boundary layer. In fact, Panerai [5] compared different chemical models when constructing the S-curves and, for high pressures, the model chosen influences these curves considerably. Thereafter, the chemical models implemented in the numerical solvers are not good to capture the physics underlying the flow characteristics.

5. Concluding remarks

Experiments in the Plasmatron facility enable characterizing the catalytic properties of a TPS sample by combining direct measurements and a numerical reconstruction based on boundary layer simulations. However, experimental and numerical models are subjected to uncertainties, which must be taken into account during the inference process. The Bayesian inference approach followed in this work combines all set of available measurements to infer the catalytic properties of the ceramic materials considering measurement and model uncertainties.

In this work, a comprehensive study concerning the catalytic properties of thermal protection systems was carried, based on experiments performed at the VKI Plasmatron, under a proper Bayesian inference framework for uncertainties estimation.

This 3-probes testing methodology proved to be a good experimental approach to characterize ceramic materials of typical use in today's spacecraft. The fact that the TPS material laid in between the two materials at the opposite limits of its catalytic behaviour (copper and quartz), made the determination of the CMC material behavior more certain. Overall, the posterior

distributions and enthalpy presented peaky and narrow distributions. For the cases whose S-curves were very close together, the range of possible enthalpies was very wide, making the TPS posterior distributions yield bimodal distributions, due to the similar support given by the similar behavior of each of the materials.

For low static pressures, when varying the reference heat flux and, consequently, the wall heat fluxes, temperatures, enthalpies and flow velocities, all the cases presented TPS posterior distributions with a very similar mean and interval range. Hence, one can conclude that, for the same low pressure, the TPS catalytic parameter is not influenced by the conditions of the flow. When increasing the static pressure, the distance between the S-curves increases, leading to non-existence of a solution, meaning that the catalytic properties cannot be inferred. In these cases, the chemical models implemented in the numerical solvers are not good to capture the underlying chemical reactions occurring in the boundary layer. For the same reference heat flux, when increasing the pressure, the catalytic parameter of the TPS material decreases, as expected. This increase of pressure leads to more recombination in the gas and, consequently, to less recombination at the wall.

Overall, the Bayesian inference framework proved to be a reliable way of characterizing ceramic materials with proper uncertainty distributions. In this approach, no assumptions are made concerning the reference materials (copper and quartz), which are estimated together with the TPS material parameter with no differences in their prior knowledge. Additionally, no assumptions are made for the enthalpy of the flow, being the distribution of this parameter also estimated during the rebuilding process.

Acknowledgments

This work is partially funded by the European Commission H2020 programme, through the UTOPIAE Marie Curie Innovative Training Network, H2020-MSCA-ITN-2016, Grant Agreement number 722734.

References

[1] O. Chazot, F. Panerai, High enthalpy facilities and plasma wind tunnels for aerothermodynamics ground testing in: Hypersonic Nonequilibrium Flows: Fundamentals and Recent Advances, Ed. Eswar Josyula ARLF, 2015.

[2] T. Magin, A model for inductive plasma wind tunnels, Ph.D. thesis, ULB/VKI (2004).

[3] B. Laub, E. Venkatapathy, Thermal protection system technology and facility needs for demanding future planetary missions, in: Proceedings of international workshop on planetary probe atmospheric entry and descent trajectory analysis and science, 2004, pp. 239 – 247.

[4] R. Goulard, On catalytic recombination rates in hypersonic stagnation heat transfer, Journal of Jet Propulsion 28 (11) (1958) 737–745.

[5] F. Panerai, Aerothermochemistry characterization of thermal protection systems, Ph.D. thesis, von Karman Institute for Fluid Dynamics and Università degli Studi di Perugia (2012).

[6] A. Viladegut, Assessment of gas-surface interaction modelling for lifting body re-entry flight design, Ph.D. thesis, von Karman Institute for Fluid Dynamics and Universitat Politècnica de Catalunya (2017).

[7] F. Sanson, F. Panerai, T. E. Magin, P. M. Congedo, Robust reconstruction of the catalytic properties of thermal protection materials from sparse high-enthalpy facility experimental data, Experimental Thermal and Fluid Science 96 (2018) 482492.

[8] B. Bottin, O. Chazot, M. Carbonaro, V. Van Der Haegen, S. Paris, The VKI Plasmatron characteristics and performance, Measurement Techniques for High Enthalpy and Plasma Flows.

[9] B. Bottin, Aerothermodynamic model of an inductively-coupled plasma wind tunnel: Numerical and experimental determination of the facility performance, Ph.D. thesis, von Karman Institue for Fluid Dynamics (1999).

[10] B. Helber, Calibration curves, private communication.

[11] A. Lani, N. Villedieu, K. Bensassi, L. Kapa, M. Vymazal, M. S. Yalim, M. Panesi, COOLFluiD: an open computational platform for multi-physics simulation and research, in: 21st AIAA Computational Fluid Dynamics Conference, San Diego, CA, 2013.

[12] D. LeQuang, Spectroscopic measurements of sub- and supersonic plasma flows for the investigation of atmospheric reentry shock layer radiation, Ph.D. thesis, von Karman Institute for Fluid Dynamics and Université Blaise Pascal (2014).

[13] G. Degrez, P. Barbante, M. de la Llave, T. Magin, O. Chazot, Determination of the catalytic properties of TPS materials in the VKI ICP facilities, in: European Congress on Computational Methods in Applied Sciences and Engineering - ECCOMAS Computational Fluid Dynamics Conference, Swansea, Wales, UK, 2001.

[14] P. F. Barbante, Accurate and efficient modelling of high temperature nonequilibrium air flow, Ph.D. thesis, von Karman Institute for Fluid Dynamics and Université Libre de Bruxelles (2001).

[15] F. Sanson, N. Villedieu, F. Panerai, O. Chazot, P. M. Congedo, T. E. Magin, Quantification of uncertainty on the catalytic property of reusable thermal protection materials from high enthalpy experiments, Experimental Thermal and Fluid Science 82 (2017) 414–423.

[16] D. S. Sivia, J. Skilling, Data Analysis: A Bayesian tutorial, Oxford Science Publications, 2006.

[17] J. A. Nelder, R. Mead, A simplex method for function minimization, Computer Journal 7 (4).

[18] M. D. McKay, R. J. Beckman, W. J. Conover, A comparison of three methods for selecting values of input variables in the analysis of output from a computer code, Technometrics 21 (2) (1979) 239–245.

[19] C. E. Rasmussen, C. K. I. Williams, Gaussian Processes for Machine Learning, the MIT Press, 2006.

[20] J. Kaipio, E. Somersalo, Statistical and Computational Inverse Problems, Springer-Verlag, 2005.

[21] A. Fagnani, Plasma testing methodology for demise phenomena analysis, Project report, von Karman Institute for Fluid Dynamics (June 2018).

[22] B. Helber, Material response characterization of low-density ablators in atmospheric entry plasmas, Ph.D. thesis, von Karman Institute for Fluid Dynamics and Vrije Universiteit Brussel (January 2016).

Gradient-informed sampling of Bayesian posteriors in probabilistic inversion of pyrolysis models

Joffrey Coheur

Aeronautics and Aerospace Department, von Karman Institute for Fluid Dynamics, Belgium, joffrey.coheur@vki.ac.be

Supervisor: Thierry Magin

Professor, Aeronautics and Aerospace Department, von Karman Institute for Fluid Dynamics, Belgium, magin@vki.ac.be

University Supervisor: Maarten Arnst

Assistant Professor, Aerospatial & Mechanical Engineering, Université de Liège, Belgium, maarten.arnst@uliege.be

University Supervisor: Philippe Chatelain

Professor, Institute of mechanics, materials and civil engineering, Université catholique de Louvain, Belgium, philippe.chatelain@uclouvain.be

Abstract

We compare two gradient-informed Markov chain Monte Carlo algorithms, namely the Hamiltonian Monte Carlo (HMC) and the Itô stochastic differential equation (Itô-SDE) methods for sampling Bayesian posterior probability density functions (PDFs) in probabilistic inversion of pyrolysis models. In order to sample efficiently, we use a change of measure based either on the support of the posterior PDF or directly on the pyrolysis models and a change of scales that is based on an estimate of the posterior covariance that is adapted iteratively. We show that the adaptation procedure improves significantly the convergence towards the PDF and is robust to an inaccurate estimate of the initial posterior covariance matrix. In the absence of the change of measure or the adaptation of the estimate of the posterior covariance (when applying the change of measure based on the support of the posterior PDF) convergence toward the PDF is slow, thus emphasizing the need for both a change of measure and a change of scales.

Keywords: inverse problem, Bayesian, chemical kinetics, pyrolysis, thermal protection materials

1. Introduction

Ablative porous thermal protection materials (TPMs) are used for the heat shield of spacecraft of extra-orbital high-velocity entry missions. They can accommodate the high heating rates and heat loads encountered during hypersonic entry ([1]) through phase change and mass loss ([2]). First, the resin is progressively pyrolyzed, producing pyrolysis gases that percolate through the material and leave a carbonaceous residue on the fibers, the char. Then, this charred material is ablated simultaneously by heterogeneous chemical reactions, sublimation, and mechanical erosion.

Although baseline predictions are nowadays performed using high-fidelity simulation tools, the estimation of their associated uncertainties has received less attention. The first step for the quantification of uncertainty in numerical simulations is the characterization of input uncertainties by means of probability density functions (PDFs) that rely on experimental data; these PDFs can then be propagated through numerical solvers to assess error margins. This paper investigates gradient-informed sampling methods for complex PDFs obtained from the parameter inference relevant to pyrolysis experiments for thermal protection materials.

1.1. Literature review

Studies on ablative materials date back to the 60's with the development of early material response codes ([3; 4]) based on the experiments of [5] and [6]. Since then, these materials have been investigated from both the numerical and the experimental perspective. For predicting the material thermal decomposition, current models are still based on those previous experiments, although nowadays computer solvers allow the use of more accurate models ([7; 8; 9; 10; 11; 12; 13]). Several experiments have been carried out more recently to get new insight into the pyrolysis of the resin ([14; 15; 16; 17; 18; 19]) and improve models for numerical solvers. In particular, there have been several efforts to infer the kinetic parameters in order to update the models based on these recent experiments. Most of the inference is performed in a deterministic framework, mainly by using optimization solvers to obtain best-fit estimates ([20]). For the application to TPMs, Torres-Herrador ([21]) performed deterministic optimization using genetic algorithms in the experiments of [19]. Although those algorithms can be very efficient and the results accurately reproduced the experiments, they do not account for the uncertainty on the parameters stemming from experimental measurement uncertainty, model inadequacy, parameter variability, etc. A correct characterization of those uncertainties is required to obtain a robust estimation of errors in numerical simulations for a better assessment of safety margins.

Investigations on pyrolysis experiments from a stochastic view have been performed for fire technology ([22]) using an adaptive random-walk sampling algorithm. For the pyrolysis of TPMs in aerospace engineering, a first study using Bayesian inference was already applied in [23] for parameter inference of the pyrolysis of phenolic materials using thermogravimetric analysis (TGA) data and gas production curves. In the stochastic framework, rather than optimizing a cost function, we wish to obtain the probability density function of the parameters considering their uncertainties using Bayes formula

$$\pi(\boldsymbol{w}|\boldsymbol{y}^{\text{obs}}) = \frac{\pi(\boldsymbol{y}^{\text{obs}}|\boldsymbol{w})\pi_0(\boldsymbol{w})}{\int_{\mathbb{R}^m} \pi(\boldsymbol{y}^{\text{obs}}|\boldsymbol{w})\pi_0(\boldsymbol{w})d\boldsymbol{w}}, \qquad (1)$$

where $\boldsymbol{w} \in \mathbb{R}^n$ is the vector of input parameters, $\boldsymbol{y}^{\text{obs}} \in \mathbb{R}^d$ the vector of observations, $\pi_0(\cdot)$ the prior density, $\pi(\cdot|\boldsymbol{y}^{\text{obs}})$ the posterior density, and $\pi(\boldsymbol{y}^{\text{obs}}|\cdot)$ the likelihood function.

Bayesian inference applied to general pyrolysis decomposition laws (competitive reactions) is investigated in [24]; however, a slow convergence toward the posterior distribution was observed and attributed to the complex dependence structure of the PDF. The objectives of this paper are therefore to study more efficient sampling algorithms based on either the reparametrization of the posterior PDF or the evaluation of its gradients or both. Gradient-informed algorithms take into account evaluations of the posterior PDF as well as the evaluation of its gradients and can be advantageous for posterior PDFs with complex dependence structure. Of course the evaluation of the gradients increases the computational complexity. The particular case of the application presented here has the advantage that the the solution and its gradient are known analytically. For other applications, methods for computing gradients efficiently are needed (e.g. automatic differentiation).

The model for the pyrolysis reactions applied to the decomposition of thermal protection materials is first presented (Sect. 2). The gradient-based algorithms that are investigated are then presented (Sect. 3) and for this class of algorithms we introduce the change of measure and the change of scale that can be applied in order to improve the convergence of the sampling. Results using those algorithms are presented and their efficiency are then compared (Sect. 4). We consider the case of the experimental data from [19] for the production of a single species, namely CH_4 in order to have a simple application easy for comparison but whose posterior PDF shows a complex structure (correlated and non-Gaussian).

2. Multi-component single-step pyrolysis model

The mathematical description of a general reaction scheme of pyrolysis processes for aerospace applications was introduced in a previous paper [24]. We recall here the notations and the general equations and we specify the hypotheses used for the type of reactions under investigation in this work. Let ρ_i denote the density of component i, with $i = 1, .., n$, which can be either a gaseous product $i \in I_{\mathcal{G}}$ or a solid component (product or reactant) $i \in I_{\mathcal{S}}$, thus $i \in \{I_{\mathcal{S}}, I_{\mathcal{G}}\}$. The number of elements in each set is $|I_{\mathcal{G}}| = n_{\mathcal{G}}$ and $|I_{\mathcal{S}}| = n_{\mathcal{S}}$ respectively with the total number of elements $n = n_{\mathcal{G}} + n_{\mathcal{S}}$. Competitive mechanisms occur on the i-th component ρ_i following the reaction rate $k_{i,j}$ where j is the index for the j-th competitive branch. The number of competitive reactions for the component ρ_i is n_{p_i}. Each reaction may generate more than one product from either $I_{\mathcal{S}}$ or $I_{\mathcal{G}}$, thus stoichiometric

coefficients $\gamma_{i,j,l}$ are introduced. The general reaction scheme writes

$$\frac{d\rho_i}{dt} = \underbrace{-\sum_{j=1}^{n_{\mathrm{p}_i}} k_{i,j}\,\rho_i}_{\text{destruction of } \rho_i} + \underbrace{\sum_{l=1}^{n}\sum_{j=1}^{n_{\mathrm{p}_j}} k_{j,l}\,\gamma_{j,l,i}\,\rho_j}_{\text{production of } \rho_i}. \tag{2}$$

In this work, the following assumptions are made:

1. No competitive reactions ($n_{\mathrm{p}_i} = 1\ \forall i$), which simplifies Eq. 2 to obtain

$$\frac{d\rho_i}{dt} = -k_i\rho_i + \sum_{l=1}^{n} k_l\gamma_{l,i}\rho_l. \tag{3}$$

2. Each fictitious component produces only gas and no other solid component ($\gamma_{l,i} = 0\ \forall l \in I_{\mathcal{S}}$).
3. Gaseous products do not deposit ($\gamma_{l,i} = 0\ \forall i \in I_{\mathcal{G}}$) and there are no secondary reactions (frozen chemistry) among gaseous species ($k_i = 0\ \forall i \in I_{\mathcal{G}}$).

In matrix form, Eq. 3 together with hypotheses 2 and 3 lead to the following system of ODEs:

$$\frac{d\boldsymbol{\rho}_{\mathcal{S}}}{dt} = K\boldsymbol{\rho}_{\mathcal{S}}, \tag{4}$$

where $K = \mathrm{diag}(k_1, k_2, \ldots, k_{n_{\mathcal{S}}})$ and Γ is the $n_{\mathcal{G}} \times n_{\mathcal{S}}$ matrix of coefficients for the production of gaseous species which is given by the right-hand side of Eq. 3 for $i \in I_{\mathcal{G}}$, $l \in I_{\mathcal{S}}$. The fact that K is diagonal, resulting in the independence of each $\rho_i,\ i \in I_{\mathcal{S}}$ from each other, follows from hypothesis 2. Therefore, each differential equation for $i \in I_{\mathcal{S}}$ can be solved independently. The solution for the gaseous product is then found from

$$\frac{d\boldsymbol{\rho}_{\mathcal{G}}}{dt} = K\,\Gamma\boldsymbol{\rho}_{\mathcal{G}}, \quad \text{with } \Gamma = \begin{bmatrix} \gamma_{11} & \gamma_{12} & \cdots & \gamma_{1n} \\ \gamma_{21} & \gamma_{22} & \cdots & \gamma_{2n} \\ \vdots & \vdots & \ddots & \vdots \\ \gamma_{n1} & \gamma_{n2} & \cdots & \gamma_{nn}. \end{bmatrix} \tag{5}$$

Matrix Γ completely defines the finite rate chemistry produced by the decomposition of the solid material and the elements of the matrix are unknowns during the inference process. Kinetic rates appearing in K are modeled using a first-order Arrhenius equation of the form

$$k_i = \mathcal{A}_i \exp(-\mathcal{E}_i/\mathcal{R}T), \tag{6}$$

where $\mathcal{R}$ is the universal gas constant, $\mathcal{A}_i$ is the pre-exponential factor, and $\mathcal{E}_i$ is the activation energy for the i-th reaction. Furthermore, we assume that the reaction rates can be nonlinear with reaction order n_i, and we express the differential equation using an advancement of reaction ξ_i to end up with the widely used formulation

$$\frac{d\xi_i}{dt} = \mathcal{A}_i \exp\left\{\frac{-\mathcal{E}_i}{\mathcal{R}T}\right\}(1-\xi_i)^{m_i}. \tag{7}$$

This equation has an analytical solution for the two experimental set-ups considered in this work, namely constant (piecewise or not) and linear heating rates. Analytical expressions of the Jacobian and gradients are also available and their use in the sampling method significantly speeds up the computational time of each evaluation of the model response and its gradients.

For the pyrolysis decomposition model (Eqs. 3 and 6) the uncertain parameter set is the vector of the calibration parameters $\boldsymbol{w} = \{\mathcal{A}_i, \mathcal{E}_i, \gamma_i\}$. The time (or temperature) in Eq.7 is assumed to be known with certainty from experiments. The experimental data are the total production of species given by

$$\pi(t) = \sum_i \rho_{\mathrm{v}}\gamma_i\tau\partial_T\xi_i \tag{8}$$

where ρ_{v} is the virgin density, τ is the heating rate, and F_i the mass fraction coming from reaction i.

3. Markov chain Monte Carlo methods

A technique that is widely used to sample directly from the posterior distribution, instead of evaluating directly Eq. 1, is the Markov chain Monte Carlo (MCMC) method. Several classical algorithms for constructing Markov chains were presented in [25]. We focus here on gradient-informed methods for generating samples from the posterior distribution. The first method presented (Sect. 3.1) is the Hamiltonian Monte Carlo method and the second one (Sect. 3.2) is the Itô-SDE algorithm. We then present two methods for improving the convergence of the Markov chains using a change of measure (Sect. 3.3) and an additional change of scale (Sect. 3.4).

3.1. Hamiltonian Monte Carlo

References for the Hamiltonian Monte Carlo method can be found in [26; 27]. HMC allows new states to be quite distant from the current state, while nevertheless keeping a high acceptance ratio. This property is particularly advantageous to address issues of slow exploration of the posterior distribution that can be encountered when using a random-walk

proposal distribution. The classical Hamiltonian dynamics describes the conservation of a system characterized by its position $\boldsymbol{p}$ and momentum $\boldsymbol{q}$ which total energy is defined by the Hamiltonian $\mathcal{H}$. The time evolution of the system is uniquely defined by Hamilton's equations

$$\frac{\mathrm{d}p_i}{\mathrm{d}t} = \frac{\partial \mathcal{H}}{\partial q_i} \tag{9}$$

$$\frac{\mathrm{d}q_i}{\mathrm{d}t} = -\frac{\partial \mathcal{H}}{\partial p_i} \tag{10}$$

The Hamiltonian is usually defined as the sum of a potential energy and the total kinetic energy of the system $\mathcal{H}(\boldsymbol{p}, \boldsymbol{q}) = \mathcal{U}(\boldsymbol{p}) + \mathcal{K}(\boldsymbol{q})$. Hamiltonian dynamics possess several properties that are necessary for constructing MCMC updates:

1. reversibility;
2. invariance;
3. symplecticness (in particular, volume preservation).

The numerical solution of the Hamiltonian equations is usually carried out using a discretization scheme that respects volume preservation. The most common scheme is the leapfrog method which leads to the following system of equations

$$q_i\left(t + \frac{\varepsilon}{2}\right) = q_i(t) - \frac{\varepsilon}{2}\frac{\partial \mathcal{U}(\boldsymbol{p}(t))}{\partial p_i}, \tag{11}$$

$$p_i(t+\varepsilon) = p_i(t) + \varepsilon \frac{\partial \mathcal{K}\left(\boldsymbol{q}\left(t + \frac{\varepsilon}{2}\right)\right)}{\partial q_i}, \tag{12}$$

$$q_i(t+\varepsilon) = q_i\left(t + \frac{\varepsilon}{2}\right) - \frac{\varepsilon}{2}\frac{\partial \mathcal{U}\left(\boldsymbol{p}\left(t+\varepsilon\right)\right)}{\partial p_i}, \tag{13}$$

where ε is the time step. The first equation is a half Euler step for the momentum, then one full step using the already computed momentum, then finally an other half step for the momentum with the already computed position.

The potential energy function in the Hamiltonian is related to the probability distribution we wish to sample from. In the Bayesian framework, this will be minus the log of the posterior and the position variable $\boldsymbol{p}$ becomes our variable of interest $\boldsymbol{w}$. The momentum variable remains the same and is used for the Hamiltonian dynamics to work. Potential and kinetic energy of the Hamiltonian thus write

$$\mathcal{U}(\boldsymbol{w}) = -\log(\pi(\boldsymbol{w}|\boldsymbol{y})), \tag{14}$$

$$\mathcal{K}(\boldsymbol{q}) = \frac{1}{2}\boldsymbol{q}^{\mathrm{T}}[M]^{-1}\boldsymbol{q}. \tag{15}$$

where $[M]$ is a symmetric, positive-definite matrix (or "mass matrix"'). Derivatives are $\frac{\partial \mathcal{K}(\boldsymbol{q})}{\partial \boldsymbol{q}} = [M]^{-1}\boldsymbol{q}$ and the derivative of the potential that must be computed numerically or analytically.

Thus, in the Metropolis-Hastings step, the proposal value is obtained from the resolution of the Hamiltonian dynamics. Once the system is solved and we have the new sample value $\boldsymbol{w}^*$, the acceptance ratio is then computed from

$$r = \exp(-\mathcal{U}(\boldsymbol{w}^*) + \mathcal{U}(\boldsymbol{w}) - \mathcal{K}(\boldsymbol{q}^*) + \mathcal{K}(\boldsymbol{q})). \tag{16}$$

3.2. Itô-SDE algorithm

This section describes the generalized version of an other type of gradient-informed MCMC algorithm built on the solution of an Itô stochastic differential equation (Itô-SDE-MCMC) ([28; 29; 30]). This Itô-SDE-based MCMC is not a Metropolis-Hastings method as there is no rejection step but is closer to a Gibbs sampler. [31], [32] applied a generalized version of the Itô-SDE-based MCMC of Soize for characterizing the uncertainty in mechanical properties of metal steel. The approach we will use for characterizing the uncertainty on pyrolysis will be similar as to [31], except that the number of repeated experiments is much smaller and the observable is varying with time.

[30] divides in three categories the support of the parameter space: either the support is the entire space $\mathbb{R}^n$, or the support is a known bounded (or semi-bounded) subset $\mathbb{S}_n \subset \mathbb{R}^n$, or the support is unknown, but we know a set of realizations and in this case we have to learn about the structure of a manifold. The case in which we are interested is the second case for which the subset $\mathbb{S}_n$ is determined by physical constraints on the parameters, like ensuring the positiveness of some parameters (for instance for the bulk modulus or activation energy). In this case, a regularization method or a rejection method ([33]) can be applied, but if there exists a bijection which transforms $z \to \mathbf{1}(z)\phi(z)$ on $\mathbb{S}_n$ into $z' \to \phi(z')$ on $\mathbb{R}^n$ we can take advantage of it.

The Itô-SDE introduced by [28] describes a dissipative Hamiltonian system with a stochastic forcing term. This stochastic differential equation describes a second-order system that contains a damping parameter and subject to a potential ϕ

$$d\boldsymbol{p} = [\hat{C}]\boldsymbol{q}dt, \tag{17}$$

$$d\boldsymbol{q} = -\boldsymbol{\nabla}_{\boldsymbol{p}}\phi(\boldsymbol{p})dt - \frac{1}{2}\zeta_0\boldsymbol{q}dt + \sqrt{\zeta_0}[L_{\hat{C}}]^{-\mathrm{T}}d\boldsymbol{W}, \tag{18}$$

where $[\hat{C}] = [L_{\hat{C}}][L_{\hat{C}}]^{\mathrm{T}}$ is the approximation of the covariance matrix, ζ_0 is a free parameter ([32]) that controls the amplitude of the deterministic damping and the stochastic forcing. In the limit of zero damping, the system is similar to the conservative Hamiltonian system describes in Sect. 3.1

To solve the irreversible (non-Hamiltonian) systems, symplectic integrators also show a favourable long-time behavior ([34]). They will have the advantage of being able to solve the system in the long term behavior even for low damping values and the same leafpfrog discretization as for the Hamiltonian system is applicable. [35; 33; 32] use the leapfrog discretization with the slight modification of [36], which allows to have an error in the variance of the momentum variable that is independent of the damping parameter ([37]), that is referred subsequently to as the Stormer-Verlet method

$$\boldsymbol{p}^{(\ell+\frac{1}{2})} = \boldsymbol{p}^{(\ell)} + \frac{\varepsilon}{2}[\hat{C}]\boldsymbol{q}^{(\ell)}, \tag{19}$$

$$\boldsymbol{q}^{(\ell+1)} = \frac{1-b}{1+b}\boldsymbol{q}^{(\ell)} - \frac{\varepsilon}{1+b}\nabla_p\phi\left(\boldsymbol{p}^{(\ell+\frac{1}{2})}\right) + \cdots \frac{\sqrt{\zeta_0}}{1+b}[L_{\hat{C}}]^{-\mathrm{T}}\Delta\boldsymbol{W}^{(\ell+1)}, \tag{20}$$

$$\boldsymbol{p}^{(\ell+1)} = \boldsymbol{p}^{(\ell+\frac{1}{2})} + \frac{\triangle t}{2}[\hat{C}]\boldsymbol{q}^{(\ell+1)}, \tag{21}$$

where $b = \zeta_0\varepsilon/4$.

[28] show that under some regularity conditions regarding the potential function ϕ, the stationnary density of $\boldsymbol{p}, \boldsymbol{q}$ is independent of the damping parameter and is given by

$$\pi(\boldsymbol{q}, \boldsymbol{p}) \propto \exp\left(-\phi(\boldsymbol{q}) - \frac{\boldsymbol{p}^{\mathrm{T}}[\hat{C}]\boldsymbol{p}}{2}\right). \tag{22}$$

By choosing a potential function that corresponds to $\phi = -\log(\pi(\mathbf{d}^{\mathrm{obs}}|\boldsymbol{w}))$, the marginal stationnary density for $\boldsymbol{p}$ will be exactly the distribution we wish to sample (e.g. the Bayesian posterior).

3.3. Change of measure

Convergence of the Markov chain Monte Carlo algorithms toward the posterior distribution can be slow for complex target distributions. It is typically the case of strongly correlated parameters with unknown covariance matrix that requires a lot of tuning and trial and error test, and for non-Gaussian posterior PDFs. In the present case, the posterior PDF for the Arrhenius parameter pairs $(\mathcal{A}_i, \mathcal{E}_i)$ shows both a strong correlated and non-Gaussian shape. In order to reach a faster convergence of the Markov chain, we propose here to use a reparametrization ([38]) of the Arrhenius equation for pyrolysis modeling based on the work of [39] that is extended to the pyrolysis modeling of TPMs Eq. 7. We show that this reparametrization is suitable for the Metropolis-Hastings algorithms since it can achieve fast convergence in a relatively small number of iterations.

3.3.1. Change of measure based on the support of the physical parameter space

When the support of the variable is a subset $\mathbb{S} \subset \mathbb{R}$, we apply a change of variables from $\mathbb{S}$ to $\mathbb{R}$. In the case where $\mathbb{S}$ is bounded from above and below with $\mathbb{S} = [L_{\mathrm{b}}, U_{\mathrm{b}}]$, we choose change of variables of the following form

$$\tilde{p} = \tan\left\{\left(\frac{p - L_{\mathrm{b}}}{U_{\mathrm{b}} - L_{\mathrm{b}}} - \frac{1}{2}\right)\pi\right\}, \tag{23}$$

$$\frac{\mathrm{d}\tilde{p}}{\mathrm{d}p} = \left[1 + \tan^2\left\{\left(\frac{p - L_{\mathrm{b}}}{U_{\mathrm{b}} - L_{\mathrm{b}}} - \frac{1}{2}\right)\pi\right\}\right]\frac{\pi}{U_{\mathrm{b}} - L_{\mathrm{b}}}. \tag{24}$$

3.3.2. Change of measure based on the structure of the equations

A proposed change of measured based on the structure of the pyrolysis model was introduced in [25] and its effect on the sampling of the posterior distribution was shown. This section briefly recalls this change of measure as it will be used also for the HMC algorithm. We consider the parameter set $\boldsymbol{w}$ introduced in Sect. 2 with N_{p} different reaction rates. We apply the same reparametrization for $\mathcal{A}_i$ and $\mathcal{E}_i$ as in [39] and [40] for deterministic parameter estimation, and we introduce two additional scaling factors for m_i and F_{ij}

$$\tilde{\mathcal{A}}_i = \ln \mathcal{A}_i - \mathcal{E}_i/(\mathcal{R}\overline{T}_i), \tag{25}$$

$$\tilde{\mathcal{E}}_i = \mathcal{E}_i/\overline{\mathcal{E}}_i, \tag{26}$$

$$\tilde{m}_i = m_i/\bar{m}_i, \tag{27}$$

$$\tilde{\gamma}_i = \gamma_i/\overline{\gamma}_i. \tag{28}$$

This parametrization does not affect the reaction rates k_i and the observed data, thus making this expression very convenient for the current modeling. A normalization common in combustion literature was also discussed by [41] for its use in uncertainty quantification, but this normalization does not consider the logarithmic dependence of the pair $\mathcal{A}_i$ and $\mathcal{E}_i$, or the translation used in Eq. (25).

Considering these new parameters, reaction rates are now expressed as

$$k_i = \exp\left(\tilde{\mathcal{A}}_i + \tilde{\mathcal{E}}_i\tilde{T}_i(t)\right), \tag{29}$$

where $\tilde{T}_i = \overline{\mathcal{E}}_i/\mathcal{R}(1/T + 1/\overline{T}_i)$ is called the local reciprocal temperature ([40]). Both $\tilde{\mathcal{A}}_i$ and $\tilde{\mathcal{E}}_i$ are scaled parameters that now appear in the exponential term, thus making the search more robust and the MCMC proposal covariance matrix easier to tune. We denote the scaling factors by $\overline{\boldsymbol{w}} = \left\{\overline{\mathcal{A}}_i, \overline{\mathcal{E}}_i, \overline{m}_i, \overline{F}_{ij}\right\}$. An appropriate choice of the scaling factors $\overline{\boldsymbol{w}}$ is very important and we strive to tune the reparametrization so that it has the effect of rescaling the posterior density to a smaller range of values around 1. We will show in the next section on a two-step pyrolysis process starting from known parameters that this reparametrization improves convergence and facilitates the process of estimating the covariance matrix for the proposal function.

3.4. Change of scales: approximation of the covariance

Covariance matrix estimation is crucial for the mixing and stationnarity (convergence) of the Markov chain towards the posterior distribution. For the random-walk Metropolis-Hastings algorithms (RWMH), the covariance estimation is used directly in the proposal distribution and is often sought as to be as close as possible to the posterior distribution. For the HMC and Itô-SDE, the covariance is used for the rescaling of the momentum variable.

We propose two strategies to improve the convergence of the Markov chains based on the estimation of the covariance matrix. The first one is concerned with using an approximation of the covariance matrix from the calculation of the inverse of the Hessian matrix at the maximum likelihood, or at an initial estimate close to it. However, we will see that this estimation can sometimes lead to inaccurate results. We therefore propose a second approach that is based on an adaptive procedure for the HMC and Itô-SDE that will adapt the covariance estimate based on previous sampled values, similar to the adaptive Metropolis-hastings from [42; 43].

It worth noting that in the case where we apply first the change of measure based on the pyrolysis model, it induces a transformation and rescaling of the posterior distribution. The tuning for the covariance matrix is thus reduced and close to identity if the scales appearing in the change of measure are chosen carefully.

3.4.1. Approximating the covariance from the inverse of the Hessian

For the Itô-SDE, [31; 32] use a scaling matrix $[\hat{C}]$ to account for scale and correlations where $[\hat{C}]$ is based on the estimate of the Hessian of the negative of the logarithm of the posterior PDF at the maximum likelihood estimator. Hessian matrix is computed either numerically using for instance finite differences or analytically if second order derivatives are available. However, it is not the case in practice and the numerical methods will be preferred.

3.4.2. Adaptive procedure for the estimation of the covariance matrix

The estimate of the covariance matrix can lack accuracy, for instance if

- the initial guess for the maximum likelihood estimator is poor, resulting in a poor covariance estimate that can even lead to an approximation of the covariance that is not positive semi-definite (PSD);
- the posterior PDF is far from Gaussian, thus the approximation using the inverse of the Hessian of the logarithm of the posterior PDF is not accurate.

Therefore, we seek other ways of approximating it. An alternative is based on the linearisation of the inverse problem investigated in [32] which relies only on the computation of the Jacobian and is always PSD. However, this approximation can still be poor for non-Gaussian distributions and strongly nonlinear inverse problems. It worth mentioning that other methods based on finding the nearest PSD matrix from [44] could also be applied based on a polar decomposition of the non PSD matrix as well as iterative methods, but preliminary uses of those methods weren't successful in the present case because of numerical issues due to bad conditioning of the Hessian in some cases.

We therefore propose to apply an adaptive procedure for the estimation of the covariance matrix based on previous iterations as in [42; 43]. We show that this method is robust independently of the initial covariance matrix estimate $[\hat{C}_0]$. We distinguish three different cases for the initial matrix $[\hat{C}_0]$:

1. The initial estimate $[\hat{C}_0]$ can be set to the identity matrix, $[\hat{C}_0] = [I]$, or in other words, we do not provide any information about scales and correlations. Because of this, care must be taken for the initial value of Δt. For the ISDE, the initial time step will require to adapt the time step if the scales represented by the identity matrix are larger or smaller than the scales of the problem.

2. Secondly, the use of the diagonal of the Hessian-estimate can be easily made PSD by taking the absolute value of the diagonal elements and represent the local scales.
3. Finally if the local Hessian can be computed and is PSD, this one can still be used with the adaptive procedure. The result will be a smaller burn-in phase in the Markov chain.

We denote n_0 the iteration at which we start the adaptive procedure and Δn_{adapt} the frequency at which the covariance is adapted. The first adaptation is based on the covariance estimation of the n_0 iterations. Then we apply a recursive formula for estimating the covariance as a function of each iteration to avoid saving all the sample values [42]. Considering that we have just sampled a new value $\boldsymbol{w}_{n+1}$ from the posterior distribution with the covariance estimate $[\hat{C}_n]$, we compute the new covariance matrix estimate $[\hat{C}_{n+1}]$ using the $(n+2)$ samples

$$[\hat{C}'_{n+1}] = \frac{n+1}{n+2}[\hat{C}'_n] + \cdots \tag{30}$$

$$\frac{1}{n+2}\left((n+1)\bar{\boldsymbol{w}}_n\bar{\boldsymbol{w}}_n^{\mathrm{T}} - (n+2)\bar{\boldsymbol{w}}_{n+1}\bar{\boldsymbol{w}}_{n+1}^{\mathrm{T}} + \boldsymbol{w}_{n+1}\boldsymbol{w}_{n+1}^{\mathrm{T}}\right),$$

$$\bar{\boldsymbol{w}}_{n+1} = \frac{1}{n+2}\left((n+1)\bar{\boldsymbol{w}}_n + \boldsymbol{w}_{n+1}\right), \tag{31}$$

$$[\hat{C}_{n+1}] = s_d[\hat{C}'_{n+1}] + s_d\epsilon I_d \tag{32}$$

where s_d is an additional scaling parameter that depends only on the dimension d of the parameter space, ϵ is a correcting parameter and I_d is the d-dimensional identity matrix. The parameter s_d is used to improve the acceptance rate and [45] showed that the optimal scaling for a Gaussian distribution using a random-walk algorithm was $s_d = 2.38^2/d$. We also keep this parameter as it was also observed that the posterior distribution was sampled more efficiently using it. The correcting parameter ϵ is set to zero in the following and the covariance is finally adapted after every $\Delta n_{\text{adapt}} = 200$ iterations when $n > n_0 = 1000$.

4. Results

The different algorithms with the change of measure and change of scale presented in the two previous sections are compared in order to assess their efficiency. For the comparison, we consider a simple case for the pyrolysis of a PICA sample using the experimental results from [19] for the production of CH_4 represented in Fig. 1 (left). The reason for considering CH_4 is because it is characterized by a single production peak that is relatively well located and can be simulated using only one single reaction. The two uncertain parameters that are considered are $\mathcal{A}$ and $\mathcal{E}$ in order to observe the strong kinetic compensation (strong correlation) effect and for which the posterior probability distribution is non-Gaussian. This low dimensional case allows the comparison of the results of the different sampling algorithms and to validate it against the analytical computation of the posterior distribution evaluated directly from the Bayesian posterior. The two other parameters of the single reaction equation, namely F_{CH4} and n, are fixed according to the maximum likelihood estimator obtained from optimization beforehand. The time step ε in the HMC and Itô-SDE is chosen by a few trial-and-error simulations. It should neither be to small, in which case the sampling is inefficient, or too large in which case the numerical scheme is not stable. For HMC, $\varepsilon = 0.05$ and for Itô-SDE $\varepsilon = 0.1$. It worth to mention for future investigation that the time step could also be adapted together with the covariance matrix in order to further improve the sampling.

The evaluation of the posterior distribution directly from Bayes formula in Eq. 1 is shown in Fig. 1 (right). In Eq. 1, the prior is a uniform distribution and the likelihood is Gaussian using all the observations ([23; 25]). As expected, we can observe a strong correlation between $\mathcal{A}$ and $\mathcal{E}$ emphasized by the large values they take and a non-Gaussian shape of the posterior. This high correlation is sometimes referred to as the kinetic compensation effect and has already been observed in past kinetics studies [22; 46; 47; 24]. This results in a wide range of values for the pre-exponential factor $\mathcal{A}$ and the activation energy $\mathcal{E}$ that can give satisfactory fits to the data.

The comparison of the efficiency of the different algorithms are shown in Fig. 2. In order to assess their efficiency, the marginal mean value of the posterior distribution as a function of the iterations are computed for $\mathcal{A}$ and $\mathcal{E}$, respectively. It is worth first mentioning that the change of measure corresponding to the pyrolysis equations proposed applied to the random-walk Metropolis Hastings (RWMH) has improved significantly the sampling of the posterior distribution (RWMH-CVR), while the RWMH was far from convergence even if the proposal covariance was already carefully tuned. The change of measure corresponding to the pyrolysis equations is also applied to the HMC algorithm (HMC-CVR). In this case, both diagonal and full matrix covariance approximation from the inverse of the Hessian provide good results and there is no need to adapt the covariance. When the

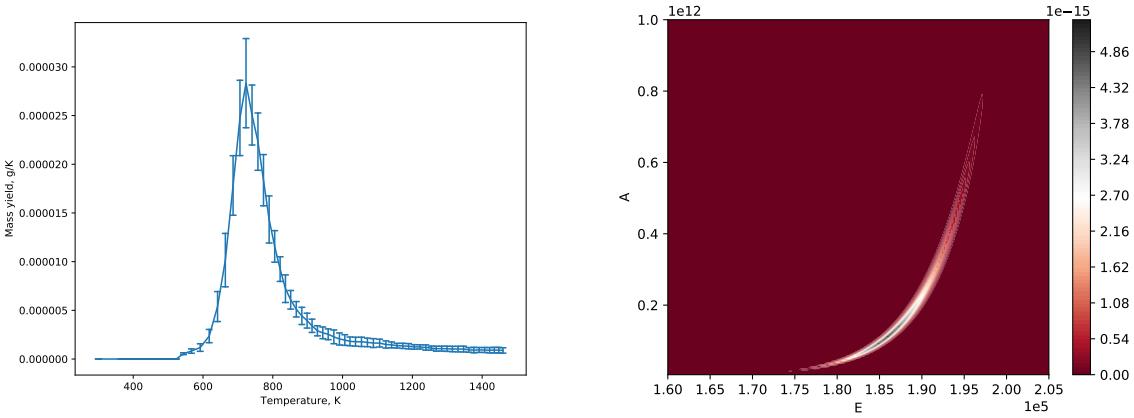

Figure 1: (Left) Experimental data for CH_4; (right) bivariate posterior PDF for $\mathcal{A}$ and $\mathcal{E}$ resulting from the Bayesian inference on the experimental data.

change of measure based on the support of the posterior PDF is applied using a poor approximation of the covariance (diagonal), both Itô-SDE (ISDE-D) and HMC (HMC-CVI-D) are far from convergence. However, they both show good performances when this poor estimation of the covariance matrix is adapted (ISDE-DA and HMC-CVI-DA), with the adaptation step here equal to 200 iterations, or if we use the approximation from the inverse of the full Hessian (ISDE and HMC-CVI). This last result shows that the adaptive HMC and ISDE are robust to a poor estimation for the initial covariance matrix.

We finally compare visually the effect of the different changes of scales proposed using the RWMH and Itô-SDE algorithms in Fig. 3. The random walk only stays in a part of the posterior PDF, even for an optimised covariance proposal using a full matrix (top left). The other cases are for the Itô-SDE with the different approaches for the covariance estimates: using the inverse of the diagonal of the Hessian (top right); from the inverse of the diagonal of the Hessian with adaptation of the covariance every 200 iterations (bottom left); and using the inverse of the full Hessian estimation (bottom right). The adaptation of the covariance can be observed on the bottom left picture where we see a higher density of sample in the high probability region close to the initial starting value (+ symbol on the graph). This would be removed ultimately by allowing a short burnin-phase and discarding the first samples drawn from the posterior distribution.

The non-Gaussian behavior is the reason why the classic random-walk algorithm does not sample the posterior distribution efficiently. Because the change of measure proposed here is adapted to the pyrolysis equation, the RWMH after this change of measure is very efficient with a simple covariance proposal that requires only a few trial-and-error adaptation for its tuning. One possibility to remove this tuning is to avoid the random-walk and motivates the use of gradient based MCMC algorithms. However, even gradient-based algorithms still require to be scaled according to the directions of the posterior distribution that are not known a priori. This covariance estimate was shown to be essential in particular when the change of measure is not adapted to the equations considered. Further improvements to the adaptation of the covariance estimate for gradient-based algorithms could be to consider locally adaptive covariance based on state-dependent scaling as already suggested in [48].

5. Conclusions

We presented gradient-informed sampling algorithms for performing Bayesian inference of unknown parameters. We explored improvements of those algorithms using a change of measure (reparametrization) based on physical constraints of the parameter space or based on the structure of the equations of the model. We presented improvements also using changes of scales from the estimation of the covariance matrix using inverse Hessian computation. When such approximation is not possible, we introduced a new approach for the gradient-informed algorithm, built on the adaptation of the estimation of the covariance matrix. This procedure was already known

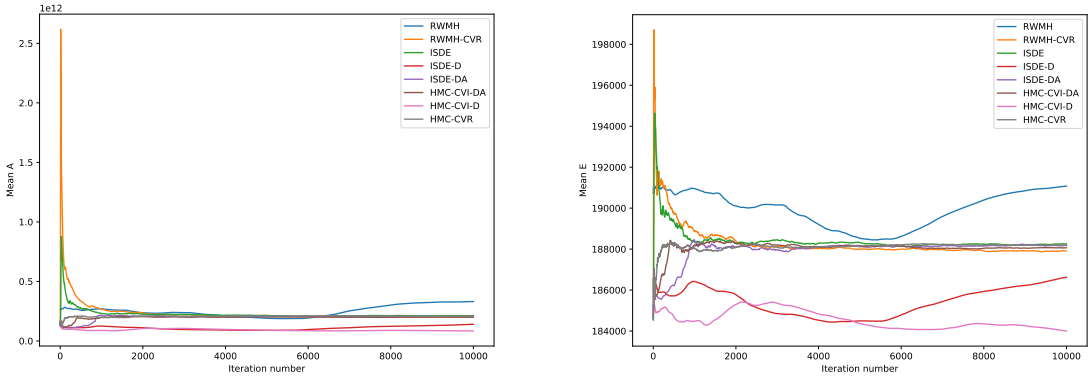

Figure 2: Convergence of the mean for $\mathcal{A}$ (left) and $\mathcal{E}$ (right). Random-Walk Metropolis-Hastings (RWMH); RWMH with change of measure adapted to pyrolysis equations (RWMH-CVR); Itô-SDE will full Hessian approximation (ISDE); Itô-SDE with diagonal Hessian approximation (ISDE-D); ISDE-D with adaptation of the covariance (ISDE-DA); HMC with full Hessian and change of variable adapted ty pyrolysis equation (HMC-CVR); HMC with diagonal Hessian and change of varianble based on paraeter space (HMC-CVI-D); HMC-CVI-D with adaptation (HMW-CVI-DA); .

for the random-walk Metropolis-Hastings with adaptive proposal covariance and was applied here for the inverse Hessian estimation. Practical use of this was shown on a simple 2 dimensional test case from experimental data on the production of CH_4 from the pyrolysis of PICA thermal protection material.

The reparametrization from a bounded set to an unbounded set provides already improved results. For the RWMH, it still requires some tuning of the proposal covariance but this could be avoided by applying covariance matrix estimation methods or adaptive procedures. The best results are obtained with the reparametrization, which provides results similar to HMC and Itô-SDE. HMC with no change of measure cannot be applied without a tuning of the mass matrix (change of scale) in the present case, and the estimation is made complex because of the non positive definiteness of the inverse of the Hessian. Thus, only scaling can be provided and improved with the iterations using the adaptive procedure proposed here.

With the change of measure based on the parameter space, both Itô-SDE and HMC tend to sample mainly the high probability region of the posterior PDF when the covariance matrix is not adapted. But when the covariance matrix is adapted, both algorithms show similar performances. However, we keep in mind that one difference between the Itô-SDE and the HMC is the single time step used at each iteration when solving the Itô equations in time and thus requiring one model evaluation with its gradients, while the HMC needs several leapfrog steps before taking the new sample.

These results emphasize the need to provide a change of measure when sampling from PDFs with complex structure. A change of measure based on the knowledge of the equations is the best that can be achieved, with a proposal from HMC. The use of RWMH algorithm was suitable in this work because the change of measure applied was making the posterior close to a Gaussian density function. However, it is unlikely to be the case in higher dimensions and a gradient-informed method will be preferred. When no such knowledge of a relevant change of measure is available, a change of measure based on physical constraints can still be applied. We also proposed to improve the convergence rate by applying an adaptive change of scale for the HMC and theItô-SDE. For the Itô-SDE in the version of [31] the change of measure is constrained also by the parameter space that must be unbounded, while for the HMC there is more freedom to chose it.

Acknowledgments

The first author work is supported by the Fund for Research Training in Industry and Agriculture (FRIA) provided by the Belgian Fund for Scientific Research (F.R.S.-FNRS). The first author would like to thanks K. Bulthuis for its thorough reading of the paper.

References

[1] J. D. Anderson, Hypersonic and High Temperature Gas Dynamics, 2nd Edition, AIAA Education Series, 2006.

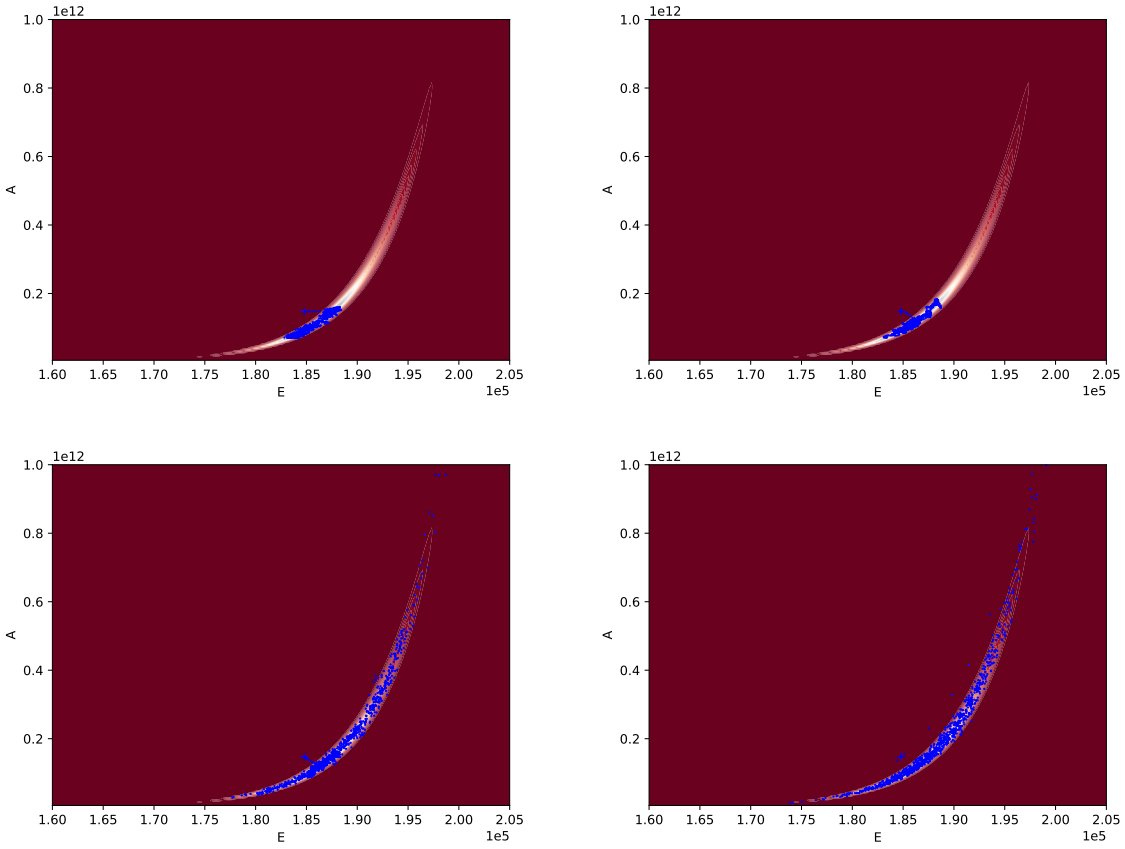

Figure 3: Comparison of the random-walk Metropolis-Hastings (RWMH) with the different covariance estimation for the Itô-SDE. (Top left) RWMH, (top right) ISDE with diagonal Hessian, (bottom left) ISDE diagonal Hessian with adaptation, (bottom-right) ISDE with full Hessian. In total, 1000 samples are show on each graph for clarity and emphasizing the adaptation of the covariance. They were obtained from a single run of 10000 samples from which we took the first 2000 samples every 2 iterations.

[2] G. Duffa, Ablative thermal protection systems modeling, American Institute of Aeronautics and Astronautics, Inc., Reston, Virginia, 2013.

[3] R. M. Kendall, E. P. Barlett, R. A. Rindal, C. B. Moyer, An Analysis of the Coupled Chemically Reacting Boundary Layer and Charring Ablator: Part I., CR-1060, NASA (1968).

[4] Y.-K. Chen, F. S. Milos, Ablation and thermal response program for spacecraft heatshield analysis, Journal of Spacecraft and Rockets 36 (3) (1999) 475–483.

[5] G. F. Sykes, Decomposition Characteristics of a Char-Forming Phenolic Polymer Used for Ablative Composites, Tech. rep., NASA TN D-3810 (1967).

[6] H. E. Goldstein, Pyrolysis Kinetics of Nylon 6-6, Phenolic Resin, and Their Composites, Journal of Macromolecular Science: Pt. A - Chemistry 3 (4) (1969) 649–673.

[7] D. Bianchi, A. Turchi, N. Francesco, O. Marcello, Coupled CFD analysis of thermochemical erosion and unsteady heat conduction in solid rocket nozzles, in: 48th AIAA/ASME/ASEE Joint Propulsion Conference & Exhibit, Atlanta, GA, 2012, pp. 1–15. doi:10.2514/6.2012-4318.

[8] A. Martin, Volume averaged modeling of the oxidation of porous carbon fiber material, in: 44th AIAA Thermophysics Conference, San Diego, CA, 2013, pp. 1–14.

[9] Y.-K. Chen, T. Gökçen, Implicit coupling approach for simulation of charring carbon ablators, Journal of Spacecraft and Rockets 51 (3) (2014) 779–788.

[10] A. Martin, I. Boyd, Strongly coupled computation of material response and nonequilibrium flow for hypersonic ablation, Journal of Spacecraft and Rockets 52 (1) (2015) 89–104.

[11] P. Schrooyen, K. Hillewaert, T. E. Magin, P. Chatelain, Fully Implicit Discontinuous Galerkin Solver to Study Surface and Volume Ablation Competition in Atmospheric Entry Flows, International Journal of Heat and Mass Transfer 103 (2016) 108–124. doi:http://dx.doi.org/10.1016/j.ijheatmasstransfer.2016.07.022.

[12] J. Lachaud, J. Scoggins, T. Magin, M. Meyer, N. Mansour, A generic local thermal equilibrium model for porous reactive materials submitted to high temperatures, International Journal of Heat and Mass Transfer 108 (2017) 1406–1417. doi:10.1016/j.ijheatmasstransfer.2016.11.067.

[13] J. Coheur, A. Turchi, P. Schrooyen, T. Magin, Development of a unified model for flow-material interaction applied to porous charring ablators, in: 47th AIAA Thermophysics Conference, American Institute of Aeronautics and Astronautics, Denver,

CO, US, 2017, pp. 1–13. doi:https://doi.org/10.2514/6.2017-3684.

[14] K. A. Trick, T. E. Saliba, Mechanisms of the pyrolysis of phenolic resin in a carbon/phenolic composite, Carbon 33 (11) (1995) 1509–1515.

[15] K. A. Trick, T. E. Saliba, S. S. Sandhu, A kinetic model of the pyrolysis of phenolic resin in a carbon/phenolic composite, Carbon 35 (3) (1997) 393–401.

[16] H.-W. Wong, J. Peck, R. Bonomi, J. Assif, F. Panerai, G. Reinish, J. Lachaud, N. Mansour, Quantitative determination of species production from phenol-formaldehyde resin pyrolysis, Polymer Degradation and Stability 112 (2015) 122–131.

[17] H.-W. Wong, J. Peck, J. Assif, F. Panerai, J. Lachaud, N. Mansour, Detailed analysis of species production from the pyrolysis of the phenolic impregnated carbon ablator, Journal of Analytical and Applied Pyrolysis 122 (2016) 258–267.

[18] B. K. Bessire, S. A. Lahankar, T. K. Minton, Pyrolysis of Phenolic Impregnated Carbon Ablator (PICA), ACS Appl. Mater. Inter. 7 (3) (2015) 1383–1395.

[19] B. K. Bessire, T. K. Minton, Decomposition of phenolic impregnated carbon ablator (PICA) as a function of temperature and heating rate, ACS Appl. Mater. Inter. 9 (2017) 21422–21437.

[20] C. Lautenberger, C. Fernander-Pello, Optimization algorithms for material pyrolysis property estimation, Fire Safety Science 10 (2011) 751–764. doi:10.3801/IAFSS.FSS.10-751.

[21] F. Torres-Herrador, J. B. Meurisse, F. Panerai, J. Blondeau, J. Lachaud, B. K. Bessire, T. E. Magin, N. N. Mansour, A high heating rate pyrolysis model for the phenolic impregnated carbon ablator (PICA) based on mass spectroscopy experiments, Journal of Analytical and Applied Pyrolysis (2019) 104625doi:10.1016/j.jaap.2019.05.014.

[22] M. Bruns, Inferring and propagatin kinetic parameter uncertainty for condensed phase burning models, Fire Technology 52 (2016) 93–120.

[23] J. Coheur, M. Arnst, P. Chatelain, T. Magin, A first step towards the bayesian inference of uncertain kinetic parameters of pyrolysis decomposition laws, in: 9th VKI PhD Symposium, Rhodes-Saint-Genèse, Belgium, 2018, pp. 1–9.

[24] F. Torres-Herrador, J. Coheur, F. Panerai, T. Magin, M. Arnst, N. Mansour, J. Blondeau, Competitive kinetic model for the pyrolysis of the phenolic impregnated carbon ablator, Under review in Aerospace Science and Technology.

[25] J. Coheur, M. Arnst, P. Chatelain, T. Magin, Bayesian parameter inference for PICA devolatilization pyrolysis at high heating rates, in: 10th VKI PhD Symposium, Rhodes-Saint-Genèse, Belgium, 2019, pp. 1–12.

[26] R. M. Neal, MCMC using hamiltonian dynamics, in: G. J. S. Brooks, A. Gelman, X.-L. Meng (Eds.), Handbook of Markov Chain Monte Carlo, Boca Raton: Chapman and Hall-CRC, 2010, pp. 113–162.

[27] A. Gelman, J. B. Carlin, H. S. Stern, D. B. Dunson, A. Vehtari, D. B. Rubin, Bayesian Data Analysis, 3rd Edition, Chapman & Hall/CRC, London, 2014.

[28] C. Soize, Construction of probability distributions in high dimension using the maximum entropy principle: Applications to stochastic processes, random fields and random matrices, International Journal for Numerical Methods in Engineering 76 (10) (2008) 1583–1611. doi:DOI: 10.1002/nme.2385.

[29] C. Soize, Polynomial chaos expansion of a multimodal random vector, SIAM/ASA Journal on Uncertainty Quantification 3 (1) (2015) 34–60. doi:10.1137/140968495.

[30] C. Soize, Uncertainty Quantification, Springer International Publishing, 2017. doi:10.1007/978-3-319-54339-0.

[31] M. Arnst, B. A. Álvarez, J.-P. Ponthot, R. Boman, Itô-SDE MCMC method for bayesian characterization of errors associated with data limitations in stochastic expansion methods for uncertainty quantification, Journal of Computational Physics 349 (2017) 59–79. doi:http://dx.doi.org/10.1016/j.jcp.2017.08.005.

[32] M. Arnst, C. Soize, Identification and sampling of bayesian posteriors of high-dimensional symmetric positive-definite matrices for data-driven updating of computational models, Computer Methods in Applied Mechanics and Engineering 352 (2019) 300–323. doi:10.1016/j.cma.2019.04.025.

[33] J. Guilleminot, C. Soize, Itô SDE–based generator for a class of non-gaussian vector-valued random fields in uncertainty quantification, SIAM Journal on Scientific Computing 36 (6) (2014) A2763–A2786. doi:10.1137/130948586.

[34] E. Hairer, C. Lubich, G. Wanner, Geometric Numerical Integration, Springer-Verlag, 2006. doi:10.1007/3-540-30666-8.

[35] C. Soize, R. Ghanem, Data-driven probability concentration and sampling on manifold, Journal of Computational Physics 321 (2016) 242–258. doi:10.1016/j.jcp.2016.05.044.

[36] R. Mannella, Numerical stochastic integration for quasi-symplectic flows, SIAM Journal on Scientific Computing 27 (6) (2006) 2121–2139. doi:10.1137/040620965.

[37] K. Burrage, I. Lenane, G. Lythe, Numerical methods for second-order stochastic differential equations, SIAM Journal on Scientific Computing 29 (1) (2007) 245–264. doi:10.1137/050646032.

[38] W. R. Gilks, S. Richardson, D. J. Spiegelhalter, Markov Chain Monte Carlo in Practice, Chapman & Hall/CRC, London, 1996.

[39] O. E. Rodionova, A. L. Pomerantsev, Estimating the parameters of the Arrhenius equation, Kinetics and Catalysis 46 (3) (2005) 305–308. doi:10.1007/s10975-005-0077-9.

[40] A. L. Pomerantsev, A. V. Kutsenova, O. Y. Rodionova, Kinetic analysis of non-isothermal solid-state reactions: multistage modeling without assumptions in the reaction mechanism, Physical Chemistry Chemical Physics 19 (5) (2017) 3606–3615. doi:10.1039/c6cp07529k.

[41] J. Urzay, N. Kseib, P. G. Constantine, D. F. Davidson, G. Iaccarino, Uncertainty-quantifying models for chemical-kinetic rates, Center for Turbulence Research Annual Briefs.

[42] H. Haario, E. Saksman, J. Tamminen, An adaptive Metropolis algorithm, Bernoulli 7 (2) (2001) 223–242.

[43] Y. F. Atchadé, J. S. Rosenthal, On adaptive Markov chain Monte Carlo algorithms, Bernoulli 11 (5) (2005) 815–828.

[44] N. J. Higham, Computing a nearest symmetric positive semidefinite matrix, Linear Algebra and its Applications 103 (1988) 103–118. doi:10.1016/0024-3795(88)90223-6.

[45] A. G. Gelman, G. O. Roberts, W. R. Gilks, Efficient Metropolis jumping rules, in: J. M. Bernardo, J. O. Berger, A. F. David, A. F. M. Smith (Eds.), Bayesian Statistics V, Oxford University Press, 1996, pp. 599–608.

[46] N. Koga, A review of the mutual dependence of Arrhenius parameters evaluated by the thermoanalytical study of solid-state reactions: the kinetic compensation effect, Thermochimica Acta 244 (1994) 1–20.

[47] A. K. Galwey, M. E. Brown, Thermal Decomposition of Ionic Solids, Elsevier, Amsterdam, 1999.

[48] J. Rosenthal, Optimal proposal distributions and adaptive MCMC, in: S. Brooks, A. Gelman, G. L. Jones, X.-L. Meng (Eds.), Handbook of Markov Chain Monte Carlo, Chapman & Hall/CRC, London, 2011, Ch. 4, pp. 93–111.

Development of a robust framework for space debris material testing in the VKI Plasmatron facility

Andrea Fagnani

Aeronautics and Aerospace Department, von Karman Institute for Fluid Dynamics, Belgium, andrea.fagnani@vki.ac.be

Supervisor: Olivier Chazot

Head of Department and Professor, Aeronautics and Aerospace Department, von Karman Institute for Fluid Dynamics, Belgium, chazot@vki.ac.be

University Supervisor: Annick Hubin

Professor at Department of Materials and Chemistry, Vrjie Universiteit Brussel, Belgium, annick.hubin@vub.be

Abstract

The number of space debris in Earth's orbit has drastically increased over the last decades, leading to a major concern about future sustainability for the space environment. Moreover, on-ground casualty risk assessment is nowadays imposed by space agencies worldwide, demanding innovative cost-effective strategies to ensure safe end-of-life disposal of space objects upon uncontrolled re-entry. Combined theoretical, numerical and experimental research is required to improve our understanding of the complex gas/surface interaction and material response of space debris materials during atmospheric entry. In this paper, we review the high-enthalpy ground testing capabilities at the von Karman Institute for Fluid Dynamics, combining novel techniques with tools inherited from the sound expertise on thermal protection systems testing, to pave the way for space debris material experimentation.

Keywords:
Space debris, aerothermochemistry, plasma wind tunnels

1. Introduction

Satellites orbiting Earth offer unrivalled possibilities for research and commercial applications; however, space activities over the last decades have left more than 20000 large objects in orbit which are no longer functional, namely, space debris [1]. Their number is predicted to increase exponentially in the future and, due to their hypervelocity motion, collision with existing and new missions can lead to a catastrophic break up, generating even more debris in a cascade effect, known as the Kessler syndrome [2]. Space debris, mitigation guidelines [3], suggested by the United Nations in 2007, were embraced by the European Commission and implemented by the European Space Agency (ESA) through the Clean Space Initiative. These measures aim at reducing the generation of new debris, limiting the break-up probability, requiring passivation procedures and implementing disposal strategies, such as re-orbiting and de-orbiting at the end-of-life [4]. Moreover, on average over the past decade, an object with mass above 800 kg has re-entered the atmosphere every week [5]. As often witnessed during these events, ground recoveries are the clear testimony of non-demisability of some spacecraft components [6]. As a result, space agencies and nations have discussed requirements to limit the on-ground casualty risk for future missions. Compliance to this requirement can be safely achieved through controlled re-entry and ground impact over large unpopulated areas. Yet, this solution has major consequences at system level, possibly requiring a full redesign of the spacecraft and leading to higher mass and thus increased mission cost [7]. Among the alternative strategies, the Design for Demise (D4D) refers to all measures taken in the design of a space object to increase the potential for demise, i.e. complete degradation, upon an uncontrolled re-entry at the end-of-

life. The latter, in addition, has the advantage to be cost effective (e.g., no additional propellant is needed) and features less stringent design requirements [8]. Thus, the ultimate goal of the D4D is to predict the complex multi-physical and multi-scale response of space materials to the extreme conditions of atmospheric entry, so as guarantee, at a design level, their complete demise. Yet, as it will be further detailed later on, this estimation is a complex task and current scientific and technological capabilities do not allow such predictive characterizations [9]. Hence, D4D demands a strong research effort in modeling, numerical simulations and experimental activities.

1.1. Aerothermal phenomena of demising metals and silicates

During atmospheric entry, the bow shock, formed in from of the spacecraft travelling at hypersonic speed produces a high-temperature plasma ($T \approx 10\,000$ K). If not suitably protected, this interaction causes a series of degradation phenomena, which are known as ablation [10]. If the latter proceeds until the entire material mass is consumed, demise is achieved. This process can be regarded as a multi-physics gas-surface interaction phenomenon. In particular, aerothermal heating of the material induces melting and formation of gas-liquid and liquid-solid interfaces. The liquid layer can be removed by surface shear forces, imposed by the surrounding flow, or by thermo-chemical phenomena such as evaporation. Injection of vapour into the boundary layer, in turn, affects the aerodynamic heat transfer and the gas-phase chemistry [11], producing a coupled flow-material problem. Additionally, molecular species dissociate due to the extreme temperatures, recombine in the boundary layer and diffuse towards the surface. At the wall, heterogeneous chemistry occurs, including catalysis, nitridation and oxidation. The latter is of paramount importance in the survivability of metallic components due to the formation of stable metallic oxide with high melting temperature [9].

1.2. Ground testing and experimental data demands

The aspiration for a cleaner and more sustainable future for the space environment, allowing to benefit both from its scientific and economical applications, advocates for a revolutionary effort in the design of new demisable systems. Combined theoretical, numerical and experimental research is then required to improve our understanding of the complex gas/surface interaction and material response of space debris materials in atmospheric entry flows.

Ground testing in plasma wind-tunnels is currently the only affordable possibility for both material qualification and validation of material response codes [12]. Due to the multiplicity of the phenomena involved in the space debris demise, however, ground reproduction of a full re-entry scenario seems infeasible. The leading path is then represented by a model development strategy based on consistent wind tunnel experiments, which must isolate each critical phenomenon. However, a withstanding challenge in high-enthalpy facilities experimentation is the correct scaling of all the driving physical phenomena [13]. For the specific case of multiphase melting-ablation, this challenge is hardly addressed in the existing literature.

Leveraging on the strong expertise of the VKI in the ground testing of reusable [14] and ablative [10] thermal protection systems, in this work we propose to adapt and improve existing tools and complement them with novel capabilities, chiefly blending numerical models and advanced data processing techniques, to provide a consistent framework to carry out state-of-the-art experimentation on space debris materials. The goal is to improve the ground testing reliability and reducing uncertainties to develop new thermo-chemical ablation models.

2. VKI Plasmatron facility

The VKI Plasmatron is the worlds largest Inductively Coupled Plasma (ICP) facility, equipped with a 160 mm diameter torch powered by a high-frequency, high-power, high-voltage (400 kHz, 1.2 MW, 2 kV) electric generator. The flow regime is typically subsonic, although sonic and supersonic flow conditions can also be achieved by means of a nozzle configuration. Since the gas is heated by electromagnetic induction, the main advantage of ICP torches with respect to arc-jet heaters is the high purity of the plasma flows, due to the absence of chemical pollution associated to the erosion of the electrodes. A water-cooled copper probe, holding a 14 mm copper calorimeter in the center of the front face, is used to calibrate the plasma flow conditions. The Cold Wall (CW) ($T_{\mathrm{cw}} = 350$K) stagnation point heat flux ($\dot{q}_{\mathrm{cw}}$) is determined by the cooling water mass flow, controlled by a calibrated rotameter, and the inlet/outlet temperature difference, measured by two type-E thermocouples. A water-cooled Pitot probe is used to perform dynamic pressure (p_{dyn}) measurements. The pressure line is connected to a Validyne variable reluctance pressure transducer and a voltage demodulator amplifies the signal. Validyne and amplifier are calibrated prior to

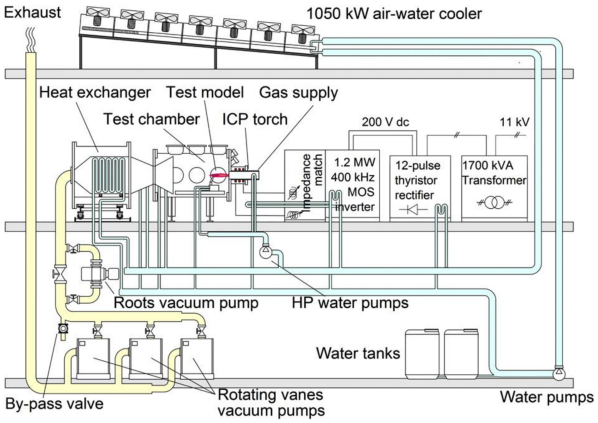

Figure 1: Schematic of the VKI Plasmatron facility.

the test by means of a Betz water manometer. An absolute pressure transducer (Memberanovac DM 12, Leybold Vacuum) measures the static pressure (p_s) in the Plasmatron test chamber. As the plasma jet is low subsonic (Ma $\approx$ 0.1), the static pressure can be assumed constant in the whole test chamber. The gas mass flow rate ($\dot{m}_{gas}$) supplied to the torch is monitored through a calibrated gas rotameter, while the Plasmatron control system allows to record the electric power ($\mathbb{P}_{el}$) supplied to the induction coil.

3. Advances in plasma flow characterization

To ensure repeatability of the test conditions and to provide accurate data for flow and material response simulations, the correct characterization of the plasma flow conditions is a necessary step. Due to the extreme temperatures of the gas, direct measurements of all the physical quantities of interest is often unfeasible. To this purpose, experimental and numerical tools must be properly combined in order to determine the quantities of interest. Traditionally, the process involves a three-step procedure. First, cold-wall heat flux and Pitot pressure measurements are taken on a reference copper probe. Then, magnetohydrodynamic simulations of the plasma flow are performed with the VKI ICP CODE, under the assumption of Local Thermodynamic Equilibrium (LTE), to retrieve the hydrodynamic parameters describing the boundary layer around the test article. Finally, one-dimensional computations of the boundary layer in chemical non-equilibrium on the stagnation line are performed, allowing to rebuild the gas flow enthalpy at the boundary layer edge. When doing so, however, one must ensure the consistency of the numerical simulations with respect to the actual experimental environment. Following the work of Le Quang [15], here we set-up an optical emission spectroscopy system, able to provide spatially resolved light emission measurement. A full data processing suite was developed to retrieve locally resolved gas temperature measurements. Then, a novel approach, based on the comparison of the experimental data to the plasma jet simulations allows to determine critical parameters to provide the correct numerical rebuilding [16]. Consistency between the different parts of the procedure is finally ensured.

3.1. Numerical tools

3.1.1. VKI ICP code simulations

The subsonic steady-state plasma flow-field in the Plasmatron chamber is numerically simulated using an in-house magnetohydrodynamics solver, which couples the Maxwell equations with the Navier-Stokes equations under LTE and axisymmetric steady flow assumptions (VKI ICP CODE [17; 14]). Free-stream simulations (Fig. 2) can be produced, as well as around a test article shape. In the latter case, the hydrodynamic parameters describing the Boundary Layer (BL) on the stagnation line in front of the test article, namely, the BL thickness δ, the radial velocity gradient β, its axial gradient $\partial\beta/\partial x$ and the velocity u are then represented by five Non-Dimensional

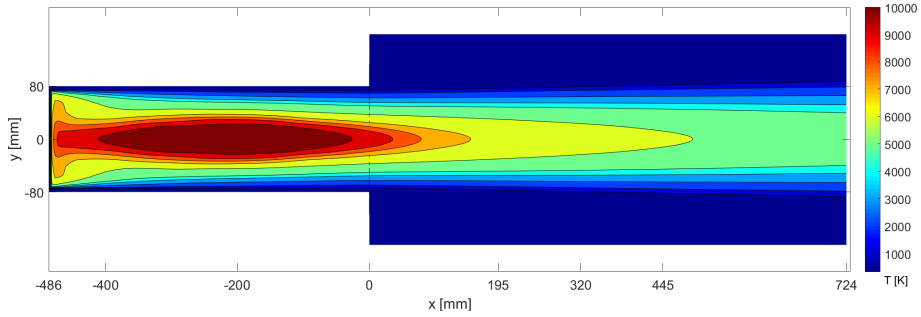

Figure 2: Example of free-stream temperature field of the VKI Plasmatron ICP torch simulated with the VKI ICP code for $p_s = 100\,\text{mbar}$, $\dot{m}_{\text{gas=16}}$ g/s, $\mathbb{P}_{\text{el}}^{\text{eff}} = 70\,\text{kW}$.

Parameters (NDPs)

$$\begin{cases} \Pi_1 = \delta / R_{\text{ref}} \\ \Pi_2 = \beta_e \cdot R_{\text{ref}} / u_t \\ \Pi_3 = -\partial \beta_e / \partial x \cdot R_{\text{ref}}^2 / u_t \\ \Pi_4 = u_e / u_t \\ \Pi_5 = u_e / u_{\text{fs}}, \end{cases} \tag{1}$$

where the subscripts e, fs and t represent the BL edge, free-stream point and torch exit locations, respectively.

The input parameters for the simulations are the static pressure p_s in the Plasmatron chamber, the gas mass flow rate $\dot{m}_{\text{gas}}$ supplied to the torch and the effective power $\mathbb{P}_{\text{el}}^{\text{eff}}$ dissipated in the plasma by electromagnetic induction. p_s and $\dot{m}_{\text{gas}}$ are experimentally measured during the test with an absolute pressure transducer and a calibrated gas rotameter, respectively. As far as $\mathbb{P}_{\text{el}}^{\text{eff}}$ is concerned, instead, its exact value is unknown and generally a power efficiency $\eta = \mathbb{P}_{\text{el}}^{\text{eff}} / \mathbb{P}_{\text{el}}$ equal to 50% is accounted for. In the following analysis, instead, we propose an improved procedure to retrieve a more accurate value of the induction efficiency based on the comparison to experimental measurements of the gas temperature.

3.1.2. VKI boundary layer code

The VKI Boundary Layer code NEBOULA [18] solves the axially symmetric stagnation line boundary layer over a catalytic surface under the assumption of chemical non-equilibrium and thermal equilibrium conditions. The flow is assumed to be laminar and only steady-state is considered. To be representative of the low-Reynolds number, highly viscous plasma flow, a finite thickness formulation is included. The catalytic boundary condition traditionally considers only two independent surface reactions ($O + O \rightarrow O_2$ and $N + N \rightarrow N_2$), with the same recombination efficiency and complete accommodation of the exothermic recombination energy. To run the code, one needs to specify the hydrodynamic parameters describing the boundary layer, i.e., the NDPs, along with boundary layer edge conditions (temperature, pressure and gas composition) and the wall conditions (temperature and catalytic efficiency). For the purpose of rebuilding the gas flow enthalpy at the boundary layer edge, the BL code is run iteratively on the boundary layer edge temperature, assuming a reference recombination coefficient at the wall, until the measured cold-wall heat flux $\dot{q}_{\text{cw}}$ is matched.

3.2. Experimental plasma free-stream investigation by means of optical emission spectroscopy

In Optical Emission Spectroscopy (OES), the electromagnetic radiation emitted by the plasma is recorded, spectrally resolved and interpreted in terms of parameters of the gas or characteristics of the radiating atoms, ions or molecules [19]. In Inductively Coupled Plasma (ICP) facilities, atomic and molecular excited states are mostly generated during electron-neutral and neutral-neutral particle collisions, resulting in energy transfer to bound electrons. Spontaneous de-excitation occurs, so that radiative transitions between allowed energetic states give rise to a spectrum in the ultra-violet and visible ranges [15], when electronic transitions are involved, as well as in the infrared and microwave ranges, in case of vibrational and rotational transitions. In LTE plasmas, a single temperature characterizes all internal energy modes (vibrational, rotational and electronic). This temperature can be determined from the absolute intensity of any atomic or molecular feature, or from Boltzmann plots of vibrational or rotational population distributions [20].

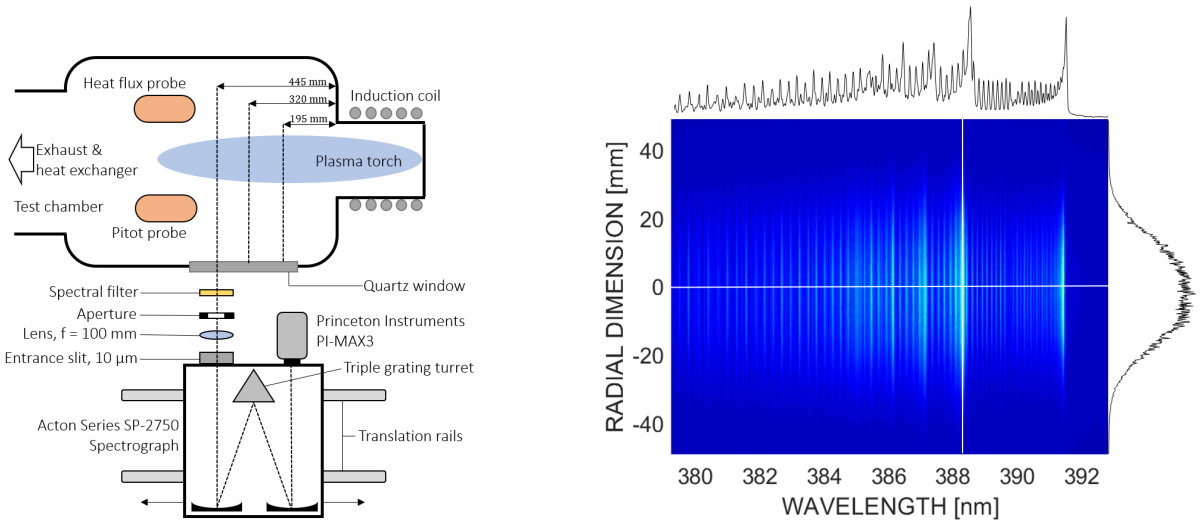

(a) (b)

Figure 3: (a) Schematic of experimental set-up for spatially resolved optical emission spectroscopy, showing the Plasmatron chamber and the components of the spectral imaging system; (b) example of high-resolution spectral imaging of the CN violet B-X and N_2^+ B-X rovibronic systems. The plasma emission is spectrally resolved in the horizontal direction and spatially resolved in the vertical direction.

3.2.1. Overview of the emission spectroscopy system

Fig. 3(a) illustrates a schematic of the instrumentation set-up at the VKI Plasmatron facility. The optical system consists of a 750 mm focal length Acton Series SP-2750 Czerny-Turner spectrograph, a 100 mm focal length lens with variable aperture and a removable spectral filter to avoid contamination by second order dispersion at wavelengths greater than 500 nm. The spectrograph is equipped with a triple grating turret to vary the spectral resolution. The 100 mm focal length plano-convex lens is placed at 1.7 m from the plasma jet axis, allowing to image the full jet diameter (21 cm) on the slit entrance, while the aperture ratio is adjusted to f/10 in order for the optical depth to be of the same size of the jet diameter itself. An intensified CCD detector (Princeton Instruments PI-MAX3) with a resolution of 1024×1024 pixels and a pixel size of 12.8 µm is connected to the exit slit of the spectrograph. The achieved spatial resolution across the jet diameter is 0.2 mm/pixel. The integration time and intensifier gain are interactively adjusted during the test to reach a high Signal to Noise Ratio (SNR) for each spectral range and test condition. After subtracting a background image, a total of 10 frames were averaged within few seconds to further increase the SNR. The entrance slit width is set to 10 µm to match the pixel size of the CCD detector, hence avoiding any loss of spectral resolution. The apparatus function was characterized with the help of a low pressure mercury lamp in the range 200-500 nm and a low-pressure argon lamp in the range 500-1000 nm. It was found that the lineshape was best represented by a Voigt profile with a Full Width Half Maximum (FWHM) of 0.0446 nm and 0.0336 nm at a wavelength of 427 and 727 nm respectively. The optical diagnostic bench was mounted on translation rails, allowing to perform measurement at different axial positions of the jet. Three locations were investigated, namely, at 195 mm, 320 mm and 445 mm from the torch exit, corresponding to 1.22, 2 and 2.78 torch diameters respectively.

The light emitted by the plasma jet is spectrally dispersed by the grating and collected by the intensified CCD camera placed at the spectrograph focal plane. For each recording, a data matrix is obtained: each row contains the spectrally resolved radiance at a certain radial position along the plasma jet, as highlighted in Fig. 3(b). The intensity calibration of the whole system in the measurement wavelength ranges was performed after the test campaign with the help of a tungsten ribbon lamp (OSRAM WI 17G) with a known spectral radiance, placed inside the test chamber on the jet axis.

After intensity calibration, each pixel of the acquired frame yields the radiance emitted at the surface of the plasma, resolved in the spectral and ra-

dial dimensions. However, as the plasma jet is observed in the side direction, the recorded signal by each frame pixel is the result of the local plasma emission intensity integrated along the line-of-sight. If we assume axial symmetry of the source and an optically thin medium, the inverse Abel transformation allows to rebuild the local spectral emission intensity. The relation between the spectral radiance L_λ (in $W/m^2/sr/nm$) and the local spectral emission intensity ϵ_λ (in $W/m^3/sr/nm$) as a function of the radial coordinate r, originating at the plasma jet axis, can be expressed as

$$\epsilon_\lambda(r) = -\frac{1}{\pi}\int_r^R \frac{dL_\lambda(y)}{dy}\frac{dy}{\sqrt{y^2-r^2}}, \tag{2}$$

with R being the maximum radial dimension of the plasma jet, i.e., where the recorded signal approaches zero. Following the work of Pretzier [21], we computed the numerical solution of eq. 2 based on the principle of Fourier analysis. The unknown radial distribution $\epsilon_\lambda(r)$ is expanded in a series of cosine functions, whose amplitudes are then obtained by least-squares-fitting of the direct Abel transform of such series to the measured data.

3.2.2. Measurement of local plasma LTE temperatures

An atomic spectral line is emitted when a bound electron undergoes a transition from an upper level (u) of energy E_u to a lower level (l) of energy E_l. The local emission intensity of the line is given by [19]

$$\epsilon_\mathrm{ul} = \frac{E_\mathrm{u}-E_\mathrm{l}}{4\pi}\mathcal{A}_\mathrm{ul}n_{\mathrm{u},i}, \tag{3}$$

where $\mathcal{A}_\mathrm{ul}$ is the Einstein coefficient of spontaneous emission for the specific transition $\mathrm{u}\rightarrow\mathrm{l}$ and $n_{\mathrm{u},i}$ is the population density of the exited states of the atomic species i. Assuming LTE conditions, $n_{\mathrm{u},i}$ can be related to the gas temperature (T_LTE) through the Boltzmann distribution

$$n_{\mathrm{u},i} = n_i(T_\mathrm{LTE},p)\frac{g_{\mathrm{u},i}\exp(-\frac{E_{\mathrm{u},i}}{k_\mathrm{B}T_\mathrm{LTE}})}{Q_{\mathrm{int},i}(T_\mathrm{LTE})}, \tag{4}$$

where n_i is the number density of species i in the mixture, $g_{\mathrm{u},i}$ is the degeneracy of the energy level $E_{\mathrm{u},i}$, k_B is the Boltzmann's constant and $Q_{\mathrm{int},i}$ is the internal partition function of the atomic species i. The NIST database [22] is selected to obtain the Einstein's coefficients, degeneracies and energy levels for the considered atomic transitions. The partition function is computed from ref. [23]. Under the assumption of LTE, once the pressure p is fixed, n_i depends only on temperature. Hence, comparison between the analytically computed emission intensity with the experimentally measured one yields the local plasma LTE temperature.

Table 1: Plasmatron operating conditions.

ID	p_s mbar	$\dot{m}_\mathrm{gas}$ g/s	$\dot{q}_\mathrm{cw}$ kW/m^2	p_dyn Pa	$\mathbb{P}_\mathrm{el}$ kW
$\mathbb{C}1$	100 ± 0.2	16	1089 ± 131	19.8 ± 2.0	192.2
$\mathbb{C}2$	200 ± 0.4	16	972 ± 116	11.8 ± 1.2	204.7

In the case of molecular rovibronic transitions, instead, one can estimate the gas temperature by fitting the experimental spectrum with the one simulated by a radiation code. Molecular emission of the air plasma radiation was simulated using Specair 3.0 [24]. The radiation model was used to generate a synthetic spectra database for the required pressures, in a range of temperature between 4000 K and 8000 K, with 100 K resolution, between 360 nm and 430 nm. For the purpose of this work we only considered LTE conditions, i.e., equilibrium chemical composition and one-temperature model. The fitting was performed by minimising the norm of residual between the absolute intensities of the measured (meas) and synthetic (synt) spectra respectively

$$Res = \sum_i^N [\epsilon_\lambda^\mathrm{meas}(\lambda_i) - \epsilon_\lambda^\mathrm{synt}(\lambda_i)]^2, \tag{5}$$

where λ_i is the wavelength at which both spectra are evaluated. An example of spectral fitting is reported in fig. 4.

The equilibrium chemical composition of the air plasma was computed with the Mutation++ library, developed at VKI by Scoggins and Magin [25], for a 16 species air mixture model with an elemental composition consisting of 78.8% nitrogen, 21.18% oxygen and 0.02% carbon, corresponding to a CO_2 concentration of 410 ppm at ambient temperature.

3.2.3. Determination of the induction efficiency

Two test conditions, as reported in table 1, were selected to apply the procedure. The subsonic plasma flow-field in the Plasmatron torch and test chamber was simulated using the VKI ICP code. The computed temperature at $x = 445$ mm, $r = 0$ mm is then compared to the experimental value and the simulation which produces the closest agreement is selected for comparison. To this purpose, an arithmetic average of the atomic line temperatures is then performed

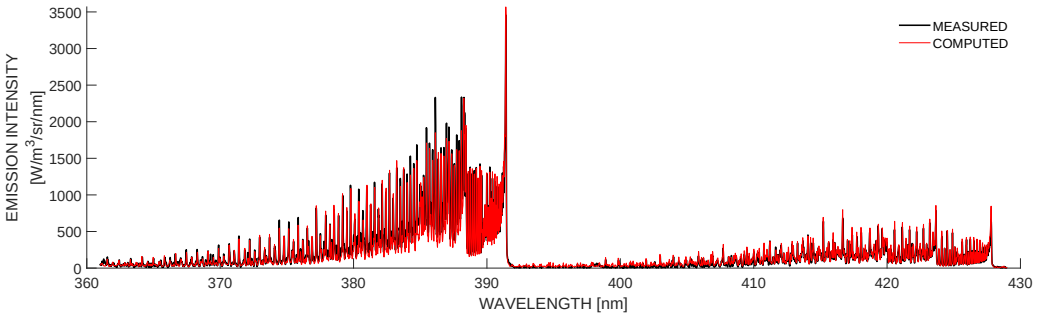

(a) $x = 195$ mm, $r = 0$ mm

Figure 4: Example of fitting of the absolute experimental spectra (black) with synthetic spectra (red) for the radial position at $r = 0$ mm at the axial location $x = 195$ mm, for the test condition $\mathbb{C}2$.

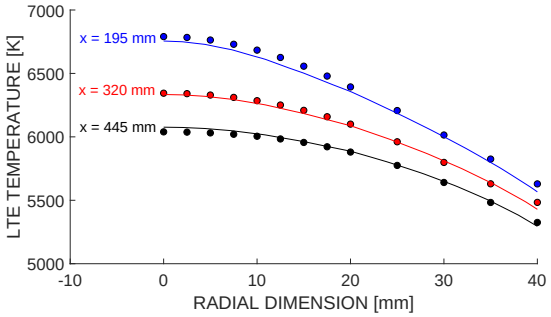

Figure 5: Test condition $\mathbb{C}1$: comparison between $T_{\mathrm{LTE}}^{\mathrm{avg}}$ (symbols) and the temperature profiles (solid lines) extracted from the MHD simulations of the plasma jet at the three axial positions for $\mathbb{P}_{\mathrm{el}}{}^{\mathrm{eff}} = 70$ kW.

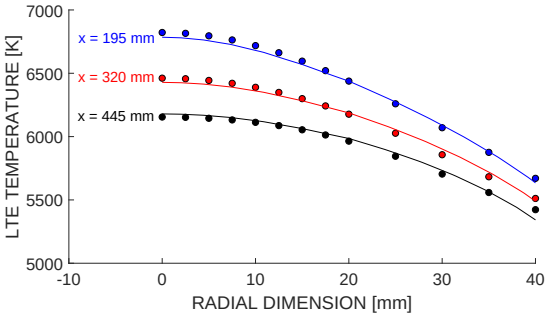

Figure 6: Test condition $\mathbb{C}2$: comparison between $T_{\mathrm{LTE}}^{\mathrm{avg}}$ (symbols) and the temperature profiles (solid lines) extracted from the MHD simulations of the plasma jet at the three axial positions for $\mathbb{P}_{\mathrm{el}}{}^{\mathrm{eff}} = 67.5$ kW.

at each radial location and for each axial position, providing $T_{\mathrm{LTE}}^{\mathrm{avg}}$. For condition $\mathbb{C}1$, the best match is found for $\mathbb{P}_{\mathrm{el}}^{\mathrm{eff}} = 70$ kW, corresponding to a power efficiency $\eta \approx 36\%$. For test condition $\mathbb{C}2$, the best match is found for $\mathbb{P}_{\mathrm{el}}^{\mathrm{eff}} = 67.5$kW, corresponding to a power efficiency $\eta \approx 33\%$. Figures 5 and 6 compare $T_{\mathrm{LTE}}^{\mathrm{avg}}$ with the temperature profiles extracted from the numerical simulations at the three axial positions. A remarkable agreement is found on the radial temperature distribution at every axial location. It is important to notice how the retrieved power efficiency is lower then the estimated value of 50%. We thus believe that such procedure could provide improved plasma flow characterization capabilities.

4. Material response investigation

Experimental and numerical capabilities must be also combined to correctly estimate the material response of the material sample exposed to the plasma flow. This capability reveals to be a crucial aspect in the design of valuable experiments, able to produce reliable and repeatable data for model development. For instance, surface temperature and recession rate should be estimated before the test to adequately adapt the experimental instrumentation to capture the observed phenomena. Test conditions, as far as heat flux and static pressure are concerned, should be chosen following a rigorous approach, in order to highlight and possibly isolate different demise mechanisms, e.g., evaporation, melting and shear ablation. Moreover, since reduced dimensional models are typically applied both for data reduction techniques as well as to rebuild experimental results, multidimensional heat transfer effects should be taken into account to provide the most accurate measurements. Hence, our approach follows a systematic procedure, which aims at including simulation tools at the experiment design level, trying to optimize the test config-

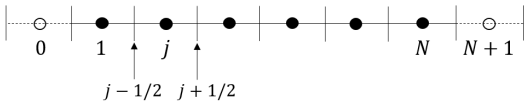

Figure 7: Discretization of the on-dimensional domain in N cells and N+1 interfaces.

uration for each specific condition.

4.1. Numerical approach

Building on the prior research of Dias et al. [26], who developed a coupled flow-material solver for the simulation of the ablation of Earth impacting meteoroids, we propose to complement and adapt such tool to ground testing of demisable materials.

The melting of the slab is a phase change problem, characterized by discontinuities in the thermophysical properties at material melting temperature. In such case, the integral form of the energy conservation, along with the equation of state expressing the temperature dependence of the enthalpy, contain all the physical information needed to determine the evolution of the phases [27].

Following the approach presented in ref. [27], the one-dimensional integral conservation law

$$\frac{d}{dt}\int_{\Omega_j} H + \oint_{\partial\Omega_j} \dot{\mathbf{q}}\cdot\mathbf{n} = \int_{\Omega_j} \dot{s}, \tag{6}$$

where H is the enthalpy per unit volume, $\dot{\mathbf{q}}$ is the heat flux and $\dot{s}$ is a volumetric source term, can be discretized in Cartesian coordinates (see Fig. 7) as

$$\begin{aligned} H_j^{n+1} &= H_j^n - \frac{\Delta t}{\Delta x}[F_{j+1/2} - F_{j-1/2})] \\ &+ s_j^{n+1} - s_j^n. \end{aligned} \tag{7}$$

The discrete approximation of the conservative variable is

$$H_j(t) = \frac{1}{\Delta x}\int_{\Delta x} H(x,t)dx, \tag{8}$$

while the numerical fluxes are

$$F_{j\pm1/2} = \frac{1}{\Delta t}\int_{t^n}^{t^{n+1}} \dot{q}_x(H(x_{j\pm1/2},t))dt. \tag{9}$$

The latter can be expressed with first order finite differences as

$$F_{j+1/2} = \dot{q}_{j+1/2} = -\frac{T_{j+1} - T_j}{R_{j+1/2}}, \tag{10}$$

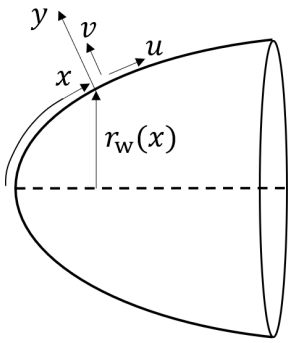

Figure 8: Sketch of the reference frame used to write the liquid layer equations.

being $R_{j+1/2}$ the heat resistance at the cell interface

$$R_{j+1/2} = \frac{1}{2}\left(\frac{\Delta x_{j+1}}{k_{j+1}} + \frac{\Delta x_j}{k_j}\right). \tag{11}$$

The equation of state provides the thermodynamic closure, giving the material enthalpy as a function of temperature

$$\begin{aligned} H(x,t) &= H(T_{\text{ref}}) \\ &+ \rho(T(x,t))\int_{T_{\text{ref}}}^{T(x,t)} c_p(\tau)d\tau \\ &+ \text{step}(T(x,t) - T_{\text{melt}})\cdot\rho(T_{\text{melt}})L_{\text{melt}}. \end{aligned} \tag{12}$$

where $\text{step}(T - T_{\text{melt}})$ is the Heaviside step function and L_{melt} is the latent heat of fusion. The previous relation can be easily inverted using an iterative procedure to compute the primitive variable as a function of the conservative variable.

Considering the particular case of space debris material samples exposed to high-temperature plasma flows, when subjected to aerodynamic heat transfer, pressure gradients and shear forces, they will form a flowing liquid layer. The equations governing the liquid layer are nearly the same as for the case of an incompressible gas boundary layer, the difference being a variation of viscosity with temperature [11]. Considering the reference frame depicted in fig. 8, the conservation of mass and momentum reduce to the following [28]

$$\begin{cases} \frac{\partial(r_w(x)u)}{\partial x} + \frac{\partial(r_w(x)v)}{\partial y} = 0 \\ \rho u\frac{\partial u}{\partial x} + \rho v\frac{\partial u}{\partial y} = \frac{\partial}{\partial y}[\mu\frac{\partial u}{\partial y}] - \frac{\partial p}{\partial x} \\ \frac{\partial p}{\partial y} = 0. \end{cases} \tag{13}$$

If we consider that the thickness of the molten layer is small and that the gradient of the thickness along

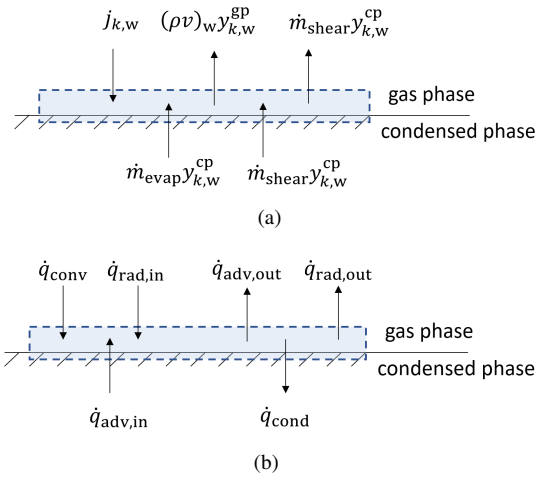

Figure 9: Schematic of the surface mass (a) and energy (b) balances for an infinitesimally thin control volume, fixed to the ablating surface.

the molten surface is small, we can neglect the convective terms in the x - momentum equation of 13 [11]. Moreover, considering that $\partial p/\partial y = 0$, we have $\partial p/\partial x = dp_w/dx$. Furthermore, in the stagnation region we have $r_w = x$, hence we obtain the simplified equations, valid around the stagnation point

$$\begin{cases} \frac{1}{x}\frac{\partial(xu)}{\partial x} + \frac{\partial v}{\partial y} = 0 \\ \frac{\partial}{\partial y}(\mu \frac{\partial u}{\partial y}) = \frac{dp_w}{dx}. \end{cases} \tag{14}$$

The latter system is then integrated in the liquid layer thickness δ to provide the normal recession velocity due to the motion of the molten layer

$$v_{melt} = \int_0^{\delta} 2 \cdot \left[\int_0^{y} \left(\frac{\tau'_w + p''_w(\eta - \delta)}{\mu(\eta)} \right) d\eta \right] dy, \tag{15}$$

where τ_w and p_w are the tangential shear stress and pressure. Thus, the ablating mass flux due to the motion of the liquid layer can be estimated as $\dot{m}_{shear} = \rho^{cp}_w v_{melt}$.

As far as the evaporation boundary condition is concerned, $\mathcal{B}'$ tables are widely used in the aerospace community to estimate the evaporation mass loss rate as a function of temperature and pressure for thermal protection materials [12]. In this case, surface mass and energy balances at thermodynamic equilibrium couple the atmosphere of interest with the ablating surface, as sketched in Fig. 9, with an imaginary thin control volume fixed to the receding wall.

Considering Fig. 9(a), the conservation of the element mass yields

$$j^{gp}_{k,w} + \dot{m}_{pg} y^{pg}_{k,w} + \dot{m}_{evap} y^{cp}_{k,w} = (\rho v)^{gp}_w y^{gp}_{k,w}. \tag{16}$$

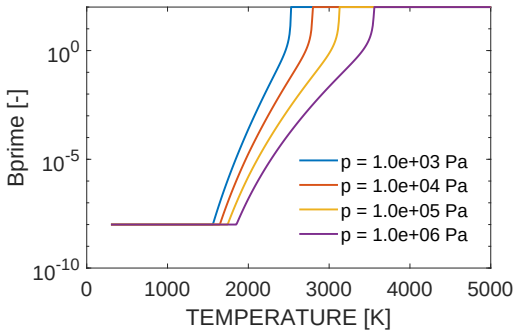

Figure 10: Temperature and pressure dependence of $\mathcal{B}'$ for a multiphase mixture of SiO_2 and air.

In particular, one can notice that the ablated mass flux due to shear $\dot{m}_{shear}$ does not participate in the net balance, since by assumption it does not undergo any phase change. By summing over all the elements and considering that $\sum_k j^{gp}_{k,w} = 0$, we obtain $(\rho v)^{gp}_w = \dot{m}_{evap}$. Finally, introducing the dimensionless blowing coefficient

$$\mathcal{B}' = \frac{\dot{m}_{evap}}{\rho_e u_e c_m}, \tag{17}$$

eq. 16 can be rewritten as

$$\mathcal{B}' = \frac{y^{gp}_{k,e} - y^{gp}_{k,w}}{y^{gp}_{k,w} - y^{cp}_{k,w}}. \tag{18}$$

The gas phase equilibrium composition $y^{gp}_{k,w}$ of the multiphase system is computed with the MUTATION++ library, allowing to obtain $\mathcal{B}'$ tables as a function of the surface temperature and pressure (see Fig. 10). Once the ablating mass flux $\dot{m} = \dot{m}_{evap} + \dot{m}_{shear}$ is computed, one can determine the recession speed as

$$\dot{s}_w = \frac{\dot{m}}{\rho^{cp}_w}. \tag{19}$$

Considering now the control volume sketched in fig. 9(b), under common transfer coefficient assumptions [12], the surface energy balance yields

$$\begin{aligned} \dot{q}_{cond} &= -k\nabla T \cdot \hat{\mathbf{n}} = \\ &= \rho_e u_e c_h (h^{gp}_r - h^{gp}_w) - \sigma\varepsilon(T^4_w - T^4_{amb}) \\ &- \dot{m}_{evap}(h^{gp}_w - h^{cp}_w) \end{aligned} \tag{20}$$

where $\hat{\mathbf{n}}$ is the outgoing normal to the boundary. In particular, we can notice that $\dot{q}_{adv,out} - \dot{q}_{adv,in} = \dot{m}_{evap}(h^{gp}_w - h^{cp}_w)$, i.e., the ablated energy due to shear forces does not contribute to the net balance, since by assumption it does not undergo any phase change.

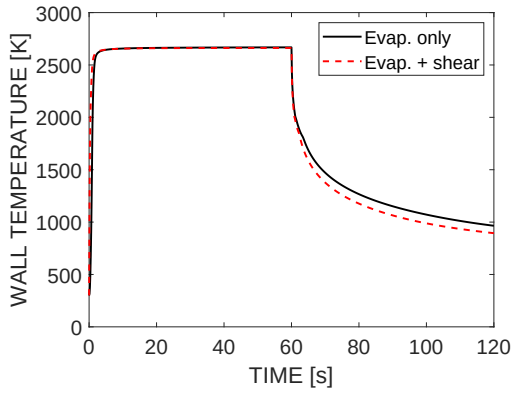

(a)

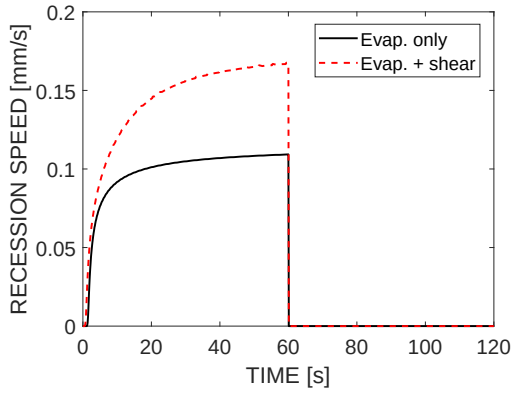

(b)

Figure 11: Time evolution of the surface temperature (a) and recession speed (b), comparing the two ablation mechanisms, i.e., evaporation and shear ablation.

Hence, once the multiphase equilibrium and surface mass balance are computed, h_w^{gp} and $\dot{m}_{evap} = \mathcal{B}' \cdot \rho_e u_e C_h$ are known, and the conductive flux $\dot{q}_{cond}$ at the boundary can be computed. This can be directly exploited as a boundary flux to update the solution at the following time step. The solver has been validated against analytical solution for transient heat conduction, one- and two-phase melting and similar ablative material response codes [29]. As an application example, Fig. 11 shows the transient wall temperature and recession speed estimated for a 50 mm silica test sample, exposed to representative Plasmatron flow conditions.

4.1.1. *Coupling with the VKI boundary layer solver*

The melting-ablation solver has been coupled to the VKI boundary layer solver NEBOULA by means of a loosely coupled approach [30]. The main assumption here is that the flow time scale is much smaller than the material time scale ($\tau_{flow} \ll \tau_{mat}$). Assuming that the boundary layer edge conditions are constant, a steady-state flow solution is computed with the surface temperature provided by the material code, hence the resulting wall heat flux is provided to the latter. The transient thermal solution in the material is then recomputed in a macro time step, until the surface temperature or recession length exceed a predefined threshold value. Hence the next steady-state flow solution is computed with the new surface temperature provided by the material solver.

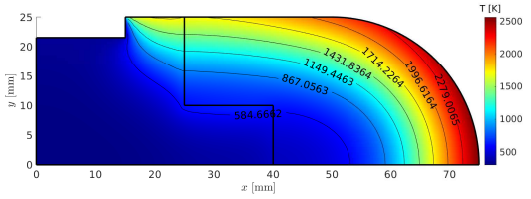

Figure 12: Snapshot of the two-dimensional unsteady heat transfer simulation used to extract $\partial \dot{q}_r / \partial r(x,t)$ for the correction on the one-dimensional solver.

4.1.2. *Correction for two-dimensional conduction effects*

Our previous work showed that the thermal behaviour of the material sample exposed to the plasma flow can be far from the one-dimensional approximation [31]. As a result, the two-dimensional axially symmetric transient thermal solution (Fig. 12) is computed on the initial sample shape and the radial conduction gradient $\partial \dot{q}_r / \partial r(x,t)$ is extracted. The latter, then, can be used as a source term in the one-dimensional computations to recover a more realistic approximation, yet maintaining the computational efficiency of the one-dimensional solver.

4.2. *Experimental methods for ablation characterization*

A schematic of the experimental setup for in situ ablation measurements can be found in Fig. 13. Optical and intrusive temperature measurements offer reliable means of comparison with computational models. Two-colour pyrometry provides direct information of the material surface temperature. Used in combination with broadband radiometry, the total directional emissivity can be measured in situ, at high temperature and in a time-resolve fashion. Such information is critical for accurate numerical simulations, as radiation is the primary means of cooling at extreme

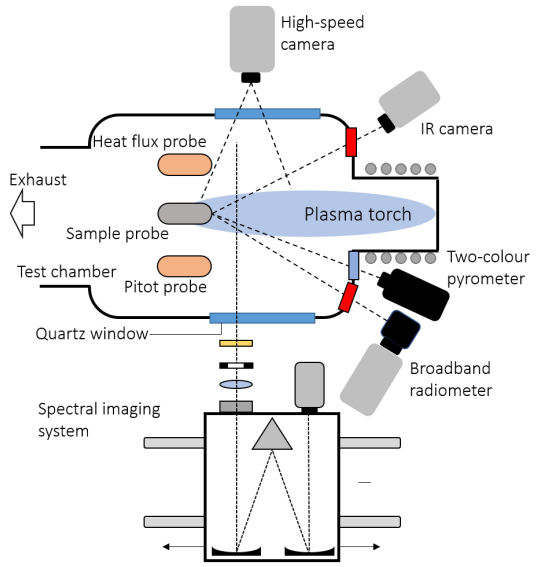

Figure 13: Snapshot of the two-dimensional unsteady heat transfer simulation used to extract $\partial \dot{q}_r / \partial r(x,t)$ for the correction on the one-dimensional solver.

re-entry conditions. Test models can be additionally instrumented with high-temperature type-K and type-R thermocouples, in order to monitor the temperature evolution in specific points. Moreover, infrared thermography allows to determine surface temperature maps over the entire sample material, while high-speed camera imaging provides information about the material surface recession rate.

4.2.1. Recession and shape measurements

When exposed to the high-temperature plasma flow, the material sample (see Fig. 14(a)) can undergo significant surface recession due to ablation phenomena (Fig. 14(b)). To this purpose, the Vision Research Phantom 7.1 CMOS high-speed camera is adopted for the in-situ recession analysis of the ablating test sample. A calibration chessboard, placed at the initial sample location, provides the necessary pixel to length calibration. The recession rate is then retrieved by applying edge detection algorithms to the recoded frames. Finally, under the assumption of axisymmetry, the three-dimensional object shape can be easily inferred from the observed two-dimensional projection. Further data processing techniques, which allow to measure the local radius of curvature around the stagnation point, are being developed. This measurement reveals important to account for the change in the boundary layer structure as the material ablates.

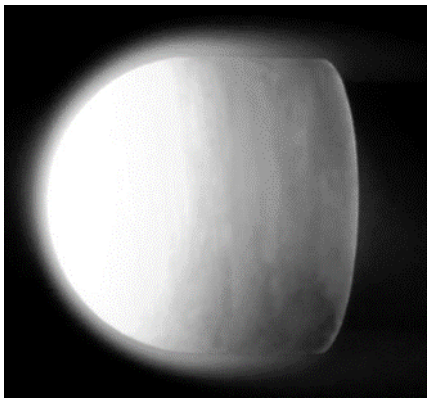

(a)

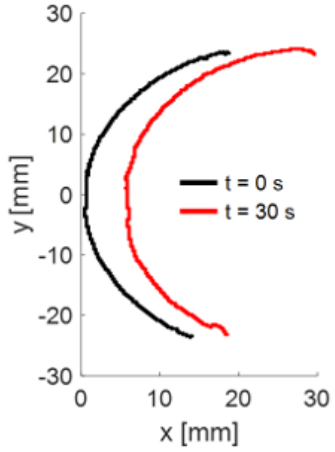

(b)

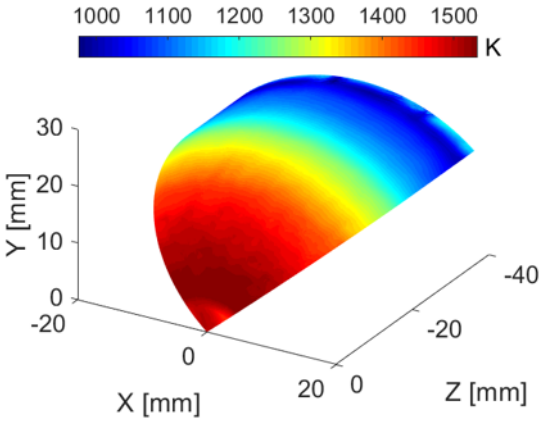

(c)

Figure 14: Time evolution of the surface temperature (a) and recession speed (b), comparing the two ablation mechanisms.

4.2.2. 3D temperature map reconstruction on an ablating surface

After proper intensity calibration and correction for emissivity, IR thermography provides a two-dimensional projection of an object temperature map. To exploit the multidimensional temperature information for quantitative measurements, however, it is required to establish the correspondence between the points of the observed surface and the pixels of the thermal image [32]. This procedure requires dedicated processing techniques if the object has a non-planar geometry. The optical calibration model here adopted exploits the camera calibration toolbox developed by Bouguet [33], which is based on the perspective projection model with lens distortion proposed by Heikkila [34]. In particular, this model is based on the combination of linear and nonlinear techniques. Extrinsic parameters (translation and rotation matrices) and intrinsic parameters (focal length, pixel position and pixel ratio) are employed to project a point from the real world coordinates to the image frame. Additionally, radial and tangential distortion components are used to compensate for the deviation of the light rays by the lens system. All the calibration parameters are found with a minimization of the root mean square difference between the known image coordinates of the calibration points and their position computed by means of the camera model. A suitable calibration target, equipped with thermally detectable spots, is adopted to provide the reference image for such procedure. Fig. 14(c) shows an example of the reconstructed three-dimensional temperature map over the observed sample.

5. Conclusions and future work

Ground testing of space debris metallic and silicate materials requires improvements in the existing experimental capabilities. In this paper, we reviewed and updated critical procedures in the VKI Plasmatron set-up and data processing techniques, which allow to perform more robust and repeatable measurements. As far as the flow characterization is concerned, locally resolved emission spectroscopy and an advanced data processing suite allows to perform local gas temperature measurement. Hence, a consistent power efficiency can be retrieved for the correct numerical simulations of the plasma flow. On the material investigation, instead, simulation tools, able to estimate melting and recession for evaporation and shear stresses, and corrected for multidimensional heat transfer effects, are being introduced at the experiment design level. The in situ material response characterization, featuring traditional techniques such as pyrometry, radiometry and high-speed camera imaging, has been improved with 3D temperature map reconstruction techniques, combined with recession measurement on an ablating surface.

Acknowledgement

The author would like to acknowledge B. Helber and D. Le Quang for the precious experimental support, B. Dias for the fruitful discussions about the melting-ablation modelling and A. Rizza for the help in the development of the material response code. F. Torres Herrador is aknwoledged for the review of this paper. The research of A. Fagnani is supported by a doctoral fellowship awarded from the Research Foundation Flanders (FWO, dossier 1SB3219N).

References

[1] H. Klinkrad, Space Debris, Vol. 60 of Springer Praxis Books, Springer Berlin Heidelberg, 2006. doi:10.1007/3-540-37674-7.
URL http://link.springer.com/10.1007/3-540-37674-7

[2] D. J. Kessler, N. L. Johnson, J. C. Liou, M. Matney, Kessler Syndrome-AAS Paper.pdf, Advances in the Astronautical Sciences.
URL https://pdfs.semanticscholar.org/2276/55e022441d1379dfdc395173ed2e776d54ee.pdf

[3] United Nations Office For Outer Space Affairs, Committee on the Peaceful Uses of Outer Space, Space Debris Mitigation Guidelines of the Committee on the Peaceful Uses of Outer Space, United Nations Publication (2010) 1arXiv:SalesNo.E.99.I.17.
URL http://www.unoosa.org/pdf/publications/st{_}space{_}49E.pdf

[4] ESA Space Debris Mitigation WG, ESA Space Debris Mitigation Compliance Verification Guidelines (1.0) (2015) 1–95.

[5] S. Lemmens, Q. Funke, H. Krag, On-ground casualty risk reduction by structural design for demise, Advances in Space Research 55 (11) (2015) 2592–2606. doi:10.1016/j.asr.2015.02.017.
URL http://dx.doi.org/10.1016/j.asr.2015.02.017

[6] Y. Prevereaud, Contribution à la modélisation de la rentrée atmosphérique des débris spatiaux, Université de Toulouse, 2014.

[7] S. Heinrich, J. Martin, J. Pouzin, Satellite design for demise thermal characterisation in early re-entry for dismantlement mechanisms, Acta Astronautica 158 (2019) 161–171. doi:10.1016/j.actaastro.2018.03.021.
URL https://doi.org/10.1016/j.actaastro.2018.03.021

[8] P. M. Waswa, M. Elliot, J. A. Hoffman, Spacecraft Design-for-Demise implementation strategy & decision-making methodology for low earth orbit missions, Advances in Space Research 51 (9) (2013) 1627–1637.

doi:10.1016/j.asr.2012.11.020.
URL http://dx.doi.org/10.1016/j.asr.2012.11.020

[9] Y. Prévereaud, J. L. Vérant, M. Balat-Pichelin, J. M. Moschetta, Numerical and experimental study of the thermal degradation process during the atmospheric re-entry of a TiAl6V4 tank, Acta Astronautica 122 (2016) 258–286. doi:10.1016/j.actaastro.2016.02.009.
URL http://dx.doi.org/10.1016/j.actaastro.2016.02.009

[10] B. Helber, Material Response Characterization of Low-density Ablators in Atmospheric Entry Plasmas, 2016.

[11] H. A. Bethe, M. C. Adams, A Theory for the Ablation of Glassy Materials, Journal of the Aerospace Sciences 26 (6) (1959) 321–328. doi:10.2514/8.8080.
URL http://arc.aiaa.org/doi/10.2514/8.8080

[12] B. Helber, A. Turchi, J. B. Scoggins, A. Hubin, T. E. Magin, Experimental investigation of ablation and pyrolysis processes of carbon-phenolic ablators in atmospheric entry plasmas, International Journal of Heat and Mass Transfer 100 (2016) 810–824. doi:10.1016/j.ijheatmasstransfer.2016.04.072.
URL http://dx.doi.org/10.1016/j.ijheatmasstransfer.2016.04.072

[13] P. F. Barbante, O. Chazot, Flight extrapolation of plasma wind tunnel stagnation region flowfield, Journal of Thermophysics and Heat Transfer 20 (3) (2006) 493–499. doi:10.2514/1.17185.

[14] D. Vanden Abeele, G. Degrez, Efficient computational model for inductive plasma flows, AIAA journal 38 (2) (2000) 234–242. doi:10.2514/3.14402.

[15] D. Le Quang Huy, Spectroscopic Measurements of Sub- and Supersonic Plasma Flows for the Investigation of Atmospheric Re-entry Shock Layer Radiation., von Karman Institute for Fluid Dynamics, 2015.

[16] A. Fagnani, D. Le Quang Huy, B. Helber, S. Demange, A. Turchi, O. Chazot, A. Hubin, Investigation of a Free-Stream Air Plasma Flow by Optical Emission Spectroscopy and Comparison to Magnetohydrodynamics Simulations (2020) 1–15doi:10.2514/6.2020-0382.

[17] G. Degrez, D. V. Abeele, P. Barbante, B. Bottin, Numerical simulation of inductively coupled plasma flows under chemical non-equilibrium, International Journal of Numerical Methods for Heat and Fluid Flow 14 (4) (2004) 538–558. doi:10.1108/09615530410532286.

[18] P. Barbante, Accurate and Efficient Modelling of High Temperature Nonequilibrium Air Flows (2001).

[19] H.-J. Kunze, Introduction to Plasma Spectroscopy, Vol. 56 of Springer Series on Atomic, Optical, and Plasma Physics, Springer Berlin Heidelberg, Berlin, Heidelberg, 2009. doi:10.1007/978-3-642-02233-3.
URL http://link.springer.com/10.1007/978-3-642-02233-3

[20] C. O. Laux, T. G. Spence, C. H. Kruger, R. N. Zare, Optical diagnostics of atmospheric pressure air plasmas, Plasma Sources Science and Technology 12 (2) (2003) 125–138. doi:10.1088/0963-0252/12/2/301.

[21] G. Pretzier, A New Method for Numerical Abel-Inversion, Zeitschrift für Naturforschung A 46 (7) (1991) 639–641. arXiv:arXiv:1011.1669v3, doi:10.1515/zna-1991-0715.
URL http://www.degruyter.com/view/j/zna.1991.46.issue-7/zna-1991-0715/zna-1991-0715.xml

[22] A. Kramida, Y. Ralchenko, J. Reader, NIST Atomic Spectra Database, Accessed in November 2019 (April 2014).
URL http://physics.nist.gov/PhysRefData/ASD/index.html

[23] S. Chauveau, C. Deron, M. Y. Perrin, P. Riviére, A. Soufiani, Radiative transfer in lte air plasmas for temperatures up to 15,000 k, Journal of Quantitative Spectroscopy and Radiative Transfer 77 (4) (2003) 113–130.

[24] C. O. Laux, Radiation and nonequilibrium collisional-radiative models, VKI Special course on Physico-chemical models for high enthalpy and plasma flow modelling (2002) 1–55.

[25] J. B. Scoggins, Development of numerical methods and study of coupled flow, radiation, and ablation phenomena for atmospheric entry, Ph.D. thesis, von Karman Institute for Fluid Dynamics & CentraleSupélec (2017).

[26] B. Dias, F. Bariselli, A. Turchi, A. Frezzotti, P. Chatelain, T. Magin, Development of a melting model for meteors, in: AIP Conference Proceedings, Vol. 1786, 2016, p. 160004. doi:10.1063/1.4967661.
URL http://aip.scitation.org/doi/abs/10.1063/1.4967661

[27] V. Alexiades, A. D. Solomon, Mathematical Modeling Of Melting And Freezing Processes, CRC Press, 1992.

[28] H. Schlichting, K. Gersten, Boundary-Layer Theory, 9th Edition, Springer Berlin Heidelberg, Berlin, Heidelberg, 2017. doi:10.1007/978-3-662-52919-5.
URL http://link.springer.com/10.1007/978-3-662-52919-5

[29] A. Fagnani, Development of a one-dimensional melting ablation solver (2019).

[30] P. Schrooyen, Numerical Simulation of Aerothermal Flows Through Ablative Thermal Protection Systems, Doctoral Dissertation 3 (1) (2014) 123–139. doi:10.1080/19301944.2009.10781364.

[31] A. Fagnani, B. Helber, O. Chazot, Evaluation of Probe-Material Thermal Interaction in Plasma Wind Tunnel Tests by Means of IR Thermography and Thermal Inverse Modellingdoi:10.13009/EUCASS2019-413.

[32] G. Cardone, A. Ianiro, G. Dello Ioio, A. Passaro, Temperature maps measurements on 3D surfaces with infrared thermography, Experiments in Fluids 52 (2) (2012) 375–385. doi:10.1007/s00348-011-1225-9.

[33] J.-Y. Bouguet, Camera calibration toolbox for matlab, available at: http://www.vision.caltech.edu/bouguetj. Accessed on 2019-05.

[34] J. Heikkila, Geometric camera calibration using circular control points, IEEE Transactions on Pattern Analysis and Machine Intelligence 22 (10) (2000) 1066–1077. doi:10.1109/34.879788.
URL http://ieeexplore.ieee.org/document/879788/

Towards a high-fidelity multiphase solver with application to space debris aerothermal ablation modeling

David Henneaux

Aeronautics and Aerospace Department, von Karman Institute for Fluid Dynamics, Belgium, david.henneaux@vki.ac.be

Supervisor: Thierry Magin

Professor, Aeronautics and Aerospace Department, von Karman Institute for Fluid Dynamics, Belgium, magin@vki.ac.be

University Supervisor: Philippe Chatelain

Professor, Institute of Mechanical, Materials and Civil Engineering, Université catholique de Louvain, Belgium, philippe.chatelain@uclouvain.be

Abstract

This work focuses on the first developments of a high-order sharp interface method to treat the gas-liquid interface that appears in the ablation of metallic space debris during an atmospheric entry. The coupling of both phases through interface jump conditions as well as the algorithm followed to impose them are explained. Some first verification test cases are considered, showing the potential of the method to deal with this situation.

Keywords: Compressible Multiphase Flows, High-Order Method, Sharp Interface

1. Introduction

Multiphase flows have become increasingly important in the last decades in a wide variety of engineering applications for their optimum design and safe operations. The mathematical representation and the numerical treatment of this kind of flows are made much more complicated than for single phase flows due to the existence of deformable and moving interfaces. Across those significant discontinuities of fluid properties exist, usually accompanied by phase transitions and complex flow features. While most commercial solvers today rely on the assumption of incompressible multiphase flows, high temperatures and/or high pressures can be encountered which violate this hypothesis. These conditions can be found in a large number of engineering applications for which accurate modeling and simulation are crucial. In particular, the prediction of space debris ablation by means of numerical simulations requires the elaboration of a method able to deal with the complex interface separating the surrounding gas from the condensed phase. The physical phenomena involved in this particular situation shall be described in more details below.

When a debris reenters the Earth's atmosphere from the low Earth orbit (LEO), which is by far the most congested one, it is subjected to extreme temperatures and heat fluxes due to its hypersonic velocity of about 8 km/s. This intense aerothermodynamic heating comes from the hot plasma air surrounding the body that has come through a strong shock wave and the viscous dissipation of the high-kinetic-energy flow in the boundary layer adjacent to the body surface. The degradation of metallic and glassy materials, which shares a lot of similarities with the degradation of meteors, is a recent research field which has gotten increased interest with the implementation of space debris mitigation projects [1]. The peculiarity of this class of materials is the strongly coupled interaction between the gas, liquid and solid phases during ablation. Exposed to high-enthalpy flow, metallic debris undergoes melting with the subsequent apparition of a flowing liquid molten layer over the solid surface, whose dynamic is influenced by surface tension effects. The extreme temperature gradients that develop in the vicinity of the object prevent the assump-

tion of a solenoidal velocity field and compressible[1] equations must be considered to describe correctly the thermal dilatation of the metallic liquid layer [2]. This liquid layer is progressively removed by intense evaporation and shear forces exerted by the surrounding gas, while the surface of the solid recedes as the melting front progresses. This results in the aerothermal ablation of the debris, sketched in Fig. 1.

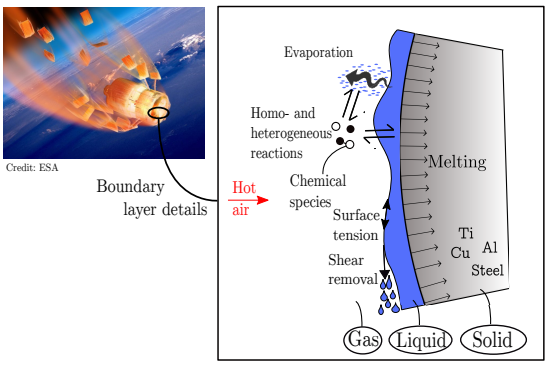

Figure 1: Schematic representation of the ablation of a metallic space debris during an atmospheric reentry with the associated physico-chemical phenomena. A two-phase compressible solver is needed to treat the gas-liquid interface.

The present work is part of a project whose ambition is the development of an unified numerical tool for producing high-fidelity simulations of the aerothermal ablation of metallic re-entering space debris. One of the main elements of this tool is the development of an accurate compressible multiphase solver which will be able to deal with the important jumps in properties between the gas and the condensed phase while taking into account the various physical phenomena described before. There exists different approaches in the literature to cope with this kind of situations and the one selected in this work is compared to some of the main existing methods in the following paragraph.

The treatment of multiphase compressible flows brings additional difficulties compared to the treatment of their incompressible counterparts. Indeed, hydrodynamics and thermodynamics are strongly coupled through equations of state in the bulk of each phase, which are moreover different in the case of gas-liquid flows (typically the perfect gas EOS for the gas and a more elaborated stiff EOS for the liquid). The main difficulty is therefore related to the elaboration of a consistent numerical strategy to treat the discontinuous nature of the interface together with the related physical interface processes such as surface tension or phase change [3]. Two approaches can be identified to tackle these challenges: diffuse and sharp interface methods. In the first approach, which is the most common one, a set of averaged equations governing mean values of flow quantities are usually considered. Many variants that are often derived from the Baer-Nunziato model [4] exist. The averaging procedure introduces additional terms to be modeled that represent the interfacial transfer mechanisms between the phases. In the case of dispersed two-phase flows where one phase is scattered in the other, the averaging approach is the only possible one. However, for separated multiphase flows in which clear material interfaces can be identified, the use of this technique can lead to an important loss of accuracy in the representation of the interfacial phenomena, due to the smearing introduced by the averaging. In this situation, to which the ablation of space debris belongs, it is preferable to have a sharp representation of the interface in order to model with accuracy the phenomena driving the physics of the interface. This can be accomplished by modifying the numerical scheme to capture the jumps across the interface, without any smoothing. This is realized by coupling at the interface the field equations valid in the bulk of each phase through the resolution of some jump conditions. Different strategies have been developed with this respect, among which the moving grid [5], the ghost-fluid [6] or the cut-cell [7] methods are the most popular. In this work, a novel sharp interface method based on the discontinuous Galerkin method (DGM) is considered. This method, called the eXtended discontinuous Galerkin (XDG) method, was proposed, for example, in [8] and further developed in [9] or [10]. In the existing multi-physics DG platform ARGO[2] [11], this method has been implemented by Schrooyen et al. and first results were presented in [12; 13]. The XDGM directly takes advantage of the appealing properties of the DG method and it allows to preserve its high-order convergence in the vicinity of a material interface. With the ever more

[1] By "compressible" equations, we mean equations in which the density variations with temperature are too important to be modeled by the Boussinesq approximation and must be taken into account in the continuity equation. The liquid phase remains however nearly incompressible, as the density is very weakly dependent on pressure variations.

[2] ARGO is a proprietary code developed by the Belgian research center Cenaero.

stringent accuracy requirements imposed in many industrial flow problems whose space debris ablation is clearly part of, such high-order methods have an essential role to play.

The present work will exploit the great potential of this new sharp interface method by extending its capabilities to compressible multi-phase flows. In order to achieve this goal, the single-phase compressible solver inside Argo has been first extended to solve the Navier-Stokes equations closed by general equations of state (EOS) under an analytical form. Single-phase compressible test cases with immersed boundaries treated by the XDGM were considered as a first step [14]. The new module has then been coupled to the XDG solver and dedicated techniques were developed to couple the two phases at the interface through jump conditions. They are detailed in Sec. 3 after a description of the numerical method in itself. The first results concerning simple verification test cases are analyzed in Sec. 4. It is important to note that at this stage, only inviscid flows without phase transition have been considered. The perspectives to extend the capabilities of the solver are presented in Sec. 5.

2. Physical modeling

2.1. Governing equations in the bulk of each phase

The general compressible multispecies Navier-Stokes equations that will be considered in the gas and in the liquid phases [3] in future work can be written by splitting the convective and diffusive fluxes, neglecting any chemical reactions or radiation in this case, as:

$$\frac{\partial \mathbf{u}_k}{\partial t} + \nabla \cdot \mathbf{F}^c = \nabla \cdot \mathbf{F}^d \,, \tag{1}$$

where the conservative variables, the convective fluxes and the diffusive fluxes are given respectively by

$$\begin{aligned} &\mathbf{u}_k = \begin{bmatrix} \rho_{k,i} \\ \rho_k \mathbf{v}_k \\ \rho_k E_k \end{bmatrix}, \quad \mathbf{F}^c(\mathbf{u}_k) = \begin{bmatrix} \rho_{k,i}\mathbf{v}_k \\ \rho_k \mathbf{v}_k \mathbf{v}_k + p_k \mathbf{I} \\ \rho_k \mathbf{v}_k H_k \end{bmatrix}, \\ &\mathbf{F}^d(\mathbf{u}_k, \nabla \mathbf{u}_k) = \begin{bmatrix} -\rho_{k,i}\mathbf{V}_{k,i} \\ \boldsymbol{\tau}_k \\ \boldsymbol{\tau}_k \cdot \mathbf{v}_k - \mathbf{q}_k \end{bmatrix}, \quad \forall i \in \{1, N_s\} \,, \end{aligned} \tag{2}$$

[3] As the computation of transport properties for multispecies liquid phase is made particularly difficult due to the absence of general models, a single species liquid (composed of multiple elements) will most probably be considered instead.

in which N_s is the number of species in the whole system (i.e. including the species inside the gas and the liquid phases), the density of the ith-species in the kth-phase is noted $\rho_{k,i}$, the velocity vector $\mathbf{v}_k$, the diffusion velocity $\mathbf{V}_{k,i}$ and the static pressure p_k. The total energy E_k and the total enthalpy H_k per unit mass both include thermal and kinetic contributions

$$E_k = e_k + \frac{\mathbf{v}_k \cdot \mathbf{v}_k}{2}, \quad H_k = h_k + \frac{\mathbf{v}_k \cdot \mathbf{v}_k}{2} = e_k + \frac{p_k}{\rho_k} + \frac{\mathbf{v}_k \cdot \mathbf{v}_k}{2}, \tag{3}$$

with the specific internal energy e_k and the specific enthalpy h_k. The constitutive equations for the shear stress tensor $\boldsymbol{\tau}_k$ and the heat flux $\mathbf{q}_k$ are written as

$$\begin{aligned} \boldsymbol{\tau}_k &= \mu_k \left[\nabla \mathbf{v}_k + (\nabla \mathbf{v}_k)^T - \frac{2}{3} \nabla \cdot \mathbf{v}_k \mathbf{I} \right], \\ \mathbf{q}_k &= -\lambda_k \nabla T_k + \sum_{i=1}^{N_s} \rho_{k,i} h_{k,i} \mathbf{V}_{k,i} \,, \end{aligned} \tag{4}$$

following the assumption of a Newtonian fluid and the Fourier law, with the dynamic viscosity μ_k, the thermal conductivity λ_k and the temperature T_k.
In the present work, inviscid single species equations with constant heat capacities are considered. The Euler equations that are solved by the solver in the bulk of the kth-phase can therefore be written as

$$\frac{\partial \mathbf{u}_k}{\partial t} + \nabla \cdot \mathbf{F}^c = \mathbf{0} \,, \tag{5}$$

where

$$\mathbf{u}_k = \begin{bmatrix} \rho_k \\ \rho_k \mathbf{v}_k \\ \rho_k E_k \end{bmatrix}, \quad \mathbf{F}^c(\mathbf{u}_k) = \begin{bmatrix} \rho_k \mathbf{v}_k \\ \rho_k \mathbf{v}_k \mathbf{v}_k + p_k \mathbf{I} \\ \rho_k \mathbf{v}_k H_k \end{bmatrix}, \tag{6}$$

To close the system of Eqs. (5), it must be supplemented by constitutive relations relating intensive thermodynamic properties at equilibrium. For this purpose, it is needed to provide two so-called incomplete EOS that unequivocally determine the state of the fluid inside each phase k, which are a volumetric, i.e. $p_k = p_k(\rho_k, T_k)$, and a caloric, i.e. $e_k = e_k(\rho_k, T_k)$, EOS [15]. These two relations can be expressed, for example, under a general analytical form, known as the Mie-Grüneisen form:

$$\begin{cases} p_k(\rho_k, T_k) = p_{\text{ref},k}(\rho_k) + \rho_k \, \Gamma_k(\rho_k) \, e_{\text{th},k}(\rho_k, T_k) \,, \\ e_k(\rho_k, T_k) = e_{\text{ref},k}(\rho_k) + e_{\text{th},k}(\rho_k, T_k) \,, \end{cases} \tag{7}$$

where the Grüneisen coefficient is given by

$$\Gamma_k(\rho_k) = \frac{1}{\rho_k} \left(\frac{\partial p_k}{\partial e_k} \right)_{\rho_k = \text{const}} \,, \tag{8}$$

and the thermal part of the internal energy by

$$e_{\mathrm{th},k}(\rho_k, T_k) = e_{0,k} + \int_{T_{0,k}}^{T_k} C_{v,k}(\rho_k, T^{'})\,\mathrm{d}T^{'}\ , \quad (9)$$

with a reference state $\bullet_{0,k}$ and the specific heat at constant volume $C_{v,k}$. $p_{\mathrm{ref},k}$ and $e_{\mathrm{ref},k}$ are the properly chosen states of the pressure and internal energy along some reference curve (e.g. along an isentrope or a single shock Hugoniot) in order to match the experimental data of the material being examined [16]. This type of EOS is an adequate approximation to a wide variety of materials, as long as the state of the fluid remains near the reference curve [17]. In particular, it has been used to model the behavior of compressible liquid metals [18; 2], which makes it a good candidate to model the condensed phase (i.e. the liquid and the solid) of a metallic ablating space debris. That is why this general EOS is chosen as a basis to derive more specific EOS. The extension of the DG solver to general EOS requires also the definition of some thermodynamic derivatives that are used to express the speed of sound, as well as to build the Jacobian matrices for the implicit time-stepping scheme. More details can be found in [14].

2.2. Jump conditions at the interface

The use of a sharp interface method in this work leads to a so-called local instant formulation requiring the resolution of some jump conditions at the interface. These conditions specify the exchanges of mass, momentum, and energy through the interface and stand as matching conditions between the two phases. Considering the projections of the momentum jump conditions along the normal $\mathbf{n}_{int}$ and the tangent $\mathbf{t}_{int}$ to the interface, they read:

$$\begin{aligned}
&-v_{int,n}[\![\rho]\!] + [\![\rho v_n]\!] = 0\ ,\\
&-v_{int,n}[\![\rho v_n]\!] + [\![\rho v_n^2 + p]\!] = \Delta p_\sigma + [\![\boldsymbol{\tau}\cdot\mathbf{n}_{int}\cdot\mathbf{n}_{int}]\!]\ ,\\
&0 = [\![\boldsymbol{\tau}\cdot\mathbf{n}_{int}\cdot\mathbf{t}_{int}]\!] + \nabla_s\sigma\cdot\mathbf{t}_{int}\ ,\\
&-v_{int,n}[\![\rho E]\!] + [\![(\rho E + p)\,v_n]\!] + [\![\mathbf{q}\cdot\mathbf{n}_{int}]\!]\\
&\qquad = \Delta p_\sigma v_{int,n} + [\![\boldsymbol{\tau}\cdot\mathbf{v}\cdot\mathbf{n}_{int}]\!]\ ,
\end{aligned} \quad (10)$$

where the jump operator across the interface with position $\mathbf{x}$ for some quantity α defined in the bulk of each phase is given by

$$[\![\alpha]\!] = (\alpha_2 - \alpha_1)\ , \quad \text{with} \quad \alpha_k = \lim_{\epsilon\to 0,\epsilon>0} \alpha(\mathbf{x} \pm \epsilon\mathbf{n}_{int})\ , \quad (11)$$

$v_{int,n}$ and v_n are the normal components of the interfacial and the bulk velocities, respectively, $\Delta p_\sigma = \sigma\kappa$ represents the pressure jump induced by surface tension effects, with the surface tension coefficient σ and the interface curvature κ, and $\nabla_s\sigma$ is the derivative of the surface tension coefficient along the interface, which is responsible for Marangoni effects if different from zero. Note that non-slip condition at the interface has been assumed in the tangential momentum balance:

$$[\![\mathbf{v}\cdot\mathbf{t}_{int}]\!] = 0\ . \quad (12)$$

The interfacial jump conditions Eqs. (10) with the no-slip condition Eq. (12) do not constitute sufficient matching conditions which are necessary to define the problem uniquely. Consequently, they must be supplemented by an additional condition expressing the net mass flux associated to phase changes, defined as

$$\dot{m}_{int} = \rho_k(v_{int,n} - v_{n,k})\ . \quad (13)$$

Several possibilities exist and can be roughly categorized in thermodynamic equilibrium and non-equilibrium models, each one of them including models for single component or multi-components systems. Since we restrict ourselves to an inviscid model with no phase transition for the moment, the net mass flux across the interface Eq. (13) is zero, the additional relation for expressing it is not needed and the jump conditions that are considered converge to the hydrodynamic equilibrium between both phases:

$$\begin{aligned}
[\![v_n]\!] &= 0\ ,\\
[\![p]\!] &= \Delta p_\sigma\ .
\end{aligned} \quad (14)$$

Note that the pressure laws $p_i = p_i(\rho_i, e_i)$ are allowed to be different in the two phases. The main goal and challenge of this work is to incorporate the jump conditions Eqs. (14) in the framework of the XDGM. The strategy to reach this objective is explained in Sec. 3.3.

3. Numerical methods

3.1. Extended discontinuous Galerkin method

As stated before, the XDGM belongs to the class of sharp interface methods and thus preserves the high-order of convergence of the DGM in the vicinity of the interface by avoiding any degradation of the solution. One of the most interesting features of the XDGM is that the mesh is kept fixed and does not need to conform with the interface. The simulation

of ablating materials, which is the final goal of this work, involves inevitably important interface deformations with complex dynamics. For such applications, remeshing process can be time-consuming and complicated. It might be advantageous in this case to use a fixed and simple mesh instead and to track the position of the interface with a dedicated technique. The difficulty is then for the method to be able to handle discontinuous fields inside the elements. In what follows, it is explained how this can be achieved with the XDGM, in the context of two-phase inviscid compressible flows.

Let formulate the discretized weak formulation of the governing Euler Eqs. (5) as follows: find $\mathbf{u}^h \in \mathcal{V}^h$ such that

$$\mathcal{E}(\mathbf{u}^h, \mathbf{v}^h) = \sum_{m=1}^{M} \mathcal{E}_m(\mathbf{u}_m^h, \mathbf{v}_m^h) = 0\,, \quad \forall \mathbf{v}^h \in \mathcal{V}^h\,,$$

in which the subscript $\bullet_m$ denotes the m-th element, and $\mathbf{u}^h$ and $\mathbf{v}^h$ are the approximated discrete solutions and test functions, respectively, both expressed as linear combinations of some shape functions forming a base for the finite dimensional space $\mathcal{V}^h$. Developing the contribution of a single element to the global formulation, the distinction is made between:

- an element Ω_m with edges $\partial\Omega_m$ in the bulk of phase k:

$$\begin{aligned}\mathcal{E}_m = &\int_{\Omega_m} \mathbf{v}_m^h \cdot \frac{\partial \mathbf{u}_m^h}{\partial t}\,\mathrm{d}V \\ &- \int_{\Omega_m} \nabla^h \mathbf{v}_m^h : \mathbf{F}^c(\mathbf{u}_m^h)\,\mathrm{d}V \\ &+ \int_{\partial\Omega_m} \mathbf{v}_m^h \cdot \underbrace{(\mathbf{F}^c(\mathbf{u}_m^h)\cdot\mathbf{n}_{\partial\Omega_m})}_{\mathcal{H}(\mathbf{u}_m^{h,+},\,\mathbf{u}_m^{h,-})}\,\mathrm{d}S\,,\end{aligned} \tag{15}$$

  where $\mathcal{H}$ is a numerical flux function depending on both the interior and exterior solutions, $\mathbf{u}_m^{h,+}$ and $\mathbf{u}_m^{h,-}$, on the element edges;

- an element $\Omega_m = \Omega_{m,1} \cup \Omega_{m,2}$ with edges $\partial\Omega_m = \partial\Omega_{m,1} \cup \partial\Omega_{m,2}$ cut by the phase interface Γ_m (see Fig. 2):

$$\begin{aligned}\mathcal{E}_m = \sum_{k=1}^{2}\Bigg[&\int_{\Omega_{m,k}} \mathbf{v}_{m,k}^h \cdot \frac{\partial \mathbf{u}_{m,k}^h}{\partial t}\,\mathrm{d}V \\ &- \int_{\Omega_{m,k}} \nabla^h \mathbf{v}_{m,k}^h : \mathbf{F}^c(\mathbf{u}_{m,k}^h)\,\mathrm{d}V \\ &+ \int_{\partial\Omega_{m,k}} \mathbf{v}_{m,k}^h \cdot \underbrace{(\mathbf{F}^c(\mathbf{u}_{m,k}^h)\cdot\mathbf{n}_{\partial\Omega_m})}_{\mathcal{H}(\mathbf{u}_{m,k}^{h,+},\,\mathbf{u}_{m,k}^{h,-})}\,\mathrm{d}S \\ &+ \int_{\Gamma_m} \mathbf{v}_{m,k}^h \cdot \underbrace{(\mathbf{F}^c(\mathbf{u}_{m,k}^h)\cdot\mathbf{n}_{\Gamma_m})}_{\mathcal{H}_\Gamma(\mathbf{u}_{m,k}^h,\,\mathbf{u}_{m,k^*}^h)}\,\mathrm{d}S\Bigg],\ k^* = \{2,1\}\,,\end{aligned} \tag{16}$$

  where $\mathcal{H}_\Gamma$ is a numerical flux function depending on the solutions in both phases, $\mathbf{u}_{m,1}^h$ and $\mathbf{u}_{m,2}^h$. Eq. (16) is an extension to two-phase flows of the approach proposed in [10] for immersed boundary problems.

The following remarks can be made based on Eqs. (15, 16):

- the number of degrees of freedom on a cut element is doubled in order to have two separate representations of the solution, $\mathbf{u}_{m,1}^h$ and $\mathbf{u}_{m,2}^h$, as illustrated in Fig. 2. Those two representations are then truncated at the interface, resulting in a sharp solution;
- the assembling of the weak form in the cut element requires the evaluation of three kind of integrals:
  - over the cut volumes $\Omega_{m,k}$ ($k = \{1,2\}$);
  - over the cell edges $\partial\Omega_{m,k}$ ($k = \{1,2\}$);
  - over the phase interface Γ_m.

  The computation of those integrals, which can not be done by classical quadrature rules, is briefly explained in Sec. 3.2;
- the convective numerical flux function across the interface, $\mathcal{H}_\Gamma$, is not based on the classical Riemann solvers used for the flux functions across the element edges, $\mathcal{H}$. The concept of multiphase Riemann solvers on which it relies is presented in Sec. 3.3;
- finally, the position of the interface Γ_m, which is needed to perform the different integrals mentioned before, is identified by a signed distance level-set function. A short overview of this technique is given in Sec. 3.4.

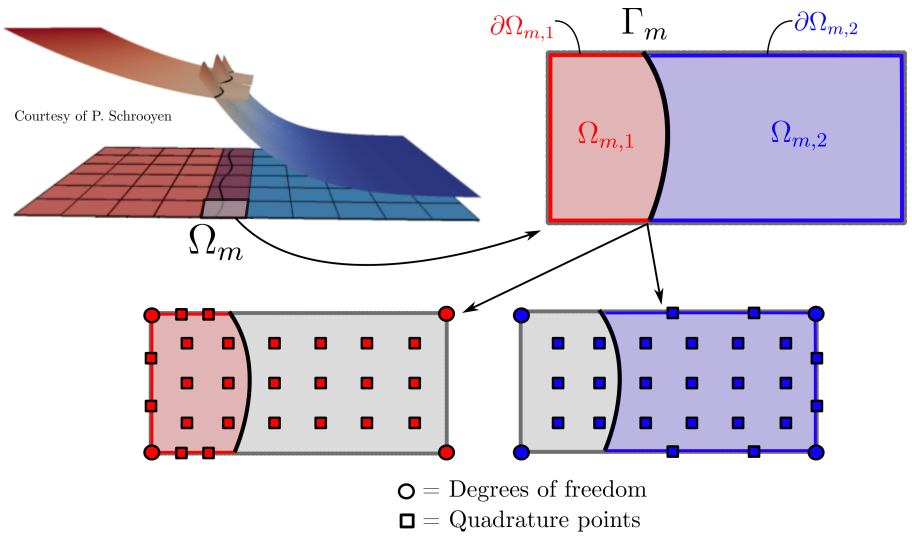

Figure 2: Principle of the XDGM. The degrees of freedom (here for a $p1$-element) are doubled on the cut elements in order to capture exactly the discontinuity at the phase interface Γ_m. The integrals of the weak form are evaluated inside the volume $\Omega_{m,k}$, on the element boundaries $\partial\Omega_{m,k}$ and along the interface Γ_m, based on cut quadrature rules (here the HMF method).

3.2. *Evaluation of integrals on cut elements*

The capacity of the XDGM of reaching high-order accuracy is directly linked to the accuracy with which the integrals in Eq. (16) can be computed. Contrary to normal elements on which standard quadrature rules can be applied to evaluate the integrals, for a cut element the integrals need to be computed over surfaces which are defined implicitly via a fixed isosurface of a smooth scalar function. A special procedure for numerical integration is therefore requested which will build a quadrature for each cut element, i.e. a set of quadrature nodes and weights. Two different approaches are available in Argo:

- a hierarchical moment-fitting (HMF) method proposed in [19] and implemented into Argo by Schrooyen at al. [13];
- a high-order quadrature method for implicitly defined domains in hyperrectangles [20], included as a library.

The main difference between both approaches, of interest for the present application, is the following. While the HMF method uses quadrature points on the entire element (for both $\int_{\Omega_{m,k}} \mathrm{d}V$ and $\int_{\Gamma_m} \mathrm{d}S$), the second method defines them strictly inside their respective phase (for $\int_{\Omega_{m,k}} \mathrm{d}V$) or on the zero isocontour of the level-set (for $\int_{\Gamma_m} \mathrm{d}S$). For two-phase flows, and in particular for compressible flows, evaluating the field variables at positions strictly inside their respective phase is preferable. The second quadrature method is therefore chosen in this work.
In addition to the quadrature rules, a cell-agglomeration strategy, discussed in [10], was included by Schrooyen et al. in the code to circumvent the problem of elements with small volume fractions. Indeed, when the ratio between the surface occupied by one phase in an element is much smaller than the surface occupied by the other phase, this could render the method impractical due to the extreme time-step restriction imposed by the configuration.

3.3. *Resolution of the jump conditions: multiphase Riemann solver*

In order to capture correctly the sharp transition between the two phases, the two distinct solutions on the cut elements must satisfy the jump relations Eqs. (14) at the interface. This is done by computing appropriate fluxes contained in the last terms of Eq. (16). For the inviscid model without phase transition considered in this work, we propose to rely on the concept of multiphase Riemann solvers. With the variables in the different phases $\mathbf{U}_1$ and $\mathbf{U}_2$ at each quadrature point associated to the interface, we seek for the solutions $\mathbf{U}_1^*$ and $\mathbf{U}_2^*$ that match the structure illustrated in Fig. 3

: one standard elementary wave (shock or rarefaction wave) in phase $k = 1$ starting from the left state, an intermediate phase boundary and one elementary wave in phase $k = 2$ connecting to the right state [21]. Across the phase interface, the jump conditions Eqs. (14) are imposed. Thus the resolution of this Riemann problem provides the solution states on both sides of the interface satisfying the prescribed jumps. The interfacial fluxes are then evaluated based on $\mathbf{U}_1^*$ and $\mathbf{U}_2^*$. Contrary to single-valued intercell fluxes coupling the solutions at the element edges, two different fluxes are defined in this case, as it is done in the idea of the ghost-fluid approach in [22]: one from phase 1 to phase 2, the other one from phase 2 to phase 1. Doing so, the mixing between the two fluids obeying possibly dissimilar thermodynamic models is avoided. On the other hand, the conservation can no longer be satisfied locally.

The approximate HLLC multiphase Riemann solver of [22] is chosen in this work. The numerical flux function across the phase interface is then expressed as:

$$\mathcal{H}_\Gamma(\mathbf{U}_1, \mathbf{U}_2) = \begin{cases} \mathbf{F}^c(\mathbf{U}_1)\cdot\mathbf{n}_\Gamma + S_1(\mathbf{U}_1^* - \mathbf{U}_1) & \text{for phase 1,} \\ \mathbf{F}^c(\mathbf{U}_2)\cdot\mathbf{n}_\Gamma + S_2(\mathbf{U}_2^* - \mathbf{U}_2) & \text{for phase 2,} \end{cases} \tag{17}$$

where S_1 and S_2 are the two shock speeds estimated from the linearization of wave curves. Note that the use of an approximate solver avoids the need of an iterative root-finding algorithm, which is desirable in terms of cost and robustness.

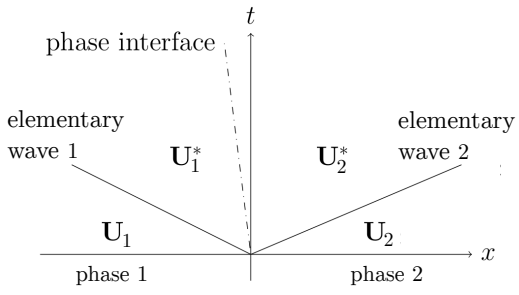

Figure 3: General Riemann wave structure for an inviscid two-phase flow without phase transition.

3.4. Interface tracking: the level-set method

In the XDGM, the interface is represented implicitly as the zero iso-contour of a smooth level-set function φ, for which an advection equation is solved at each time step to update its position. If we write the level-set equation under a conservative form, a source term appears that is non-zero for compressible flows [3]:

$$\frac{\partial\varphi}{\partial t} + \nabla\cdot(\varphi\mathbf{v}_{int}) = \varphi\nabla\cdot(\mathbf{v}_{int}), \tag{18}$$

where $\varphi = 0$ indicates the current position of the interface between the two phases, $\varphi \gtrless 0$ signals the presence of one or the other phase and

$$\mathbf{v}_{int} = v_{int,n}\mathbf{n}_{int} + (\mathbf{v}_{int}\cdot\mathbf{t}_{int})\mathbf{t}_{int}\ . \tag{19}$$

is the velocity of the interface whose normal component is obtained from the resolution of the multiphase Riemann problem.

It is important to remark that the governing equations of the flow problem Eqs. (5), discretized by the XDGM , and the level-set Eq. (18), discretized with a classical DG formulation, are not solved simultaneously. The level-set equation is first advanced in time and then the governing equations, before starting a new time step. Within a time step, the interface position can be kept constant or its motion can be taken into account with a cell-agglomeration procedure [23].

The computation of the normal to the interface and its curvature are needed in the jump conditions and are related to the level-set function via the Bonnet's formula:

$$\mathbf{n}_{int} = \frac{\nabla\varphi}{|\nabla\varphi|}\ , \quad \kappa = \nabla\cdot\mathbf{n}_{int}\ . \tag{20}$$

Following Marchandise approach [24], a lifting procedure is used to compute the gradient of the level-set $\mathbf{G}_\varphi$ inside each element

$$\int_{\Omega_m}\left(\mathbf{G}_\varphi - \nabla\varphi\right)\mathbf{v}_m^h\,\mathrm{d}V = 0\,, \tag{21}$$

that is subsequently integrated by parts to transform the unknown gradient term $\nabla\varphi$. The curvature is also multiplied by a test function $\mathbf{v}^h$, integrated over the element volume and integrated by parts. Unfortunately, this direct approach of computing interfacial geometric quantities leads to inaccurate and oscillatory results for the curvature, as it is shown in Fig. 4. As expected, the curvature field shows an oscillatory behavior because the high frequencies contained in the level-set field are magnified after taking its second derivative. The computation of the curvature was not necessary for the one-dimensional test cases treated in this paper but it will be important to smooth the curvature field for future work.

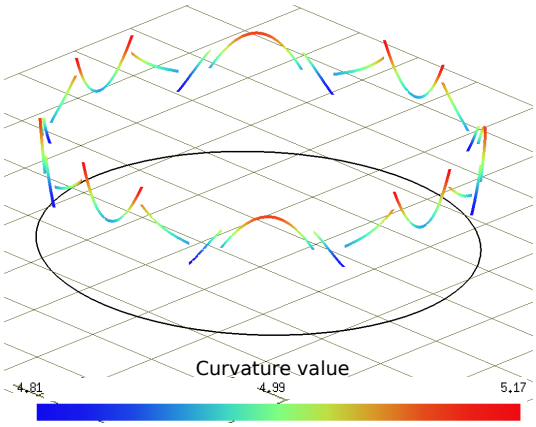

Figure 4: Value of the curvature of a circle at the position of the iso-zero of the level-set. The exact value is $\kappa = 5.0\,m^{-1}$

3.5. Artificial viscosity method coupled with the XDGM

Due to its hypersonic velocity, a strong shock will appear in front a space debris reentering the atmosphere. In high-order methods, special techniques are required in order to remove spurious oscillations in the vicinity of the discontinuity. In Argo, a shock-capturing artificial viscosity technique is present, largely based on the method by [25] and the improvement proposed by [26]. Although this technique is not robust in the hypersonic regime and others approaches like limiting methods should be favoured, is has been considered in this work because of its availability in Argo and its ease of extension to the XDGM.

Contrary to material interfaces that are tracked by a technique like the level-set, one needs to identify the *a priori* unknown position of the shock by an appropriate detector. The detector of Persson and Peraire works on the principle that polynomial expansions of the solutions of two different orders will give similar values in regions where the solution is smooth but will be different when it contains discontinuities. In each element, the polynomial expansion of order p is expressed as

$$\mathbf{u}_m^h(\mathbf{x}) = \sum_{n=1}^{N_m} \phi_{m,n}(\mathbf{x})\mathbf{U}_{m,n}\,, \quad \mathbf{x} \in \Omega_m\,, \tag{22}$$

where the subscripts $\bullet_m$ and $\bullet_n$ refer to the mth element and the nth degree of freedom on this element, respectively. The shape functions $\phi_{m,n}$ are in this case elementwise Lagrange polynomials of order p. A truncated solution $\hat{\mathbf{u}}_m^h$ is also introduced by projecting the solution on a function space of order $p-1$. Discontinuities can then be detected by comparing the two expansions of different orders, which gives the following cell-local sensor:

$$S_{\Omega_m} = \frac{\int_{\Omega_m} (\mathbf{u}_m^h - \hat{\mathbf{u}}_m^h)\cdot(\mathbf{u}_m^h - \hat{\mathbf{u}}_m^h)\,\mathrm{d}V}{\int_{\Omega_m} (\mathbf{u}_m^h \cdot \mathbf{u}_m^h)\,\mathrm{d}V} \tag{23}$$

Following [27], the sensor is reformulated on cells cut by the interface. In the kth-phase on the mth-element, the sensor is therefore computed by

$$S_{\Omega_{m,k}} = \frac{\int_{\Omega_{m,k}} (\mathbf{u}_{m,k}^h - \hat{\mathbf{u}}_{m,k}^h)\cdot(\mathbf{u}_{m,k}^h - \hat{\mathbf{u}}_{m,k}^h)\,\mathrm{d}V}{\int_{\Omega_{m,k}} (\mathbf{u}_{m,k}^h \cdot \mathbf{u}_{m,k}^h)\,\mathrm{d}V}\,, \tag{24}$$

using the available quadrature rules on cut cells presented in Sec. 3.2.

When a troubled cell has been detected, artificial viscosity has to be added depending on the strength of the shock through a parameter ϵ. For the exact expression of this parameter, the reader is referred to [28]. Artificial viscosity is finally added to the equations in the form of a Laplacian term in the diffusive fluxes:

$$\mathbf{F}^d(\mathbf{u}, \nabla\mathbf{u}) = \epsilon\nabla\mathbf{u}\,. \tag{25}$$

Although the Euler equations are solved in this work, the diffusive fluxes must be taken into account in the discretization due to the addition of the artificial viscosity. Those are treated with an interior penalty method (IPM) [11].

4. Some preliminary test cases

The various test cases presented in the following are preliminary in the sense that they do not represent any real physical phenomena and concern simple theoretical situations in one dimension. They were however used as verification test cases in the implementation processes of the different numerical elements described in this paper and will be used as the starting point for more complex simulations in the future.

4.1. 1-D translating interface

This test case comes from [29] with the initial values given in Tab. 1. It concerns a column of dense perfect gas pushing a column of 1000 times less dense perfect gas from the left to the right, at uniformly constant speed and pressure. The result in Fig. 5 shows that the important jump in density is perfectly preserved after the translation of the interface until the end of the domain.

	ρ	v_n	p	EOS	γ
Left fluid	1000.0	1.0	1.0	Perfect gas	1.4
Right fluid	1.0	1.0	1.0	Perfect gas	1.6

Table 1: Initial values for the two-fluid translating interface problem

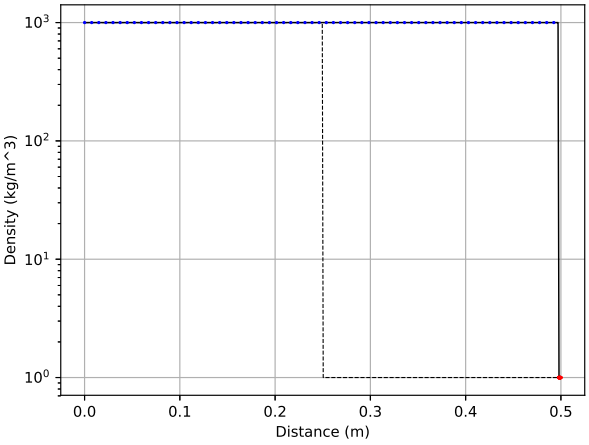

Figure 5: Comparison between the exact (plain) and the numerical (dots) density field of the translating interface problem at $t = 0.2475\,s$ for 100 equidistant cells at order $p = 2$; initial solution in dashed.

4.2. *Sod Riemann test case with pressure jump*

The original Sod test case is modified by imposing a pressure jump $\Delta p_\sigma = 0.2$ across the contact discontinuity, as done in [22]. In this situation, the apparition of the rarefaction fan on the left and especially the presence of the shock propagating to the right require the use of artificial viscosity to damp the oscillations near the strong gradients regions. At the beginning of the simulation, the shock starts to develop in the cells cut by the interface and it is therefore important to have a correct way of estimating the artificial viscosity, which is the one presented in Sec. 3.5. The values of the parameters of the method are taken from [28].

The results in Fig. 6 are found to be in excellent agreement with the exact solution. The contact discontinuity is successfully kept sharp and its movement is accurately predicted. The jump in pressure at the contact discontinuity is also perfectly imposed.

	ρ	v_n	p	EOS	γ
Left fluid	1.0	0.0	1.0	Perfect gas	1.4
Right fluid	0.125	0.0	0.1	Perfect gas	1.4

Table 2: Initial values for the two-phase Sod Riemann problem with pressure jump.

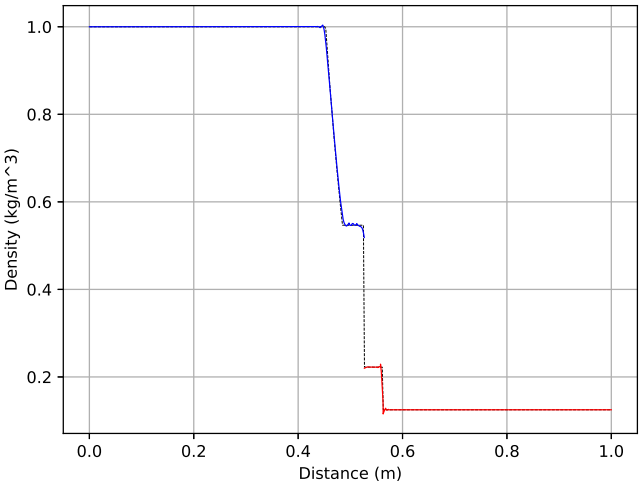

(a) Density

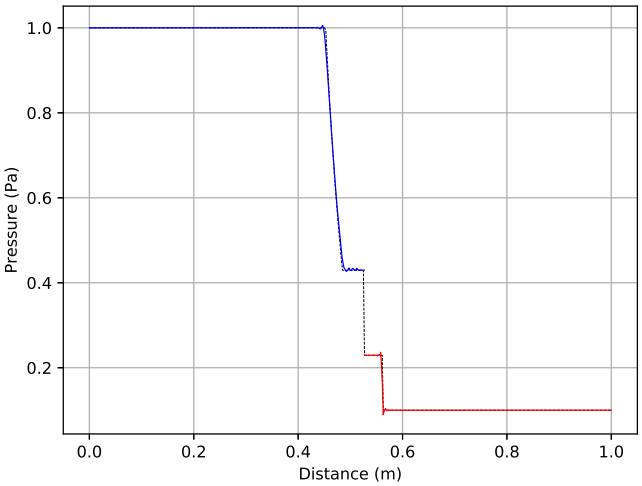

(b) Pressure

Figure 6: Comparison between the exact (dashed) and the numerical (plain) solutions of the Sod test case with pressure jump at $t = 0.04\,s$ for 200 equidistant cells at order $p = 2$.

4.3. *Gas-Liquid Riemann test case*

The purpose of this last test case is to demonstrate the performance of the method in a two-phase setting

under challenging conditions and is inspired from the one proposed in [30]. It deals with a gas-liquid flow with initial ratio of pressure and density equal to 100. The gas is represented by a perfect gas EOS while the liquid obeys a stiffened gas EOS. The different parameters are listed in Tab. 3. In addition, a pressure jump between both phases is imposed:

$$\Delta p_\sigma = 10\ bar\,.$$

	ρ (kg/m^3)	v_n (m/s)	p (bar)	EOS	γ /	p_∞ (bar)
Gas	10	10	100	Perfect gas	1.4	/
Liquid	1000	0	1	Stiffened gas	5.5	4900

Table 3: Initial values for the gas-liquid Riemann problem

Fig. 7 shows that the important discontinuity in the density field across the phase interface is perfectly captured by the numerical scheme. The imposed pressure jump is respected while the normal velocity is continuous between both phases. The effect of the artificial viscosity is also illustrated on the velocity field where the important spurious oscillations are removed near the shock and rarefaction waves.

5. Conclusions and perspectives

The ablation of metallic space debris involves the interaction between the air atmosphere and a metallic liquid molten layer at the surface. In order to represent the physical phenomena of this situation with high fidelity, it is proposed in this project to rely on a novel sharp interface method. This high-order method, built in a discontinuous Galerkin framework, has been extended to inviscid compressible two-phase flows. The next steps to be explored in order to overcome the remaining challenges towards the simulation of the targeted application are discussed below:

- multiphase Riemann solver accounting for phase transition: by inserting an additional wave inside the HLLC solver considered in this work, it is possible to resolve the jump conditions with phase transition at the interface [31]. In this situation, non-linear systems need to be solved, even for approximate Riemann solvers. To this end, the robust global Newton methods that have been implemented in Argo will be useful. A coupling with the external library Mutation++ will also be considered to provide different models for the estimation of the evaporation mass flux;

- viscous jump conditions: a strategy to incorporate the viscous effects in the jump relations will have to be developed;

- smoothing technique for the curvature: in order to filter out the high-frequency components of the curvature field, a smoothing technique like the least squares method proposed by [24] will be necessary and will be introduced in future work;

References

[1] R. Wormnes, L. Le Letty, R. Summerer, R. Schonenborg, O. Dubois-Matra, E. Luraschi, A. Cropp, H. Krag, J. Delaval, Esa technologies for space debris remediation, in: European Space Agency - Publications, 6th European conference on space debris, 2013, darmstadt, Germany.

[2] M. Latige, Simulation numrique de l'ablation liquide, Ph.D. thesis, Université de Bordeaux (2013).

[3] S. Fechter, Compressible multi-phase simulation at extreme conditions using a discontinuous galerkin scheme, Ph.D. thesis, Universitat Stuttgart (2015).

[4] M. Baer, J. Nunziato, A two-phase mixture theory for the deflagration-to-detonation transition (ddt) in reactive granular materials, International journal of multiphase flow 12 (6) (1986) 861–889.

[5] M. Dumbser, W. Boscheri, High-order unstructured lagrangian one-step weno finite volume schemes for non-conservative hyperbolic systems: applications to compressible multi-phase flows, Computers & Fluids 86 (2013) 405–432.

[6] B. M. R.P. Fedwik, T. Aslam, S. Osher, A non-oscillatory eulerian approach to interfaces in multimaterial flows (the ghost fluid method), Journal of Computational Physics 152 (1999) 457–492.

[7] R. R. Nourgaliev, M.-S. Liou, T. G. Theofanous, Numerical prediction of interfacial instabilities: Sharp interface method (sim), Journal of Computational Physics 227 (8) (2008) 3940–3970.

[8] F. Kummer, M. Oberlack, An extension of the discontinuous galerkin method for the singular poisson equation, SIAM Journal on Scientific Computing 35 (2) (2013) A603–A622.

[9] F. Kummer, Extended discontinuous galerkin methods for two-phase flows: the spatial discretization, International Journal for Computational Methods in Engineering 109 (2017) 259–289.

[10] B. Müller, S. Krämer-Eis, F. Kummer, M. Oberlack, A high-order discontinuous galerkin method for compressible flows with immersed boundaries, Internal Journal For Numerical Methods in Engineering 110 (2017) 3–30.

[11] K. Hillewaert, Development of the discontinuous galerkin method for high-resolution, large scale cfd and acoustics in industrial geometries, Ph.D. thesis, Universit catholique de Louvain (2013).

[12] P. Schrooyen, J.-S. Cagnogne, N. Poletz, K. Hillewaert, A high-order extended discontinuous galerkin method for moving immersed interface problem, in: XDMS Conference, Umea.

[13] P. Schrooyen, L. Arbaoui, J.-S. Cagnone, N. Poletz, K. Hillewaert, A high-order extended discontinuous galerkin method to treat hydrodynamics problems, in: ECCM-ECFD Conference, Glasgow (UK), 2018.
[14] D. Henneaux, P. Schrooyen, B. Dias, A. Turchi, P. Chatelain, T. Magin, Towards a high-fidelity multiphase solver with application to space debris aerothermal ablation modeling, in: AIAA Aviation 2019 Forum, 2019, p. 2876.
[15] S. Vitale, M. Pini, P. Colonna, G. Gori, A. Guardone, T. Economon, F. Palacios, J. Alonso, Extension of the su2 open source cfd code to the simulation of turbulent flows of fluids modelled with complex thermophysical laws, in: 22nd AIAA Computational Fluid Dynamics Conference, 2015.
[16] K.-M. Shyue, A fluid-mixture type algorithm for compressible multicomponent flow with miegruneisen equation of state, Journal of Computational Physics 171 (2001) 678707.
[17] R. Menikoff, B. Plohr, The riemann problem for fluid flow of real materials, Reviews of Modern Physics 61.
[18] S. Peluchon, Approximation numrique et modlisation de ablation liquide, Ph.D. thesis, Université de Bordeaux (2017).
[19] B. Müller, F. Kummer, M. Oberlack, Highly accurate surface and volume integration on implicit domains by means of moment-fitting, Internal Journal For Numerical Methods in Engineering 96 (2013) 512–528.
[20] R. Saye, High-order quadrature methods for implicitly defined surfaces and volumes in hyperrectangles, SIAM Journal on Scientific Computing 37 (2) (2015) A993–A1019.
[21] C. Zeiler, Liquid vapor phase transitions: modeling, riemann solvers and computation, Ph.D. thesis, University of Stuttgart (2016).
[22] S. Fechter, F. Jaegle, V. Schleper, Exact and approximate riemann solvers at phase boundaries, Computers & Fluids 75 (2013) 112–126.
[23] F. Kummer, B. Müller, T. Utz, Time integration for extended discontinuous galerkin methods with moving domains, International Journal for Numerical Methods in Engineering 113 (5) (2018) 767–788.
[24] E. Marchandise, Simulation of three-dimensional two-phase flows : coupling of a stabilized finite element method with a discontinuous level set approach, Ph.D. thesis, Universite catholique de Louvain (2006).
[25] P.-O. Persson, J. Peraire, Sub-cell shock capturing for discontinuous galerkin methods, in: 44th AIAA Aerospace Sciences Meeting and Exhibit, 2006, p. 112.
[26] G. E. Barter, D. L. Darmofal, Shock capturing with pde-based artificial viscosity for dgfem: Part i. formulation, Journal of Computational Physics 229 (5) (2010) 1810–1827.
[27] M. Geisenhofer, F. Kummer, B. Müller, A discontinuous galerkin immersed boundary solver for compressible flows: Adaptive local time stepping for artificial viscosity–based shock-capturing on cut cells, International Journal for Numerical Methods in Fluids 91 (9) (2019) 448–472.
[28] M. Cruellas Bordes, A study of an artificial viscosity technique for high-order discontinuous galerkin methods, Master's thesis, Delft University (2019).
[29] J. J. Kreeft, B. Koren, A new formulation of kapilas five-equation model for compressible two-fluid flow, and its numerical treatment, Journal of Computational Physics 229 (18) (2010) 6220–6242.
[30] S. Rouy, P. Helluy, S. Kokh, Test-case number 13: Shock tubes(pa), Multiphase Science and Technology 16 (1-3).
[31] S. Fechter, C.-D. Munz, C. Rohde, C. Zeiler, A sharp interface method for compressible liquid–vapor flow with phase transition and surface tension, Journal of Computational Physics 336 (2017) 347–374.

Acknowledgments

The first author is supported by the Fonds de la Recherche Scientifique (FNRS) under a FRIA Grant. The first author would like to thank Pierre Schrooyen from Cenaero for all his advice on the implementation strategy into Argo and his help with the XDG method.

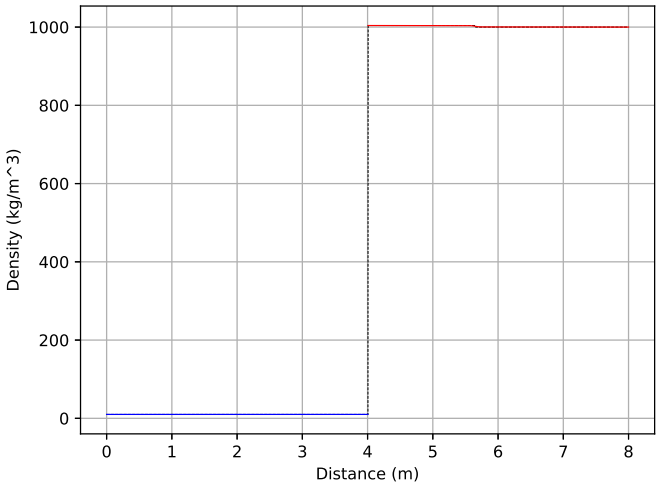

(a) Density

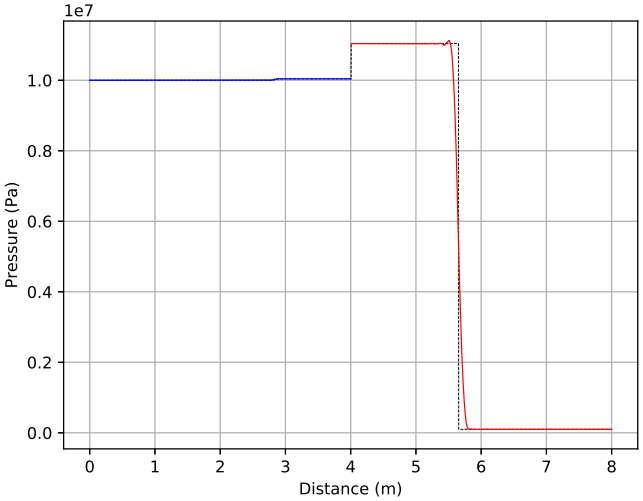

(b) Pressure

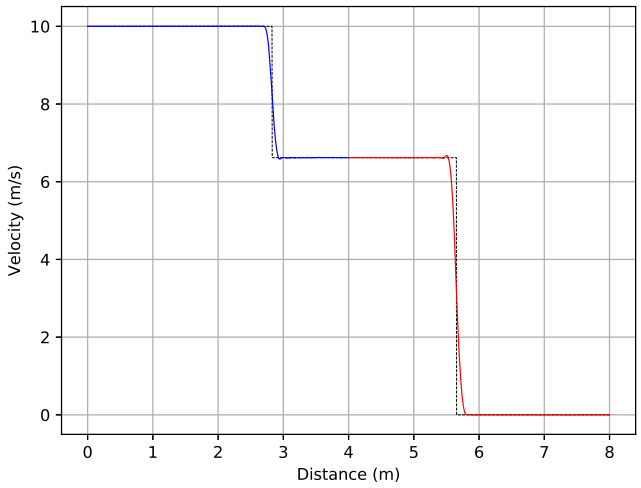

(c) Velocity with artificial viscosity

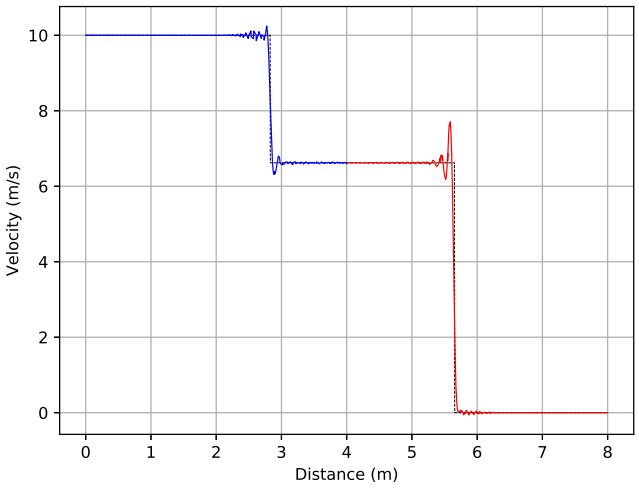

(d) Velocity without artificial viscosity

Figure 7: Comparison between the exact (dashed) and the numerical (plain) solutions of the gas-liquid test case with pressure jump at $t = 0.001\ s$ for 200 equidistant cells at order $p = 2$.

Characterization of the thermal degradation of carbon-phenolic materials: an experimental effort on the ZURAM® ablator.

Francisco Torres Herrador

Aeronautics and Aerospace Department, von Karman Institute for Fluid Dynamics, Belgium, fratorhe@vki.ac.be

Supervisor: Olivier Chazot

Head of Department and Professor, Aeronautics and Aerospace Department, von Karman Institute for Fluid Dynamics, Belgium, chazot@vki.ac.be

Supervisor: Thierry Magin

Professor, Aeronautics and Aerospace Department, von Karman Institute for Fluid Dynamics, Belgium, magin@vki.ac.be

University Supervisor: Julien Blondeau

Professor, Thermo and Fluid dynamics (FLOW), Faculty of Engineering, Vrije Universiteit Brussel, Belgium, jublonde@vub.ac.be

University Supervisor: Kevin M. Van Geem

Professor, Laboratory for Chemical Technology (LCT), Faculty of Engineering and Architecture, Ghent University, Belgium, kevin.VanGeem@UGent.be

Abstract

Carbon/phenolic ablators are commonly used as thermal protection material for spacecraft. Nevertheless, their complex thermal degradation is not yet fully understood. One of the current limitations preventing significant advancements in the modeling of the decomposition process and its effects on the material thermal response is the scarcity of detailed and reliable experimental data on these materials. In addition, there is not a standard material that can be used as a reference for model validation. In this paper, we give an insight into the different thermal analysis techniques and preliminary results of an extensive experimental campaign to characterize different properties of the carbon/phenolic ablator ZURAM®. We have characterized the heat capacity, the elemental composition and the pyrolysis products. Our experiments show that the elemental composition of ZURAM® resembles that of other carbon/phenolic ablators (e.g. PICA). In addition, more than 40 different products of the pyrolysis of ZURAM® have been identified using a unique micropyrolysis setup. Improved knowledge on material properties will reduce safety margins on spacecraft heatshield design.

Keywords: carbon/phenolic, thermal degradation, thermal analysis

1. Introduction

Atmospheric entry is an engineering challenge. The hypersonic speed of the spacecraft generates a bow shock in front of the vehicle whose surface may reach temperatures higher than 3000 K. To protect the spacecraft integrity, Thermal Protection Materials (TPMs) are used. A common type of TPMs are ablative materials. These materials originated during the Apollo Program, precisely 50 years ago. Recently, there has been a renewed interest in ablative TPM with the development of carbon/phenolic composites [1; 2].These materials are made of a short carbon fiber ($\sim$ 1 mm) felt which is impregnated with a phenolic resin. These resins are then cured providing structural integrity to the composite. During an atmospheric entry, the resin undergoes a series of chemical transformations in a globally endothermic process known as pyrolysis[3; 4; 5; 6]. During pyrolysis, the resin decomposes absorbing heat and releasing gases that will

partially block the incoming heat.

In recent years, there has been a large development on material response codes to simulate the thermal degradation of these composites. However, due to the scarcity of available experimental data (material properties, pyrolysis gas characterization, plasma wind tunnel tests, etc), most codes have only been verified against other codes or theoretical materials [7; 8; 9]. In an attempt to provide a reference material, the German Aerospace Agency (DLR) has developed ZURAM®, a carbon/phenolic material that can be shared among the scientific community. The von Karman Institute along with other institutions is carrying out an important effort to help advancing the thermal response modeling of this material [10; 11].

In this paper, we first introduce the different experimental techniques that have been used for this characterization (section 2): simultaneous thermal analysis, elemental analysis, and micropyrolysis. Then, we present the material used during this study (ZURAM®) and explain the preparation of the samples (section 3). Finally, we show the preliminary results(section 4): heat capacity, elemental composition and pyrolysis gas composition.

2. Experimental Techniques

In this section, we briefly introduce the three different experimental facilities that have been used during this campaign.

2.1. Simultaneous Thermal Analysis

Simultaneous Thermal Analysis (STA, Figure 1) is a analytical technique which combines two complementary techniques: Thermo-Gravimetric Analysis (TGA) and Differential Scanning Calorimetry (DSC). For both TGA and DSC, the temperature is typically monitored and linearly increased at a constant heating rate β. On the one hand, TGA monitors the mass of a sample. On the other hand, DSC measures small differences of temperature between the sample of interest and a reference (typically an empty crucible), these small temperature differences arise for two reasons: energy required to heat up the sample and transformations (physical or chemical) of the sample.

Among other applications, STA can be used to determine material properties particularly important for TPMs such as mass loss, kinetics [12], pyrolysis enthalpy or heat capacity. In the present study, we focus on the determination of the heat capacity c_p.

The heat capacity of a material is typically obtained applying the standard procedure ISO 11357 - sapphire

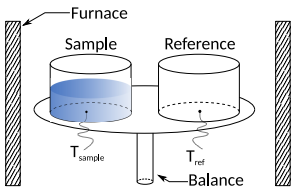

Figure 1: Schematic of a STA device.

method. In this procedure, the c_p of an unknown sample is obtained by comparison to a known substance: pure sapphire. In this case, the $c_\mathrm{p}^{\mathrm{sample}}$ is computed as:

$$c_\mathrm{p}^{\mathrm{sample}} = \frac{DSC^{\mathrm{sample}}}{DSC^{\mathrm{sapphire}}} c_\mathrm{p}^{\mathrm{sapphire}}, \tag{1}$$

Where DSC refers to the STA signal expressed in $\mathrm{mW \cdot mg^{-1}}$ of substance. $c_\mathrm{p}^{\mathrm{sapphire}}$ is the theoretical heat capacity of pure sapphire sample, typically provided by its manufacturer.

For a decomposing material such as carbon/phenolic ablators, a correction with the mass evolution (TGA^{sample}) should be applied:

$$DSC^{\mathrm{sample}} = \frac{DSC_\mathrm{v}^{\mathrm{sample}}}{TGA^{\mathrm{sample}}} = \frac{DSC_\mathrm{v}^{\mathrm{sample}}}{m^{\mathrm{sample}}/m_\mathrm{v}^{\mathrm{sample}}}, \tag{2}$$

where the sub-index v refers to the virgin material.

Replacing Eq. 2 in Eq. 1, we have:

$$c_\mathrm{p}^{\mathrm{sample}} = \frac{DSC_\mathrm{v}^{\mathrm{sample}} m_\mathrm{v}^{\mathrm{sample}}}{DSC^{\mathrm{sapphire}} m^{\mathrm{sample}}} c_\mathrm{p}^{\mathrm{sapphire}}, \tag{3}$$

For each sample measurement, three measurements are required:

- Blank measurement: both *sample* and *reference* crucibles are empty, it is used to compensate for buoyancy effects and the difference in mass of the two crucibles, providing a baseline to be subtracted in the subsequent measurements.
- Reference measurement: performed with a 0.7 mm sapphire disk in the *sample* crucible, and *reference* crucible remains empty to provide DSC^{sapphire}.
- Sample measurement: actual sample of interest in *sample* crucible, and *reference* crucible still remains empty. This measurement provides TGA^{sample} and DSC^{sample}.

The experiments were performed using a STA NETZSCH 449 F3 Jupiter which performs both TGA

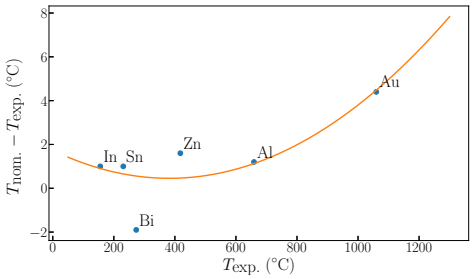

(a) Temperature calibration using a 2nd order polynomial.

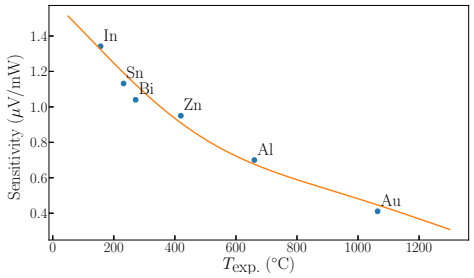

(b) Sensitivity calibration for DSC measurements.

Figure 2: Calibration results using 7 different high purity metals.

and DSC measurements simultaneously. The STA is located in an argon glove-box in order to avoid any oxidation or humidity absorption. For accurate c_p measurements, the recommended configuration of the device is as follows: Platinum furnace, DSC sample carrier with radiation shielding, sample holder with thermocouples type S, Rhodium/platinum crucibles with alumina liner, argon atmosphere (purging 50ml/min, protective 20ml/min).

2.2. Calibration

The STA was calibrated following the manufacturers standard procedure using the melting temperature and enthalpy of 7 different high purity metals (min 99.999 %) in identical conditions of those to be used during the actual measurements. A second order polynomial was used for the calibration in temperature (Fig. 2). It can be seen that the error increases with temperature. Nonetheless, in terms of percentage with respect to the actual temperature, the uncertainty is about a 0.3 %. For the DSC calibration, a sensitivity curve is retrieved. These two calibrations are internally applied by the manufacturer's software.

A verification of the calibration was performed using two sapphire disks of different thicknesses. The 0.7 mm disk was used as *reference* and the 1 mm disk as unknown *sample*. The determined heat capacity (Eq. 3) is compared with the manufacturer's provided data in Fig. 3. It can be seen that the experimentally determined c_p closely follows the theoretical within a 2 % uncertainty in the whole range. The slight deviation found at the beginning is attributed to the thermal lag due to the difference in mass of the two samples, while at high temperatures it is attributed to a slight loss of accuracy.

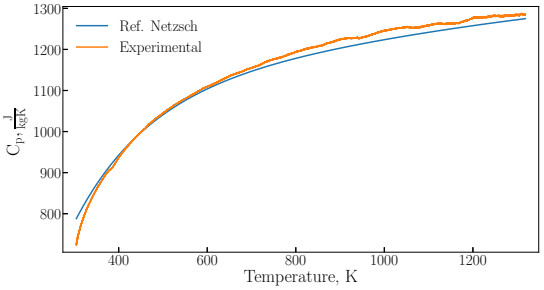

Figure 3: c_p measurement verification: comparison between the experimentally determined c_p of sapphire and the one provided by the manufacturer.

2.3. Elemental Analysis

Elemental analysis is a technique commonly used for polymer characterization. This measurement allows to obtain the elemental fractions of the typical elements (CHON) that make up the compound under study.

The analyzer has two functioning modes: oxidation and pyrolysis (Figure 4). The first mode, oxidation, uses the classical formula of a combustion in excess of oxygen. In this mode, C and H can be detected from CO_2 and H_2O molecules. In addition, N can be also measured from N_2, which will not react. In the pyrolysis mode, the pyrolysis reaction occurs in excess of carbon, which generates CO.

When the sample is dropped inside the reactor, it undergoes one of the aforementioned processes (depending on the chosen configuration). Then, the produced gas flow will be swept away by a carried gas (generally He) to the Gas Chromatograph (GC). In the chromatograph, the different compounds get separated by molecular weight (different retention times). Finally, a Thermal Conductivity Detector (TCD) detects a voltage signal proportional to the quantity of gas, which is recorded. In order to convert this voltage signal into mass % of each element, a calibration with

a high purity standard material is performed (BBOT, $C_{26}H_{26}N_2O_2S$).

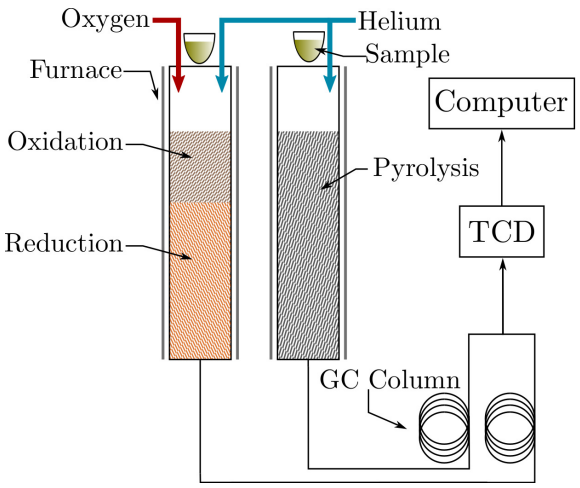

Figure 4: Typical elemental analysis set-up.

2.4. *Micropyrolysis Setup*

Characterizing the gases released during pyrolysis is essential for an accurate modeling. Different approaches have been applied in the past [4; 5; 6] with different limitations in each case (e.g. long residence times, only certain molecules detected, etc). In order to have a better characterization on the pyrolysis gases, we propose to use a micropyrolyzer setup [13]. This setup was initially developed for biomass pyrolysis characterization but it is being extended to other applications such as aerospace materials or plastic waste.

This setup consists of an isothermal reactor where the sample gets pyrolyzed at a constant temperature. Three non-dimensional numbers (Bi $<$ 1, $\mathrm{Py^I} >$ 1, $\mathrm{Py^{II}} >$ 1) will ensure that: 1) sample is isothermal, 2) heat transfer inside the sample is fast compared to pyrolysis, 3) heat transfer by convection is fast compared to pyrolysis to ensure same temperature as the furnace [14; 15; 16]. Particularizing for $\sim$ 200 µg of Zuram® at 700 °C:

$$\mathrm{Bi} = \frac{t_{\mathrm{cond}}}{t_{\mathrm{conv}}} = \frac{L_c h}{\lambda_z} = 0.004 \tag{4}$$

$$\mathrm{Py^I} = \frac{t_{\mathrm{pyro}}}{t_{\mathrm{cond}}} = \frac{\lambda_z}{\rho_z c_{p_z} L_c^2 \mathcal{A} \exp\left(\frac{-\mathcal{E}}{RT}\right)} = 4600 \tag{5}$$

$$\mathrm{Py^{II}} = \frac{t_{\mathrm{pyro}}}{t_{\mathrm{conv}}} = \frac{h}{\rho_z c_{p_z} L_c \mathcal{A} \exp\left(\frac{-\mathcal{E}}{RT}\right)} = 21 \tag{6}$$

Where L_c is the characteristic length of the sample cup, h is the heat transfer coefficient, the subindex z refers to Zuram®, λ_z is its thermal conductivity, ρ_z is the intrinsic density, c_{p_z} is the heat capacity, and $\mathcal{A} \exp\left(\frac{-\mathcal{E}}{RT}\right)$ is the kinetic rate (estimated from TACOT data [9]). For unknown parameters, worst case scenario based on literature [13] have been used.

As it can be seen, Bi is much smaller than 1 ensuring homogeneous temperature of the sample. $\mathrm{Py^I}$ greater than 1 indicates that the pyrolysis front is thick, thus the whole sample is undergoing pyrolysis at the same rate, in other words, the process is kinetically controlled. Finally, $\mathrm{Py^{II}}$ greater than 1 indicates that the sample reaches the pyrolysis temperature by convection quickly compared to the pyrolysis time, thus the assumption of the particle being at the same temperature of the furnace during pyrolysis is considered appropriate.

After pyrolysis, the produced gases are rapidly swept away by the carrier gas (He) and trapped by a cryo-trap (liquid nitrogen, 77 K) which is used to focus the products. Then, the products are slowly released by heating up the GC oven at a given heating rate (3-5 $\mathrm{K \cdot min^{-1}}$). The analysis section is composed by: 1) a 2-dimensional GC (GCxGC, Rtx-PONA and BPX-50 for 1st and 2nd dimension respectively) equipped with a Fire Ionization Detector (FID) and a Time-of-flight Mass Spectrometer (TOF-MS) and 2) a customized GC with TCD to detect permanent gases and other light compounds (water, methanol, etc). This configuration allows the detection and quantification of the different molecules formed due to the pyrolysis of a carbon/phenolic ablator.

In the present case, we only focused on the identification of the different molecules from the TOF-MS which is a preliminary step to an accurate quantification.

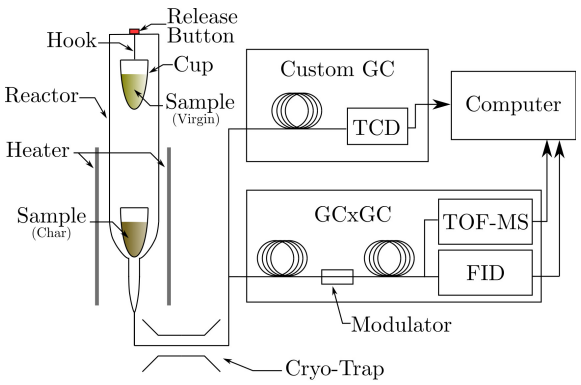

Figure 5: Schematic of the micropyrolysis setup.

3. Material and sample preparation

The material used to carry out this study is Zuram®. This lightweight carbon/phenolic ablator was developed by DRL as a reference material which could be shared among scientists and institutions without restrictions neither for the material itself nor the data [17]. This is useful to compare data from different facilities (reliability and repeatability of measurements) and to develop and verify numerical tools.

Zuram® is made of a rigid carbon fiber preform (CBCF 18-2000) which is infiltrated with a liquid phenolic resin and later polymerized [17; 18]. There are different versions of Zuram® depending on the proportions in weight of carbon fibers and phenolic resin. In the present study, the version of Zuram® is 18/50 which is 50 % carbon fibers and 50 % resin in mass (more on this in Sec. 4.2). This combination leads to a density of $\rho = 430(30)\,\mathrm{kg \cdot m^{-3}}$.

To characterize the c_p of the charred material, we first pre-charred a piece of Zuram® in a furnace at 1100 °C during 6 h in an inert argon atmosphere and using a carbon preform plenum to avoid any possible oxidation due to leaking of atmospheric air inside the furnace.

In addition, cured phenolic resin from the same batch has also been analyzed independently from the fibers.

During the first STA experimental runs, we found out some limitations on the accuracy and repeatability of tests due to the low density of Zuram®. Therefore, it was decided to crush and powder the material into a fine powder [19; 20]. This has three positive impacts: 1) higher density and thus higher mass in the crucible or sample cup, 2) improved contact with the crucible, required for accurate DSC measurements and 3) more homogeneous and representative samples. Since we are only interested in intrinsic quantities, powdering the sample should not have any effect in those quantities.

The different materials (Zuram®, phenolic resin, and pre-charred Zuram®) were stored each in glass vials. During the experiments, the samples were taken at random from the vials. The sample mass is different depending on the type of experiment:

- For c_p determination samples of 20 mg.
- Elemental analysis typically samples of 1-2 mg.
- Micropyrolysis uses samples of 0.1-0.2 mg.

4. Results

In the following, we provide results for the different measurements performed in these experimental campaigns.

4.1. Heat capacity determination with DSC

In the following, we first provide the results on the different forms of Zuram® (virgin, pre-charred and resin). Secondly, we provide the evolution of the heat capacity as function of temperature where the thermal degradation and the pass from virgin to char can be observed.

4.1.1. Pre-charred Zuram®

As previously mentioned, this material was pre-charred in an argon atmosphere during 6 h at 1100 °C to ensure completion of pyrolysis. However, as it can be seen in Figure 6a (red dots), the process was not fully completed: during the first measurement of each sample the material lost ~ 3.5 % of mass. While still significant, the mass loss of this pre-charred sample is small compared with the typical mass loss from a virgin sample (~ 20 %).

Afterwards, the same sample was re-heated in several cycles without observing a significant mass loss (Rep. 1-3 in Figure 6a). This can also be observed in the DSC (Figure 6b) where the reacting sample produce changes to the DSC signal (red dots) which seems to be related to an endothermic reaction around 1000 K.

The repeatability in DSC for the non-reacting sample during heating and cooling cycles (Figure 6b) is excellent. However, when the sample is changed, the repeatability slightly worsens (Figure 6c). The positioning of the crucible and its lid in the sample holder is one of the main reasons of this variability. This effect has been previously studied for biomass applications with uncertainties up to 20 % on c_p determination [21].

The c_p of charred Zuram® can be calculated applying Eq. 1 to the DSC data. Seven measurements were performed using 3 different samples Fig. 7. A polynomial fit was performed for the whole dataset. The shape of the polynomial was chosen based on graphite material [22]. The fitting procedure was carried out using a MonteCarlo approach taking into account the uncertainties mentioned in Section 2. The shadowed area represents the plus and minus 1-σ (standard deviation) for the fitted parameters. This same approach is used in the following sections for the other materials analyzed.

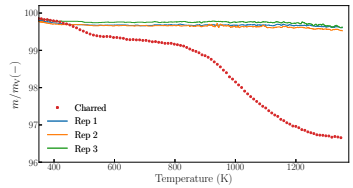

(a) TGA of a pre-charred ZURAM® sample submitted to heating cycles. The first measurement (●) shows appreciable mass loss due to an incomplete pyrolysis in the sample preparation process.

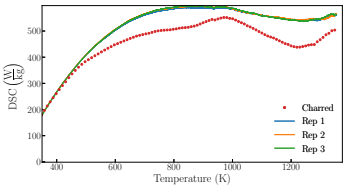

(b) DSC of a pre-charred ZURAM® sample submitted to heating cycles. An endothermic process is observed at 1000 K for the first measurement ●. Subsequent repetitions show excellent repeatability and no reactions occur.

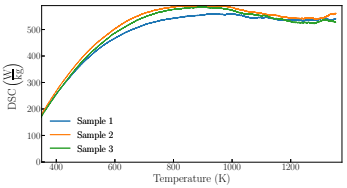

(c) DSC of different non-reacting pre-charred ZURAM® samples. Good repeatability is observed.

Figure 6: TGA/DSC measurements on pre-charred ZURAM®.

$$c_{\mathrm{p}}^{\mathrm{char}}(T) = \mathrm{a}+\mathrm{b}T+\frac{\mathrm{c}}{T}\left(\frac{\mathrm{J}}{\mathrm{kg}\cdot\mathrm{K}}\right)\begin{cases}\mathrm{a} = 1850.384 \pm 37.674\\ \mathrm{b} = 0.248 \pm 0.005\\ \mathrm{c} = -393964.868 \pm 8021.225\end{cases} \tag{7}$$

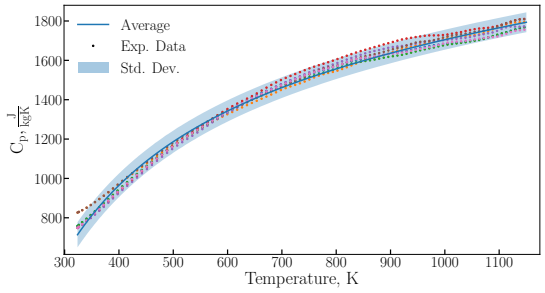

Figure 7: Heat capacity of charred ZURAM®. The dots represent the experimental measurements with the different repetitions. The blue line represents the average fit for the datapoints taking into account the experimental uncertainties and the shadowed area represents the standard deviation.

4.1.2. *Virgin* ZURAM®

The STA measurements on ZURAM® were performed analogously to the pre-charred. However, it is not possible to access the c_{p} of the virgin material at high temperatures due to the different chemical reactions occurring to the material. The common approach in such cases is to measure the property up to the maximum temperature without decomposition, and then to extrapolate the property to higher temperatures using a polynomial fit with the same shape used for the charred material. In this case, the maximum temperature without thermal degradation is 500 K (Fig. 8).

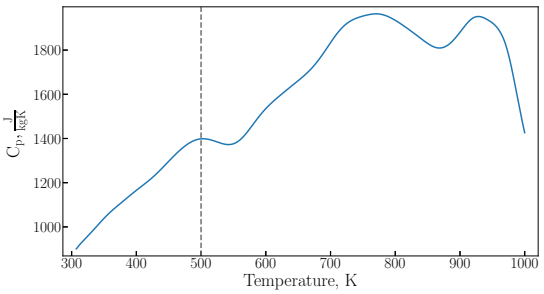

Figure 8: Apparent c_{p} of ZURAM®. After 500 K reactions are overlap the c_{p}, thus material cannot be considered in the virgin state.

We can then reduce the range of the different measurements up to 500 K so that no reactions are observed. Then, we perform a polynomial fit to those data (Fig. 9, blue). Finally, the polynomial is extrapolated to high temperatures (orange).

$$c_{\mathrm{p}}^{\mathrm{virgin}}(T) = \mathrm{a}+\mathrm{b}T+\frac{\mathrm{c}}{T}\left(\frac{\mathrm{J}}{\mathrm{kg}\cdot\mathrm{K}}\right)\begin{cases}\mathrm{a} = 1724.514 \pm 35.109\\ \mathrm{b} = 0.656 \pm 0.014\\ \mathrm{c} = -311009.512 \pm 6333.753\end{cases} \tag{8}$$

4.1.3. *Phenolic resin*

Samples of phenolic resin from the same ZURAM® batch were also analyzed. The low density of the resin is an obstacle to obtain reliable and repeatable measurements. Even though compressing the material using an in-house designed mini-press relieved the problem allowing mass of ~ 16 mg barely enough to perform an accurate measurement. The samples of resin were analyzed up to 500 K again due to the effect of the pyrolysis and the thermal degradation of the

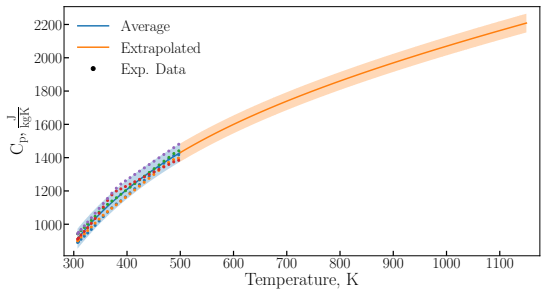

Figure 9: c_p of virgin ZURAM®. The experimental results (dots) are shown up to 500 K (no reactions). Fit to these experiments (blue line) is extrapolated to higher temperatures (orange) where the virgin state does not exist.

material, then it was extrapolated to higher temperatures using the same polynomial shape. The c_p of resin (Fig. 10) is significantly higher than ZURAM®.

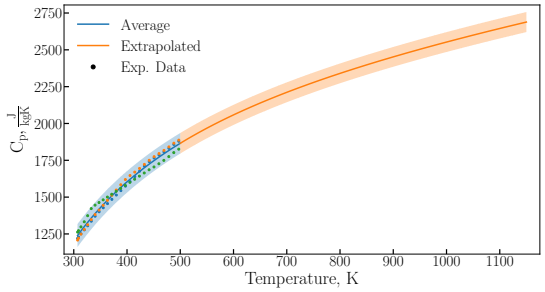

Figure 10: c_p of virgin phenolic resin. The experimental results (dots) are shown up to 500 K (no reactions). Fit to these experiments (blue line) is extrapolated to higher temperatures (orange) where the virgin state does not exist.

$$c_p^{\text{resin}}(T) = \text{a}+\text{b}T+\frac{\text{c}}{T}\left(\frac{\text{J}}{\text{kg}\cdot\text{K}}\right)\begin{cases}\text{a} = 2422.642 \pm 47.729\\ \text{b} = 0.545 \pm 0.011\\ \text{c} = -414779.268 \pm 8176.467\end{cases} \quad (9)$$

4.1.4. *Heat capacity of* ZURAM®*: from virgin to char*

The data described in the previous section can be exploited to study the evolution of the c_p during thermal degradation of ZURAM®. As previously mentioned, the heat capacity can only be accessed in absence of physico-chemical transformations. For a thermally decomposing material, one option is to measure the charred material over the whole temperature range, then measure the virgin material up to the maximum temperature were no transformations occur and extrapolate to higher temperatures. Finally, for a given temperature, the heat capacity of the decomposing sample is computed as:

$$c_p^{\text{ZURAM®}} = \frac{1}{1-\chi(1-\gamma)}\left[(1-\chi)c_p^{\text{virgin}} + \chi\gamma c_p^{\text{char}}\right], \quad (10)$$

Where the parameters χ and γ are the advancement of reaction and the conversion ratio respectively. These two parameters can be easily determined from TGA measurements from the initial mass m_0, the final mass m_∞, and the current mass m as:

$$\chi(T) = \frac{m_0 - m(T)}{m_0 - m_\infty} \quad (11)$$

$$\gamma = \frac{m_\infty}{m_0}. \quad (12)$$

Using the experimentally determined c_p for ZURAM® and pre-charred material (Eqs. 7, 8) in Eq. 10, and determining $\chi(T)$ and γ from the measurements performed, one obtains the evolution of the heat capacity of ZURAM® (Fig. 11)

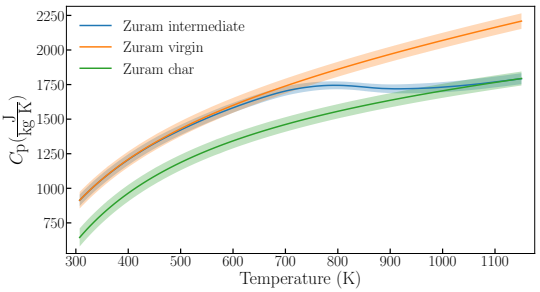

Figure 11: In orange virgin ZURAM® extrapolated to high temperatures. When heated, the material degrades and c_p evolves as ZURAM® intermediate (blue), leading to a char c_p (green)

It can be seen that the c_p of ZURAM® smoothly transitions from virgin to char at ~ 800 K, when the pyrolysis reactions are taking place.

4.2. *Elemental Analysis*

For each material (virgin ZURAM® and phenolic resin), both oxidation and pyrolysis tests were performed in triplets to ensure repeatability. This resulted in 12 measurements which are summarized in the following. In addition, a calcination test (900 °C during 3 hours) was also performed which resulted in negligible residual mass (ash content) for both ZURAM® and the phenolic resin.

4.2.1. *Phenolic resin*

The phenolic resin of ZURAM® is mostly composed of carbon (~ 75.25%) and oxygen (~ 14.13%) and small quantities of hydrogen (~ 5.83%) and nitrogen (~ 1.45%) in mass (Table 1). The mass balance is closed at 96.7%. These results are in great agreement with the measurements on by Sykes [23] on a similar resin.

Table 1: Summary of elemental analysis results for phenolic resin

	C	O	H	N	Total
Avg (%mass)	75.25	14.18	5.83	1.45	96.71
Std (%mass)	0.39	0.14	0.06	0.01	0.42

4.2.2. ZURAM®

It can be seen that ZURAM® has a greater content of carbon (~ 87.3%) than the resin alone due to the contribution from the carbon fiber preform. Consequently, the percentage of the remaining elements has decreased: oxygen (~ 6.97%), hydrogen (~ 2.5%) and nitrogen (~ 0.53%). In this case, the mass balance is closed at 97.3% (Table 2).

Table 2: Summary of elemental analysis results for ZURAM®

	C	O	H	N	Total
Avg (%mass)	87.30	6.97	2.53	0.53	97.33
Std (%mass)	0.22	0.34	0.08	0.02	0.41

ZURAM® is assumed to be made of 50 % carbon fiber preform and 50 % phenolic resin in mass. However, these data was provided by the manufacturer and it needs to be confirmed for further analyses. With the elemental composition, we can perform this check.

Two hypothesis are considered here:

1. The ashes content is negligible (< 3 %, as observed in the calcination test).
2. Carbon fibers are pure carbon.

Assuming that the 1:1 ratio in mass is true, and the aforementioned hypotheses, the composition of ZURAM® computed from the elemental analysis of the phenolic resin (Table 1) should be as described in Table 3. It can be seen that this computed composition is very close to the measurements on ZURAM® (Table 2), hence validating the hypothesis of 1:1 mass ratio of carbon/phenolic in the composite material.

4.3. *Micropyrolysis*

As mentioned in Section 2.4, the results presented in this part are a preliminary work on the molecule identification using the GCxGC and TOF-MS instruments.

Table 3: Computed composition of ZURAM® for 1:1 ratio carbon/phenolic based on the elemental analysis of the phenolic resin

	C	O	H	N	Total
Resin (%mass)	39.69	7.163	2.599	0.548	50
Fibers (%mass)	50	0	0	0	50
Composite (%mass)	89.69	7.163	2.599	0.548	100

The result of a GCxGC is a 2D map of retention times as shown in Figure 12. The horizontal axis refers to the first retention time –first column– while the vertical refers to the second column. It should be highlighted that the scales of the two axis are different: minutes for the first, and seconds for the second column. Different compounds are highlighted with circles (permanent gases, phenols and diphenols) showing the large variety of compounds. In addition, usual compounds found in the past [6] (benzene, toluene, phenol, etc.) are also provided.

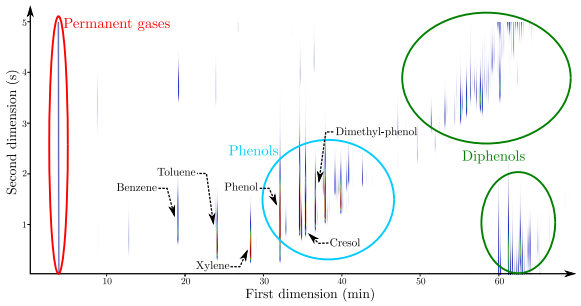

Figure 12: GCxGC map of ZURAM® at 700 °C with the different compounds identified using TOF-MS. The circles depict different types of compounds. Commonly found compounds are specified with dashed arrows. Higher retention times (first dimension) indicate higher molecular weight.

Due to the first column separation based on boiling point and its "direct" relation with molecular weight, compounds with higher retention times on the horizontal axis will have higher carbon number. Certain isomers will elute at the same retention time on the first dimension. These compounds will get separated in the second column which is based on polarity.

In these first tests, we have identified over 40 different molecules product of the pyrolysis on ZURAM® and its phenolic resin at 700 °C. The detailed list is provided in Table 4. This list contains not only the products detected by previous studies [3; 4; 5; 6], but also many high molecular weight (up to C_{15}) compounds. We hypothesize that those previous studies could not observe those molecules due to three main reasons: 1) long residence times which may lead to homogeneous chemistry in the gas phase [3; 4], 2) small number

of those heavier molecules which may hinder their detection [5; 6], and 3) large sample sizes which do not ensure intrinsic kinetics regime.

Table 4: Molecules found with TOF-MS for ZURAM® sample.

Ret. Time (min)	Compound	Mol. mass
3.83	CO	28
9.00	CO2	44
9.33	Cyclopropane (prob 47%)	42
12.33	1-Pentene	70
19.17	Benzene	78
21.00	1-Heptene	98
24.00	Toluene	92
25.50	1-Octene	112
28.25	p-Xylene	106
32.50	Phenol	94
33.00	Benzofuran	118
34.75	2-Methyl Phenol (prob. 30.5%)	108
35.50	p-Cresol (prob. 23.21%)	108
36.83	2,4-dimethyl-phenol (prob. 12%)	122
37.00	Benzofuran, 2-methyl	132
37.58	Benzonitrile, 2-hydroxy-	119
38.08	Phenol, 2,4-dimethyl	122
38.58	Phenol, 3-ethyl-	122
38.83	Phenol, 3,5-dimethyl	122
39.08	Phenol, 2,3-dimethyl	122
40.08	Phenol, 2,3,5-trimethyl-	136
41.58	Hydroquinone	110
43.33	Napthalene, 1-methyl-	142
44.33	Benzaldehyne, 3-hydroxy	122
49.83	Benzene, 1-methyl-3-(phenylmethyl)-	182
51.58	Fluorene (C13H10)	166
52.08	Benzene, 1-methyl-3-((4-methylphenyl)methyl)-	196
53.08	9H-Xanthene	182
54.58	9H-Fluorene, 9-methyl-	180
54.83	p-Benzylphenol	184
55.58	4-Methyl-2-Benzylphenol	198
56.58	Methanol, bis(o-tolyl)-	212
57.83	1,1'-Biphenyl, 3, 3', 4, 4'-tetramethyl	210
58.58	1,1'-Biphenyl, 3, 3', 4, 4'-tetramethyl	210
59.33	Anthracene, 2-methyl-	192
60.17	Phenol, 2, 2'-methylenebis-	200
61.42	Phenol, 4, 4'-methylenebis-	200
62.42	Phenol, 2, 2'-methylenebis(4-methyl-	228
62.67	Phenol, 2, 2'-methylenebis(4-methyl-	228
64.17	Phenol, 2, 2'-methylenebis(4-methyl-	228

From the tests, we can evaluate the conversion ratio for ZURAM® at different temperatures by measuring the initial –virgin– mass and the final as depicted in Fig. 13. It can be seen that as temperature increases, γ tends to a plateau of 0.4, which coherent with TGA measurements on ZURAM® [11].

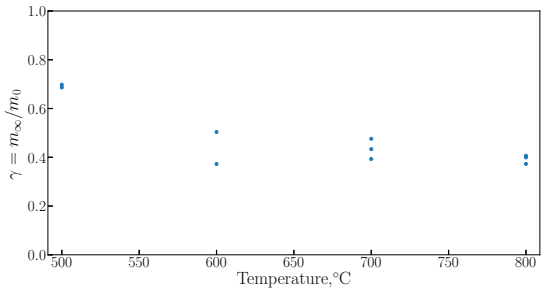

Figure 13: Evolution of the conversion ratio with temperature

We also provide here a first quantification (uncalibrated) of some of the main products of the pyrolysis of phenolic resin of ZURAM® (Fig. 14)[1]. The scaling applied in the y-axis is based on the blob volume computed with the software GCImage, the initial mass of the sample, and the range applied in the FID detector (either 1 or 10). It can be seen that as temperature increases the formation of the different aromatics increases reaching a plateau, except with phenol. This gas seems to achieve a maximum at $\sim 700\,°C$ and then decrease again at $800\,°C$.

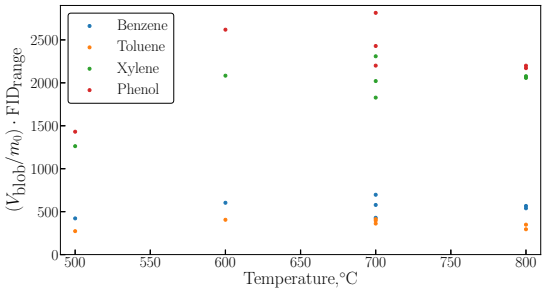

Figure 14: Evolution of the main pyrolysis products for different temperatures.

5. Conclusions

In this work, we have presented three analytical techniques to characterize the thermal degradation of a carbon/phenolic ablator –ZURAM®– at high temperatures.

Simultaneous Thermal Analysis is a powerful technique to characterize the c_p of decomposing materials. We have characterized the c_p of ZURAM® and its components. In addition, we have computed a decomposing c_p considering both virgin and char state and TGA data. Accurate characterization of c_p is required in order to obtain properties from other tests such as the thermal conductivity from Laser Flash Analysis.

Elemental Analysis (CHON) allows to easily obtain the elemental composition of an organic compound. These data are useful to 1) obtain the empirical formula of compounds such as the phenolic resin of ZURAM®, 2) verify the mass ratio resin/fibers in unknown samples and 3) to verify completion of pyrolysis from other analyses.

The micropyrolyzer setup is a novel technique to characterize the pyrolysis of carbon/phenolic. We have identified more than 40 different molecules from the pyrolysis of ZURAM® including high molecular weight compounds which have never been reported in literature. This identification capability is mainly due to the good separation of compounds using a tandem of GC (GCxGC). Further work will allow quantification under different conditions of temperature and advancement of reaction.

[1] Note that comparisons among gases is not possible at this stage since calibration factors need to be determined using a calibration standard.

Acknowledgments

The research of F. Torres Herrador is supported by SB PhD fellowship 1S58718N of the Research Foundation Flanders (FWO). This work is partially supported by ESA contract no. 4000122914/18/NL/KML (AblaNTIS). We acknowledge Thomas Reimer and Christian Zuber (DLR Stuttgart) for providing the materials used in this project. Diana Vargas, Sri Bala Gorugantu (Ghent University) are acknowledged for their help during the elemental analysis and the micropyrolysis experiments. We thank Gertjan Glabeke (VKI) for his support during the STA experiments. Bernd Helber and Alessandro Turchi (VKI) are acknowledged for the comments and support provided through this work. Michele Capriati is acknoleged for revising this manuscript.

References

[1] F. S. Milos, Y.-K. Chen, M. Congdon, J. M. Thornton, Mars Pathfinder Entry Temperature Data, Aerothermal Heating, and Heatshield Material Response, Journal of Spacecraft and Rockets - J SPACECRAFT ROCKET 36 (1999) 380–391. doi:10/cd3xtz.

[2] F. S. Milos, R. Brewer, Y. Chen, T. Squire, Analysis of Galileo Probe Heatshield Ablation and Temperature Data, Journal of Spacecraft and Rockets - J SPACECRAFT ROCKET 36 (1999) 298–306. doi:10/fb3phw.

[3] H.-W. Wong, J. Peck, R. E. Bonomi, J. Assif, F. Panerai, G. Reinisch, J. Lachaud, N. N. Mansour, Quantitative determination of species production from phenol-formaldehyde resin pyrolysis, Polymer Degradation and Stability 112 (2015) 122–131. doi:10.1016/j.polymdegradstab.2014.12.020.
URL http://www.sciencedirect.com/science/article/pii/S0141391014004534

[4] H.-W. Wong, J. Peck, J. Assif, F. Panerai, J. Lachaud, N. N. Mansour, Detailed analysis of species production from the pyrolysis of the Phenolic Impregnated Carbon Ablator, Journal of Analytical and Applied Pyrolysis 122 (2016) 258–267. doi:10/f9h46d.
URL http://www.sciencedirect.com/science/article/pii/S016523701630211X

[5] B. K. Bessire, S. A. Lahankar, T. K. Minton, Pyrolysis of Phenolic Impregnated Carbon Ablator (PICA), ACS Applied Materials & Interfaces 7 (3) (2015) 1383–1395. doi:10/f62x9w.
URL https://doi.org/10.1021/am507816f

[6] B. K. Bessire, T. K. Minton, Decomposition of Phenolic Impregnated Carbon Ablator (PICA) as a Function of Temperature and Heating Rate, ACS Applied Materials & Interfaces 9 (25) (2017) 21422–21437. doi:10.1021/acsami.7b03919.
URL http://dx.doi.org/10.1021/acsami.7b03919

[7] J. Lachaud, A. Martin, I. Cozmuta, B. Laub, Ablation Test Case 1, in: 4th Ablation Workshop, Albuquerque, New Mexico, 2011.

[8] J. Lachaud, A. Martin, T. van Eekelen, I. Cozmuta, Ablation Test Case 2, in: 5th Ablation Workshop, Lexingotn, Kentucky, 2012.

[9] T. van Eekelen, I. Cozmuta, A. Martin, J. Lachaud, Ablation Test Case 3, in: 6th Ablation Workshop, Illinois, 2014.

[10] B. Helber, F. Torres Herrador, V. Leroy, A. Turchi, O. Chazot, T. E. Magin, Experiments of the ZURAM carbon-phenolic ablator for test case definition and material code validation., in: 9th Ablation Workshop, Bozeman, Montana USA, 2017.

[11] F. Torres-Herrador, T. E. Magin, B. Helber, A. Turchi, A. Fagnani, O. Chazot, Material properties and ablation performance of the ZURAM ablator for material response code validation, in: 10th Ablation Workshop, Burlington, Vermont USA, 2018.

[12] F. Torres-Herrador, J. Coheur, J. Blondeau, J. Meurisse, F. Panerai, J. Lachaud, T. Magin, N. N. Mansour, Comparison between traditional and competitive reaction models for the pyrolysis of high temperature aerospace materials, in: AIAA Aviation 2019 Forum, American Institute of Aeronautics and Astronautics, 2019. doi:10.2514/6.2019-3361.
URL https://arc.aiaa.org/doi/abs/10.2514/6.2019-3361

[13] H. E. Toraman, Fast Pyrolysis for the Circular Economy: from Plastic Waste to Genetically Engineered Poplar, Ph.D. thesis, Ghent University (2016).
URL http://hdl.handle.net/1854/LU-8602450

[14] J. Blondeau, Investigation of pulverised biomass combustion: detailed modelling of particle pyrolysis and experimental analysis of ash deposition, Ph.D. thesis, Universit catholique de Louvain (May 2013).

[15] D. L. Pyle, C. A. Zaror, Heat transfer and kinetics in the low temperature pyrolysis of solids, Chemical Engineering Science 39 (1) (1984) 147–158. doi:10/c9244q.
URL http://www.sciencedirect.com/science/article/pii/0009250984801402

[16] S. Maduskar, G. G. Facas, C. Papageorgiou, C. L. Williams, P. J. Dauenhauer, Five Rules for Measuring Biomass Pyrolysis Rates: Pulse-Heated Analysis of Solid Reaction Kinetics of Lignocellulosic Biomass, ACS Sustainable Chemistry & Engineering 6 (1) (2018) 1387–1399. doi:10/gct7j4.
URL https://doi.org/10.1021/acssuschemeng.7b03785

[17] T. Rothermel, G. Herdrich, L. Walpot, C. Zuber, A lightweight ablative material for research purposes, in: 6th Ablation Workshop, University of Kentucky, 2014.

[18] T. Reimer, C. Zuber, J. Rieser, T. Rothermel, Determination of the Mechanical Properties of the Lightweight Ablative Material Zuram (Feb. 2018). doi:10.1002/9781119423829.ch28.

[19] Mettler-Toledo, Investigating unknown samples, Thermal Analysis UserCom.
URL http://us.mt.com/content/us/en/home/supportive_content/usercom/TA_UserCom29.html

[20] Mettler-Toledo, Interpreting DSC Curves, Thermal Analysis UserCom.
URL http://us.mt.com/content/us/en/home/supportive_content/usercom/TA_UserCom11.html

[21] Q. Chen, R. Yang, B. Zhao, Y. Li, S. Wang, H. Wu, Y. Zhuo, C. Chen, Investigation of heat of biomass pyrolysis and secondary reactions by simultaneous thermogravimetry and differential scanning calorimetry, Fuel 134 (2014) 467–476. doi:10/f6crd2.
URL http://www.sciencedirect.com/science/article/pii/S0016236114005547

[22] H. O. Pierson, Handbook of Carbon, Graphite, Diamonds and Fullerenes, Elsevier, 1994.

[23] G. F. Sykes, Decomposition Characteristics of a Char-Forming Phenolic Polymer Used for Ablative Composites., Tech. Rep. TN D-3810 (1967).

ENVIRONMENTAL FLOWS AND SAFETY

VMS implementation for CBRN dispersion modeling in the atmosphere

Yoshiyuki Nishio

Department of Mechanics, Royal Military Academy (RMA), Belgium, yoshiyuki.nishio@rma.ac.be
Environmental and applied fluid dynamics department, von Karman Institute for Fluid Dynamics (VKI), Belgium

Supervisor: Jeroen van Beeck

Professor, Environmental and applied fluid dynamics department, von Karman Institute for Fluid Dynamics (VKI), Belgium, vanbeeck@vki.ac.be

Supervisor: Bart Janssens

Associate Professor, Department of Mechanics, Royal Military Academy (RMA), Belgium, bart.janssens@rmi.ac.be

University supervisor: Karim Limam

Professor, LaSie, Université de La Rochelle (ULR), France, klimam01@univ-lr.fr

Abstract

In the context of a Chemical, Biological, Radiological and Nuclear (CBRN) application for the Belgian Defense, the aim of the current work is to propose a LES model, derived from the code developed in the thesis of Janssens, B. to predict the dispersion of particles in the atmosphere. The code uses the Finite Element Method (FEM) for both the fluid and the dispersed solid phase.

This article starts with a brief recall on the context leading to the aim of the work.

Subsequently, a section is dedicated to theory. In this section, the formulation for the Navier-Stokes equations in FEM is enounced and the application of the SUPG method is formulated. Especially, its assembly matrix and stabilization coefficients are detailed. After having presented the SUPG method, the VMS method is presented, first, by presenting its specific structure. For this structure, the different stages and steps are developped. Secondly, the VMS algorithm is enunciated, especially the corresponding assembly matrix and its stabilization coefficients. Then, by comparing these assembly matrix, it is demonstrated that the VMS can be considered as a more general version of the SUPG method. This is done by indicating the similarities and differences.

The third part is more focused on the results of the implementation. It is shown that the predictor / multi-corrector stages structure is properly implemented. It is also shown that the implementation of the algorithm itself is not yet correct although aspiring to the right direction.

Eventually, when the VMS implementation will be completed, it will offer a robust foundation to explore the VMS capacities.

Keywords: ABL, CFD, FEM, LES, SUPG , Turbulent Flow, VMS

Nomenclature

N_i	[-]	Shape function
Δt	[s]	$= t_{n+1} - t_n$
Ω	[m^3]	Space domain
α_X	[-]	α-method parameter
ν	[m^2/s]	Kinematic viscosity
τ_X	[-]	Stabilization coefficient for X
$\tilde{u}_{adv}$	[m/s^2]	Reference advection velocity
p	[$kg/(ms^2)$]	Pressure
t	[s]	Time
u	[m/s]	Velocity

Acronyms

γ	α-method parameter
A_e	Assembly matrix for the elements
R^X	Residual vector for X
ABL	Atmospheric Boundary Layer
BU	Bulk viscosity stabilization
CBRN	Chemical, Biological, Radiological and Nuclear
CFD	Computational Fluid Dynamics
FEM	Finite Elements Method
LES	Large Eddy Simulation
PG	Petrov–Galerkin
PS	Pressure Stabilization
SU	Streamline Upwind
USA	United States of America
VMS	Variational MultiScale method

Superscripts and Subscripts

adv	Advection
BU	Coefficient for the bulk viscosity stabilization
e	Per element
F, M	α-method parameters
l	Multi-corrector iteration number
M, C	Momentum, Continuity
n	Timestep
PS	Coefficient for the PSPG stabilization
SU	Coefficient for the SUPG stabilization
T	Transpose

1. Introduction

1.1. Context

In March 2019, a petrochemical storage facility took fire near Houston, USA. The smoke rapidly expanded above the city, inciting fear with the population. Questions concerning air pollution and health care brought significant doubt surrounding the safety measures that were taken. Being able to predict the smoke dispersion while taking into account the city's topography and to the weather conditions could have avoided such a situation and therefore protected civilians.



Figure 1: Smoke dispersion's above Houston (source: [1])

With regard to CBRN military applications, succeeding in predicting the propagation direction of a gas or aerosol can be very useful for both the attacker and the defender. The former could use the information to find the optimal position to arm the diffusion source. The latter will have a clear idea on the area of contamination and how it could evolve. For both cases, the weather forecast and the topography of the considered area are key parameters.

1.2. Previous Works and Evolutions

In 2014, a DNS model for fluids laden with small particles was developed in the thesis of Janssens, B. [2]. The model, using FEM for both the fluid and the dispersed phase, was validated by reference and experimental CFD case studies (e. g. "Turbulent channel flow" case, "Taylor-Green vortex flow" case and "Turbulence-induced coalescence in aerosols" case).

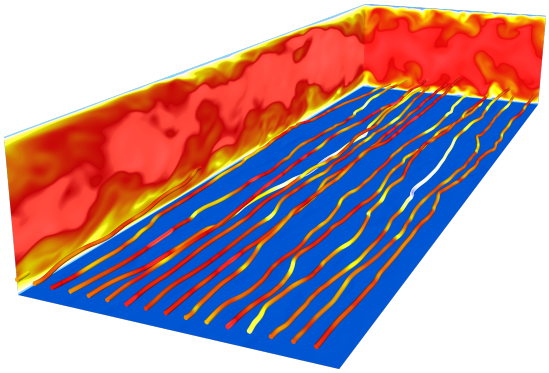

Figure 2: Turbulent channel flow (source: [2])

Furthermore, thanks to the significant improvement in computing resources the last decades, CFD codes increased their simulations capabilities, in terms of

model dimensions, processing time and resolution. As a consequence, it becomes more realistic to study, jointly, smaller turbulent scales and meso-scales effects.

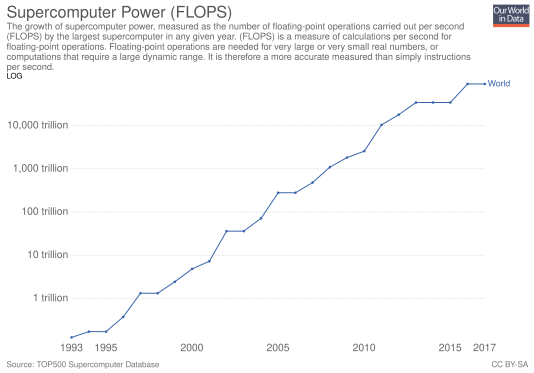

Figure 3: Supercomputer power in FLOPS (source: [3])

Consequently to these validations and to the computing resources' improvement, the aim of the proposed CFD model is to predict the dispersion of particles in the atmosphere, for an area on the order of the hectometer, taking into account detailed geometries of the topography. However, correctly resolving the atmospheric boundary layer is not straightforward and its representation needs to be validated first.

In article [4], a Schumann's wall model was implemented and tested in 2D. It used the Streamline-Upwind Petrov-Galerkin (SUPG) stabilization method implemented by Janssens, B. [2] to stabilize the numerical oscillations. The results were encouraging but in 3D, spurious numerical fluctuations near the wall were observed.

There are suspicions concerning the stabilization currently used in our finite element method. It appears as insufficient to damp the oscillations occuring with high Reynolds number flow. So we intend to amend it using the techniques from the Variational Multiscale Method (VMS), which provides a combined framework for stabilization and turbulence modeling.

In this article, the proposed solution is first described and then compared theoretically to the SUPG method.

In the second part, a comparison is proposed on the Taylor-Green test case and the results are being analyzed.

2. Theory

In current work, the described methods are implicit. Thus, the system of equations is coupling the velocity and the pressure. In a next article, after validation, it will have to be extended to a semi-implicit method to boost the scalability.

2.1. Navier-Stokes in FEM

The model that is being implemented is based on the incompressible two Navier-Stokes transport equations. These can be written following [2]:

$$\nabla \cdot u = 0$$
$$\frac{\partial u}{\partial t} + (u \cdot \nabla)u + \frac{u(\nabla \cdot u)}{2} + \nabla p - \nu \nabla^2 u = 0 \qquad (1)$$

The finite element formulation can be achieved by multiplying these equations with weigthing functions. The unknown variables can be interpolated between the discrete nodes by using shape functions and eventually, these equations can be integrated over the whole domain. The expressions can be simplified by choosing weighting functions equal to shape functions, which leads to a Galerkin formulation.

After applying a θ-method to the time derivative and because the shape functions are non-zero only on their respective node and surrounding element, the integrals for all the elements can be replaced by a sum of the integral on each element. By solving this discrete system, the pressure and the velocity for the next timestep can be found:

$$\sum_{e=1}^{N} \left(\frac{1}{\Delta t} T_e + \theta A_e \right) \left(x_e^{n+1} - x_e^n \right) = -A_e x_e^n \qquad (2)$$

where θ is set to 1 for a forward Euler scheme or 0.5 for a Crank-Nicolson scheme. By default, it is set to 0.5 in [2]. The unknown x_e^n for each element, grouped by nodal values, have following format for a 3D element with $m + 1$ nodes:

$$x_e^n = \left[p_0^n \cdots p_m^n (u_0^n)_0 \cdots (u_0^n)_m \cdots (u_2^n)_m \right] \qquad (3)$$

Matrices A_e and T_e have the following structure:

$$A_e = \begin{bmatrix} A_{pp} & A_{pu} \\ A_{up} & A_{uu} \end{bmatrix} = \begin{bmatrix} A_{pp} & A_{pu_0} & A_{pu_1} & A_{pu_2} \\ A_{u_0 p} & A_{u_0 u_0} & A_{u_0 u_1} & A_{u_0 u_2} \\ A_{u_1 p} & A_{u_1 u_0} & A_{u_1 u_1} & A_{u_1 u_2} \\ A_{u_2 p} & A_{u_2 u_0} & A_{u_2 u_1} & A_{u_2 u_2} \end{bmatrix} \qquad (4)$$

2.2. SUPG Stabilization method

By applying the SUPG stabilization method detailed in [5] to Eq. 1, each block of A_e can be formulated as follows:

$$A_{pp} = \int_{\Omega_e} \tau_{PS} \nabla N_p^T \nabla N_p d\Omega_e \tag{5}$$

$$A_{pu_i} = \int_{\Omega_e} \left(\left(N_p + \frac{\tau_{PS} \tilde{u}_{adv} \nabla N_p}{2} \right)^T (\nabla N_u)_i + \tau_{PS} \left(\nabla N_p \right)_i^T \tilde{u}_{adv} \nabla N_u \right) d\Omega_e \tag{6}$$

$$A_{u_i p} = \int_{\Omega_e} \left(N_u + \tau_{SU} \tilde{u}_{adv} \nabla N_u \right)^T \nabla N_p d\Omega_e \tag{7}$$

$$A_{u_i u_i} = \int_{\Omega_e} \left(\nu \nabla N_u^T \nabla N_u + \left(N_u + \tau_{SU} \tilde{u}_{adv} \nabla N_u \right)^T \tilde{u}_{adv} \nabla N_u \right) d\Omega_e + A_{u_i u_j} \tag{8}$$

$$A_{u_i u_j} = \int_{\Omega_e} \left(\tau_{BU} \left(\nabla N_u \right)_i + \frac{1}{2} \left(\tilde{u}_{adv} \right)_i \left(N_u + \tau_{SU} u \nabla N_u \right) \right)^T \left(\nabla N_u \right)_j d\Omega_e \tag{9}$$

$$T_{pu_i} = \int_{\Omega_e} \tau_{PS} \left(\nabla N_p \right)_i^T N_u d\Omega_e \tag{10}$$

$$T_{u_i u_i} = \int_{\Omega_e} \left(N_u + \tau_{SU} \tilde{u}_{adv} \nabla N_u \right)^T N_u d\Omega_e \tag{11}$$

where $\tilde{u}_{adv}$ is the advection velocity, obtained, in [2], by a Taylor expansion of the previous velocities. And where the stabilization terms, multiplied by their respective stabilization coefficients ($\tau_{PS,SU,BU}$), are presented in [6].

To better understand the difference between SUPG and VMS methodologies, these terms are briefly depicted.

1. The PSPG term has an influence both on the A_{pp} and A_{pu_i} blocks. The most impacted is the former, the laplacian of the pressure, that is non-zero when $\tau_{PS} \neq 0$.
2. The SUPG terms increase the weight of the upstream nodes, relative to the stream direction.
3. The bulk viscosity term is influencing advection flows.

These coefficients have to be chosen in such a manner that the numerical values are properly stabilized but not over-dissipated.

Hereafter, the definition proposed by [7], based on the element metric tensor G_{ij} (i.e. the element shape function inverse Jacobian matrix multiplied with its transpose).

$$\tau_{SU1}^2 = \frac{1}{u_i G_{ij} u_j} \tag{12}$$

$$\tau_{SU2} = \frac{\Delta t}{2} \tag{13}$$

$$\tau_{SU3}^2 = \frac{1}{\nu^2 G_{ij} G_{ij}} \tag{14}$$

$$\tau_{SU} = \left(\frac{1}{\tau_{SU1}^2} + \frac{c_1^2}{\tau_{SU2}^2} + \frac{c_2}{\tau_{SU3}^2} \right)^{-1/2} \tag{15}$$

$$\tau_{PS} = \tau_{SU} \tag{16}$$

$$\tau_{BU} = \frac{1}{\tau_{SU} G_{ij}} \tag{17}$$

where c_1 and c_2 are tuning parameters set to $4 \leq c_1 \leq 16$ and $c_2 = 36$ by the author in [7], for an advection flow.

This stabilization method was implemented by B. Janssens in [2] and successfully helped to solve oscillations for reasonable Reynolds simulation (e.g. the channel flow test case).

Nevertheless, to be able to tackle the spurious numerical oscillations observed in [8], the idea is to use a generalized version of the SUPG stabilization method, called Variational Multiscale method (VMS). It was introduced by T.J.R. Hughes in [9] and Y. Bazilevs proposed an algorithm in [10].

The next section will present an implementation of the latter, following the convention proposed by Y. Bazilevs, with the notation used in this section.

2.3. Variational Multiscale method (VMS)

The VMS applies the scale separation (coarse vs fine) primarly and only approximate the fines scales. In these small scales, the stabilization terms appear naturally.

2.3.1. Structure

The proposed VMS method derives from [10] and follows a Newton structure, also called predictor / multi-corrector structure, schematized in Figure 4. This method has more parameters than the standard SUPG method, allowing it to better respond to numerical oscillations.

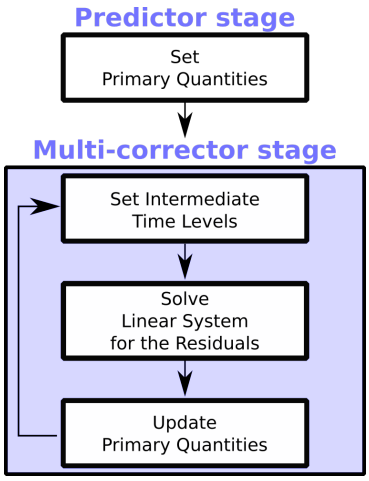

Figure 4: Predictor / Multi-corrector's structure

2.3.2. Stages

2.3.2.1. Predictor stage. For each timestep, during the first stage, the predictor stage, the three variables (velocity u, derivative of the velocity $\dot{u}$ and pressure p) are set according to previous timestep.

$$U_{n+1,(0)} = U_n \tag{18}$$

$$\dot{U}_{n+1,(0)} = \frac{\gamma - 1}{\gamma} \dot{U}_n \tag{19}$$

$$P_{n+1,(0)} = P_n \tag{20}$$

γ (as well as α_f and α_m that are presented in 2.3.2.2) is a real-valued parameter defining the α-method. It is developped in [11] and especially for fluid dynamics in [12].

2.3.2.2. Multi-corrector stage. Then, during the second stage (that is, the nonlinear multi-corrector stage), a number of iterations ($l = 1, 2, ..., l_{max}$) is performed (typically between 2 and 4) to converge to steady values, or in other words, the residuals for, both, the continuity and momentum equations of Eq. (1) are minimized.

To be more explicit, during these iterations, the following steps are performed:

(1) The first step is to set the intermediate time levels:

$$\dot{U}_{n+\alpha_m,(l)} = \dot{U}_n + \alpha_m \left(\dot{U}_{n+1,(l-1)} - \dot{U}_n \right) \tag{21}$$

$$U_{n+\alpha_f,(l)} = U_n + \alpha_f \left(U_{n+1,(l-1)} - U_n \right) \tag{22}$$

$$P_{n+1,(l)} = P_{n+1,(l-1)} \tag{23}$$

α_f and α_m are intermediate time level parameters. They (as well as previously mentionned γ) are selected, taking accuracy and stability considerations into account. According to [12], obtaining second-order accuracy in time is possible if:

$$\gamma = 1/2 + \alpha_m - \alpha_f \tag{24}$$

and the method is unconditionally stable if:

$$\alpha_m \geqslant \alpha_f \geqslant 1/2 \tag{25}$$

For the latter, α_f and α_m can be expressed as a function of one single parameter: ρ_∞. That is, the spectral radius of the amplification matrix when $\Delta t \to \infty$.

$$\alpha_m = \frac{1}{2}\left(\frac{3 - \rho_\infty}{1 + \rho_\infty}\right) \quad \textit{and} \quad \alpha_f = \frac{1}{1 + \rho_\infty} \tag{26}$$

Further details on how this single parameter controls the dissipation for high-frequencies is extensively described in [13]. Therefore, by selecting a γ agreeing with Eq. (24) and by defining the proper ρ_∞, one can ensure the time integration scheme is unconditionally stable.

(2) These intermediate values are used to assemble the residuals of the continuity and momentum equations and solve the following linear system:

$$A_{\dot{u}\dot{u}} \Delta\dot{U}_{n+1,(l)} + A_{\dot{u}p} \Delta P_{n+1,(l)} = -R^M_{(l)} \tag{27}$$

$$A_{p\dot{u}} \Delta\dot{U}_{n+1,(l)} + A_{pp} \Delta P_{n+1,(l)} = -R^C_{(l)} \tag{28}$$

that can be rearranged as below:

$$\begin{bmatrix} A_{\dot{u}\dot{u}} & A_{\dot{u}p} \\ A_{p\dot{u}} & A_{pp} \end{bmatrix} \begin{bmatrix} \Delta\dot{U}_{n+1,(l)} \\ \Delta P_{n+1,(l)} \end{bmatrix} = \begin{bmatrix} -R^M_{(l)} \\ -R^C_{(l)} \end{bmatrix} \tag{29}$$

(3) This will provide values for the derivative of the velocity and the pressure that can be updated in the last step of the multi-stage corrector:

$$\dot{U}_{n+1,(l)} = \dot{U}_{n+1,(l-1)} + \Delta\dot{U}_{n+1,(l)} \tag{30}$$

$$U_{n+1,(l)} = U_{n+1,(l-1)} + \gamma \Delta t \Delta\dot{U}_{n+1,(l)} \tag{31}$$

$$P_{n+1,(l)} = P_{n+1,(l-1)} + \Delta P_{n+1,(l)} \tag{32}$$

In terms of computation, the second step of the multi-corrector stage, namely, assembling and solving the linear system, is the most costly.

2.3.3. VMS Assembly matrix A_e

Below, compared to Eq. (5)-(11), a slightly different assembly matrix A_e is provided:

$$A_e = \begin{bmatrix} A_{\dot{u}\dot{u}} & A_{\dot{u}p} \\ A_{p\dot{u}} & A_{pp} \end{bmatrix} = \begin{bmatrix} A_{\dot{u}_0\dot{u}_0} & A_{\dot{u}_0\dot{u}_1} & A_{\dot{u}_0\dot{u}_2} & A_{\dot{u}_0 p} \\ A_{\dot{u}_1\dot{u}_0} & A_{\dot{u}_1\dot{u}_1} & A_{\dot{u}_1\dot{u}_2} & A_{\dot{u}_1 p} \\ A_{\dot{u}_2\dot{u}_0} & A_{\dot{u}_2\dot{u}_1} & A_{\dot{u}_2\dot{u}_2} & A_{\dot{u}_2 p} \\ A_{p\dot{u}_0} & A_{p\dot{u}_1} & A_{p\dot{u}_2} & A_{pp} \end{bmatrix} \tag{33}$$

Indeed, in this case, the first block depends on the derivative of the velocity $\dot{u}$ and the last block on the pressure p. This structure was chosen to match the proposed implementation of [10] but it is equivalent to the one presente in the SUPG section (2.2).

For each block, the expression is detailed hereafter:

$$\begin{aligned} A_{\dot{u}_i\dot{u}_i} = \int_{\Omega_e} \Big(& \alpha_m N_{\dot{u}}^T N_{\dot{u}} \\ & + \alpha_m \left(u\tau_M \nabla N_{\dot{u}}\right)^T N_{\dot{u}} \\ & + \alpha_f \gamma \Delta t N_{\dot{u}}^T u \nabla N_{\dot{u}} \\ & + \alpha_f \gamma \Delta t \left(\nabla N_{\dot{u}} \nu\right)^T \nabla N_{\dot{u}} \\ & + \alpha_f \gamma \Delta t \left(u \nabla N_{\dot{u}} \tau_M\right)^T \left(u \nabla N_{\dot{u}}\right) \Big) d\Omega_e \end{aligned} \tag{34}$$

$$\begin{aligned} A_{\dot{u}_i\dot{u}_j} = \int_{\Omega_e} \Big(& \alpha_f \gamma \Delta t \left(\nabla N_{\dot{u}}\right)_j^T \nu \left(\nabla N_{\dot{u}}\right)_i \\ & + \alpha_f \gamma \Delta t \left(\nabla N_{\dot{u}}\right)_i^T \tau_C \left(\nabla N_{\dot{u}}\right)_j \Big) d\Omega_e \end{aligned} \tag{35}$$

$$\begin{aligned} A_{\dot{u}_i p} = \int_{\Omega_e} & - \left(\nabla N_{\dot{u}}\right)_i^T N_p \\ & + \left(u^T \tau_M \left(\nabla N_{\dot{u}}\right)_i\right)^T \nabla N_p d\Omega_e \end{aligned} \tag{36}$$

$$\begin{aligned} A_{p\dot{u}_i} = \int_{\Omega_e} \Big(& \alpha_f \gamma \Delta t N_p^T \left(\nabla N_{\dot{u}}\right)_i \\ & + \alpha_f \gamma \Delta t \left(\nabla N_p\right)_i^T \tau_M u \nabla N_{\dot{u}} \\ & + \alpha_m \left(\nabla N_p\right)_i^T \tau_M N_{\dot{u}} \Big) d\Omega_e \end{aligned} \tag{37}$$

$$A_{pp} = \int_{\Omega_e} \left(\nabla N_p\right)^T \tau_M \nabla N_p d\Omega_e \tag{38}$$

As previously described, the $N_{[\dot{u},p]}$ represent the shape functions, the $\alpha_{[f,m]}$ and γ represent the intermediate time level parameters, Δt represents the difference between timestep t_{n+1} and t_n, u is the advection velocity (different of $\tilde{u_{adv}}$ because computed during the simulation and not constructed from a Taylor serie), ν is the kinematic viscosity, and at last, $\tau_{[C,M]}$ are the stabilizing coefficients.

All these components have been defined except the two stabilizing coefficients. Next section will describe them thoroughly.

2.3.4. Defining the stabilizing coefficients

Two stabilizing coefficients are defined: τ_m and τ_c. The first one is the stabilization coefficient associated to the momentum equation and the second, to the continuity equation.

Below, their respective expressions:

$$\tau_m = \left(\frac{4}{\Delta t^2} + u \cdot Gu + C_1 \nu^2 G : G\right)^{-1/2} \tag{39}$$

$$\tau_c = \left(\tau_m g \cdot g\right)^{-1} \tag{40}$$

where C_1 is a positive constant, derived from an element-wise inverse estimate described in [14] and set to 1 in our work. And where three specific operations have to be introduced:

1. the tensor product $G : G$
2. the advection term $u \cdot Gu$
3. the vector product $g \cdot g$

To compute all these items, similarly to the SUPG method (cf. 2.2), the element shape function inverse Jacobian matrix $J^{-1} = \left(\frac{\partial x_i}{\partial \xi_k}\right)^{-1}$ has to be computed.

Items one and two are found by, first, defining the element metric tensor $G_{ij} = \sum_{k=1}^{3} J_{k,i}^{-1} \left(J_{k,j}^{-1}\right)^T$. Second, item one is reached by computing the tensor product of G_{ij} and item two, by determining the scalar product of the velocity by the product of the inverse jacobian tensor and the velocity:

1. $G : G = \sum_{i,j=1}^{3} G_{ij} G_{ij}$
2. $u^h \cdot Gu^h = \sum_{i,j=1}^{3} u_i^h G_{ij} (u_j^h)^T$

For the last item, first the sum of the inverse of the jacobian is formed and then, its product is column-wise summed.

1. $g_i = \sum_{j=1}^{3} (J^{-1})_{j,i}$
2. $g \cdot g = \sum_{i=1}^{3} g_i (g_i)^T$

When looking to the SUPG method (2.2), Eq.(17) (i.e. τ_{BU}) is equivalent to Eq.(40) (i.e. τ_c).

For the relation between τ_m and τ_{SU} (and thus τ_{PS}), these are the same, when looking to Eq.(15) and Eq.(39), except for the tuning parameters.

2.4. SUPG vs VMS Assembly matrix comparison

Now that both SUPG (2.2) and VMS (2.3) are described, it is convenient to show that, indeed, the VMS method can be considered as a generalized version of the older and more used SUPG method.

To ease the comprehension, the viscosity term will be colored in green, the stabilization terms in blue. Moreover, to simplify the expressions, the intermediate time level parameters will be set to unity: $\alpha_f = \alpha_m = \gamma = 1$. Furthermore, because the SUPG assembly matrices have the velocity and the pressure as unknowns whereas VMS assembly matrix has the derivative of the velocity and the pressure as unknowns, to be able to compare them, Δt is set equal to 1 making the value of $\dot{u}$ and u equal.

In the next equations, each block of the assembly matrices will be re-written for comparison.

1. PP block:

$$SUPG\ (Eq.\ (5)) : A_{pp} = \int_{\Omega_e} \tau_{PS} \nabla N_p^T \nabla N_p d\Omega_e$$

$$VMS\ (Eq.\ (38)) : A_{pp} = \int_{\Omega_e} \nabla N_p^T \tau_M \nabla N_p d\Omega_e$$

Both equations are expressing the shape functions related to the pressure and can be considered equivalent, assuming $\tau_{PS} \equiv \tau_M$

2. PU_i block:

$$SUPG\ (Eq.\ (6)) :$$

$$A_{pu_i} = \int_{\Omega_e} \left(\left(N_p + \frac{\tau_{PS} \tilde{u}_{adv} \nabla N_p}{2} \right)^T (\nabla N_u)_i + \tau_{PS} \left(\nabla N_p \right)_i^T \tilde{u}_{adv} \nabla N_u \right) d\Omega_e$$

$$SUPG\ (Eq.\ (10)) :$$

$$T_{pu_i} = \int_{\Omega_e} \tau_{PS} \left(\nabla N_p \right)_i^T N_u d\Omega_e$$

$$VMS\ (Eq.\ (37)) :$$

$$A_{pu_i} = \int_{\Omega_e} \left(\alpha_f \gamma \Delta t N_p^T (\nabla N_{\dot{u}})_i + \alpha_f \gamma \Delta t \left(\nabla N_p \right)_i^T \tau_M u \nabla N_{\dot{u}} + \alpha_m \left(\nabla N_p \right)_i^T \tau_M N_{\dot{u}} \right) d\Omega_e$$

First observation is that both the assembly matrix A_e and T_e for the SUPG method are gathered into the assembly matrix A_e in the VMS method.

Second observation is that Eq. (6) is proportional to the two first terms of Eq. (37), while the third term in Eq. (37) is equivalent to Eq. (10).
Note that the second term of the SUPG formulation is written in skew symmetric form to improve its stability and accuracy properties.

3. U_iP block:

$$SUPG\ (Eq.\ (7)) :$$

$$A_{u_ip} = \int_{\Omega_e} (N_u + \tau_{SU} \tilde{u}_{adv} \nabla N_u)^T (\nabla N_p)_i d\Omega_e$$

$$VMS\ (Eq.\ (36)) :$$

$$A_{u_ip} = \int_{\Omega_e} - (\nabla N_{\dot{u}})_i^T N_p + (u \tau_M \nabla N_{\dot{u}})^T (\nabla N_p)_i d\Omega_e$$

After developing the integration by parts, the first term of Eq. (7) can be expressed as the first term of Eq. (36). The second terms are directly equivalent.
This also implies that, for setting the pressure to 0 on a boundary (i.e. at the outlet), nothing has to be done. It is the do-nothing boundary condition ([15]).

4. U_iU_i block:

$$SUPG\ (Eq.\ (8)) :$$

$$A_{u_iu_i} = \int_{\Omega_e} \left(\nu \nabla N_u^T \nabla N_u + (N_u + \tau_{SU} \tilde{u}_{adv} \nabla N_u)^T \tilde{u}_{adv} \nabla N_u \right) d\Omega_e + A_{u_iu_j}$$

$$SUPG\ (Eq.\ (11)) :$$

$$T_{u_iu_i} = \int_{\Omega_e} (N_u + \tau_{SU} \tilde{u}_{adv} \nabla N_u)^T N_u d\Omega_e$$

$$VMS\ (Eq.\ (34)) :$$

$$A_{u_iu_i} = \int_{\Omega_e} \left(\alpha_m N_{\dot{u}}^T N_{\dot{u}} + \alpha_m (u \tau_M \nabla N_{\dot{u}})^T N_{\dot{u}} + \alpha_f \gamma \Delta t N_{\dot{u}}^T u \nabla N_{\dot{u}} + \alpha_f \gamma \Delta t (\nabla N_{\dot{u}} \nu)^T \nabla N_{\dot{u}} + \alpha_f \gamma \Delta t (u \nabla N_{\dot{u}} \tau_M)^T (u \nabla N_{\dot{u}}) \right) d\Omega_e + A_{u_iu_j}$$

For U_iU_i block, when comparing the two SUPG blocks to the VMS block, all the terms are identical: there is one term (in green) for viscosity, two terms (in blue) for stabilization and two terms for the shape functions time derivative and the advection.

5. $U_i U_j$ block:

$$SUPG\ (Eq.\ (9)):$$
$$\int_{\Omega_e} \left(\tau_{BU} \left(\nabla N_u\right)_i + \frac{1}{2} \left(\tilde{u}_{adv}\right)_i \left(N_u + \tau_{SU} u \nabla N_u\right) \right)^T \left(\nabla N_u\right)_j d\Omega_e$$

$$VMS\ (Eq.\ (35)):$$
$$\int_{\Omega_e} \left(\alpha_f \gamma \Delta t \left(\nabla N_{\dot{u}}\right)_j^T \nu \left(\nabla N_{\dot{u}}\right)_i + \alpha_f \gamma \Delta t \left(\nabla N_{\dot{u}}\right)_i^T \tau_C \left(\nabla N_{\dot{u}}\right)_j \right) d\Omega_e$$

The last block, $A_{u_i u_j}$ is interesting since there is a clear distinction between the SUPG and the VMS formulation. For the first term of Eq. (9), supposing $\tau_{BU} \equiv \tau_C$, it can be considered equivalent to the second term of Eq. (35). The second term of Eq. (9) is the skew-symmetric form in the SUPG matrix while the viscous tensor in VMS is treated differently.

3. Results

Now that the VMS theory that is implemented has been described, a few tests will be presented.

Note that, to reduce the computer cost, all tests are performed in 2D. Indeed, thanks to the use of FEM, moving from a simulation in 2D to a simulation in 3D only requires to use a different element type while the algorithm implementation remains identical.

The first section is focused on the structure of the algorithm whereas the second section concentrates more on the implementation of the algorithm itself.

3.0.1. Mesh properties

Preliminary to the results, the properties of the mesh are listed, to allow one to compare its results to the one presented below.

For the tests related to the structure, a mesh of 16x16 segments was used, with a reference velocity of $1m/s$ in x-direction (horizontal) for the poisson equation and in the x and y-directions for the Taylor-Green equation.

For the test related to the algorithm, the number of segments was reduced to 2x2 and the θ-value appearing in the finite element formulation from Eq. (2) was set to 1 (in other words, the Euler form) to be able to compare the combination of the SUPG assembly matrices, A_e and T_e, to the VMS assembly matrix, A_e.

3.1. Tests for the VMS Structure

The VMS structure described in section 2.3.1 is a predictor / multi-corrector structure. To confirm the correctnes of our implementation, it was first tested with classical and already existing equations.

3.1.1. Poisson equation

The first test, the Poisson equation, defined by $\Delta\varphi = f$, was used because of its simple implementation, its analytical resolution and no use of periodical boundary condition.

The outcome was directly and successfully compared to the result of the simulation performed, using a standard steady Poisson implementation. No quantitative analysis were performed.

To illustrate the simulation, hereafter, a contour view of the velocity:

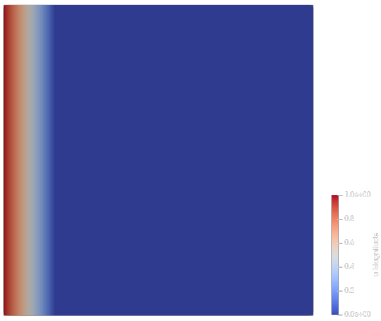

Figure 5: Poisson test case ; $V_{inlet} = 0.5$

On Figure 5, the inlet velocity on the left side was set to $1m/s$.

3.1.2. Taylor-Green equation

After having gained some confidence in the structure's implementation, it was tested on a test case with periodical boundary conditions: The Taylor-Green test case.

Once more, the test case was used because it has an analytical solution and because the standard Navier-Stokes implementation already exists.

The comparison is purely qualitative and the aim is not to obtain a nicely converged simulation but to reproduce the result captured, using the same number of timesteps and the same model parameters, with a standard Navier-Stokes implementation.

Hereafter a contour view of the result:

The objective of this test was to ensure the output, with the new structure, would correlate with the one produced with a standard Navier-Stokes structure.

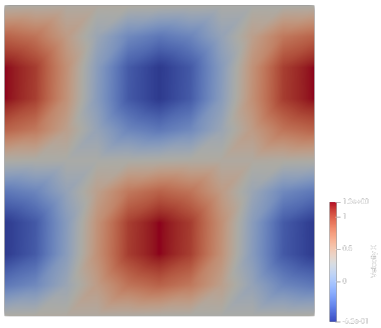

Figure 6: Taylor-Green test case

3.2. *Tests for the VMS implementation*

Having acquired confidence in the structure, it is time to test the algorithm's implementation. The latter is more complicated because the only comparison that can be performed is to compare the assembly matrix A_e between the SUPG implementation and the VMS algorithm implementation, when both the viscosity ν and the stabilization coefficients τ_x are reduced to zero.

To better analyse how each equation described in section 2.3.3 is influencing A_e, they are schemed with blocks in Table 1. Note that each block is actually a 3x3 matrix.

Table 1: A_e structure

$A_{u_iu_i}$	$A_{u_iu_j}$	A_{u_ip}
$A_{u_iu_j}$	$A_{u_iu_i}$	A_{u_ip}
A_{pu_i}	A_{pu_i}	A_{pp}

To ease the reading, the A_e matrix will be printed, limited to 3 decimals (sufficient to see the differences).

3.2.1. *Results with $\nu = \tau_x = 0$*

A simulation was performed, for an identical mesh, with both the SUPG implementation and the VMS implementation. Table 2 displays A_e for the SUPG implementation. This is the reference result.

In Table 2, one can see the matrix is symmetrical, considering the blocks. Another observation is that $A_{u_iu_j}$ and A_{pp} blocks are null value. Eventually, all blocks have a column structure (values varying only column-wise).

The next table (Table 3) proposes the VMS implementation (Eq. 34-38).

Table 2: A_e with $\nu = 0$ for SUPG

-0.182	0	0.182	0	0	0	-0.083	0.083	0
-0.182	0	0.182	0	0	0	-0.083	0.083	0
-0.182	0	0.182	0	0	0	-0.083	0.083	0
0	0	0	-0.182	0	0.182	0	-0.083	0.083
0	0	0	-0.182	0	0.182	0	-0.083	0.083
0	0	0	-0.182	0	0.182	0	-0.083	0.083
-0.083	0.083	0	0	-0.083	0.083	0	0	0
-0.083	0.083	0	0	-0.083	0.083	0	0	0
-0.083	0.083	0	0	-0.083	0.083	0	0	0

Table 3: A_e with $u = 0$ for VMS

-0.083	0	0.083	0	0	0	0.083	0.083	0.083
-0.083	0	0.083	0	0	0	-0.083	-0.083	-0.083
-0.083	0	0.083	0	0	0	0	0	0
0	0	0	-0.083	0	0.083	0	0	0
0	0	0	-0.083	0	0.083	0.083	0.083	0.083
0	0	0	-0.083	0	0.083	-0.083	-0.083	-0.083
-0.083	0.083	0	0	-0.083	0.083	0	0	0
-0.083	0.083	0	0	-0.083	0.083	0	0	0
-0.083	0.083	0	0	-0.083	0.083	0	0	0

When analysing Table 3 for the similarities, the observation is that the null valued blocks are identical. For the differences, the first remark is that A_e is column-wise except for A_{u_ip} that is row-wise and has the opposite sign, compared to SUPG values. Second, the $A_{u_iu_i}$ values are not equal to SUPG ones.

After modifying A_{u_ip} by transposing it and taking its opposite value, Table 3 becomes Table 4.

Table 4: Modified A_e with $u = 0$ for VMS

-0.083	0	0.083	0	0	0	-0.083	0.083	0
-0.083	0	0.083	0	0	0	-0.083	0.083	0
-0.083	0	0.083	0	0	0	-0.083	0.083	0
0	0	0	-0.083	0	0.083	0	-0.083	0.083
0	0	0	-0.083	0	0.083	0	-0.083	0.083
0	0	0	-0.083	0	0.083	0	-0.083	0.083
-0.083	0.083	0	0	-0.083	0.083	0	0	0
-0.083	0.083	0	0	-0.083	0.083	0	0	0
-0.083	0.083	0	0	-0.083	0.083	0	0	0

In the latter, the only difference resides in $A_{u_iu_i}$. This issue is still under investigation.

When the issue will be solved, the next step will be to reactivate the stabilization coefficients and the viscosity to study their behaviour.

4. Conclusion

In this article, after having acknowledged the purpose of the work and its context, the aim was to present the Variational Multiscale Method, to describe the chosen implementation, to demonstrate that it can be considered as a more general version of the SUPG method, and to present its similarities and differences with that method.

In the first part, the main objective of the work and its context were briefly recalled.

Then, in the second part, a theoretical explanation was provided for these two methods. Their respective assembly matrices were described and a comparison revealed their characteristics.

The third part was more focused on the results of the implementation. It was shown that the predictor / multi-corrector stages structure was properly implemented. It was also shown that the implementation of the algorithm itself is not yet correct although evolving in the right direction.

Eventually, when the VMS implementation will reflect perfectly the SUPG (for the non viscous case), it will offer a robust foundation to explore the VMS capacities.

5. Acknowledgments

This study is promoted by the Royal Military Academy (RMA), in cotutelle with the Université de La Rochelle (ULR) and the von Karman Institute for Fluid Dynamics (VKI). The author is thankful to these three institutions to give him the opportunity to work on this subject.

References

[1] Air pollution from harvey was bad. this houston petrochemical fire is worse., `https://grist.org/article/air-pollution-from-harvey-was-bad-this-houston-petrochemical-fire-is-worse/`, accessed: 2019-03-19.

[2] B. Janssens, Numerical modeling and experimental investigation of fine particle coagulation and dispersion in dilute flows, Ph.D. thesis, Université de La Rochelle (2014).

[3] Supercomputer power (flops), `https://ourworldindata.org/grapher/supercomputer-power-flops`, accessed: 2019-01-21.

[4] Y. Nishio, B. Janssens, J. van Beeck, K. Limam, Cbrn dispersion modeling in the atmosphere, in: Review of the VKI Doctoral Research 2018-2019, Von Karmann Institute for Fluid Dynamics, Belgium, 2019, pp. –.

[5] T. Bányai, D. V. Abeele, H. Deconinck, A fast fully-coupled solution algorithm for the unsteady incompressible navier-stokes equations, in: Conference on Modelling Fluid Flow (CMFF06). Budapest, Hungary, 2006, pp. –.

[6] M. Braack, E. Burman, V. John, G. Lube, Stabilized finite element methods for the generalized oseen problem, Computer Methods in Applied Mechanics and Engineering 196 (4-6) (2007) 853–866.

[7] A. V. Trofimova, A. E. Tejada-Martínez, K. E. Jansen, R. T. Lahey Jr, Direct numerical simulation of turbulent channel flows using a stabilized finite element method, Computers & fluids 38 (4) (2009) 924–938.

[8] Y. Nishio, B. Janssens, K. Limam, J. van Beeck, Multiphase flow modeling for cbrn applications, in: International Conference on Materials and Energy (ICOME18). San Sebastian, Spain, 2018.

[9] T. J. Hughes, L. Mazzei, K. E. Jansen, Large Eddy Simulation and the variational multiscale method, Computing and Visualization in Science 3 (1-2) (2000) 47–59. doi:10.1007/s007910050051.

[10] Y. Bazilevs, V. Calo, J. Cottrell, T. Hughes, A. Reali, G. Scovazzi, Variational multiscale residual-based turbulence modeling for large eddy simulation of incompressible flows, Computer Methods in Applied Mechanics and Engineering 197 (1-4) (2007) 173–201.

[11] J. Chung, G. M. Hulbert, A Time Integration Algorithm for Structural Dynamics With Improved Numerical Dissipation: The Generalized-α Method, Journal of Applied Mechanics 60 (2) (1993) 371–375. doi:10.1115/1.2900803.

[12] K. E. Jansen, C. H. Whiting, G. M. Hulbert, A generalized-α method for integrating the filtered navierstokes equations with a stabilized finite element method, Computer Methods in Applied Mechanics and Engineering 190 (3) (2000) 305 – 319. doi:10.1016/S0045-7825(00)00203-6.

[13] T. J. Hughes, The finite element method: linear static and dynamic finite element analysis, Courier Corporation, 2012.

[14] C. Johnson, Numerical solution of partial differential equations by the finite element method, Courier Corporation, 2012.

[15] M. Braack, P. B. Mucha, Directional do-nothing condition for the navier-stokes equations, Journal of Computational Mathematics (2014) 507–521.

A new one-dimensional planetary boundary layer (PBL) scheme from large-eddy simulations: VKIPBL-01

Cem Berk Senel

Environmental and Applied Fluid Dynamics Department, von Karman Institute for Fluid Dynamics, Belgium, cem.berk.senel@vki.ac.be

Supervisor: Jeroen van Beeck

Professor, Environmental and Applied Fluid Dynamics Department, von Karman Institute for Fluid Dynamics, Belgium, vanbeeck@vki.ac.be

University Supervisor: Alessandro Parente

Professor, Aero-Thermo-Mechanics Department, Université Libre de Bruxelles, Belgium, Alessandro.Parente@ulb.ac.be

Abstract

A new one-dimensional planetary boundary layer (PBL) scheme, VKIPBL-01, is developed from high-resolution large eddy simulations (LES) for different atmospheric stability levels. LES results are compared with the wind speed measurements from the meteorological mast at the Test Centre for Large Wind Turbines at Høvsøre, Denmark. A generic formulation for the determination of mixing length scale is proposed and incorporated into the initial version, VKIPBL-00, developed by Temel et al. (2018) [1]. The new PBL scheme is implemented into the Weather Research and Forecasting (WRF) model to perform mesoscale simulations for the Høvsøre test site as an idealized case as well as for a real-data case at the eXperimental Planetary boundary layer Instrumentation Assessment (XPIA) campaign. Results reveal that a significant improvement has been achieved to represent the boundary layer characteristics by the proposed VKIPBL-01 scheme. This research has been published in Journal of Advances in Earth Modeling Systems (Senel et al., 2019, https://doi.org/10.1029/2018MS001580).

Keywords: Planetary boundary layer scheme, large-eddy simulation, atmospheric turbulence

1. Introduction

The planetary boundary layer (PBL) is the lowest part of the troposphere, involving complex turbulent structures induced by the solar radiation. Except for the cases, where the spatial resolution is sufficiently high to use large-eddy simulation (LES) techniques, turbulent fluxes are parameterized using planetary boundary layer (PBL) schemes, which are based on the eddy diffusivity concept. This approach basically assumes a relation between turbulent fluxes and mean velocity gradients where this proportionality is called the eddy diffusivity. To calculate the vertical turbulent fluxes, eddy diffusivity is either determined by algebraic closures, e.g. Yonsei University (YSU) scheme [2], or by turbulence kinetic energy (TKE) closures, which solve a transport equation for the TKE and empirically models its sink term, the dissipation rate [3]. Several different TKE closures were proposed in the literature, e.g. Bougeault-Lacarrere (BouLac) scheme [4], Mellor-Yamada-Janjic (MYJ) scheme [3], Mellor-Yamada-Nakanishi-Niino (MYNN) scheme [5]. The main difference depends mainly on the formulation of the length scale and closure coefficients for the calculation of the eddy momentum/heat diffusuvities. These TKE closures are used as the one-dimensional turbulence closures by neglecting streamwise and spanwise turbulent fluxes as well as all the horizontal derivatives. Although these schemes are suitable for mesoscale simulations, however, in case of high horizontal grid resolutions, the microscale atmospheric turbulence must be regarded as a three dimensional process [6]. For such circumstances, large-eddy simulation (LES) technique has been widely used, e.g. [7; 8; 9]. Furthermore, LES studies can be used to improve the existing TKE closures like the derivation of the MYNN scheme [10] and the improved Tim-Marht (TM) scheme [11]. Another approach is to implement

3D PBL schemes to model flows over complex terrain by using high-resolution models [9]. In either case, attention should be paid to PBL schemes with varying stability parameters for high spatial resolution models, where the span- and streamwise turbulence can not be neglected. This can lead to realizability issues meaning that the predicted turbulence kinetic energy would become negative [12].

In numerical weather prediction (NWP) models, turbulent fluxes are parameterized using a turbulent transport coefficients, i.e. eddy diffusivity. This is calculated as a function of a velocity scale, a length scale and a model coefficient, the eddy diffusivity coefficient. It has been shown that in case of using high eddy diffusivity coefficients for the flows with high velocity gradients, such as flow over complex terrain, the turbulence model can become unrealizable. In terms of the threshold value for the eddy diffusivity coefficient, various suggestions have been proposed for industrial flows [13]. However, a similar investigation, regarding the realizability issues in modeling the horizontal turbulent fluxes, is missing. Therefore, a turbulence model with constant closure coefficients would stand as a more promising starting point to develop future 3D PBL schemes. Based on this idea, [1] have revised the BouLac scheme conducting a theoretical investigation under realizability constraints. A new formulation was in turn proposed for the turbulent Prandtl number. However, for this latest version of the revised BouLac scheme (VKIPBL-00), the classical Blackadar length scale [14] is used.

In the present study, a new PBL scheme (hereafter VKIPBL-01) is presented using a turbulence mixing length scale parameterization derived from a set of LES results. It incorporates the turbulent Prandtl number definition proposed by Temel et al. (2018) [1]. LES simulations are compared with the wind mast measurements in Høvsøre, Denmark [15]. Then, the new PBL scheme is implemented into the Weather Research and Forecasting (WRF) model. The performance of the proposed model is investigated by performing idealized mesoscale simulations. The results obtained by the new PBL scheme are compared with the reference Høvsøre LES and two state-of-the-art PBL schemes: BouLac and MYNN. This can be regarded as the baseline of the proposed model for various aspects. Finally, the new PBL scheme is applied to the XPIA campaign in Boulder, Colorado [16] to perform real-case mesoscale simulations. Simulation results are investigated comparing the time evolution of the wind speed, temperature, PBL height, friction velocity, mixing length scale, wind direction, turbulence kinetic energy and its dissipation rate.

2. Description of the new 1D planetary boundary layer scheme

The new planetary boundary scheme is a non-local turbulence kinetic energy (TKE) closure. So that the one-dimensional transport equation for the TKE can be defined as,

$$\frac{\partial k}{\partial t} = \frac{\partial}{\partial z}\left[lk^{0.5}S_k\frac{\partial k}{\partial z}\right] + P_s + P_b - \epsilon \tag{1}$$

The source and sink terms on the right hand side of Eq. 1 stand for the shear production of turbulence, P_s, the buoyancy production/destruction of turbulence, P_b, and the dissipation rate of turbulence, ϵ, which can be calculated as follows,

$$P_s = K_m\left[\left(\frac{\partial u}{\partial z}\right)^2 + \left(\frac{\partial v}{\partial z}\right)^2\right] \tag{2}$$

$$P_b = -\beta g K_h\frac{\partial \theta_v}{\partial z} \tag{3}$$

$$\epsilon = \frac{k^{1.5}}{B_1 l} \tag{4}$$

In Eq. 1, l is the turbulent mixing length scale and S_k is the TKE diffusion coefficient. K_m is the eddy diffusivity of momentum in Eq. 2. K_h is the eddy diffusivity of heat, $\beta = 1/300K$ is the thermal expansion coefficient and g is the gravitational acceleration in Eq. 3. B_1 is the dissipation coefficient in Eq. 4. The K_m and K_h are calculated as follows,

$$K_m = S_m k^{0.5} l \tag{5}$$

$$K_h = S_h k^{0.5} l \tag{6}$$

where S_m and S_h denote the stability functions of momentum and heat.

One of the main differences among mesoscale PBL schemes is based on the turbulence mixing length scale formulation. This allows in turn to compute the eddy diffusivities and dissipation rate as can be seen in Eq. 4, 5 and 6. To find out a generic expression for the mixing length scale, the turbulence kinetic energy and dissipation rate are needed according to Eq. 4, i.e. $l = k^{1.5}/(\epsilon\, B_1)$. To do this, k and ϵ fields are computed from high-resolution large-eddy simulations by solving the one-dimensional TKE budget equation (see the details of TKE budget analysis in Senel et al. [17]), i.e.

$$0 = \underbrace{-\langle\widetilde{w}\rangle\frac{\mathrm{d}\langle k\rangle}{\mathrm{d}z}}_{\mathcal{A}=0} \underbrace{-\frac{\mathrm{d}}{\mathrm{d}z}\langle kw'\rangle}_{T^T} \underbrace{-\frac{1}{\rho_0}\frac{\mathrm{d}}{\mathrm{d}z}\langle p'w'\rangle}_{T^P} \underbrace{-\frac{\mathrm{d}}{\mathrm{d}z}\left\langle\tau^{D'}_{i3}\widetilde{u}'_i\right\rangle}_{T^{sgs}} \underbrace{-\langle u'w'\rangle\frac{\mathrm{d}\langle\widetilde{u}\rangle}{\mathrm{d}z} - \langle v'w'\rangle\frac{\mathrm{d}\langle\widetilde{v}\rangle}{\mathrm{d}z}}_{P^S} + \underbrace{\frac{g}{\theta_0}\langle w'\theta'\rangle}_{P^B} + \underbrace{\left\langle\tau^{D'}_{ij}S'_{ij}\right\rangle}_{\epsilon} \tag{7}$$

where $\mathcal{A}$ denotes the advection, T^T, T^P, T^{sgs} denote the turbulence, pressure and SGS transport, respectively. P^S and P^B are the shear and buoyancy productions and ϵ stands for the dissipation. Note that, the brackets, i.e. $\langle\cdot\rangle$, denote the horizontal-averaging operator. The advection term here is negligible in Eq. 7 since the horizontally-averaged $\langle\widetilde{w}\rangle = 0$ as a consequence of the continuity equation. Since our aim is to get the dissipation field for the determination of the mixing length scale, we do not follow the modeled expressions which are based on Kolmogorov hypothesis and common in the literature, e.g. [18; 19; 20]. Instead, we determine directly as the double inner product of two second-rank tensors which are the fluctuating components of the deviatoric SGS stress tensor and the strain-rate tensor, $\epsilon = \left\langle \tau_{ij}^{D'} S'_{ij} \right\rangle$. Accordingly, both k and ϵ are determined to be utilized in the following step, i.e. modeling of mixing length scale. This starts with the classical [14] formulation that is basically the harmonic average of two length scales,

$$\frac{1}{l_{Blackadar}} = \frac{1}{l_0} + \frac{1}{l_s} \tag{8}$$

where l_0 and l_s denote the asymptotic and surface layer length scales. By this way, Blackadar's mixing length scale switches from the surface layer throughout the well-mixed boundary layer limit. This approach constitutes the basis of different PBL schemes as well, for instance, the UW PBL scheme of [21], the scale-adaptive TKE closure of [22] and MYJ scheme [3]. For the latter, [3] set the asymptotic component of Blackadar's mixing length scale, l_0, to

$$l_0 = \alpha \frac{\int_{p_t}^{p_s} q\, z\, dp}{\int_{p_t}^{p_s} q\, dp} \tag{9}$$

where p_s and p_t are the pressures at the bottom and top of the model atmosphere, α is an empirical constant to be 0.30 and $q = \sqrt{k}$ is the square root of TKE. Later on, this length scale (Eq. 9) is used in the MYNN scheme by setting $\alpha = 0.23$ where they named the l_0 "the length scale dependent on the PBL depth".

According to proposed model, above the surface layer, asymptotic component of Blackadar's mixing length scale is expanded to two components, i.e. $l_0 = (1/l_k + 1/l_\lambda)^{-1}$. These are TKE length scale, l_k, related to turbulence kinetic energy of the PBL and asymptotic length scale, which is used to fit the mixing length scale to our reference LES data along the mixed layer. Furthermore, the mixing length scale becomes constant above the surface layer and it asymptotically converges to a constant value since the grid resolution

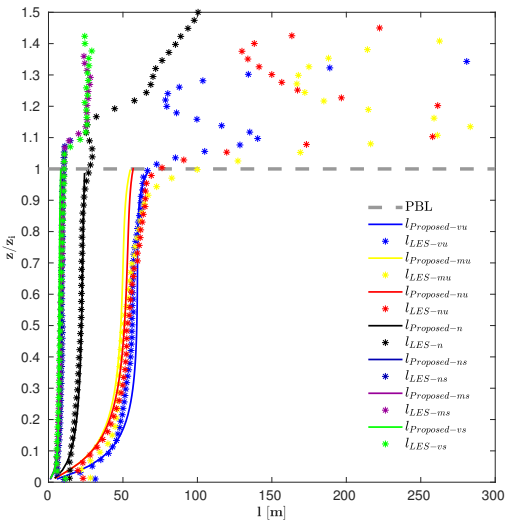

Figure 1: Vertical profiles of the proposed mixing length scale compared to LES results. Solid lines refer to the proposed model and circular markers refer to LES results. The gray dashed lines refer to the PBL height.

of mesoscale simulations falls in the mesoscale limit, $\Delta_{meso} > L$, where L denotes the size of energy containing eddies [23]. This is consistent with the observations of [24] where they find the dissipation length scale converges to a unique value at the mesoscale limit. Considering the study of [24], the mixing length scale becomes constant above the surface layer, i.e. $\partial l/\partial z \rightarrow 0 \quad if\ z > z_s$. [24] also showed that the vertical profiles of dissipation length scale, $l_\epsilon = B_1 l$, reach to a nearly asymptotic shape if the horizontal grid resolution approaches to the mesoscale limit. In other words, as the grid resolution increases from LES limit towards the mesoscale limit, i.e.

$$\lim_{\Delta \rightarrow \Delta_{meso}} \langle B_1\, l \rangle = \langle B_1\, l \rangle (\infty) \tag{10}$$

where the infinity symbol denotes this asymptote. Note that, the angular bracket denotes the horizontal-averaging operator applied in the horizontal directions, i.e. streamwise (x) and spanwise (y), similar to [25]. In this context, the total contribution of our l_k and l_λ tends to be constant in the mixed layer as the altitude increases similar to [24]. In addition to this, the sum of l_k and l_λ reach to an asymptotic value independent from the grid resolution. As discussed above, this is because the length scale profiles coincide at the mesoscale limit in accordance with the self-similarity. Since the l_λ brings the l_k towards the

mixed-layer asymptote at the mesoscale limit, we call the l_λ "asymptotic" length scale.

Another essential point is to adjust the value of the B_1 coefficient. Since B_1 l is equal to $k^{1.5}/\epsilon$ and considering the value of B_1 l converges to a constant value (from the Eq. 10). The problem itself becomes independent from the selection of B_1 at the mesoscale limit, Δ_{meso}. From this aspect, we simply set B_1 to 24 following the MYNN model. Consequently, we define the length scale based on MYNN's harmonic mean of three length scales, i.e.

$$\frac{1}{l} = \frac{1}{l_k} + \frac{1}{l_\lambda} + \frac{1}{l_s} \tag{11}$$

$$l_k = \kappa \frac{\int_0^\infty k\, z\, dz}{\int_0^\infty k\, dz} \tag{12}$$

$$l_\lambda = \lambda e^{\zeta_1} z_i \begin{cases} \lambda = 0.150, & -1000m \le L_O < 0 \quad (unstable) \\ \lambda = 0.100, & |L_O| > 1000m \quad (neutral) \\ \lambda = 0.032, & 0 < L_O \le 1000m \quad (stable) \end{cases} \tag{13}$$

$$l_s = \begin{cases} \kappa z\,(1 - 80\,\zeta)^{1/4}, & -1000m \le L_O < 0 \quad (unstable) \\ 2.5\kappa z, & |L_O| > 1000m \quad (neutral) \\ \kappa z\left(1 + \kappa^{-1}\,\zeta\right), & 0 < L_O \le 1000m \quad (stable) \end{cases} \tag{14}$$

where l_k is the TKE length scale, l_λ is the asymptotic length scale and l_s is the surface layer length scale. If we further introduce this parameterization, the functional form of the proposed TKE length scale in Eq. 12 is based on [26],

$$l_k = \alpha \frac{\int_0^\infty q\, z\, dz}{\int_0^\infty q\, dz} \tag{15}$$

as the ratio of the first to the zeroth moment of the TKE velocity scale, $q = \sqrt{2k}$. This definition can be interpreted as the TKE tendency of the length scale related to changes in the atmospheric stability and the altitude. Accordingly, the turbulence kinetic energy tends to decay with the stability and the altitude as can be seen (cbs:cite). Both k and q are able to represent this description, however, we prefer the TKE itself for its direct implementation rather than its velocity scale. Note that, the closure constant, α, has been selected to be 0.10 in [26], 0.30 in MYJ scheme [3] and 0.23 in MYNN scheme [5]. In this study, we choose $\alpha = \kappa$ where $\kappa = 0.40$ denotes the von Karman constant. The reason can be explained by the physical representation of l_k, such that it corresponds to the center of TKE analogous to the center of gravity of a particular object. If α is 1, this gives the absolute center of TKE where $z \to \infty$. To make the l_k more dominant along the middle boundary layer, the center of TKE can be moved to $z = 0.40 z_i$. This location can be determined as the center of $z = 0.80 z_i$ where the middle boundary layer is still effective, before the top boundary layer starts.

According to our asymptotic length scale parameterization, it enables the mixing length scale to fit our reference LES results above the surface layer, i.e.

$$l_0 = (1/l_k + 1/l_\lambda)^{-1} \to l_{LES} \quad if\ z > z_s \tag{16}$$

We introduce this parameterization by postulating that the asymptotic length scale be the function of the PBL height, z_i, and the non-dimensional stability parameter, i.e. $\zeta_1 = z_1/L_O$, at the first wall adjacent cell center, z_1, where L_O is the Obukhov length scale,

$$L_O = \frac{-u_*^3}{\kappa \frac{g}{\theta_0} \overline{w'\theta'}_s} \tag{17}$$

where u_* is the surface friction velocity, g/θ_0 is the buoyancy parameter and $\overline{w'\theta'}_s$ is the kinematic heat flux at the surface. Then,

$$l_\lambda = f(z_i, \zeta_1) \tag{18}$$

similar to the University of Washington (UW) scheme [21], which is

$$l_{\lambda,UW} = z_i \eta \tag{19}$$

where they adjust $\eta = 0.085\left(2 - e^{[min(Ri^{CL},0)]}\right)$ by using LES results. Note that, Ri^{CL} is the bulk Richardson number for the convective turbulent layer. Recalling our postulate given in Eq. 18, a curve fitting is made by the linear regression considering the quasi-linear behaviour of mixing length scale above the surface layer. Supposing that the PBL height is proportional to the asymptotic length scale with the power of 1, i.e.

$$l_\lambda \propto z_i^{p=1} \tag{20}$$

This enables l_λ to satisfy the unit of meter. Then, $l_\lambda \propto z_i$ can be linked to the LES results through the atmospheric stability in different functional forms (logarithmic, exponential, hyperbolic tangent, etc.), i.e. $l_\lambda = \mathcal{F}(\lambda, \zeta_1) z_i$. Note that, here λ is the fitting parameter. Following the UW scheme [21], the exponential function provided the best agreement for our l_λ model in our regression analysis. Beside this, since

the exponential function tended to be more aware of the stability, we choose the exponential form as,

$$l_\lambda = e^{(ln\lambda+\zeta_1)} z_i = \lambda e^{\zeta_1} z_i \tag{21}$$

Then, the asymptotic length scale is defined as a piecewise function in three different stability regimes based on the classification of [15], in Eq. 13. By this way, the model itself tends to be adaptive to the atmospheric stability.

If the functional form of the surface layer length scale is addressed, it can be assumed to be proportional with the altitude based on [27], [28] and [15], $l_{s,neutral} = 2.5\kappa z$ where $\kappa = 0.4$ is the von Karman constant. This selected value matches well with our LES results for the near-neutral condition (LES-n case). On the other hand, for non-neutral conditions, we begin with the functional form of l_s from MYNN scheme as $l_{s,unstable} = \kappa z(1 - a_1\zeta)^{p_1}$ and $l_{s,stable} = (1 + a_2\zeta)^{p_2}$. Then, by means of curve fitting to the predicted LES results, we end up with the final functional form for the non-neutral conditions given in Eq. 14.

The results of the proposed length scale model are depicted in Fig. 1 in comparison to the Høvsøre LES results (see the details of LES setup and results in Senel et al. [17]). The proposed length scale matches well with these LES results until $0.9z_i$ for all the stability conditions. However, above which, a deviation initiates particularly for the convective PBL. This is because our model does not presently account for the entrainment and inversion effects that exist between the upper PBL and free atmosphere. Therefore, for the altitudes higher than $0.9z_i$, the mixing length scale is determined based on the MYJ scheme [3], as follows

$$l = 0.23\Delta z \tag{22}$$

where Δz corresponds to the vertical grid spacing.

As mentioned earlier, a new length scale formulation is proposed to build a new PBL scheme which later can be used as a baseline for further extension, for instance towards a 3D PBL scheme. After applying the closure assumption for dissipation rate (Eq. 4) into Eq. 5, then the turbulent viscosity can be redefined independent from the mixing length scale,

$$K_m = \frac{S_m}{B_1}\frac{k^2}{\epsilon} \tag{23}$$

where S_m/B_1 is the equivalent closure coefficient of C_μ appearing in computational fluid dynamics (CFD) simulations of turbulent flows by using three-dimensional turbulence closures. Based on the realizability constraints [12], C_μ is set to 0.09 [29] for industrial flow applications and to 0.033 for wind engineering applications [30]. In this present study, B_1 and S_m are taken to be 24.0 and 0.144, which is equivalent to a smaller value of $C_\mu = 0.006$, ensuring the realizability of the turbulence closure for further extensions as a 3D PBL scheme. Finally, the eddy heat diffusivity coefficient is computed by utilizing the formulation of turbulent Prandtl number, i.e. $Pr_t = S_m/S_h$, proposed by [1] as,

$$Pr_t = \begin{cases} 1.25 & Ri < 0.23 \\ \frac{Ri}{1-\left(\frac{\phi_e}{\phi_m}\right)_{|\zeta|=1.0}} & Ri > 0.23 \end{cases} \tag{24}$$

where ϕ_m is the stability function of Monin-Obukhov theory for velocity gradient and ϕ_e is the stability function for potential temperature gradient [27]. Ri stands for the gradient Richardson number,

$$Ri = \frac{g\beta\frac{\partial\theta_v}{\partial z}}{\left(\frac{\partial u}{\partial z}\right)^2} \tag{25}$$

Moreover, similar to the MYJ scheme, the minimum value for the turbulence kinetic energy is set to $0.01\ m^2/s^2$. For determination of the boundary layer height, the way of BouLac scheme, which is similar to the 1.5-theta-increase method [31], is applied. In the original BouLac scheme [4], the boundary layer height is determined at the first height where the potential temperature is increased by 0.5K for all stability levels. We keep this value for the convective atmosphere, however it is set to 1.0K to avoid the possible instantaneous temperature rise at the near surface for non-convective conditions. As noted before, the present PBL scheme is a non-local scheme, thus the non-local term is computed in the following equation suggested by [32] (see Section 4.2, Eq. 40).

$$\overline{w'\theta'} = -K_h\left(\frac{\partial\theta}{\partial z} - \gamma_{cg}\right) \tag{26}$$

3. Idealized PBL Simulations

In this section, results of idealized PBL simulations in comparison to Høvsøre LES results are presented. The idealized PBL simulations are performed by using an open-source numerical weather prediction code, i.e. the Weather Research and Forecasting (WRF) model version 3.5.1 [33]. The model forcing is conducted by imposing different surface heat

Table 1: Mean absolute errors of three PBL schemes compared to the Høvsøre LES results in terms of horizontally-averaged potential temperature and wind speed where $z \leq z_{i,LES}$. Bold values denote the best performance as the lowest MAE among the three PBL schemes.

$MAE_{\langle\theta\rangle}$ $[K]$	*vu*	*mu*	*nu*	*n*	*ns*	*ms*	*vs*
VKIPBL-01	0.076	**0.055**	0.077	**0.142**	**0.320**	0.318	0.362
MYNN	0.117	0.089	0.105	0.190	0.377	**0.294**	**0.309**
BouLac	**0.034**	0.134	**0.063**	0.595	0.689	0.569	0.586
$MAE_{\langle U\rangle}$ $[m/s]$	*vu*	*mu*	*nu*	*n*	*ns*	*ms*	*vs*
VKIPBL-01	**0.261**	**0.462**	**0.437**	**0.770**	1.750	**1.447**	1.730
MYNN	0.445	0.754	0.727	1.695	**1.212**	1.695	**1.223**
BouLac	0.471	0.849	0.932	1.626	2.716	2.417	2.421

fluxes presented in Senel et al. (2019) [17]. However, the momentum flux is calculated by using a surface layer scheme, MM5 similarity scheme [34]. In this section, we make use of LES results to verify our proposed model. The concept of using high-fidelity simulations, such as LES, as a verification tool for PBL parameterization schemes, has been widely applied in the literature when a novel turbulence closure is initially designed [21; 5; 35]. Even if the LES and mesoscale models used for this comparison are different, a recent LES intercomparison study by [36] has shown that both dynamical cores (SOWFA and WRF) provide comparable results in canonical PBL simulations. As described in Section 2, it is possible to state that our proposed PBL scheme has some similarities both with MYNN and BouLac schemes. The mixing length scale parameterization is based on three components as it is in case of MYNN scheme and the closure coefficient to determine turbulent viscosity is constant similar to the BouLac scheme. Therefore, idealized PBL simulations are also performed by using MYNN [5] and BouLac schemes [4], enabling us to evaluate the performance of our model against these two state-of-the-art PBL schemes. As far as the computational details are concerned, the horizontal domain size is set to $L_{x,y} = 15km\ x\ 15km$ for unstable PBL, $L_{x,y} = 9km\ x\ 9km$ for neutral PBL, $L_{x,y} = 4km\ x\ 4km$ for stable PBL. The horizontal grid resolution is taken to be $1km$ in order to avoid passing the gray-zone. It is worth noting that the horizontal length of the mesoscale domain does not affect the results of idealized PBL simulations due to the idealized conditions. The vertical height is set to $2km$ where 80 grid points are located along this direction, by clustering near the ground. Time integration is conducted setting time step to $\Delta t = 5s$. The total simulation time is same as our LES computations, i.e. $\mathcal{T} = 23400s$ for unstable condition and $\mathcal{T} = 24000s$ for neutral and stable conditions. Note that, periodic boundary conditions are applied to lateral boundaries and the Coriolis force is accounted consistently with our Høvsøre LES database (see Senel et al., 2019 [17]).

As noted before, the idealized PBL simulations are performed for the same stability conditions presented in the Høvsøre LES database. Compared to the LES results, vertical profiles of horizontally-averaged potential temperature predicted by VKIPBL-01, MYNN and BouLac schemes, are presented in Fig. 2. As presented in Fig. 2, within the mixed layer of unstable PBLs, VKIPBL-01 and BouLac provide better predictions than the MYNN scheme. However, potential temperature gradient is overestimated within the surface layer by VKIPBL-01 scheme compared to both schemes. Considering the mixed layer characteristics, VKIPBL-01 presents the best agreement in moderately unstable PBL where BouLac significantly overestimates the potential temperature. However, BouLac is slightly better than VKIPBL-01 for very and near-neutral unstable conditions. MYNN scheme underestimates the potential temperature in the mixed layer where it underestimates the potential temperature. In Table 1, this behaviour is quantified with a performance metric, i.e. mean absolute error (MAE), against to the Høvsøre LES results. VKIPBL-01 produces the lowest error of potential temperature for moderately-unstable PBL, while BouLac is the best in case of very and near-unstable PBLs. For the stable PBL, although VKIPBL-01 and MYNN schemes perform very similarly, VKIPBL-01 stands slightly better than MYNN below the PBL height except for near the ground. While VKIPBL-01 improves near-neutral stable PBL with the lowest MAE, MYNN is slightly better than VKIPBL-01 for moderately stable and very stable PBLs. For the BouLac scheme, it significantly overestimates the potential temperature all along the stable boundary layer. Note that, none of the PBL schemes is able to predict correctly the capping inversion, showing the intrin-

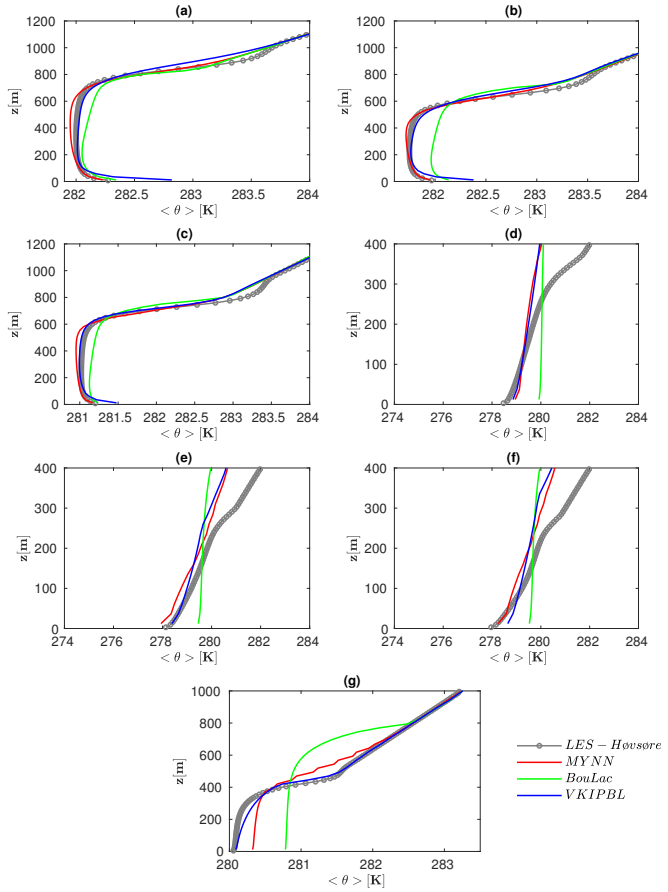

Figure 2: Horizontally-averaged potential temperature predictions. Gray line with circle markers denotes Høvsøre LES results. Red, blue and green lines show the MYNN, BouLac and VKIPBL-01 schemes. Panels refer to very unstable (a), moderately unstable (b), near-neutral unstable (c) near-neutral stable (d), moderately stable (e), very stable (f) and near-neutral (g) conditions from left to right.

sic limitations of these PBL schemes for stably stratified boundary layer. Regarding the near-neutral condition, VKIPBL-01 performs superior than other two PBL schemes considering its mixing layer and PBL top behaviour. Its MAE is equal to 0.142 which is much lower than that of MYNN and BouLac schemes. The latter fails predicting correctly the potential temperature both below and above the PBL for the neutral conditions (Fig. 2-g). Along with the potential temperature profiles, predicted wind speed profiles for three PBL schemes in comparison to LES results are presented in [17]. For all the stability levels, BouLac scheme fails to represent a good agreement with LES results. However, although VKIPBL-01 scheme overestimates the potential temperature gradient near the ground for convective cases, it provides better estimation for the wind speed compared to the MYNN scheme. VKIPBL-01 performs better also through the convective mixed-layer. Quantitatively, VKIPBL-01 gives the lowest mean absolute errors for all the stability levels except for near-neutral and very stable PBLs where MYNN improves the wind speed slightly better than VKIPBL-01.

4. Application to the XPIA field campaign

In the previous section, the proposed model is verified with the LES results to some degree that despite its simpler closure coefficient formulation, the new PBL scheme is able to provide similar predictions to

MYNN scheme, which solves a set of algebraic equations to determine the closure coefficients. However, the validity of the newly proposed PBL scheme for a real case study should also be tested based on a full-scale field campaign. In this section, we present the mesoscale simulations for the eXperimental Planetary boundary layer Instrumentation Assessment (XPIA) campaign (40.05°N, 105°W) conducted at the Boulder Atmospheric Observatory (BAO) from March 2nd to May 31st in 2015 [16]. The BAO tower contains a total of 12 three-dimensional sonic anemometers (Campbell CSAT3) mounted on northwesterly (NW, 334°) and southeasterly (SE, 154°) pointing booms every 50 m starting from 50 m above ground level up to 300 m. This experimental campaign involves high-frequency 20-Hz measurements of wind, temperature and relative humidity. Recently, [37] derived the turbulence dissipation rate, ϵ, within the planetary boundary layer using these sonic anemometer measurements. These results are available at $z = 50$ m and they are classified into daytime/convective and nighttime/stable conditions.

These measurements will help us to validate mesoscale simulations, performed by the new PBL scheme and again compare with MYNN and BouLac schemes. The mesoscale domain depicted in Fig. 3 consists of two one-way nested domains, the largest domain has a horizontal resolution of 27 km with a domain size of 3375 x 2700 km^2. The smallest domain, on the other hand, has a horizontal resolution of 9 km with a domain size of 1332 x 1197 km^2. For the vertical discretization, 53 grid points are used with the finest resolution of 2.5 m close to the ground, while the upper boundary is located at 15 km. Boundary and initial conditions are extracted from the National Centre of Environmental Prediction (NCEP) North American Regional Reanalysis (NARR) datasets. For the PBL parameterization, BouLac, MYNN and VKIPBL-01 schemes are used. In addition to the PBL schemes, the other physical parameterizations utilized for the WRF set-up are the longwave and shortwave Rapid Radiative Transfer Model (RRTM) [38] for the radiation, the Thompson microphysics parameterization [39], MM5 Similarity Scheme [34] for the surface layer parameterization and the Community Land Model version 4 [40] for the land surface coupling.

Nested mesoscale simulations are performed during the 6th-9th of March in 2015 at the XPIA field campaign for 72 hours, but the first 24 hours is discarded considering the model spin-up so that the results are presented between the 7th-9th of March. In

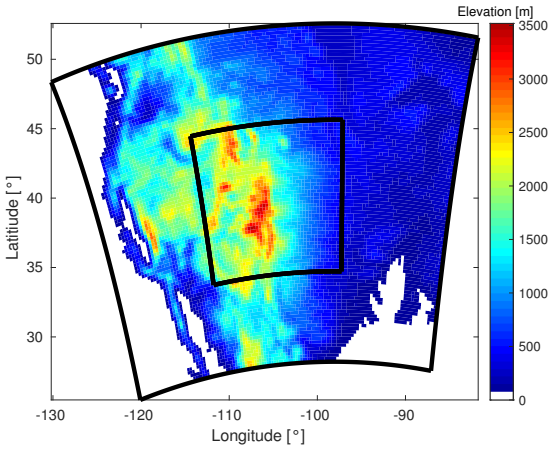

Figure 3: WRF domain for the mesoscale simulation with the terrain elevation [m] where it is located at the Boulder Atmospheric Observatory (BAO) in Colorado (40.05°N, 105°W). The outer black line encircles the outer zone with the resolution 27 km where the inner region demonstrates the inner zone with 9 km resolution.

Fig. 4, mesoscale simulations are compared against to sonic anemometer measurements at $z = 50$ m. Fig. 4-a and Fig. 4-b present the time evolution of the turbulence kinetic energy and dissipation rate respectively. Compared to the MYNN and BouLac schemes, VKIPBL-01 matches well with the XPIA measurements presenting the best agreement where it is able to reproduce the diurnal evolution of the boundary layer. Both MYNN and BouLac significantly underestimate the TKE and dissipation rate profiles during the first ($t = 7.0 - 7.5$ day) and second ($t = 8.0 - 8.5$ day) nighttime. Such that, VKIPBL-01 and XPIA profiles are $\sim O(10^{-2})$ for TKE and $\sim O(10^{-4})$ for the dissipation rate. However, TKE for MYNN and BouLac are $\sim O(10^{-3})$ and $\sim O(10^{-4})$ where dissipation rate for MYNN and BouLac are $\sim O(10^{-5})$ and $\sim O(10^{-7})$, respectively. Although MYNN and BouLac schemes predict the TKE better during the daytime, VKIPBL-01 is much better for the dissipation rate in case of convective conditions. In Table 2, in order to evaluate the performance of simulated PBL schemes, mean absolute errors (MAE) for TKE, its dissipation rate, temperature and wind speed are presented against to XPIA measurements from [37]. VKIPBL-01 reproduces the dissipation rate better by reducing MAE compared to MYNN and BouLac schemes. However for the MAE of k, MYNN scheme produces slightly lower error than both PBL schemes. On the other hand, Fig. 4-c and Fig. 4-d show the time evolution of wind speed and temperature at $z = 50$ m

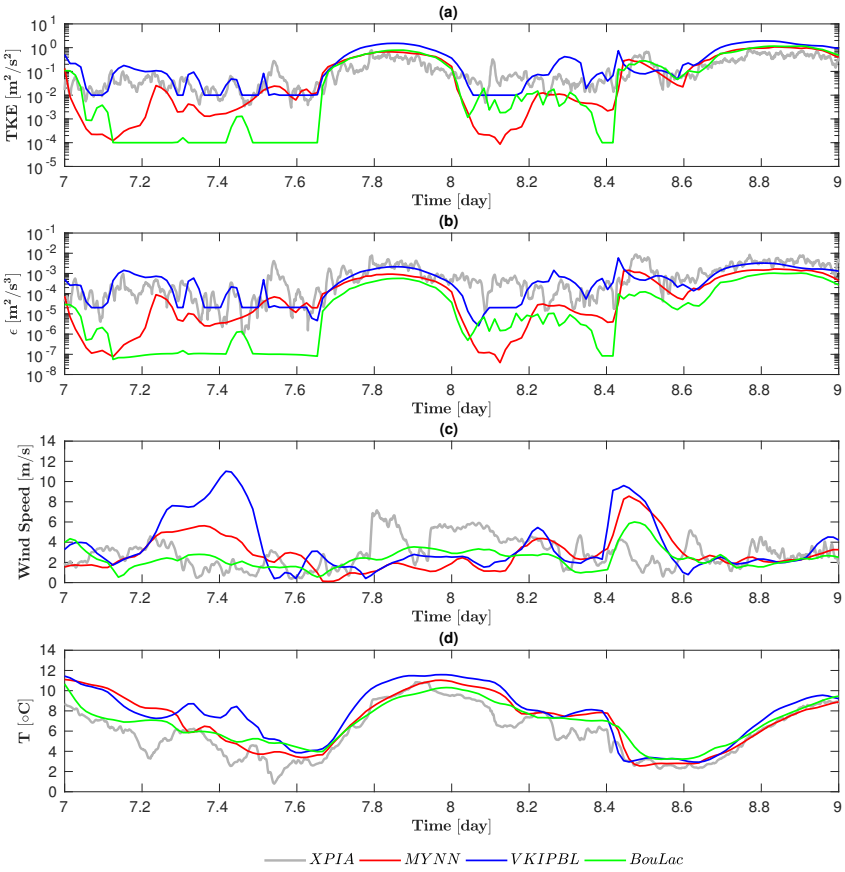

Figure 4: Time evolution of the turbulence kinetic energy, k, (top-left), dissipation rate, ϵ, (top-right), wind speed (bottom-left) and temperature (bottom-right) profiles at $z = 50\ m$ obtained from the VKIPBL-01 (blue line), MYNN (red line), BouLac (green line) schemes. Gray solid line denotes the sonic anemometer measurements during March 7th-9th in 2015 at the XPIA field campaign from [37].

for three PBL schemes. Even though the wind speed profiles are able to capture the general behaviour of the diurnal pattern at the XPIA campaign, all the PBL schemes, particularly VKIPBL-01, overpredict the wind speed during nighttime conditions. While they underestimate it during the daytime condition (i.e. $t = 7.7-8.2$ day). But in general, BouLac scheme predicts the wind speed much better. In Fig. 4-d, the time evolution of the temperature acquired by three PBL schemes are depicted. It can be stated that all the performed PBL schemes seem in a good agreement except for the first night untill the first morning transition, i.e. $t = 7.0 - 7.5$ day. Eventually, if the mean absolute errors are concerned, BouLac scheme improves both wind speed and temperature predictions, resulting in the lowest errors as $MAE_U = 1.14\ m/s$ and $MAE_T = 1.04\ ^\circ C$ respectively.

To evaluate the performance of proposed VKIPBL scheme, a further investigation is conducted to compare the time evolution of wind direction and vertical speed against to the sonic anemometer measurements at $z = 50$ m. Besides these, an inter-comparison among three PBL schemes are performed in terms of PBL characteristics, i.e. friction velocity, near-ground temperature, PBL height and mixing length scale. For the details, the reader is referred to Senel et al. [17].

5. Conclusion

In the present study, we presented a new PBL scheme, VKI01. Our proposed scheme incorporates with a new formulation for the mixing length scale, which has been applied to idealized and real test cases,

Table 2: RMS logarithmic errors (RMSLE) of TKE, its dissipation rate and mean absolute errors (MAE) of temperature and wind speed obtained by three PBL schemes in comparison to XPIA sonic anemometer measurements at $z = 50m$ from [37]. Bold values denote the best performance as the lowest error among the three PBL schemes.

PBL scheme	$RMSLE_k$ $[m^2/s^2]$	$RMSLE_\epsilon$ $[m^2/s^3]$	MAE_T $[^\circ C]$	MAE_U $[m/s]$
VKIPBL-01	$\mathbf{0.5\ 10^{-1}}$	$\mathbf{0.6\ 10^{-1}}$	1.83	2.24
MYNN	$1.3\ 10^{-1}$	$1.1\ 10^{-1}$	1.20	1.90
BouLac	$1.4\ 10^{-1}$	$1.7\ 10^{-1}$	**1.04**	**1.14**

and benchmarked against two state-of-the-art PBL schemes (MYNN and BouLac PBL schemes).

Considering both idealized and real-case tests, the developed PBL scheme gives promising predictions despite some aforementioned exceptions. Even though, it is possible to state that the objective has not been to propose an ultimately improved PBL scheme, but to develop a new formulation that can be considered as a baseline for further studies to develop a three-dimensional PBL scheme. Our proposed PBL scheme is based on the use of constant closure coefficients to determine eddy diffusivities, as opposed to the MYNN scheme. In this way, our proposed formulation stands as a baseline for a more straightforward extension to a three-dimensional PBL parameterization. However, it must be noted that the development of a three-dimensional parameterization will require further LES studies in order to quantify the contribution of horizontal turbulent fluxes in both horizontally-homogeneous PBLs as well as flow over complex terrain, including various stability conditions. Finally, these idealized PBL simulations are performed in order to verify the implementation of our new PBL scheme. And, as expected, our model performs mostly better than the other schemes thanks to the fact that its mixing length definition is derived from the Høvsøre LES dataset, which is also used to be compared. Therefore, the present results do not discard the applicability of the other PBL schemes. In order to perform a quantitative realistic inter-comparison study of various PBL schemes, long-term mesoscale simulations must be performed and compared with near-surface meteorological observations [41], which is beyond the scope of the present study.

Acknowledgments

This research has been published in Journal of Advances in Earth Modeling Systems (Senel et al., 2019 [17]) https://doi.org/10.1029/2018MS001580. The proposed model, VKIPBL-01, is the updated version of VKIPBL-00, firstly developed by Temel et al. (2018) [1]. I am grateful to Dr. Orkun Temel, Sara Porchetta and Dr. Domingo Muñoz-Esparza for their continuous support during the model-development. This research has been supported and funded by the von Karman Institute for Fluid Dynamics. A portion of this work was performed at the Royal Observatory of Belgium. NCEP Reanalysis data is provided by the NOAA/OAR/ESRL PSD, Boulder, Colorado, USA, from their website at http://www.esrl.noaa.gov/psd/. The proposed planetary boundary layer scheme is available by request from the author Cem Berk Senel, as well as the simulation results.

References

[1] O. Temel, L. Bricteux, J. van Beeck, Coupled wrf-openfoam study of wind flow over complex terrain, Journal of Wind Engineering and Industrial Aerodynamics 174 (2018) 152–169.

[2] S.-Y. Hong, Y. Noh, J. Dudhia, A new vertical diffusion package with an explicit treatment of entrainment processes, Monthly weather review 134 (9) (2006) 2318–2341.

[3] Z. I. Janjić, The step-mountain eta coordinate model: Further developments of the convection, viscous sublayer, and turbulence closure schemes, Monthly Weather Review 122 (5) (1994) 927–945.

[4] P. Bougeault, P. Lacarrere, Parameterization of orographyinduced turbulence in a mesobetascale model., Mon. Wea. Rev. 117 (1989) 1872–1890.

[5] M. Nakanishi, H. Niino, Development of an improved turbulence closure model for the atmospheric boundary layer, Journal of the Meteorological Society of Japan. Ser. II 87 (5) (2009) 895–912.

[6] D. Muñoz-Esparza, J. Sauer, R. Linn, B. Kosović, Limitations of one-dimensional mesoscale pbl parameterizations in reproducing mountain-wave flows, Journal of the Atmospheric Sciences 73 (7) (2016) 2603–2614.

[7] F. K. Chow, A. P. Weigel, R. L. Street, M. W. Rotach, M. Xue, High-resolution large-eddy simulations of flow in a steep alpine valley. part i: Methodology, verification, and sensitivity experiments, Journal of Applied Meteorology and Climatology 45 (1) (2006) 63–86.

[8] R. Rotunno, Y. Chen, W. Wang, C. Davis, J. Dudhia, G. Holland, Large-eddy simulation of an idealized tropical cyclone, Bulletin of the American Meteorological Society 90 (12) (2009) 1783–1788.

[9] B. Kosović, P. Jimenez, S. Haupt, A. Martilli, J. Olson, J. Bao, Recent developments and assessment of a three-dimensional pbl parameterization for improved wind forecasting over complex terrain, in: AGU Fall Meeting Abstracts, 2017.

[10] M. Nakanishi, Improvement of the mellor–yamada turbulence closure model based on large-eddy simulation data, Boundary-layer meteorology 99 (3) (2001) 349–378.
[11] Y. Noh, W. Cheon, S. Hong, S. Raasch, Improvement of the k-profile model for the planetary boundary layer based on large eddy simulation data, Boundary-layer meteorology 107 (2) (2003) 401–427.
[12] T.-H. Shih, W. W. Liou, A. Shabbir, Z. Yang, J. Zhu, A new k-ϵ eddy viscosity model for high reynolds number turbulent flows, Computers & Fluids 24 (3) (1995) 227–238.
[13] T.-H. Shih, J. Zhu, J. L. Lumley, A new reynolds stress algebraic equation model, Computer methods in applied mechanics and engineering 125 (1-4) (1995) 287–302.
[14] A. K. Blackadar, The vertical distribution of wind and turbulent exchange in a neutral atmosphere, Journal of Geophysical Research 67.8 (1962) 3095–3102.
[15] S. E. Gryning, E. Batchvarova, B. Brummer, H. Jorgensen, S. Larsen, On the extension of the wind profile over homogeneous terrain beyond the surface boundary layer, Boundary-Layer Meteorology 124 (2) (2007) 251–268.
[16] J. K. Lundquist, J. M. Wilczak, R. Ashton, L. Bianco, W. A. Brewer, A. Choukulkar, A. Clifton, M. Debnath, R. Delgado, K. Friedrich, et al., Assessing state-of-the-art capabilities for probing the atmospheric boundary layer: the xpia field campaign, Bulletin of the American Meteorological Society 98 (2) (2017) 289–314.
[17] C. B. Senel, O. Temel, S. Porchetta, D. Muñoz-Esparza, J. van Beeck, A new planetary boundary layer scheme based on les: Application to the xpia campaign, Journal of Advances in Modeling Earth Systems 11 (8) (2019) 2655–2679.
[18] P. P. Sullivan, E. G. Patton, The effect of mesh resolution on convective boundary layer statistics and structures generated by large-eddy simulation, Journal of the Atmospheric Sciences 68 (10) (2011) 2395–2415.
[19] S. Ramachandran, J. C. Wyngaard, Subfilter-scale modelling using transport equations: large-eddy simulation of the moderately convective atmospheric boundary layer, Boundary-layer meteorology 139 (1) (2011) 1–35.
[20] B. Kosović, J. A. Curry, A large eddy simulation study of a quasi-steady, stably stratified atmospheric boundary layer, Journal of the atmospheric sciences 57 (8) (2000) 1052–1068.
[21] C. S. Bretherton, S. Park, A new moist turbulence parameterization in the community atmosphere model, Journal of Climate 22 (12) (2009) 3422–3448.
[22] M. J. Kurowski, J. Teixeira, A scale-adaptive turbulent kinetic energy closure for the dry convective boundary layer, Journal of the Atmospheric Sciences 75 (2) (2018) 675–690.
[23] J. C. Wyngaard, Toward numerical modeling in the terra incognita, Journal of the atmospheric sciences 61 (14) (2004) 1816–1826.
[24] J. Ito, H. Niino, M. Nakanishi, C. H. Moeng, An extension of the mellor–yamada model to the terra incognita zone for dry convective mixed layers in the free convection regime, Boundary-layer meteorology 157 (1) (2015) 23–43.
[25] F. Catalano, C. H. Moeng, Large-eddy simulation of the daytime boundary layer in an idealized valley using the weather research and forecasting numerical model, Boundary-layer meteorology 137 (1) (2010) 49–75.
[26] G. L. Mellor, T. Yamada, A hierarchy of turbulence closure models for planetary boundary layers, Journal of the Atmospheric Sciences 31 (7) (1974) 1791–1806.
[27] J. A. Businger, J. C. Wyngaard, Y. Izumi, E. F. Bradley, Flux-profile relationships in the atmospheric surface layer, Journal of the atmospheric Sciences 28 (2) (1971) 181–189.
[28] A. J. Dyer, B. B. Hicks, Flux-gradient relationships in the constant flux layer, Quarterly Journal of the Royal Meteorological Society 96 (410) (1970) 715–721.
[29] W. Rodi, Turbulence models and their application in hydraulics, Routledge, 2017.
[30] C. Alinot, C. Masson, k-ϵ model for the atmospheric boundary layer under various thermal stratifications, Journal of Solar Energy Engineering 127 (4) (2005) 438–443.
[31] J. W. Nielsen-Gammon, C. L. Powell, M. J. Mahoney, W. M. Angevine, C. Senff, A. White, C. Berkowitz, C. Doran, K. Knupp, Multisensor estimation of mixing heights over a coastal city, Journal of Applied Meteorology and Climatology 47 (1) (2008) 27–43.
[32] G. Therry, P. Lacarrère, Improving the eddy kinetic energy model for planetary boundary layer description, Boundary-Layer Meteorology 25 (1) (1983) 63–88.
[33] W. C. Skamarock, J. B. Klemp, J. Dudhia, D. M. Barker, M. G. Duda, X. Y. Huang, W. Wang, J. G. Powers, A description of the advanced research wrf version 3, Tech. rep., NCAR - National Center for Atmospheric Research Technical Notes (NCAR/TN-475+STR) (2008).
[34] A. C. Beljaars, The parametrization of surface fluxes in large-scale models under free convection, Quarterly Journal of the Royal Meteorological Society 121 (522) (1995) 255–270.
[35] G. Efstathiou, R. J. Beare, Quantifying and improving sub-grid diffusion in the boundary-layer grey zone, Quarterly Journal of the Royal Meteorological Society 141 (693) (2015) 3006–3017.
[36] J. D. Mirocha, M. J. Churchfield, D. Muñoz-Esparza, R. K. Rai, Y. Feng, B. Kosović, S. E. Haupt, B. Brown, B. L. Ennis, C. Draxl, et al., Large-eddy simulation sensitivities to variations of configuration and forcing parameters in canonical boundary-layer flows for wind energy applications, Tech. rep., National Renewable Energy Lab.(NREL), Golden, CO (United States) (2017).
[37] D. Muñoz-Esparza, R. D. Sharman, J. K. Lundquist, Turbulence dissipation rate in the atmospheric boundary layer: Observations and wrf mesoscale modeling during the xpia field campaign, Monthly Weather Review 146 (1) (2018) 351–371.
[38] M. J. Iacono, J. S. Delamere, E. J. Mlawer, M. W. Shephard, S. A. Clough, W. D. Collins, Radiative forcing by long-lived greenhouse gases: Calculations with the aer radiative transfer models, Journal of Geophysical Research: Atmospheres 113 (D13).
[39] G. Thompson, P. R. Field, R. M. Rasmussen, W. D. Hall, Explicit forecasts of winter precipitation using an improved bulk microphysics scheme. part ii: Implementation of a new snow parameterization, Monthly Weather Review 136 (12) (2008) 5095–5115.
[40] D. M. Lawrence, K. W. Oleson, M. G. Flanner, P. E. Thornton, S. C. Swenson, P. J. Lawrence, X. Zeng, Z.-L. Yang, S. Levis, K. Sakaguchi, et al., Parameterization improvements and functional and structural advances in version 4 of the community land model, Journal of Advances in Modeling Earth Systems 3 (1).
[41] X.-M. Hu, J. W. Nielsen-Gammon, F. Zhang, Evaluation of three planetary boundary layer schemes in the wrf model, Journal of Applied Meteorology and Climatology 49 (9) (2010) 1831–1844.

Visualization and quantitative analysis of muzzle flow

Abdelhafidh Moumen

Environmental and Applied Fluid Dynamics Department, von Karman Institute for Fluid Dynamics, Belgium, abdelhafidh.moumen@gmail.com

Supervisor: Delphine Laboureur

Associate Professor , Environmental and Applied Fluid Dynamics Department , von Karman Institute for Fluid Dynamics, Belgium, delphine.laboureur@vki.ac.be

University Supervisors: Johan Gallant and Patrick Hendrick

Professor, Dept of Weapon Systems and Ballistics, Royal Military Academy, Belgium, johan.gallant@dymasec.be

Professor, Laboratory of Aero-Thermo-Mechanics, Université Libre de Bruxelles, Belgium, patrick.hendrick@ulb.ac.be

Abstract

In the context of intermediate ballistic research, several experimental and numerical studies on muzzle blast and flow fields have been performed to fully understand this complicated phenomenon. Indeed, about 70% of the chemical energy developed by a conventional weapon system (propellant-gun) is not converted into kinetic energy of the projectile but is contained in a high-temperature, high-pressure, high-velocity reactive gas. After the projectile ejection, this gas-particle mixture discharges from the muzzle of the gun in a few milliseconds.
The deep comprehension of this flow is essential in weapon system design (mainly accessories), the projectiles exterior ballistic behavior and crew and equipment protection. However, the research in this field is limited due to the classical intrusive and local measurement methods.
In the present study, the objective is to quantitatively analyze the muzzle flow field as it expands into the surrounding atmosphere to get a deeper comprehension of these phenomena. This analysis will be based on quantitative visualization techniques. The potential and the limitations of the selected methods, in characterizing such a challenging flow field, will be investigated. The density and velocity based analysis of this flow will then be further exploited for the optimization of the muzzle devices and numerical validation.
Towards the achievement of the research objectives, during this first year, we have been focusing on the development of a density sensitive and quantitative flow visualization technique based on Background Oriented Schlieren (BOS) combined with a high-speed camera. The implemented experimental high-speed BOS set-up has demonstrated its ability to capture clearly the salient features of the precursor and the propellant gas flow fields and their interactions. The captured structures such as vortex, barrel shock, Mach disk, and blast wave show a good agreement with that issued from a realized conventional Schlieren setup and the bibliography confirming the BOS capability to visualize complex density flows in the ballistics field. Furthermore, we succeeded to capture the flow field around a projectile freely flying in the air in both subsonic and supersonic regimes. The reconstructed density showed a very good agreement when compared with numerical simulation.

Keywords: Background Oriented Schlieren , intermediate ballistics , flow visualization , muzzle flow fields

CFD modeling of a contaminant release in a subway station

Loreline Faugier

Mechanical Engineering Department, Royal Military Academy, Belgium, loreline.faugier@rma.ac.be

Supervisor: Delphine Laboureur

Associate Professor, Environmental and Applied Fluid Dynamics Department, von Karman Institute for Fluid Dynamics, Belgium, delphine.laboureur@vki.ac.be

University Supervisor: Walter Bosschaerts

Professor, Mechanics Department, Royal Military Academy, Belgium, walter.bosschaerts@rma.ac.be

University Supervisor: Benoît G. Marinus

Associate Professor, Mechanical Engineering Department, Royal Military Academy, Belgium, benoit.marinus@rma.ac.be

University Supervisor: Karim Limam

Professor, LaSIE, Universit de La Rochelle, France, karim.limam@univ-lr.fr

Abstract

In the context of CBRN applications for the Belgian Defense, this study intends to model and predict numerically the ventilation and dispersion of an airborne contaminant into a subway station, and to validate the CFD results. The toxicity assessment will allow the public transport companies and the medical services to adapt their detection infrastructure and emergency procedures. Sainte-Catherine subway station in Brussels is used as a test case to validate the CFD results.

In the Sainte-Catherine station, the ventilation is only realized by the piston effect caused by the train movement. When a train travels through a narrow tunnel, the air pushed by the train cannot completely flow to the rear end of the train. A positive pressure volume is formed at the front and discharged when entering the station, while a negative pressure and highly turbulent region appears behind the train, that will suck the air from the station. This is what we intend to simulate numerically. A simplified geometry of the station is used to implement the different scenarios, with dynamic meshing techniques. The domain far-field limits and the boundary conditions will be improved from literature and the experiments.

Experimental measurements in the station, with a hot wire for the air velocity and a Lidar laser for the metro distance, intend to confront the results of the CFD simulations. The measurements show a good accordance with the theory but it is still hard to discriminate between the different air sources. The piston wind is one of them, but the weather conditions, the presence of people on the platform, the general air circulation through the tunnel network are also likely to have an influence.

The similarity issues of building a 4 meters long scale model, with a running train within it, are currently being studied. The model will allow to perform repeatable PIV measurements in a controlled environment. The experiments will allow the verification of simplifying assumptions for our model, so a validated model could finally be used to calculate different scenarios. Feasibility of generalization to more complex station architectures will also be tested.

Monotone integrated large eddy simulation (MILES) and uncertainty quantifications for improved CFD modeling of urban environments

Tom Lauriks

Environmental and Applied Fluid Dynamics Department, von Karman Institute for Fluid Dynamics, Belgium, tom.lauriks@vki.ac.be

Supervisor: Jeroen van Beeck

Professor, Environmental and Applied Fluid Dynamics Department, von Karman Institute for Fluid Dynamics, Belgium, vanbeeck@vki.ac.be

University Supervisor: Siegfried Denys

Professor, Department of Bioscience Engineering, University of Antwerp, Belgium, siegfried.denys@uantwerpen.be

Abstract

Urban physics is well-positioned for finding solutions for the existing urban challenges, e.g. in the topics building energy performance and air pollution. In urban physics, computational fluid dynamics (CFD) models can be extremely useful, since they allow, e.g., to calculate results at every point in space [1]. However, concerns about the accuracy and computational cost of urban CFD models exist. The faster Reynolds-averaged Navier Stokes (RANS) models are not suitable to study all topics in urban physics [1; 2; 3]. In addition, the more accurate large eddy simulation (LES) models still require very large computation times [4; 5; 6]. Urban environments are, moreover, highly variable, which introduces substantial uncertainties into the modeling results. This was demonstrated, for example, for the variability of the incoming wind [5].

In the future research of the author, CFD modeling of complex urban geometries in realistic outdoor conditions will be improved, by implementing a computationally less expensive LES method, MILES. It has been successfully applied in the past [7], but the limits of its capabilities still have to be established. Besides, uncertainty quantifications will be performed to identify uncertain model parameters that have a large influence on the model results. Possibly interesting examples are uncertainties present in time-dependent inflow boundary conditions, the parametrization of geometrical details in the zone of interest [8], and deviations from neutral atmospheric conditions [9].

So far, the flow field and pollutant dispersion in the Turnhoutsebaan (street in Antwerp, Belgium) were modeled by the author, using RANS in the commercial CFD software COMSOL. Locations with increased pollutant concentrations were identified. Innovative measures to locally lower the concentration at the pollution hot spots are being modeled. (Results not yet available.)

The COMSOL results are, in addition, being compared with results of a recently improved RANS method [10]. The authors of the latter article are the developers of the improved RANS method. In general, the new RANS method seems to deliver better results. Improvements, however, still seem necessary, which justifies continuing with the planned research.

1. Preliminary results

In a part of the Turnhoutsebaan, a street in Antwerp (Belgium), the flow field and pollutant dispersion were modeled in the commercial computational fluid dynamics (CFD) software packages COMSOL and Fluent. In the Fluent simulations, a recently developed improved Reynolds-averaged Navier Stokes (RANS) method [10] was used. The author of this document built the COMSOL model and performed field measurements to validate the models. The Fluent model was built by the developers of the new RANS method. The main goal of this research, is to study the spatial distribution of air pollution in the Turnhoutsebaan and the effectiveness of locally

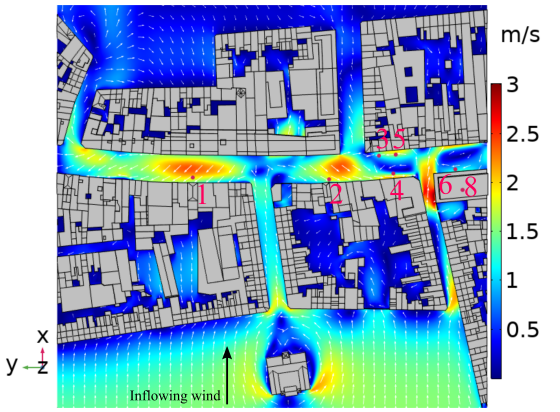

(a)

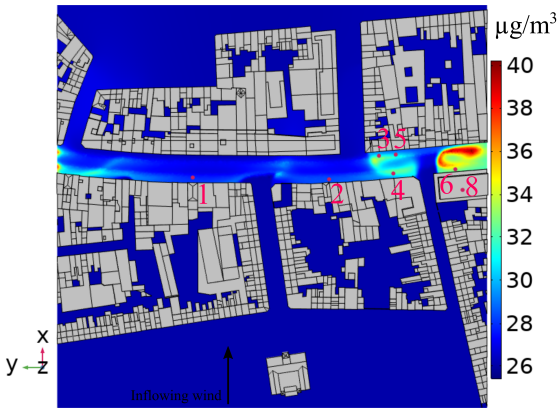

(b)

Figure 1: Turnhoutsebaan model results in the *xy* plane at $z = 1.5$ m. The red dots and corresponding numbers indicate field measurement locations. (a) Velocity, only the *xy* components. The color scale represents the magnitude (b) Concentration of particulate matter (PM_{10}), inflow concentration = 26.04 µg m^{-3}.

applied measures against said air pollution. Besides, the COMSOL and Fluent results are being compared. Fig. 1 a shows COMSOL results of the wind velocity and Fig. 1 b shows COMSOL results of the concencentration of particulate matter with a diameter of 10 µm or less (PM_{10}). Field measurements were collected at locations shown in these figures. At the measurement locations, the modeled wind directions agreed well with the measurements (results not shown). For the wind speed, in general, the improved RANS method performed better than COMSOL (results not shown). There is, however, still much room for improvement.

Fig. 1 b shows that, in the model results, locations occur with elevated pollutant concentrations. From comparing with Fig. 1 a, it is clear that these elevated concentrations occur at places with a low wind speed. These locations are recirculation areas, where the wind velocity is very low due to high buildings, placed very close to each other. With the current pollutant measurements (results not shown), it will be unlikely that hard evidence can be delivered for the existence of these pollution hot spots in the Turnhoutsebaan. The reason for this, is that the pollution measurements were performed with only one measurement device, due to the cost of such devices. As a consequence, the inflowing concentration and the concentration in the street could not be measured at the same time, which resulted in too large uncertainty on these measurements to draw solid conclusions. It can be concluded from this, that better measurements are needed, if one intends to use models for practical applications.

In the literature, measurement campaigns with a high spatial resolution performed in cities around the world were already described, e.g. in in a street in Sidney (Australia) [11], in a small scale area in Liege (a city in the Region Wallonia, Belgium) [12], in Hong Kong [13], in Oakland (California, USA) [14], and in the Berlin/Brandenburg Metropolitan Region (Germany) [15]. These campaigns indicate that notable air pollution concentration differences can indeed occur at very local scales, e.g. a difference in mean PM_{10} of more than 20 µg m^{-3} at a distance of 50 m [12].

Implementing measures to locally lower air pollution in problematic hot spots could therefore clearly be an interesting strategy in many regions of the world and the Turnhoutsebaan model is currently being used for a preliminary assessment of the effectiveness of such measures. The measures being studied are the removal of PM_{10} with electrostatic precipitation and the dilution of air pollution by building a roof top structure, termed a wind catcher, redirecting the wind to the low wind speed zones. The removal of PM_{10} from semi-enclosed parking garages with electrostatic precipitation and the effect on the surrounding urban neighborhood [2] and the removal of $PM_{2.5}$ with electrostatic precipitation from the naturally ventilated courtyard of the American embassy school in Delhi [16] were already modeled, resulting in significant locally lowered pollution levels (10-50% reduction in the vicinity of the parking garages and up to 34.1% overall volume-averaged concentration reduction in the Delhi case). The effect of a wind catcher on air pollution was already modeled for an idealized 2D street canyon case [17]. The effectiveness of both

measures was, however, not yet assessed in a realistic 3D urban street case study, such as the Turnhoutsebaan model. The modeling results of said measures are not yet available.

References

[1] P. Moonen, T. Defraeye, V. Dorer, B. Blocken, J. Carmeliet, Urban physics: Effect of the micro-climate on comfort, health and energy demand, Front. Archit. Res. 1.

[2] B. Blocken, R. Vervoort, T. van Hooff, Reduction of outdoor particulate matter concentrations by local removal in semi-enclosed parking garages: A preliminary case study for Eindhoven city center, J. Wind Eng. Ind. Aerodyn. 159 (2016) 80–98.

[3] T. Tamura, K. Nozawa, K. Kondo, AIJ guide for numerical prediction of wind loads on buildings, J. Wind Eng. Ind. Aerodyn. 96 (2008) 1974–1984.

[4] B. Blocken, LES over RANS in building simulation for outdoor and indoor applications: A foregone conclusion?, Build. Simul.

[5] C. García-Sánchez, J. van Beeck, C. Gorlé, Predictive large eddy simulations for urban flows: Challenges and opportunities, Build. Environ. 139 (2018) 146–156.

[6] J. Th, H. Yu, A critical review on the simulations of wind turbine aerodynamics focusing on hybrid RANS-LES methods, Energy 138 (2017) 257–289.

[7] G. Patnaik, J. P. Boris, T. R. Young, F. F. Grinstein, Large scale urban contaminant transport Simulations with miles, Journal of Fluids Engineering 129 (2007) 1524–1532.

[8] B. Blocken, J. Persoon, Pedestrian wind comfort around a large football stadium in an urban environment: CFD simulation, validation and application of the new Dutch wind nuisance standard, J. Wind Eng. Ind. Aerodyn. 97 (2009) 255–270.

[9] H. J. Breedt, K. J. Craig, V. D. Jothiprakasam, Monin-obukhov similarity theory and its application to wind flow modelling over complex terrain, J. Wind Eng. Ind. Aerodyn. 182 (2018) 308–321.

[10] R. Longo, M. Ferrarotti, C. García-Snchez, M. Derudi, A. Parente, Advanced turbulence models and boundary conditions for flows around different configurations of ground-mounted buildings, J. Wind Eng. Ind. Aerodyn. 167 (2017) 160–182.

[11] I. Wadlow, C. Paton-Walsh, H. Forehead, P. Perez, M. Amirghasemi, É.-A. Guérette, O. Gendek, P. Kumar, Understanding spatial variability of air quality in sydney: Part 2—a roadside case study, Atmosphere 10 (4) (2019) 217. doi:10.3390/atmos10040217.

[12] H. Merbitz, F. Detalle, G. Ketzler, C. Schneider, F. Lenartz, Small scale particulate matter measurements and dispersion modelling in the inner city of Liege, Belgium , International Journal of Environment and Pollution 50 (1–4) (2012) 234–249.

[13] Z. Li, J. C. H. Fung, A. K. H. Lau, High spatiotemporal characterization of on-road PM2.5 concentrations in high-density urban areas using mobile monitoring, Building and Environment 143 (2018) 196–205. doi:10.1016/j.buildenv.2018.07.014.

[14] J. S. Apte, K. P. Messier, S. Gani, M. Brauer, T. W. Kirchstetter, M. M. Lunden, J. D. Marshall, J. Portier, R. C. H. Vermeulen, S. P. Hamburg, High-Resolution Air Pollution Mapping with Google Street View Cars: Exploiting Big Data, Environmental Science & Technology 51 (12) (2017) 6999–7008. doi:10.1021/acs.est.7b00891.

[15] B. Bonn, E. von Schneidemesser, D. Andrich, J. Quedenau, H. Gerwig, A. Ldecke, J. Kura, A. Pietsch, C. Ehlers, D. Klemp, C. Kofahl, R. Nothard, A. Kerschbaumer, W. Junkermann, R. Grote, T. Pohl, K. Weber, B. Lode, P. Schnberger, G. Churkina, T. M. Butler, M. G. Lawrence, BAERLIN2014 – the influence of land surface types on and the horizontal heterogeneity of air pollutant levels in berlin, Atmospheric Chemistry and Physics 16 (12) (2016) 7785–7811. doi:10.5194/acp-16-7785-2016.

[16] R. Vervoort, B. Blocken, T. van Hooff, Reduction of particulate matter concentrations by local removal in a building courtyard: Case study for the delhi american embassy school, Science of The Total Environment 686 (2019) 657–680. doi:10.1016/j.scitotenv.2019.05.154.

[17] K. Zhang, G. Chen, X. Wang, S. Liu, C. M. Mak, Y. Fan, J. Hang, Numerical evaluations of urban design technique to reduce vehicular personal intake fraction in deep street canyons, Science of the Total Environment 653 (2019) 968–994. doi:10.1016/j.scitotenv.2018.10.333.

Aerothermal characterization of compact heat exchanger elements

Aude Lecardonnel

Environmental and Applied Fluid Dynamics Department, von Karman Institute for Fluid Dynamics, Belgium, aude.lecardonnel@vki.ac.be

Supervisor: Delphine Laboureur

Associate Professor, Environmental and Applied Fluid Dynamics Department, von Karman Institute for Fluid Dynamics, Belgium, delphine.laboureur@vki.ac.be

Abstract

The present work is dedicated to the study of additive manufactured heat exchangers in terms of thermal exchange and pressure losses created by the airflow, and is part of the European program CLEAN SKY 2. Temperatures and pressures were measured at different locations by mean of thermocouples and taps. Fanning and Colburn factors were retrieved to compare the samples.

Keywords: Heat exchanger, Additive manufacturing

The evolution of darker wings improves flight efficiency in seabirds

Svana Rogalla

Environmental and Applied Fluid Dynamics Department, von Karman Institute for Fluid Dynamics, Belgium, Svana.Rogalla@UGent.be

Supervisor: Jeroen van Beeck

Professor, Environmental and Applied Fluid Dynamics Department, von Karman Institute for Fluid Dynamics, Belgium, vanbeeck@vki.ac.be

University Supervisor: Matthew D. Shawkey

Professor, Department of Biology, Ghent University, K. L. Ledeganckstraat 35, 9000 Gent, Belgium, Matthew.Shawkey@UGent.be

Abstract

Avian flight is considered a key innovation that allowed birds to diversify into the ecologically, morphologically and species diverse group we know today. In order to fly, birds need to produce lift to oppose their own body weight and thrust to overcome drag. Every increase in lift or reduction in drag will thus improve the lift/drag ratio, i.e. the flight efficiency of a bird. Previous studies have shown that black wing coloration might positively affect the lift/drag ratio due to photothermal heating (Hassanalian 2017). Indeed, differently colored feathers show different heating rates, even during flight. We used a combination of wind tunnel tests and phylogenetic comparative analyses to show that the temperature differential across the cross section of the wing created by heat absorption differences improves flight efficiency. To test whether birds with a higher wing loading, thus larger flight costs, are more likely to evolve darker wings, we measured wing reflectance on seabird museum specimens and modelled darkness in function of wing loading and flight mode performing an ancestral state reconstruction. We found that drag did not differ, but lift increased with increasing temperature differentials between suction and pressure side. Thus, the lift/drag ratio, i.e. the flight efficiency, increased with increasing larger differentials. We further found that seabirds with higher wing loadings are more likely to evolve dark wings independently from their applied flight mode. However, even lighter birds evolved dark wings, suggesting that all birds may profit from the efficiency increment. Our results indicate that birds with darker wings profit from an improved flight efficiency.

PROPULSION

Gas-liquid interface dynamics in non-isothermal sloshing: experimental analysis and simplified modeling

Domenico Fiorini

Environmental and Applied Fluid Dynamics Department, von Karman Institute for Fluid Dynamics, Belgium, domenico.fiorini@vki.ac.be
Department of Materials Engineering, KU Leuven, Belgium,

Supervisor: Miguel Alfonso Mendez

Assistant Professor, Environmental and Applied Fluid Dynamics Department, von Karman Institute for Fluid Dynamics, Belgium, miguel.alfonso.mendez@vki.ac.be

University Supervisor: David Seveno

Associate professor, Department of Materials Engineering, KU Leuven, Belgium, david.seveno@kuleuven.be

University Co-Supervisor: Johan Steelant

Associate professor, Department of Mechanical Engineering, KU Leuven, Belgium, Johan.Steelant@esa.int

Abstract

The motion of any fluid interface near a solid strongly depends on the *dynamic contact angle* which the gas-fluid interface itself forms at the wall. Industrial applications and literature studies found that current dynamic contact angle models are unsatisfactory for all the cases where the contact point is subjected to accelerations and non-isothermal wall conditions, as it is for fluid sloshing in space tanks. Hence, we need to develop new models from experiments, particularly concerning cryogenic space fuels, which hold a near-zero *equilibrium contact angle* which optical methods can hardly quantify with accuracy. To overcome this limit and investigate the phenomenology of accelerating contact lines we designed a multi-purpose experimental test-case constituted by a U-shaped quasi-capillary tube, partially filled with cryogenic fuels-substitute. Our measurement method considers the tracking of the fluid interface oscillations in time and the reconstruction of the dynamic contact angle data through an inverse method of regression. Gene programming and other approaches for system identification will be used to build the contact angle correlations. So far, we achieved an optimized design of the facility and we tested the method against synthetic data and similar literature test-cases such as capillary rise problems. We point out the limits of existing correlations, along with the critical aspects of dynamic contact angle modeling for cryogenic fuels.

Keywords: Dynamic contact angle – Cryogenic – Inertial wetting – Capillary rise – Inverse method

1. Introduction

The equilibrium between three phases is a delicate subject whose features we still don't understand entirely. In the field of wetting, this situation arises when a gas-liquid interface meets a solid surface, delineating a micro-region where the physics in the vicinity of the contact point affects the behaviour of the whole free surface of the liquid. This impacts a large number of industrial flow cases where the surface-gas-fluid interaction is essential as boundary condition for the fluid models. Moreover, when a moving contact line is involved, we have additional difficulties in implementing these conditions, since the classic formulation with no-slip boundary condition at the solid cannot be used due to the non-integrable stress singularity arising at the moving contact point where the particles on the wall are suddenly asked to move. As a consequence, the curvature of the interface at the wall cannot be found

but needs to be prescribed through a *contact angle*.
The contact angle is a fundamental parameter for many applications such as curtain coating and deposition of photographic films, where one of the main challenges is to account for the dynamic behaviour of the contact angle into the stabilization of the coating film (hydrodynamic assist). The dynamics of the contact angle plays a role also for ink-jet printing and drying paints applications where the velocity field near the contact line leads to the accumulation of the die particles towards the contact line resulting into the well- known coffee stain effect. In bio-engineering, the contact angle is one of the most important parameters quantifying the bio-compatibility between tissues and bio-materials, e.g. contact lenses, including problems of hydration of human body parts as the eyes. The contact angle is also relevant for a large number of industrial processes as magnetic disk production, wetting of powders and polymer processing. In this project we target the control of the fuel behavior in space tanks, which is based on the ability to predict the movement of the liquid free surface when the fuel is subjected to specific operational conditions as unsteady accelerations or heat transfer. The contact angle deeply affects the interface motion since in space the forces driving the fluid motion, which is called *sloshing*, change drastically compared to earth gravity conditions: the free surface displacement becomes capillary dominated and natural or free convection may be replaced by thermo-capillary convection [1]. The control of cryogenic propellant behavior compared to isothermal storable propellants is furthermore complex since additional phenomena are present such as thermal stratification while even phase change of the liquid may occur [1], the management of such fluids in a compensated gravity environment is of strategic interest for future space exploration including the anticipation of sending humans to Mars.

The dynamics of the contact angle has a long history of investigations both theoretical and experimental, unfortunately, most of the literature focus on a limited set of *steady* regimes which were on interest for terrestrial application [2]. Therefore, existing models have limited applicability to space problems where the *unsteadiness* is a fundamental feature and as a result, numerical simulations of space sloshing still show discrepancies comparing with experiments in terms of velocity and thermal fields, phase transition and free surface response, when the liquid in the tanks is subjected to impulsive accelerations during the transients. An improvement of the prediction of the surface response is addressed to a more physically accurate definition of the contact angle boundary condition at the contact line [2; 3; 4; 5; 6; 7].

This research project aims to provide additional understanding on contact angle dynamics by investigating the aspects that are missing in current literature and that results to be important for space as well for other terrestrial applications. In detail, the objectives of this research are twofold: First, it is intended to provide experimental data for the dynamics of the contact angle for cryogenic and non-cryogenic fluids in different acceleration conditions, testing different regimes of motion, emphasizing the difference between steady and unsteady conditions and the impact on the contact angle itself.
The second challenge is to develop a methodology to accurately measure near zero dynamically changing contact angles. We investigated an innovative inverse method of system identification which we validated on literature test cases where the flow is known to be capillary dominated. The method will be implemented also on a newly developed test case, in order to develop new physical models for the dynamics of the contact angle to be integrated into computational fluid dynamic solvers.
The target scenario of this study is deep space exploration. In particular, the missing requirements for accurate modeling of the liquid/gas/solid contact region where viscosity, phase change and surface tension are dominant. The propellants addressed in this study are preferably cryogens, such as hydrogen and methane as propellants and oxygen as oxidizer.

The paper is structured as following. In sec. 2 the fundamental definitions, models and most relevant experimental test-cases are discussed. In sec. 3, the methodology with which the contact angle problem is approached is explained. In sec. 4 the method is validated against synthetic and literature test-cases and finally in sec. 5 the conclusions on the current status are withdrawn.

2. Fundamentals

In a wetting configuration as in fig. 1 when cohesion and adhesion forces are balanced the system is said to be in a meta-stable state of equilibrium and the corresponding contact angle is called *static* (SCA or θ_S). When the contact line is out of equilibrium, i.e. it is moving, the contact angle is called *dynamic* (DCA

or θ_D). The equation of Young-Dupre' (1905)[8] is the first and most basic description which relates the balance of forces at the contact line with the fluid static contact angle:

$$\gamma_{SG} - \gamma_{SL} = \gamma \cos\theta_{eq} \tag{1}$$

Where γ_{SG}, γ_{SL} and γ are respectively the surface tension at the solid-gas interface, the solid-liquid interface and the well-know surface tension at the liquid-gas interface. The equation is exact for pure fluids on smooth surfaces.

On the other hand, dynamic contact angle models are still argument of scientific debate, we distinguish two categories: theoretical and empirical models. The model of Voinov (1976)[9] is one of the pillars of contact angle theory, it is derived by applying hydrodynamic lubrication theory at the meniscus region (reason why it is also called *hydrodynamic theory* (HT)) and sets the difference between the CA in the outer region (θ) and the CA inner region (θ_m). The first is linked to the second by viscous bending of the interface in an intermediate mesoscopic range (Figure 1). Therefore, the CA acquires a *multiscale* characteristics where the CA observed experimentally is only *macroscopic* or *apparent*, which is on interest for practical numerical cases where the mesh size at the surfaces cannot be too small.

The main limit of Voinov Law model is that it is applicable only to systems with a liquid/inviscid-gas interface. Cox (1986) [10] proposed a more complete and general model based on HT, which is applicable to systems with two viscous fluids. For $\theta_D < 3/4\pi$, Capillary number and Reynolds number lower that one [11; 12], Voinov law can be written in a simple form as:

$$\cos\theta_D = \cos\left(\theta_{eq}^3 + \frac{u_i \mu}{\sigma} F_T\right)^{\frac{1}{3}} \tag{2}$$

Where the ratio $u_i\mu/\sigma$ is the above mentioned "Capillary number". The constant $F_T = 9 \ln \frac{L_M}{l_m}$, where L_M is a typical macro-length of the flow, assumed as the distance from the contact line at which the contact angle is measured [11], l_m is the molecular length-scale which corresponds to the distance from the wall the solution of the HT model is truncated, θ_{eq} is the contact angle at equilibrium condition, which is generally assumed equal to θ_m. We need to emphasize that eq. 2 has been developed only for advancing contact lines, which is the main interest for industrial processes, but is has been generally assumed to be valid even for receding contact lines [13]. The difference between the fluid advancing contact angle and receding contact angle is named *contact angle hysteresis*.

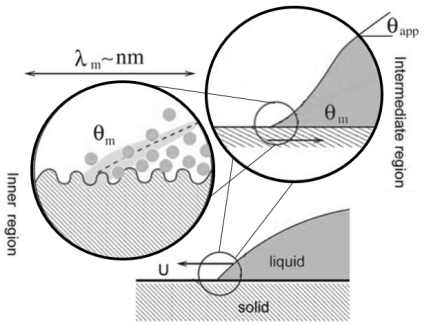

Figure 1: Multi-scale property of the contact angle, adapted from [14]

The second theoretical pillar is the molecular-kinetic theory (MKT) of T. Blake [15] (1969). Differently from HT model, the statistical dynamics of the fluid molecules at the three phase contact point determines the contact angle in the inner, microscopic, region. The model requires a spatial resolution in the order of the nano-meter and cannot be applied in the conventional continuum mechanics approach. On the other hand, it is fundamental to relate the micro-dynamic physics at the contact line to the macro-hydrodynamics. For $\kappa_B T >> \sigma/n$, with n the number of absorption sites per unit area, MKT model can be written as:

$$cos\theta_A - cos\theta_m = \frac{\kappa_B T}{\kappa_0 \lambda^3} \frac{u_i}{\sigma} \tag{3}$$

Where κ_B is the Boltzmann constant, T is the absolute temperature, θ_m is the microscopic contact angle, λ is the distance between the absorption sites on the solid surface (generally between 0.4 and 1.8 nm) and κ_0 is the frequency of the molecular displacements, this last value can vary widely, it is inversely proportional to viscosity and to the exponential of the work of adhesion.

The two models differ in two important aspects. The first is the targeted system resolution, which with MKT is near the molecular size while in HT is of the order of some microns. The second aspect relates with the physics involved: HT model doesn't account for the physical interaction with the solid surface, while on the other hand, the MKT model doesn't consider any viscous dissipation due to the velocity field in the meniscus. For these reasons another category of *combined models* have been developed [16] in order to ac-

counts for the characteristics of both models.
A relevant drawback of both HT ad in MKT models is that the physical constants appearing in the models are not strictly defined and are often conveniently chosen. A reasonable estimation for the logarithmic term of HT is of the order of 10 since the molecular distance is of the order of $1nm$ and the macro-length is of the order of $10\mu m$.
Concerning the MKT, some example values are presented in table 1.

Table 1: Parameters obtained by applying MKT to experimental data for various systems.[11]

System	$\lambda(nm)$	$\kappa_0(s^{-1})$
Water on PET	0.36	$8.6x10^9$
16% glyc. in Water/PET	0.46	$3.6x10^9$
86% glyc. in Water/PET	0.46	$3.5x10^7$
Di-n-butylphthalate/PET	1.8	$1.1x10^5$
Silicon oil/glass (0.958 Pas)	0.8	$2.3x10^5$
Silicon oil/glass (98.8 Pas)	0.8	$2.3x10^3$

Even if reasonable ranges can be established, values of F_T, λ or κ_0 for a specific experiment cannot be predicted in advance. Indeed, these values are generally adjusted in order to describe experiments *a posteriori* and they have no predictive power since a wide range of possibilities can be found even among similar experiments.
Among the theoretical models, it is necessary to mention also the one recently proposed by Shikhmurzaev (1993) [17] which is a generalization of the classical boundary conditions at the free surface and contact line. The novelty of this method is to consider the fluid-gas-solid interface as a thermodynamic system with mass, momentum and energy exchange with the bulk. As the interface moves it needs to reorganize itself due to the change of equilibrium properties. A natural tension gradient arises at the interface due to the change of material densities and the microscopic contact angle will naturally change as a result of the change of equilibrium of the surface tension (see equation 1), viscous bending of the interface will be present as a result of the flow motion. Unfortunately, as for HT and MKT models, also this last theory holds the disadvantage of requiring a number of phenomenological coefficients which are difficult to be estimated a-priory.

The second category of DCA models is based on scattered data, due to their nature they are naturally subjected to the possibility of errors in the measurements and additionally, it is suggested that a larger amount of parameters influencing the DCA, which have not been investigated up to now, may impact the experimental results [11]. Among the empirical models it is important to mention the model of Hoffman (1975) [18], which has a formulation similar to Voinov law, Bracke (1989)[19], Seebergh (1992) [20] and the more recent model of Yokoi (2009) [21].

Both theoretical and empirical models surprisingly account only for the contact line instantaneous velocity, neglecting any possible role of the contact line acceleration, which is strange considering that the angle is called *dynamic*. The definition as *dynamic contact angle* can be traced back to Hoffman [18], who classified as *dynamic studies* experiments involving a quasi-steady contact line velocity and *relaxation studies* experiments involving accelerating contact lines. As a consequence, in the literature, both the cases of theoretical and empirical dynamic CA models assumed that the dynamic contact angle monotonically increases (or decreases) only with the contact line instantaneous velocity [9][10][22] neglecting any unsteady contribution. This may explain the large scatter found on experimental data but more importantly this feature theoretically prevents correlations derived upon a steady contact line velocity assumption to be strictly applicable over sloshing contact line cases, where the contact point is subjected to non-negligible accelerations.
Relaxation studies haven't gained a lot of attention in the wetting literature. The problem has been explored theoretically by Golestanian *et al.* [23][24] whose test case was recently reproduced experimentally by Delon *et al.* [25]. The main outcome of these studies determined that a perturbation induced on a steadily moving meniscus decays exponentially with a relaxation rate $p = (2\pi\sigma)/(\lambda\mu)f(Ca)$, where λ is the wavelength of the perturbation and $f(Ca)$ is a function of the Capillary number strongly linked to the relation $\theta_d = f(Ca)$.

The dynamic contact angle is measured with mainly two methods: droplet spreading and capillary rise experiments. The droplet spread generally follows an impact or a growth through an injection and it is the most popular among the two methods [26; 27; 28]. During the experiment the height and radius of the droplet are monitored along with the contact angle which is measured visually through side view imaging [27] or other approaches as interferometry [29].

We concluded that this method is not suited to explore the wide range of regimes requested by the our study with the needed accuracy. Moreover, a large amount of phenomena is involved in a droplet impact and spreading which imply that additional uncertainty would be added to the conclusions on the experimental result and this would also prevent to apply safely inverse methods as the one described in section 3.

Capillary rise experiments gained popularity only in the 21th century thanks to the experiments of Quere' (1997) [30] which emphasized the key role of contact angle modeling on the prediction of the transient of the capillary rise. This test case has some favorable features: the experiment is confined and the physics involved is limited almost to the capillary action. Experimental techniques such as side view imaging and our inverse methods of regression (see sec. 3) are applicable simultaneously promising, along with multiple data, a strong validation.

Despite the recent development, the capillary rise is known since the experiments of Jurin (1718)[31], who gives the name to the famous Jurin's law, which establishes the final height of a fluid column in a capillary tube, $h_{end} = 2L_c^2 r^{-1} cos\Theta_s$, where r is the capillary tube radius and $L_c = \sqrt{\gamma/(\rho g)}$ is the capillary length of the fluid. The first model for the transient height appeared much later with the well-known non-linear, first order, differential equation of Washburn-Lucas (1921) [32], which Bosanquet (1923) [33] improved in order to include the effect of flow inertia. Later on, a large number of new formulations have been published adding corrections to take into account additional phenomena involved, Zhong *et al.* [34] present a review of the most relevant models. The formulation that holds the simplest form, while taking into account all the relevant physics is the equation of Levine (1976) [35] which we will use for all the comparisons of section 4.

$$\left(h + \frac{37}{36}\right)\ddot{h} - \frac{2\gamma\cos\theta}{\rho r} + \frac{8\mu}{\rho r^2}h\dot{h} + gh + \frac{1}{2}\left(\frac{4\mu}{\rho r}\dot{h} + \frac{7}{3}\dot{h}^2\right) = 0 \tag{4}$$

The dot-symbol indicates the time derivatives of the transient height. Interestingly, this equation considers many phenomena (e.g. entrance effects into capillary tubes), but originally doesn't account the dynamic behaviour of the contact angle, which leads to a substantial mismatch with a large number of experimental cases where the capillary rise is relatively fast (see sec. 4).

3. Inverse method

Contact angle measurements have an overall accuracy of one degree for standard fluids [36]. However, this doesn't hold for near zero CA values ($\theta < 10°$, e.g. cryogenic fluids) and since this may hide the contribute of the quantities of interest on the dynamic contact angle, we developed an alternative accurate measurement approach which uses the experimental data of fluid-interface motion and link them to the dynamic contact angle. The accuracy of the method is determined by the impact of the dynamic contact angle on the motion of the fluid interface of the specific test case, which should allow to simply model the free surface displacement in order to test contact angle correlations and reversibly, draw out empirical new forms which include parameters of interest for sloshing (e.g. acceleration of contact line). In simple terms, our algorithm reproduces the displacement of the fluid interface in the chosen test case (e.g. free oscillations in a U-tube manometer) by using a theoretical 1D model leaving the contact angle correlation as a free parameter. The simulation is compared with the experimental displacement of the interface. By using a *best fitting* objective function the method determines the unknown parameters of the contact angle model necessary to match the prediction of the interface motion with the corresponding experiment. This measurement approach is therefore called inverse method, since the contact angle correlation is retrieved by the regression of the data on the free surface displacement. A genetic algorithm (GA) is used to minimize objective function which is preliminary defined as:

$$fitness = \sqrt{\frac{1}{N-1}\int_0^{t_{end}} \sum_0^N \left(\frac{\hat{h} - \hat{h}^*}{\hat{h_0}^*}\right)^2 dt} \tag{5}$$

where $\hat{h}$ is the non-dimensional position of the interface as predicted by the model and $\hat{h}^*$ it the experimentally observed interface position. $N = t_{end}/f_{acq}$ is the number of samples from the experiment, where the experiment duration t_{end} is set by the design parameter of the setup, which determine the number and the amplitude of the oscillations. While monitoring the height of the fluid interface in time through high-speed imaging the behaviour of the contact line will be tentatively observed also by a camera, placed on the side, with the visualization of the interface enhanced by back-light illumination.

Experiments will be done for two sizes of the setup, the first size will be large enough to imply a negligible influence of the contact line on the flow behaviour,

allowing to validate the formulation of the model in terms of the parameters that are considered to be known without the necessity of modeling correctly the behavior of the *unknown* contact line. The inverse method is applied on the second configuration which, on the opposite, will be of dimensions such as to maximize the impact of the dynamic contact angle on the oscillations of the fluid interface, maximizing also the accuracy of the method.

The chosen test case for dynamic contact angle experiments is a U-tube manometer, filled with the test-liquid, where the fluid slug oscillates after release from the initial conditions. In order to derive the 1D-model for the motion of the fluid interface, we assume the flow to be laminar and the fluid in-compressible. Furthermore we consider that any other secondary effect as end effect of the liquid, falling film and curvature of the tube are negligible. The velocity components along the radial and tangential direction are negligible and the velocity profile is constant along the slug length (not in time) and axial-symmetric. Consequently, the momentum equation for the fluid motion along the tube axis is of the form:

$$\rho\frac{\partial u}{\partial t} = -\frac{\partial p}{\partial z} + \frac{\mu}{r}\left[\frac{\partial}{\partial r}r\frac{\partial u}{\partial r}\right] + F \tag{6}$$

where $F = -2\rho g\frac{h_i}{l} + \frac{\gamma}{rl}(cos\theta_A - cos\theta_R)$ and h_i is a variable external to the fluid slug, different from its z coordinate, varying with the position of the slug interface in the pipe and equal to the displacement from equilibrium position of the slug. θ is the contact angle of the fluid. Integrating eq. 6 over the pipe cross section and subsequently over the length "l" of the liquid slug leads to the following integral equation for the motion of the interface of the liquid slug in the pipe.

$$\begin{aligned}&\frac{du_i}{dt} + \frac{\mu}{\rho}\frac{1}{\pi R^2}\int_0^R \frac{\partial}{\partial r}\left(r\frac{\partial u}{\partial r}\right)2\pi r dr = \\ &2\frac{g}{l}h_i + 2\frac{\sigma}{R\rho l}\Delta_\Theta\end{aligned} \tag{7}$$

Where with the subscript "i" we refer respectively to the velocity of the slug interface u_i and its displacement h_i respect to the equilibrium position. The variable $\Delta_\Theta = \cos\theta_A - \cos\theta_R$ synthetize the unknown behaviour of the contact angle. In order to evaluate the integral of eq. 7 we need to know the profile of the axial velocity, a simple assumption is represented by a Pouseuille-type velocity distribution of the form:

$$u(r,t) = 2u_i\left(1 - \frac{r^2}{R^2}\right) \tag{8}$$

Assuming $u_i = dh_i/dt$ we can write eq. 7 as:

$$h_i'' + \frac{8\mu}{R^2\rho}h_i' + 2\frac{g}{l}h_i - 2\frac{\sigma}{R\rho l}\Delta_\Theta = 0 \tag{9}$$

This attractive form of the equation has been similarly obtained by Weislogel in 1996 [37] for forced flow movement in a U-tube manometer where the driving force was induced by different wetting properties in the two sides of the U-manometer. We emphasize that Pouseuille flow is verified for steady case conditions, in cases were the flow can be considered as quasi-steady (e.g. capillary rise), this condition can be relaxed. Concerning free oscillations in U-tubes still it is not clear under which limits a Pouseuille flow assumption is verified since some authors claim that the velocity profile in U-tubes may be different from the classic parabolic shape due to the intrinsic unsteadiness of the flow [38; 39; 40]. A more general formulation for the velocity profile would be:

$$\begin{aligned}u(r,t) =& 2u_i\left(1 - \frac{r^2}{R^2}\right) - 16u_i\sum_{n=1}^{\infty}\frac{1}{\lambda_n^3}\frac{J_0(\lambda_n r/R)}{J_1(\lambda_n)}e^{-\lambda_n^2\frac{\nu t}{R^2}} \\ & J_0(\lambda_n) = 0\end{aligned} \tag{10}$$

$J_0(\lambda_n r/R)$	is the Bessel function of the first kind of order zero
λ_n	positive roots of J_0
$J_1(\lambda_n)$	is the Bessel function of the first kind of order one

To the author knowledge, the term accounting for the increased resistance to the movement of the liquid slug due to the surface tension of the fluid has never been considered up to now for free oscillations in a U-tube manometer.
We emphasize that if the contact angle is assumed to be constant, the surface tension term in equation 9 cancels out and it is not accounted in the movement of the liquid slug. Differently, if we consider a model for the dynamic contact angle, with a receding behavior for the receding interface of the slug, and an advancing model for the progressing front of the liquid slug, then we have an additional damping of the fluid oscillation.

The comparison of the U-tube test case with other applications requires scaling of the governing equation and discussion about the similarity in terms of dynamic contact angle. In sloshing, it is commonly

assumed as scaling length the radius of the container [41], in our case we prefer to emphasize the role of the capillary effects, which have small typical length scales and the capillary length of the fluid $L_c = \sqrt{\sigma/\rho g}$ becomes a more suitable choice. The scaling pressure becomes a "capillary pressure" of the form $\delta p_0 = \sqrt{\sigma\rho g}$. Another unknown parameter is the scaling velocity U_0. We assume that the accelerations of the problems are representative scaled by a multiple (even 1) of the earth-gravity acceleration $a_0 = (n)g = U_0/t_0$. Considering $t_0 = L/U_0$, the scaled velocity can be expressed by combining this two relations in $U_0 = \sqrt{L_c g}$, which corresponds to a *critical flow* condition ($Fr \approx 1$), where the typical velocity of the flow is equal to the wave velocity generated by a disturbance. Accordingly, the typical timescale of the problem becomes $t_0 = (\sigma/\rho g^3)^{\frac{1}{4}}$.
As a consequence of these choices, we obtain the following typical numbers:

$\tilde{u} = \sqrt{l_c g}$	typical velocity of a capillary dominated flow (few meters per seconds)
$\tilde{t} = \sqrt{l_c/g}$	typical timescale of a capillary dominated flow (of the order of half a second)

Therefore, equation 9 can be made dimension-less by using the quantities introduced above and eq. 7 becomes:

$$\ddot{\bar{h}}_i + \frac{8Oh_{cb}}{\bar{R}^2}\dot{\bar{h}}_i + \frac{2}{\bar{l}}\bar{h}_i - \frac{2}{\bar{R}\bar{l}}\Delta_\Theta = 0 \qquad (11)$$

Where $\bar{R}$ and $\bar{l}$ are respectively the ratio between the tube diameter and the capillary length and the ratio between the liquid column length and the capillary length. The Ohnesorge number computed using the capillary length of the fluid, defined here as *Capillary Ohnesorge number*, represents the damping characteristic intrinsic of the specific fluid and relates viscous forces to inertial and surface tension forces, typical values ranges from 2.3e-03 for water to 8.3e-03 for HFE 7500, while extremely viscous fluids can have high values as 1.7e-01 for dypropilene glycol.
In the next section we use the formulation for the flow movement in a quasi-capillary U-tube to preliminary test capabilities and performances of the inverse method.

4. Results

We used the model developed in section 3 to optimize the design of the quasi-capillary U-tube manometer. We aim to maximize the impact of an hypothetical contact angle correlation on the interface displacement in order to allow an accurate application of the inverse method on the regression of contact angle data. We use a genetic algorithm of optimization for the tube diameter, constrained to obtain the maximal fitness function in the form of eq. 5, where we substituted the experimental profile with a synthetic one obtained with a constant contact angle correlation. Once the fluid is fixed, the design variables are $\bar{R}$ and $\bar{l}$. In the field of research of the GA, the optimum $\bar{l}$ results always to be the smallest in the population of the GA, meaning that the impact of flow inertia on the fluid oscillations needs to be minimized in order to achieve a strong sensitivity of the model to the dynamic contact angle. Hence, we constrained this term to his minimal value $\bar{l} = 2\bar{h_0} + \pi/2\bar{D}_u$, where the first term accounts for the maximum starting position of the fluid column and the second term keeps the semicircular section of the tube completely filled (avoiding correction for the gravity-term in 11), D_u is the distance between the U-tube columns which has been set to $D_u = 3D = 6R$ according to the design in figure 2. We perform another optimization step with fixed $\bar{l}$. Surprisingly, the optimum diameter results to be slightly bigger than the capillar value ($\approx 8L_c$). This is justified by the high impact of the viscous forces on a thin tube, they slow down the flow and bring the contact angles close to the static values. On the opposite, too large tube diameters imply an high inertia of the flow and again a low impact of the dynamic contact angle. The best solution is clearly a compromise between these extreme cases.

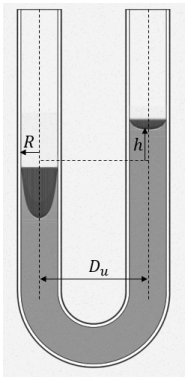

Figure 2: Design model of quasi capillary tube

In order to validate the inverse method approach, eq. 11 is used to generate synthetic data of a U-tube experiment. Before the synthetic test, we pro-

vide to the U-tube model of eq. 11 a test-correlation for the contact angle, the data on the height in time are then corrupted with different levels of Gaussian noise standard deviations [0, 0.05 ,0.1], and acquisition frequency is tested for [15, 33, 67] Hz.
We use the GA inverse method on these synthetic experimental data to retrieve the best coefficients for the input correlation of the contact angle that would fit the synthetic experiment, the test is successful if the input coefficient are retrieved. Test correlation is of the form:

$$\theta_D = (aOh_{cb}\dot{\bar{h}})^b \tag{12}$$

The results of table 2 are obtained for input values of $a = 90$ and $b = 0.33$. The domain of research is set within $30 < a_d < 250$ and $0.05 < b_d < 1$.

Table 2: Test on GA inverse method uniqueness and accuracy.

Test	$f_{acq}(Hz)$	Noise Std (mm)	a_{GA}	b_{GA}
1	67	0	90.0	0.330
2	33	0	90.6	0.332
3	67	0.05	92.1	0.333
4	67	0.1	86.4	0.324
5	15	0	90.0	0.330
6	15	0.1	98.3	0.344

We conclude that increased level of noise deteriorate the accuracy of the method. The sampling frequency appears to not have a strong impact on the GA performances. For each test-case of table 2, we performed a few number of runs of the GA, for the test with 0.0 Noise Std, a variance on the prediction of the coefficient a of ±0.9% and of ±0.3% for coefficient b has been estimated, these values increases with increase levels of noise. We emphasize that, even for the worst case of table 2, test 6, differences in height between the exact model and the GA reconstruction are of the order of $100\mu m$ (see figure 3), differences in the computed DCA are of the order of half a degree. Given these features we consider the behaviour of the model satisfactory for the sake of these preliminary analysis. The accuracy of the method can be improved by tuning the input parameters for the GA.

We can provide a stronger validation of our methodology by applying it on experimental data. To the best of our knowledge, the literature lacks of experiments in capillary U-tube, except the case of [37], whose configuration is anyway different from ours. However, capillary rise experiments holds a very

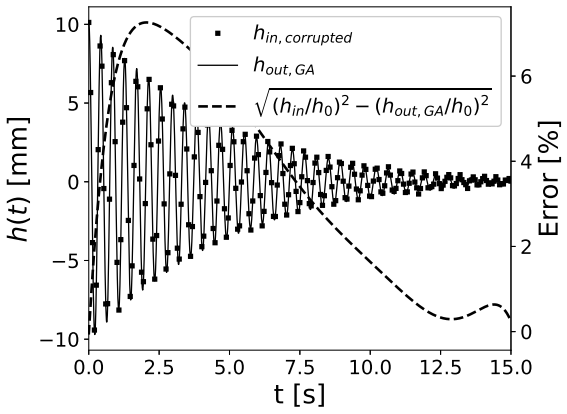

Figure 3: Simulation of Utube experiment. Comparison between synthetic experimental points, $h_{in,corrupeted}$, and reconstruction through GA-based inverse method $h_{out,GA}$, test 6 of table 2. h_{in} corresponds to $f_{acq} = 1500$, $std = 0.0$, $a = 90$, $b = 0.33$ used as *exact* reference.

similar configuration and despite being the governing equation [35] sensibly different from eq. 9, our inverse method can be applied with the same methodology of a U-tube test-case. The literature has a large number of data, with different fluids, that can be used for our purposes [30; 42; 43; 44; 45; 46; 47; 48]. The most interesting capillary rise experiment in the literature is the case of Quere' [30] (ether-on-glass). Figure 4 shows the comparison of different predictions made through the model of Levine [35], improved with a dynamic contact angle correlation, with Quere' experimental data. In the first case (continuous line) we consider only an equilibrium contact angle value θ_{eq} and consequently, we observe an high error in the prediction of the damping of the fluid column. With the dashed line prediction, we introduce a dynamic contact angle model, based on the hydrodynamic theory, with a standard theoretical coefficient $F_T = 90$ (see eq. 2), the prediction improved considerably but still with an observable mismatch (about 7% on the first peak height). The best prediction is obtained by adjusting the coefficients of the contact angle correlation through application of the inverse method, in a spirit that belongs to Hoffman empirical correlation $\Theta_D = c_t Ca^{0.33}$, where $Ca = \mu\dot{h}/\gamma$ is the *capillary number*. The resulted dotted line show still a small difference compared to the experiment, probably due to the fact we are constraining the main form of the dynamic contact angle equation.

At this point, we understand that in order to make time-accurate predictions in a capillary dominated

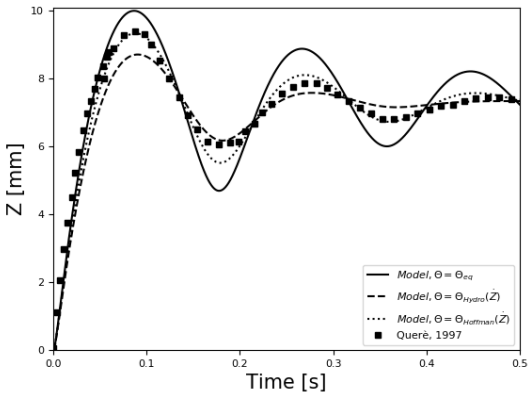

Figure 4: Quere' experiment (1997). Ether on glass tube.

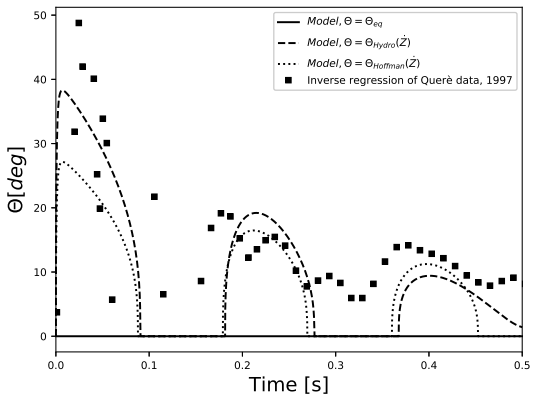

Figure 5: Comparison between different contact angle models and Quere' experiment (1997). Ether on glass tube.

flow situation we need a dynamic contact angle model which accounts for all the physics involved, this feature is still not possessed by standard models. Indeed, we often need to tune the DCA models parameters to be able to *describe* the problem.
We compared the models also by computing the contact angle in time, (fig. 5). In this case, we need also to compute the DCA for Quere' experiment, which is not provided by the paper [30] (as for most of the studies about capillary rise). We use Levine model to derive an explicit equation of the contact angle, function of the position, velocity and acceleration of the interface.

$$\cos\theta_D = \frac{\rho r}{2\gamma}\left[\left(h + \frac{37}{36}r\right)\ddot{h_i} + 8\frac{\mu}{\rho r^2}h_i\dot{h_i} + \frac{1}{2}\left(\frac{4\mu}{\rho r}\dot{h_i} + \frac{7}{3}\dot{h_i}^2\right) + gh_i\right] \tag{13}$$

We observed that this kind of contact angle regression needs to be handled with extreme care. We compute the interface velocity and acceleration by applying a simple gradient operator to the original data, which we smooth by convolution with *Savitzky-Golay filter* [49]. In this procedure we observed a very high sensitivity of the computed contact angle to the resolution and noise on the data of the transient height. We simulated the experiment of Quere' using different sampling frequencies and we found out that an insufficient frequency of acquisition may introduce a shift of the CA curve in time.

The receding phase of the liquid column rebound differs the most from the predictions of the model (fig. 5). According to theory, for a receding contact line the DCA assumes values below the equilibrium CA, for zero contact angle fluids this value is necessary limited to the equilibrium value itself (i.e. $\theta_eq = 0°$ since a negative value is physically meaningless. The indirect measurements of 5 show that the contact angle doesn't respond immediately to the contact line velocity, it is yet decreasing along with the decrease of the mean velocity of the oscillations.
Moreover, we observed that a better match of the transient height is not necessary due to a better match of the contact angle prediction. This could be due to uncertainties linked to the model of the transient height that is used, which could not incorporate every factor. Studies dealing with the transient of the capillary rise shows clearly that the rising velocity is unsteady and that inertial phenomena should be taken into account. Classic correlation based on hydrodynamic theory or empirical formulation based on Hoffman method are too simple to correctly describe the contact angle behaviour in many cases of the literature. They don't consider inertial effect neither a saturation of the contact angle with the contact line velocity. This last point, even if it is reasonably important has been little considered in the literature except of some author who proposed new contact angle correlations which have received little attention e.g. Sciffer correlation (2000) [50].

For the sake of a broader comparison, we computed the contact angle through eq. 13 for a large set of of literature capillary rise experiment and we compared the large number of DCA data points with classic hydrodynamic prediction 6. We observed a large scatter-

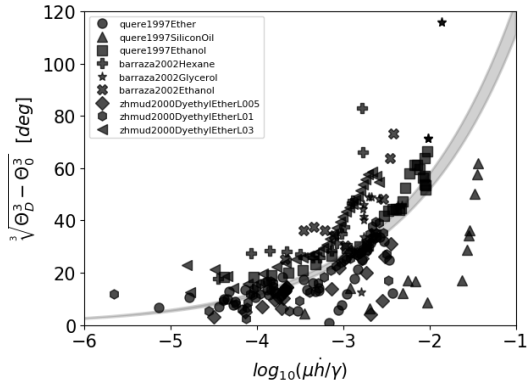

Figure 6: Dynamic contact angle data retrieved through inverse regression of literature data, shaded area is theoretical prediction using Voinov eq. with F_T bounds between 75 and 105 (see eq. 2)

ing of the data around the theoretical prediction even if large bound are allowed for the theoretical coefficient F_T. It is clear that even experiments involving the same couple fluid/material lead to different conclusions about the contact angle behavior, this behaviour has been tentatively emphasized in terms of interface acceleration but this is not the case for all the data points in fig. 6. It is necessary then to elaborate a test-case where the control on the maximum number of parameters involved is guaranteed, and it is possible to separate the inertial behaviour by the steady feature of contact lines. As hinted before, we aim to fulfill these conditions through the U-tube test-case we preliminary tested.

5. Conclusions

1. The oscillating flow in a U-tube may behave in a complex way due its intrinsic unsteady behavior which may need to be introduced at all the levels for the correlations used (wall shear stress and capillarity).
2. We validated an inverse method of contact angle data regression on synthetic data generated using the model equation and superimposed random noise. Very good sensitivities have been achieved and input equations were retrieved with a satisfactory level of accuracy.
   Moreover we demonstrated also the uniqueness of fitness function for the inverse method with several test for an hypothesized theoretical correlation, more test will be carried in the future to prove uniqueness with other test-correlations for CA.
3. Literature data about capillary rise experiment are a big source of information, however the correct retrieval of the contact angle values requires extreme care. In these cases we found standard DCA correlations unable to describe CA behaviour. It is clear that the correlations need to be upgraded in order to take into account the additional physics involved in unsteady cases as accelerating or oscillating contact lines.
4. Future work will be devoted to upgrade the inverse method to be free from any input correlation and determine the most suitable form of the CA using only input experimental data. Genetic programming will be the approach to achieve the desired instrument.
5. The indirect method will be applied to U-tube experimental data as soon as the facility will be available.

Acknowledgments

Part of this work was supported by Fonds WetenschappelijkOnderzoek, FWO project number 1S96120N. We would like to thank also Alessia Simonini for he strong support from the experimental side of the work.

References

[1] M. Dreyer, Free surface flows under compensated gravity conditions, Vol. 221, Springer, 2007.
[2] S. Van Mourik, A. Veldman, M. Dreyer, Simulation of capillary flow with a dynamic contact angle, Microgravity-Science and Technology 17 (3) (2005) 87.
[3] J. Billingham, Nonlinear sloshing in zero gravity, Journal of Fluid Mechanics 464 (2002) 365–391.
[4] A. E. Veldman, J. Gerrits, R. Luppes, J. A. Helder, J. Vreeburg, The numerical simulation of liquid sloshing on board spacecraft, Journal of Computational Physics 224 (1) (2007) 82–99.
[5] R. Luppes, J. A. Helder, A. E. Veldman, The numerical simulation of liquid sloshing in microgravity, in: Computational Fluid Dynamics 2006, Springer, 2009, pp. 607–612.
[6] M. El-Kamali, Ballottement des liquides avec tension superficielle: études statique et dynamique, Ph.D. thesis (2010).
[7] Y. Tang, B. Yue, Y. Yan, Improved method for implementing contact angle condition in simulation of liquid sloshing under microgravity, International Journal for Numerical Methods in Fluids 89 (4-5) (2019) 123–142.
[8] T. Young, Iii. an essay on the cohesion of fluids, Philosophical transactions of the royal society of London (95) (1805) 65–87.
[9] O. Voinov, Hydrodynamics of wetting, Fluid dynamics 11 (5) (1976) 714–721.
[10] R. Cox, The dynamics of the spreading of liquids on a solid surface. part 1. viscous flow, Journal of Fluid Mechanics 168 (1986) 169–194.

[11] T. D. Blake, The physics of moving wetting lines, Journal of colloid and interface science 299 (1) (2006) 1–13.
[12] H. Eral, J. Oh, et al., Contact angle hysteresis: a review of fundamentals and applications, Colloid and polymer science 291 (2) (2013) 247–260.
[13] J. Eggers, Existence of receding and advancing contact lines, Physics of Fluids 17 (8) (2005) 082106.
[14] J. H. Snoeijer, B. Andreotti, Moving contact lines: scales, regimes, and dynamical transitions, Annual review of fluid mechanics 45 (2013) 269–292.
[15] T. Blake, J. Haynes, Kinetics of liquidliquid displacement, Journal of colloid and interface science 30 (3) (1969) 421–423.
[16] P. Petrov, I. Petrov, A combined molecular-hydrodynamic approach to wetting kinetics, Langmuir 8 (7) (1992) 1762–1767.
[17] Y. D. Shikhmurzaev, The moving contact line on a smooth solid surface, International Journal of Multiphase Flow 19 (4) (1993) 589–610.
[18] R. L. Hoffman, A study of the advancing interface. i. interface shape in liquidgas systems, Journal of colloid and interface science 50 (2) (1975) 228–241.
[19] M. Bracke, F. De Voeght, P. Joos, The kinetics of wetting: the dynamic contact angle, in: Trends in Colloid and Interface Science III, Springer, 1989, pp. 142–149.
[20] J. E. Seebergh, J. C. Berg, Dynamic wetting in the low capillary number regime, Chemical Engineering Science 47 (17-18) (1992) 4455–4464.
[21] K. Yokoi, D. Vadillo, J. Hinch, I. Hutchings, Numerical studies of the influence of the dynamic contact angle on a droplet impacting on a dry surface, Physics of Fluids 21 (7) (2009) 072102.
[22] P.-G. De Gennes, Wetting: statics and dynamics, Reviews of modern physics 57 (3) (1985) 827.
[23] R. Golestanian, E. Raphaël, Dissipation in dynamics of a moving contact line, Physical Review E 64 (3) (2001) 031601.
[24] R. Golestanian, E. Raphaël, Relaxation of a moving contact line and the landau-levich effect, EPL (Europhysics Letters) 55 (2) (2001) 228.
[25] G. Delon, M. Fermigier, J. H. Snoeijer, B. Andreotti, Relaxation of a dewetting contact line. part 2. experiments, Journal of Fluid Mechanics 604 (2008) 55–75.
[26] A. Neumann, R. Good, Techniques of measuring contact angles, in: Surface and colloid science, Springer, 1979, pp. 31–91.
[27] L. Tanner, The spreading of silicone oil drops on horizontal surfaces, Journal of Physics D: Applied Physics 12 (9) (1979) 1473.
[28] R. J. Hunter, Foundations of colloid science, Oxford university press, 2001.
[29] S. Dehaeck, Y. Tsoumpas, P. Colinet, Analyzing closed-fringe images using two-dimensional fan wavelets, Applied optics 54 (10) (2015) 2939–2952.
[30] D. Quéré, Inertial capillarity, EPL (Europhysics Letters) 39 (5) (1997) 533.
[31] J. Jurin, Ii. an account of some experiments shown before the royal society; with an enquiry into the cause of the ascent and suspension of water in capillary tubes., Philosophical Transactions of the Royal Society of London 30 (355) (1718) 739–747.
[32] E. W. Washburn, The dynamics of capillary flow, Physical review 17 (3) (1921) 273.
[33] C. Bosanquet, Lv. on the flow of liquids into capillary tubes, The London, Edinburgh, and Dublin Philosophical Magazine and Journal of Science 45 (267) (1923) 525–531.
[34] X. Zhong, B. Sun, S. Liao, Analytic solutions of the rise dynamics of liquid in a vertical cylindrical capillary, European Journal of Mechanics-B/Fluids 78 (2019) 1–10.
[35] S. Levine, P. Reed, E. Watson, G. Neale, A theory of the rate of rise of a liquid in a capillary, Colloid and interface science 3 (1976) 403–419.
[36] Y. Yuan, T. R. Lee, Contact angle and wetting properties, in: Surface science techniques, Springer, 2013, pp. 3–34.
[37] M. M. Weislogel, Steady capillary driven flow.
[38] M. Iguchi, M. Ohmi, K. Maegawa, Analysis of free oscillating flow in a u-shaped tube, Bulletin of JSME 25 (207) (1982) 1398–1405.
[39] E. Shuy, Approximate wall shear equation for unsteady laminar pipe flows, Journal of Hydraulic Research 33 (4) (1995) 457–469.
[40] A. Ogawa, S. Tokiwa, M. Mutou, K. Mogi, T. Sugawara, M. Watanabe, K. Satou, T. Kikawada, K. Shishido, N. Matumoto, Damped oscillation of liquid column in vertical u-tube for newtonian and non-newtonian liquids, Journal of Thermal science 16 (4) (2007) 289–300.
[41] F. T. Dodge, et al., The new" dynamic behavior of liquids in moving containers", Southwest Research Inst. San Antonio, TX, 2000.
[42] H. J. Barraza, S. Kunapuli, A. Edgar, Advancing contact angles of newtonian fluids during high velocity, transient, capillary-driven flow in a parallel plate geometry, The Journal of Physical Chemistry B 106 (19) (2002) 4979–4987.
[43] B. Zhmud, F. Tiberg, K. Hallstensson, Dynamics of capillary rise, Journal of colloid and interface science 228 (2) (2000) 263–269.
[44] A. Siebold, M. Nardin, J. Schultz, A. Walliser, M. Oppliger, Effect of dynamic contact angle on capillary rise phenomena, Colloids and surfaces A: Physicochemical and engineering aspects 161 (1) (2000) 81–87.
[45] G. R. Willmott, C. Neto, S. C. Hendy, Uptake of water droplets by non-wetting capillaries, Soft Matter 7 (6) (2011) 2357–2363.
[46] F. F. Ouali, G. McHale, H. Javed, C. Trabi, N. J. Shirtcliffe, M. I. Newton, Wetting considerations in capillary rise and imbibition in closed square tubes and open rectangular cross-section channels, Microfluidics and nanofluidics 15 (3) (2013) 309–326.
[47] O. Shardt, P. R. Waghmare, J. Derksen, S. K. Mitra, Inertial rise in short capillary tubes, Rsc Advances 4 (28) (2014) 14781–14785.
[48] J. Delannoy, S. Lafon, Y. Koga, E. Reyssat, D. Quéré, The dual role of viscosity in capillary rise, Soft matter 15 (13) (2019) 2757–2761.
[49] A. Savitzky, M. J. Golay, Smoothing and differentiation of data by simplified least squares procedures., Analytical chemistry 36 (8) (1964) 1627–1639.
[50] S. Sciffer, A phenomenological model of dynamic contact angle, Chemical engineering science 55 (23) (2000) 5933–5936.

Toward densified propellants for space launchers: the effect of solid particles on the convective heat transfer coefficient in slurry pipe flows

Maria Teresa Scelzo

Environmental and Applied Fluid Dynamics Department, von Karman Institute for Fluid Dynamics, Belgium, mariateresa.scelzo@vki.ac.be

Supervisors: Jean-Marie Buchlin, Delphine Laboureur and Laura Peveroni

Professor, Environmental and Applied Fluid Dynamics Department, von Karman Institute for Fluid Dynamics, Belgium, buchlin@vki.ac.be

Assistant Professor, Environmental and Applied Fluid Dynamics Department, von Karman Institute for Fluid Dynamics, Belgium, laboureur@vki.ac.be

Project Manager, Aeronautics and Aerospace Department, von Karman Institute for Fluid Dynamics, Belgium, peveroni@vki.ac.be

University Supervisor: Gérard Degrez

Professor, Aéro-Thermo-Mechanics Departement, Université Libre de Bruxelles, Belgium, degrez@ulb.ac.be

Abstract

Slush is a solid-liquid mixture at the thermodynamic triple point characterized by higher density and higher specific enthalpy than the liquid phase. These aspects qualify slush as a promising substitute for rocket propellants, enabling reduced volume tank and longer fuel holding time. However, the presence of solid particles dispersed in the liquid phase modifies the hydraulic transport and heat transfer features, requiring ad-hoc investigations to build suitable design correlations for fuel feed pipelines. This work shows the effect of millimetric particles seeding a liquid turbulent pipe flow on the temperature profiles development and the flow heat transfer coefficient when applying constant heat flux at the boundaries. In order to decouple the thermal features modification from the melting phenomenon that would take place in a slush, the working fluid employed during the experiments is a mixture of water and polystyrene particles, with density ratio of 1.05. The flow Reynolds number spans from 4000 to 20000, and the solid volume fraction is in the range 0-7%.

Keywords: two-phase flow, slurry, heat transfer.

1. Introduction

This project intends to characterize and model slush flows as a propellant for future launcher engines. Nowadays, cryogenic liquids are widely used as fuel in rocket engines due to the high specific impulse they provide. However, given their low density and highly thermo-sensitive nature, they still lead to large storage volume requirements and short holding time. One promising way to reduce these problems is to substitute the liquids with their slush state [1].

Slush is a solid-liquid mixture at the thermodynamic triple point characterized by higher density and higher specific enthalpy than the liquid phase [2]. Recent studies conducted at the SART department of DLR have shown a potential improvement on the gross payload of about 20% if slush replaces the liquid propellant [3]. However, the presence of solid particles in the liquid suspension changes the flow hydraulic transport and thermal properties.This implies that during the design phase of slush pipelines, the standard correlations for the liquid flow pressure drop and heat transfer coefficient are no longer valid.

The first step of the project was the characterization of the pressure drop of an isothermal solid-liquid mixture [4] [5] in flow similarity with slush hydrogen. Mixtures in which the two phases belong to two different species and melting does not occur, are referred to as slurries [6]. The second part of the project, described in this article, studies the effect of millimetric particles on the flow heat transfer coefficient.

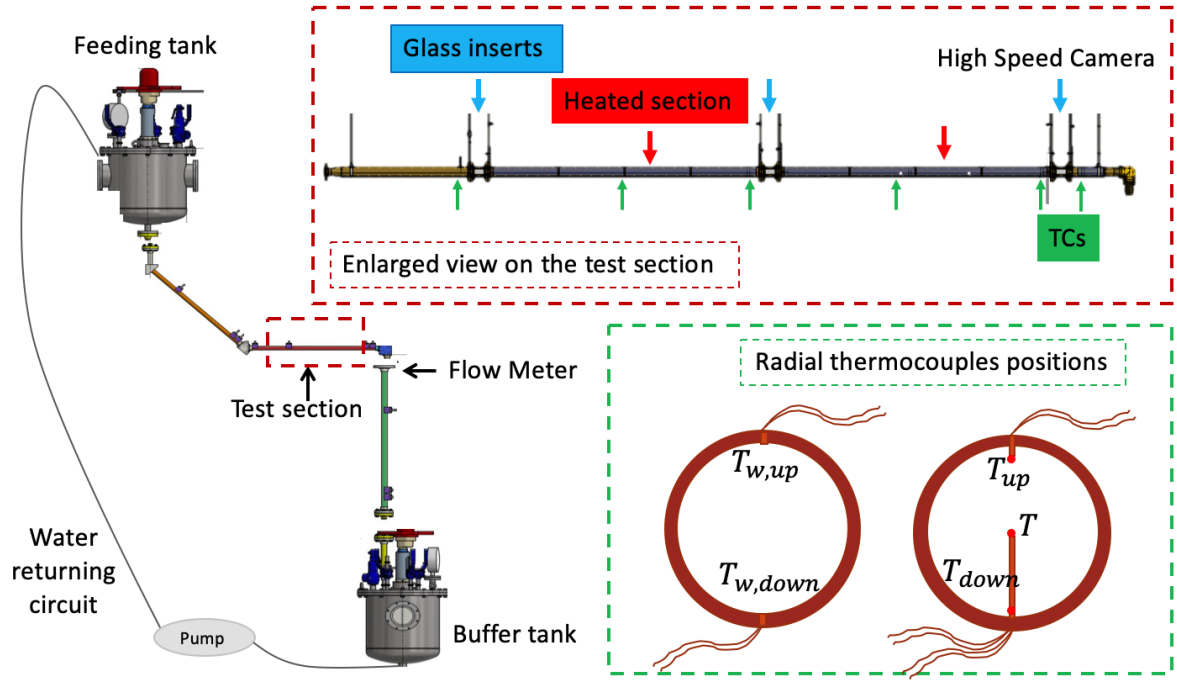

Figure 1: Schematic of the VKI PREDICT facility with water returning circuit; enlarged view of the copper horizontal test section details; radial position of the thermocouples along the pipe cross section.

Experiments are performed in a horizontal pipe, providing heat constant wall heat flux to a turbulent water based slurry, with solid volume fraction up to 7%. This article reports the experimental results found in terms of temperature profile modification and heat transfer coefficient enhancement, when polystyrene spherical particles ($d = 1mm$) seed the liquid flow.

The experimental database is currently being used to verify the capabilities of a Euler-Euler URANS model in OpenFOAM to predict the features of slush flow in non-isothermal conditions.

2. Experimental methods

2.1. Facility and measurements techniques

The experiments are conducted in the VKI PREDICT (PRopEllant DensiIication CompaTibility) facility shown in Figure 1, designed for the experimental characterization of slurry flow in pipelines. The upstream feeding tank is connected to the facility by means of an on-off valve. An electrical stirrer is activated to mix the slurry before and during the experiments, to facilitate the mixture to flow out, towards the test section. The latter is a horizontal copper pipe (internal diameter D=30mm and wall thickness s=5mm) reported schematically in Figure 1. The test section is instrumented with type K (sensor diameter 0.18mm) thermocouples, three across the pipe test section (T_{up},T, T_{down}) and two for wall temperature measurement ($T_{w,up}$, $T_{w,down}$), at six axial positions (green arrows in Figure 1).

The heated test section extends for 2.5 m (corresponding to the red arrows in Figure 1). Electric resistive films (manufactured by Captec France), glued around the copper pipe, provide constant wall heat flux through the Joule effect. The heaters are electrically supplied at 230 V (Solcon TPS31) on three balanced current phases, being the circuit designed to provide up to $50kW/m^2$. The test section presents three glass windows (blue arrows in Figure 1) to allow qualitative flow visualization (with high speed camera Phantom v7) and the evaluation of the solid volume fraction through image post-processing.

On the vertical segment of the facility, the Coriolis meter (Yokogawa Rotamass Prime40) measures the values of mass flow rate and fluid density. About 35 diameters downstream the Coriolis meter, the flow regulation valve aperture defines the flow rate of the slurry passing through the test section and connects the pipeline to the slurry buffer tank.

Table 1: Properties of the slurry phases: liquid phase, water and solid phase, polystyrene particles

slurry phase /material	ρ $[kg/m^3]$	μ $Pa \cdot s$	d $[mm]$	k $[W/mK]$
water	999	0.00089	-	0.6
polystyrene particles	1050	-	0.85-1	1.33

2.2. Test procedure and post processing techniques

The working slurry is a mixture of water and polystyrene particles whose properties are collected in Table 1. These properties enable reduced density ratio ($\beta = \rho_s/\rho_l$) to avoid fast settling of the solid phase in the feeding tank. At the same time, they allow flow conditions similar to those expected in a slush feed pipeline of a typical real launcher's engine.

The experiments are conducted at a constant mass flow rate and for a time long enough to reach constant temperature, i.e. thermal steady-state conditions.

The transient time is evaluated, in first approximation, by solving the 1D unsteady energy equation for the bulk flow and the 1D transient conduction equation for the pipe wall simultaneously (Eq.s 1-2). The system of PDEs is solved with the finite difference method in Matlab, marching in time with an Euler scheme and solving the derivatives in space with a first-order upwind scheme.

$$\rho_f c_f \frac{\partial T}{\partial t} + \rho_f c_f U \frac{\partial T}{\partial x} = h(T_w - T_f) \tag{1}$$

$$\rho_w c_w S \frac{\partial T_w}{\partial t} = \frac{P}{\pi D L} - h(T_w - T_f) \tag{2}$$

In Eq.s 1-2,P is the heat power provided by Joule effect, the subscripts w and f indicates the fluid and the wall properties; ρ is the density and c the specific thermal capacity; U is the flow velocity, L the length of the test section. h is the theoretical heat transfer coefficient evaluated from the Nusselt number (Nu) in Eq. 3, where k is the fluid thermal conductivity. In turn, Nu is calculated according to the Gnielinski's [7] correlation reported in Eq. 4.

$$h = \frac{kNu}{D} \tag{3}$$

$$Nu = \frac{f/8(Re - 1000}{1.07 + 12.7\sqrt{f/8}(Pr^{2/3} - 1)} \tag{4}$$

The Reynolds number (Re) is calculated as in Eq.5.

$$Re = \frac{UD\rho}{\mu_f} \tag{5}$$

It's worth noticing that, in the definition of the Reynolds number throughout this work, ρ is the density of the flow, liquid or slurry, and μ is the viscosity of the liquid. The flow friction factor is calculated as in Eq. 6 [7].

$$f = 1.82(Log(Re_l) - 1.64)^2 \tag{6}$$

The flow Prandt number (Pr) is evaluated at the flow bulk temperature.

Figure 2 shows a typical time evolution of the temperature in a fully liquid test at the outlet section of the horizontal pipe (Position 6). The plot features the numerical calculation and the experimental signal, hence showing the validation of the numerical 1D model *a posteriori*.

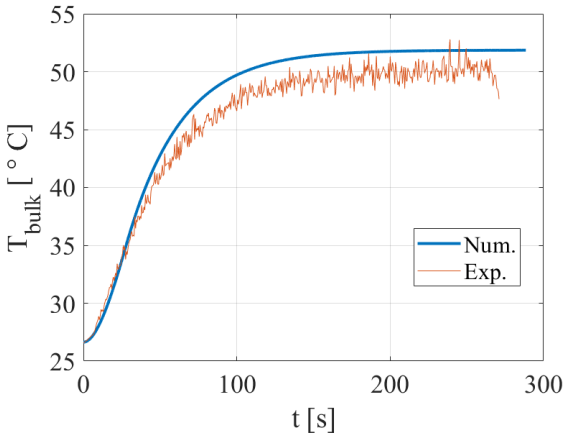

Figure 2: Typical bulk temperature T_f evolution in a fully liquid test, resulting from the experiments (orange curve) and from the solution of Eq.1-2 (blue curve), for $m = 0.06kg/s$ and $P = 6kW$

At $t = 0$ the heaters are switched on. Given the assumption of 1D and fully developed flow, a discrepancy between the experiments and the numerical modelling exists. However, this first calculation gave an order of magnitude of the time needed for the flow to reach the steady state. In the case of Figure 2, with mass flow rate $m = 0.06kg/s$, the transient time is of the order of 110sec.

The VKI PREDICT installation functioned originally in open-loop configuration. This choice avoided undesired accumulation of solid particles in the pump or in the returning circuit, resulting in an unwanted change of solid mass concentration during the test. However, in this case the time to reach the thermal steady state is longer than the testing time allowed by the volume of the feeding tank. Therefore, a pump connects buffer and feeding tanks to have sufficient

test time, thus operating the facility in closed-loop configuration, as shown in Figure 1.

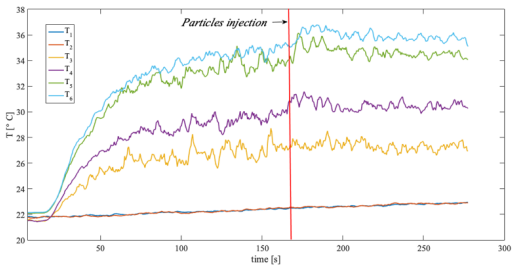

Figure 3: Typical flow temperature evolution recorded at the six axial positions during a slurry test. At t=120sec, after the liquid flow transient time, particles are injected in the feeding tank and slurry flows in the test section

Figure 3 shows a typical evolution of the flow temperature during a slurry test, at the reference six axial positions (highlighted in Figure 1). Once the steady-state in fully liquid conditions is reached, particles are injected in the tank and the slurry flows in the test section. A filter placed in the buffer tank collects the particles, while the water continuously circulates in closed loop. The experimental values reported in the next sections represent the average of minimum 7 seconds of tests during which temperature, mass flow rate and slurry solid volume fraction are constant.

In order to account for the thermal losses, the heat flux is calculated from the energy balance along the test section, as in Eq.7:

$$\dot{q} = \frac{mc(T_{outlet} - T_{inlet})}{\pi DL} \tag{7}$$

where T_{outlet} and T_{inlet} are the outlet and inlet bulk temperature, calculated as in Eq.8:

$$T = \frac{1}{D}\int_0^D Tydy \tag{8}$$

y being the radial coordinate that ranges from 0 to D.

When not otherwise specified, the experimental results presented derive from the last section, in position 6, to ensure the maximum thermal development of the flow. Ultimately, the heat transfer coefficient reads as in Eq.9.

$$h = \frac{\dot{q}}{T_w(x) - T_f(x)} \tag{9}$$

where the wall temperature T_w is the average of the bottom and upper wall temperature values.

2.3. *Experimental uncertainty evaluation*

According to Eq.s 7-8-9, the main source of error on the heat transfer coefficient values is the temperature sensor, being the uncertainty on the pipe section area and mass flow rate negligible. After the thermocouples calibration, the uncertainty of the temperature measurement in one point is estimated equal to maximum $\pm 0.2°C$. According to the law of uncertainty propagation, the uncertainty on h is given by Eq. 10.

$$\frac{\delta h}{h} = \sqrt{2}\frac{\delta \Delta T}{\Delta T} \tag{10}$$

$\delta\Delta T$ is the uncertainty on the sum $T_w - T_f$ and it is estimated equal to a fixed value of $\pm 0.45°C$.

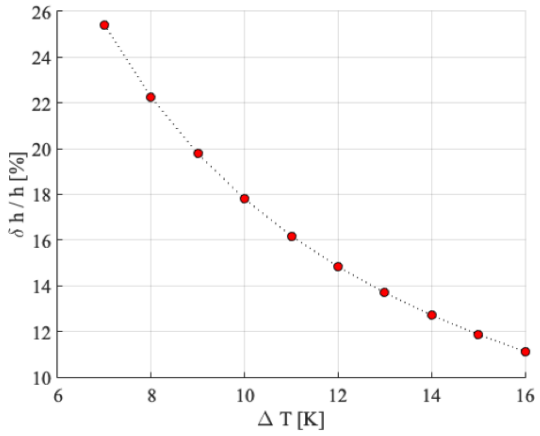

Figure 4: Uncertainty on the heat transfer coefficient values in function of the temperature difference between pipe wall and bulk temperature

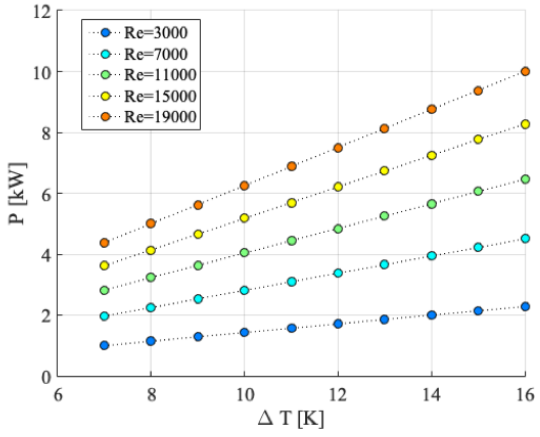

Figure 5: Heat power (P) required to achieve a desired ΔT between wall and bulk fluid for different values of Reynolds number (Re).

Figure 4 shows the expected uncertainty on the value of h depending on the temperature difference achieved between the pipe wall and the bulk flow. Diminishing ΔT produces higher uncertainty on the heat transfer coefficient values. To achieve the desired high values of ΔT, a certain heat power must be provided to the test section, depending on the flow Reynolds number, as illustrated in Figure 5. In theory, the power supply provides current intensity high enough to enable the lowest value of uncertainty on the heat transfer coefficient value (corresponding to $\Delta T = 16°C$) for all the flow conditions. However, the heat power is constrained by the maximum temperature achievable on the heating films surface, $120°C$, thus, it is modulated depending on the flow Reynolds number. This results in a ΔT around $9°C$, leading to an expected uncertainty on h of around 20% for the entire range of Reynolds number.

3. Fully liquid conditions

The first experiments are performed in fully liquid conditions. The goal is twofold: to verify the correct functioning of the newly designed experimental test section; and to have the reference conditions to evaluate the effect of the solid particles on temperature profiles and heat transfer coefficient.

Figure 6 shows the Nusselt number resulted from the experiments in comparison with the Gnielinsky correlation, reported in Eq.4.

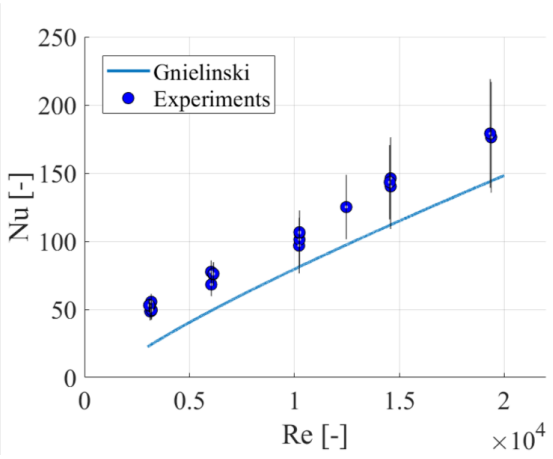

Figure 6: Experimental results of Nusselt number for fully liquid flow in comparison with the Gnielinsky correlation

The deviation between the experimental results with their error bars and the correlation remains below the 25%, common value in heat transfer measurements [8]. However, for the low values of Reynolds number, the discrepancy between experiments and correlation increases up to 110%. This might be due to the only partial thermal and hydraulic development of the flow at low values of Reynolds number. Nevertheless, for the entire range of Reynolds number (Re=3000-20000), the experiments in fully liquid conditions represent the reference case to evaluate the effect of the solid particles, as shown in the next section.

4. Slurry flow conditions

4.1. Temperature profiles analysis

This section reports the analysis of the slurry flow temperature profiles in comparison with the fully liquid conditions at the same mass flow rate and provided heat flux. The two conditions in fact, belong to the same experiment, as described in Section 2.2.

Figures 7 show three exemplary frames acquired with the high speed camera in background light configuration. They correspond to three different slurry flow regimes: (a) full suspension, m=0.28kg/s and α=0.4 %; (b) heterogeneous suspension, m=0.3 kg/s and α= 4 % ; (c) moving bed, m = 0.28kg/s and α=5.4 %. In all the three cases, the temperature profile of the slurry flow (blue line in Figures 7) is higher than the fully liquid conditions (red line in Figures 7).

It is worth noticing that the temperature profile in fully liquid conditions is not symmetric across the pipe section. The asymmetry correlates with the Reynolds number - as Re decreases the asymmetry worsens, and with the heat power - the asymmetry strengthens at the highest heat power values. This behaviour might stem from the influence of the 45° bend upstream the test section (Figure 1) together with natural convection occurring at the pipe outside boundaries. This fact, however, does not prevent to evaluate the effect of the solid particles on the temperature profile and on the flow heat transfer coefficient.

For fully suspended slurry (Figure 7 (a)), the temperature increases uniformly along the pipe cross-section. On the other hand, when the distribution of particles is heterogeneous (Figure 7 (b-c)), the temperature shows an increase at the bottom part of the pipe higher than the upper positions. As expected, the enhancement of the temperature values depends on the slurry solid content.

In fact, according to the energy conservation equation, given a fixed heat flux, the mixture is expected to increase its outlet temperature depending on the specif heat of the mixture, as expressed in Eq. 11.

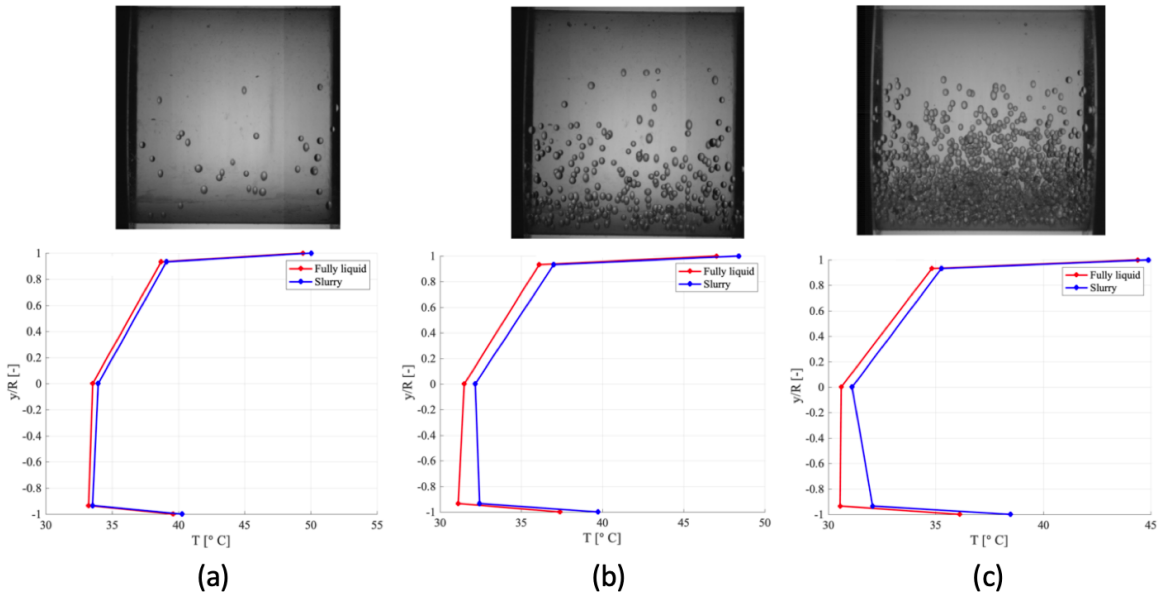

Figure 7: Exemplary flow conditions and temperature profiles for (a) full suspension, m=0.28kg/s and α=0.4 %; (b) heterogeneous suspension, m=0.3 kg/s and α= 4 % ; (c) moving bed, m = 0.28kg/s and α=5 %.

$$[T - T_l]_{out} = \frac{q}{\dot{m}}\left(\frac{1}{c} - \frac{1}{c_l}\right) \tag{11}$$

The specif heat of the mixture c can be evaluated as the averaged of the two phases weighted on the solid volume fraction, as in Eq.12.

$$c = c_s\alpha + c_l(1 - \alpha). \tag{12}$$

Figure 8 shows the comparison between the expected enhancement of the temperature profile $[T - T_l]_{out}$ and the one calculated from the experimental temperature profiles. The vertical error bars represent the experimental uncertainty on the quantity $[T - T_l]_{out}$, being T the bulk temperature at the outlet section.

In order to combine the effect of the mass flow rate and the solid volume fraction, the experimental data are classified according to a modified Richardson number as in Eq. 13.

$$Ri^* = \frac{U^2}{gD}\frac{1}{1 + (\beta - 1)\alpha} \tag{13}$$

This quantity represents the ratio between the gravitational inertia of the mixture over the shear flow of the liquid phase. According to the definition, Ri^* decreases at low mass flow rate and high solid volume fraction. These conditions favor the settling of the solid particles enabling the transition of the slurry from suspension to moving bed.

According to this approach, at values of Richardson number higher than 0.28, the behavior predicted by the theory meets the experiments within the uncertainty of the measurements. On the other hand, for lower values of Richardson number, the particles undergo strong settling toward the bottom pipe wall where the flow velocity decreases and the solid volume fraction increases. These conditions cause an overheating of the lower part of the pipe and the departing of the bulk temperature from the expected behaviour predicted by Eq.11 and represented by the continuous black line in Figure 8. This suggests that the temperature modification is driven by the solid volume fraction as well as by the slurry flow regime, hence, by the proposed Richardson number.

The overheating of the bottom wall in slurry horizontal pipe flow is reported also by Rozenblit et al. [9]. The slurry was a mixture of water and plastic acetal particles; the Reynolds number was between 19000 and 55000, and the concentration of solid particles was between 6% and 15%. The authors measured the pipe wall by means of an electro-resistance sensor and infrared imaging. The measurements showed that the bed of particles produces a screen effect, so that the temperature of the wall increases.

On a final note, the flow regime influences also

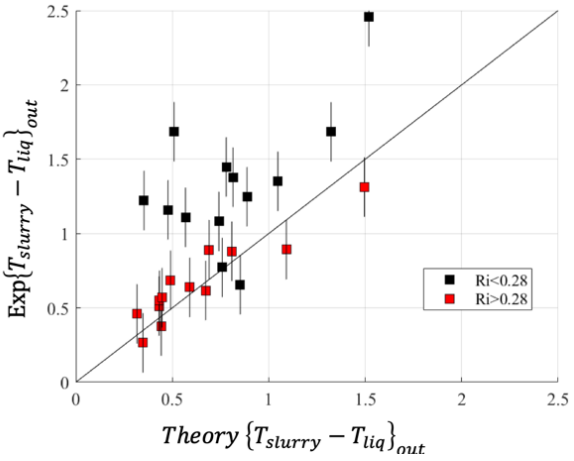

Figure 8: Enhancement of the slurry bulk temperature with respect to the fully liquid conditions; experimental results are compared with the energy equation.

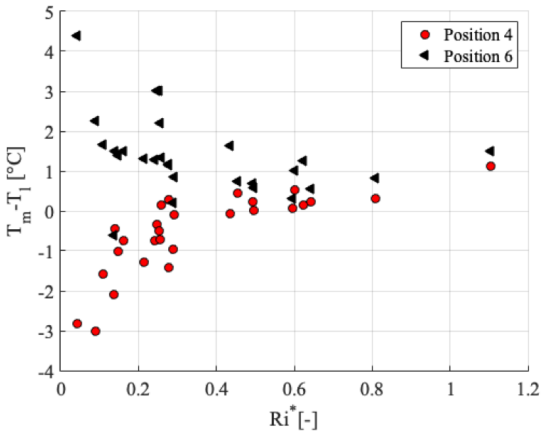

Figure 9: $[T_w - T_{wl}]$ at the bottom pipe wall in function of Ri^*, at position 4 (red marks) and at position 6 (black marks).

the slurry thermal development in the pipe axial direction. Figure 9 shows the difference between the slurry and the liquid temperature profile at the wall $[T_w - T_{wl}]_{bottom}$.Let us consider positions 4 and 6 of the test section (Figure 1) represented with two different marks in the plot. The difference $[T_w - T_{wl}]_{bottom}$ is shown in function of the modified Richardson number. At large value of R^*, the flow is already established at position 4, thus the difference $[T_w - T_{wl}]_{bottom}$ remains nearly constant until the last position 6. On the other hand, at flow conditions corresponding to moving bed and heavily concentrated suspension (at $Ri < 0.28$), the temperature profiles keep evolving along the section. Previous studies about slurry flows and heat transfer do not report analog studies or investigation on slurry temperature profiles. The hypothesis of later slurry development at low Ri^* will be supported by flow visualization in multiple sections along the horizontal segment. The results will possibly confirm that this trend links to the particles distribution evolution along the pipe axial direction. On the other hand, the solid phase increases the apparent viscosity of the mixture, leading to a decreased equivalent Reynolds number (calculated with the mixture viscosity) than the liquid flow at the same mass flow rate, hence, to a later thermal development of the flow.

4.2. Slurry flow heat transfer coefficient

Past studies concerning the thermal features' modification due to the presence of solid particles, solely focused on the effect of the dispersed phase on the flow heat transfer coefficient. Indeed, among the techniques to enhance the heat transfer coefficient (for example, secondary flows for heat exchangers), seeding the flow with particles has gained increasing importance.

The effect of the solid volume fraction on the convective heat transfer coefficient was first analyzed by Zisselmar et al. [10]. Experiments were performed with particles of mean diameter between 12 μm and 120 μm, in a water slurry at Reynolds number between 88000 and 164000. The heat transfer coefficient enhancement, defined as in Eq. 14, showed a pick at around 3 % in solid volume fraction.

$$h^* = \frac{h_{slurry} - h_l}{h_l} \tag{14}$$

For solid content higher than 15%, the h^* reduced to negative values. The authors argued that, since the main resistance to heat transfer resides in the viscous sub-layer, an enhancement of heat transfer must be due to disturbances of this region. This happens when the flow turbulent structures are of the same order of magnitude of the slurry particles and if the particles-particles interaction is not too important. In fact, as the solid volume fraction increases, the turbulence is hampered and the heat transfer coefficient decreases.

Ever since, the key parameter to evaluate the slurry heat transfer coefficient enhancement has become the particles diameter, in particular the parameter d^* reported in Eq 15 and defined as the ratio between the particles diameter and the Kolmogorov scale of the flow.

$$d^* = \frac{d}{D} Re^{11/16} \tag{15}$$

Brandon et al. [11] conducted experiments in vertical and horizontal pipes, with glass spheres of mean diameter from 20 μm to 860 μm, at solid volume fraction lower than 2%, in a turbulent water based slurry fully suspended at Reynolds number between 20000 and 90000. The authors showed that the enhancement of the slurry heat transfer coefficient with respect to the fluid flow reached a pick at $d^* = 4.2$. Ozbelge et al. [12] collected experimental data for a water slurry with feldspar particles of size up to .22mm, with $\alpha < 3\%$ and Reynolds number from 14000 to 115000. The authors reported the appearance of different flow regimes such as fixed and moving bed, and heterogenous and homogeneous suspension of particles. These data were later correlated in terms of h^* and d^* [13] and showed a trend similar to [10] and [11]. For all these experiments, the peak of enhancement corresponds to a d^* equal to:

$$d^*_{max} = 11.9\left(\frac{\rho_l}{2\rho_s + \rho_l}\right)^{0.5} \tag{16}$$

It's worth mentioning that for the experiments found in literature and mentioned in this literature survey the density ratio $\beta = \rho_s/\rho_l$ was of the order of 2.5 and particles size lower than 0.8mm.

Figure 10 shows the data collected for the present work, in terms of h^* and d^*. For each experiment, the values of h_l and h_{slurry} and Re are calculated according to the definitions in Section 2.1. The maximum

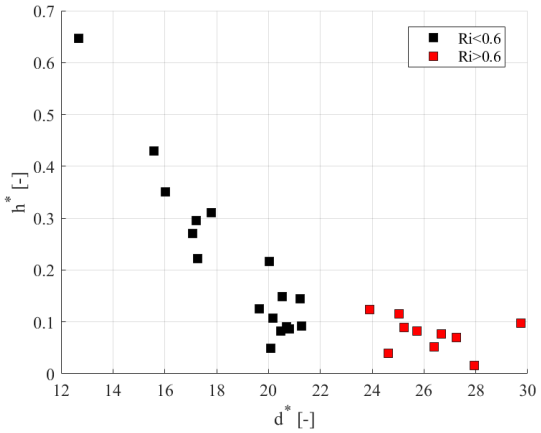

Figure 10: Heat transfer coefficient enhancement h^* in function of the dimensionless particles size d^*, classified in terms of the modified Richardson number.

enhancement expected at $d^*_{max} = 6.7$ is not reached because the particles size is fixed at 1mm and lower values of Reynolds number are not achievable in the PREDICT facility. Further experiments will be performed with particles characterized by $d = 0.4mm$ in order to complete the expected bell-shape like curve.

The data are again classified in function of the modified Richardson number. At high values of Reynolds number (cases at high Ri^*), the slurry heat transfer coefficient h shows a modest increment with respect to the liquid one h_l. At low Ri^*, h^* the significantly increases. This is due to the higher thermal conductivity of the concentrated slurry at the bottom part of the pipe. Consistently, in the upper part of the pipe, the water accelerates due to the decreased available flowing area.

A modified d^* is used to compare the present experiments with the literature ones, that is d^* multiplied by the density ratio of the correspondent mixture β. Hence, the comparison with the experimental data from Ozbege et al. [12] and [13] is shown in Figure 11. It can be concluded the heat transfer coefficient enhancement linked to the presence of the dispersed phase occurs likewise at higher values of particles size (1mm).

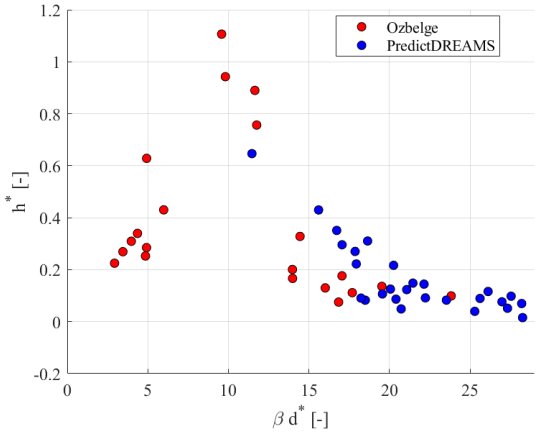

Figure 11: Heat transfer coefficient enhancement parameter h^* in function of the dimensionless particles size βd^*, compared with literature data.

5. Conclusions

This work reports on the results of the latest experimental campaign of the project PREDICT. The project aims to characterize the features of slurry transport in flow conditions similar to the ones expected for slush flowing in a real launchers'engine feed line. The chosen slurry is a mixture of water and polystyrene particles, with a narrow particles size distribution with

$d_{mean} = 1mm$ and density ratio $\beta = 1.05$. The flow Reynolds number spans from 4000 to 20000, and the solid volume fraction is in the range 0-7%.

It is shown that slurry bulk temperature is higher than the fully liquid phase at the same mass flow rate and provided heat flux. This, for $Ri^* > 0.28$ links directly to the slurry composition and to the diminished specific heat capacity c of the mixture. On the other hand, for $Ri^* < 0.28$, the particles settle on the bottom part of the pipe due to the gravity and produce an asymmetrical temperature profile. The particles, in fact, cause a screen effect at the wall increasing the bulk slurry temperature that, thus, deviates from the expected value.

The slurry regime as well affects the so called slurry thermal development. In fact, the difference between slurry and liquid temperature profiles stabilized after about 50 diameter for $Ri^* > 0.28$. Contrarily, at low values of mass flow rate, i.e. $Ri^* < 0.28$, the slurry temperature profile did not reach full development. Currently, it is unclear if this behavior is due to the partial thermal development of the flow at low Reynolds number or it stems from the dynamic of the particles settling. This point will be clarified with flow visualization in multiple sections along the pipe.

It is also found that the heat transfer coefficient of this slurry is always higher than the correspondent fully liquid conditions. The enhancement is more pronounced at lower Reynolds number due to the slurry transition between heterogeneous suspension to moving bed regime. The reason is twofold: in the upper region of the pipe, the water assumes a higher velocity because of the reduced flowing section available; in the lower part, the particles cause higher thermal conductivity.

The experimental data will be used to verify the applicability of a Euler-Euler numerical model to predict the thermal features of a slurry flow flow, temperature profiles and heat transfer coefficient enhancement.

Acknowledgments

This research project is supported by the ESA Networking/Partnering Initiative. The Ph.D. program of M.T. Scelzo is funded by FNRS through the FRIA grant. The author gratefully acknowledges the support of Mr. L. Neubourg during the experimental campaign.

References

[1] A. Friedlander, R. Zubrin, T. L. Hardy, Benefits of slush hydrogen for space missions, Cryogenics 52 (7-9) (2012) 428–440.

[2] K. Ohira, A. Ota, Y. Mukai, T. Hosono, Numerical study of flow and heat-transfer characteristics of cryogenic slush fluid in a horizontal circular pipe (slush-3d), Cryogenics 52 (7-9) (2012) 428–440.

[3] E. Dumont, S. Stappert, T. Ecker, J. Wilken, S. Karl, S. Krummen, M. Sippel, Evaluation of future ariane reusable vtol booster stages, 9 VKI Ph.D. Symposium, 5-7 March 2018.

[4] M. Scelzo, Experimental characterization of a solid-liquid mixture flowing in circular pipes, 9 VKI Ph.D. Symposium, 5-7 March 2018.

[5] M. Scelzo, Numerical simulations of a slurry flow in horizontal and vertical pipes: Effect of forces modelling, 10 VKI Ph.D. Symposium, 5-7 March 2019.

[6] C. E. Brennen, C. E. Brennen, Fundamentals of multiphase flow, Cambridge university press, 2005.

[7] V. Gnielinski, New equations for heat and mass transfer in turbulent pipe and channel flow, Int. Chem. Eng. 16 (2) (1976) 359–368.

[8] A. Bejan, A. D. Kraus, Heat transfer handbook, Vol. 1, John Wiley & Sons, 2003.

[9] R. Rozenblit, M. Simkhis, G. Hetsroni, D. Barnea, Y. Taitel, Heat transfer in horizontal solid–liquid pipe flow, International journal of multiphase flow 26 (8) (2000) 1235–1246.

[10] R. Zisselmar, O. Molerus, Investigation of solid-liquid pipe flow with regard to turbulence modification, The Chemical Engineering Journal 18 (1979) 233–239.

[11] C. A. Brandon, D. G. Thomas, Transport characteristcs of suspensions, in: Proc. 4th Int. Heat Transfer Conf. Paris 1970, 1970, pp. Paper no CT–2.

[12] T. Ozbelge, G. Somer, Hydrodynamic and heat transfer characteristics of liquid-solid suspensions in horizontal turbulent pipe flow pipe flow, The Chemical Engineering Journal 38 (1988) 111–122.

[13] T. Ozbelge, The location of peak heat transfer enhancement in suspension flows, Int. J. Multiphase Flow 19 (3) (1993) 535–538.

Multi-dimensional design and optimization of a hypersonic propulsion system

Ali Can Ispir

Aeronautics and Aerospace Department, von Karman Institute for Fluid Dynamics, Belgium, ali.can.ispir@vki.ac.be

Supervisors: Bayindir H. Saracoglu and Thierry Magin

Research Manager, Aeronautics and Aerospace Department, von Karman Institute for Fluid Dynamics, Belgium, bayindir.saracoglu@vki.ac.be

Professor, Aeronautics and Aerospace Department, von Karman Institute for Fluid Dynamics, Belgium, magin@vki.ac.be

University Supervisor: Axel Coussement

Professor, Aero-Thermo-Mechanics Department, Universit libre de Bruxelles (ULB), axcousse@ulb.ac.be

Abstract

Hypersonic aviation is a remarkable candidate as a solution for future of high-speed civilian air transportation. One of the key enabler to fly hypersonic speeds is the propulsion system design provide thrust from take-off till landing. Such propulsion plants are generally comprised of combination of two distinct engines in order to propel the hypersonic aircraft along the whole flight trajectory without on board oxidizer. The design of the engine component and the operational conditions varying along the flight trajectory play a significant role in determination of the performance of the power plant.

The first part of this doctoral research is devoted to design and optimize the combined cycle propulsion plant of STRATOFLY MR3 which is the contemporary European civil hypersonic aircraft concept. The propulsion plant of this hypersonic aircraft is comprised of six air turbo rockets (ATR) and one dual mode ramjet/scramjet engine (DMR). The aircraft is propelled by ATR engines from take-off till cruise speed of Mach 4.5. DMR engine kicks in after Mach 1.5 to contribute thrust during the supersonic acceleration phase of the flight trajectory. In order to estimate the performance of the power plant in subsonic and supersonic cruise conditions (up to M=4.5), one-dimensional transient thermodynamic model of ATR and DMR engines are created in Ecosimpro, an object-oriented multidisciplinary simulation platform. The model is also coupled with CADO which is an in-house code optimizer to set proper boundary and operational conditions for the best engine performance. It basically utilizes several analytical relations to simulate engine operation under real flight conditions. In operation of ATR engines, air flow is taken in the engine duct by a supersonic inlet, compressed by an air compressor, mixed with hydrogen fuel and burnt in a combustion chamber, after that exhaust gaseous leaves the aircraft via diverged nozzle. Before the fuel is injected to air stream, it is heated up by heat exchangers, collecting the excess heat from the combustion chamber and the nozzle, and passes through a fuel expander turbine. The mechanical power produced by the turbine is used to drive the compressor and fuel pump. The analytic relations offer to resolve combustion phenomena by using Gibbs minimum energy approach in the combustor and nozzle parts. The compression/expansion in the compressor, fuel turbine, turbo-pump and nozzle are figured out by using isentropic expressions. In addition, amount of heat picked up from the combustor and nozzle parts, and regenerated by the heat exchangers, is computed by empirical convective heat transfer correlations. The several steady state 1D thermodynamic simulations and optimization study were firstly performed for various subsonic and supersonic flight cruise speeds. In order to investigate transient engine performance along the flight trajectory, time-dependent simulations have been run by adding time derivative term to governing equations in the engine thermodynamic models.

The aircraft is propelled by only DMR engine after cruise speed of Mach 4.5. The engine consists of four main components which are intake, isolator, combustor and nozzle. The incoming air is compressed along ramps in the intake. The pressure and temperature values of the air increase along the shock wave in the isolator and

fuel is injected from struts to the air stream. When fuel air mixture reaches auto-ignition limit, it burns in the combustor and is expanded along the nozzle. The flow regime is fully supersonic in scramjet mode of the engine so combustion process of the fuel air mixture takes place in supersonic conditions. In the course of the current thesis work, a tool has been developed to calculate the scramjet performance along the hypersonic phase of the flight trajectory. It solves 1D inviscid steady flow transport equations and calculating finite rate chemistry by using Arrhenius approach for supersonic combustion.

The flow field through the DMR engine duct is rather complex due to shock compression at the inlet as well as the shock train along the combustion chamber section. One of the most important challenges is to estimate where and at which rate fuel and air are mixed. Mixing length and efficiency directly affect the reaction process and pressure rise along the duct so they have impact the engine thrust and performance level. It is worth to note that there are many parameters affecting these mixing properties in supersonic combustion such as injector properties, flight conditions, chemical properties of fuel air composition and engine duct geometry. In second part of this doctorate study, CFD simulations will be performed to investigate aforementioned parameters and data mining techniques will be coupled with the simulations to avoid excessive computational costs.

This project has received funding from the European Union's Horizon 2020 research and innovation programme under grant agreement No 769246.

Keywords: high speed propulsion, hypersonic aircraft, 1D thermodynamic simulations, supersonic flow, data mining

---

LIQUID METAL AND INDUSTRIAL FLOWS

Offline powder-gas nozzle jet characterization for coaxial Direct Laser Deposition

Zoé Jardon

Environmental and Applied Fluid Dynamics Department, von Karman Institute for Fluid Dynamics, Belgium, zoe.jardon@vki.ac.be

Mechanical Department, Vrije Universiteit Brussel, Belgium, zoe.jardon@vub.be

Supervisor: Jeroen van Beeck

Head of department and Professor, Environmental and Applied Fluid Dynamics Department, von Karman Institute for Fluid Dynamics, Belgium, vanbeeck@vki.ac.be

University Supervisor: Patrick Guillaume

Head of department and Professor, Mechanical Department, Vrije Universiteit Brussel, Belgium, patrick.guillaume@vub.be

Abstract

One of the major challenges faced by Direct Laser Deposition (DLD) is the process efficiency. This efficiency is significantly affected by the percentage of blown powder that effectively reaches the spherical metal melt pool. Increasing the process efficiency would allow to reduce the overall costs of the DLD process and consequently reduce the printed part cost. The present work focuses on the experimental characterization of the powder-gas jet in terms of powder stream shape, stand-off distance and powder-jet focus diameter. The previous parameters are linked to the blown powder settings (carrier gas, shielding gas, powder feed rate) and optimized to maximize the deposition efficiency and minimize the powder waste. The determination of the optimal powder settings is also essential to obtain good thermo-mechanical properties and a high microstructure quality of the printed parts. The study is performed for metal powders with different particle diameter distributions.

Keywords: Direct Laser Deposition, Coaxial nozzle, Powder jet, Stand-off, Powder-jet focus, Blown powder

1. Introduction

1.1. Additive Manufacturing of metals

Metal Additive Manufacturing (AM), more commonly known as 3D metal printing, introduces the "imagination is the limit" concept in the manufacturing. 3D printing is a promising technology with maximum design freedom, to which there is often referred to as "rapid prototyping". Building layer by layer, the technique prints components with highly complex geometries from almost any digital model. Therefore, the determining factor for the cost of a printed component is different with respect to components made by conventional manufacturing techniques. This factor switches from component complexity to component size and/or the amount of material used.

1.2. Direct Laser Deposition

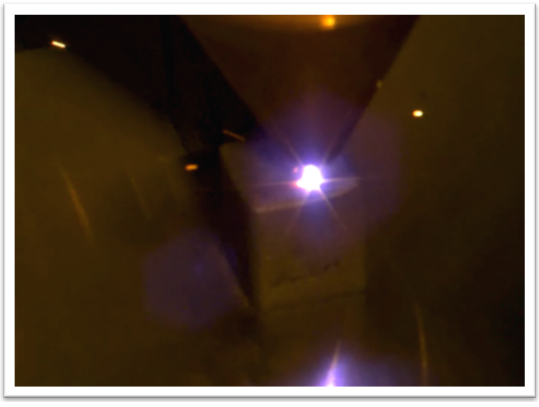

Figure 1: Direct Laser Deposition process (MiCLAD machine of Vrije Universiteit Brussel : print of cube with dimension 9x9x9mm)

Presently, a variety of different metal additive manufacturing technologies exist on the market. Direct Energy Deposition (DED) and Powder Bed Fusion (PBF) are the most known and widespread technologies for metal 3D printing. Both processes rely on the deposition of metal that is fused by a concentrated heat source (laser or electron beam). Direct Laser Deposition (DLD) is a type of DED technology and is defined as an additive manufacturing process that uses a laser heat source to melt and fuse either metal wire, filament or powder.

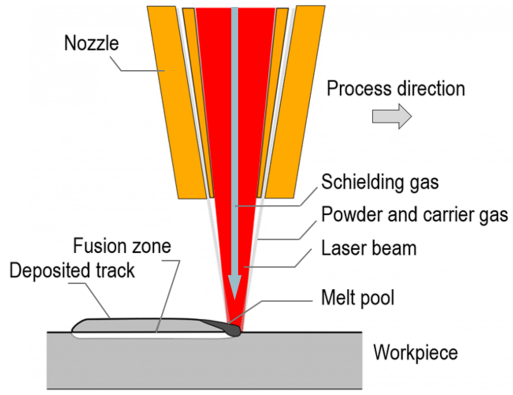

Figure 2: Direct Laser Melting process principle

The present work is more specifically based on the Direct Laser Melting (DLM) or Laser Metal Deposition (LMD) additive manufacturing technique, characterized by the simultaneous laser and powder delivery, see Fig. 1. The DLM process is used in multiple industries such as aviation, aerospace, automotive, medical and energy industry. As presented in Fig. 2, metal powder particles are carried by means of a carrier gas through channels in the nozzle head. The laser heat source goes through the inner nozzle cone and locally initiates a liquid metal melt pool on the workpiece surface in which the fine metal powder particles are melted and subsequently fused with the base material. The shielding gas going through the inner nozzle cone is used to minimize oxidation of the workpiece surface and to protect the optical system in the nozzle head from any possible damage during the printing process (for example ricocheting heated metal particles).

1.3. Powder-gas nozzle jet

In a very short time, during the layer-wise bounding of the material, many complex interconnected physical phenomena take place during the DLM process (thermal energy transfer, laser/powder/gas interactions, melt pool initiation, localized solidification, ...) [1]-[2]. Therefore, it is essential to characterize the powder-gas jet as an initial step for further understanding and quantification of these different physical phenomena as well as their effect on the printed part quality.

For the DLM process, different nozzle configurations exist, see [3]. Multi-jet or discrete coaxial powder nozzles (minimum of 3 powder jets) are robust nozzles and are generally used to deposit wider tracks and thicker metal layers. Coaxial multi-directional powder nozzles on the other hand, are convenient for narrow deposition tracks (and small powder-jet focus diameters) and to obtain a high powder efficiency. Coaxial nozzles are furthermore easier to use and have the advantage to be omni-directional. The present study focuses on coaxial nozzle flow and therefore the nozzle cut shown in Fig. 3. represents an axisymmetric cut of the used nozzle.

The flow generated by the coaxial nozzle is a 3-dimensional two-phase gas-powder turbulent flow. The parameters influencing the flow behavior, process efficiency and final component quality are the carrier gas volumetric flow rate (in l/min), shielding gas volumetric flow rate (in l/min), powder mass flow rate (in g/min) and the metal powder characteristics (particle shape, particle size distribution and production technique).

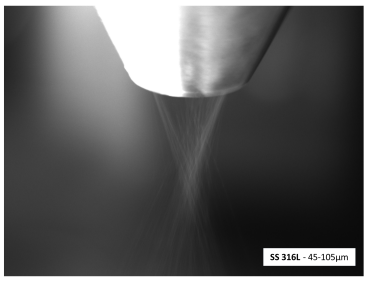

Figure 3: Long exposure powder-gas nozzle jet visualization

1.4. Objectives and methodology

In comparison with the wire-fed process, DLM allows to deposit finer features and facilitates the real time control of powder dynamics. However, the

main drawback is the powder waste and slower print-process in comparison with fire-fed [4].

One of the major challenges faced by Direct Laser Deposition (DLD) and more precisely Direct Laser Melting (DLM) is the process efficiency. The efficiency is significantly affected by the percentage of blown powder that effectively reaches the spherical melt pool. Increasing the process efficiency would allow to reduce the overall costs of the DLD process and consequently reduce the printed part cost. The determination of the optimal powder settings is also essential to obtain good thermo-mechanical properties and a high microstructure quality of the printed parts.

The present work focuses on the experimental characterization of the powder-gas jet in terms of powder stream shape, stand-off distance and powder-jet focus diameter. The stand-off distance represents the distance between the nozzle tip and the focus of the nozzle jet. During the print process itself, the stand-off distance must be set as nozzle tip - melt pool distance in order to optimize the process efficiency. The powder-jet focus diameter represents the width of the nozzle jet in the focus plane. For optimal efficiency, the powder-jet focus should have a similar or smaller dimension as the melt pool size (that has about the same dimension as the laser spot). Note that the laser spot size is determinant for the printing precision and therefore cannot be enlarged without consequences. The two previously cited parameters are linked to the blown powder settings (carrier gas - CG, shielding gas - SG, powder feed rate - FR) and optimized to maximize the deposition efficiency and minimize the powder waste.

To perform this experimental study, different in-situ optical (high-speed) image-based techniques [5]-[9] are compared in terms of stand-off distance and powder-jet focus diameter. The study is performed for powders with different particle diameter distributions and the effect of powder particle diameter on the powder-gas jet characterization is analyzed. Note that the study is carried out on free nozzle flow, without the presence of a substrate/melt pool under the nozzle head.

2. Experimental study: high speed powder jet visualization and characterization

2.1. Set-up description

An experimental set-up is designed to visualize and characterize the powder gas nozzle jet flow during the Direct Laser Melting deposition process. The experiments are performed on the MiCLAD hybrid Direct Laser Melting in-house developed machine by the Additive Manufacturing Research Group of the Vrije Universiteit Brussel and are non-intrusive. Fig. 4. shows the experimental set-up and identifies every component.

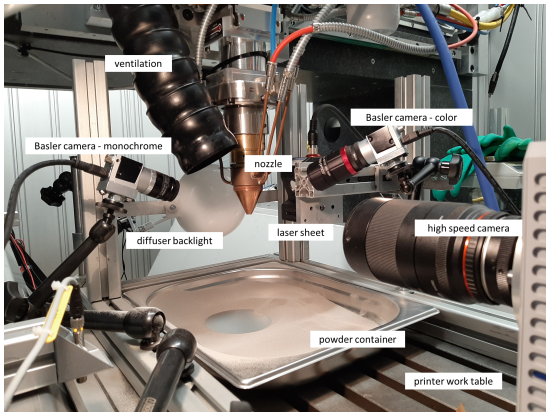

Figure 4: Set-up description powder-jet characterization on MiCLAD machine

The used nozzle is a Fraunhofer ILT COAX-40-S coaxial nozzle with nozzle tip of 7.5mm diameter. Argon is used as both carrier gas and shielding gas. The metal powder particles used for the experiments are gas atomized 316L stainless steel powders from Carpenter Additive, known to be near-spherical. Powders with two different particle size distributions are used. A sieve analysis of the powders resulted in the following particle size ranges : 15-45μm and 45-106μm. Powders of different sizes show both microscopic and macroscopic differences. Microscopic differences between metal powder can among others be seen on Scanning Electron Microscopy (SEM) micrographs. Fig. 5. shows a SEM image of the 316L 45-106μm powder used for the experiments of this study. On the other hand, powders can also show macroscopic differences in terms of flowability, cohesiveness and electric charge that can influence the powder-jet behavior.

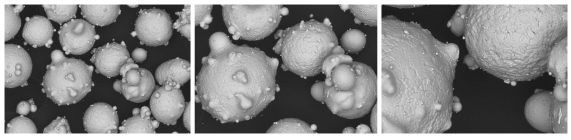

Figure 5: Scanning Electron micrograph of 316L powder particles with magnification x300, x500, x1000 from Additive Carpenter

A ventilation unit is used to extract the smaller metal particles that are ”floating” around the nozzle. An experimental verification was performed to confirm the non-influence of the ventilation on the powder-jet flow. The powder coming from the nozzle is caught by a powder container placed on the printer worktable. Two Basler cameras (acA720–540uc color, ac A720–540um monochrome) with adapted objectives are mounted on both sides of the nozzle head. A Photron SA1.1 high speed camera is mounted in the front of the nozzle and used to acquire high speed images of the metal powder flow.

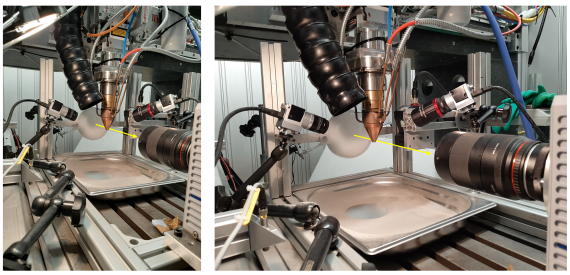

Figure 6: Back-light illumination set-up (1)

In terms of illumination, 3 configurations are tested and compared. The first configuration, shown in Fig. 6, relies on the maximization of the contrast between the powder particles and background. For this purpose, and for a good detection of the metal particle contours, back-light illumination is used and set by means of a LED lamp (KDP Bulb LED MR16 GU5.3 12V, 2800K, 5W) connected to a DC voltage supply in order to avoid flickering phenomena on the acquired images. A spherical diffuser is placed in front of the light source to have a uniform background on the acquired images.

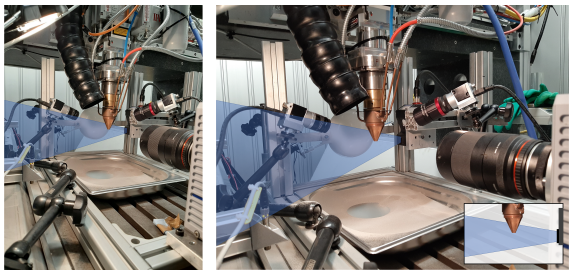

Figure 7: Vertical laser sheet illumination set-up (2)

As second light source, a visible line laser of wavelength 405nm with output power of 4.8mW (class 2 laser product) is used for the second and third configuration of the experiments. According to the laser specifications, the line thickness is approximately 50μm. In practice, from visual measurements performed with a calibration plate, the line shows a larger thickness of approximately 0.5mm. This line laser is mounted both horizontally and vertically with respect to the nozzle axis. Both configurations are clarified hereunder in Fig. 7 and Fig. 8.

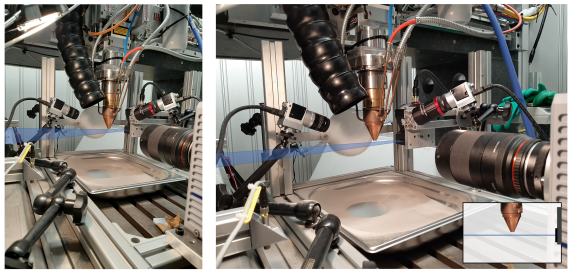

Figure 8: Horizontal laser sheet illumination set-up (3)

For the 3 configurations it is assumed that the light attenuation (conf. 1) or light scattering (conf. 2,3) caught by the camera sensors are linearly proportional to the particle concentration, according to Mie's Theory [10]-[11] :

$$L = \frac{I_{v,ref} r^2}{A} = \frac{I_{inc} n V}{k^2 A} F(\delta, \Phi) \qquad (1)$$

Which relates L, the average luminance of the scattering element, with I_{ref}, the light reflected at distance r by the n particles contained in volume v. I_{inc} stands for the incident light on the particles. K is the wave number, F_i is a dimensionless function of the orientation of the particle and the state of polarization of the incident light and A is the projected area of the volume. Since only a relative value for particle concentration is needed to find the focal plane, no calibration is required.

2.2. Results: Powder-gas nozzle jet characterization

Back-light jet characterization

The raw images obtained with the back-light configuration for both powder distributions are shown in Fig. 9. The nozzle tip is visible in black on the top of the images. The powder jet images are acquired with maximal camera aperture in order to reduce the focal plane width as much as possible. Care is taken to set

the focal plane in the middle of the nozzle depth. In this way, the system is optimized to catch non-blurry metal particles only in 1 plane, namely the focal plane. The 45-105μm images are acquired at 5400 fps with 25μs exposure time. Note that the images for the 15-45μm powder are generally darker and have a lower signal to noise ratio due to the higher fps (9000 fps) and lower exposure time (6.5μs) needed to properly catch the particles. This can be explained by their faster travelling speed (reduced mass per unit) and by their smaller diameter that therefore reduces the number of pixels per particle and by consequence the contrast between particle and background. It is observed in the images that due to shape and diameter differences between particles, not all the particles are travelling at the same speed. All the following results in the present paragraph will be given for the next reference set of gas/powder settings : SG 3.5l/min, CG 8l/min, FR 5 g/min.

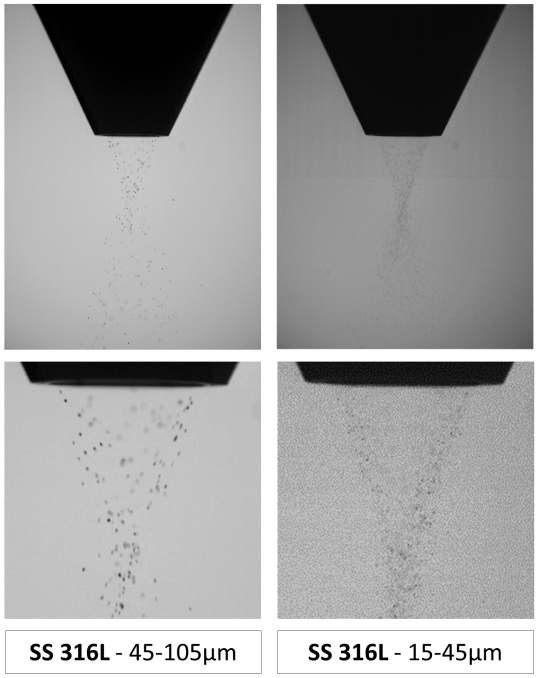

Figure 9: (up) Raw back-light images : SG 3.5l/min, CG 8l/min, FR 5 g/min, (down) zoom

An image post-processing algorithm is set-up to improve the quality of the raw high-speed images of the powder jet. For every measurement, a background subtraction is applied to improve the contrast and measurement quality. The contrast of the images is further increased by applying a sequence of image post-processing techniques and the blurry (out of focal plane) particles are discarded by applying image binarization with threshold, see Fig. 10.

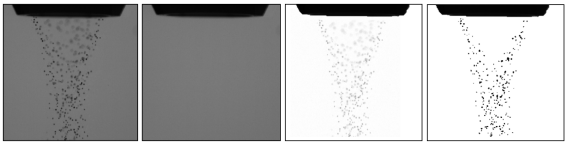

Figure 10: Image post-processing (256x256px) ((1) raw image, (2) background, (3) background subtraction, (4) final image)

The particle concentration or pixel intensity map of the gas-powder cone is obtained by averaging 30k post-processed images and is shown in Fig. 11. A convergence analysis is completed to find the optimal number of frames needed for the averaging. As can be observed on the particle concentration map, the powder stream diverges into a wider stream from the moment it exits the nozzle channel. It was noticed from the high speed images that smaller particles travel at higher velocities and therefore diverges less when exiting the nozzle. As stated by Lin [10], an inner stream core with higher powder concentration is observable, which is surrounded by an outer stream shell with lower concentration. This coincides with the typical Gaussian distribution of powder streams.

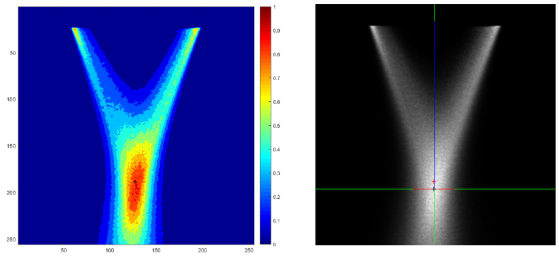

Figure 11: Particle concentration map (left,right), stand-off and powder-jet focus diameter identification (right)

Image intensity curves are extracted from the averaged image for every pixel line (horizontal) and pixel column (vertical). An example is given for 5 pixel lines in Fig. 12. A one-term Gaussian fit is realized on all the intensity/concentration profiles (for both lines and columns). The height along the powder cone at which the maximal peak value of the horizontal Gaussian intensity profiles arises defines the stand-off distance. The powder-jet focus diameter is defined as the minimum width (or diameter) of the particle cone that contains 86% of the total amount of particles at the

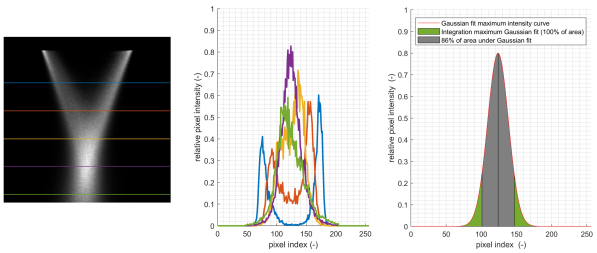

Figure 12: Pixel intensity profile (SG 3.5l/min, CG 8l/min, FR 5g/min for 15-45μm and 45-106μm 316L powder)

corresponding stand-off distance, see left graph of Fig. 12. The calibration is performed based on the nozzle diameter that can be extracted from the images and has a known measured value.

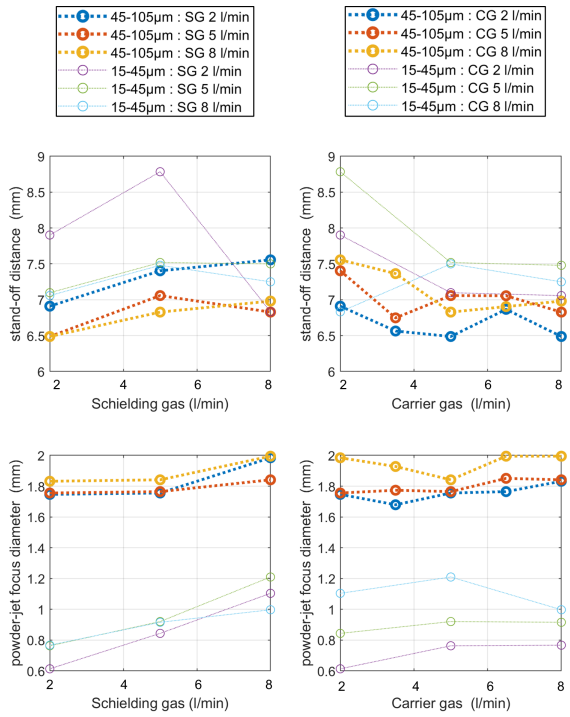

Figure 13: Back-light results : Effect of shielding gas (left) and carrier gas (right) on stand-off distance (up) and powder-jet focus diameter (down) (for FR 3g/min of 15-45μm and 45-106μm 316L powder)

The powder-jet focus diameter and stand-off distance are respectively indicated in red and blue on Fig. 11 (right). Both green lines are used to highlight respectively their height and axial position. The measurements are performed for 27 different gas/powder settings chosen within the optimal setting range of the COAX-40-S nozzle. The measurements are carried out for both 45-105μm (large line-width) and 15-45μm (small line-width) powder and for PF 3, PF 5 and PF 7 g/min in respectively Fig. 13, Fig. 14 and Fig. 15.

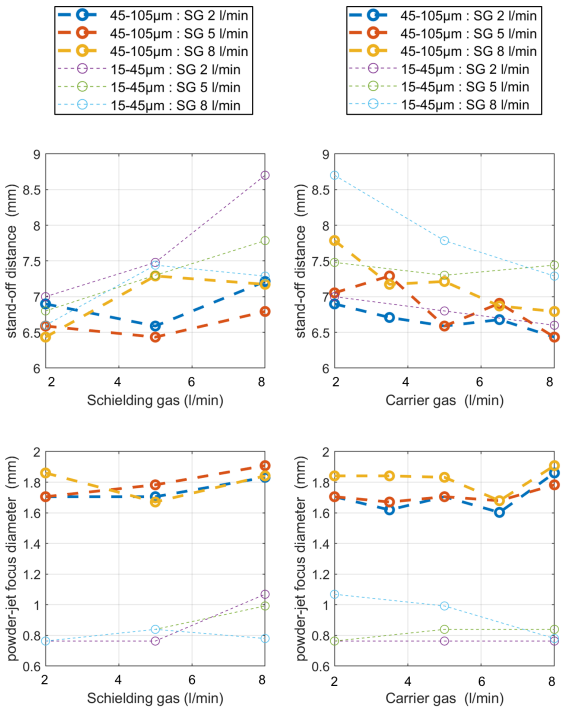

Figure 14: Back-light results : Effect of shielding gas (left) and carrier gas (right) on stand-off distance (up) and powder-jet focus diameter (down) (for FR 5g/min of 15-45μm and 45-106μm 316L powder)

The obtained values for the stand-off distance and powder-jet focus diameter are respectively situated in the ranges [6.3-7.8]mm and [1.5-2]mm for the 45-105μm particles and [6.9-8.9]mm and [0.63-1.1]mm for the 15-45μm particles. As can be concluded from the graphs, an increasing SG results in a small increase stand-off distance and powder-jet focus diameter. The SG pushes the focal plane down and has a broadening effect on the powder cone. On the other side, a higher CG decreases the stand-off distance and flattens the powder cone due to the higher carrying force applied by the CG on the particles.

No effect of the CG on the powder-jet focus diameter seems to be observable in the present results. Increasing the PF increases both the stand-off and powder-jet focus diameter. This was clearly observable for FR values higher than the one presented here. The effects described above seems to be more pronounced for increasing powder volumetric flow rate (effects more pronounced for 7g/min w.r.t. 3g/min).

To finish, reducing the particle diameter of the metal powder used, reduces the powder-jet focus diameter in a significant way and increases the stand-off distance. The use of smaller metal particles allows a reduction of powder-jet focus diameter up to 50% for the powders used for these experiments. Therefore, to increase the process efficiency for a given laser spot size, smaller particles should be used carried by CG with higher volumetric flow rate. In this way, more metal particles will be caught by the metlpool, the overall process efficiency will increase and the powder waste will be reduced.

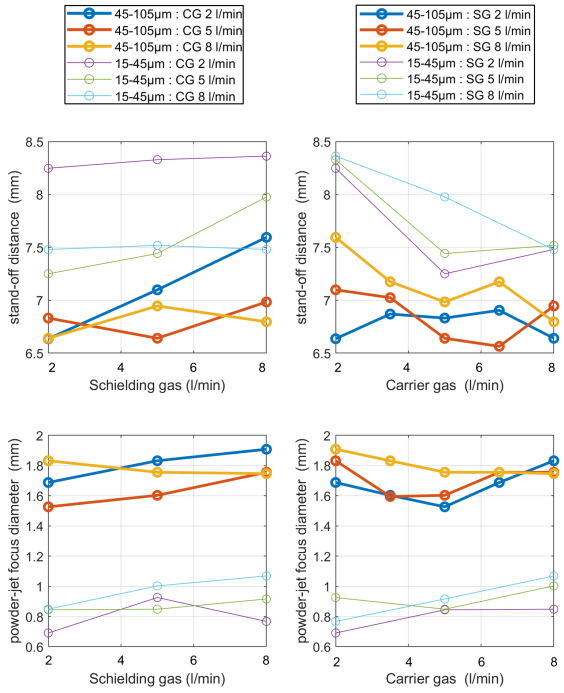

Figure 15: Back-light results : Effect of shielding gas (left) and carrier gas (right) on stand-off distance (up) and powder-jet focus diameter (down) (for FR 7g/min of 15-45μm and 45-106μm 316L powder)

Horizontal laser sheet jet characterization

The horizontal laser sheet jet characterization is presented for the reference set of powder/gas settings (SG 3.5l/min, CG 8l/min, PF 5g/min). The laser sheet has a fixed position during the measurements and the z-position of the nozzle is varied in order to scan the complete powder cone. Fig. 16 (up) gives a superposition of results at 5 different z-positions of the nozzle. A lowering of the powder focus diameter is observed for increasing stand-off distance till reaching the focal height, after which the powder cone diverges again. On the high exposure images taken at focal height (down), the powder cone and powder slice at stand-off distance are visible for both particle distributions. A smaller focus diameter is observed for the smaller particles.

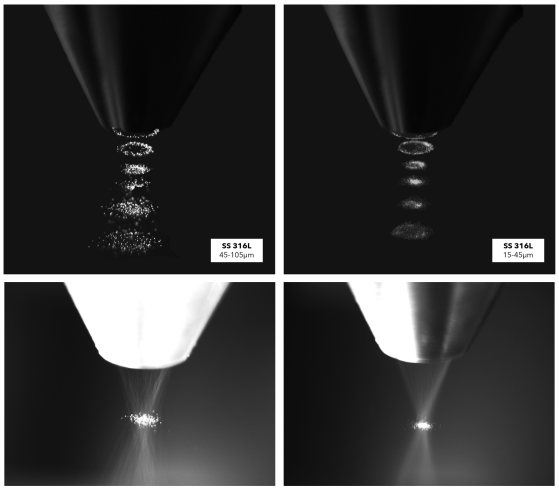

Figure 16: : Side view raw images horizontal laser sheet illumination (up) short exposure at 5 nozzle distances (down) long exposure in focal plane

The corresponding quantitative results shown in Fig. 17. are extracted from the front view high speed camera. As for configuration 1, a convergence analysis is performed to define the required number of images for averaging. The intensity/concentration curves are extracted from the mean image at different stand-off distances (left), and their local maxima (middle) is used for the powder cone reconstruction (right). Based on these results, stand-off distance and powder-jet focus diameter are extracted.

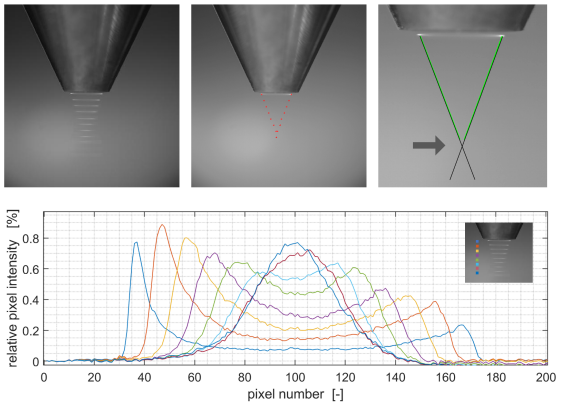

Figure 17: (up,left) Superposed front view mean images, (up,middle) Local maxima of intensity Gaussian fits, (up,right) Stand-off distance definition (down) Relative pixel intensity curves

Vertical laser sheet jet characterization

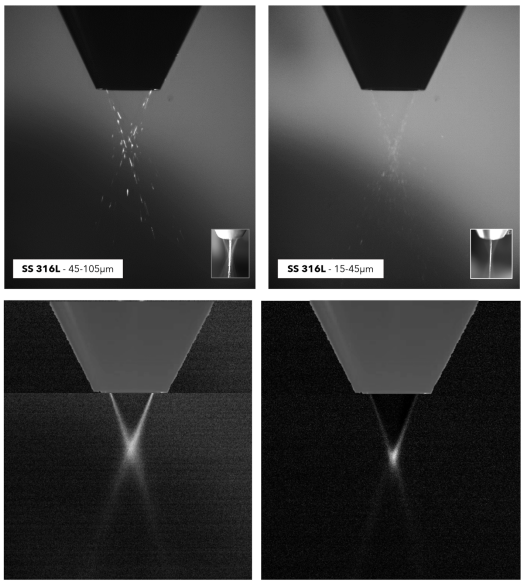

Figure 18: Front view raw images vertical laser sheet illumination (up), Mean front view images (down)

As for the previous measurements, the same reference settings are considered and similar post-processing techniques are applied. It is clearly observable in Fig. 18. that the smaller particles (15-45μm) are reflecting less light as the larger ones (45-105μm) due to their reduced mean diameter. The present optical measurement shows the advantage of only capturing particles in 1 plane, avoiding the need of post-processing to discard particles out of focus plane (as it is the case for the back-light method). This is clearly visible on the averaged image, in which the inner empty cone (without particles) is defined more precisely and is deeper w.r.t. the back-light method. Also here, stand-off distance and powder-jet focus diameter are extracted in the same way.

Comparison of the optical methods for reference settings

The results (stand-off distance/powder-jet focus diameter) given in Table 1 highlights a concordance and similar trend for the different optical methods. The back-light and horizontal laser sheet results are coinciding for both particle diameter ranges (between $2-7\%$ error with respect to the back-light results). For the vertical laser sheet visualization an overestimation ($15-28\%$ error) is observed. However, to relatively compare different gas/powder settings cases, the 3 techniques/configurations showed their efficiency and can be used separately.

Optical set-up	**Powder diameter range** (µm)	**Stand-off distance** (mm)	**Powder-jet focus diameter** (mm)
Back-light	45-105	6.90	1.77
	15-45	7.21	0.99
Horizontal laser sheet	45-105	6.99	1.89
	15-45	7.14	0.95
Vertical laser sheet	45-105	6.95	2.27
	15-45	7.44	1.14

Table 1: Comparison of optical methods for reference settings : SG 3.5l/min, CG 8l/min, FR 5 g/min

2.3. DLM process efficiency

On the DLM 3D printer on which the experiments are performed, an infrared/visible redPOWER® QUBE fiber laser of 900-1250nm with a power of 300W-2kW is mounted. The diameter of the laser beam is approximately 1mm and follows a near flat-top intensity profile. Fig.19 shows an image taken with an optical metallographic microscope of a polished cross section of a DLM printed track. The laser spot size is indicated in red and the track width can

be extracted based on the observable change in microstructure between built plate and track. The choice of optimal gas/powder settings is important to decrease the powder-jet focus diameter, in order to have a higher number of metal particles reaching the melt pool. This results in an increasing process efficiency and therefore in layer thickness. Consequently, the ratio of laser spot size (or melt pool width) and powder focus diameter is a very important parameter to obtain a good process efficiency. Moreover, it was observed that this ratio is also essential to achieve a good printing quality.

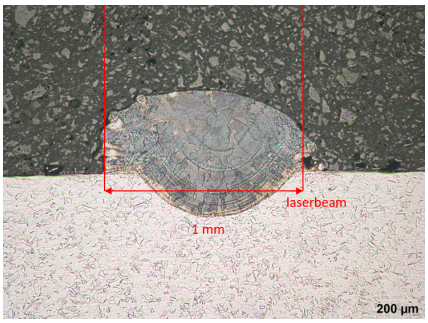

Figure 19: Optical metallographic microscope image of DLM printed track

3. Conclusion and future work

The results show that the powder-gas jet (in terms of stand-off distance and powder-jet focus diameter) and consequently the process efficiency are affected by the chosen gas and powder settings (SG, CG, PF, particle diameter distribution). The three optical methods presented in the study give comparable results and the same trends. However, care should be taken for the choice of the image recording parameters (exposure time and frames per second). The optical measurement with smaller metal particles are less straightforward and require more post-processing since the particles reflect/attenuate less light. A solution would be to increase the light source intensity to make the particles scatter/attenuate more light and to increase the signal-to-noise ratio. Note that the experimental measurements based on high speed imaging techniques are computationally expensive in terms of data storage and post-processing. The process efficiency can mainly be improved by using metal particles with smaller diameter. In terms of gas settings, a high CG volumetric flow rate combined with a not too high SG volumetric flow rate is reducing the powder-jet focus diameter and by consequence should have a positive impact on the process efficiency. Knowing the complexity of coaxial multiphase flows, it is very difficult to compare these results with analytical models, this is why numerical simulations would be interesting for comparison in the future.

References

[1] S. M. Thompson, L. Bian, N. Shamsaei, A. Yadollahi, An overview of direct laser deposition for additive manufacturing: Part i: Transport phenomena, modeling and diagnostics, Additive Manufacturing 8 (2015) 36–62.

[2] W. Devesse, D. De Baere, P. Guillaume, Modeling of laser beam and powder flow interaction in laser cladding using ray-tracing, Journal of Laser Applications 27(S2) (2015) S29208.

[3] U. E. Lamikiz A., Tabernero I., M. S., Current designs of coaxial nozzles for laser cladding, Recent Patents on Mechanical Engineering 4(1) (2011) 29—36, doi:10.2174/2212797611104010029.

[4] N. Shamsaei, A. Yadollahi, L. Bian, S. M. Thompson, An overview of direct laser deposition for additive manufacturing: Part ii: Mechanical behavior, process parameter optimization and control, Additive Manufacturing 8 (2015) 12–35.

[5] P. Balu, P. Leggett, R. Kovacevic, Parametric study on a coaxial multi-material powder flow in laser-based powder deposition process, Journal of Materials Processing Technology 212 (2012) 1598–1610.

[6] H. Pan, T. Sparks, Y. Thakar, F. Liou, The investigation of gravity-driven metal powder flow in coaxial nozzle for laser-aided direct metal deposition process, Journal of Manufacturing Science and Engineering 128(2) (2006) 541–553.

[7] S. Zekovic, R. Dwivedi, R. Kovacevic, Numerical simulation and experimental investigation of gas-powder flow from radially symmetrical nozzles in laser-based direct metal deposition, International Journal of Machine Tools & Manufacture 47(1) (2007) 112–123.

[8] O. Kovalev, A. Zaitsev, D. Novichenko, I. Smurov, Theoretical and experimental investigation of gas flows, powder transport and heating in coaxial laser direct metal deposition (dmd) process, Journal of Thermal Spray Technology 8 (2010) 465–478.

[9] S. Mann, O. Nottrodt, New sensor and system technology for higher process stability in lmd, Conference on Additive Manufacturing Technologies, Bangalore, India (February 2019) doi: 10.1117/12.2506776.

[10] J. Lin, Concentration mode of the powder stream in coaxial laser cladding, Opt. Laser Technol. 31 (1999) 251–257.

[11] A. J. Pinkerton, L. Li, Modeling powder concentration distribution from a coaxial deposition nozzle for laser-based rapid tooling, J. Manuf. Sci. Eng. 126 (2004) 33–41.

Acknowledgments

This research work was financed by the OZR mandate (No. VOZ/R&D/2018009) of the Vrije Universiteit Brussel.

Feedback control of liquid metal coating

Fabio Pino

Environmental and Applied Fluid Dynamics Department, von Karman Institute for Fluid Dynamics, Belgium, fabio.pino@vki.ac.be

Supervisor: Miguel Alfonso Mendez

Assistant Professor, Environmental and Applied Fluid Dynamics Department, von Karman Institute for Fluid Dynamics, Belgium, miguel.alfonso.mendez@vki.ac.be

University Supervisor: Benoit Scheid

Professor, TIPs laboratory, Universit Libre de Bruxelles, Belgium, bscheid@ulb.ac.be

Abstract

One of the most commonly used technique for protecting steel plates from corrosion is hot-dip galvanisation. This process consists in dipping the metal into a bath of molten zinc and then withdrawing it to create a thin protective layer on the surface. Although being a simple, continuous and cost-effective configuration, it has a major drawback. Certain operating conditions are limited by the occurrence of an hydrodynamic instability which results in harmful undulation of the final coat surface with an impact on the final product quality.

Within this context this research project is aimed at exploring various control strategies to attenuate –and ideally prevent– the formation of these undulation patterns. The peculiar aspect is the amount of expertises involved and so the need for a strongly multidisciplinary approach encompassing theoretical modelling liquid films, numerical methods for solving partial differential equations, advanced feedback and adaptive control theory and machine learning.

The problem will be approached in several different ways. (1) The first consists in relying on the stability equations of the system and defining the control strategy based on the solution of a response problem. This strategy goes under the name of white-box, given that all the information about the mathematical modelling of the system are known. (2) The second outlook is called grey-box approach which comprises a limited knowledge of the physics and it relies on the construction of a simplified model based on data-driven system identification approached to design the controller. (3) The last method is the black-box technique where the system is obscure to the controller and the control policy is determined exclusively with model-free machine learning paradigms such as Genetic Programming or Reinforcement Learning. These control strategies will be implemented in a numerical environment where the controller could interact, through sensors and actuators, with a 3D CFD solver reproducing the coating flow in various industrial conditions. Alongside a modelling of the actuators and sensors in the virtual environments will be performed.

More broadly, the investigated control task can be generalised to any non-linear dynamical systems, hence extending the potential impact of this work to many other critical technologies.

Keywords: coating flows, interface instabilities, control theory, optimisation, adjoint methods, machine learning, data-driven science, applied mathematics, reduced order models, numerical methods

Modeling particle-laden flows in two dimensions, an optimization-based multivariate quadrature moment method

Maxim Van Cappellen

Environmental and Applied Fluid Dynamics Department, von Karman Institute for Fluid Dynamics, Belgium, maxim.van.cappellen@vki.ac.be

Supervisor: Delphine Laboureur

Associate Professor, Environmental and Applied Fluid Dynamics Department, von Karman Institute for Fluid Dynamics, Belgium, delphine.laboureur@vki.ac.be

University Supervisor: Maria Rosaria Vetrano

Associate Professor, Faculty of Engineering Science, Katholieke Universiteit Leuven, Belgium, rosaria.vetrano@kuleuven.be

Abstract

In this paper we present a novel solution for solving two-dimensional kinetic equations in the framework of quadrature based moments methods (QBMM). The main contribution of this work is a novel optimization-based multivariate quadrature inversion algorithm. The proposed method is evaluated qualitatively on simple two dimensional test cases for which a well established reference solution is available. The main focus of these test cases is particle trajectory crossing. A physical phenomena in which particle paths cross unhindered. The results here presented are promising and show that by incorporating the right mixed moments in the transport system we can exactly reproduce PTC events using a minimal number of moments.

Keywords: Poly-kinetic, particle-laden flows, particle trajectory crossing, method of moments, QBMM, multivariate quadrature, Eulerian particle kinetics.

1. Introduction

The kinetics of a population of inertial particles suspended in a fluid can conveniently be described by a number density function (NDF) that complies with the general population balance equation (GPBE) [1; 2]. This GPBE can be solved by numerous numerical models, generally divided into two classes of solvers: the Lagrangian methods which directly solve the GPBE on a mesoscale level and the Eulerian models that apply an averaging procedure to find the transport equations of certain lower order statistics of the NDF (*i.e. macroscale methods*).

Conventionally, the kinetics of particles with high Stokes and Knudsen number are solved using the Lagrangian methods. However, these methods suffer from statistical noise when coupled with the Eulerian physics of the carrier flow. Furthermore, they are expensive for large populations of particles. These disadvantages create a high demand for Eulerian models that can describe the kinetics of particle-laden flows across a wide range of regimes.

In the last decade, a new type of Eulerian solvers has emerged to meet this demand, the so-called quadrature-based moment methods (QBMM) [3; 4; 5; 6; 7; 2; 8; 9]. One of the most challenging problem all QBMM have to face when describing a poly-kinetic population of particles, is the multivariate moment-inversion problem. The inversion from power moments to quadrature weights and abscissas can be solved using numerous algorithms when the underlying NDF is univariate (e.g. Chebyshev algorithm [10] or PD-algorithm [2]). For multivariate problems no algorithm yet exists that can find a direct and unique inversion from moments to quadrature points. Several approximate solutions have been proposed, with the currently most common method being the conditional quadrature method of moments (CQMOM)

[5; 9; 8]. However this method suffers from some rather important flaws. First, the resulting quadrature of the moment-inversion depends on the ordering of the conditional variables, so different permutations result in different quadratures. This means that we have to compute the quadrature for each permutation of the set of internal variables. Secondly, the inversion algorithm can fail due to unrealizable conditional moments and therefore does not guarantee to reproduce the moments exactly. Lastly, the moment matrix quickly becomes large for increasing order and increasing number of internal variables (*i.e. curse of dimensionality*), heavily decreasing the computational efficiency.

In this work we investigate an novel approach to the multivariate moment inversion problem. Our objective is to create a bivariate moment-inversion algorithm that: (1) Reproduced the moments with high accuracy (2) is always realizable (3) is permutation invariant (4) results in a hyperbolic closure of the fluxes (*delta-shock free solution*) (5) works for arbitrary quadrature order (6) is computational efficient and most importantly (7) produces an accurate and reliable approximation of the Lagrangian particle kinetics.

The remainder of the this work is organized as follows: first we demonstrate the use of the moment transformation to reduce the number of degrees of freedom a typical kinetic equation. Secondly we describe the multivariate quadrature problem, followed by our proposed solution. In section 5 we discretize the governing equations and lastly in section 6 we test our model on various two dimensional test cases for which a well established reference solution can be found.

2. The moment transport equation

Consider the kinetic equation for the velocity-based number density function $f(t, \boldsymbol{x}, \boldsymbol{u})$ of mono-sized particles in two dimensions:

$$\partial_t f + \partial_{\boldsymbol{x}} \cdot \boldsymbol{u} f = S(f) \tag{1}$$

with $\boldsymbol{u} = (u, v)$ the particle velocity vector and $S(f)$ represents the forces acting on the particles due for example fluid-particle forces or collisions. Applying the bivariate power moments transformation, defined by

$$M_{k,l} = \int_{\mathbb{R}} \int_{\mathbb{R}} u^k v^l f(t, x, y, \boldsymbol{u})\, du\, dv, \tag{2}$$

results in the (*unclosed*) moment transport equations

$$\partial_t M_{k,l} + \partial_x M_{k+1,l} + \partial_y M_{k,l+1} = S_{k,l} \tag{3}$$

with $S_{k,l} = \int \int u^k v^l S(f)\, du\, dv$.

3. The multivariate quadrature problem

In the framework of the QMOM, we seek to find a moment closure of the form:

$$M_{k,l} = \sum_{\alpha=1}^{N} \rho_\alpha u_\alpha^k v_\alpha^l \tag{4}$$

that is exact for a limited number of lower order power moments. Here, ρ_α are called the weights, u_α, v_α the abscissas and N the order of the quadrature. Unlike for univariate moments, this system of equations has no established methodology.

4. Optimization-based multivariate quadrature

As mentioned in the introduction, our objective is to find a solution for eq. (4) using a symmetric set of moments. One multivariate closure method that uses a symmetric moment matrix is the tensor-product closure defined in [3]. However due to the use of the Cholesky decomposition (used in order to find the abscissas in a coordinate system that minimizes the variance of the distribution), the moment matrix contains a large number of mixed moments which for large orders N and higher dimensional distributions will cause problems with the overall computational efficiency. Furthermore is this method not permutation invariant. Therefor we propose an alternative solution which we explain using an example. Assume we know a subset of the moment matrix $\boldsymbol{M_{k,l}}$:

$$\boldsymbol{M_{k,l}} = \begin{bmatrix} M_{0,0} & M_{0,1} & M_{0,2} & M_{0,3} & M_{0,4} & M_{0,5} \\ M_{1,0} & M_{1,1} & M_{1,2} & M_{1,3} & M_{1,4} & M_{1,5} \\ M_{2,0} & M_{2,1} & M_{2,2} & M_{2,3} & M_{2,4} & M_{2,5} \\ M_{3,0} & M_{3,1} & M_{3,2} & M_{3,3} & M_{3,4} & M_{3,5} \\ M_{4,0} & M_{4,1} & M_{4,2} & M_{4,3} & M_{4,4} & M_{4,5} \\ M_{5,0} & M_{5,1} & M_{5,2} & M_{5,3} & M_{5,4} & M_{5,5} \end{bmatrix}, \tag{5}$$

indicated by the dashed line. We calculate the 1D-quadrature (*using the Chebyschev algorithm* [10]) in the x-direction from the moments $(M_{0,0}, M_{1,0}, \cdots, M_{5,0})$. Resulting in

$$f(u) \approx \sum_{\beta=1}^{3} \rho_\beta \delta(u - u_\beta) \tag{6}$$

We do the same for the y-direction with moments $(M_{0,0}, M_{0,1}, \cdots, M_{0,5})$ and obtain

$$f(v) \approx \sum_{\beta=1}^{3} \rho_\beta \delta(v - v_\beta) \tag{7}$$

We define the approximate bivariate NDF by

$$f(u,v) \approx \sum_{\alpha=1}^{3^2} \rho_\alpha \delta(u - u_\alpha)\delta(v - v_\alpha) \tag{8}$$

where the nine quadrature points are defined using the tensor product of the one dimensional abscissas.

$$\begin{array}{lll} (u_1, v_1) & (u_1, v_2) & (u_1, v_3) \\ (u_2, v_1) & (u_2, v_2) & (u_2, v_3) \\ (u_3, v_1) & (u_3, v_2) & (u_3, v_3) \end{array} \tag{9}$$

In order to find the weights ρ_α of eq. (8) we use an optimization based approach in order to minimize the linear system

$$||M_{k,l} - \sum_{\alpha=1}^{N^2} \rho_\alpha u_\alpha^k v_\alpha^l||_2 \tag{10}$$

for all the moments in eq. (5) with the constraint $\rho_\alpha \geq 0$. In this work we use the active set-method found in [11]. Using this optimization-based approach we are free to select the mixed moments ($M_{k,l}$ *with* $k \neq 0$ *and* $l \neq 0$) of the moment matrix. In the next section we demonstrate how to numerically solve eq. (3) using our optimization-based quadrature.

5. Kinetic based finite volume method

Let us denote the volume averaged moments on a uniform mesh with spacing $(\Delta x, \Delta y)$ at time t and cell-center (x_i, y_i).

$$M_{k,l}|_{i,j}^t = \frac{1}{\Delta x \Delta y} \int_{x_i - \Delta x/2}^{x_i + \Delta x/2} \int_{y_i - \Delta y/2}^{y_i + \Delta y/2} M_{k,l}(t,x,y)\, dx\, dy. \tag{11}$$

Making use of the quadrature representation of the moments eq. (4) we can write a kinetic based flux splitting finite volume scheme. For a single step forward Euler temporal discretization and a first order upwind flux scheme we get the following numerical scheme:

$$\begin{aligned} M_{k,l}|_{i,j}^{t+\Delta t} &= M_{k,l}|_{i,j}^t \\ &- \frac{\Delta t}{\Delta x}\left(M_{k+1,l}^{+u}|_{i,j}^t - M_{k+1,l}^{+u}|_{i-1,j}^t + M_{k+1,l}^{-u}|_{i+1,j}^t - M_{k+1,l}^{-u}|_{i,j}^t\right) \\ &- \frac{\Delta t}{\Delta y}\left(M_{k,l+1}^{+v}|_{i,j}^t - M_{k,l+1}^{+v}|_{i,j-1}^t + M_{k,l+1}^{-v}|_{i,j+1}^t - M_{k,l+1}^{-v}|_{i,j}^t\right) \end{aligned} \tag{12}$$

with the flux splitted moments defined by

$$\begin{aligned} M_{k,l}^{+u} &= \sum_{\alpha=1}^{N} \rho_\alpha \max(0, u_\alpha)^k\, v^l \\ M_{k,l}^{-u} &= \sum_{\alpha=1}^{N} \rho_\alpha \min(0, u_\alpha)^k\, v^l \\ M_{k,l}^{+v} &= \sum_{\alpha=1}^{N} \rho_\alpha u^k \max(0, v_\alpha)^l \\ M_{k,l}^{-v} &= \sum_{\alpha=1}^{N} \rho_\alpha u^k \min(0, v_\alpha)^l \end{aligned} \tag{13}$$

This particular scheme is both conditionally stable and realizable if:

$$\Delta t \leq \frac{\Delta x}{\max(|u_\alpha|)} + \frac{\Delta y}{\max(|v_\alpha|)} \tag{14}$$

[12].

6. Results and discussion

6.1. Jets in vacuum

In this section we investigate two key aspects of the numerical model. First, the correctness of the optimization-based multivariate quadrature method of moments will be tested. In this novel multivariate quadrature the mixed moments can be freely chosen and the influence of selecting specific mixed moments will be investigated. Secondly, the hyperbolic quadrature closure we proposed in [13] will be tested in order to evaluate if our hypothesis holds for a bivariate quadrature. In order to make an objective evaluation, we simulate 2D crossing jets in a vacuum. In this idealized case, the jets should travel in straight path without influencing one another. The initial solution is described in fig. 1 and all numerical results are obtained on a 100 by 100 uniform grid.

6.1.1. Cumulative reference solution

Because all jets start from a one point velocity distribution, the correct multivariate poly-kinetic numerical solution is equal to the sum of the multivariate mono-kinetic numerical solution of the individual jets. The evolution of an individual jet can easily be calculated from the moment transport equations:

$$\begin{cases} \partial_t M_{0,0} + \partial_x M_{1,0} + \partial_y M_{0,1} = 0 \\ \partial_t M_{1,0} + \partial_x \overline{M}_{2,0} + \partial_y \overline{M}_{1,1} = 0 \\ \partial_t M_{0,1} + \partial_x \overline{M}_{1,1} + \partial_y \overline{M}_{0,2} = 0 \end{cases} \tag{15}$$

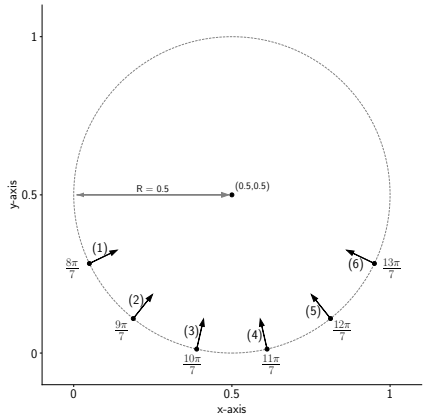

Figure 1: Location of the sources of the jets. The jets are located on a circle around the center of the domain $(x, y = 0.5, 0.5)$ with radius $R = 0.5$. The individual jets are identified by their index $(1) \cdots (6)$ with the angle of rotation given next to arrow. The absolute velocity of all jets is equal to one and oriented towards the center of the domain. The initial number concentration at the source points is set to one.

where the unclosed moments are found by a one node tensor-product closure in eq. (16).

$$\overline{M}_{2,0} = \frac{M_{1,0}^2}{M_{0,0}}, \quad \overline{M}_{0,2} = \frac{M_{0,1}^2}{M_{0,0}}, \quad \overline{M}_{1,1} = \frac{M_{0,1}M_{1,0}}{M_{0,0}} \tag{16}$$

It is important to note that this closure is exact for a mono-kinetic jet in a vacuum. The cumulative reference solution is obtained by summing the moments found from the evolution of the individual jets. The advantage of using the cumulative reference solution over the analytic solution is that we can ignore the effects of numerical diffusion.

6.1.2. Three jets in a vacuum

The results obtained for three jets crossing with our optimization-based quadrature are found in fig. 2. In fig. 2a the cumulative reference solution is show. The three other figures show the results for a different mixed moment. All results where obtained using a third order marginal moment sets for the x and y direction. The total number of moments used in the closure is indicated at the bottom of each plot by $\#M$. In the first simulation (fig. 2b) we do not select a mixed moments. Hence the closure is obtained by back-projecting the marginal quadratures in order to obtain the weights. Using such a quadrature forces the particles to move statistically independent in the x and y direction. This is because the approximated joint number density function is now equal to the product of the marginal density functions (*i.e.* $f(u, v) = f(u)f(v)$). Before the crossing point this closure behave the same as the reference solution. After the crossing we see that the particles have lost crucial information about their initial trajectories. In the second test case (fig. 2c) we add $M_{1,1}$ to the moment matrix. Now the jets follow more closely the reference solution. However, the trajectories are clearly influenced by the crossing event. The same can be said when selecting $M_{1,2}$ as mixed moment (fig. 2d), which produces slightly better results. In the last two tests (fig. 2e and fig. 2f), we select respectively $M_{2,1}$ and $M_{2,2}$ as the mixed moment. Now the reference solution is exactly reproduced. The exact reason why selecting $M_{2,1}$ or $M_{2,2}$ produces satisfactory results is unknown. However, what both these test have in common is that the mixed moment is always positive. Thus we suspect that when the sign of the mixed moment is the same for the whole region where PTC occurs, the optimization based quadrature produced a sufficiently accurate solution. This can always be ensured by optimizing the quadrature for mixed moments $M_{k,l}$ where both $k \neq 0$ and $l \neq 0$ are even. Therefor, in the remainder of this work the mixed moment is always $M_{2,2}$.

6.1.3. Four, five and six jets in a vacuum

Since the optimization based quadrature is directly related to the abscissas of 1D-quadratures, this method can be easily applied with higher quadrature orders. In order to demonstrate this, we simulated the crossing of four, five and six jets in a vacuum. The 1D-quadrature order used for each case is equal to the number of jets and the mixed moment is $M_{2,2}$. The results are shown in fig. 3. Again we observe that the optimization based quadrature reproduces exactly the crossing events.

6.1.4. Hyperbolicity

In our previous work we investigated the hyperbolic nature of the QMOM closure used for solving 1D kinetic equations and proposed a novel quadrature closure that ensures the moment transport system to be strictly hyperbolic for arbitrary quadrature order. Due to the direct relation between the optimization based multivariate quadrature and 1D Gaussian quadrature, our 1D-hyperbolic QMOM closure can be directly applied. Analytically proving whether the resulting 2D closure will result in a strictly hyperbolic transport system is not possible. Since the weights are obtained

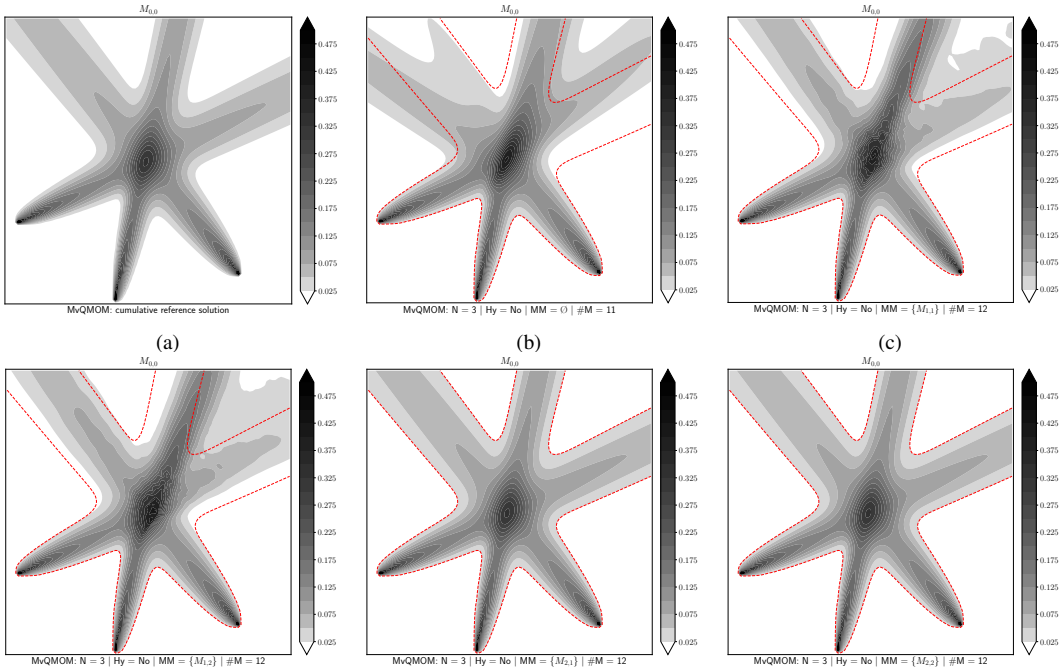

(a) (b) (c)

(d) (e) (f)

Figure 2: Three jets crossing in a vacuum. Influence of the choice of the mixed moments in the optimization-based multivariate quadrature. The red outline represents the contour at $M_{0,0} = 0.025$ of the cumulative reference solution

from an iterative optimization problem and can thus not be written as an analytic expression. However, since we now that a weakly hyperbolic system produces delta-shocks whenever a PTC event occurs that has more distinct velocities (u, v) than there are abscissas (u_α, v_α), we can numerically test our closure. In order to do so, we revisit the case of six crossing jets in a vacuum. The results are shown in fig. 4. In the left column we show the reference solution, in the middle column we use a hyperbolic 1D-quadrature and in the right column we use the classic QMOM closure. In each row we increase the order of the quadrature, until $N = 6$. In which case there are a sufficient number of distinct abscissas in x and y direction to avoid the formation of delta-shocks, even if the system is weakly hyperbolic. In fig. 4c we clearly see the formation of a delta-shock in the middle of the domain. In fig. 4b we use the hyperbolic QMOM closure with the same order N. It is clear that now no delta-shocks are created. The same behavior can be seen for the higher order quadratures. From this numerical experiment we can conclude two things: 1) The optimization based quadrature using a Gaussian-quadrature in order to determine the abscissas, results in a weakly-hyperbolic moment transport system. 2) The optimization based quadrature using the hyperbolic QMOM in order to determine the abscissas, results in a delta-shock-free moment transport system for vorticity-free flows.

6.2. *Jets in a compressible flow*

In this last section, we test our model on a one-way coupled problem, namely jets in a compressible carrier flow. This test case is the same as in [14] and [9], with the slight modification that we have rotated the flow field and initial conditions 45° around $(0, 0)$. This is done in order to ensure that the velocities u and v are statistically dependent. Note that the non-rotated test case has a constant velocity in the x-direction and can thus be solved using only a 1D-quadrature for the velocity in the y-direction. The carrier flow velocity is given by:

$$u_g(x_r, y_r) = u_{g,0}, \quad v_g(x_r, y_r) = -\epsilon y_r \tag{17}$$

where x_r and y_r are the coordinates in a reference frame rotated 45° around $(0, 0)$, $u_{g,0} = 0.2$ m/s is the axial gas velocity and $\epsilon = 1\ \mathrm{s}^{-1}$ is the rate of strain in the vertical direction. The influence of the carrier

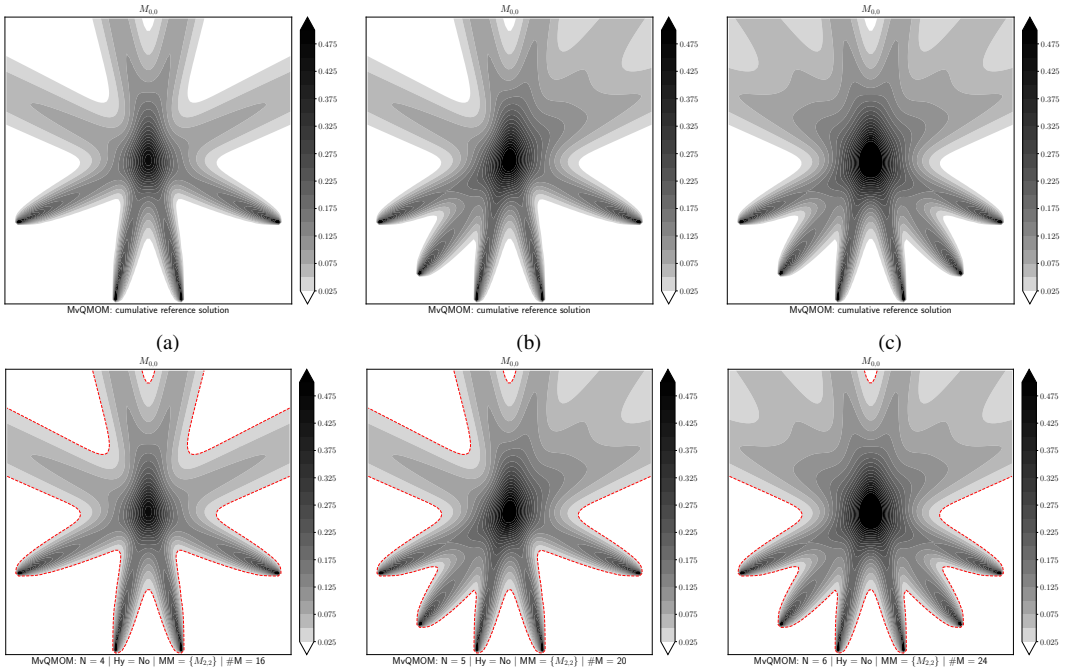

Figure 3: Four, five and six jets in a vacuum, shown respectively in the left, middle and right column. Top row shows the cumulative reference solutions, the bottom row the solution using the optimization based quadrature. The red outline represents the contour at $M_{0,0} = 0.025$ of the cumulative reference solution

flow on the particles is modeled by Stokes drag. The acceleration term in eq. (1) is thus given by:

$$S(f) = \frac{1}{\tau_p}(u - u_g) + \frac{1}{\tau_p}(v - v_g) \tag{18}$$

The behavior of particles in this flow field can be divided into two regimes, based on the particle Stokes number $\mathrm{St} = \epsilon\tau_p$. Below the critical Stokes number $\mathrm{St}_c = 1/4$ the particle will converge towards the center-line ($y_r = 0$) without oscillations. When $\mathrm{St} > \mathrm{St}_c$ the particles will oscillate around the center-line while eventually converging at the center-line. The carrier flow field is illustrated in fig. 5a. At $t = 0$ two mono-kinetic jets enter the domain at $(x_r, y_r) = (0, 0.5)$ and $(x_r, y_r) = (0, -0.5)$ with initial velocities $(u_r, v_r) = (0.2, 0)$ and $\mathrm{St} = 20\mathrm{St}_c$. The reference trajectories of the two jets si found from the analytic solution given in [14]. The numerical solution for this case is given in fig. 5b and was computed on a 200 by 200 uniform grid with a hyperbolic closure ($N = 3$) and mixed moment $M_{2,2}$. It can be seen that our numerical model can correctly approximate the trajectories of the jets as well as the crossing events.

7. Conclusion

In this paper we investigated the possibility to use an optimization-based multivariate quadrature for closing the moment transport equations describing the kinetics of a population of particles. We evaluated our model based on qualitative comparison of the computed distribution of particles. The main focus of the presented results is particle trajectory crossing. For particle moving in vacuum the exact Eulerian solution was obtained for any number of crossing jets, as long as the order of the marginal moments was equal or higher as the number of crossing trajectories. In the case the order is lower as the number of crossings, delta-shocks are observed. In order to deal with this non-physical behavior, the hyperbolic 1D quadrature introduced in [13] was applied, successfully producing a delta-shock-free and accurate approximation of the exact solution. With this novel bivariate quadrature inversion algorithm the mixed moments that are tracked are free to choose. This allows for great flexibility in selecting which properties of the distribution will be included in the closure. However, even for the simple test cases considered in this work, the influence of the selected mixed moments had a significant

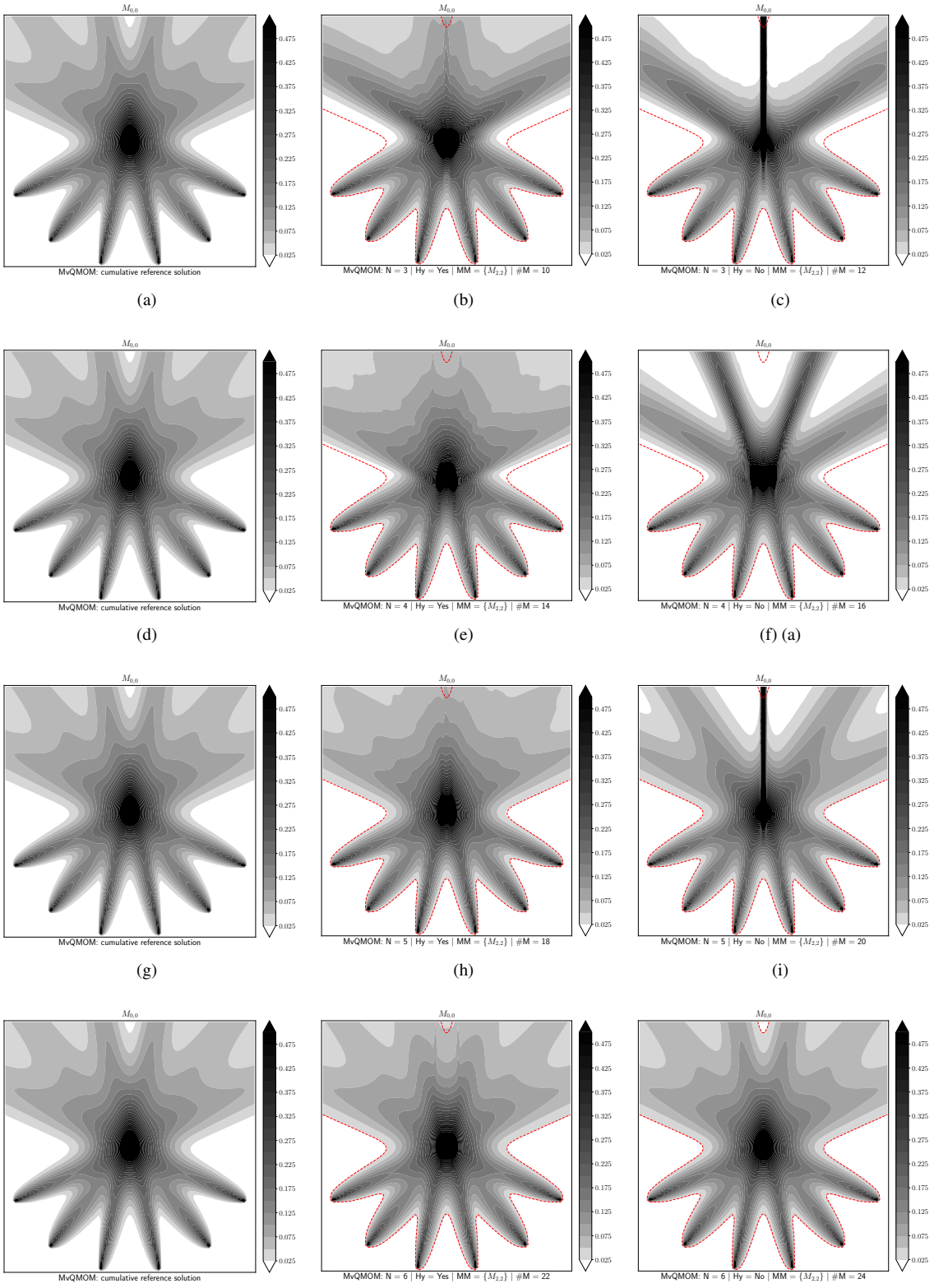

(a) (b) (c)

(d) (e) (f) (a)

(g) (h) (i)

(j) (k) (l)

Figure 4: Six jets crossing in a vacuum. Formation of delta-shocks when the abscissas are found from a Gaussian quadrature (right) and the delta-shock free solution obtained by applying the hyperbolic Gaussian closure (left) introduced in [13].

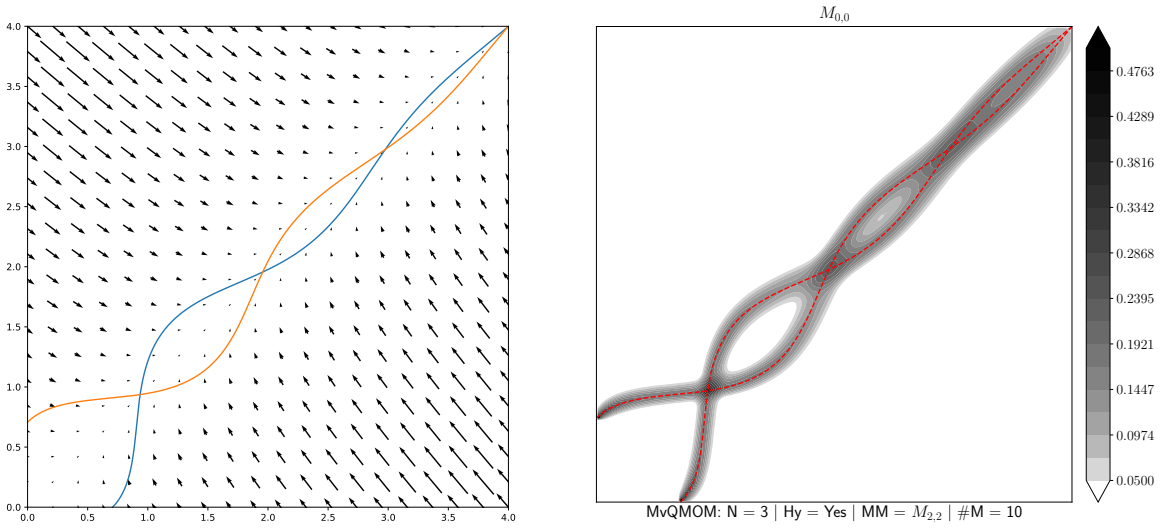

(a) (b)

Figure 5: Jets in a compressible flow. Left: Compressible flow field (black arrows) and analytic trajectory of the two jets (colored lines). Right: Numerical number density with the analytic trajectories in red dashed lines. St = $20\mathrm{St}_c$

impact on the outcome. Future work, in which we will evaluate quantitatively the numerical results, will have to shed light on which mixed moments are required in order to obtain a reliable moment approximation of the Lagrangian physics.

Acknowledgments

This work is funded by the PhD fellowship Strategic Basic Research of the Research Foundation-Flanders (FWO), as part of the project (1S C61 19N).

References

[1] D. Ramkrishna, Population Balances, Vol. 1, 2000.

[2] D. L. Marchisio, R. O. Fox, Computational Models for Polydisperse Particulate and Multiphase Systems, Cambridge Series in Chemical Engineering, 2013.

[3] R. O. Fox, A quadrature-based third-order moment method for dilute gas-particle flows, Journal of Computational Physics 227 (12) (2008) 6313–6350.

[4] C. Chalons, R. Fox, M. Massot, A multi-gaussian quadrature method of moments for gas-particle flows in a les framework, Studying Turbulence Using Numerical Simulation Databases, Center for Turbulence Research, Summer Program 2010, Stanford University (2010) 347–.

[5] C. Yuan, R. Fox, Conditional quadrature method of moments for kinetic equations, Journal of Computational Physics 230 (22) (2011) 8216–8246.

[6] F. Laurent, A. Vié, C. Chalons, R. O. Fox, M. Massot, A hierarchy of Eulerian models for trajectory crossing in particle-laden turbulent flows over a wide range of Stokes numbers, Proceedings of the Summer Program 2012 - Center for Turbulence Research (2012) 193–204.

[7] C. Chalons, D. Kah, M. Massot, Beyond pressureless gas dynamics: Quadrature-based velocity moment models, Communications in Mathematical Sciences 10 (4) (2012) 1241–1272.

[8] C. Chalons, F. Laurent, M. Massot, A. Vié, Multivariate Gaussian extended quadrature method of moments for turbulent disperse multiphase flow.

[9] R. O. Fox, F. Laurent, A. Vié, Conditional hyperbolic quadrature method of moments for kinetic equations, Journal of Computational Physics 365 (2018) 269–293.

[10] W. Gautschi, Orthogonal Polynomials, Quadrature, and Approximation: Computational Methods and Software (in Matlab) BT - Orthogonal Polynomials and Special Functions: Computation and Applications, Springer Berlin Heidelberg, Berlin, Heidelberg, 2006, pp. 1–77.

[11] C. L. Lawson, R. J. Hanson, Solving Least Squares Problems, 1995.

[12] V. Vikas, Z. J. Wang, A. Passalacqua, R. O. Fox, Realizable high-order finite-volume schemes for quadrature-based moment methods, Journal of Computational Physics 230 (13) (2011) 5328–5352.

[13] M. Van Cappellen, Solving kinetic equations using quadrature based moment methods: hyperbolicity and the frontier of moment space, Journal of Computational Physics (*ready for submission*).

[14] A. Vié, F. Doisneau, M. Massot, A. Vié, F. Doisneau, M. Massot, A. Gaussian, A. Vi, On the Anisotropic Gaussian velocity closure for inertial- particle laden flows To cite this version : HAL Id : hal-00912319 On the Anisotropic Gaussian velocity closure for inertial- particle laden flows, Communications in Computational Physics 17 (2015) 1–46.

Numerical Investigation of the Effect of Buoyancy Forces on the Deflagration of Hydrogen in the Thai Facility

Andrea Attavino

Environmental and Applied Fluid Dynamics Department, von Karman Institute for Fluid Dynamics, Belgium, andrea.attavino@vki.ac.be

Supervisor: Philippe Planquart and Jean-Marie Buchlin

Research Manager, Environmental and Applied Fluid Dynamics Department, von Karman Institute for Fluid Dynamics, Belgium, philippe.planquart@vki.ac.be

Full Professor, Environmental and Applied Fluid Dynamics Department, von Karman Institute for Fluid Dynamics, Belgium, buchlin@vki.ac.be

University Supervisor: Alessandro Parente

Associate Professor, Aero-Thermo-Mechanics Department, Université Libre de Bruxelles, Belgium, alessandro.parente@ulb.ac.be

Abstract

Accumulation of hydrogen in the building of a nuclear reactor, during a severe accident, can lead to a deflagration event, resulting in high dynamic pressure loads which could threaten the containment structures and the operability of technical equipment. Hydrogen is usually released in the building alongside a large amount of steam. The presence of steam, which acts as a diluent, together with the absence of a strong initial flow field in the building, makes deflagration event relatively slow. In this case the propagation of the flame front is mostly controlled by the self-wrinkling of the flame and by buoyancy forces. For this work, CFD computations of hydrogen deflagration in a closed compartment have been performed, with the aim of studying the effect of buoyancy forces on the flame front propagation. The cases considered are the experiments HD-15, HD-16, HD-22 and HD-23 performed in the THAI facility in the framework of the OECD/NEA THAI project [1]. In the experiments the facility has been filled with a mixture of air, hydrogen and steam. The igniter is located either in the upper or the lower area of the facility, resulting in a different direction of the flame propagation in the four tests. The numerical calculations have been performed using the open source software OpenFOAM. The flame front propagation has been described using the model developed by Weller derived by means of a conditional averaging technique on the transport equations [2]. Comparison between the computed pressure history and flame front position with experimental results will be presented.

Keywords: Hydrogen combustion, Hydrogen deflagration, Computational fluid dynamics, Severe accidents

1. Introduction

During a severe nuclear accident, a large amount of hydrogen can be produced due to core degradation in the reactor pressure vessel and released in the atmosphere of the containment building, alongside a large amount of steam, e.g. due to operation of depressurization systems or in case of breaks in the reactor coolant system. After vessel failure, hydrogen, as well as other gases, can be produced due to molten core concrete interaction. As the released gases accumulates in the building, the concentration of hydrogen may exceed the flammability limit. The presence of a combustible mixture in the building represents a serious threat to the integrity of the containment. For this reason, hydrogen mitigation systems are installed, and the building is designed to be able to withstand a deflagration event. Thermal and pressure loads caused by the combustion in conditions representative of containment operation are key parameters that needs to be correctly simulated by code calculations used for

safety analyses. These parameters are strongly dependent on the concentration profile of hydrogen and steam in the building, as well as the geometry and the materials of the wall, if the heat transfer is not negligible. Moreover, the presence of a flow field and turbulence in the building, due to a ventilation system or natural convection, can influence the combustion process, leading to flame acceleration and, in the worst case, transition of the deflagration to the detonation regime with a consequent increase in the over pressure reached. The estimation of the thermal and pressure loads requires knowledge of the thermochemical properties of the combustible mixture that forms in the containment building. Those parameters can be divided in two categories, the equilibrium parameters, which depends only on the energetics of the mixture, and nonequilibrium parameters, which depends on the chemical kinetics and transport rates [3]. As described by Sherman [4], the first category of parameters can be used to estimate the result of a deflagration that happens in simple configurations, such the combustion of a premixed gas in single compartments with negligible heat transfer. Among those parameters the most relevant ones are the flammability limits and the Adiabatic Isochoric Complete Combustion pressure. The flammability limits are defined as the critical composition of the fuel air inert diluent mixture beyond which the mixture cannot sustain steady flame propagation. This parameter depends on the initial thermophysical state of the mixture [5], as well as the direction of the flame propagation due to buoyancy effects [6] and can be computed to high accuracy using data from thermodynamic tables [7]. The AICC pressure, also called constant volume explosion pressure, is the pressure reached after a combustion event that happens in a constant volume enclosure with perfectly isolated walls and in which the burned gases are in thermochemical equilibrium (complete combustion). However, in many practical cases it is not possible to use the aforementioned assumptions. When the concentration of hydrogen is close to the flammability limit, the deflagration process is particularly slow, the convective and radiative heat transfer to the structures becomes relevant, and the combustion process is strongly influenced by buoyancy forces and turbulence. The description of the combustion phenomena becomes more complex and simple correlations cannot predict accurately the magnitude of the thermal and pressure loads. For this reason, Computational Fluid Dynamics and Lumped Parameters codes can be of great aid in the hydrogen analysis of the containments and safety systems of nuclear reactors. However, due to the small dimension of the flame front, compared with the dimension of the containment, even CFD codes are not capable of fully describe the combustion event. Many features of the flame, such as the wrinkling due to turbulence and hydrodynamic instabilities, particularly important for lean hydrogen mixtures, have to be modelled. For that reason, extensive validation of CFD is a prerequisite, to improve the reliability of their results. In this paper results of CFD simulations of hydrogen deflagration test, performed in the THAI test facility, will be shown. The aim of the work is to validate the flame wrinkling model that has been implemented in the CFD code OpenFOAM and show how the propagating direction of the flame and the presence of steam in the combustible mixture affects the pressure peak of a deflagration event in a large scale facility.

2. Governing Equations

A complete description of the combustion phenomena is extremely computationally expensive because of the high amount of equations that have to be solved and the small dimension of the flame front, compared to the dimension of a large-scale facility. In order to reduce the computational cost of combustion simulations Weller et al. [8] developed a new model in which the laminar-flamelet approach is used with conditional averaging to create a set of equations that can be used to describe the complex combustion phenomenon.

The governing equations are conditionally averaged by multiplying by an indicator function I, which is 0 in the burnt zone and 1 in the unburned one, and by applying conventional averaging technique, density weighted or otherwise. The form of the averaged continuity and momentum transport equations are the same as the canonical Favre averaged equations. They are then coupled with the energy transport equation for the burned and unburned mixture. The last equation to be solved is the transport of the density weighted regress variable $\tilde{b}$, defined as:

$$\tilde{b} = \frac{\tilde{f} - f_b}{f_u - f_b}. \tag{1}$$

Where $\tilde{f}$ is the density weighted fuel mass fraction and the subscripts u and b denote respectively the unburned and burned mixture. Following this approach, a generic property of the fluid ϕ can be expressed as:

$$\phi = \tilde{b}\phi_u + \left(1 - \tilde{b}\right)\phi_b. \tag{2}$$

The transport equation for $\tilde{b}$ yields:

$$\frac{\delta\bar{\rho}\tilde{b}}{\delta t} + \nabla\left(\bar{\rho}\tilde{\mathbf{U}}\tilde{b}\right) - \nabla\left(\rho\mathcal{D}\nabla\tilde{b}\right) = -\bar{\rho}_u S_l \Xi \left|\nabla\tilde{b}\right|. \quad (3)$$

Where $\bar{\rho}$ is the averaged density, $\tilde{\mathbf{U}}$ the density average velocity, $\mathcal{D}$ the turbulent diffusion coefficient, $\bar{\rho}_u$ the averaged unburnt density, S_l the laminar flame speed and Ξ the flame wrinkling factor. The term on the right-hand side of the equation represent the evolution of the flame due to the chemical reactions, and it includes all the parameters that affects the combustion process. The laminar flame S_l speed is computed using a correlation derived by Bentaib et al. [9]:

$$S_l(\phi,\psi,T,p) = \alpha(\phi)\cdot\beta(\psi)\cdot\left(\frac{T}{T_{ref}}\right)^{2.2}\cdot\left(\frac{p}{p_{ref}}\right)^{-0.5}. \quad (4)$$

$$\alpha(\phi) = 1.44\phi^2 + 1.7\phi - 0.29.$$

$$\beta(\phi) = (1-\psi)^4.$$

Where ϕ is the equivalence ratio of the hydrogen-air mixture, ψ the molar fraction of the diluent, T_u the temperature of the unburned gas, p the pressure, $p_{ref} = 10^5\ Pa$ and $T_{ref} = 298\ K$.
The flame wrinkling Ξ function, appearing in the r.h.s. of equation (3) represents the ratio between the average flame area per unit of volume in the cell, over the average flame area projected onto the mean propagation direction in the cell. To compute this function Weller proposes to solve a transport equation, where the terms representing the generation and removal of surface area are only linked to the turbulent quantities of the flow. However, in the case considered in this study there is absence of flow and turbulence at the beginning of the test, and the flame propagation is mostly controlled by self-wrinkling. For this reason, we used a model proposed by Molkov [10], which uses a modified version of the Yakhot equation [11] yelding:

$$\Xi = \Xi_K \cdot \Xi_f \cdot \Xi_{lp} \cdot \Xi_t. \quad (5)$$

The four terms on the r.h.s. of equation (6) are representative of the different mechanism whereby flame surface area is generated. Ξ_K is the wrinkling factor due to the turbulence generated by the flame front itself. This parameter increases gradually with the distance the flame has travelled from its ignition point, to mimic the transition from the laminar regime to the fully developed turbulent flame:

$$\Xi_K = 1 + (1 - \Xi_K^{MAX})\left(1 - exp\left(-\frac{R}{R_0}\right)\right). \quad (6)$$

Where R is the distance from the ignition ignition point, R_0 a reference distance set equal to 1 m and Ξ_K^{MAX} the maximum value of the self-wrinkling which can be calculated as [12]:

$$\Xi_K^{MAX} = \frac{E_i - 1}{\sqrt{3}}. \quad (7)$$

Where E_i is the expansion coefficient of the combustion products.

Ξ_f is the wrinkling factor due to the fractal evolution of the flame front, it is assumed that this term has an effect only after transition to the turbulent self similar regime:

$$\Xi_f = \begin{cases} 1 & \text{if } R < R_0 \\ \left(\frac{R}{R_0}\right)^{D-2} & \text{if } R \geq R_0 \end{cases}. \quad (8)$$

The value of the fractal dimension D has been set equal to 7/3 in agreement with experimental evidence [13].

Ξ_{lp} is the enhancement of turbulent burning velocity due to the leading point mechanism, which is linked to the negative Markstein length of lean hydrogen flames. The high diffusivity of hydrogen increase the flame speed in the cusps that are formed due to instabilities effect, leading in an increase in area of the flame wrinkles. It is assumed that the leading point coefficient increases linearly with the distance R until it reaches its maximum value $\Xi_{lp}^{MAX} = 2.4$:

$$\Xi_{lp} = \begin{cases} 1 + (1 - \Xi_{lp}^{MAX})\left(\frac{R}{R_0}\right) & \text{if } R < R_0 \\ \Xi_{lp}^{MAX} & \text{if } R \geq R_0 \end{cases}. \quad (9)$$

The last term Ξ_t is the flame wrinkling generated due to the turbulence in the flow. Since there is no initial flow field this and the turbulence fluctuation u' is really small, a simple algebraic relation has been used:

$$\Xi_t = 1 + 0.62\left(\frac{u'}{S_l}\right). \quad (10)$$

The model has been implemented in the opensource CFD platform OpenFOAM.

3. The THAI test facility and experiments

The model has been tested against experiments of hydrogen deflagration in the test facility THAI (Thermal hydraulics, Hydrogen, Aerosols, and Iodine), which is a containment test facility located at Eschborn, Germany. As shown in Fig. 1, the main component of the facility is a 60 m^3 stainless steel vessel, 9.2 m high, and 3.2 m in diameter, and the outer wall is insulated by a 120-mm rock-wool layer. The container is equipped with three independent oil jackets to control the wall temperature during the tests and to precondition the atmosphere inside the facility.

Thanks to its modular structure and the presence of appropriate feeding/generation devices for different gases, experimental configuration and operating conditions typical of those for PWR or BWR can be produced in the THAI vessel.

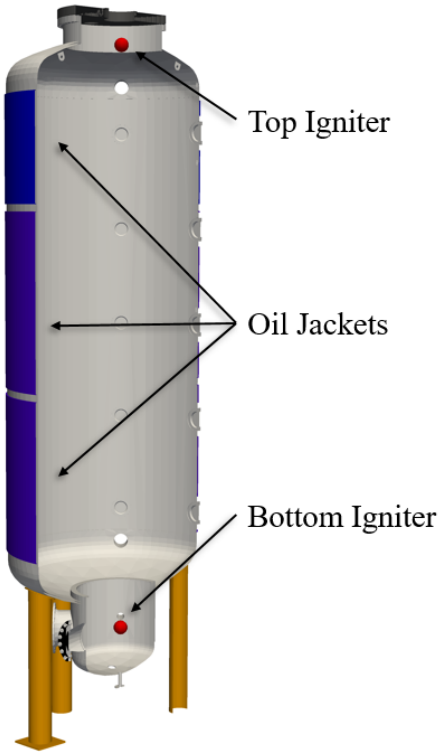

Figure 1: Schematic of the THAI test facility.

In the framework of the OECD-NEA THAI-1 project [14], a series of tests has been performed to investigate the deflagration of hydrogen-air-steam mixture, under the conditions that can be found in a containment of a nuclear reactor during a severe accident. Among those tests, four of them have been selected to be simulated in this study.

In the first two tests, HD-15 and HD-16, the facility has been filled with a mixture composed of only hydrogen and air. The pressure and temperature in the facilities, prior to ignition, has been set respectively to 1.5 bar and 90 . A recirculation fan has been used to homogenize the atmosphere inside the facility. In the HD-15 test the deflagration is started by the igniter positioned in the bottom part of the vessel, while in the HD-16 test the top igniter has been used. The tests HD-22 and HD-23, are analogous to the previous one except that the mixture has been diluted with steam. A summary of the test conditions is shown in Table 1.

Table 1: Summary of the computational grids used in the CFD simulations

Test	Vol. H_2	Direction	Vol. H_2O
HD-15	10	$\uparrow\uparrow$	0
HD-16	12	$\downarrow\downarrow$	0
HD-22	10	$\uparrow\uparrow$	25
HD-23	12	$\downarrow\downarrow$	25

During the tests 43 fast sheathed thermocouples were installed at 13 different elevations to monitor the flame front propagation and the temperature during the combustion, while 4 fast pressure transducers (strain gauge type) were used to monitor the transient deflagration pressure.

4. Simulations Setup

The combustion models are implemented in the solver XiFoam, which has been modified to take into account the effect of flame self-acceleration, not considered in the original model. Three unstructured axisymmetric meshes have been generated using the meshing utility snappyHexMesh. The computational grids have a uniform cell size in the whole domain, with an exception for the wall and the area around the igniter, where the mesh is finer, as shown in Fig. 2.

The reactants and products composition have been set according to the specification of each test, and completeness of the combustion process has been assumed. The initial temperature and pressure have been set equal to 90 $^{\circ}C$ and 1.5 bar for all the tests. The atmosphere has been considered at rest. The system of averaged equations is closed with the k-SST turbulence model, the initial value of the turbulent fluctuation u' has been set equal to 10^{-2} m/s and

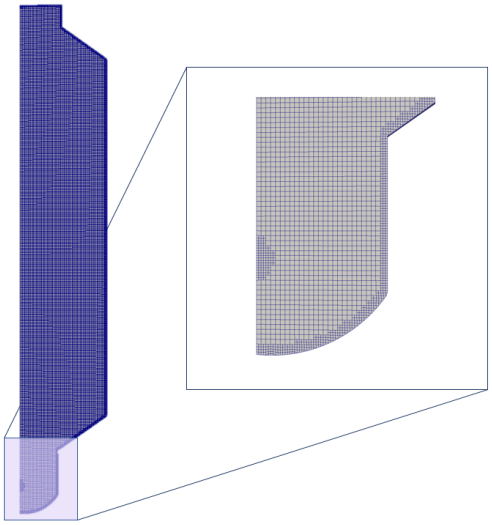

Figure 2: Mesh of the THAI facility for the simulation of the test HD-15.

the dissipation rate has been set in order to obtain a value of the turbulent viscosity lower than the molecular one, as suggested in the test report [15]. All the variable have been discretized using a second order upwind scheme, while the turbulent kinetic energy k and the dissipation rate ω have been discretized with a first order upwind scheme. Concerning the temporal discretization, the first order Euler scheme have been used. Radiation has been considered in the solution of the energy equation. The emissivity of the gas has been computed using the weighted sum of gray gases model [16], while the radiative transport has been modelled using the P1 radiation model.

The boundary of the domain is composed of a single wall. A no slip boundary condition has been applied to the velocity field, while wall functions have been used for the turbulence equations. The wall, of the THAI facility is made of a 22 mm tick steel structure. Compared to the energy released during the combustion the thermal inertia of the structure is relatively high. If the heat released during the deflagration would be evenly distributed over the whole metal structure, its temperature would increase of only 3 K degrees. For this reason, the boundary condition for the energy equation has been set to a constant value, equal to the initial one. This assumption leads to an error in the later stages of the simulation, when the inner part of the metal structure starts to heat up and the convective and radiative heat transfer to the walls should reduce.

Table 2: Cases used for testing the performance of the combustion model.

Test	N Cells	Cell Size [cm]	CPUh
Mesh 1	1598	10	80
Mesh 2	6113	5	178
Mesh 2	22479	1.5	732

5. Results

The ignition in the simulation has been started at time $t = 0\ s$, however, it is described in the experimental report that the ignition of the mixture does not happen at the exact time of the igniter activation. For this reason, all the results shown in this section have been shifted in order to match the beginning of the calculations with the ignition time of the experiments. Moreover, the igniter, which operates at a frequency of 1 Hz, is kept active for several seconds during the tests. In the simulation the ignition is modelled as a sink term in the regress variable equation, in agreement with the experiment description, and this sink was kept active during the first 2 seconds of simulation.

5.1. HD-15 Test

For the test HD-15 three simulations have been performed using the three different grids, characterized by a different cell size. The pressure transients obtained in the different simulations are shown in Figure 3 and they are compared with the experimental results.

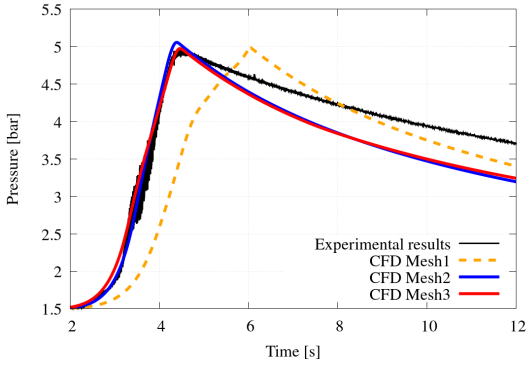

Figure 3: Comparison between the results obtained with numerical computations on the three different grids and the experimental results of the test HD-15.

The dashed orange line represents the pressure computed using the coarsest mesh. The other two simulations, performed with the more refined grids, yields

similar results, however, the pressure peak computed with the intermediate mesh is slightly overestimated. The small difference between the second and third simulation is a consequence of the small influence that the flow field has on the flame propagation. The absence of an initial flow field makes the turbulence level at the beginning of the test really small and then the combustion process is mostly controlled by the self acceleration mechanisms described in equations (6)-(9), which depend only on the distance from the ignition point and the gradient of the regress variable itself, as shown in equation (3). The only effect due to the flow is the presence of the buoyancy force which enhances the flame speed by pushing upward the burned gases, like a bubble of light gas surrounded by a heavier medium.

The first mesh however was too coarse, and the numerical error on the gradient of the regress variable becomes too high when the flame travels outside of the more refined ignition area. It was not possible then, to capture the correct evolution of the flame front during the deflagration.

All the simulations have been running on a 16 core AMD Ryzen processor. As it can be seen in Table 2 the computational time is relatively small for the first 2 simulations, while it drastically rises for the last simulation. The calculations for the other tests have been performed using the intermediate grid, due to the short computational time required and the small difference with the results obtained with the finer mesh.

Figure 4 shows the evolution of the temperature field during the simulation of the test. In the initial time steps the flames assumes the shape of a mushroom cloud, after a short time the flame evolves into an elongated shape. For most of the combustion time the hot gases are not in contact with the cold walls of the facility.

This effect, combined with the relatively short combustion time results in a correct prediction of the peak pressure, even though the temperature of the wall is kept constant in the simulation and therefore the heat transfer is overestimated in the second part of the simulation. The temperature signal recorded by the thermocouples has been used to calculate the position of the flame front in the center line of the facility. Figure 5a shows the comparison between the experimental curve represented by the black dots and the computed one represented by the blue curve. The curves agree well except in the very last half second. This difference is due to a distortion of the flame near the top flange of the facility which is not observed in the numerical calculations that have been performed using an axisymmetric domain. Overall the numerical and experimental results agree well, proving that the flame wrinkling model shown in section 2 is well suited to compute a deflagration process that happens in a single compartment.

The temperature computed trough the CFD calculation could not be directly compared with the data of the experimental database, because of the time response of the probes. For this reason, a simple algebraic model, as described by Pantazis at al. in [17], has been applied to take into account the effect of heat transfer from the fluid to the probe and the thermal capacity of the probes themselves. In the model applied the heat transfer coefficient has been calculated using a correlation for heat transfer over a cylinder [18]. The flow is considered to be always perpendicular to the flame front and the velocity used to compute the Nusselt number is equal to the magnitude of the instantaneous velocity in the point where the probe is located in the CFD domain. The processed results (dashed lines) are shown in figure 5b, where they are compared with the experimental data (continuous lines). All the probes are located at different height over the central axis of the domain. For the points that are located in the lowest area of the domain, near the ignition point, the temperature evolution during the combustion process agrees very well with the experimental data, while after the combustion has ended the temperature decrease is significantly overestimated. Concerning the probes located in the upper area of the domain, it can be observed that the time in which the flame front reaches the probes is accurately computed however the peak temperature result being overestimated. This difference is due to a distortion of the flame near the top flange of the facility which is not observed in the numerical calculations that have been performed using an axisymmetric domain.

5.2. HD-16 Test

Differently from the previous test, the flame in the experiment HD-16 propagates in the downward direction. In this case the buoyancy force is directed in the opposite direction than the flame propagation. When the mixture is ignited, the initial flame bubble is pushed upward against the ceiling of the facility. It then starts propagation downward, assuming a flat shape as can be seen in Figure 6. During most of the test the hot burned gases are in contact with the cold wall. For this reason, the peak pressure is underestimated as shown in Figure 7a, while the flame propagates at the correct speed, compared to the measurements, shown in Figure 7b. The peak pressure and

temperatures are overall higher than the one observed during the test HD-15, this is due to the higher concentration of hydrogen in the mixture. In this case the wrinkling model is again capable of predicting the correct propagation of the flame, the flame speed and time at which the combustion is ended is well predicted. The error on the pressure peak computed shows the importance of applying a correct boundary condition for the temperature, not yet implemented in the current version of the solver.

5.3. HD-22 HD-23 Tests

In the tests HD-22 and HD-23 steam was added to the initial mixture. The steam concentration has been kept equal to 25% and for the whole duration of the test the partial pressure of the steam is lower than the saturation pressure.

The presence of steam raises the concentration of diluents in the mixture, which was previously only composed of Nitrogen, but since the hydrogen concentration is kept constant the overall equivalence ratio of the combustible mixture increases, resulting in a value of the flame speed computed trough equation (4) which is around 40% lower than the values computed for the previous tests. As a result, the combustion process is slower than the tests conducted without steam, as it is shown in Figure 8 (c)-(d). In the case of the flame propagating in the upward direction this slowing effect is damped by the buoyancy force acting on the raising flame bubble. For this reason, and because of the elongated shape of upward propagating flames, the pressure peaks of tests HD-15 and HD-22 are comparable, while the highest pressure measured and computed for the test HD-23 is considerably lower than the one of the HD-16 test, as it is shown in figure 8 (a)-(b). In the latest case the hot gases transfer energy to the walls for a considerably longer time during the combustion event. On the other side, the heat transfer during the second part of the test, after the combustion has ended, is lower due to the lower temperature of the burned gases. In these cases, a larger discrepancy is observed between the pressure evolution and the tracked flame front position. A possible reason could be that the parameters used, such as the fractal dimension in equation (8) and the wrinkling of the flame due to the leading point in equation (9), are not suited for simulations of mixture with high fractions of steam as a diluent.

6. Conclusion and Future Work

It has been shown that the model implemented in OpenFOAM, is capable of describing the deflagration of a hydrogen-air mixture. The pressure transient and the position of the flame front agrees well with the experimental results. A large discrepancy in the results occur after the end of the deflagration due to the boundary condition for the temperature, which have been set uniform and equal to the initial value for all the duration of the simulation. In the future a 1D conjugate heat transfer model will be added to the solver, to resolve properly the heat transfer to the metal structure of the THAI vessel.
When steam is added to the mixture however a large difference in the results of the numerical calculations and the experimental one can be observed. Additional work is necessary to adapt the models to the presence of a diluent.

Acknowledgments

We thank BelV for sponsoring this work, and the OECD-NEA for providing the experimental database.

References

[1] S. Gupta, Experimental investigations relevant for Hydrogen and Fission Product issues raised by the Fukushima accident, Nuclear Engineering and Technology 47 (2015) 11–25.
[2] H. Weller, The development of a New Flame Area Combustion Model Using Conditional Averaging, Pr, Department of Mechanical Engineering, Imperial College of Science Technology and Medicine March (1993).
[3] J.H.S. Lee, M. Berman, Hydrogen Combustion and Its Application to Nuclear reactor Safety , Advances in Heat Transfer 29 (1997) 59–127.
[4] M.P. Sherman, Hydrogen Combustion in Nuclear Power Plant Accidents and Associated Containment Loads, Nuclear Engineering and Design 82 (1984) 13–24.
[5] H. F. Coward, G. W. Jones, Limits of Flammability of Gases and Vapors, Tech. rep., United States printing Office (1952).
[6] D.W. Stamps, M. Berman, High-Temperature Hydrogen Combustion in Reactor Safety Applications, Nuclear Science and Engineering 109 (1991) 39–48.
[7] D. R. Stull, H. Prophet, JANAF Thermochemical Tables (second edition), Tech. rep., United States printing Office (1952).
[8] H.G. Weller, G. Tabor, A.D. Gosman, C. Fureby, Application of a flame-wrinkling les combustion model to a turbulent mixing layer, Symposium (International) on Combustion 27 (1998) 899–907.
[9] A., Bentaib, A. Bleyer, N. Meynet, N. Chaumeix, B. Schramm, M. Hhne, P. Kostka, M. Movahed, S. Worapittayaporn, T. Brhler, H. Seok-Kang, M. Povilaitis, I. Kljenak, P. Sathiah, SARNET hydrogen deflagration benchmarks: Main outcomes and conclusions, Annals of Nuclear Energy 74 (2014) 143–152.

[10] V. Molkov, Fundamentals of Hydrogen Safety Engineering II, www.bookboon.com, 2012.
[11] V. Yakhot, Propagation Velocity of Turbulent Premixed Flames, Combustion Science and Technology 60 (1988) 191–214.
[12] B. Karlovits, D.W. Denniston, F.E. Wells, Investigation of turbulent flames, Journal of Chemical Physics 19 (1951) 541–547.
[13] H. Kobayashi, H. Kawazoe, Flame instability effects on the smallest wrinkling scale and burning velocity of high-pressure turbulent premixed flames, Proceedings of the Combustion Institute 28 (2000) 375–382.
[14] OECD/NEA THAI Project Final Report - Hydrogen and Fission Product issues relevant for containment safety assessment under severe accident conditions, Tech. rep., NEA/CSNI/R (2007).
[15] T. Kanzleiter, G. Langer, Quick Look Report, Hydrogen Deflagration Tests HD-22 and HD-23, Tech. rep., Tech. rep., Becker Technologies GmbH (2010).
[16] T.F. Smith, Z.F. Shen, Evaluation of Coefficients for the Weighted Sum of Gray Gases Model, Journal of Heat Transfer 104.
[17] S. Pantazis, J. Buthig, K. Jousten, Conjugate heat transfer simulations of a thermocouple sensor in a low temperature nitrogen gas ambient, International Journal of Heat and Mass Transfer 70 (2014) 536–544.
[18] S. W. Churchill, M. Bernstein, A Correlating Equation for Forced Convection From Gases and Liquids to a Circular Cylinder in Crossflow., J. Heat Transfer 99(2) (1977) 300 306.

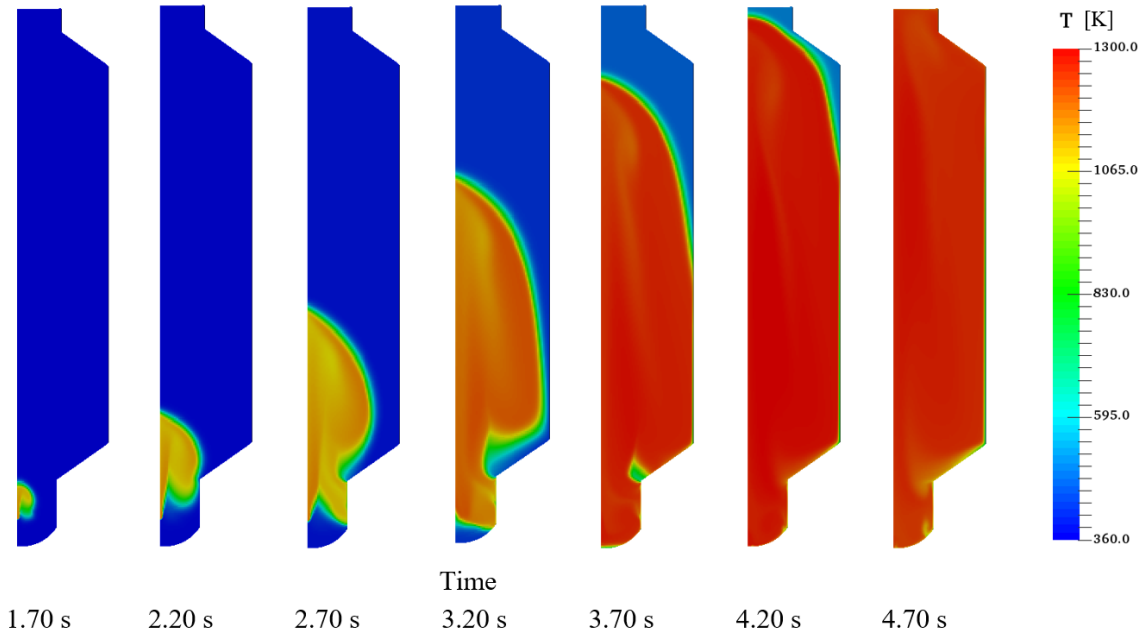

Figure 4: Temporal evolution of the temperature profile during the test HD-15.

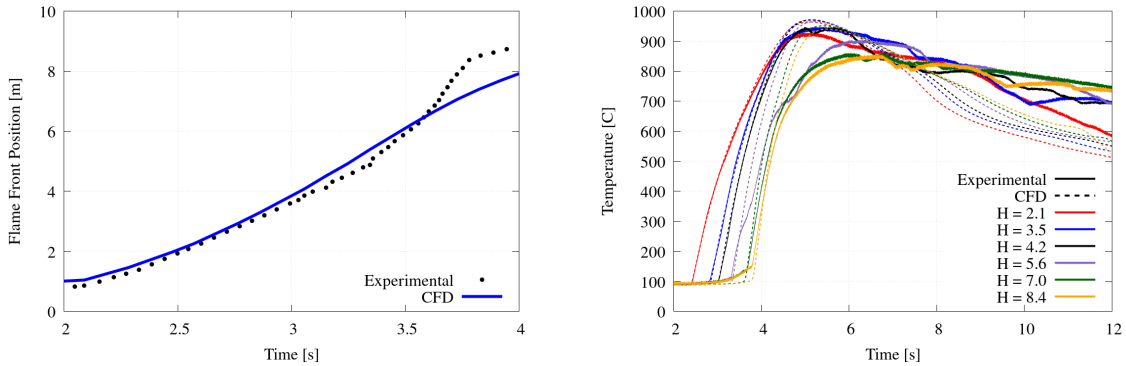

(a) (b)

Figure 5: Comparison between the measured position of the flame front and the simulated one for the test HD-15 (a) and Comparison between the measured position of the flame front and the simulated one for the test HD-15.

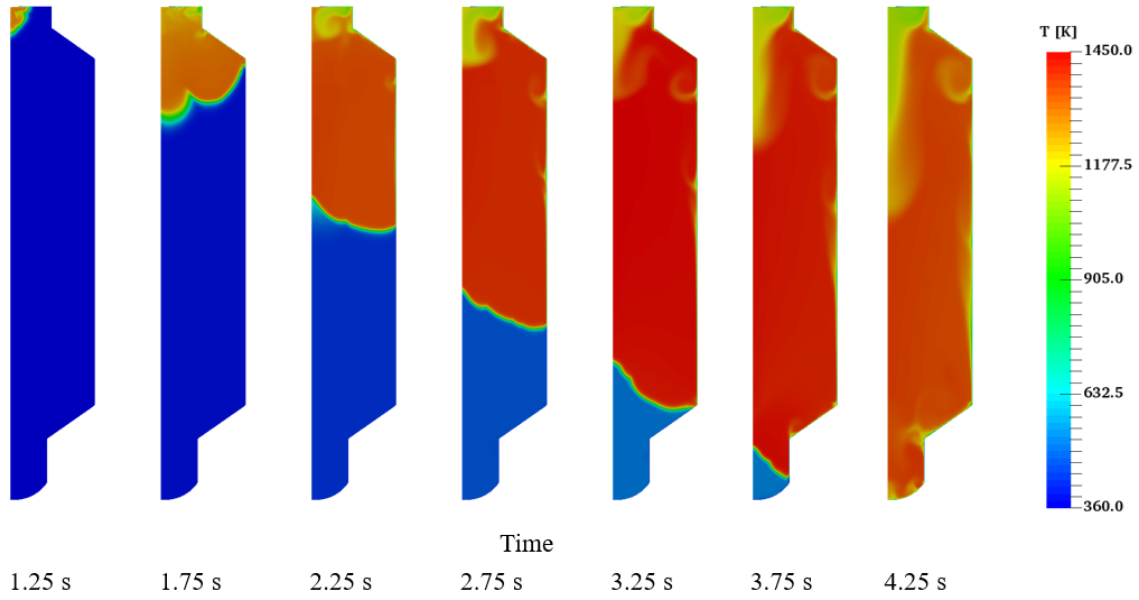

Figure 6: Temporal evolution of the temperature profile during the test HD-16.

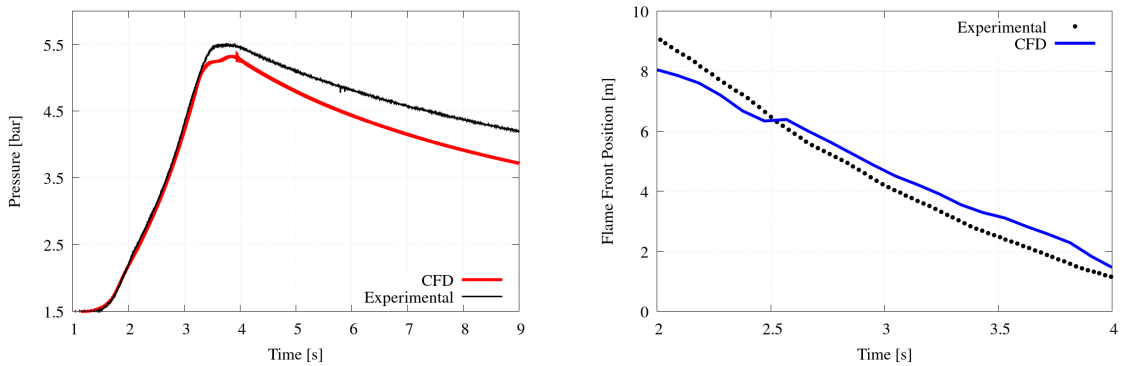

(a) (b)

Figure 7: Pressure history of test HD-16 (a) and position of the flame front on the center line of the THAI facility during the test HD-16 (b).

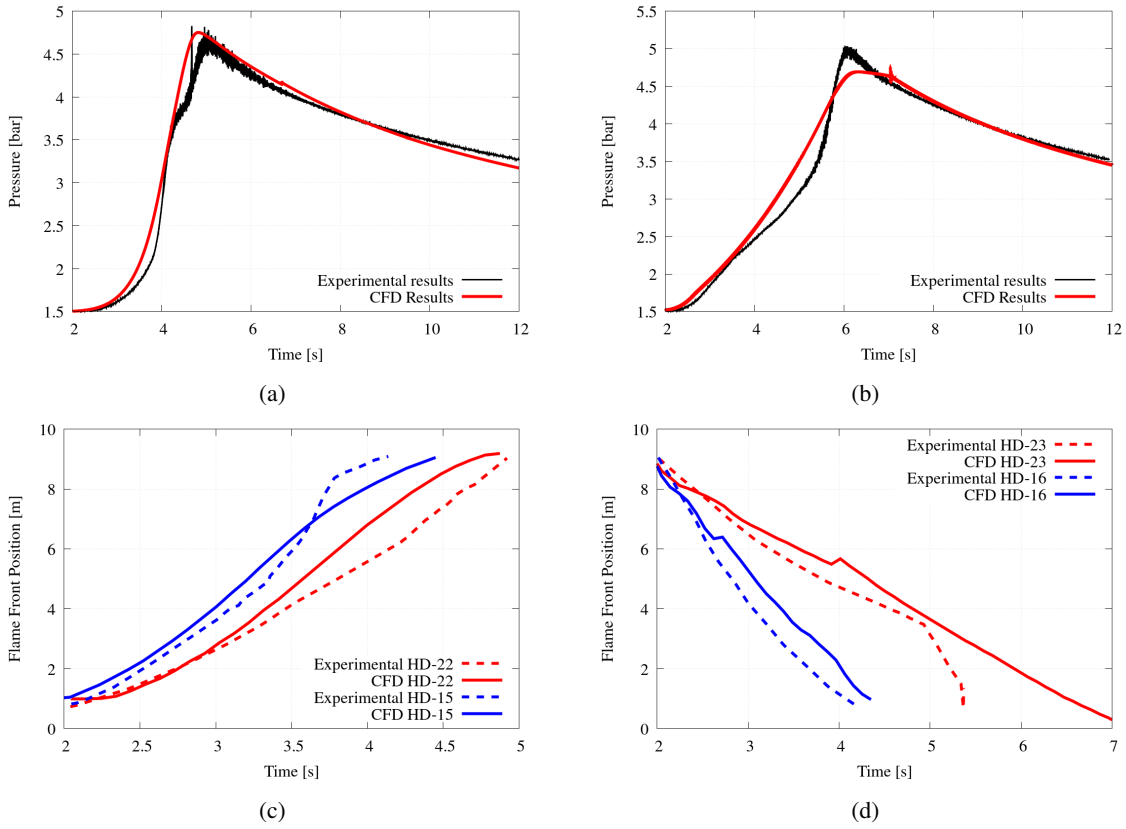

Figure 8: . Pressure history of tests HD-22 (a) and HD-23 (b). Comparison between the flame front position during the tests performed without steam (blue lines) and the one containing steam in the mixture (red lines), for upward (c) and downward (d) propagating flames.

Thermal turbulence modelling of liquid metal flows via data analysis and machine learning

Matilde Fiore

Environmental and Applied Fluid Dynamics Department, von Karman Institute for Fluid Dynamics, Belgium, matilde.fiore@vki.ac.be

Supervisor: Lilla Koloszar

Research Engineer, Environmental and Applied Fluid Dynamics Department, von Karman Institute for Fluid Dynamics, Belgium, lilla.koloszar@vki.ac.be

Supervisor: Miguel Alfonso Mendez

Assistant Professor, Environmental and Applied Fluid Dynamics Department, von Karman Institute for Fluid Dynamics, Belgium, miguel.alfonso.mendez@vki.ac.be

Supervisor: Jeroen van Beeck

Dean of Faculty, Environmental and Applied Fluid Dynamics Department, von Karman Institute for Fluid Dynamics, Belgium, vanbeeck@vki.ac.be

University Supervisor: Yann Bartosiewicz

Professor, Mechanical Engineering Department, Universite catholique de Louvain UCL, Belgium, yann.bartosiewicz@uclouvain.be

Abstract

Liquid metals play a central role in many flow configurations of industrial and academic interest, including Sun and Earth core discovery, materials processing, development of liquid metals batteries and high-performance cooling systems in nuclear reactors. Many relevant applications involve large-scale problems, for which the Reynolds Average Navier-Stokes (RANS) equations are preferred to obtain cost-effective predictions. The numerical RANS simulation of non-isothermal flows requires an appropriate closure of the averaged energy equation, and an engineering model must then be introduced to replace the complete description of the thermal turbulence.
The very low Prandtl numbers of liquid metals prevent to use widely accepted assumptions in thermal turbulence modelling, as isotropicity and similarity between momentum and thermal boundary layers. Given the limitations of the most popular RANS thermal models, low-Prandtl number turbulent flows are currently studied with the use of second order closure models and algebraic models for the turbulent heat flux, which are characterized by many a priori assumptions and are generally tailored towards the validation databases they were validated on.
Such assumptions will be relaxed in the framework of this project, to construct a general thermal model for low Prandtl number fluid flows. For such purpose, a physics constrained data-driven method will be adopted, to open a wider parameter space and enable an efficient non-linear mapping within the constraints of a general model structure that should be consistent with the physics. The proposed method is based on a complementary use of analytical methods, correlation analysis and unsupervised learning techniques (PCA, autoencoders) for a good features selection. Then, the remaining unclosed parameters will be modelled by Artificial Neural Networks (ANN), which will be trained using available high-fidelity DNS data covering natural, mixed and forced convection regimes. The validation of the model against DNS simulations and experiments will be accomplished, such that the range of applicability of the resulting model in terms of Prandtl number could be highlighted as one of the most important outcomes. Given the comprehensive set of flow configurations covered by the training data and the lack of a priori simplifications, a wide range of applicability is expected, which explains the choice of this relatively new methodology in fluid dynamics to yield a reliable Reynolds thermal closure.

Keywords: RANS modelling, liquid metals, Prandtl number, artificial neural networks (ANN)

A numerical study on the jet wiping process using LES and VOF methods

David Barreiro

Escuela Politcnica Superior, Universidade da Corua, Spain, david.barreiro1@udc.es

Environmental and Applied Fluid Dynamics Department, von Karman Institute for Fluid Dynamics, Belgium, david.barreiro@vki.ac.be

Supervisor: Miguel Alfonso Mendez

Assistant Professor, Environmental and Applied Fluid Dynamics Department, von Karman Institute for Fluid Dynamics, Belgium, miguel.alfonso.mendez@vki.ac.be

University Supervisor: Anne Gosset

Professor, Escuela Politcnica Superior, Universidade da Corua, Spain, anne.gosset@udc.es

Abstract

In metallurgy, coatings are used to protect the final products from corrosion. In the galvanization process, a coating film is applied on the ferrous substrate by submerging the latter in a molten zinc bath at 460 C. Jet wiping is a metering technique that uses a plane gas impinging jet to reduce and control the thickness of the dragged coating. The gas jet/liquid film interaction that takes place in this process is inherently unsteady, affecting the final product quality due to the formation of undulations on the final coating. It was shown to be produced by a low frequency coupling between the gas jet and the descending waves on the runback flow.

The numerical work carried out in this thesis to understand the undulation mechanism is articulated through two different strategies. One is based on high fidelity CFD simulations consisting in 3D two-phase simulations using the Smagorinsky one equation Large Eddy Simulation model for an accurate estimation of the turbulent behaviour of the gas jet and the Volume of Fluid method for the tracking of the interface. This approach is validated in laboratory conditions via confrontation with extensive experimental data. In that way, it can be later used for ”numerical experiments” which will provide reference data for the study of the mechanism in industrial conditions. The other strategy focuses on the development of a hybrid solver to build a bridge between high fidelity simulations of the gas jet and integral boundary layer model for the liquid film. It consists in a single phase high fidelity simulation fully coupled with an integral model. The jet wiping actuators are estimated by the former and the liquid interface by the latter. The models are fed by each other, overcoming the limitations they present when used separately.

Keywords: free surface flows, jet wiping, air-knife coating, two-phase CFD, integral boundary layer

AEROACOUSTICS

Inferring empirical wall pressure spectral models using Gene Expression Programing

Joachim Dominique

Environmental and Applied Fluid Dynamics Department, von Karman Institute for Fluid Dynamics, Belgium, joachim.dominique@vki.ac.be

Supervisor: Christophe Schram

Full Professor, Environmental and Applied Fluid Dynamics Department, von Karman Institute for Fluid Dynamics, Belgium, christophe.schram@vki.ac.be

University Supervisor: Wim Desmet

Professor, Production Engineering, Machine Design and Automation (PMA) Section, KU Leuven, Belgium, wim.desmet@kuleuven.be

Abstract

In many aerospace applications, it is critical to be able to model the pressure spectra beneath a turbulent boundary layer. This paper presents a new, data-driven, approach to build empirical models for turbulent boundary layer wall-pressure spectrum. Those new empirical models are not given by extending previously existing ones but directly built from the data at our disposal. Using this approach, the definition of new wall-pressure model becomes a symbolic regression problem that can be investigated using a genetic algorithm: the Gene Expression Programming. In order to prove the validity of such approach, the Gene Expression Programming has been used in this paper to retrieve the well-known models of Chase-Howe and Goody from a synthetic noisy dataset.

Keywords: Genetic Algorithm, Gene Expression Programing, Wall Pressure Models, Turbulent Boundary Layer

1. Introduction

The modelling of the vibration and noise induced beneath a turbulent boundary layer is common to a broad range of applications in the aeronautics and automotive field. Indeed, the noise generated by the interaction of the turbulent boundary layer with a sharp surface such as an airfoil trailing edge is often considered as an indicator of the minimum sound level for a fan or an airfoil in a clean airflow [1]. In the automotive sector, wind noise originated from the interaction between the turbulent boundary layer and the vehicle surface is considered to be the dominating sound source for cars above 100km/h [2].

The pressure fluctuations beneath a turbulent boundary layer in a flow at low Mach number are given by the divergence of the Navier-Stokes equations

$$\frac{1}{c^2}\frac{\partial^2 p}{\partial t^2} - \frac{\partial^2 p}{\partial x_i^2} = \frac{\partial^2 \left(\rho v_i v_j - \langle \rho v_i v_j \rangle\right)}{\partial x_i \partial x_j}, \qquad (1)$$

where ρ is the fluid density, c is the speed of sound and the bracket denotes an ensemble average. This reduces to the Poisson equation in the case of strictly incompressible flows. However, such an integral model is undoubtedly complex for three reasons: (1) As indicated in the integral equation, velocity fluctuations in all parts of the boundary layer participate to the wall pressure fluctuations; (2) Within the boundary layer, the turbulent velocity fluctuations are convected at different speeds; (3) There is not a single scaling to describe the velocity field in the boundary layer [3].

The complexity of the phenomena has motivated the research on wall pressure turbulence since the 1960s [4]. Over the years, many researchers such as Amiets [5] or Howe [6] proposed simplified empirical models of increasing complexity for engineering applications. The empirical model of Chase-Howe was improved by Goody in 2004 [7] to take into account the effects of Reynolds number and correct its high frequency discrepancy. A review of all existing models was performed by Hwang et al in 2007

and proved Goody's models to be the most accurate one for boundary layers without pressure gradient [8]. More recently, several authors (Kumruzzaman in 2010, Rozenberg in 2012, Hu in 2017, ...) have proposed models to capture the effect of pressure gradients on the turbulent boundary layer pressure fluctuations. Those models were reviewed by Lee et al in 2017 and it was shown that although each model fit well their own validation data, they tend to fail to provide consistently accurate results for all datasets available [9].

Until now, the approach preferred to extend wall pressure fluctuation models to pressure gradient flows consists in adapting the coefficients of a known mathematical expression often inspired from the model proposed by Goody. This methodology will be referred here as the *physics-based* approach. However, the growing number of available experimental datasets and the recent improvements of data analysis techniques have made possible to consider a new approach where the underlying mathematical expression is no longer obtained from the Goody model but directly built from data using symbolic regression. Such *data-based* approach will be investigated in this work using the symbolic regression algorithm called Gene Expression Programing (GEP).

This paper presents an implementation of GEP for the symbolic regression of wall spectral pressure fluctuations models using the open source Python library Geppy. We start by describing the GEP algorithm and its extension for an effective finding of decimal power. We use this algorithm on synthetic noisy data to retrieve the previously proposed models of Chase-Howe and Goody. Finally, we will use the results to discuss the applicability of GEP as a data-based method to investigated new wall pressure spectral models.

2. Traditional gene expression programing

Gene expression programing is an evolutionary algorithm that builds mathematical models from data [10]. Over the past decade, GEP has been used with success in different fields such as time series regression, data mining or knowledge discovery, but it will be mostly employed in this work as a symbolic regression tool [11]. It should be pointed out that this paper is not the first application of GEP to the field of fluid dynamics as this method has already be applied for the generation of various kind of turbulence models from high fidelity numerical data [12; 13; 14; 15].

Like other evolutionary algorithms, GEP optimizes solutions by iteratively modifying non-deterministically a population of individuals using a process that mimics natural selection and survival of the fittest (Fig. 1). Among an initial population of candidate solutions, the best individuals are selected based on their fitness while the less fitting ones are rejected. Those least-fit individuals are later replaced by new candidates that are build from random genetic variations.

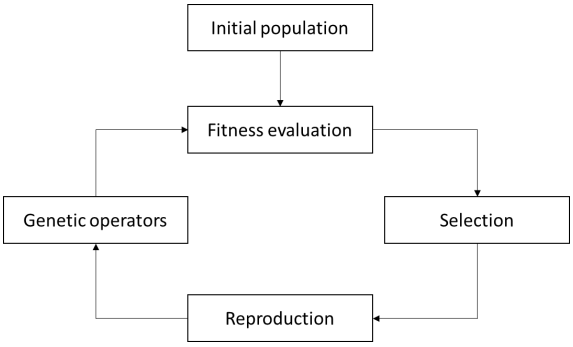

Figure 1: Gene expression programing uses the evolutionary optimization flowchart

In this section we will illustrate in details the different steps of the traditional GEP optimization starting with the construction of the individuals and the mean used to evaluate their fitness. Then, the procedure used to select and reproduce the best fitting candidates will be discussed along with the operators used to introduce genetic variations into the remaining pool of candidates. We will conclude this section by discussing specific issues that such an algorithm can face, such as the determination of numerical constants.

2.1. Individuals

2.1.1. Single-gene individuals

In GEP, the individuals are encoded as linear strings of fixed length. Each element of the string is either a function or a terminal selected among predefined sets. As an illustration, the string in Fig. 2 has been constructed from the function set F : $[Q, +, -, \times]$ and the terminal set T : $[a, b]$, where Q is the square root operator and $[a, b]$ are numerical variables.

The linear string translates into an expression tree which corresponds to a specific valid equation. In this case, the linear string has a fixed total length of 21 elements but the corresponding length of the expression tree may vary. Indeed, Fig. 2 shows an expression tree that only uses the first 11 elements of the linear string. This is known as the concept of Open Reading Frame (ORF). Such a formulation allows to create

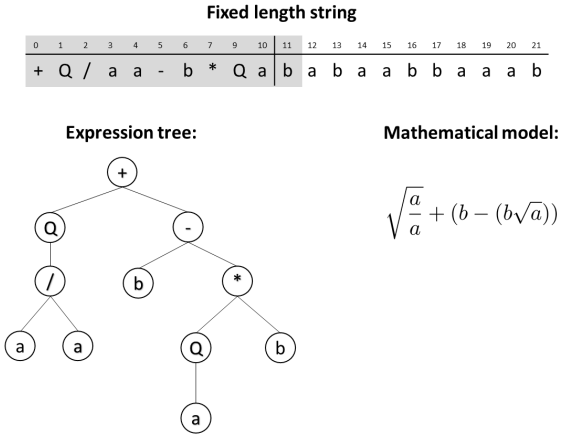

Figure 2: Example of an individual representation

solutions of different length while conserving a fixed length string representation. For example, when the element 11 of the individual is changed from b to + in Fig. 3, the length of the expression tree increases by two.

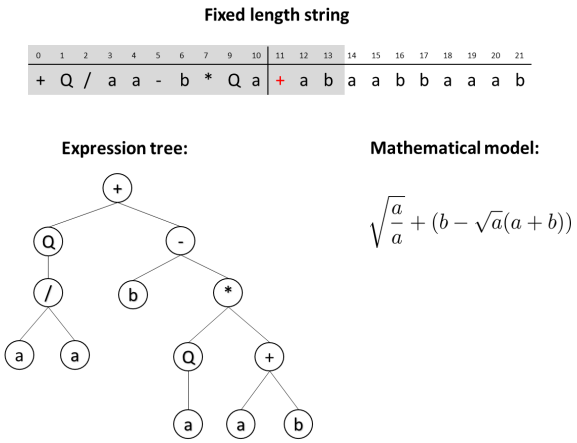

Figure 3: Modification of element 11 from the previous individual example

To ensure that every expression tree results in a correct mathematical model, every branch of the expression tree must finish by a terminal. This is achieved by dividing the linear string in two parts called respectively *the head* and *the tail*. The first h elements of the string are the head and consist of mathematical operators OR terminal functions. The tail of length $t = h(n_{max} - 1) + 1$, where n_{max} is the maximum arity of the functional set, is only composed of terminals. Therefore, regardless of the number of operators used within the head region, there always will be enough terminals inside the tail to provide a valid mathematical expression. In the previous examples, the head length is $h = 10$ and the tail length is $t = h(2 - 1) + 1 = 11$.

2.1.2. Multigenic individuals

Individuals are usually composed of not one but multiple genes. When you combine multiple genes of similar length, you compose a solution of multiple sub-expression trees which are able to evolve separately from each other as independent entities. This facilitates the findings of relevant shorter solutions.

To connect the different genes together and form a valid mathematical model, the individual must be provided with a linking function. Three different types of linking functions are discussed here:

- Prescribed linking functions : All sub expression trees are linked together by a prescribed mathematical function that remains unchanged during the evolution process as illustrated in Fig. 4. This restricts the search space of the algorithm as the genes will always be arranged in the same way.
- Random linking functions : The linking functions are chosen randomly among a set of operators. This allows the shape of the individuals to change during the evolution as the same gene can interact in a variety of ways and produce different solutions. However, since the connection between the genes is always a linear combination of the operators, non-linear gene structure can never be created. Indeed, $f = G_1/G_2 + G_3$ is not equivalent to $f = \frac{G_1}{G_2+G_3}$. This also restricts the search space of solutions that individuals can represent.
- Automatically Defined Functions (ADF): Another additional gene is added at the end of the multi-genic structure that describes how the sub expression trees are linked together, this solution allows both the global shape to evolve during the evolution and also the creation of non-linear entities. It is also the most difficult method to implement.

2.2. Fitness

The fitness of an individual is defined as its capability to reproduce a set of points. It is also considered as an indicator of its quality and it is the quantity that we are trying to minimize through the optimization process. In the context of symbolic regression, the set of

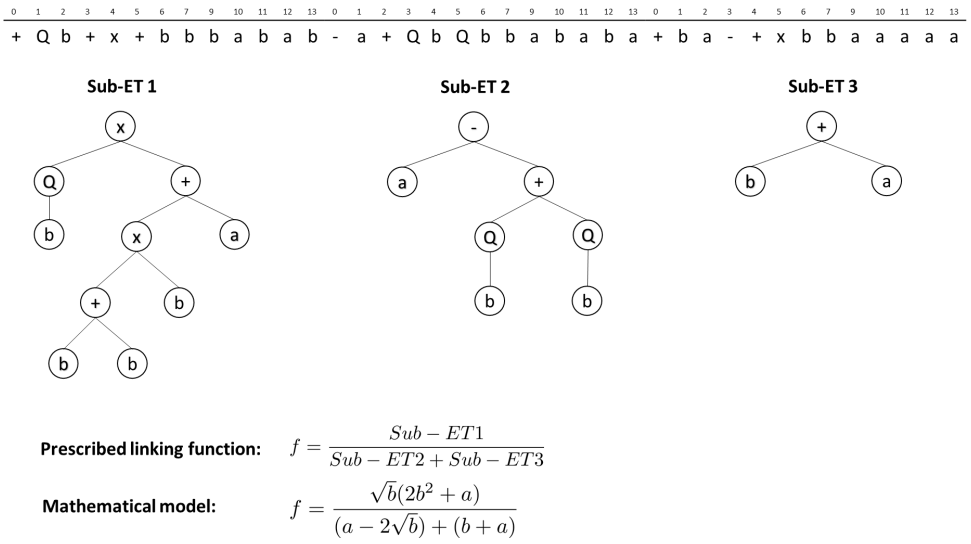

Figure 4: Contruction of multigenic individual using prescribed linking function

points used represent the training dataset that we are trying to fit with a function. Assuming a set of n training points (f_n, x_n, y_n) and an individual function f_{ind}, the fitness is defined as the mean square error (MSE):

$$\text{MSE} = \frac{1}{n}\sum_{k=1}^{n}(f_{ind}(x_k, y_k) - f_k)^2 \qquad (2)$$

It should be stressed that GEP differs from other evolutionary algorithms because the selection/mutation process and fitness computation are performed on different entities. Here, the selection and mutation process are performed on the linear string formulation which is linear, compact and easy to manipulate genetically, while the fitness is computed from the expression tree which is a complex nonlinear expression. The compactness of the representation of the linear string entities, combined with the complexity of the expression tree formulation, is the strength of the GEP algorithm.

2.3. Selection and reproduction

At each generation, the best members of the population are selected based on their fitness (Eq. 2) to breed a new population of individuals through evolutionary processes. Such selection is accomplished using what is called tournament selection. This is a competition between individuals where *n* randomly selected individuals compete with each other *k* times and the less fitting ones of each tournament are eliminated. This selection is used to remove badly adapted solutions from the pool of candidates. The *k* winners of the tournament are passed to the population of the next generation. To fill the empty spots in this new population, the winners will reproduce sometimes with modifications due to mutations.

Another possible method is called roulette wheel selection. In this method each individual has a probability proportional to their fitness to be selected for the next generation. This enables good candidates to have a higher chance to be selected and conserved to the next generation. The wheel is turned as many time as necessary to fill the next generation. Although this method seems more elaborate it has been shown to converge less rapidly than the tournament selection [16]. Therefore, the tournament selection was preferred in this work.

2.4. Mutation Operators

Using selection only, the pool of candidates remains unchanged and the algorithm cannot create new and better fitting solutions. To trigger those changes, GEP uses a process call mutation where each individual of the selected population has a chance to modify part of its solution using mutation operators. Those mutation operators describe how evolution is introduced in the algorithm. They are usually separated into three groups: Mutation, transposition and recombination.

2.4.1. Mutation

Mutation is the most basic operator where a random element of different genes is changed. This allows to

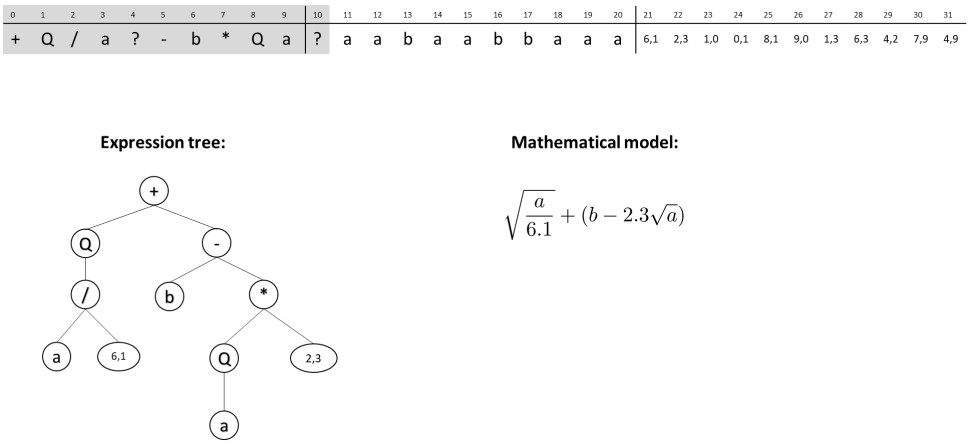

Figure 5: Construction of an individual including RNC terminals and an DC array

create diversity into the selected pool of candidates. It is described by two probabilities: The first (p_m^1) gives the probability of a given individual to be selected for mutation. The second (p_m^2) describes the probability of each gene to be randomly changed into another function or terminal. For instance, a large (p_m^1) and a small (p_m^2) implies that many individuals will be slightly modified, and vice-versa. It should also be noted that this operator must respect the structure of the individual. In the head a gene can be transformed into a function or a terminal but in the tail only a terminal can be selected.

2.4.2. Transposition

The second type of mutation operator, transposition, is when part of a gene is moved to another location within the same gene. The numbers of element moved is variable, it can be a single element or multiple functions and terminals. When the sequence is moved at the root of the individual this process is called RIS transposition and when it is moved at another position it is called IS transposition. They have respectively transposition rate of p_T^1 and p_T^2.

2.4.3. Recombination

Recombination, the last type of mutation operator, is when a single element or a sequence of elements are exchanged between different genes. There are three types of recombination:

- one-point recombination (p_r^1) : A position is randomly selected in two genes and all the information past this point is exchanged.
- two-points recombination (p_r^2) : The information exchange between genes is everything in between two randomly selected positions.
- Gene recombination (p_r^3) : This only occurs in multigenic individuals, all the information of a gene is exchanged between two individuals.

All those mutation operators are not necessarily applied to every individual simultaneously due to their respective rates. As a result, some individuals might be affected by several mutation operators and others by none. In fact, their probabilistic rate affects strongly the convergence of the GEP algorithm. The best convergence of the algorithm is obtained by balancing selection and mutation. When there is not enough mutation, the algorithm does not generate many new individuals and tends to converge toward local minima. On the contrary, when there are too many mutations, the selection and evolutionary process cannot take place and the GEP reduces to a random search algorithm.

2.5. Numerical constants

The determination of numerical constants has always been a bottleneck for non-gradient based methods such as genetic algorithms. As a result, GEP suffers from the same limitations. In the past, numerical constants were introduced within the GEP using mostly two methods: Random Numerical Constants (RNC) or Ephemeral Numerical Constants (ENC).

RNC work as a particular type of terminal because it also introduces a new array of genes that comes after the tails named the DC domain. As illustrated in Fig. 5 this domain is constituted of numerical constants that

can evolve (using the same selection-mutation process as other genes) during the optimization. Every time the RNC terminal ? is encountered, the numerical constants from the DC array are inserted from left to right into the expression tree. To ensure that there are always enough RNC variables available, the length of the DC array should always be as long as the tail of the individual.

ENC works in a similar fashion, except that the pool of numerical constants is not selected from an additional array but randomly selected within a user-defined range. This implies that the search region of the algorithm is reduced but that the numerical constants do not have the chance to evolve as the optimization carries on.

3. Existing wall pressure spectral model

As previously discussed in the introduction, wall pressure models have been subject of ongoing research for the last 50 years. Today, dozens of semi-empirical models of various complexity and accuracy are available and almost all of those models were generated using a *physics-based* approach. Since we propose to investigate a new *data-based* approach, the first step is to prove that such an approach can yields equally meaningful results by comparing it to already existing models.

In this section, we will apply the GEP to two training datasets constituted of points obtained from existing wall pressure models: the Chase-Howe [6] model and the Goody model [7]. We are going to evaluate the quality of the GEP solutions regarding 1) their capability to reproduce their training dataset (the fitness of the model); and 2) the similarity between the proposed GEP mathematical expression and the true model. In particular, specific attention will be given to the ability of the GEP to retrieve meaningful trends of the models such as the Reynolds dependency or the high and low frequency trend.

Initially, the GEP algorithm showed some difficulties retrieving the model of Goody. In order to overcome those limitations, two modifications of the traditional GEP algorithm were implemented: a new type of power terminal and a local optimization loop. In this section, we will start by discussing the modifications applied to the traditional GEP algorithm and we will later discuss the results obtained by investigating the datasets built from the existing wall pressure models.

3.1. Modification of the traditional GEP algorithm

Most wall pressure spectral models include multiple variables with high fractional exponent values. To approach such exponent using the traditional function set $[+, -, /, \times, Q]$, the GEP must create long tree structures as illustrated in Fig. 6. This makes the convergences of the algorithm weak as a very long linear string must be considered. As a result, the algorithm provides very long and complicated mathematical expressions which are often not similar to the existing wall pressure models.

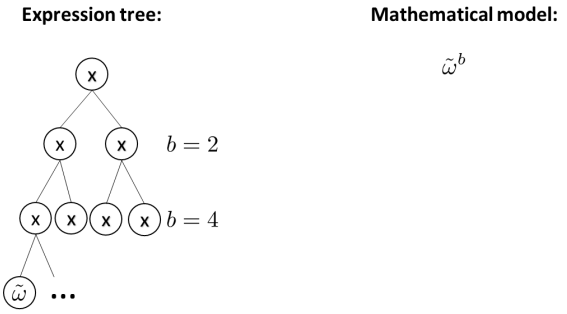

Figure 6: Illustration of the problem due to the approximation of high exponent variables

An elegant solution to this problem is to introduce a new type of terminal named the *pow* terminal. The said *pow* terminal works similarly to an RNC terminal, except that the numerical constants selected act as a numerical exponent to a variable. As an example, the pow terminal of the variable named a can be written as $a^?$ where ? is a numerical constant selected among the DC terminal. This formulation permits an easy creation of variables with large fractional exponent and relatively short linear string.

As we have discussed in the previous section, evolutionary algorithms are non-gradient based optimization techniques. Therefore, they have trouble to correctly approach numerical constants. This is normally not an issue, but the introduction of the *pow* terminal that uses numerical constants from the DC array as exponent value for some variables has put additional strain on the ability of the GEP to accurately approach numerical constants. For this reason, an additional local optimization loop was added to the traditional evolutionary algorithm as shown in Fig. 7. This local optimizer has the effect that every time that the condition is satisfied the numerical constants in the DC array of some selected individuals are changed to their best fitting values using a least-square regression. The least square regression is far slower than the

reproduction/mutation optimization performed within the evolutionary process. However, by controlling its occurrence rate through the condition, we can feed to the optimization process with well-fitting numerical constants while not penalizing too much the convergence time. In addition, not all the training dataset is used for the least-square optimisation. A randomly selected subset of the training data is used each time the optimization loop is activated leading to a so-called *stochastic least square regression* for the numerical constants determination.

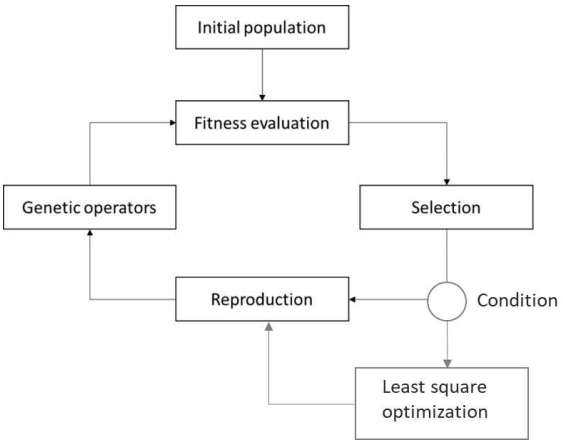

Figure 7: Local optimization in the GEP flowchart

3.2. Validation on Chase-Howe model

Using the theoretical development of Chase, Howe proposed a semi-empirical model that describes the behavior of the wall-pressure field at low Mach number based on mixed variables:

$$\frac{\Phi_{pp}U_e}{\tau_w^2\delta^*} = \frac{2\tilde{\omega}^2}{(\tilde{\omega}^2 + 0.0144)^{3/2}} + N, \tag{3}$$

where Φ_{pp} is the surface pressure spectrum, U_e is the external boundary layer velocity, τ_w is the wall shear stress, δ^* is the displacement thickness and $\tilde{\omega} = \frac{\omega\delta^*}{U_e}$. This model scales as $\tilde{\omega}^2$ at low frequency and as $\tilde{\omega}^{-1}$ at high frequency but it does not provide the expected stronger negative slope at higher frequencies and does not account for the Reynolds number effect. The Chase-Howe model was shown to not be the most accurate but its simple mathematical expression makes it a good candidate to try the GEP approach. Indeed, the Chase-Howe model describes the behaviour of the wall pressure fluctuations using a single variables $\tilde{\omega}$ and only one numerical constant $C_1 = 0.0144$.

The training dataset used within the GEP algorithm will be constituted of 1000 points obtained from Eq. 3 with additional Gaussian noise N that is used to represent the uncertainty that can be found in experimental data. Two Gaussian noise sources are considered in this investigation such that $N = N_1 + N_2$. The first noise source is proportional to 5% of the amplitude of $\frac{\Phi_{pp}U_e}{\tau_w^2\delta^*}$ while the second noise source is a normal Gaussian noise with a constant amplitude of 0.01 used to model the background noise.

To approach Eq. 3, the function and terminal set will be set respectively to F : $[+, \times, /, Q]$ and T : $[\tilde{\omega}, 1.0]$. It was decided to approach the numerical constant $C_1 = 0.0144$ using an RNC terminal and a DC array composed of strictly positive constants. When defining those sets, it is of utmost importance to ensure that any combination of operators and terminals cannot result in an inconsistent solution. For example, we must ensure that the algorithm cannot perform divisions by zeros or roots of negative numbers. Since $\tilde{\omega}$ is strictly positive and non-null, such mathematical operations will never happen in this simulation. Otherwise, some conditions must be implemented within the optimization loop to avoid those operations. For this simple model, we are using the traditional GEP, not using any of the additional modifications previously discussed.

Next, the number of genes and the head length that describes the shape of the solution need to be defined. The number of genes considered usually depends on the type of linking functions used to connect the genes. Since we know from theory the mathematical model used to create the dataset, we can use a prescribed linking function of similar shape to facilitate the convergence. In this case, we are going to consider 3 genes connected using the following linking function : $f = \frac{G_1}{(G_2 \times G_3)}$. The head length sets the maximum length of the individuals. If the head is too short, the solutions proposed by the algorithm will not be complex enough to accurately fit the dataset. But, if the head is too long, the mathematical solution proposed will tend to overfit by proposing unnecessary complex solutions for the problem. This prevents the GEP algorithm to retrieve physically meaningful mathematical expressions from the dataset. Therefore, the head length h should be chosen as the smallest value that allows to capture the complexity of the training dataset. Figure 8 shows the evolution of the mean fitness over 10 solutions for different head lengths. It can be seen that for $h \geq 3$ the mean fitness is no longer strongly impacted by the size of the solutions allowing us to set

the head length to 3.

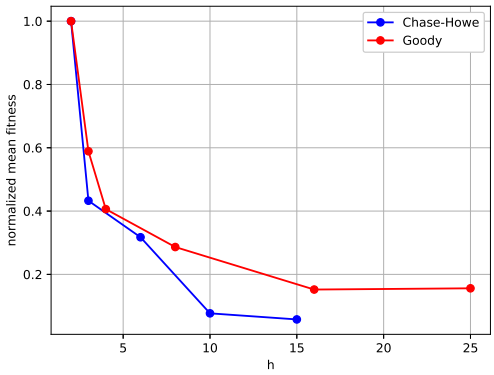

Figure 8: Representation of the minimum length of the linear string

Below, we can inspect 4 different solutions proposed by the GEP approach in Tab. 1 and represented in Fig. 9. It can directly be seen from Fig. 9-left that the fit with the noisy data is excellent for all solutions. However, the solution expressed in log scales in Fig. 10-right shows that finding the correct trends at low and high frequency is more difficult. Indeed, only solution 4 was able to retrieve the expected trend of $\tilde{\omega}^{-1}$ and $\tilde{\omega}^2$ at high and low frequency. It is surprising to observe that this solution is not the one that led to the lowest fitness, although it gives the best representation of the physics of the model.

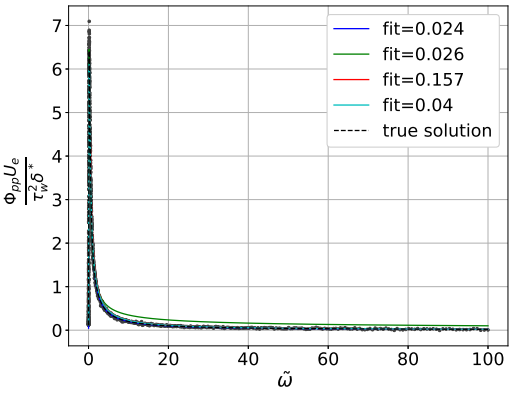

Figure 9: Comparison between the GEP solutions and the Chase-Howe model. The grey dots represent the training set and the black dotted line is the true Chase-Howe model. The four different GEP models expressed in Tab. 1 are represented in coloured lines

Overall, all the solutions proposed using the GEP algorithm have a high resemblance to the equation of

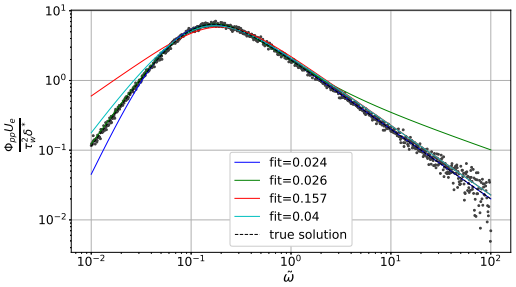

Figure 10: Same plot as before but with the trends highlighted in log-log representation

the model of Chase and Howe, and it would take very little engineering judgment to move from the set of approximate equations to the real one. The biggest differences observable between the GEP models and the model proposed by Chase and Howe is due to the approximations of numerical constants that is difficult within the GEP optimization and the evaluation of the correct exponent values.

3.3. *Validation on Goody model*

The results obtained for the Chase-Howe model are sufficiently good to encourage the investigation of the more complex but also more realistic model of Goody. Starting from the Chase and Howe model, Goody proposed another model that accounts for the third slope at high frequency and includes a correction for the effect of the Reynolds number:

$$\frac{\Phi_{pp}U_e}{\tau_w^2\delta} = \frac{C_2(\omega\delta/U_e)^2}{((\omega\delta/U_e)^{0.75} + C_1)^{3.7} + (C_3(\omega\delta/U_e))^7} + N, \tag{4}$$

where $C_1 = 0.5$, $C_2 = 3.0$ and $C_3 = 1.1R_T^{-0.57}$ describes the effect of Reynold number. As one can see, the scaling of the Goody model depends on the boundary layer thickness δ instead of the displacement thickness δ^* in Eq. 3. Other than that, the wall pressure spectrum and frequency scaling $\tilde{\omega} = \frac{\omega\delta}{U_e}$ remain unchanged. This model depends on two variables: $\tilde{\omega}$ and R_T and has a longer mathematical expression with several numerical constants. Therefore, Goody model is likely to be more difficult to approach using GEP. However the Goody model is often considered today as the starting point to derive new spectral wall pressure models that account for other physical effects such as the pressure gradient [17]. Validating the GEP approach with this model would prove the

validity of our approach to derive new wall pressure fluctuations models.

The dataset used for this model comprises, as before, of 1000 points for 5 different Reynolds numbers $R_T = [1, 3.16, 10, 31.62, 100]$ for a total of 5000 points in the training set. The noise N is modelled as in the Chase-Howe model with two Gaussian noise sources. The functional and terminal set considered are defined as F : $[+, \times, /, Q]$ and T : $[\tilde{\omega}, 1.0, \tilde{\omega}^2, R_T^2]$. As shown, the terminal set is composed of the modified power terminal discussed in the previous section. However, at first, we will not be using the local optimization loop. Later in this section, we will redo the same GEP approach using the local optimization to show its impact on the quality of the solutions.

The number of genes selected to approach this model was set to 3 and they are connected using the prescribed linking function $f = \frac{G_1}{G_2+G_3}$. The head length was also chosen as $h = 4$ in order to be the smallest value of h that allows to capture the complexity of the training dataset as illustrated in Fig. 8.

Below, 4 different solutions proposed by the GEP approach are shown in Tab. 2 and represented in Fig. 11. Those results are very satisfactory because all the models proposed are alike and resemble strongly the model proposed by Goody. In addition, the use of the power terminal allowed to find trends for the different variables very close to the ones expected from the model. Indeed, the Goody model predicted a Reynolds dependency as R_T^4 and exhibits a decrease as $\tilde{\omega}^{-5}$ at high frequency. Only the trend as $\tilde{\omega}^2$ at low frequency is not observed for every solution in Tab. 2. This is likely due to the Gaussian noise that is always positive and affects the trend a low frequency.

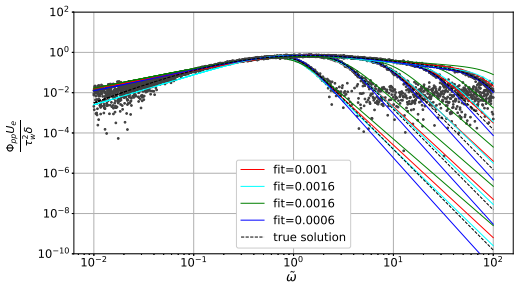

Figure 11: Comparison between the GEP solutions and the Goody model. The grey dots represent the training set and the black dotted line is the true Goody model. The four different GEP models expressed in Tab. 2 are represented in coloured lines

As in the Chase-Howe model, below a given threshold, the fitness gives little indication on the quality of the results. Again, the model that is the closest to the Goody model (Solution 2) is not the one with the lowest fitness.

We can now investigate the impact of the local optimization loop using the least square method. The same parameters as before were used inside the GEP except that we enable the local optimization at each generation. This implies that at each generation, three individuals have their numerical constant in the DC array transformed through a least-square regression.

The solutions for this optimization are shown inTab. 3 and represented in Fig. 12. Using the local optimization not only allows improving the prediction of the numerical constant and the fitness of the individuals, it also improved the accuracy of the model's trends. Indeed, the trend at low and high frequency are now predicted with a better accuracy.

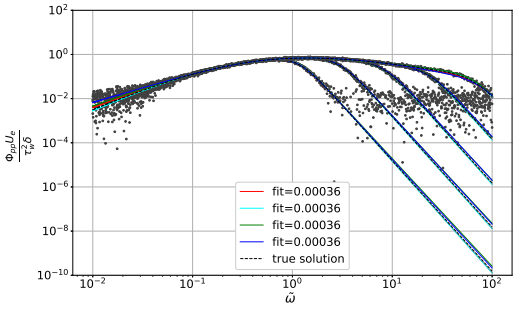

Figure 12: Comparison between the GEP solutions and the Goody model using the local optimization loop. The grey dots represent the training set and the black dotted line is the true Chase-Howe model. The four different GEP models expressed in Tab. 3 are represented in coloured lines

It can be seen that the fitness values are almost identical for all solutions although there are four different solutions. Once again, we can see that below a given threshold, the fitness defined as a MSE is not a good criterium to characterize the quality of candidate solutions.

N	Expression	Simplified	Fitness	$\tilde{\omega} \to 0$	$\tilde{\omega} \to \infty$
Solution 1	$\frac{2\tilde{\omega}}{(\tilde{\omega}+\frac{0.021}{\tilde{\omega}})(\tilde{\omega}+\frac{0.002}{\tilde{\omega}})}$	$\frac{2\tilde{\omega}^3}{(\tilde{\omega}^2+0.021)(\tilde{\omega}^2+0.002)}$	0.024	$\tilde{\omega}^3$	$\tilde{\omega}^{-1}$
Solution 2	$\frac{(1.06+\tilde{\omega})}{(\sqrt{\tilde{\omega}}+\frac{0.05}{\tilde{\omega}})(\tilde{\omega}+\frac{0.017}{\tilde{\omega}})}$	$\frac{(1.06+\tilde{\omega})\tilde{\omega}^2}{(\tilde{\omega}^{3/2}+0.05)(\tilde{\omega}^2+0.017)}$	0.026	$\tilde{\omega}^2$	$\tilde{\omega}^{-1/2}$
Solution 3	$\frac{\tilde{\omega}}{(0.038+\tilde{\omega}^2)(0.037)^{0.25}}$	$\frac{\tilde{\omega}}{(0.038+\tilde{\omega}^2)(0.037)^{0.25}}$	0.157	$\tilde{\omega}$	$\tilde{\omega}^{-1}$
Solution 4	$\frac{2.076}{(\tilde{\omega}+\frac{0.017}{\tilde{\omega}})(1+\frac{0.065}{\tilde{\omega}})}$	$\frac{2.076\tilde{\omega}^2}{(\tilde{\omega}^2+0.017)(\tilde{\omega}+0.065)}$	0.04	$\tilde{\omega}^2$	$\tilde{\omega}^{-1}$

Table 1: Representation of 4 different solution proposed by the GEP to approach Chase-Howe model

N	Simplified	Fitness	Reynold dependency	$\tilde{\omega} \to 0$	$\tilde{\omega} \to \infty$
Solution 1	$\frac{\tilde{\omega}^{0.9}}{\tilde{\omega}^{5.5}R_T^{-3.8}+\sqrt{1+\tilde{\omega}^{2.7}}}$	0.001	$R_T^{3.8}$	$\tilde{\omega}^{0.9}$	$\tilde{\omega}^{-4.6}$
Solution 2	$\frac{\tilde{\omega}^{3/2}}{0.4+\tilde{\omega}^2+\tilde{\omega}^{6.3}R_T^{-4.1}}$	0.0016	$R_T^{4.1}$	$\tilde{\omega}^{1.5}$	$\tilde{\omega}^{-4.8}$
Solution 3	$\frac{\tilde{\omega}}{0.6+\tilde{\omega}^{1.4}+\tilde{\omega}^{6.3}R_T^{-3.9}}$	0.0016	$R_T^{3.9}$	$\tilde{\omega}$	$\tilde{\omega}^{-5.3}$
Solution 4	$\frac{2\tilde{\omega}}{1.7+\tilde{\omega}^{1.8}+\tilde{\omega}^{5.8}R_T^{-3.7}}$	0.0006	$R_T^{3.7}$	$\tilde{\omega}$	$\tilde{\omega}^{-4.8}$

Table 2: Representation of 4 different solution proposed by the GEP to approach the Goody model

N	Simplified	Fitness	Reynold dependency	$\tilde{\omega} \to 0$	$\tilde{\omega} \to \infty$
Solution 1	$\frac{\tilde{\omega}^{1.72}/(\tilde{\omega}+0.18)}{3.93+\frac{4.8\tilde{\omega}^{5.79}}{R_T^{4.02}}+5.78\tilde{\omega}+\tilde{\omega}^{1.72}}$	3.6×10^{-4}	$R_T^{4.02}$	$\tilde{\omega}^{1.72}$	$\tilde{\omega}^{-5.07}$
Solution 2	$\frac{1.65\tilde{\omega}^{0.63}}{0.24(\tilde{\omega}^{0.76}+\tilde{\omega}^{0.82})+\frac{\tilde{\omega}^{5.68}}{R_T^{4.01}}+\tilde{\omega}^{1.24}+1.37}$	3.6×10^{-4}	$R_T^{4.01}$	$\tilde{\omega}^{0.63}$	$\tilde{\omega}^{-5.05}$
Solution 3	$\frac{1.46\tilde{\omega}^{1.64}}{0.15+\tilde{\omega}+\frac{\tilde{\omega}^{6.51}}{R_T^{3.9}}+\tilde{\omega}^{2.21}}$	3.6×10^{-4}	$R_T^{3.9}$	$\tilde{\omega}^{1.64}$	$\tilde{\omega}^{-4.87}$
Solution 4	$\frac{1.46\tilde{\omega}^{1.34}}{0.25\tilde{\omega}^{2.34}+1.46\tilde{\omega}^{1.34}+0.47+\frac{\tilde{\omega}^{6.26}}{R_T^{3.97}}}$	3.6×10^{-4}	$R_T^{3.97}$	$\tilde{\omega}^{1.34}$	$\tilde{\omega}^{-4.92}$

Table 3: Representation of 4 GEP solution for the Goody model using the local optimization loop for the determination of constants

4. Conclusion

A close approximation of the Goody model for wall pressure fluctuations was obtained from a purely data-driven approach. This requires the use of a modified version of the Gene Expression Programing with 1) a new type of terminal called the power terminal and 2) a local optimization loop based on a least-square regression. Using those two modifications, it was possible to retrieve very accurately the model proposed by Goody from a noisy synthetic dataset while making very little assumptions on the physics of the system. In addition to the close fit of the dataset, the Gene Expression Programing is also able to provide an explicit mathematical function of the model. This was used to show that the constructed models were consistent with the physics-based model used to generate the training data. This shows that Gene Expression Programing can be use to device new models AND to unveil physical relationship between data in complex numerical dataset. However, such approach is pending on the selection of many meta-parameters such as population size, mutation operators probabilities, individuals architecture, functional and terminal sets. Those parameters can be difficult to define when you have no prior knowledge of the physics of the problem investigated. Nonetheless, the Gene Expression Programing data-based approach is a very promising tool to device future algebraic wall pressure models from a combination of different measurements and simulations dataset.

Acknowledgments

This research was partly supported by the French global automotive Valeo in the context of a thesis for the investigation of noise induced by HAVC systems. The authors thank Pr. Sandberg from Melbourne University for his help and advices in this study.

References

[1] M. Roger, S. Moreau, Back-scattering correction and further extensions of amiets trailing-edge noise model. part 1: theory, Journal of Sound and Vibration (286) (2005) 477, 506. doi:10.1016/j.jsv.2004.10.054.

[2] N. Van de Wyer, A. Zapata, D. Nogueira, C. Schram, Development of a test rig for the measurement of turbulent boundary layer wall pressure statistics, 2018 AIAA/CEAS Aeroacoustics Conferencedoi:10.2514/6.2018-3122.

[3] K. Bull, M, Wall-pressure fluctuations beneath turbulent boundary layers: Some reflections on forty years of research, Journal of Sound and Vibration (190) (1996) 299, 315. doi:10.1006/jsvi.1996.0066.

[4] H. Kraichnan, R, Pressure fluctuations in turbulent flow over a flat plate, The Journal of the Acoustical Society of America 28 (3).

[5] K. Amiet, R, Noise due to turbulent flow past a trailing edge, Journal of Sound and Vibration 47 (3) (1976) 387, 393.

[6] M. Howe, Acoustic of fluid structure interactions, Cambridge Univ press.

[7] M. Goody, Empirical spectral model of surface pressure fluctuations, AIAA Journal 42 (9). doi:10.2514/1.9433.

[8] F. Hwang, Y, K. William, S. Bonness, A. Hambric, Comparison of semi-empirical models for turbulent boundary layer wall pressure spectra, Journal of Sound and Vibration (319) (2007) 199, 217. doi:10.1016/j.jsv.2008.06.002.

[9] A. Lee, S andVillaescusa, Comparison and assessment of recent empirical models for turbulent boundary layer wall pressure spectrum, 23rd AIAA/CEAS Aeroacoustics Conferencedoi:10.2514/6.2017-3688.

[10] C. Ferreira, Gene Expression Programming: Mathematical Modeling by an Artificial Intelligence, 1st Edition, Springer-Verlag, 2006.

[11] J. Zhong, L. Feng, Y.-S. Ong, Gene expression programming: A survey, IEEE Computational Intelligence Magazine 12 (3) (2017) 54–72.

[12] J. Weatheritt, R. Sandberg, A novel evolutionary algorithm applied to algebraic modifications of the rans stress–strain relationship, Journal of Computational Physics 325 (2016) 22–37.

[13] C. Lav, R. D. Sandberg, J. Philip, A framework to develop data-driven turbulence models for flows with organised unsteadiness, Journal of Computational Physics 383 (2019) 148–165.

[14] J. Weatheritt, R. D. Sandberg, Hybrid reynolds-averaged/large-eddy simulation methodology from symbolic regression: formulation and application, AIAA Journal (2017) 3734–3746.

[15] M. Schoepplein, J. Weatheritt, R. Sandberg, M. Talei, M. Klein, Application of an evolutionary algorithm to les modelling of turbulent transport in premixed flames, Journal of Computational Physics 374 (2018) 1166–1179.

[16] T. Verstraete, Multidisciplinary turbomachinery component optimization considering performance, stress, and internal heat transfer, Ph.D. thesis, Karman Institute (2008).

[17] Y. Rozenberg, G. Robert, S. Moreau, Wall-pressure spectral model including the adverse pressure gradient effects, AIAA journal 50 (10) (2012) 2168–2179.

Influence of forward-swept blades on low-order acoustic prediction for low-speed fans

Alessandro Zarri

Environmental and Applied Fluid Dynamics Department, von Karman Institute for Fluid Dynamics, Belgium, alessandro.zarrri@vki.ac.be

Supervisors: Christophe Schram and Julien Christophe

Full Professor, Environmental and Applied Fluid Dynamics Department and Aeronautics and Aerospace Department, von Karman Institute for Fluid Dynamics, Belgium, christophe.schram@vki.ac.be

Senior Research Engineer, Environmental and Applied Fluid Dyanmics Department, von Karman Institute for Fluid Dynamics, Belgium, julien.christophe@vki.ac.be

University Supervisor: Michel Roger

Professor, Laboratoire de Mécanique des Fluides et d'Acoustique, École Centrale de Lyon, France, michel.roger@ec-lyon.fr

Abstract

The low-speed fans that are used for automotive engine cooling contribute to a significant part of the global noise emitted by the vehicle. Automotive engine cooling manufacturers are therefore interested in developing low-order noise prediction methodologies that include the radiated sound in pre-design optimization cycles. Two among the most influential broadband noise mechanisms characterizing the automotive axial cooling-fans spectra in operating conditions are the turbulence-impingement noise and the trailing-edge noise. We modelled them through the application of a semi-analytical method called Amiet's airfoil theory, appropriately adapted via a strip-theory approach, in order to take the rotating motion into account. In modern fan designs, the fan blades are strongly forward-swept, meaning that the blade edges are not always perpendicular to the tangential-to-rotation velocity vector. This is particularly true at the tip of the blades where the sweep angle often reaches its maximum value, and where most of the noise is expected. Sweep was shown to reduce the noise emitted by isolated airfoils, but its effect on rotating machines is not yet well understood. Its prediction requires an extension to the classical Amiet's theory, which has been implemented in this work, permitting to assess the importance of varying sweep on the acoustic far-field radiation. Amiet's theory is therefore applied for the two noise mechanisms mentioned above, starting from steady CFD simulations, reproducing the ventilator geometry operating at its maximum-efficiency condition. In contrast with the classical unswept formulation, the predicted results considering the sweep variation along the blade span better compare with the experimental measured ones in the VKI anechoic chamber, especially for high frequencies.

Keywords: aeroacoustics, noise prediction, low-speed fan, Amiet's theory, sweep angle.

1. Introduction

Several industrial fields, such as the aeronautical, automotive, and wind turbines sector are concerned by the acoustic radiations of rotational machinery [1; 2; 3]. Manufacturing ventilators with swept blades is considered as a classical technique in order to mitigate the far-field emissions, as well as to enhance the aerodynamic efficiency [4]. In the automotive field, low-speed cooling fans [5] are used to cool down the engines of the cars by extracting hot air out of heat exchangers. Several noise generating mechanisms of tonal and broadband nature occur in this application [6] where backward-swept and forward-swept propellers are often employed [7]. Among the most influencing sound source mechanisms, one can distinguish the turbulence-interaction or leading-

The content of this paper will be presented at ISROMAC 18 International Symposium.

edge one and the trailing-edge or self-noise mechanism. Following the semi-analytical works carried out in [8; 9; 10; 11] for the previous two broadband mechanisms, the aim of this study is to implement semi-analytical methods, based on Amiet's airfoil noise theory [12; 13], able to take into account the effect of having fan blades with varying swept leading- and trailing-edges. Although these methodologies have already proven to accurately model the noise emitted by isolated swept airfoils, to the authors knowledge, no application to low-speed rotating blades has been carried out so far, in order to predict the overall broadband emitted sound. Nevertheless, the work of Roger & Carazo [11] aimed at modelling tonal noise emissions by Contra-Rotating Open Rotors (CRORs) and was instrumental in deriving the set of equations hereafter adapted to model the leading-edge noise for low-speed cooling fans.

In the recent work [14], the authors implemented a low-order prediction methodology that was only including the trailing-edge noise modelling neglecting the acoustic influence of blades with varying sweep angle. The following study is intended to be a continuation of the just mentioned one and thus, the same experimental measurements and CFD simulation are considered.

Hereafter, the leading-edge noise prediction has been included in the low-order acoustic methodology and both the trailing- and leading-edge noise formulations are now considering the presence of a radius-dependent sweep angle.

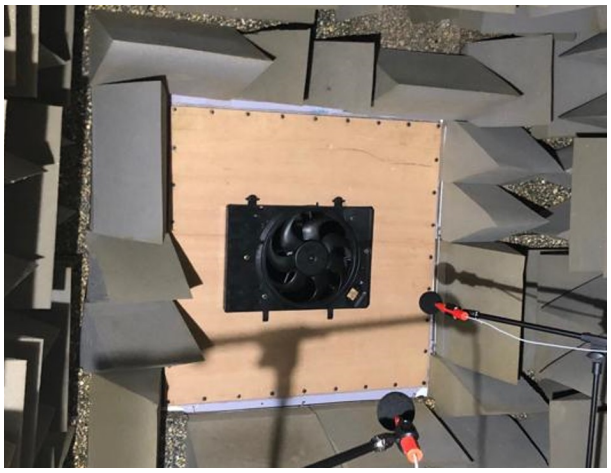

(a)

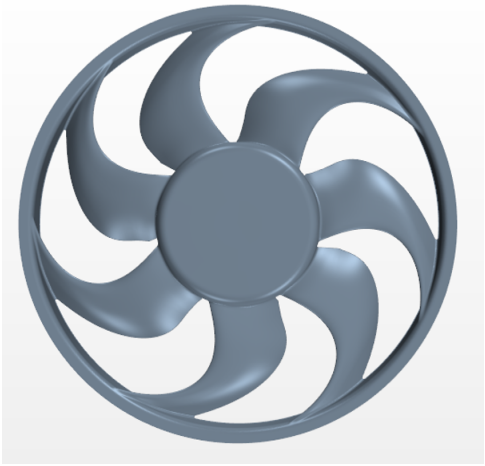

(b)

Figure 1: (a) ALCOVES anechoic chamber: upstream room with B&K microphones and open-rotor configuration from [14]. (b) Suction-side 3D CAD model of the Valeo fan employed in the simulation.

2. Experimental Setup and CFD Computation

The experimental campaign and the CFD study carried out at the von Karman Institute for Fluid Dynamics in [14] are used as a base to investigate the sweep-angle effect inclusion within the proposed analytical formulation and in order to compare it with a real application. In the ALCOVES anechoic chamber, the cooling module has been mounted in an open-rotor configuration as depicted in Fig. 1a and its far-field sound spectrum has been measured for the fan maximum-efficiency working condition. The laboratory has been designed by Bilka *et al.* [15] to have low turbulence level at the inlet and an acoustic cut-off frequency of 150 Hz. A value of 200 Hz is later adopted in the sound spectrum to be conservative. The chosen fan has 7 almost-equally-spaced blades which are forward skewed, with high sweep-angle values particularly at the tip of the blades, which result to be the most influenced regions by the sweep. A 3D modelling of the fan has been employed and it is shown in Fig. 1b. Steady Reynolds Averaged Navier-Stokes simulations (RANS), coupled with SST $K-\omega$ turbulence model [16] are chosen as a fair compromise between the computational cost and the simulation accuracy in describing the near-field flow characteristics. The aim of the simulation is to collect the leading-edge upstream local flow information (turbulence kinetic energy k_t, specific rate of dissipation ω_t and mean relative velocity U_0) as well as to reconstruct the velocity profiles around the blade trailing edge in order to model the wall-pressure spectrum with semi-empirical methods [17]. In Fig. 2a, an iso-radial cut

is performed at the blade region. The seven blades present similar aerolic properties, where in the tip the highest values of velocities and turbulence kinetic energy k are achieved. More details are given in [14]. A parametric study, not shown in here for writing-space limits, was carried out to clarify the dependency of the acoustic results on the extraction points at the leading-edge upstream and at the trailing-edge boundary layer. Especially at the tip region it is not trivial to define the correct locations where to extract this information. As shown by an unsteady RANS computation of the same fan in Fig. 2b, the Q-criterion technique depicts a complex vortical structure developing all around the rotating ring. This suggests the presence of large coherent eddies that are not captured by steady calculations and that are probably responsible for the typical sub-harmonic humps characterizing the low-frequency spectrum, as discussed in [18]. Higher-order methods could be taken into account if one is interested in including these coherent structures in the noise prediction.

3. Theoretical Background

An extension of Amiet's theory to rotating blades, initially developed by Schlinker and Amiet [19] and subsequently by Rozenberg *et al.* [20], is firstly proposed in order to take into account leading-edge and trailing-edge noise mechanisms. Although the two models present consistent similarities, a distinction will be made when implementing the sweep-angle formulations for the two different noise mechanisms.

3.1. Noise Emitted by Rotating Blades

To deal with spanwise-varying conditions, the fan blade is subdivided into strips (or segments) through iso-radial cuts such that each strip encounters its own flow condition. The overall radiated fan noise is calculated as the summation of the sound individually emitted by each strip to which the single-airfoil theory is applied, assuming that the circular motion can be approximated by an equivalent local translation. The relative motion between the listener and the source is afterwards considered by including a Doppler factor and taking into account all the azimuthal blade locations as shown in Fig. 3a and expressed by Eq. 1.

For a given angular frequency ω, the fan radiated noise is calculated as:

$$S_{pp}(\vec{x},\omega) = \frac{B}{2\pi}\int_0^{2\pi}\left(\frac{\omega_e(\Psi)}{\omega}\right)^2 S_{pp}^{\Psi}(\vec{y},\omega_e)\,d\Psi, \quad (1)$$

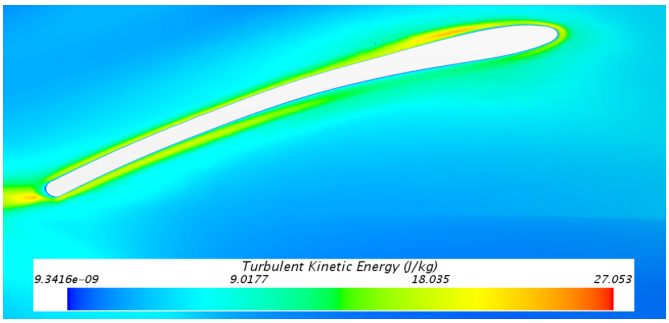

(a)

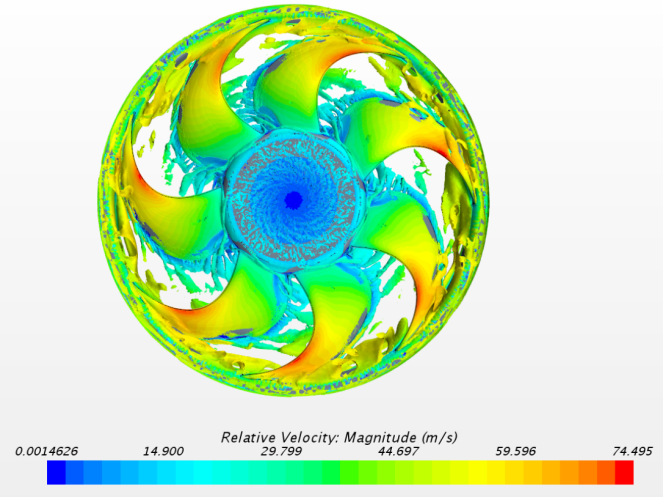

(b)

Figure 2: (a) An iso-radius cut is performed at the blade tip region and the turbulent kinetic region is shown. (b) The relative velocity is plotted on the iso-surface obtained with the Q-criterion technique. Large vortical structures are depicted in particular close to the ring and in the trailing-edge recirculating region.

where $\vec{x}$ is the vectorial listener's position, whereas $\vec{y}$ is the source location; B represents the blades number, $\omega_e(\Psi)$ is the source emitted frequency for a certain azimuthal position expressed by the angle $\Psi = \Omega t$, as depicted in Fig. 3a. The Doppler factor has to be squared as proven by Sinayoko *et al.* [21] and for low-Mach number is given by the relation:

$$\frac{\omega_e(\Psi)}{\omega} = 1 + M_r \sin\Psi \sin\Theta, \quad (2)$$

in which M_r is the Mach number of the source relative to the fluid. The term $S_{pp}^{\Psi}(\vec{y},\omega_e)$ of Eq. 1 is obtained from the single-airfoil theory as the sum of

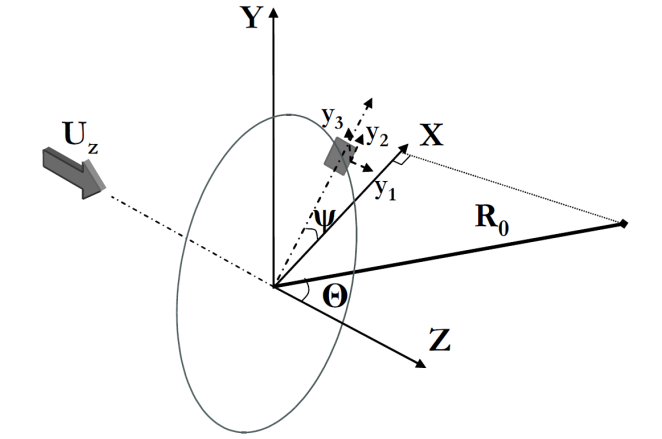

(a)

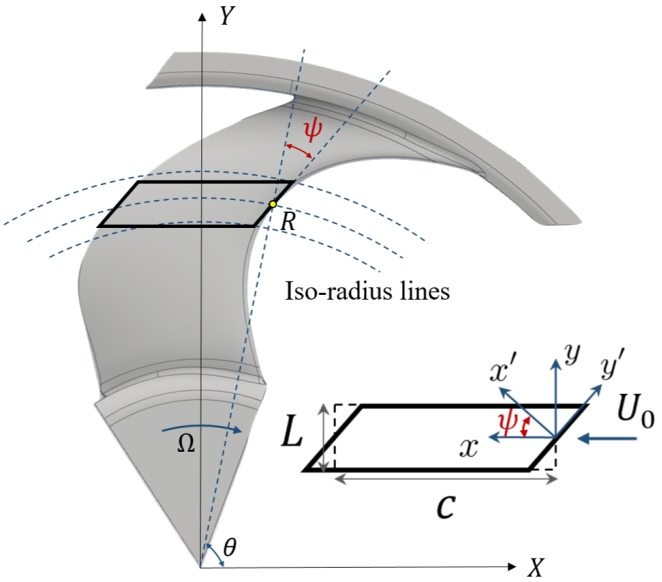

(b)

Figure 3: (a) From [10], the rotating local airfoil reference frame is denoted. The fixed reference frame $\vec{x} = (X, Y, Z)$ defines the observer's position. (b) Sweep-angle definition over the leading edge of the fan blade; the rotated local reference frame (x', y', z) is determined.

the trailing-edge and leading-edge noise contributions such that $S_{pp}^{\Psi} = S_{pp}^{TE} + S_{pp}^{LE}$, discussed in the next paragraphs.

3.2. Leading-Edge Noise Formulation

Based on the classical Amiet's analytical gust-airfoil interaction noise model [12], Roger & Carazo in [11] extended the formulation to account for swept blades in order to predict tonal noise emitted by CRORs. In the following work, these developments are used to predict broadband sound sources as carried out for an isolated airfoil in the work of Giez *et al.* [9]. The sweep angle is defined as the angle between the fan radius line and the line locally tangent to the edge of the blade, as depicted in Fig. 3b. The chord c and span L of the blade segment are indicated in the same figure. A local reference frame (x, y, z) is defined, with the x axis parallel to the flow direction $U_0 = \Omega R$ (with the fan angular rotation Ω), the z axis perpendicular to the blade-strip plane and the y axis orthogonal to the previous two. A second local reference frame (x', y', z) is obtained by rotating around the z axis by the sweep angle ψ; the y' axis is now laying on the leading edge of the blade segment. It is worth noticing that in the latest figure, the sweep angle has been defined for the leading edge, but its definition is going to be equivalent for the trailing-edge case as long as the reference frames are centered on the trailing-edge of the blade. To have further information about the following formulation, the interested reader can refer to [1; 9; 11; 22]. We define the acoustic wavenumber $k_a = \frac{\omega}{c_0}$ and the observer corrected distance S_0 to take into account the convection effects as:

$$S_0^2 = \beta_y^2 X^2 + \beta_x^2 Y^2 + \beta_0^2 Z^2, \tag{3}$$

$$\text{where} \quad \beta_{y,x,0} = \sqrt{1 - \left(\frac{U_{y,x,0}}{c_0}\right)^2},$$

Hence, the velocity component $U_x = \frac{U_0}{\cos\psi}$ perpendicular to the swept leading edge and the one parallel to the swept edge $U_y = \frac{U_0}{\sin\psi}$ are determined. The turbulence is assumed as isotropic, frozen, and expanded into harmonics gusts. We write the power spectral density (PSD) of the far-field acoustic pressure for a fluid with the speed of sound c_0 and the density ρ_0, with the assumption of large aspect ratio. This choice has been done in order to have a simpler mathematical expression of the PSD reported in Eq. 4:

$$S_{pp}^{LE}(\vec{x}, \omega) = \left(\frac{\rho_0 k_a c \cos\psi Z}{2 S_0^2}\right)^2 \pi U_x \frac{L}{2} \Phi_{ww}\left(K_x', K_y'\right) \left|\mathcal{L}^{LE}\left(X, K_x', K_y'\right)\right|^2, \tag{4}$$

where K_y' is the only involved gust, which is always

supercritical [1] and is expressed as:

$$K'_y = \frac{k_a}{\beta_0^2}\left(\frac{\beta_x^2 Y}{S_0} - \frac{U_y}{c_0}\right), \tag{5}$$

Given the dispersion equation:

$$\mathbf{U_0} \cdot \mathbf{K} = U_x K'_x + U_y K'_y,$$

the x'-wavenumber is defined as:

$$K'_x = \frac{\omega - K'_y U_y}{U_x}. \tag{6}$$

The mathematically-derived aeroacoustic wavenumber term $\mathcal{L}^{LE}$ does not consider the contribution of the trailing-edge back-scattering derived in [23], which is typically much smaller if compared to the main contribution shown in Eq. 7.

$$\mathcal{L}^{LE} = -\frac{e^{-i\Theta_2}}{\pi}\sqrt{\frac{2}{\left(\bar{K}'_x + \beta_x^2\kappa\right)\Theta_1}}E\left[2\Theta_1\right], \tag{7}$$

We define the parameter κ as:

$$\kappa^2 = \frac{\bar{K}'^2_x U_x^2}{c_0\beta_x^4} - \frac{\bar{K}'^2_y}{\beta_x^2},$$

where $\bar{K}'_x$ and $\bar{K}'_y$ are the dimensionless wavenumbers; $E[-]$ is the Fresnel integral, whereas the expressions of Θ_1 and Θ_2 can be found for instance in [9].

The von Karman turbulence model is used to calculate the two-wavenumber spectrum $\Phi_{ww}(K'_x, K'_y)$ analogously to what has been done by Christophe in [24]. In fact, starting off from the steady RANS computation of section 2, we can write the two-wavenumber spectrum as:

$$\Phi_{ww}\left(K'_x, K'_y\right) = \frac{4}{9\pi}\frac{\bar{u}^2}{k_e^2}\frac{\bar{K}'^2_x + \bar{K}'^2_y}{\left(1 + \bar{K}'^2_x + \bar{K}'^2_y\right)^{7/3}}, \tag{8}$$

with $\bar{u}^2$ as the square of the RMS of the streamwise fluctuations, which is related to the RANS scalar turbulent kinetic energy k_t as: $\bar{u}^2 = \frac{2}{3}k_t$.

The average wavenumber of the energy-containing eddies k_e in Eq. 8 is defined in [24] as:

$$k_e = \frac{\sqrt{\pi}}{\Lambda_f}\frac{\Gamma(5/6)}{\Gamma(1/3)}, \tag{9}$$

where Λ_f is the streamwise integral scale of the turbulence, function of the RANS-output scalar specific dissipation ratio ω_t as:

$$\Lambda_f = \frac{B_t k_t^{1/2}}{\omega_t C_\mu}, \tag{10}$$

with the empirical constant $B_t = 0.4$ given in [25] and $C_\mu = 0.09$ given in [26].

3.3. Trailing-Edge Noise Formulation

According to the original derivation by Amiet [13], afterwards extended by Roger & Moreau [23], the inclusion of the sweep-angle effect for the trailing-edge noise modelling in this work followed the recent work of Grasso *et al.* [8]. The PSD of the far-field noise for the large aspect ratio is given as:

$$S_{pp}^{TE}(\vec{x}, \omega) = \left(\frac{k_a c \cos\psi Z}{2S_0^2}\right)^2 \frac{L}{2\pi^2}\varphi_{pp}(\omega) l_y\left(\omega/U_c, K'_y\right) \left|\mathcal{L}^{TE}\left(K'_c, K'_y\right)\right|^2, \tag{11}$$

coherently with the leading-edge formulation in the previous section, the main contribution of the aeroacoustic transfer function is written:

$$\mathcal{L}^{TE} = -\frac{\mathrm{e}^{2\mathrm{i}C/\cos\psi}}{\mathrm{i}C}\left\{(1+\mathrm{i})\mathrm{e}^{-2\mathrm{i}C/\cos\psi}\sqrt{\frac{2B}{\cos\psi}}\mathrm{ES}\left[\frac{2(B-C)}{\cos\psi}\right] + -(1+\mathrm{i})\mathrm{E}^*\left[\frac{2B}{\cos\psi}\right] + 1 - \mathrm{e}^{-2\mathrm{i}C/\cos\psi}\right\}, \tag{12}$$

where the mathematical expressions of the terms B, C, $E^*[-]$ and $ES[-]$ are given in [8].

The K'_y term is given by Eq. 5, whilst the rotated convective wavenumber is shown in Eq. 13, assuming the frozen turbulence hypothesis can be applied such that the convective velocity is determined as $U_c = U_0/\alpha$, with $\alpha = 1/0.7$.

$$K'_c = \frac{\omega}{U_c\cos\psi} - K'_y\tan\psi. \tag{13}$$

The Rozenberg's model [27], suited for airfoils generating boundary layers with relevant adverse-pressure gradients, has been employed to determine the wall-pressure spectrum $\phi_{pp}(\omega)$ in Eq. 11, by exploiting the trailing-edge boundary-layer information, as illustrated in [14]. The Generalized Corco's model derived in [28] is used following Section IV of [8] to find the analytical expression of the spanwise correlation length $l_y\left(\omega/U_c, K'_y\right)$.

4. Acoustic Far-Field Results

The implementation of the single-airfoil Amiet's analytical formulations including the sweep-angle effect has been compared and validated with the work of

Giez *et al.* [9] for the leading-edge noise case and with the work of Grasso *et al.* [8] for the trailing-edge noise case. For example, in the latest case, the strip-theory approach can be visualized in Fig. 4 a, where 4 blade planes have been generated together with their local reference frames at the trailing edge. An improvement taking into account the sweep angle is shown in Fig. 4 b, where the trailing-edges of the blade planes are now locally parallel to the forward-skewed curvature of the blade. Similar blade segments are defined but not illustrated for the leading-edge noise formulation. For the two noise mechanisms, the unswept

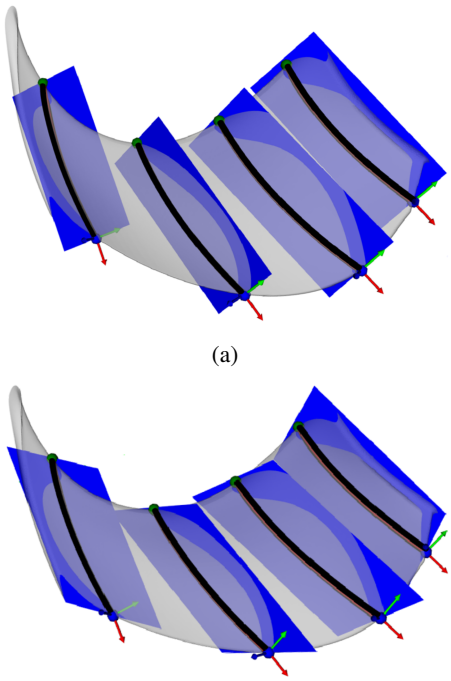

(a)

(b)

Figure 4: For the trailing-edge case, the blade is divided into 4 segments: in (a), a classical unswept trailing-edge formulation can be used; in (b), the effect of the sweep is evaluated with blade strips which have locally parallel trailing-edges, following the blade forward-skewed curvature.

classical Amiet's formulations [12; 13] are retrieved as a limit case where $\psi = 0$. The acoustic far-field results are plotted in Fig. 5 for the fan maximum-efficiency operational condition. The measured experimental overall noise presents tonal contributions, particularly at the blade-passing frequency (around 400 Hz) and its harmonics, not accounted for in the prediction methodology. When including the sweep contribution (SW), the leading-edge noise mechanism appears to be relevant at low-frequency, whereas the trailing-edge at higher frequency [6]. This behaviour is fairly similar to the one encountered in the work of Sanjose & Moreau [29] and with the beamforming study carried out by Herold *et al.* [7]. As in their beamforming experiments, also in this noise prediction, most of the noise is emitted by the blade segments approximating the tip of the blade, where the relative velocities reach the highest values and where the sweep angle is at its maximum along the blade span. For both the noise mechanisms, the effect of the sweep is to reduce the emitted noise, especially from medium to high frequencies. The sum of the trailing-edge (TE) and leading-edge (LE) noise mechanisms in the swept case results to be in fairly good agreement with the experimental case, especially at high frequencies. The unswept case instead, results to over-predict the radiated noise in this frequency range. In the two cases, the methodology is not suited to model the sound spectrum for low-frequencies; in this region in fact, most of the radiated sound is expected to be generated by sub-harmonic coherent vortical structures convected upstream within the gap between the fan shroud and the rotating ring [30; 31]. Secondary flows with more broadband behaviour as well as recirculation bubbles under the trailing-edge pressure-side of the blade can also take place in the tip region [18], but their modelling would require higher-order CFD inputs to feed in semi-analytical methods.

5. Conclusions

The aim of the present work was to extend the low-order noise prediction methodology developed in [14], exploiting the same near-field steady RANS computation and experimentally measured sound emitted by an automotive fan. We implemented a semi-analytical methodology, based on Amiet's theory, to predict the leading-edge noise and the trailing-edge noise mechanisms for a fan with forward-swept blades. These have been divided into strips through iso-radius cuts where the single-airfoil Amiet's theory has been calculated, taking into account the local sweep angles for the leading and trailing edges separately. The overall effect of considering swept blades with respect to the classical Amiet's formulations, is a reduction of the predicted noise for both the sound mechanisms that is in good agreement with the experimental measurements acquired in the AL-COVES anechoic chamber of the von Karman Institute for Fluid Dynamics. Although the tip region of the blade is the most influenced by the sweep-sound

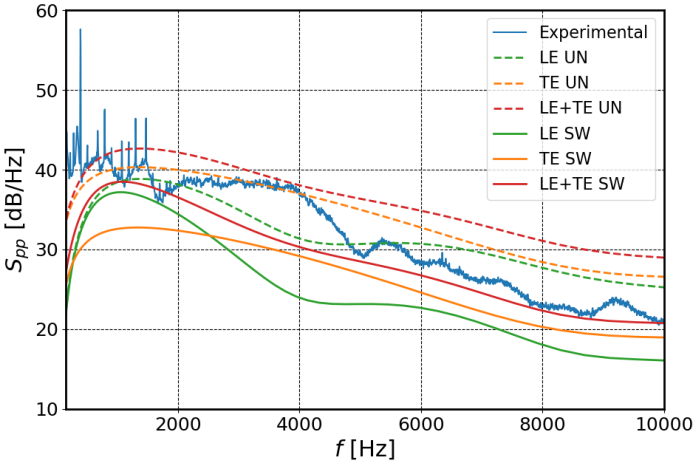

Figure 5: PSD of the far-field emitted sound by the fan at its maximum-efficiency operational point: the solid red line representing the summation of trailing-edge (TE) and leading-edge (LE) noise contributions for the swept case (SW) is in fairly good agreement with the experimental curve in solid blue, especially at high frequency, resulting into a better description of the noise emission with respect to the unswept (UN) classical Amiet's formulation shown in dashed line.

mitigation, yet it remains the one radiating most of the noise due to the highest relative velocities. The trailing-edge noise appears to be dominant at high frequency, in agreement with [29]. The under-prediction of the far-field noise can be justified, especially for low-frequencies, by the typical presence of large turbulence structures and secondary flows, hardly detectable by steady RANS. This motivates further investigations and developments to include these noise mechanisms in the prediction methodology.

Acknowledgments

The European Commission's Framework Program "Horizon 2020", with the Marie Skłodowska-Curie Innovative Training Networks (ITN) "SmartAnswer - Smart mitigation of flow-induced acoustic radiation and transmission" grant agreement No. 722401 are acknowledged for funding and supporting the present study. Moreover, the authors acknowledge the École Centrale de Lyon for the received technical support.

References

[1] S. Moreau, M. Roger, Advanced noise modeling for future propulsion systems, International Journal of Aeroacoustics 17 (6-8) (2018) 576–599.

[2] S. Allam, M. Åbom, Noise reduction for automotive radiator cooling fans, in: FAN 2015, 2015.

[3] S. Oerlemans, Reduction of wind turbine noise using blade trailing edge devices, in: 22nd AIAA/CEAS Aeroacoustics Conference, Lyon, France, 2016.

[4] F. B. Metzger, C. Rohrbach, Benefits of blade sweep for advanced turboprops, Journal of Propulsion and Power 2 (6) (1986) 534–540.

[5] M. Henner, B. Demory, F. Franquelin, Y. Beddadi, Z. Zhang, Test Rig Effect on Performance Measurement for Low Loaded Large Diameter Fan for Automotive Application, in: Volume 1A: Aircraft Engine; Fans and Blowers, American Society of Mechanical Engineers, Dsseldorf, Germany, 2014.

[6] S. Moreau, M. Roger, Competing Broadband Noise Mechanisms in Low-Speed Axial Fans, AIAA Journal 45 (1) (2007) 48–57.

[7] G. Herold, F. Zenger, E. Sarradj, Influence of blade skew on axial fan component noise, International Journal of Aeroacoustics 16 (4-5) (2017) 418–430.

[8] G. Grasso, M. Roger, S. Moreau, Effect of sweep angle and of wall-pressure statistics on the free-field directivity of airfoil trailing-edge noise, in: 25th AIAA/CEAS Aeroacoustics Conference, Delft, The Netherlands, 2019.

[9] J. Giez, L. Vion, M. Roger, S. Moreau, Effect of the Edge-and-Tip Vortex on Airfoil Selfnoise and Turbulence Impingement Noise, in: 22nd AIAA/CEAS Aeroacoustics Conference, American Institute of Aeronautics and Astronautics, Lyon, France, 2016.

[10] Y. Rozenberg, M. Roger, A. Gudel, S. Moreau, Rotating Blade Self Noise: Experimental Validation of Analytical Models, in: 13th AIAA/CEAS Aeroacoustics Conference (28th AIAA Aeroacoustics Conference), 2007.

[11] M. Roger, A. Carazo, Blade-Geometry Considerations in Analytical Gust-Airfoil Interaction Noise Models, in: 16th AIAA/CEAS Aeroacoustics Conference, Stockholm, Sweden, 2010.

[12] R. Amiet, Acoustic radiation from an airfoil in a turbulent stream, Journal of Sound and Vibration 41 (4) (1975) 407–420.

[13] R. Amiet, Noise due to turbulent flow past a trailing edge, Journal of Sound and Vibration 47 (3) (1976) 387–393. doi:10.1016/0022-460X(76)90948-2.

[14] A. Zarri, J. Christophe, C. F. Schram, Low-order aeroacoustic prediction of low-speed axial fan noise, in: 25th AIAA/CEAS Aeroacoustics Conference, 2019, p. 2760.

[15] M. Bilka, J. Anthoine, C. Schram, Design and evaluation of an aeroacoustic wind tunnel for measurement of axial flow fans, The Journal of the Acoustical Society of America 130 (6) (2011) 3788–3796.

[16] F. R. Menter, Two-equation eddy-viscosity turbulence models for engineering applications, AIAA Journal 32 (8) (1994) 1598–1605.

[17] Y. C. Kkosman, J. Christophe, C. Schram, Trailing edge noise prediction based on wall pressure spectrum models for NACA0012 airfoil, Journal of Wind Engineering and Industrial Aerodynamics 175 (2018) 305–316.

[18] M. Sanjose, D. Lallier-Daniels, S. Moreau, Aeroacoustic Analysis of a Low-Subsonic Axial Fan, in: Volume 1: Aircraft Engine; Fans and Blowers; Marine, American Society of Mechanical Engineers, Montreal, Quebec, Canada, 2015.

[19] R. Schlinker, R. Amiet, Helicopter rotor trailing edge noise, in: 7th Aeroacoustics Conference, American Institute of Aeronautics and Astronautics, Palo Alto,CA,U.S.A., 1981.
[20] Y. Rozenberg, M. Roger, S. Moreau, Rotating Blade Trailing-Edge Noise: Experimental Validation of Analytical Model, AIAA Journal 48 (5) (2010) 951–962.
[21] S. Sinayoko, M. Kingan, A. Agarwal, Trailing edge noise theory for rotating blades in uniform flow, Proceedings of the Royal Society A: Mathematical, Physical and Engineering Sciences 469 (2157).
[22] M. Roger, C. Schram, S. Moreau, On vortexairfoil interaction noise including span-end effects, with application to open-rotor aeroacoustics, Journal of Sound and Vibration 333 (1) (2014) 283–306. doi:10.1016/j.jsv.2013.09.012.
[23] M. Roger, S. Moreau, Back-scattering correction and further extensions of Amiet's trailing-edge noise model. Part 1: theory, Journal of Sound and Vibration 286 (3) (2005) 477–506.
[24] J. Christophe, Application of Hybrid Methods to High Frequency Aeroacoustics, PhD Thesis, ULB - VKI.
[25] K. R. Sreenivasan, On the universality of the Kolmogorov constant, Physics of Fluids 7 (11) (1995) 2778–2784.
[26] H. K. Versteeg, W. Malalasekera, An introduction to computational fluid dynamics: the finite volume method, 2nd Edition, Pearson Education Ltd, Harlow, England ; New York, 2007.
[27] Y. Rozenberg, G. Robert, S. Moreau, Wall-Pressure Spectral Model Including the Adverse Pressure Gradient Effects, AIAA Journal 50 (10) (2012) 2168–2179.
[28] A. Caiazzo, R. DAmico, W. Desmet, A Generalized Corcos model for modelling turbulent boundary layer wall pressure fluctuations, Journal of Sound and Vibration 372 (2016) 192–210.
[29] M. Sanjos, S. Moreau, Fast and accurate analytical modeling of broadband noise for a low-speed fan, The Journal of the Acoustical Society of America 143 (5) (2018) 3103–3113. doi:10.1121/1.5038265.
[30] S. Magne, S. Moreau, A. Berry, Subharmonic tonal noise from backflow vortices radiated by a low-speed ring fan in uniform inlet flow, The Journal of the Acoustical Society of America 137 (1) (2015) 228–237.
[31] S. Moreau, M. Sanjose, Sub-harmonic broadband humps and tip noise in low-speed ring fans, The Journal of the Acoustical Society of America 139 (1) (2016) 118–127.

Experimental investigation of the distortion of turbulence interacting with a porous airfoil

Riccardo Zamponi

Environmental and Applied Fluid Dynamics Department, von Karman Institute for Fluid Dynamics, Belgium, riccardo.zamponi@vki.ac.be

Supervisor: Christophe Schram

Full Professor, Aeronautics and Aerospace Department & Environmental and Applied Fluid Dynamics Department, von Karman Institute for Fluid Dynamics, Belgium, christophe.schram@vki.ac.be

University Supervisor: Daniele Ragni

Associate Professor, Delft University of Technology, Delft 2629 HS, the Netherlands, d.ragni@tudelft.nl

Abstract

A possible strategy for the reduction of the aeroacoustic noise generated by turbulence interacting with a wing profile, also referred to as leading-edge noise, is represented by the implementation of a porous medium in the structure of the airfoil. However, the physical mechanisms involved in this noise mitigation technique remain unclear. The present work aims at elucidating these phenomena and particularly how the porosity affects the incoming turbulence characteristics in the immediate vicinity of a NACA-0024 airfoil. On the basis of the results obtained, an interpretation of the phenomena occurring in the turbulence-interaction noise reduction due to a porous treatment of the airfoil is given with reference to the theoretical inputs of the Rapid Distortion Theory.

Keywords: aeroacoustics, leading-edge noise reduction, porous materials, turbulence distortion

1. Introduction

The interaction between an airfoil and incident turbulence is an important source of aerodynamic noise in numerous applications that have a high societal impact, such as turbo engines, cooling systems for automotive and construction industries or high-lift devices on aircraft wings. In these examples, the turbulence is generally produced by elements that are installed upstream of the wing profile and generate inflow distortions.

The turbulent eddies interacting with the leading edge of the airfoil are subjected to a rapid deformation that scatters part of their kinetic energy into sound [1]. A fundamental study on the noise emitted by this mechanism was performed by Amiet [2], who proposed a theory to predict the far-field acoustic power spectral density generated by an airfoil immersed in a turbulent flow. In this case, the spanwise correlation length and the integral length scale of the upwash turbulent velocity fluctuations constitute the key parameters for the prediction of the noise generated by the interaction with the incoming turbulence. Experimentally, the leading-edge noise generation process has been addressed by several authors. Paterson and Amiet [3] measured the emitted far-field noise and the unsteady surface pressure field of a NACA-0012 airfoil installed downstream of a turbulence grid and concluded that the prediction of incident turbulence-interaction noise can be carried out if the inflow properties are sufficiently documented. Olsen and Wagner [4] analyzed the broadband noise generated by the impingement of turbulence on airfoils characterized by different shapes and observed that an increasing airfoil thickness corresponded to a reduced turbulence-interaction noise. Similar conclusions were drawn by Oerlemans and Migliore [5], who performed wind tunnel tests for six different airfoils at several angles of attack in a grid-generated turbulent flow. Moreau *et al.* [6] investigated the effect of the angle of attack and the airfoil shape by studying the noise emitted by three different mock-ups (a flat plate, a thin

Controlled-Diffusion (CD) airfoil, and a thick NACA-0012 airfoil) interacting with a turbulent flow in a grid-airfoil configuration. The results of the experiments confirmed the previously mentioned thickness effect of the airfoil, whereas the impact of the angle of attack and the camber was found to be limited. Devenport *et al.* [7] also confirmed the analysis of the effects of these parameters by testing three airfoils in a wind tunnel equipped with a turbulence grid. Additional numerical investigations on this influence were also carried out by Gill *et al.* [8] and Kim *et al.* [9].

The effective distortion of the turbulent vortical structures at the leading edge must be taken into account in order to obtain an accurate prediction of the leading-edge noise when the wing profile exceeds a minimum thickness [6; 10; 11]. In this regard, a useful analytical tool that can be considered for estimating the turbulence distortion around an airfoil with a significant thickness is the Rapid Distortion Theory (RDT), formulated by Hunt [12] and based on the work of Batchelor and Proudman [13]. This theory assumes a particular distortion to occur rapidly enough to have a negligible contribution from the turbulence to the relative motion of the fluid particles when these are convected through the non-uniform mean flow region. In addition, the turbulent velocity fluctuations are supposed to be small compared with the free-stream velocity. Recently, experimental evidence of the turbulence properties alteration predicted by the RDT for the case of a relatively thick airfoil was provided by De Santana *et al.* [11].

Since acting on the turbulence intensity of the incident flow is typically unfeasible, one possible leading-edge noise mitigation strategy is to make the airfoil less affected by local disturbances. The usage of absorbing materials, e.g. porous media, as part of the airfoil structure has the potential of achieving such a goal. Several researchers have already proposed technological solutions for the implementation of porous materials in the design of a wing profile in the last two decades. Among them, Roger *et al.* [1; 14] filled a NACA-0012 profile with steel wool to study the leading-edge noise reduction from a grid-airfoil and rod-airfoil interaction. They found that a reduction ranging from 2.5 dB to 6 dB was achievable for a part of the spectrum that was related to the characteristic length of the porous medium. Likewise, Geyer *et al.* [15] manufactured numerous porous airfoils characterized by different materials and tested them with various grid-generated turbulent flows. They also focused their attention on the influence of the parameters characterizing the porous media, observing how the noise reduction performance was strongly related to the material properties. Particularly, they found that lower values of static air flow resistivity could lead to a higher noise reduction.

All these studies demonstrated the potential of a porous treatment of the airfoil as a turbulence-interaction noise reduction technique. However, no definitive explanation about the physical mechanisms involved in the noise mitigation has been found yet. One possible mechanism is linked to the dissipation of the acoustic energy by the viscous and thermal losses occurring during the oscillatory fluid motion in the pores of the material [16]. A second one is related to the hydrodynamic absorption of the turbulent eddies due to the interaction with a penetrable surface. As a consequence of this, the distortion experienced by the turbulence in the immediate vicinity of the airfoil may be affected by the porous treatment. The present research has the purpose of investigating experimentally the latter mechanism.

The experimental campaign presented in this paper has been conducted in the JAFAR facility of the von Karman Institute for Fluid Dynamics (VKI). The comparison between the solid and the porous cases has been performed considering a zero-lift angle of attack and a jet outlet flow speed of $30\,\mathrm{m\,s^{-1}}$. The incident turbulence has been generated by placing a cylindrical rod upstream of the airfoil. In this arrangement, firstly proposed by Jacob *et al.* [17] as an aeroacoustic benchmark problem, the airfoil undergoes a broadband perturbation dominated by a shedding frequency, similarly to landing-gear applications [18].

2. Materials and methods

2.1. Rod-airfoil configuration

Fig. 1 shows a scheme of the rod-airfoil configuration installed in the JAFAR facility of von Karman Institute for Fluid Dynamics (VKI). A circular-to-rectangular contraction designed by De Santanta [19] adapts the circular geometry of the upstream duct to the rectangular geometry of the exhaust nozzle. The area ratio is 2.35 to 1 and the nozzle exit has a span of $s = 0.200\,\mathrm{m}$ and a width of $l = 0.150\,\mathrm{m}$. Two side plates guide the flow and support the $d = 0.020\,\mathrm{m}$ diameter cylindrical rod and the NACA-0024 airfoil, separated from each other by a distance of $0.174\,\mathrm{m}$ ($x/d = 8.20$). The airfoil chord is $c = 0.157\,\mathrm{m}$ ($c/d = 7.85$) and the maximum thickness is approximately $t = 0.038\,\mathrm{m}$ ($t/d = 1.90$). This value has been designed in order to have the same radius for the airfoil leading edge and the rod.

The following reference system, indicated by the red arrows in Fig. 1, has been adopted for the presentation of the results: the x-axis is aligned with the flow direction, the z-axis is aligned with the spanwise direction of the airfoil and the y-axis is oriented in the normal direction in order to form a right-handed coordinate system. The origin is set at midspan and at the leading edge of the airfoil mock-up.

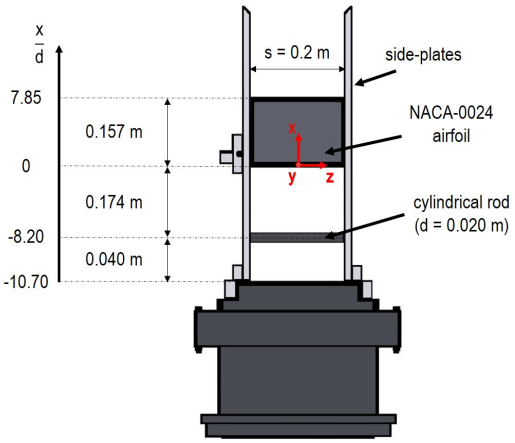

Figure 1: Sketch of the rod-airfoil configuration installed in the JAFAR facility of VKI. The red arrows denote the coordinate axes of the reference system.

2.2. *Design of the airfoils*

The same manufacturing technique has been used to design both the solid and the porous versions of the airfoil [20]. For both of them, a hard plastic exoskeleton with a thickness of 0.002 m preserves the structural integrity of the model. This is made of two components, one per each side of the airfoil surface, which have been glued together at the leading edge and the trailing edge. The porous airfoil exoskeleton features hexagonal openings throughout its surface, with a side-to-side length of 0.004 m and an equivalent open area ratio of 80 % to allow for the penetration of the air flow into the inner region. The volume of the wing profile has been filled with melamine foam. A hard plastic impenetrable center-plane avoids the cross-flow between the two sides of the airfoil. However, its extent does not cover the first 6.4 % of the chord (one leading-edge radius) to allow for the penetration of the air flow at the stagnation point. Moreover, both wing profiles have been coated with the same metallic wire mesh, which protects the materials and guarantees an adequate quality surface roughness. This is characterized by an aperture of 0.198 mm, a wire diameter of 0.056 mm and an open area ratio of 60.8 %. Fig. 2 provides a sketch of the different parts of the porous airfoil.

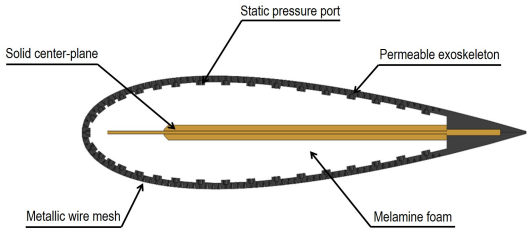

Figure 2: Representation of the porous NACA-0024 profile featuring the solid center-plane, the hard-plastic exoskeleton, the metallic wire mesh and the static pressure ports.

Finally, the solid and the porous airfoils have been equipped with 35 static pressure sensors distributed along both sides of the airfoils, at corresponding streamwise locations (Fig. 2). The transducers have been placed at the corners of the hexagonal openings in the midspan of the exoskeleton, thereby minimizing the alterations of the local open area ratio. The x-coordinates of the sensors range from 1 % to almost 80 % of the chord. Furthermore, an additional measurement position has been designed at the airfoil leading edge in order to acquire the stagnation pressure. The ports have then been connected to an in-house acquisition system for the evaluation of the mean wall-pressure distributions and the data have been acquired at a sampling frequency of 500 Hz and with an acquisition time of 15 s.

2.3. *Characterization of the porous medium*

According to the Johnson-Champoux-Allard-Lafarge (JCAL) model [21; 22; 23], the six parameters that are necessary to fully characterize the porous material are the static air flow resistivity, σ, the porosity, ϕ, the tortuosity, α_∞, the viscous characteristic length, Λ, the thermal characteristic length, Λ', and the static thermal permeability, k'. Besides these, another property used to define a porous medium is the static viscous permeability, k, which is directly linked to σ by the relationship $k = \mu/\sigma$, μ being the dynamic viscosity of air.

The characterization of the melamine foam parameters has been carried out in collaboration with the Laboratoire d'Acoustique de l'Université du Maine (LAUM). An inverse method based on the measurement of the scattering matrix by means of a 4-microphone impedance tube has been adopted [24].

Table 1: JCAL model parameters characterizing the melamine foam of the porous airfoil.

σ [Pa s m^{-2}]	ϕ [-]	α_∞ [-]	Λ [m]	Λ' [m]	k [m^2]	k' [m^2]
13 003.9	0.986	1.02	1.344×10^{-4}	1.942×10^{-4}	1.410×10^{-9}	2.305×10^{-9}

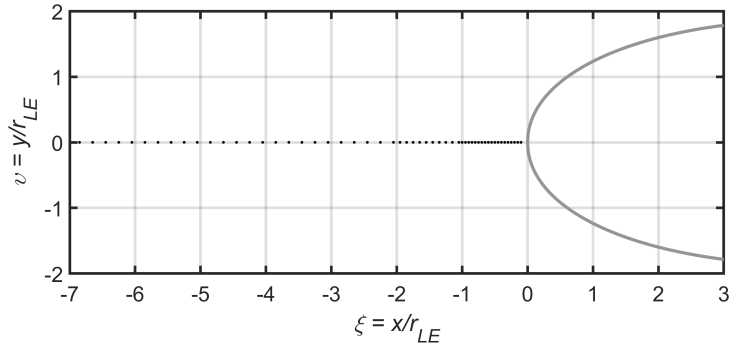

Figure 3: Traverse designed for the characterization of the stagnation streamline by means of hot-wire anemometry consisting of approximately 55 points at $z = 0$. The distance between the points is 2.0 mm, 1.0 mm and 0.5 mm for respectively the first 50 mm (5 r_{LE}), the following 10 mm (1 r_{LE}) and the final 10 mm (1 r_{LE}) of the traverse, whereas the minimum distance of the probe from the surface is 0.5 mm.

The results are listed in Table 1. Furthermore, additional measurements have been performed at Centre de Transfert de Technologie du Mans (CTTM), using samples of the exoskeleton and the wire mesh. The static air resistivity of the two layers has been found to be negligible compared with that of the melamine foam. The measured parameters have been used by Satcunanathan *et al.* [25] for calibrating and validating a direct hybrid LES/CAA method.

2.4. Flow field characterization

The experiments have been carried out at a free-stream flow velocity of $U_\infty = 30\,\mathrm{m\,s^{-1}}$ that corresponds to a Reynolds number based on the rod diameter of $Re_d = 4.1 \times 10^4$. The airfoil is set at zero angle of attack, which has been verified by the mean wall-pressure distribution.

The investigation of the stagnation region surrounding the airfoil leading edge has been conducted using a single hot-wire L-shaped probe connected to an in-house anemometer and installed in a carriage system that enables the automatic movement of the sensor along the x-direction, at y and z corresponding to the midspan of the airfoil leading edge. The wire has been mounted on a straight probe oriented perpendicular to the flow direction. The sampling frequency has been set to 51.2 kHz, whereas the acquisition time has been extended to 10 s in order to ensure statistical convergence in the computation of the velocity power spectral density (PSD). This quantity has been processed by means of the Welch method [26], with blocks of 2^{13} samples windowed using a Hanning weighting function characterized by a 50 % data overlap, thus providing a frequency resolution of about 6.25 Hz. In this case, the temperature variations have also been corrected, following the model proposed by Bruun [27].

Fig. 3 illustrates the measurement positions of the single traverse achieved at the midspan along the stagnation streamline. The x-coordinate is normalized by the leading-edge radius, r_{LE}. The traverse has been designed at $z = 0.1s$ in order to avoid the influence of the static pressure port on the measurement points close to the airfoil surface. 55 measurement points have been considered, with the probe moving in the streamwise direction from the upstream flow region towards the airfoil leading edge. The distance between consecutive measurement positions varies from 2.0 mm, to 1.0 mm and finally to 0.5 mm as shown in Fig. 3. The minimum distance of the probe from the surface less than 0.5 mm has been evaluated using a dummy sensor having the same geometry as the hot-wire probe. In this way, it has been possible to optically determine the exact position at which the prongs of the sensor touch the surface of the airfoil at the

leading edge, without harming the actual probe.

2.5. Acoustic beamforming setup

The noise reduction performance that is achieved with a porous treatment of the wing profile is evaluated by means of acoustic beamforming. A seven arms Dougherty array [28] has been used for the measurements. This has been placed at 1.160 m from the airfoil, out of the flow, and its center has been approximately aligned with the midspan of the leading edge. The array has an aperture of 1.500 m and is equipped with 64 capacitor-based Knowles electret microphones model FG-23329-P07 (frequency response: ±3 dB; frequency range: from 100 Hz to 10 kHz), calibrated in amplitude and in phase. Their coordinates are reported in Fig. 4. The data have been acquired at a sampling frequency of 51.2 kHz for 60 s. The cross-spectral matrix of the measured signals has been computed by employing the Welch method [26], with blocks of 2^{13} samples windowed using a Hanning weighting function characterized by a 50 % data overlap, thus providing a frequency resolution of 6.25 Hz.

The acoustic data have been post-processed using a Generalized Inverse Beamforming (GIBF) technique developed at VKI and validated with both numerical and experimental benchmark datasets [29; 30; 31; 32]. The use of an advanced beamforming algorithm turns out to be crucial to properly isolate the different noise source contributions. Particularly, the rod-noise has been found to be the dominant source for a major part of the sound spectrum, making it difficult to measure the leading-edge noise produced by the airfoil with a single microphone. This is a consequence of the thickness effect of the NACA-0024 profile that decreases the efficiency of the noise generation mechanism, as mentioned in Section 1.

A proper handling of the background noise is also required to ensure a better evaluation of the sound maps. Hence, an advanced subtraction technique based on the eigendecomposition of the cross-spectral matrix [33] has been employed. In this case, the acquired background noise corresponds to a configuration where the airfoil has been removed. Indeed, the distance between the rod and the wing profile is such that the vortex shedding is not suppressed by the presence of the body and the vortex-shedding frequency remains unaltered, making it feasible to perform the subtraction. Furthermore, corrections to account for the convection of the flow and the refraction of the shear layer have been applied, following the method proposed by Sijtsma [34]. A similar approach has been adopted in Zamponi *et al.* [35].

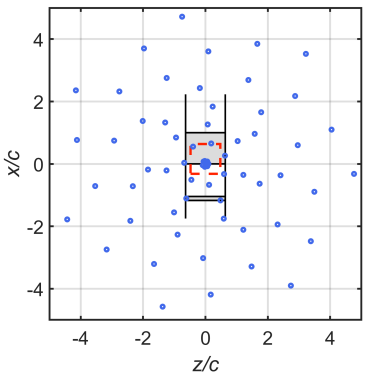

Figure 4: Configuration of the beamforming sound map, with the black lines indicating side-plates, rod and airfoil leading edge and trailing edge, the red dashed lines denoting the area considered for the integration of the sound maps and the blue circles illustrating the 64 microphones positions.

The focus of the present analysis is on the low-frequency range in order to investigate the noise reduction around the vortex shedding frequency. At low frequencies, the resolution of the beamforming sound maps is typically too low to exhibit a clear representation of the distributed noise sources along the leading edge due to the beamwidth characteristics of the microphone array. Nevertheless, the information on the source strength is preserved and it can be evaluated by integrating the sound maps after their decontamination from the background noise. The integration is then performed by summing the pressure values of each scanning grid point within a square region surrounding the airfoil leading edge. A sketch of the experimental setup to yield the sound maps is illustrated in Fig. 4. The scanning grid ranges between $-2 < z/c < 2$ and $-2 < x/c < 2$, with a spatial resolution of 0.010 m. The vertical black lines indicate the test section side-walls, the cylindrical rod, the leading edge, and the trailing edge of the airfoil. The red dashed lines indicate the considered integration area, whose dimension is 0.15 m × 0.15 m.

3. Results

3.1. Aeroacoustic Measurements

Fig. 5a and Fig. 5b show the GIBF sound maps for the solid and the porous airfoils respectively and refer to the one-third octave band center frequency $f_{1/3}$ = 250 Hz, which corresponds to the band that includes

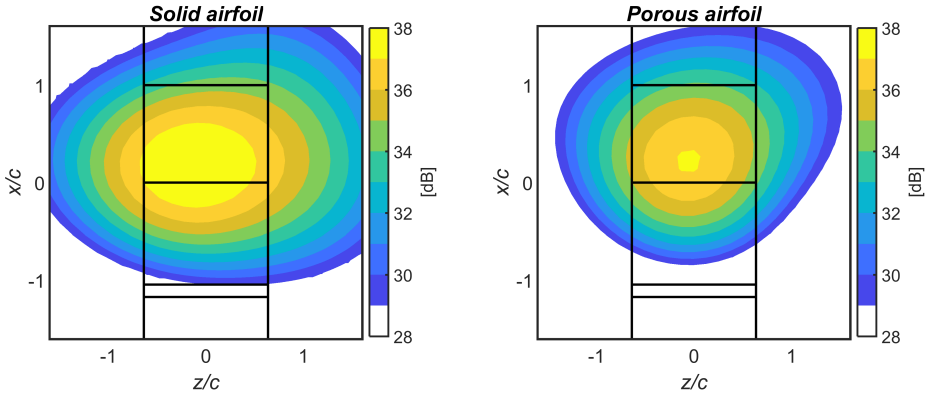

(a) (b)

Figure 5: GIBF sound maps for the solid (a) and porous (b) airfoil at $f_{1/3} = 250\,\text{Hz}$ plotted with the same 5 dB dynamic range for both cases and computed with a reference pressure of $p_{\text{ref}} = 20\,\mu\text{Pa}$. A background subtraction technique is applied to reduce the rod-noise contribution.

the vortex shedding frequency. The maps provide the one-third octave band sound pressure level $L_{\text{p(1/3)}}$ calculated with a reference pressure of $p_{\text{ref}} = 20\,\mu\text{Pa}$ and they are presented considering the same dynamic range of 10 dB. As already mentioned in Section 2.5, the noise source region does not appear distributed at the leading edge but extends over most of the airfoil surface for both solid and porous cases. Nevertheless, the adopted dynamic range allows for a visual estimation of the noise reduction achieved at this frequency range due to the porous treatment.

Furthermore, inverse beamforming methods such as GIBF display the source distribution contours instead of the peak source intensity, differently from direct techniques [36]. Hence, the integration of the maps is required to assess the actual noise source strength. This explains the relatively low levels of the sound maps in Fig. 5.

The resulting sound maps for one-third octave band center frequencies ranging from 250 Hz to 800 Hz have been subsequently integrated with reference to the center of the array. For each frequency, one eigenmode[1] is found to be dominant and therefore has been computed by the algorithm. The integrated spectra for both airfoils are presented in Fig. 6. The greatest noise abatement occurs at lower frequencies, in correspondence with the band containing the tonal component at the shedding frequency, and amounts to about 2.5 dB.

[1]GIBF is based on the eigendecomposition of the cross-spectral matrix of the microphone signals and each eigenvalue is linked to a coherent source distribution under constraint of orthogonality [36].

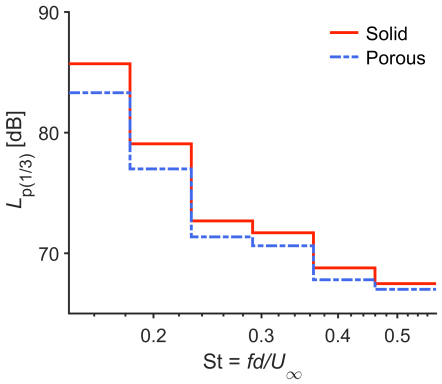

Figure 6: GIBF integrated one-third octave band spectra referred to the one-third octave band center frequencies ranging from 250 Hz to 800 Hz for the solid airfoil (red solid line) and the porous airfoil (blue dash-dotted line) and computed with a reference pressure of $p_{\text{ref}} = 20\,\mu\text{Pa}$.

For higher St, the noise reduction gradually decreases and solid and porous spectra start converging.

3.2. Static pressure distribution

The results of the mean wall-pressure distribution measurements are presented by defining the pressure coefficient C_p as

$$C_p = \frac{p - p_\infty}{p_{0,\text{s}} - p_\infty}, \tag{1}$$

where p is the measured mean wall-pressure and p_∞ and $p_{0,\text{s}}$ are respectively the static pressure in the free-

stream and the stagnation pressure measured at the leading edge of the solid airfoil.

The C_p distributions along the chord for the solid and porous airfoils are shown in Fig. 7. Each point of the curve has been calculated by averaging the mean wall-pressure acquired on the two sides of the airfoil at the same chord position.

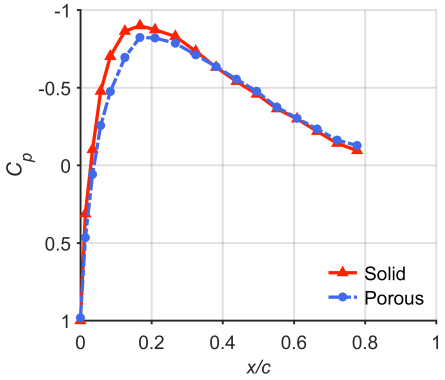

Figure 7: C_p distribution along the airfoil chord measured for the solid (red solid line) and the porous (blue dash-dotted line) airfoil for $U_\infty = 30\,\mathrm{m\,s^{-1}}$ and for a 0° angle of attack.

The alteration of the mean pressure field by the porous treatment appears to be confined to the upstream 30 % of the airfoil, despite the fact that the melamine foam fills the wing profile up to 80 % of the chord in the porous case. The two airfoils exhibit almost the same pressure in the stagnation point, although this value does not correspond to the free-stream dynamic pressure since the airfoil is immersed in the wake of the rod.

The negative C_p peak for the two wing profiles occurs at 17 % of the chord and is almost preserved, being its absolute value 6.7 % reduced for the porous case than for the solid one. Moreover, for the porous airfoil, this peak is reached in a more gradual way. The discrepancy can be explained by the partial penetration of the air flow through the pores of the melamine foam that tends to level out the pressure differences along the surface and reduces the flow displacement by the NACA-0024 profile. This would most likely degrade the lift of the airfoil if placed at some non-zero angle of attack, as reported in similar works [37; 38].

3.3. Mean and fluctuating velocity field along the stagnation streamline

The hot-wire anemometry results indicate that the implementation of the porous material in the airfoil preserves the airfoil's potential effect with regard to the upstream flow. Fig. 8a illustrates the mean velocity profile along the stagnation streamline for the solid and the porous airfoils. $\bar{U}$ is normalized by the free-stream velocity. As can be observed, the experimental data for the two cases follow the same trend up to the immediate vicinity of the leading edge. This conclusion is supported also by the relatively small deviation in the solid and porous C_p distributions of Fig. 7.

The most striking effect of porosity is on the evolution of the turbulent velocity fluctuations in the immediate vicinity of the leading edge. The velocity fluctuation profile along the stagnation streamline for the solid and the porous airfoil is depicted in Fig. 8b. The velocity U' is normalized with an upstream reference value, U'_{ref}, which corresponds to the r.m.s. of the velocity fluctuations that has not been affected by the presence of the body yet. This notation is consistent with the one by Batchelor and Proudman [13], Bearman [39], Hunt [12], and Britter *et al.* [40] in their investigations of the turbulence distortion. U'_{ref} has been evaluated at $\xi = -7$ and refers to the solid case. As can be seen from the plot, the experimental data present a similar trend up to about 0.5 r_{LE} from the leading edge, with a constant value equal to 1 for $\xi < -2$ and a decrease in the region $-2 \leq \xi < -0.5$. After this threshold, the solid and the porous cases diverge significantly, the former starts to increase and the latter keeps decreasing.

For small turbulence levels, a single normal hot-wire responds only to fluctuations in the direction of the mean velocity [41]. Therefore, in the region for $\xi < -2$, where the flow has a preferred direction along the x-axis, U' is dominated by the streamwise velocity fluctuations, which are constant. When the stagnation region is being approached, these are attenuated accordingly with the decrease of mean velocity due to the potential effect of the airfoil. However, near the stagnation point, the mean flow field further reduces and the hot-wire detects also the velocity fluctuations in the y-direction. This assumption is verified by the trend observed for the solid case, where the contribution of the upwash component of the velocity fluctuations is visible. In this case, indeed, the no-penetration condition imposed by the rigid surface forces the streamwise velocity fluctuations to be zero, leading to a transfer of momentum to the upwash com-

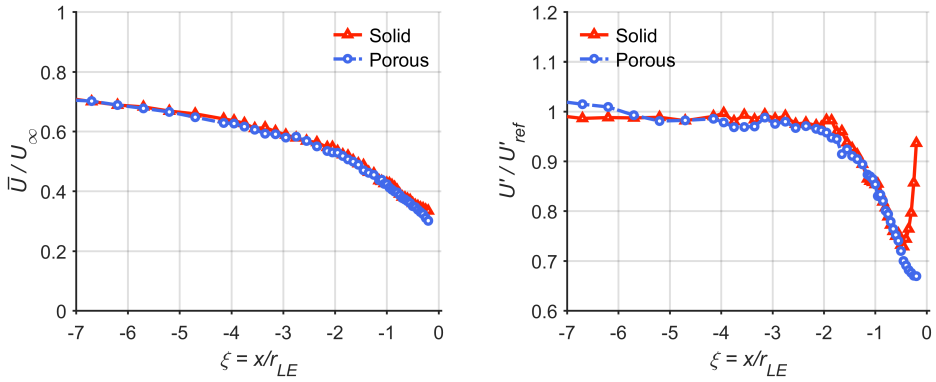

(a) (b)

Figure 8: Mean velocity profile (a) and velocity fluctuation profile (b) of the solid (in red) and porous (in blue) airfoil along the stagnation streamline for $U_\infty = 30\,\mathrm{m\,s^{-1}}$ and for a 0° angle of attack. U'_{ref} corresponds to the r.m.s. of the velocity fluctuations evaluated at $\xi = -7$ for the solid case.

ponent. This is the origin of the strong increase of velocity fluctuations in Fig. 8b for the solid airfoil.

In view of the above, it is possible to relate the damping effect of the porosity on U' to the attenuation of the upwash component of the velocity fluctuations. This outcome is in agreement with the analysis on the numerical results conducted by Satcunanathan *et al.* [42], where a strong attenuation of the Turbulent Kinetic Energy (TKE) in the stagnation region of the porous airfoil was reported. The present result constitutes a key point in understanding the physical mechanism for which the porous treatment of the airfoil affects the turbulence distortion and will be discussed in Section 4.

3.4. Turbulent velocity power spectra

The velocity power spectral density (PSD) from the experimental data extracted at four specific locations along the stagnation streamline have been computed. The results in Fig. 9 are presented in dB/St with a reference of $1\,\mathrm{m^2\,s^{-2}}$. The Strouhal number is based on the cylindrical rod diameter and the free-stream velocity. At $\xi = -6.7$ (Fig. 9a), the velocity power spectrum clearly presents two peaks corresponding to the vortex shedding frequency, found to be $St = 0.176 \pm 0.001$, and its first harmonic. At this position, no difference can be detected between the solid and the porous case, as already observed in Fig. 8b.

At $\xi = -1$ (Fig. 9b), the two considered cases still exhibit the same trend but now the vortex shedding frequency peak turns out to be fully dampened and is no longer visible in the spectra. It has been observed that this peak gradually decreases from the region downstream of the rod up to $\xi = -2$, where it disappears. Interestingly, at this location, the r.m.s. of the velocity fluctuations measured by the hot-wire starts reducing, as shown in Fig. 8b. In this intermediate region, the size of the larges eddies of the turbulent flow in the streamwise direction was derived by evaluating the integral length scale L_x from the autocorrelation function of the hot-wire time signal and from the local mean flow velocity [43] considering Taylor's frozen turbulence assumption. The resulting $L_x \approx 4.2\ r_{LE}$ will be used in Section 4 to interpret the velocity fluctuation trends by means of the RDT.

At $\xi = -0.8$, the peak at $St = 0.176 \pm 0.001$ reappears for both airfoils and increases in magnitude as the stagnation point is approached. This phenomenon is typical for stagnation-point flows [44] and might be caused by the effect of the flow deceleration that excites the instability associated with the vortex shedding and present in the oncoming flow. Indeed, vorticity of sufficiently large scale and opportunely oriented in such a way that the vortex lines are susceptible to stretching can undergo amplification as this is convected towards the stagnation region. Moreover, the solid and porous spectra start diverging from this point on, consistently with the U' trends in Fig. 8b. For the measurement point closest to the airfoil surface (Fig. 9d), the part of the spectrum that is affected by the porosity is the one at low Strouhal numbers, which corresponds to large vortical structures, whereas the high-St region is mostly unaltered.

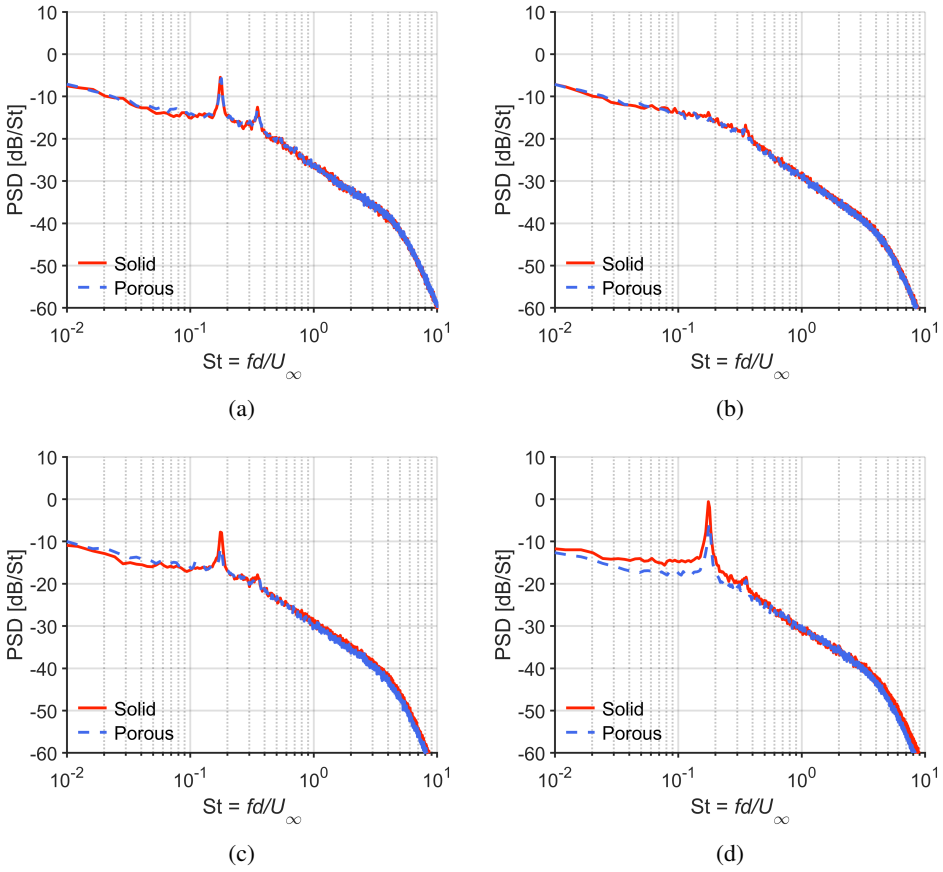

Figure 9: Velocity power spectral density for the solid (solid red line) and the porous case (dashed blue line) computed at $\xi = x/r_{LE} = -6.7$ (a), at $\xi = -1$ (b), at $\xi = -0.5$ (c) and at $\xi = -0.05$ (d) with a reference of 1 m^2 s^{-2}.

4. Discussion of the results: RDT

The results of the investigation described in Section 3 can be interpreted considering the RDT. Indeed, previous experimental studies [45; 11] have demonstrated that, in a region sufficiently close to the stagnation point, the inflow distortion experienced by an airfoil is similar to the one caused by a cylinder that has the same radius as the tangent circle at the airfoil leading edge. According to Hunt [12], there are two ways in which a bluff body can affect the incident turbulent flow:

- Through the distortion of the flow vorticity field due to potential effect of the body, which alters the mean velocity field around it and upstream of it and leads to a deflection of the streamlines.

- Through the pressure exerted by the body, which blocks the turbulence fluctuations by forcing the component of the incident velocity that is normal to its surface to be zero.

This first effect can be considered negligible if the streamwise integral length scale of the turbulent flow is much higher than the characteristic dimension of the body. For the airfoil case, the aforementioned condition can be expressed by $L_x \gg r_{LE}$. On the contrary, the body always exerts pressure on the flow, regardless of the ratio between the streamwise integral length scale of the turbulence and the leading-edge radius. The present mechanism is evident for a flat plate, which is characterized by $L_x/r_{LE} \to \infty$. In this extreme case, the vorticity field is almost unaffected by the presence of the body and the only contribution to the alteration of the turbulent velocity fluctuations comes from the second effect.

As showed in Section 3, the turbulence approaching the airfoils at $\xi = -7$ is characterized by $L_x/r_{LE} > 4$. Therefore, it is reasonable to assume that the contri-

bution of the first mechanism is negligible. Moreover, a closed-form expression of the RDT for describing the fluctuating velocity field around the body can be derived for the asymptotic case $L_x/r_{LE} \rightarrow \infty$ given the mean velocity field and the rate of change of it due to small alterations in the direction of the incident flow [12]. In his theory, Hunt assumes the mean velocity field to be inviscid and the turbulent velocity fluctuations to be small compared with the free-stream velocity. Under these assumptions, an analytical formulation of the r.m.s. of the velocity fluctuations for $L_x/r_{LE} \rightarrow \infty$ is [12]

$$\begin{cases} \mathbf{M_{11}^{(0)}} u'_\infty + \mathbf{M_{12}^{(0)}} v'_\infty = u' \\ \mathbf{M_{21}^{(0)}} u'_\infty + \mathbf{M_{22}^{(0)}} v'_\infty = v' \end{cases} \tag{2}$$

with

$$\mathbf{M_{ij}^{(0)}} = \begin{bmatrix} 1 - \frac{(1-\xi)^2-\upsilon^2}{[(1-\xi)^2+\upsilon^2]^2} & \frac{2(1-\xi)\upsilon}{[(1-\xi)^2+\upsilon^2]^2} \\ \frac{-2(1-\xi)\upsilon}{[(1-\xi)^2+\upsilon^2]^2} & 1 + \frac{(1-\xi)^2-\upsilon^2}{[(1-\xi)^2+\upsilon^2]^2} \end{bmatrix}, \tag{3}$$

where $\xi = x/r_{LE} \leq 0$, $\upsilon = y/r_{LE} \leq 0$, and u'_∞ and v'_∞ denote the free-stream values of u' and v' (similarly to the convention adopted for U'_{ref} in Fig. 8b). Along the stagnation streamline, Eq. (2) yields

$$u' = u'_\infty \left(1 - \frac{1}{(1-\xi)^2}\right), \tag{4}$$

$$v' = v'_\infty \left(1 + \frac{1}{(1-\xi)^2}\right). \tag{5}$$

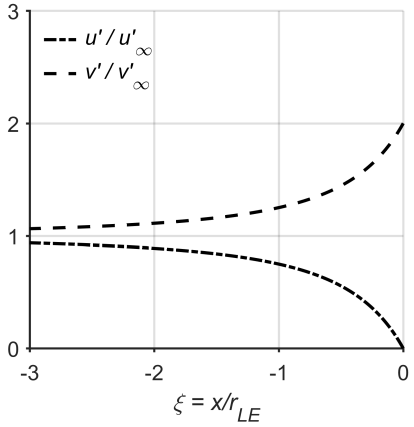

Figure 10: Trends of the r.m.s. of the velocity fluctuations along the stagnation streamline predicted by the RDT for the asymptotic case $L_x/r_{LE} \rightarrow \infty$.

The trends expressed by Eqs. (4) - (5), valid in the immediate vicinity of the stagnation point, are plotted in Fig. 10. The r.m.s. of the velocity fluctuations in the streamwise direction and the ones in the normal direction are respectively dampened and amplified with reference to their free-stream values. This asymptotic result is in qualitative agreement with what was observed in Figs. 8b for the solid airfoil and highlights the momentum transfer that occurs between u' and v' due to the no-penetration condition. However, for the porous case, the possibility for part of the incident velocity to penetrate the porous medium alters the mean velocity field around the airfoil and provides a non-zero value for the velocity at the leading edge. This constitutes a reduced geometrical discontinuity with respect to a solid wall. Hence, the porous body exerts a lower pressure on the turbulence with respect to the solid one and this leads to a damping effect on the variation of the velocity fluctuations starting from $\xi = 0.5$, as discussed in Section 3.

In view of the above, the distortion of the large vortical structures that interact with the porous airfoil leading edge is actually attenuated by the penetration of flow within the melamine foam. Physically, this leads to a decrease in the time variation of the inertia of the oncoming turbulent gusts and therefore to a less efficient conversion of their vortical energy into sound.

Finally, the fact that the turbulence is characterized by a large length scale compared to the characteristic dimension of the body implies that the dominant contribution to the incident velocity power spectrum is given by the low-frequency range [12]. This explains why the influence of the porous treatment is visible mostly in this frequency range (Fig. 9d), in agreement with the trends of the integrated acoustic power spectra reported in Fig. 6. The present link confirms the key role played by the attenuation of the distortion of the turbulent eddies in the leading-edge noise reduction mechanism.

5. Conclusion

The work described in this paper aims at elucidating the physical mechanisms responsible for the turbulence-interaction noise reduction due to a porous treatment of a thick airfoil. A NACA-0024 has been implemented with melamine foam enclosed within a permeable exoskeleton in order to perform a comparison with a solid baseline wing profile. The two airfoils have been tested in a rod-airfoil configuration, at a Reynolds number based on the cylindrical rod diameter of $Re_d = 4.1 \times 10^4$. The focus of the analysis has been put on the stagnation region near the leading edge with the purpose of examining the effect of

the porosity on the distortion of the turbulent vortical structures in the interaction with the profiles. Specifically, from the acquisition of the mean wall-pressure distributions on their surface, it has been observed that the porous treatment leads to a slight reduction of the flow displacement by the airfoil due to the possibility for the incident velocity to penetrate the inner volume. This phenomenon influences the potential effect of the airfoil and levels out the pressure differences along the surface. However, the C_p deviation between the two cases seems to be limited by the presence of the exoskeleton that preserves the shape fidelity of the NACA-0024 profile.

Furthermore, the flow field along the stagnation streamline has been characterized by means of hot-wire anemometry. The experiments showed that the fluctuating velocity field is significantly affected by the porosity when the stagnation region is being approached. In particular, the significant increase of the r.m.s. of the upwash velocity fluctuations experienced by the solid profile in the immediate vicinity of the leading edge and predicted by the RDT has not been observed in the porous case, bringing an attenuation of the TKE in the stagnation region. In addition, the analysis of the turbulent velocity power spectra suggests that the melamine foam has an effect mainly at low frequencies on the large scale structures. Therefore, the flow penetration through the pores of the melamine foam in the porous airfoil softens the distortion of the largest turbulent eddies though the presence of the body. This is supported by the results of the acoustic beamforming measurements, which indicate that the most appreciable noise abatement is achieved in the one-third octave band containing the tonal component at the shedding frequency, showing a correlation with the attenuation of the turbulent velocity fluctuations.

In summary, the absence of a no-penetration condition on the surface of the porous airfoil reduces the time variation of the vortices' inertia, making the distortion *less rapid*, and eventually leads to a less efficient conversion of vortical energy into sound. This hypothesis for explaining the role of porosity in the turbulence-interaction noise mitigation has been already formed in the past, but, to the authors' knowledge, no experimental evidence of it has ever been provided for a relatively thick airfoil.

Acknowledgments

This project has received funding from the European Union's Horizon 2020 research and innovation programme under the Marie Skłodowska-Curie grant agreement No. 722 401 in the framework of the ITN SmartAnswer.

References

[1] M. Roger, C. Schram, L. De Santana, Reduction of Airfoil Turbulence-Impingement Noise by Means of Leading-Edge Serrations and/or Porous Material, in: 19th AIAA/CEAS Aeroacoustics Conference, American Institute of Aeronautics and Astronautics, Berlin, Germany, 2013. doi:10.2514/6.2013-2108.

[2] R. K. Amiet, Acoustic radiation from an airfoil in a turbulent stream, Journal of Sound and Vibration 41 (4) (1975) 407–420. doi:10.1016/S0022-460X(75)80105-2.

[3] R. Paterson, R. Amiet, Acoustic radiation and surface pressure characteristics of an airfoil due to incident turbulence, in: 3rd Aeroacoustics Conference, American Institute of Aeronautics and Astronautics, Palo Alto,CA,U.S.A., 1976. doi:10.2514/6.1976-571.

[4] W. Olsen, J. Wagner, Effect of thickness on airfoil surface noise, AIAA Journal 20 (3) (1982) 437–439. doi:10.2514/3.7922.

[5] S. Oerlemans, P. Migliore, Aeroacoustic Wind Tunnel Tests of Wind Turbine Airfoils, in: 10th AIAA/CEAS Aeroacoustics Conference, American Institute of Aeronautics and Astronautics, Manchester, GREAT BRITAIN, 2004. doi:10.2514/6.2004-3042.

[6] S. Moreau, M. Roger, Effect of Angle of Attack and Airfoil Shape on Turbulence-Interaction Noise, in: 11th AIAA/CEAS Aeroacoustics Conference, American Institute of Aeronautics and Astronautics, Monterey, California, 2005. doi:10.2514/6.2005-2973.

[7] W. J. Devenport, J. K. Staubs, S. A. Glegg, Sound radiation from real airfoils in turbulence, Journal of Sound and Vibration 329 (17) (2010) 3470–3483. doi:10.1016/j.jsv.2010.02.022.

[8] J. Gill, X. Zhang, P. Joseph, Symmetric airfoil geometry effects on leading edge noise, The Journal of the Acoustical Society of America 134 (4) (2013) 2669–2680. doi:10.1121/1.4818769.

[9] D. Kim, G.-S. Lee, C. Cheong, Inflow broadband noise from an isolated symmetric airfoil interacting with incident turbulence, Journal of Fluids and Structures 55 (2015) 428–450. doi:10.1016/j.jfluidstructs.2015.03.015.

[10] J. Christophe, Application of Hybrid Methods to High Frequency Aeroacoustics, Ph.D. thesis, Université Libre de Bruxelles (11 2011).

[11] L. D. Santana, J. Christophe, C. Schram, W. Desmet, A Rapid Distortion Theory modified turbulence spectra for semi-analytical airfoil noise prediction, Journal of Sound and Vibration 383 (2016) 349–363. doi:10.1016/j.jsv.2016.07.026.

[12] J. C. R. Hunt, A theory of turbulent flow round two-dimensional bluff bodies, Journal of Fluid Mechanics 61 (4) (1973) 625–706. doi:10.1017/S0022112073000893.

[13] G. K. Batchelor, I. Proudman, THE EFFECT OF RAPID DISTORTION OF A FLUID IN TURBULENT MOTION, The Quarterly Journal of Mechanics and Applied Mathematics 7 (1) (1954) 83–103. doi:10.1093/qjmam/7.1.83.

[14] M. Roger, S. Moreau, Airfoil Turbulence-Impingement Noise Reduction by Porosity or Wavy Leading-Edge Cut: Experimental Investigations, in: 45th International Congress and Exposition on Noise Control Engineering, INTER-NOISE, Hamburg, Germany, 2016, p. 10.

[15] T. Geyer, E. Sarradj, J. Giesler, Application of a Beamforming Technique to the Measurement of Airfoil Leading Edge Noise, Advances in Acoustics and Vibration 2012. doi:10.1155/2012/905461.

[16] M. Kuczmarski, J. Johnston, Acoustic absorption in porous materials, Technical Report NASA/TM-2011-216995, NASA Glenn Research Center (2011).

[17] M. C. Jacob, J. Boudet, D. Casalino, M. Michard, A rod-airfoil experiment as a benchmark for broadband noise modeling, Theoretical and Computational Fluid Dynamics 19 (3) (2005) 171–196. doi:10.1007/s00162-004-0108-6.

[18] V. Lorenzoni, M. Tuinstra, F. Scarano, On the use of time-resolved particle image velocimetry for the investigation of rodairfoil aeroacoustics, Journal of Sound and Vibration 331 (23) (2012) 5012–5027. doi:10.1016/j.jsv.2012.05.034.

[19] L. D. de Santana, Semi-analytical methodologies for airfoil noise prediction, Ph.D. thesis, KU Leuven (6 2015).

[20] R. Zamponi, D. Ragni, N. Van de Wyer, C. Schram, Experimental Investigation of Airfoil Turbulence-Impingement Noise Reduction Using Porous Treatment, in: 25th AIAA/CEAS Aeroacoustics Conference, American Institute of Aeronautics and Astronautics, Delft, The Netherlands, 2019. doi:10.2514/6.2019-2649.

[21] D. L. Johnson, J. Koplik, R. Dashen, Theory of dynamic permeability and tortuosity in fluid-saturated porous media, Journal of Fluid Mechanics 176 (-1) (1987) 379. doi:10.1017/S0022112087000727.

[22] Y. Champoux, J. Allard, Dynamic tortuosity and bulk modulus in airsaturated porous media, Journal of Applied Physics 70 (4) (1991) 1975–1979. doi:10.1063/1.349482.

[23] D. Lafarge, P. Lemarinier, J. F. Allard, V. Tarnow, Dynamic compressibility of air in porous structures at audible frequencies, The Journal of the Acoustical Society of America 102 (4) (1997) 1995–2006. doi:10.1121/1.419690.

[24] M. Niskanen, J.-P. Groby, A. Duclos, O. Dazel, J. C. Le Roux, N. Poulain, T. Huttunen, T. Lhivaara, Deterministic and statistical characterization of rigid frame porous materials from impedance tube measurements, The Journal of the Acoustical Society of America 142 (4) (2017) 2407–2418. doi:10.1121/1.5008742.

[25] S. Satcunathan, R. Zamponi, M. Meinke, N. Van de Wyer, C. Schram, W. Schrder, Validation of a model for acoustic absorption in porous media, in: 48th International Congress and Exhibition on Noise Control Engineering, INTER-NOISE, Madrid, Spain, 2019.

[26] P. Welch, The use of fast Fourier transform for the estimation of power spectra: A method based on time averaging over short, modified periodograms, IEEE Transactions on Audio and Electroacoustics 15 (2) (1967) 70–73. doi:10.1109/TAU.1967.1161901.

[27] H. H. Bruun, Hot-Wire Anemometry: Principles and Signal Analysis, Measurement Science and Technology 7 (10). doi:10.1088/0957-0233/7/10/024.

[28] R. P. Dougherty, Spiral-shaped array for broadband imaging, Pat. US 5,838,284 (1998).

[29] R. Zamponi, N. V. de Wyer, C. Schram, An Improved Regularization of the Generalized Inverse Beamforming Applied to a Benchmark Database, in: 7th Berlin Beamforming Conference, BeBeC, Berlin, Germany, 2018.

[30] R. Zamponi, N. Van de Wyer, C. Schram, Benchmark Assessment of an Improved Regularization Technique for Generalized Inverse Beamforming, in: 2018 AIAA/CEAS Aeroacoustics Conference, American Institute of Aeronautics and Astronautics, Atlanta, Georgia, 2018. doi:10.2514/6.2018-4106.

[31] R. Merino-Martnez, P. Sijtsma, A. R. Carpio, R. Zamponi, S. Luesutthiviboon, A. M. Malgoezar, M. Snellen, C. Schram, D. G. Simons, Integration methods for distributed sound sources, International Journal of Aeroacoustics 18 (4-5) (2019) 444–469. doi:10.1177/1475472X19852945.

[32] R. Merino-Martnez, S. Luesutthiviboon, R. Zamponi, A. Rubio Carpio, D. Ragni, P. Sijtsma, M. Snellen, C. Schram, Assessment of the accuracy of microphone array methods for aeroacoustic measurements, Journal of Sound and Vibration 470 (2020) 115176. doi:10/gghzdf.

[33] C. J. Bahr, W. C. Horne, Advanced Background Subtraction Applied to Aeroacoustic Wind Tunnel Testing, in: 21st AIAA/CEAS Aeroacoustics Conference, American Institute of Aeronautics and Astronautics, Dallas, TX, 2015. doi:10.2514/6.2015-3272.

[34] P. Sijtsma, Phased Array Beamforming Applied to Wind Tunnel And Fly-Over Tests, Tech. rep., National Aerospace Laboratory NLR (Oct. 2010).

[35] R. Zamponi, P. Chiariotti, G. Battista, C. Schram, P. Castellini, 3D Generalized Inverse Beamforming in wind tunnel aeroacoustic testing: application to a Counter Rotating Open Rotor aircraft model, Applied Acoustics 163 (2020) 107229. doi:10.1016/j.apacoust.2020.107229.

[36] T. Suzuki, L1 generalized inverse beam-forming algorithm resolving coherent/incoherent, distributed and multipole sources, Journal of Sound and Vibration 330 (24) (2011) 5835–5851. doi:10.1016/j.jsv.2011.05.021.

[37] E. Sarradj, T. Geyer, Noise Generation by Porous Airfoils, in: 13th AIAA/CEAS Aeroacoustics Conference (28th AIAA Aeroacoustics Conference), American Institute of Aeronautics and Astronautics, Rome, Italy, 2007. doi:10.2514/6.2007-3719.

[38] T. Geyer, E. Sarradj, C. Fritzsche, Measurement of the noise generation at the trailing edge of porous airfoils, Experiments in Fluids 48 (2) (2010) 291–308. doi:10.1007/s00348-009-0739-x.

[39] P. W. Bearman, Some measurements of the distortion of turbulence approaching a two-dimensional bluff body, Journal of Fluid Mechanics 53 (03) (1972) 451. doi:10.1017/S0022112072000254.

[40] R. E. Britter, J. C. R. Hunt, J. C. Mumford, The distortion of turbulence by a circular cylinder, Journal of Fluid Mechanics 92 (02) (1979) 269. doi:10.1017/S0022112079000628.

[41] J.-D. Vagt, Hot-wire probes in low speed flow, Progress in Aerospace Sciences 18 (1979) 271–323. doi:10.1016/0376-0421(77)90010-0.

[42] S. Satcunanathan, M. H. Meinke, W. Schröder, Prediction of Noise Mitigation by Porous Media based on a Direct-Hybrid CFD/CAA Method, in: 25th AIAA/CEAS Aeroacoustics Conference, American Institute of Aeronautics and Astronautics, Delft, The Netherlands, 2019. doi:10.2514/6.2019-2696.

[43] N. V. C. Swamy, B. H. L. Gowda, V. R. Lakshminath, Autocorrelation measurements and integral time scales in three-dimensional turbulent boundary layers, Applied Scientific Research 35 (4) (1979) 237–249. doi:10.1007/BF00418215.

[44] S. P. Sutera, Vorticity amplification in stagnation-point flow and its effect on heat transfer, Journal of Fluid Mechanics 21 (3) (1965) 513–534. doi:10.1017/S0022112065000307.

[45] P. F. Mish, W. J. Devenport, An experimental investigation of unsteady surface pressure on an airfoil in turbulencePart 2: Sources and prediction of mean loading effects, Journal of Sound and Vibration 296 (3) (2006) 447–460. doi:10.1016/j.jsv.2005.08.009.

NUMERICAL METHODS

Massively parallel and robust high-order methods for transitional hypersonic flow modelling on unstructured grids

Ray Vandenhoeck

Aeronautics and Aerospace Department, von Karman Institute for Fluid Dynamics, Belgium, vandenhoeck@vki.ac.be

Supervisor: Georg May

Associate Professor, Aeronautics and Aerospace Department, von Karman Institute for Fluid Dynamics, Belgium, georg.may@vki.ac.be

Advisor: Andrea Lani

Research Expert, Aeronautics and Aerospace Department, von Karman Institute for Fluid Dynamics, Belgium, lanil@vki.ac.be

University Supervisor: Johan Steelant

Professor, Department of Mechanical Engineering, KU Leuven, Belgium, johan.steelant@kuleuven.be

Abstract

The high-order finite element-type method Flux Reconstruction (FR) is a promising scheme with a high computational efficiency and favorable properties for massively parallel computing, especially on GPUs. The present paper presents the implementation and optimization of a fully implicit FR solver that can handle hypersonic flows and its extension to GPUs. The implementation of implicit FR with an analytically computed Jacobian matrix is presented in detail. Its performance is compared to explicit FR and to implicit FR with a numerical Jacobian computation. Furthermore, the extension of the solver to GPUs is presented and its performance analyzed. The main test case used to assess the performance of the solver consists of a hypersonic viscous flow over a cone with an application to heat flux prediction. The solver is verified for this test case by comparing its results with both experimental results and numerical results from the literature.

Keywords: High-Order CFD, Flux Reconstruction, GPU, Hypersonics

1. Introduction

Over the past decade, compact high-order methods have drawn considerable attention due to an increased computational efficiency over their low-order counterparts. High-order methods generally introduce less numerical dissipation and allow for the use of coarser meshes to obtain the same accuracy as compared to low-order methods. The Flux Reconstruction (FR) formulation in particular represents one of the most recent and promising family of schemes. The FR approach is readily adaptable to heterogeneous high-performance parallel architectures due to its element-local nature and is capable of dealing with complex unstructured geometries. However, adoption of these types of methods for both academic and industrial high-speed applications has remained limited up to now due to their reduced robustness and lack of adequate shock capturing techniques.

The present paper presents the development of a fully implicit FR solver that is capable of handling viscous hypersonic flows as well as a GPU-enabled explicit FR solver. The present solver is implemented within the open-source framework for multi-physics modeling and simulations COOLFluiD[1]. More information on the development of this platform can be found in [1; 2]. More specifically, the implementation of implicit FR with an analytical Jacobian matrix is discussed as well as the extension of the present solver to GPUs.

After giving an overview of the Flux Reconstruction method in section 2, the derivation of the ana-

[1] https://github.com/andrealani/COOLFluiD/wiki

lytic Jacobian matrix is presented in section 3. Subsequently the performance of the developed FR solver is analyzed for both explicit and implicit time marching methods in section 4. Next, section 5 presents the extension of the FR solver to GPUs. Finally, the performance of the GPU-enabled solver is analyzed in section 6.

2. Flux Reconstruction Method

The FR method is a high-order Finite Element-type (FE) method that was originally developed by Huynh in [3]. The formulation of the FR approach proposed by Huynh is applicable to 1D advection problems and can be extended to quadrilateral and hexahedral (tensor) elements through tensor products of the one-dimensional base and correction functions. In [4; 5], the FR scheme was extended to advection-diffusion problems on both simplex and tensor elements. In this case, the flux also depends on the gradient of the solution, and the reconstruction procedure is applied to both the solution and the flux.

2.1. FR for Tensor Elements

Since the present FR solver works with tensor elements, an overview of the FR method for these types of elements is given in this section. Consider solving a system of N_{eq} advection-diffusion conservation equations on an arbitrary domain Ω, given by its i-th equation:

$$\frac{\partial u_i(\mathbf{x},t)}{\partial t} = -\nabla \cdot \mathbf{F}_i\left(\mathbf{u}, \nabla\mathbf{u}\right) \quad \text{for } i = \{1, \ldots, N_{eq}\} \text{ and } \mathbf{x} \in \Omega. \quad (1)$$

In this equation, t represents the time variable, $\mathbf{x}$ contains the space dimensional variables, in 3D being $\mathbf{x} = (x, y, z)$, u_i is the i-th conservative variable for which the system is solved, and $\mathbf{F}_i$ is the flux vector related to the i-th conservative variable. The Euler and Navier-Stokes equations can be written as a system of conservation equations, equivalent to expression 1. The FR method is classified as an FE-type method. Hence, the spatial domain Ω is partitioned into a finite number N of non-overlapping, non-empty, open sub-domains Ω'_n. The closed domain corresponding to the union of the open sub-domain Ω'_n and its boundary Γ_n is called an element and is denoted by $\Omega_n = \Omega'_n \cup \Gamma_n$ such that:

$$\bigcup_{n=1}^{N} \Omega_n = \Omega \quad \text{with} \quad \bigcap_{n=1}^{N} \Omega_n = \emptyset. \quad (2)$$

The exact solution vector $\mathbf{u}$ of the conservation law in 1 is approximated by a function $\mathbf{u}_n^\delta$ within each element Ω_n. This function $\mathbf{u}_n^\delta$ corresponds for each u_i to a polynomial of degree P within Ω_n and is identically zero on $\Omega \setminus \Omega_n$. These polynomials are allowed to be discontinuous across elements. $\mathbf{u}^\delta$ is constructed through summation of the elemental solutions $\mathbf{u}_n^\delta$. In the same manner, the exact flux $\mathbf{F}$ is approximated by a polynomial of degree $P+1$ within each sub-domain Ω_n, denoted by $\mathbf{F}_n^\delta$. The overall approximate flux $\mathbf{F}^\delta$ in the entire domain Ω is given by the sum of the elemental approximate fluxes such that:

$$\mathbf{u}^\delta = \sum_{n=1}^{N} \mathbf{u}_n^\delta \text{ and } \mathbf{F}^\delta = \sum_{n=1}^{N} \mathbf{F}_n^\delta. \quad (3)$$

Each element Ω_n together with the approximate solution $\mathbf{u}_n^\delta$ and flux $\mathbf{F}_n^\delta$ inside it, is transformed to a standard reference element Ω_S, which in 3D is given by: $\Omega_S = \{\boldsymbol{\xi} = (\xi, \eta, \zeta) \mid -1 \leq \xi, \eta, \zeta \leq 1\}$. In this manner, the computations for all elements are done in the same reference domain Ω_S. Consequently, the same algorithm can easily be applied to all elements. The transformation between Ω_n and Ω_S is carried out by means of a mapping function $\Theta_n(\boldsymbol{\xi})$.

The solution $\mathbf{u}_n^\delta$ within each sub-domain Ω_n can be obtained by solving the transformed conservation equation within the reference element Ω_S:

$$\frac{\partial \hat{u}_i^\delta}{\partial t} = -\nabla_{\boldsymbol{\xi}} \cdot \hat{\mathbf{F}}_i^\delta \quad \text{with} \quad \boldsymbol{\xi} \in \Omega_S, \quad (4)$$

with the transformed physical quantities given by:

$$\hat{u}_i^\delta = \hat{u}_i^\delta(\boldsymbol{\xi}, t) = J_n u_i^\delta(\Theta_n(\boldsymbol{\xi}), t) \quad \text{and} \quad \hat{\mathbf{F}}_i^\delta = \hat{\mathbf{F}}_i^\delta(\boldsymbol{\xi}, t) = \mathbf{F}_i^\delta(\Theta_n(\boldsymbol{\xi}), t). \quad (5)$$

In equation 5, J_n represents the Jacobian of the mapping $\Theta_n(\boldsymbol{\xi})$. From here on out, equations will only be considered in the standard domain and will only operate on the approximate polynomials for solution and flux. As such, hats on $\mathbf{u}$ and $\mathbf{F}$ and the superscript δ will be omitted in the rest of the present paper to make the equations more readable.

The FR method for solving equation 4 within the reference element Ω_S consists of seven subsequent steps. In the first step, a specific form for the approximate solution u_i is defined. To this end, a set of $N_s = (P+1)^{N_{dim}}$ distinct solution points are chosen where N_{dim} is the spatial dimensionality of the problem to be solved. The solution points typically have a Gauss-Legendre distribution. At these solution points the values of u_i are assumed to be known. Consequently, the approximate solution u_i is defined as a degree P polynomial of the following form:

$$u_i = \sum_{k=1}^{N_s} {}_k u_i \, l_k(\boldsymbol{\xi}), \tag{6}$$

where ${}_k u_i$ is the value of u_i at the k-th solution point, and $l_k(\boldsymbol{\xi})$ is the base function polynomial associated with the k-th solution point. For the FR method the base functions are Lagrange polynomials. It is however not necessary to construct a multivariate Lagrange basis for tensor elements since a product of one-dimensional Lagrange polynomials in each spatial direction can be taken as follows:

$$u_i = \sum_{k=1}^{N_s} {}_k u_i \, l_k(\boldsymbol{\xi}) = \sum_{k=1}^{N_s} {}_k u_i \, l_k^{\xi}(\xi) l_k^{\eta}(\eta) l_k^{\zeta}(\zeta), \tag{7}$$

where $l_k^{\xi}(\xi)$ represents a 1D Lagrange polynomial in the ξ direction related to the k-th solution point. More detailed information on this can be found in [3].

The second step consists of determining a common interface solution u_i^I at the boundaries of the standard element Ω_S. On each face of the element, $P+1$ flux points are defined with the same distribution as the solution points, where the flux points of two neighboring elements coincide. In order to compute the interface value at the f-th flux point ${}_f u_i^I$, equation 6 is evaluated in the f-th solution point. The approximate solution of the current element in f is denoted by ${}_f u_i^c$ and the solution of the neighboring element in f by ${}_f u_i^n$. Following the second approach of Bassi and Rebay (BR2), ${}_f u_i^I$ is then computed as the average of the two solutions in a flux point [6]. Figure 1 illustrates the process of computing the common interface values in 1D.

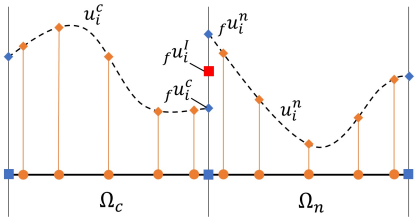

Figure 1: Computation of the common interface solutions; orange circles represent solution points and blue squares represent flux points

The third step of the FR method consists of calculating a corrected solution gradient ${}_k\mathbf{q}_i$ in each solution point k for each variable i. The previously defined interface solution values are used to obtain a continuous solution polynomial. To this end correction functions h_f for each flux point f are defined which have the following property for all flux points f and their opposite flux point g:

$$h_f(\boldsymbol{\xi}_f) = 1 \text{ and } h_f(\boldsymbol{\xi}_g) = 0. \tag{8}$$

Due to the tensor basis previously used for the solution points, these correction functions are one-dimensional and are only defined in the direction related to flux point f. Flux point g is on the same spatial direction as f but on the opposite side of the element as shown in figure 2. Furthermore from this figure it can be seen that to each solution point k there will be N_{dim} 1D Lagrange polynomials associated, each defined on a different spatial direction, shown by two dashed lines in figure 2. The form of the correction polynomials is defined by the VCJH scheme, which can be found in [7].

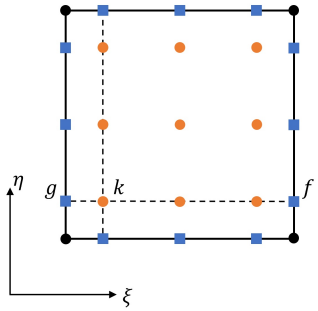

Figure 2: Illustration of tensor basis in 2D tensor element

The corrected solution gradient ${}_k\mathbf{q}_i$ is then computed via the following expression:

$${}_k\mathbf{q}_i = \nabla u_i + \sum_{f=1}^{N_f} \frac{dh_f}{d\xi^f}(\boldsymbol{\xi}_k)\left({}_f u_i^I - {}_f u_i^c\right)\mathbf{n}_f, \tag{9}$$

where N_f is the total number of flux points in an element, ξ^f the direction related to flux point f and $\mathbf{n}_f$ the normal vector in flux point f. Using equation 7 this can be written as:

$${}_k q_i^d = \sum_{s=1}^{N_s} {}_s u_i \frac{dl_s^d}{d\xi}(\xi_k) + \sum_{f=1}^{N_f} \frac{dh_f}{d\xi^f}(\boldsymbol{\xi}_k)\left({}_f u_i^I - {}_f u_i^c\right) n_f^d, \tag{10}$$

where ${}_k q_i^d$ is the i-variable gradient in solution point k in the d-direction, where d is either ξ, η or ζ, and n_f^d d-component of the normal in flux point f.

The fourth step consists of calculating the approximate discontinuous flux polynomial $\mathbf{F}_i^D(\boldsymbol{\xi})$. To this end, the flux is computed at each solution point $\boldsymbol{\xi}_k$, denoted by ${}_k\mathbf{F}_i$. In general, the flux depends on the solution and the solution gradient. Consequently, the dis-

continuous flux is evaluated using the approximate solution ${}_k u_i$, and the corrected solution gradient ${}_k \mathbf{q}_i$. The approximate discontinuous flux $\mathbf{F}_i^D(\boldsymbol{\xi})$ is then constructed as a polynomial of degree P in the same manner as u_i in equation 7:

$$\mathbf{F}_i^D(\boldsymbol{\xi}) = \sum_{k=1}^{N_s} {}_k\mathbf{F}_i({}_k u_i, {}_k\mathbf{q}_i)\, l_k(\boldsymbol{\xi}) = \sum_{k=1}^{N_s} {}_k\mathbf{F}_i({}_k u_i, {}_k\mathbf{q}_i)\, l_k^{\xi}(\xi) l_k^{\eta}(\eta) l_k^{\zeta}(\zeta). \quad (11)$$

The fifth step of the FR framework involves computing the common interface fluxes $\mathbf{F}_i^I$ at the flux points. In order to compute these interface fluxes, it is necessary to first obtain in each flux point f the values of ${}_f u_i$ and ${}_f \mathbf{q}_i$ using equations 7 and 10. The methodology for calculating the interface fluxes depends on the system of equations that needs to be solved. In the case of the Navier-Stokes equations, it is computed as the sum of a convective and a diffusive term. For the convective interface flux, an upwind biased approximate Riemann solver, like the Roe scheme [8], can be used. The diffusive interface flux is often calculated following the BR2 scheme [6].

The flux must be continuous across element boundaries in order to obtain a conservative scheme. Therefore, the sixth stage of the FR framework consists of adding a correction flux function $\mathbf{F}_i^C(\boldsymbol{\xi})$ to the approximate discontinuous flux $\mathbf{F}_i^D(\boldsymbol{\xi})$ resulting in the continuous flux $\mathbf{F}_i(\boldsymbol{\xi})$. The correction flux $\mathbf{F}_i^C$ is a polynomial of degree $P+1$ defined in such a manner that the continuous flux $\mathbf{F}_i$ equals the common interface flux $\mathbf{F}_i^I$ in the flux points, while approximating the discontinuous flux $\mathbf{F}_i^D$ within the standard element. In order to satisfy the aforementioned requirements, $\mathbf{F}_i^C$ is constructed by means of the degree $P+1$ correction functions $h_f(\xi)$ that were previously used to obtain the corrected gradient ${}_k \mathbf{q}_i$.

The correction flux function $\mathbf{F}_i^C(\boldsymbol{\xi})$ takes the following form:

$$\mathbf{F}_i^C(\boldsymbol{\xi}) = \sum_{f=1}^{N_f} h_f(\boldsymbol{\xi}) \left({}_f\mathbf{F}_i^I - {}_f\mathbf{F}_i^D \right), \quad (12)$$

where ${}_f\mathbf{F}_i^D = \mathbf{F}_i^D(\boldsymbol{\xi}_f)$. The continuous flux $\mathbf{F}_i(\boldsymbol{\xi})$ is then written as the sum of the approximated discontinuous flux and the correction flux:

$$\mathbf{F}_i(\boldsymbol{\xi}) = \mathbf{F}_i^D(\boldsymbol{\xi}) + \sum_{f=1}^{N_f} h_f(\boldsymbol{\xi}) \left({}_f\mathbf{F}_i^I - {}_f\mathbf{F}_i^D \right). \quad (13)$$

A schematic of the flux correction procedure within a 1D element with flux points f and g is given in figure 3.

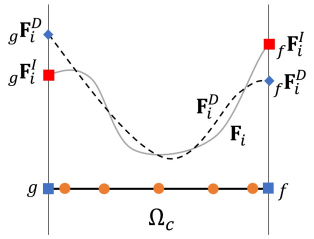

Figure 3: Correction procedure of the discontinuous flux such that the values of the total flux at the boundaries are equal to the interface value

The final step of the FR method consists of computing the divergence of the total flux $\mathbf{F}_i(\boldsymbol{\xi})$ at each solution point k. To this end the divergence of equation 13 is taken, taking into account the expression for the discontinuous flux in 11:

$$\nabla \cdot {}_k\mathbf{F}_i = \sum_{s=1}^{N_s} \sum_{d=1}^{N_{dim}} {}_s F_i^d \frac{dl_s^d}{d\xi^d}(\xi_k^d) + \sum_{f=1}^{N_f} \frac{dh_f}{d\xi^f}(\boldsymbol{\xi}_k) \left({}_f\mathbf{F}_i^I - {}_f\mathbf{F}_i^D \right) \cdot \mathbf{n}_f, \quad (14)$$

where ξ^d is the d-th spatial direction and ${}_s F_i^d$ the ξ^d-component of ${}_s\mathbf{F}_i$.

Finally, a time marching strategy such as the backward Euler method is applied to advance the approximate solution u_i in time using the following expression:

$$\frac{d_k u_i}{dt} = -\nabla \cdot {}_k\mathbf{F}_i. \quad (15)$$

3. Implicit Flux Reconstruction

Explicit time marching procedures have a stringent CFL stability condition, strongly restricting the admissible time step. The forward Euler method for example has a CFL condition for FR of:

$$CFL < \frac{1}{P+1}. \quad (16)$$

Consequently, implicit time marching methods, which do not have this stringent CFL constraint, typically allow for much faster convergence. However, implicit methods require the computation of the Jacobian matrix of the right-hand side (RHS) of equation 15.

Consider as an example the backward Euler implicit time marching scheme in solution point k that can be written as follows:

$${}_k u_i(t+\Delta t) = {}_k u_i(t) + \Delta t \left[{}_k R_i(\mathbf{u}(t+\Delta t), \mathbf{q}(\mathbf{u}(t+\Delta t))) \right], \quad (17)$$

where ${}_kR_i$ is the RHS of equation 15 in solution point k for variable i. The value of Δt can be determined by a CFL number specified by the user. At time t, the value of ${}_kR_i((\mathbf{u}(t+\Delta t), \mathbf{q}(\mathbf{u}(t+\Delta t)))$ is not readily available since ${}_k\mathbf{u}(t+\Delta t)$ is unknown. As such, expression 17 is a non-linear equation that has to be solved during each iteration. It also needs to be solved for each element in the spatial domain, resulting in a system of non-linear equations, which is linearized as follows:

$$
\begin{aligned}
&{}_ku_i(t+\Delta t) = {}_ku_i(t) + \\
&\Delta t \left[{}_kR_i(\mathbf{u}(t), \mathbf{q}(\mathbf{u}(t))) + \left.\frac{\partial_k R_i}{\partial_k \mathbf{u}}\right|_t \left({}_k\mathbf{u}(t+\Delta t) - {}_k\mathbf{u}(t) \right) \right],
\end{aligned}
\tag{18}
$$

where $\left.\frac{\partial_k R_i}{\partial_k \mathbf{u}}\right|_t$ is the Jacobian matrix of the RHS with respect to the state vectors, evaluated at time t. The resulting large linear system is then solved with for example a Generalized Minimal Residual approach (GMRES) [9].

For high-order FE-type methods, the evaluation of the Jacobian is costly and largely dictates the performance of the implicit method. The present section described two ways of computing the Jacobian: a numerical and an analytical way. In section 4 the performance of both are compared. First an overview of the numerical approach is given.

3.1. Numerical Jacobian

The Jacobian matrix is determined by numerically approximating the partial derivatives with a simple first-order finite difference scheme. It is important to note that in the FR framework, the RHS in solution point k depends on the solution and gradient in the other solution points of the element and its neighboring elements. Furthermore it is important to note that the RHS for variable i in general depends on the complete state and gradient, not only on the i-th variable state and gradient. As such, the quantities that need to be computed are the partial derivatives of the RHS of variable i in solution point k with respect to variable j and solution point l which can belong to the current element or a neighboring element. Using a first-order finite difference scheme, this partial derivative can be written as:

$$
\frac{\partial_k R_i}{\partial_l u_j} = \frac{{}_kR_i({}_lu_j + \varepsilon_j, {}_l\mathbf{q}_j({}_lu_j + \varepsilon_j)) - {}_kR_i({}_lu_j, {}_l\mathbf{q}_j({}_lu_j))}{\varepsilon_j},
\tag{19}
$$

where ε_j is a small perturbation added to ${}_lu_j$. Note that in this expression only the arguments of ${}_kR_i$ that are changed due to the perturbation are written. In the present solver, the perturbation ε_j is computed as follows:

$$
\varepsilon_j = \varepsilon \max(|{}_lu_j|, u_{j,ref}),
\tag{20}
$$

where ε is a user-defined tolerance, usually $1e-7$, and $u_{j,ref}$ a user-defined reference value for the j-th variable, usually corresponding to its free stream value.

From an implementation perspective, this approach is relatively straightforward: for each RHS ${}_kR_i$ the whole FR procedure is repeated for each solution point state variable ${}_lu_j$ that influences this RHS. As such, no significant additions need to be added to the solver for this approach. However it is very costly and does not scale well with the order of the FR method, as is illustrated in section 4. This is because superfluous computations will simply be repeated every time a new solution point variable is perturbed as the perturbation does not influence the complete FR procedure.

3.2. Analytical Jacobian

The analytical approach consists of analytically determining an expression for the Jacobian $\frac{\partial_k R_i}{\partial_l u_j}$ based on the FR formulation and the expression of the physical fluxes $\mathbf{F}_i$. The RHS is simply minus the flux divergence:

$$
{}_kR_i = -\nabla \cdot {}_k\mathbf{F}_i.
\tag{21}
$$

Consequently, to compute the Jacobian, the partial derivative of expression 14 needs to be taken:

$$
\begin{aligned}
\frac{\partial_k R_i}{\partial_l u_j} &= -\frac{\partial \nabla \cdot {}_k\mathbf{F}_i}{\partial_l u_j} \\
&= -\sum_{s=1}^{N_s} \sum_{d=1}^{N_{dim}} \frac{\partial_s F_i^d}{\partial_l u_j} \frac{dl_s^d}{d\xi^d}(\xi_k^d) \\
&\quad - \sum_{f=1}^{N_f} \frac{dh_f}{d\xi^f}(\boldsymbol{\xi}_k) \left(\frac{\partial_f \mathbf{F}_i^I}{\partial_l u_j} - \frac{\partial_f \mathbf{F}_i^D}{\partial_l u_j} \right) \cdot \mathbf{n}_f.
\end{aligned}
\tag{22}
$$

At this point it is important to note that the flux depends on the state and the gradient, which in turn depends on the state. In tensor elements the gradient in solution point m depends only on $N_{dim}(P+1)$ states in the current element and on $P+1$ states in each of the $2N_{dim}$ neighboring element, as is illustrated for 2 neighboring 2D tensor elements in figure 4. As such, consider the total number of states that influence the gradient $N_{s,q} = 3N_{dim}(P+1)$. Taking the dependence of the flux to the state and gradient into account, the following expression for the partial derivative of the flux holds:

$$\frac{\partial_k \mathbf{F}_i(\mathbf{u}, \mathbf{q}(\mathbf{u}))}{\partial_l u_j} = \left.\frac{\partial_k \mathbf{F}_i}{\partial_l u_j}\right|_{\mathbf{q}} + \sum_{m=1}^{N_{s,q}} \sum_{b=1}^{N_{dim}} \left.\frac{\partial_k \mathbf{F}_i}{\partial_m q_j^b}\right|_{\mathbf{u}, q^{\xi \neq b}} \frac{\partial_m q_j^b}{\partial_l u_j}, \quad (23)$$

where $\left.\frac{\partial_k \mathbf{F}_i}{\partial_l u_j}\right|_{\mathbf{q}}$ is the flux partial derivative to the state keeping the gradient constant and $\left.\frac{\partial_k \mathbf{F}_i}{\partial_m q_j^b}\right|_{\mathbf{u}, q^{\xi \neq b}}$ the flux partial derivative to the gradient keeping the state and all other gradients constant. Note that from here on out, this will be written in shorthand as $\left.\frac{\partial_k \mathbf{F}_i}{\partial_m q_j^b}\right|_{\mathbf{u}}$.

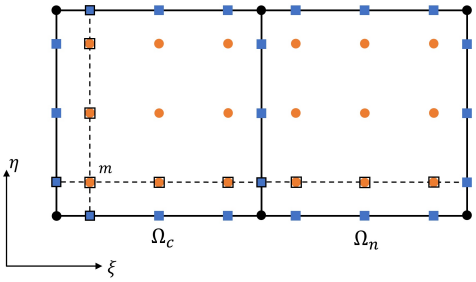

Figure 4: States in two neighboring 2D tensor elements that are used to compute the gradient in point m

Plugging expression 23 into 22 yields the following expression for the Jacobian:

$$\begin{aligned}\frac{\partial_k R_i}{\partial_l u_j} = & \underbrace{-\sum_{s=1}^{N_s} \sum_{d=1}^{N_{dim}} \left.\frac{\partial_s F_i^d}{\partial_l u_j}\right|_{\mathbf{q}} \frac{dl_s^d}{d\xi^d}(\xi_k^d)}_{J_{e,u}} \\ & \underbrace{-\sum_{s=1}^{N_s} \sum_{d=1}^{N_{dim}} \sum_{m=1}^{N_{s,q}} \sum_{b=1}^{N_{dim}} \left.\frac{\partial_s F_i^d}{\partial_m q_j^b}\right|_{\mathbf{u}} \frac{\partial_m q_j^b}{\partial_l u_j} \frac{dl_s^d}{d\xi^d}(\xi_k^d)}_{J_{e,q}} \\ & \underbrace{-\sum_{f=1}^{N_f} \frac{dh_f}{d\xi^f}(\boldsymbol{\xi}_k) \left(\left.\frac{\partial_f \mathbf{F}_i^I}{\partial_l u_j}\right|_{\mathbf{q}} - \left.\frac{\partial_f \mathbf{F}_i^D}{\partial_l u_j}\right|_{\mathbf{q}} \right) \cdot \mathbf{n}_f}_{J_{f,u}} \\ & \underbrace{-\sum_{f=1}^{N_f} \sum_{m=1}^{N_{s,q}} \sum_{b=1}^{N_{dim}} \frac{dh_f}{d\xi^f}(\boldsymbol{\xi}_k) \frac{\partial_m q_j^b}{\partial_l u_j} \left(\left.\frac{\partial_f \mathbf{F}_i^I}{\partial_m q_j^b}\right|_{\mathbf{u}} - \left.\frac{\partial_f \mathbf{F}_i^D}{\partial_m q_j^b}\right|_{\mathbf{u}} \right) \cdot \mathbf{n}_f}_{J_{f,q}} . \end{aligned} \quad (24)$$

It is clear that there are four separate terms in equation 24: a term related to the inner element and the solution derivative $J_{e,u}$, related to the inner element and the gradient derivative $J_{e,q}$, related to the faces and the solution derivative $J_{f,u}$ and related to the faces and the gradient derivative $J_{f,q}$.

Since the flux depends only on the state in the solution point in which it is evaluated when keeping the gradient constant, $J_{e,u}$ can be simplified accordingly:

$$\left.\frac{\partial_{s \neq l} F_i^d}{\partial_l u_j}\right|_{\mathbf{q}} = 0 \Rightarrow$$

$$J_{e,u} = -\sum_{d=1}^{N_{dim}} \left.\frac{\partial_l F_i^d}{\partial_l u_j}\right|_{\mathbf{q}} \frac{dl_l^d}{d\xi^d}(\xi_k^d). \quad (25)$$

For the derivative of the flux to the gradient in $J_{e,q}$, a similar reasoning can be made:

$$\left.\frac{\partial_{s \neq m} F_i^d}{\partial_m q_j^b}\right|_{\mathbf{u}} = 0 \Rightarrow$$

$$J_{e,q} = -\sum_{d=1}^{N_{dim}} \sum_{m=1}^{N_{s,q}} \sum_{b=1}^{N_{dim}} \left.\frac{\partial_m F_i^d}{\partial_m q_j^b}\right|_{\mathbf{u}} \frac{\partial_m q_j^b}{\partial_l u_j} \frac{dl_m^d}{d\xi^d}(\xi_k^d). \quad (26)$$

In $J_{f,u}$ and $J_{f,q}$ there is a term J^I related to the interface flux and a term J^D related to the extrapolated discontinuous flux. Consider these two terms separately as follows:

$$\begin{aligned} J_{f,u} = & \underbrace{-\sum_{f=1}^{N_f} \frac{dh_f}{d\xi^f}(\boldsymbol{\xi}_k) \left.\frac{\partial_f \mathbf{F}_i^I}{\partial_l u_j}\right|_{\mathbf{q}} \cdot \mathbf{n}_f}_{J_{f,u}^I} \\ & + \underbrace{\sum_{f=1}^{N_f} \frac{dh_f}{d\xi^f}(\boldsymbol{\xi}_k) \left.\frac{\partial_f \mathbf{F}_i^D}{\partial_l u_j}\right|_{\mathbf{q}} \cdot \mathbf{n}_f}_{J_{f,u}^D}, \end{aligned} \quad (27)$$

$$\begin{aligned} J_{f,q} = & \underbrace{-\sum_{f=1}^{N_f} \sum_{m=1}^{N_{s,q}} \sum_{b=1}^{N_{dim}} \frac{dh_f}{d\xi^f}(\boldsymbol{\xi}_k) \frac{\partial_m q_j^b}{\partial_l u_j} \left.\frac{\partial_f \mathbf{F}_i^I}{\partial_m q_j^b}\right|_{\mathbf{u}} \cdot \mathbf{n}_f}_{J_{f,q}^I} \\ & + \underbrace{\sum_{f=1}^{N_f} \sum_{m=1}^{N_{s,q}} \sum_{b=1}^{N_{dim}} \frac{dh_f}{d\xi^f}(\boldsymbol{\xi}_k) \frac{\partial_m q_j^b}{\partial_l u_j} \left.\frac{\partial_f \mathbf{F}_i^D}{\partial_m q_j^b}\right|_{\mathbf{u}} \cdot \mathbf{n}_f}_{J_{f,q}^D} . \end{aligned} \quad (28)$$

First, consider the J^D terms. For tensor elements, the extrapolated values of states and fluxes in a flux point only depend on $P+1$ solution points that define the 1D Lagrange polynomials in the spatial direction related

to that flux point. Consequently, using equation 11, the extrapolated discontinuous flux in flux point f can be written as:

$$ {}_f\mathbf{F}_i^D = \sum_{m=1}^{P+1} {}_m\mathbf{F}_i l_m^f(\xi_f^f). \tag{29} $$

Taking the partial derivatives and taking into account equations 25 and 26, this becomes:

$$ \left.\frac{\partial_f \mathbf{F}_i^D}{\partial_l u_j}\right|_{\mathbf{q}} = \left.\frac{\partial_l \mathbf{F}_i}{\partial_l u_j}\right|_{\mathbf{q}} l_l^f(\xi_f^f), \tag{30} $$

$$ \left.\frac{\partial_f \mathbf{F}_i^D}{\partial_m q_j^b}\right|_{\mathbf{u}} = \left.\frac{\partial_m \mathbf{F}_i}{\partial_m q_j^b}\right|_{\mathbf{u}} l_m^f(\xi_f^f). \tag{31} $$

Substituting equation 30 and 31 into respectively equation 27 and 28 yields:

$$ J_{f,u}^D = \sum_{f=1}^{N_f} \frac{dh_f}{d\xi^f}(\boldsymbol{\xi}_k) l_l^f(\xi_f^f) \left.\frac{\partial_l \mathbf{F}_i}{\partial_l u_j}\right|_{\mathbf{q}} \cdot \mathbf{n}_f, \tag{32} $$

$$ J_{f,q}^D = \sum_{f=1}^{N_f}\sum_{m=1}^{P+1}\sum_{b=1}^{N_{dim}} \frac{dh_f}{d\xi^f}(\boldsymbol{\xi}_k) l_m^f(\xi_f^f) \frac{\partial_m q_j^b}{\partial_l u_j} \left.\frac{\partial_m \mathbf{F}_i}{\partial_m q_j^b}\right|_{\mathbf{u}} \cdot \mathbf{n}_f. \tag{33} $$

The terms $J_{f,u}^I$ and $J_{f,q}^I$ of equation 27 and 28 cannot be further simplified since the scheme to compute $\mathbf{F}^I$ is not known a priori: for convective fluxes this could be any Riemann solver and for diffusive fluxes this could be a number of different schemes such as BR2, Local Approach, Interior Penalty, etc. As a consequence, the analytical expression for $\left.\frac{\partial_f \mathbf{F}_i^D}{\partial_l u_j}\right|_{\mathbf{q}}$ and $\left.\frac{\partial_f \mathbf{F}_i^D}{\partial_m q_j^b}\right|_{\mathbf{u}}$ needs to be computed for the specific interface flux scheme.

In the terms $J_{e,q}$ and $J_{f,q}$, the partial derivative of the gradient to a state appears. This can also be computed analytically. Consider the b-component of the gradient in solution point m, of variable j and the solution in solution point l and of the same variable j. Using the definition of the corrected gradient in equation 10 and taking into account that only $2N_{dim}$ flux points are needed for a gradient computation as shown in figure 4, the partial derivative can be written as follows:

$$ \frac{\partial_m q_j^b}{\partial_l u_j} = \frac{dl_l^b}{d\xi^b}(\xi_m^b) + \sum_{f=1}^{2N_{dim}} \frac{1}{2}\frac{dh_f}{d\xi^f}(\boldsymbol{\xi}_m)\left(\frac{\partial_f u_j^n}{\partial_l u_j} - \frac{\partial_f u_j^c}{\partial_l u_j}\right) n_f^f. \tag{34} $$

Using expression 6 to compute ${}_f u_j^n$ and ${}_f u_j^n$, equation 34 reduces to:

$$ \frac{\partial_m q_j^b}{\partial_l u_j} = \frac{dl_l^b}{d\xi^b}(\xi_m^b) + \sum_{f=1}^{2N_{dim}} \frac{1}{2}\frac{dh_f}{d\xi^f}(\boldsymbol{\xi}_m)\left(l_l^{f,n}(\xi_f^f) - l_l^{f,c}(\xi_f^f)\right) n_f^f, \tag{35} $$

where $l_l^{f,n}$ is the Lagrange polynomial l_l^f belonging to the neighboring element and $l_l^{f,c}$ the Lagrange polynomial l_l^f belonging to the current element. Consequently, the following applies:

$$ \text{if } {}_l u \in \Omega_c: \frac{\partial_m q_j^b}{\partial_l u_j} = \frac{dl_l^b}{d\xi^b}(\xi_m^b) - \sum_{f=1}^{2N_{dim}} \frac{1}{2}\frac{dh_f}{d\xi^f}(\boldsymbol{\xi}_m) l_l^{f,c}(\xi_f^f) n_f^f, \tag{36} $$

$$ \text{if } {}_l u \in \Omega_n: \frac{\partial_m q_j^b}{\partial_l u_j} = \frac{dl_l^b}{d\xi^b}(\xi_m^b) + \frac{1}{2}\frac{dh_f}{d\xi^f}(\boldsymbol{\xi}_m) l_l^{f,n}(\xi_f^f) n_f^f. \tag{37} $$

The only unknowns remaining in order to compute the Jacobian are:

$$ \left.\frac{\partial_l F_i^d}{\partial_l u_j}\right|_{\mathbf{q}} \text{ and } \left.\frac{\partial_m F_i^d}{\partial_m q_j^b}\right|_{\mathbf{u}}. \tag{38} $$

These partial derivatives depend on the physics of the problem to be solved. For the Euler and Navier-Stokes equations, they can easily be computed analytically. However for more complex physical applications, such as Multi-Fluid Magnetohydrodynamics, or when external libraries are used to evaluate for example transport properties of the flow, it is not feasible to compute the derivatives analytically. In that case they are computed numerically applying equation 19 to the flux instead of to the RHS. This way of computing the Jacobian is called a semi-analytical Jacobian since the FR process is taken into account analytically, but the physics in a numerical way. In the present solver, a semi-analytical method is used since the execution time of the computation of the flux derivatives is small compared to that of the analytical FR Jacobian. It is however straightforward to extend to solver to a fully analytical Jacobian.

Finally, by combining equations 25, 26, 27, 28, 36 and 37, the Jacobian can be evaluated:

$$ \frac{\partial_k R_i}{\partial_l u_j} = J_{e,u} + J_{e,q} + J_{f,u}^I + J_{f,q}^I + J_{f,u}^D + J_{f,q}^D. \tag{39} $$

4. Performance Analysis of Explicit and Implicit Flux Reconstruction

High-order methods exhibit a higher accuracy per computational Degree of Freedom (DoF) as compared to traditional low-order methods (up to second order). This has been proven for the present solver in [10; 11]. However, the computational time per DoF should be considered as well. Ideally this is constant for all orders or even decreases for higher orders. For explicit methods attaining this is feasible, however for

implicit methods, which make use of a Jacobian matrix, it is not. This is due to the Jacobian computation becoming more complex at higher orders. This can be seen from the analytical formula of the Jacobian presented in section 3.2. In one element, for each solution point k, the Jacobian with respect to each other solution point which influences it needs to be computed. This computation scales with $O(P^{N_{dim}+1})$ since the amount of solution points that influence a specific solution point scales with $O(P)$ in tensor elements and the amount of solution points scales with $O(P^{N_{dim}})$. However, when considering equation 28 for example, it is clear that the computation of one such Jacobian term scales with $O(P)$ whenever diffusive fluxes are present and the influence of the corrected gradient needs to be taken into account. As such the computational time for implicit methods using a Jacobian matrix can only scale with $O(P^2)$ at best per DoF, irrespective of the dimensionality of the problem to be solved.

To analyze the performance of the present solver, a hypersonic viscous test case is considered. More specifically the Mach 9.6 flow of nitrogen gas over a cone. The considered geometry consists of a 25° half-angle cone with a rounded nose of radius 0.5 mm. The total length of the cone in the x-direction considered is 9cm. The free stream values imposed are presented in table 1. This corresponds to Run 28 of the hypersonic flow experiments over a double cone, performed in the Large Energy National Shock (LENS) wind tunnel at the Calspan-University at Buffalo Research Center (CUBRC), presented in [12]. Relatively close agreement was found between the experimental results and several Finite Volume (FV) codes [1; 12; 13]. In the present paper only the first cone of the double cone is considered. Furthermore, the cone used in Run 28 is a sharp cone. To avoid numerical problems at the leading point of the cone, a small rounding of radius 0.5 mm is given.

Table 1: Free stream and wall values

M_∞ [−]	Re $[m^{-1}]$	p_∞ $[Pa]$	T_∞ $[K]$	T_{wall} $[K]$
9.59	140,000	36.08	185.6	293.3

The used mesh is presented in figure 5. The mesh consists of curved quadrilateral elements of second-order and contains 2000 elements: 80 along the cone and 25 in the direction normal to the cone. A zoom on the area of the mesh around the rounding of the cone is shown in figure 6. The inlet boundary is imposed as a Dirichlet boundary condition that sets the states to the free stream values. For the outlet, a supersonic outlet boundary condition is used. The cone is represented by an iso-thermal no-slip wall.

The FR method is used with a VCJH scheme for the correction functions. The distribution of both the solution and flux points is the Gauss-Legendre distribution. For the convective interface fluxes, the AUSM$^+$ scheme [14] is used. A Localized Laplacian Artificial Viscosity (LLAV) shock capturing scheme was used with the following parameters: $\kappa = 0.5$ and $S_0 = -5 \log_{10} P - 0.5$. The LLAV scheme is presented in detail in [11]. In order to simulate the flow over a cone on a 2D mesh, axisymmetric source terms are added to the Navier-Stokes equations.

The pressure contours for the fifth-order of accuracy solution are presented in figure 7a. Figure 7b shows the normalized artificial viscosity distribution for this case. It is clear that the LLAV method is only active in the shock area. Figure 8 shows the Stanton number for FR P0 up to P4 compared with the Stanton number obtained in [15] with a Discontinuous Galerkin (DG) solver for P3 and with the experimental results from [12]. Note that the Stanton number is computed as follows:

$$St = \frac{q_{wall}}{c_p \rho_\infty V_\infty (T_{t,\infty} - T_{wall})}, \tag{40}$$

where q_{wall} is the wall heat flux and $T_{t,\infty}$ the total free stream temperature.

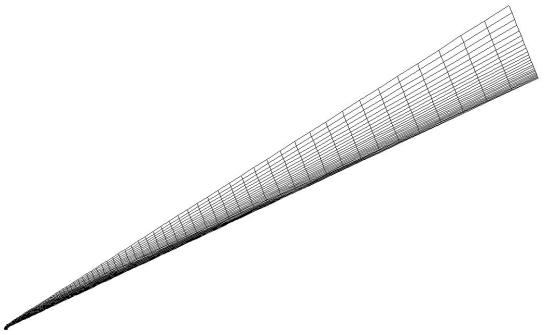

Figure 5: Mesh used for the hypersonic cone

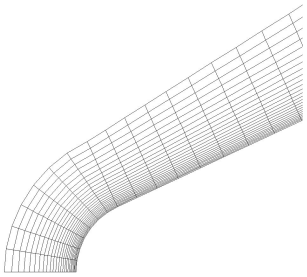

Figure 6: Zoom on the rounding of the cone

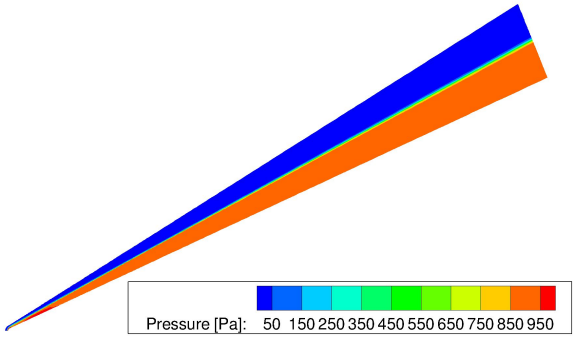

(a) Pressure

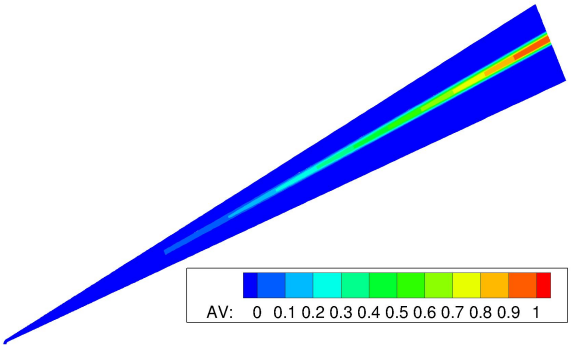

(b) Normalized artificial viscosity

Figure 7: Flow field of the hypersonic cone for P4

The performance of the solver is analyzed for this test case by running it on a single CPU core of an Intel Core i7 9700K Octa Core processor with a clock speed of 3.6 GHz and 16 GB of RAM. COOLFluiD can also be run on multiple CPU cores, more information on the parallel performance of COOLFluiD can be found in [1].

For the present explicit solver, figure 9 presents the walltime per DoF per iteration. The difference between the largest walltime (P9) and the smallest (P3) is a factor of 1.3. As such it can be concluded that the performance for explicit FR is approximately constant

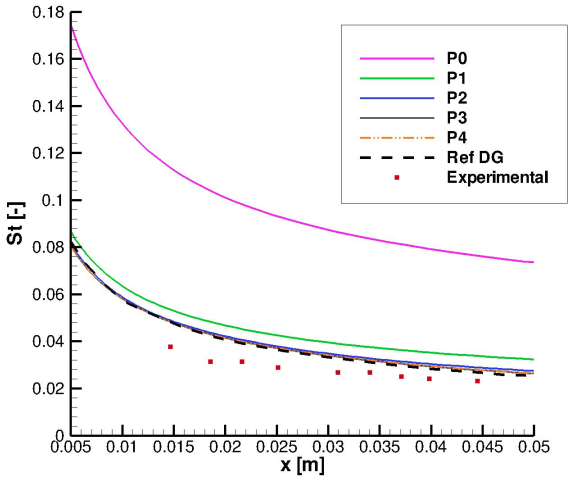

Figure 8: Stanton number for FR P0, P1, P2, P3 and P4, compared with DG P3 [15] and experimental data [12]

for the considered orders, even though there is a very slight increase towards the higher orders.

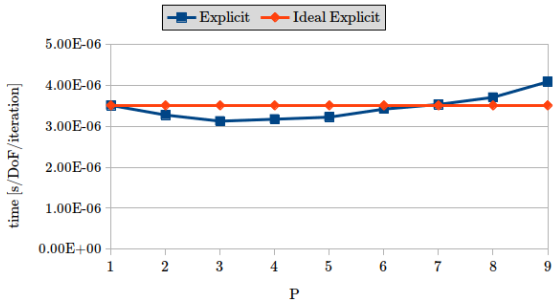

Figure 9: Walltime per DoF per iteration for explicit FR, including convective, diffusive and artificial viscosity fluxes, as a function of polynomial order

For implicit FR figure 10 presents the walltime per DoF per iteration for both a numerical and a semi-analytical Jacobian computation. In this walltime however, only the assembly of the linear system is considered, not solving the system. This is done by PETSc [16] using the GMRES algorithm. From this figure it is clear that a semi-analytical Jacobian scales much better with the order than a numerical one. However, the walltime is still not close to being constant for all orders. This is to be expected since as previously mentioned, the walltime per DoF for a semi-analytical or analytical Jacobian scales with $O(P^2)$ when diffusive fluxes are present and with $O(P)$

when only convective fluxes are present. From figure 11 it is clear that the scaling is better when only the convective fluxes are taken into account: the difference between the largest walltime (P9) and the smallest (P1) is a factor of 24 when taking all fluxes into account, while it is only 6.7 when only taking the convective fluxes into account.

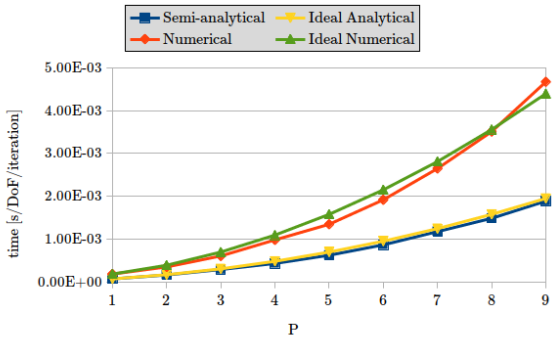

Figure 10: Walltime per DoF per iteration for implicit FR, including convective, diffusive and artificial viscosity fluxes, as a function of the polynomial order

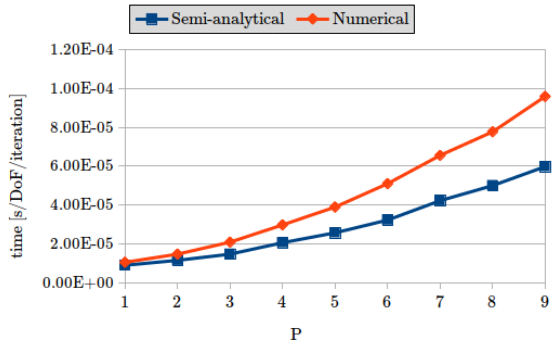

Figure 11: Walltime per DoF per iteration for implicit FR, including only convective fluxes, as a function of the polynomial order

5. Extension to GPU

The COOLFluiD platform has already been partially ported to GPUs. More specifically the FV solver for Multi-Fluid Magnetohydrodynamics is GPU-enabled. The extension to GPUs of this part of COOLFluiD is detailed in [17]. The present paper presents the extension of the explicit FR solver to GPUs. More specifically, the assembly of the residuals resulting from the FR algorithm is ported to GPUs using the NVIDIA CUDA language. The time stepper algorithm is performed on CPU.

Since CUDA does not support virtual functions, a part of the modularity of COOLFluiD has to be sacrificed when porting to GPUs. For instance the FR algorithm has to be hard coded for all different convective and diffusive flux schemes. For now, Lax-Friedrichs-Local Approach has been implemented. Furthermore, the transfer of data between the CPU and GPU and vice versa is costly, as such all the needed information should be communicated to the GPU before computing the residuals and no data transfer between CPU and GPU should occur during the residual computation. As a consequence, the GPU requires a sort of mini-data structure that contains all the information needed. Thus the first step of the FR algorithm is to transfer the needed data to the GPU. All the data is transferred in the form of arrays, which contain the following information:

1. Residual array,
2. State array,
3. Characteristic speed array for computation of time step,
4. Gradient array,
5. Array containing the normal vectors in solution and flux points,
6. Array containing the element geometrical Jacobian determinants,
7. Array containing all information related to the physics (physical constants, dimensionality, reference values, etc.),
8. Array containing all the geometrical element information defined in the standard domain (solution point - flux point - face connectivity, base function polynomial values and derivative values).

Item 1 through 4 need to transferred to the GPU before each iteration. The GPU will then fill those arrays after which they are transferred back to the CPU that will perform the time marching algorithm. All other items are transferred to the GPU before the start of the simulation and do not need to be transferred again at each iteration as this information remains unchanged during the simulation.

Next, the actual residual computation is performed. This consists of two kernels. One kernel computes the corrected gradients. The second kernel uses the corrected gradients and states to compute the flux divergence. Both kernels follow the procedure presented in section 2. Two possibilities to define the two kernels have been investigated: an element-local approach and a solution point-local approach.

Element-Local Approach. The kernels are defined in such a way that one thread is linked to one element. This is done for two reasons: it makes the implementation more straightforward since all computations can be done element-local, and it avoids doing the same computation multiple times. The efficiency of this approach can be expected to drop at higher orders since more computations need to be done per thread as the number of solution points increases. However, section 6 proofs that also at high orders substantial speedups are attained.

Solution Point-Local Approach. This approach links one thread to one solution point and exploits the shared data feature of CUDA to easily transfer information between threads linked to solution points in the same element. Since the amount of computations performed by one thread now remains approximately constant at all orders, the scaling should improve. However this approach has the disadvantage that all threads of one element need to be in the same block in order to use shared data. Considering the limited shared data size and the number of solution points per element, it is generally not possible to define a block size which is a multiple of the warp size (32). Consequently there will always be threads in the warp which are not doing any useful computations. This decreases computational efficiency substantially and causes the solution point-local approach to be outperformed by the element-local approach as demonstrated in section 6.

6. Performance Analysis of the GPU-Enabled Solver

Since the shock capturing algorithm has not yet been ported to GPUs, a subsonic viscous test case is considered to assess the performance of the GPU-enabled FR solver. More specifically, a Mach 0.15 flow over a cylinder with a Reynolds number of 40 is considered. Furthermore a Prandtl number of 0.72 is considered. In this regime, a steady laminar flow with two stable vortices behind the cylinder is expected.

The cylinder has a diameter D and is considered as an adiabatic no-slip wall. The computational domain is equal to $[-20D, 20D] \times [-20D, 20D]$. The outer circle that limits the computational domain is associated with a far field boundary condition.The present test case is similar to the test case used to verify the SD solver in [18] and the FR solver in [19]. The used mesh contains 4096 elements: 128 on the cylinder and 32 in the normal direction. Figure 12 shows a zoom around the cylinder of the mesh. The Mach contours of the solution for P3 are shown in figure 13. Streamtraces are plotted as well to visualize the re-circulation zones. This case was run on the Genius cluster of

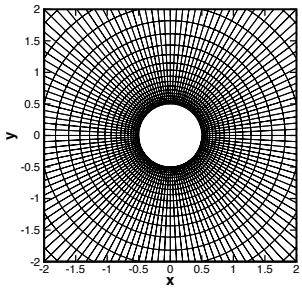

Figure 12: Mesh used for the subsonic cylinder case

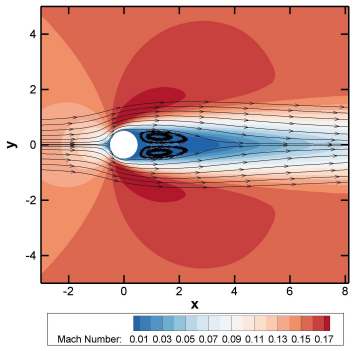

Figure 13: Mach contours for P3

the Vlaams Supercomputer Centrum. It was run using a single NVIDIA V100 SXM2 GPU and on a single Xeon 6140 CPU core of a Sky Lake node of the Genius cluster. The considered speedup is computed as follows:

$$Sp = \frac{t_{CPU}}{t_{GPU}}, \tag{41}$$

where t_{CPU} is the walltime for the case run on a CPU core and t_{GPU} the walltime when run on a GPU.

Figure 14 shows the speedup of the FR algorithm for orders ranging from P0 to P9. The largest speedup is attained at P0 and amounts to 106. The smallest speedup is attained at P9 and constitutes 65.3. However, it should be noted that for orders higher than P4 the speedup remains approximately constant. As expected, the performance declines as the order increases due to the element-local approach of the GPU-enabled FR algorithm. Furthermore, it should be noted that for this speedup only the FR algorithm itself is taken into account. The speedup of the total simulation (including the time stepping algorithm which is done on the CPU) is shown in figure 15. Due

to the necessity of returning to the CPU at each iteration to perform the time integration, the performance decreases significantly, as the maximum speedup is now only 24.7. This could be resolved by performing the time marching algorithm on the GPU as well. For implicit methods solving the linear system within the time marching method is performed on GPUs. Furthermore, for implicit methods solving the linear system as well as the Jacobian assembly are more computationally intensive than other time marching computations. As such, this problem is expected to disappear for a GPU-enabled implicit FR solver.

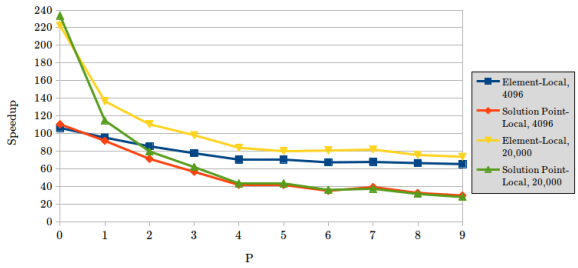

Figure 14: Speedup of the FR algorithm

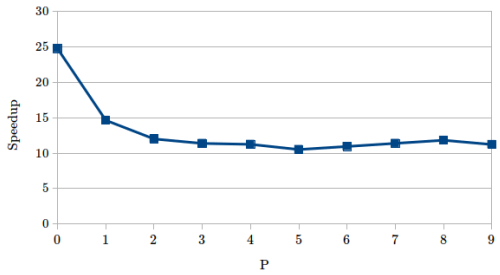

Figure 15: Speedup of the complete solver algorithm for the element-local approach

7. Conclusion

The performance of a high-order FE-type FR solver was substantially improved by implementing an analytical Jacobian computation of the implicit FR method as well as by extending the FR solver to GPUs. The performance of the implicit FR solver with both a numerical and analytical Jacobian was analyzed in detail for a hypersonic case with an application to heat flux prediction. Also the performance of the GPU-enabled solver was analyzed, considering a subsonic case. As future work, the implicit FR solver including the shock capturing scheme will be ported to GPUs and its performance will be investigated. Furthermore, a RANS local correlation-based transition model will be added to the solver to tackle more complex problems where laminar-turbulent transition is present. Finally, the solver will be applied to more complex 3D problems such as the IXV and Hexafly-INT hypersonic vehicles.

Acknowledgments

The research of Ray Vandenhoeck is supported by SB PhD fellowship 1S19918N of the FWO.

References

[1] A. Lani, An object oriented and high performance platform for aerothermodynamics simulation, Ph.D. thesis, Université Libre de Bruxelles (2008).

[2] T. Quintino, A component environment for high-performance scientific computing: design and implementation, Ph.D. thesis, Ph. D. Thesis, KU Leuven, von Karman Institute for Fluid Dynamics, Leuven (2008).

[3] H. Huynh, A flux reconstruction approach to high-order schemes including discontinuous galerkin methods, AIAA paper 4079 (2007) 2007.

[4] H. T. Huynh, A reconstruction approach to high-order schemes including discontinuous galerkin for diffusion, AIAA paper 403 (2009) 2009.

[5] H. Huynh, High-order methods including discontinuous galerkin by reconstructions on triangular meshes, AIAA Paper 44 (2011) 2011.

[6] F. Bassi, S. Rebay, A high-order accurate discontinuous finite element method for the numerical solution of the compressible navier–stokes equations, Journal of computational physics 131 (2) (1997) 267–279.

[7] P. E. Vincent, P. Castonguay, A. Jameson, A new class of high-order energy stable flux reconstruction schemes, Journal of Scientific Computing 47 (1) (2011) 50–72.

[8] P. L. Roe, Approximate riemann solvers, parameter vectors, and difference schemes, Journal of computational physics 43 (2) (1981) 357–372.

[9] Y. Saad, M. H. Schultz, GMRES: A generalized minimal residual algorithm for solving nonsymmetric linear systems, SIAM Journal on scientific and statistical computing 7 (3) (1986) 856–869.

[10] R. Vandenhoeck, A. Lani, Implicit high-order flux reconstruction positivity preserving LLAV scheme for viscous high-speed flows, in: AIAA Scitech 2019 Forum, 2019, p. 1153.

[11] R. Vandenhoeck, A. Lani, Implicit high-order flux reconstruction solver for high-speed compressible flows, Computer Physics Communications-doi:https://doi.org/10.1016/j.cpc.2019.04.015.

[12] J. Harvey, M. Holden, T. Wadhams, Code validation study of laminar shock-boundary layer and shock-shock interactions in hypersonic flow part b: Comparison with navier-stokes and DSMC solutions, in: 39th Aerospace Sciences Meeting and Exhibit, 2001, p. 1031.

[13] G. Candler, I. Nompelis, M.-C. Druguet, M. Holden, T. Wadhams, I. Boyd, W.-L. Wang, CFD validation for hypersonic flight-hypersonic double-cone flow simulations, in: 40th AIAA Aerospace Sciences Meeting & Exhibit, 2002, p. 581.

[14] M.-S. Liou, A sequel to ausm: Ausm+, Journal of computational Physics 129 (2) (1996) 364–382.

[15] E. J. Ching, Y. Lv, P. Gnoffo, M. Barnhardt, M. Ihme, Shock capturing for discontinuous galerkin methods with application to predicting heat transfer in hypersonic flows, Journal of Computational Physics 376 (2019) 54–75.

[16] S. Balay, S. Abhyankar, M. F. Adams, J. Brown, P. Brune, K. Buschelman, L. Dalcin, A. Dener, V. Eijkhout, W. D. Gropp, D. Karpeyev, D. Kaushik, M. G. Knepley, D. A. May, L. C. McInnes, R. T. Mills, T. Munson, K. Rupp, P. Sanan, B. F. Smith, S. Zampini, H. Zhang, H. Zhang, PETSc Web page, `https://www.mcs.anl.gov/petsc` (2019).

[17] I. A. Asensio, A. A. Laguna, M. H. Aissa, S. Poedts, N. Ozak, A. Lani, A GPU-enabled implicit finite volume solver for the ideal two-fluid plasma model on unstructured grids, Computer Physics Communications 239 (2019) 16–32.

[18] K. Van den Abeele, Development of high-order accurate schemes for unstructured grids, Phd thesis in Vrije Universiteit Brussel.

[19] P. Castonguay, D. M. Williams, P. E. Vincent, M. Lopez, A. Jameson, On the development of a high-order, multi-GPU enabled, compressible viscous flow solver for mixed unstructured grids, AIAA paper 3229 (2011) 2011.

R-adaptive mesh agorithms with high-order flux reconstruction scheme for simulating high-speed flows with uncertainties

Firas Ben Ameur

Aeronautics and Aerospace Department, von Karman Institute for Fluid Dynamics, Belgium, firas.benameur@vki.ac.be

Supervisor: Georg May

Associate Professor, Aeronautics and Aerospace Department, von Karman Institute for Fluid Dynamics, Belgium, georg.may@vki.ac.be

Advisor: Andrea Lani

Research Expert, Aeronautics and Aerospace Department, von Karman Institute for Fluid Dynamics, Belgium, lani@vki.ac.be

University Supervisor: Stefaan Poedts

Professor, Centre for mathematical Plasma-Astrophysics, KU Leuven, Belgium, stefaan.poedts@kuleuven.be

Abstract

The present paper addresses the development and the implementation of two different numerical tools, mainly, the first r-adaptive mesh refinement within the Flux Reconstruction (FR) solver and an Uncertainty Quantification (UQ) toolkit within the open source platform COOLFLuiD.
The r-refinement consists on nodal re-positioning while keeping their number and connectivity constants. The developed Adaptive Mesh Refinement (AMR) is based on physics-driven spring-analogies, where the mesh can be seen as a network of factious springs. While AMR increases the local mesh density, the high-order Flux Reconstruction method potentially provides a more accurate detection of complex flow features over relatively coarser mesh resolution, compared to low-order methods, which can result in considerably more efficient mesh generation process and run-time for high-speed re-entry flows.
Moreover, the Multi-Level Monte Carlo (MLMC) methods used for UQ will construct levels using p-refinement instead of h-refinement, therefore requiring, ideally, just one initial coarse mesh which will undergo polynomial upgrade (from 2nd up to ideally 10th order) for obtaining finer levels. This approach should improve the overall computational efficiency of our UQ analysis.
In this work, a concise overview of the Flux Reconstruction method, mesh adaptation and MLMC techniques will be given, followed by some promising results of the physics-based r-refinement and uncertainty quantification.

Keywords: High-Order CFD, Hypersonics, Flux Reconstruction, R-refinement, Uncertainty Quantification, Multi-Level Monte Carlo

1. Introduction

The number and complexity of mathematical models used virtually in all areas of science and engineering, to boost our understanding of the real world, is continually increasing. Similarly, the wide variety of the parameters controlling these models is expanding. Uncertainty affects almost all of these parameters. A rigorous quantification of these uncertain parameters is mandatory to define confidence intervals when analyzing the model output, where the outcome of the uncertainty quantification will be used to make engineering decisions. State-of-the-art UQ distinguishes between intrusive and non-intrusive approaches.
Intrusive methods involve the formulation of a stochastic version of the original model (i.e. implying deep modifications in the deterministic CFD codes). These methods decompose and provide, respectively, the uncertain variables and the outputs, i.e. Quantities of Interest (QoI), as basis of complete orthogo-

nal polynomials. The Galerkin polynomial chaos is the most well-known intrusive approach[1]. Yet, the implementation of an intrusive method within flow solvers is very demanding and the methods themselves are not well established for complex applications.

Non-intrusive methods treat the deterministic solver as a black-box and simply require a set of simulations for different realizations of the uncertain parameters. We distinguish between polynomial/collocation and Monte Carlo (MC) approaches [2]. The formers are efficient for smooth response and moderate number of uncertain parameters, but they lack efficiency for problems whose solutions exhibit sharp gradients and shocks (e.g. Euler and Navier-Stokes equations). (MC)-type methods overcome such deficits, being therefore preferred in his work.

This work will focuses on MC-type Forward non-intrusive methods, allowing the propagation different sources of uncertainties through a typically large number of simulations to study their effects and obtain numerical data defining the dispersity of the monitored quantities of interests. Since the classic MC method suffers from the *curse of dimension*, multi-level sampling method fortunately exists. Several instances of the multi-level methods will make UQ simulations, involving a large number of the uncertain input parameters and complex, large-scale and high-dimensional systems of partial differential equations (PDEs), affordable to solve [3; 2; 4; 5].

The vast majority of state-of-the-art Computational Fluid Dynamic (CFD) codes tackling hypersonic applications rely upon low-order solvers, categorized into Finite Volume (FV), Finite Difference (FD) and Finite Element (FE) schemes, that are robust and easy to implement. Unfortunately, achieving an accurate heat flux prediction is still a challenge even on simple geometries, leading to an unoptimized design of the space vehicle shield, i.e. Thermal Protection System (TPS) . CFD analysts acknowledge the importance of using well-designed grids to obtain accurate flow results, since mesh/shock misalignment leads to shock instability, noisy post-shock regions and poor heat flux predictions [6; 7]. State-of-the-art ATD simulations require demanding mesh generation processes and grid convergence studies resulting in a high run-time and considerable computational effort. All this makes numerical analysis more challenging and time-consuming especially for those kind of applications where high-grid density are needed, close to the space vehicle walls, in order to resolve boundary layer features and obtain accurate numerical heat fluxes [8; 9; 10]. To overcome those deficiencies, Adaptive Mesh Refinement (AMR) represent, on one hand, a robust procedure for improving the quality of the physical results, especially heat flux prediction, due to a local increase of the grid resolution and mesh/shock alignment, at the price of an increased algorithmic complexity. On the other hand, high-order methods have drawn considerable attention among researchers in the field of Computational Fluid Dynamics (CFD) due to their increased computational efficiency per degree of freedom" over their low-order counterparts [11].

In our previous work [12], a robust and efficient r-refinement algorithm (i.e. repositioning of mesh points based on the solution of a pseudo-elastic system of equations) has been developed and already applied to multiple Finite Volume test cases. The existing FV-AMR algorithm works on triangles, quadrilateral, tetrahedral and hexahedral cells, is fully parallel, implemented as a standalone module and totally physics-independent, letting the user decide which monitor physical quantity to use for driving the adaptation according to the application.

In addition, in [13; 14; 15], a state-of-the-art parallel and fully implicit high-order Flux Reconstruction (FR) code has been implemented and used to solve Euler/Navier- Stokes equations, where its structure is extremely modular and can be easily coupled to arbitrary sets of advection-diffusion-reaction PDEs.

Besides, the UQ Julia package Multilevel Estimators[1] is developed in [16] to carry on forward non-intrusive MC-type simulations of PDEs using multi-level sampling methods.

In this work, we propose first the development of AMR algorithms within the FR framework as well as the applicability of the r-refinement to multiple high-order test cases. This novel coupling will benefit from a low initial mesh resolution, increasing the order of the solution (i.e. p-refinement), shock/mesh alignment to avoid a smearing of the flow, leading to a non-physical distribution of the entropy between streamlines and finally, increasing the grid density around the shock in order to overcome the reduced order order of accuracy in the shock area (i.e. the shock is contained in a more confined space). The resulting solver has been implemented into the COOLFluiD platform[2] [17; 18] (a world-class open source framework for multi-physics modeling and simulations, particularly of hypersonic flows, radiation, laboratory and space

[1] https://github.com/PieterjanRobbe/MultilevelEstimators.jl

[2] https://github.com/andrealani/COOLFluiD/wiki

plasmas.)
As a second part of the work, the MultilevelEstimators package is coupled to the COOLFLuiD FR solver for evaluating the effect of different kind of uncertainties on the selected hypersonic testcases. The statistics of our QoI will be computed based on variance reduction using control variates and a coarse-to-fine hierarchy of models with different levels of accuracy, which will be constructed by means of p-refinement (i.e. upgrade of solution polynomial order) instead of h-refinement.

2. The Flux Reconstruction Solver– A Concise Overview:

The FR method was originally developed by Huynh in [19]. It is a compact high-order FE-type method that offers a unifying formulation for various classes of high-order schemes (e.g. nodal Discontinuous Galerkin, Spectral Finite Difference). The formulation of the FR approach proposed by Huynh is applicable to deal with advection-diffusion problems on structured and structured grids [20].
This section presents a brief review of the Flux Reconstruction method in one dimension, including the following main algorithmic steps [13; 14; 15]:

1. Consider solving the one-dimensional advection-diffusion problem within an arbitrary domain Ω, given by:
$$\frac{\partial u}{\partial t} + \frac{\partial f}{\partial x} = 0. \tag{1}$$
In Eq.1, $x \in \Omega = [x_L, x_R]$ is the one dimensional coordinate, t is the time variable, $u(x,t)$ is the conservative variable, and $f = f\left(u, \frac{\partial u}{\partial x}\right)$ is the flux which is a scalar for the 1D case. As the FR method is classified as a FE-type method, the first step of the procedure involves partitioning the spatial domain Ω into a finite number N of non-overlapping, non-empty, open sub-domains Ω'_n such that:
$$\Omega'_n = \{x \mid x_n < x < x_{n+1}\}, \tag{2}$$
where, $x_1 = x_L$ and $x_{N+1} = x_R$
2. The exact solution u of the conservation law 1 is approximated by a continuous function u_n^δ within each element Ω_n. This function u_n^δ corresponds to a polynomial of degree P within Ω_n and is identically zero on $\Omega \setminus \Omega_n$, while being generally discontinuous across elements. The approximate solution polynomial u^δ within the entire domain Ω is constructed as:
$$u^\delta = \sum_1^N u_n^\delta \tag{3}$$
In the same manner, the exact flux f is approximated by a polynomial of degree $P+1$ within each sub-domain Ω_n.
3. Each element Ω_n together with the approximate solution u_n^δ and flux f_n^δ inside, is transformed to a standard reference element $\Omega_S = \{\xi \mid -1 \le \xi \le 1\}$, where all computations are performed. The solution u_n^δ within each sub-domain Ω_n can then be obtained by solving the transformed conservation equation (Eq.1) within the reference element Ω_S:
$$\frac{\partial \hat{u}^\delta}{\partial t} + \frac{\partial \hat{f}^\delta}{\partial \xi} = 0 \quad \text{with} \quad \xi \in \Omega_S, \tag{4}$$
where=
   - $\hat{u}^\delta = \hat{u}^\delta(\xi, t) = J_n u_n^\delta(\Theta_n(\xi), t)$,
   - $\hat{f}^\delta = \hat{f}^\delta(\xi, t) = f_n^\delta(\Theta_n(\xi), t)$,
   - J_n represents the Jacobian of the mapping $\Theta_n(\xi)$.
4. The approximate solution $\hat{u}^\delta$ is defined as a degree P polynomial based on a Lagrange polynomial basis related to the set of $P+1$ distinct solution points ξ_i within Ω_S, where the two endpoints of the standard element Ω_S, i.e. $\xi = -1$ and $\xi = 1$, are referred to as the flux points.
5. This step consists of determining a common interface solution $\hat{u}^{\delta I}$ at the boundaries of the standard element Ω_S, i.e. $\xi = \pm 1$, where the flux points of two neighboring elements coincide.
$$u^{\delta I} = \frac{u^{\delta -} + u^{\delta +}}{2} \tag{5}$$
where $u^{\delta -}$ and $u^{\delta +}$ are respectively the approximate solutions evaluated at the left and right boundaries.
6. A corrected solution gradient $\hat{q}^\delta$ is computed. $\hat{q}^\delta$ is defined based on two correction functions $g_L(\xi)$ and $g_R(\xi)$ of degree $P+1$ and satisfy the following boundary conditions: [21]
$$\begin{aligned} g_L(-1) &= 1, \qquad g_R(-1) = 0 \\ g_L(1) &= 0, \qquad g_R(1) = 1. \end{aligned} \tag{6}$$
Furthermore, the correction function for the right boundary $g_R(\xi)$ is defined as the reflection of the

correction function $g_L(\xi)$ with respect to the vertical axis in order to ensure symmetry of the correction process $g_L(\xi) = g_R(-\xi)$.
The corrected solution gradient $\hat{q}^\delta$ is then computed via the following expression:

$$\hat{q}^\delta = \frac{\partial \hat{u}^\delta}{\partial \xi} + (\hat{u}_L^{\delta I} - \hat{u}_L^\delta)\frac{dg_L}{d\xi} + (\hat{u}_R^{\delta I} - \hat{u}_R^\delta)\frac{dg_R}{d\xi}, \quad (7)$$

where $\hat{u}_L^{\delta I}$ and $\hat{u}_R^{\delta I}$ are the common interface solutions at the left and right boundaries of Ω_S, and $\hat{u}_R^\delta = \hat{u}^\delta(1)$ and $\hat{u}_L^\delta = \hat{u}^\delta(-1)$ are the values of the approximate solution polynomial at the left and right boundaries. The Vincent-Castonguay-Jameson-Huynh (VCJH) scheme, in [22], is used to define the exact polynomial expression of g_L and g_R.

7. On the reference element Ω_S, the approximate discontinuous flux $\hat{f}^{\delta D}(\xi)$ is calculated. Based on $\hat{u}^\delta$ and $\hat{q}^\delta$, the approximate discontinuous flux $\hat{f}^{\delta D}$ is constructed as a polynomial of degree P in the same manner as the approximate solution $\hat{u}^\delta$.
8. The transformed common interface fluxes $\hat{f}^{\delta I}$ at the flux points of the standard element Ω_S, i.e. $\xi = \pm 1$, is calculated. $\hat{f}_L^{\delta I}$ and $\hat{f}_R^{\delta I}$ are denoted as the common interface flux at the left and right end of the standard element, respectively. In the case of the Navier-Stokes equations, it is computed as the sum of a convective and a diffusive term. More details can be found in [14; 15]
9. The flux must be continuous across element boundaries in order to obtain a conservative scheme. Therefore, a correction flux function $\hat{f}^{\delta C}$ is added to the approximate discontinuous flux $\hat{f}^{\delta D}$ in order to obtain a continuous flux $\hat{f}^\delta$. The correction flux $\hat{f}^{\delta C}$ is a polynomial of degree $P + 1$ defined as:

$$\hat{f}^{\delta C} = (\hat{f}_L^{\delta I} - \hat{f}_L^{\delta D})h_L(\xi) + (\hat{f}_R^{\delta I} - \hat{f}_R^{\delta D})h_R(\xi), \quad (8)$$

where $\hat{f}_L^{\delta D} = \hat{f}^{\delta D}(-1)$ and $\hat{f}_R^{\delta D} = \hat{f}^{\delta D}(1)$ are the values of the approximate discontinuous flux at the left and right boundaries. The continuous flux $\hat{f}^\delta$ within the standard element Ω_S is then written as the sum of the approximated discontinuous flux and the correction flux.
10. The divergence of the total flux $\hat{f}^\delta$ at each solution point ξ_i is computed. This step is relatively straightforward as the derivatives of both the Lagrange polynomials and correction functions are exactly known.
11. Finally, a time marching strategy is applied to advance the approximate solution $\hat{u}^\delta$ in time using the following expression:

$$\frac{d\hat{u}_i^\delta}{dt} = -\frac{\partial \hat{f}^\delta}{\partial \xi}(\xi_i). \quad (9)$$

The extension of the 1D philosophy of the FR method to deal with 2D quadrilateral and 3D hexahedral elements is straightforward. To this end, a tensor product basis is defined based on the one-dimensional Lagrange polynomials on the reference element, as shown in [19].
Since the FR method can obtain arbitrary high orders of accuracy simply by increasing the order of the polynomials that represent the approximated solution, the method is inherently compact and doesn't require a wide stencil at higher orders. This facts goes hand to hand with r-refinement since r-refinement also requires only compact stencils.

3. Spring-Based Adaptive Mesh Refinement

The numerical investigation of high-speed flow problems may require extremely fine meshes over narrow regions of the physical domain to resolve the steep gradients occurring in the flow. The high-gradient regions are not known to the analyst a priori. Thus, a-posteriori AMR techniques represent a robust procedure to better capture the relevant flow features, to improve the quality of the physical results and to ensure, for e.g., the alignment of the computational grid cells with the flow discontinuities at the price of an increased algorithmic complexity.
In [12], the authors have proposed and developed, within a Finite Volume framework, a physics-based r-refinement adaptation algorithm based on a user-defined flow field variable, e.g. density or pressure, that relies upon the solution of pseudo-elastic systems associated to the given mesh.

3.1. Problem Statement

This section presents a brief review of the r-refinement method that can be found in [12].

Let $n \in \mathbb{N}$ be the number of the nodes in a mesh $\mathcal{M}$ and let $\mathbf{P}$ the set of the node's positions inside $\mathcal{M}$. The incidence matrix $\mathbf{L}$ is defined as:

$$L_{ij} = \begin{cases} 1, & \text{if nodes } i \text{ and } j \text{ are edge-connected} \\ 0, & \text{otherwise.} \end{cases}$$

We want to equidistribute the mesh nodes according

to a positive scalar function $W = W(x)$. For the 1D case, between node positions x_i and x_{i+1} we have,

$$\int_{x_i}^{x_{i+1}} W(x)dx = constant. \tag{10}$$

For the multidimensional case, let $\{\mathbf{P_i},\mathbf{P_j}\}$ be a set of two node's positions such that $L_{ij} = 1$, and let $\mathbf{r}(s)$ be the edge parametrization obeying to the Eq.11

$$\mathbf{r}(s) = \mathbf{P_i} + s(\mathbf{P_j} - \mathbf{P_i}) \tag{11}$$

Then, in order to equidistribute the mesh nodes, the line integral I, expressed in Eq.12, must be constant.

$$I = \int_0^1 W(\mathbf{r}(s)) \cdot r'(s)ds = C^t \tag{12}$$

The Eq.12 is the solution of the Euler-Lagrange equation to the minimization of the energy equation (13).

$$E_{ij} = L_{ij} \int_0^1 W(\mathbf{r}(s))(\mathbf{P_j} - \mathbf{P_i})^2 ds \tag{13}$$

Where, the incidence matrix $\mathbf{L}$ is artificially added ensuring the physical meaning of the energy function E. The weight function W is considered constant between two edge-connected nodes, such that $W = W_{ij}$. Hence, the energy equation can be simplified into Eq.14

$$E_{ij} = L_{ij}W_{ij}(\mathbf{P_j} - \mathbf{P_i})^2 \tag{14}$$

Eq.14 is analogous to the spring potential energy equation with a stiffness coefficient W and equilibrium spring length set to zero. The optimization process of the nodes mesh positions is formulated through the assembly and solution of a linear system, including the following main algorithmic steps:

1. The analytic Jacobian is defined as:

$$\frac{\partial E_{ij}}{\partial \mathbf{P_i}} = -2L_{ij}W_{ij}(\mathbf{P_j} - \mathbf{P_i}) = 0. \tag{15}$$

2. After simplifying the constant and collecting the contributions of each node, we obtain:

$$\sum_{j=1}^{n} L_{ij}W_{ij}(\mathbf{P_j} - \mathbf{P_i}) = 0. \tag{16}$$

3. The resulting linear system, to be solved, can be expressed as:

$$\mathbf{AP} = \mathbf{b}, \tag{17}$$

where

$$A_{ij} = \begin{cases} -L_{ij}W_{ij}, & if\ i \neq j \\ \sum_{j=1}^{n} L_{ij}W_{ij}, & if\ i = j. \end{cases}$$

and $\mathbf{b}$ contains the non-homogeneous terms of the Dirichlet or the Neumann boundary conditions.

4. Solving the linear system using an iterative solver, i.e. the Generalized Minimal RESidual (GMRES) algorithm complemented by a parallel Additive Schwartz Preconditioner as provided by the PETSc toolkit [23; 24; 25; 26].

As a result, the nodal re-positioning obeys to the following relation:

$$\mathbf{P}^{k+m} = (1 - \omega)\mathbf{P}^k + \omega\mathbf{P}_{new}, \tag{18}$$

where $\mathbf{P}^k$ is the old node position at iteration k, $\mathbf{P}^{k+m}$ is the new *relaxed* node position at iteration $k + m$ and $\mathbf{P}_{new}$ is computed from Eq.17. An under-relaxation factor ω is also added to the nodal re-positioning equation in such to smooth the nodal displacement and to mitigate, for certain cases, the cells overlap. However, ω affects negatively the convergence rate, a trade-off between the flow solver convergence and the pseudo-elastic convergence rate was sought and found in ω $=O(10^{-2})$.

3.2. Numerical formulation of the spring network

Linear spring analogy

The linear spring analogy is based on the selected flow variables gradients. Eq.19 expresses the linear spring stiffness coefficient, k_{ij}^L, between two edge-connected nodes i and j with a respective nodal state U_i and U_j. The weight function introduced in the previous section is described as:

$$W_{ij} = k_{ij}^L = |U_j - U_i|. \tag{19}$$

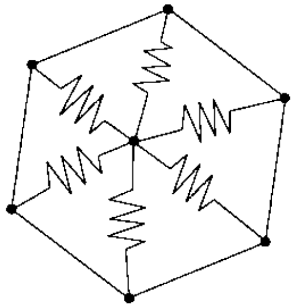

Figure 1: Linear spring analogy, a network of fictitious spring [27]

During the simulation of high-speed flows containing strong shocks, the r-refinement creates highly distorted cells due to the large node displacements and high physical gradients. Therefore, the linear spring coefficient needs to be truncated and bounded. The choice of the upper and lower bound values, referred respectively as the minimum percentile and the maximum percentile, are computed though a P^2 algorithm [28].
In order to evaluate the nodal states, the Pth-order polynomial describing the approximated solution is evaluated at the considered node coordinates as shown in Fig.2. To this end, the nodal state at a node i is evaluated as the average of the contributions of each solution polynomial inside all elements attached to the considered node i

$$U_i = \frac{1}{N} \sum_{n=1}^{N} \hat{u}_n^{\delta}(\boldsymbol{x_i}) \tag{20}$$

where $\hat{u}_n^{\delta}$ is the approximated solution polynomial within the elements n, $\boldsymbol{x_i}$ is the vector of the coordinates of the node i and N represents the number of elements attached to the node i.

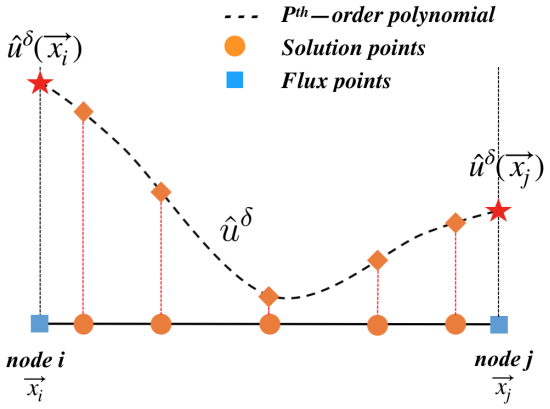

Figure 2: Evaluation of the nodal states

3.3. Preliminary Results

Preliminary results are obtained for the steady wedge channel flow. The test case conditions are presented in Tab.1, Tab.2 and Tab.3, while the test case definition and the corresponding unstructured mesh are shown in Fig.3 and Fig.4 respectively.

Table 1: Wedge – Flow characteristics

Physical Model	M	ρ [-]	ρu [-]	ρv [-]	ρE [-]
Perfect gas	2	1	2.36643	0	5.3

Table 2: Wedge – Mesh characteristics

Dimensions	Type	# Elements	
2D	Quadrilateral	3710	
BC 1	BC 2	BC 3	BC 4
Inlet	Outlet	Symmetry	no-slip wall

Table 3: Wedge – r-refinement

Spring Network	Monitor Variable	Process Rate
Linear	Density	20
Stop AMR Iteration	minPer	maxPer
7000	0.30	0.55

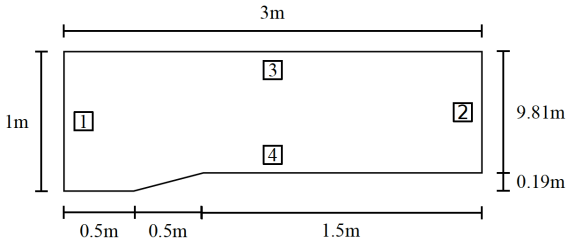

Figure 3: 2D wedge geometry

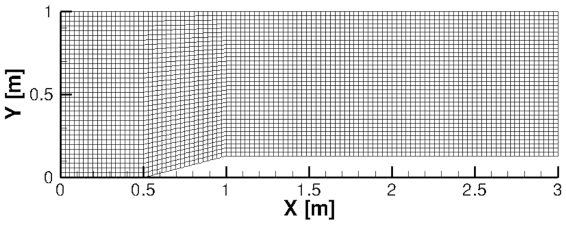

Figure 4: 2D wedge – Initial mesh

As shown in Fig.5 and Fig.6, in the final adapted solution, the oblique shock, the expansion wave and their reflections are perfectly resolved for different order, mainly $P1$ (i.e. second order of accuracy in space) and $P3$ (i.e. fourth order of accuracy in space). The best accuracy is obtained by combining the AMR algorithms and the FR solver, as demonstrated by the $P3$ adapted wedge test case (Fig.11) compared to the $P3$ non-adapted case (i.e. Fig.10).
Note: We want to draw the attention of the reader to the fact that these results are preliminary and more work need to be carried out to reach the desired accuracy of the FR-AMR solution.

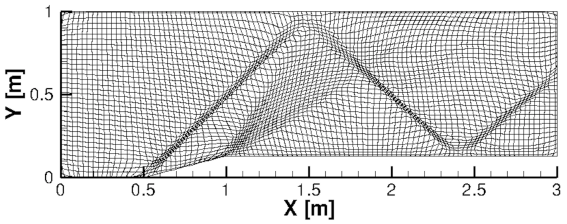

Figure 5: P1 Adapted Mesh

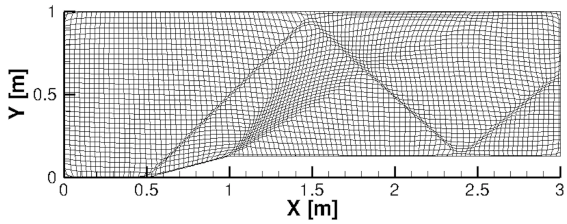

Figure 6: P3 Adapted Mesh

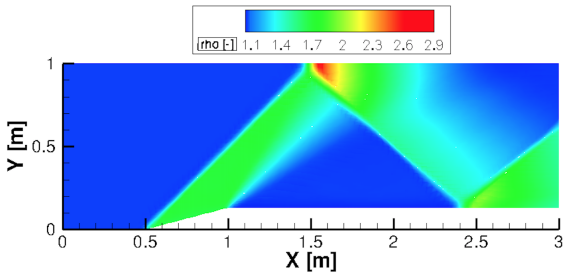

Figure 7: P1 Converged adaptive density fields

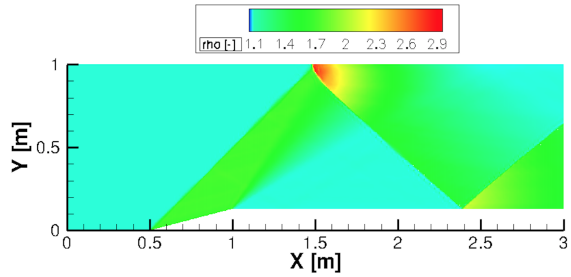

Figure 8: P3 Converged adaptive density fields

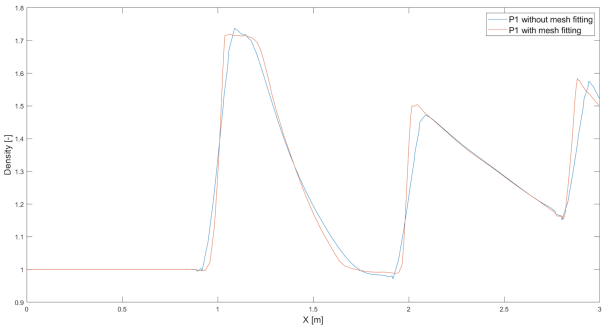

Figure 9: Density solution at a line section $Y = 0.5[m]$

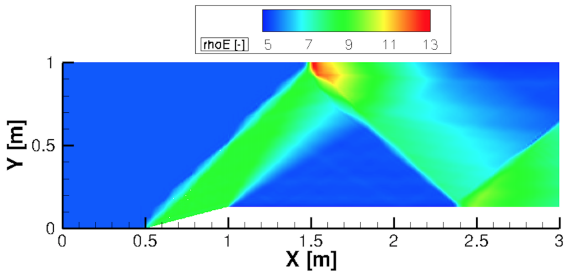

Figure 10: P3 Converged non-adaptive energy fields

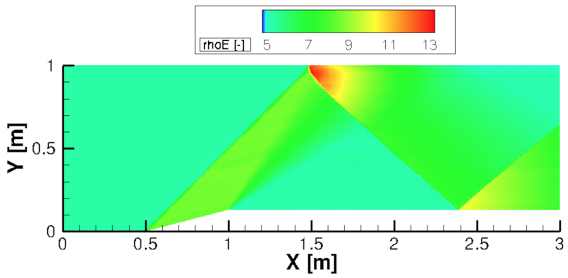

Figure 11: P3 Converged adaptive energy fields

4. Multi-Level Monte Carlo

4.1. Overview

Forward non-intrusive UQ problems consist of propagating uncertainties characterized as random variables into a computational model to quantify the output quantities of interest and study their effects based on statistical indicators (e.g. mean, variance etc...) as Fig.12 shows.

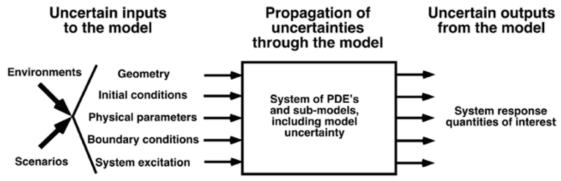

Figure 12: Forward uncertainty propagation

Our goal is to compute statistics of a quantity of interest $Q(\omega)$ that can be derived from the solution $\mathbf{u}$ of our PDE model. In particular, we will study the effect of a uniformly distributed wall temperature, denoted T_w, over the heat flux solution of the Gnoffo test case[7]. State-of-the-art MLMC uses a Multigrid method, generally based on h-refined hierarchy of meshes. Our MLMC model will benefit from the FR framework and use isotropic p-refinement to construct a coarse-to-fine hierarchy of models. Fig.13 shows the latter hierarchy, where the points inside the cells represented the solution points and the number of the dots next the cartesian grids represents the number of sampling within each grid.

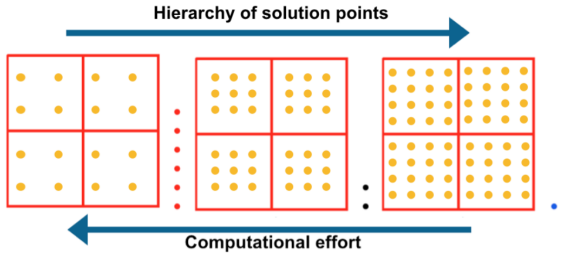

Figure 13: Illustration of the *Levels* used in our MLMC approach. Level 0 (left) – Level 1 (middle) – Level 2 (right)

4.2. MLMC sampling

The classic MC estimator Q for the expected value $\mathbb{E}[Q_L]$ is given by Eq.21:

$$\mathbb{E}[Q_L] \approx Q_{L,N} = \frac{1}{N}\sum_{0}^{N-1} Q_L^{(n)}, \tag{21}$$

where $Q_L^{(n)}$ denotes the nth independent and identically distributed (i.i.d.) sample of the QoI Q_L at level L and N is the number of independent MC samples. For every level l approximation of the QoI, we can construct, by linearity, the following telescoping sum in Eq.22:

$$\mathbb{E}[Q_L(\omega)] = \mathbb{E}[Q_0(\omega)] + \sum_{l=1}^{l=L} \mathbb{E}[Q_l(\omega) - Q_{l-1}(\omega)]. \tag{22}$$

The latter equation can be re-written as

$$\mathbb{E}[Q_L(\omega)] = \sum_{l=0}^{l=L} \mathbb{E}[\Delta Q_l], \tag{23}$$

where, $\Delta Q_l = Q_l - Q_{l-1}$ and $Q_{-1} = 0$.
Using a MC estimator for each term in Eq.23, we obtain the MLMC estimator described in Eq.24:

$$Q_{L,N_l} = \sum_{l=0}^{L} \frac{1}{N_l} \sum_{n=0}^{N_l-1} \Delta Q_l^{(n)}, \tag{24}$$

where $\Delta Q_l^{(n)}$ denotes the nth *i.i.d.* sample of ΔQ_l and N_l is the number of independent samples computed on each level $l \in [0, L]$. Eq.25 gives the variance of the estimator, since the expectations $\mathbb{E}[\Delta Q]$ are estimated independently.

$$\begin{aligned} \mathbb{V}[Q_{L,N_l}] &= \sum_{l=0}^{L} \frac{1}{N_l^2} \sum_{n=0}^{N_l-1} \mathbb{V}[\Delta Q_l] \\ &= \sum_{l=0}^{L} \frac{\mathbb{V}[\Delta Q_l]}{N_l} \end{aligned} \tag{25}$$

MLMC methods are more efficient than the one-level MC since it requires only the computations of the variance of the difference ΔQ_l on higher levels. In spite of the high cost of computing this difference, the variance is smaller, as shown in Eq.26, when a strong positive correlation is found between QoI on level l and $l-1$. Therefore, fewer and fewer samples are required to accurately estimate the expected value $\mathbb{E}[\Delta Q_l]$

$$\begin{aligned} \mathbb{V}[\Delta Q_l] &= \mathbb{V}[Q_l - Q_{l-1}] \\ &= \mathbb{V}[Q_l] + \mathbb{V}[Q_{l-1}] - 2cov(Q_l, Q_{l-1}) \\ &<< \mathbb{V}[Q_l] + \mathbb{V}[Q_{l-1}] \end{aligned} \tag{26}$$

where $cov(Q_l, Q_{l-1})$ is the covariance between Q_l and Q_{l-1}.

4.3. Implementation

Fig.14 shows our coupling between the UQ Julia package *MultilevelEstimators* and the COOLFluiD solver.

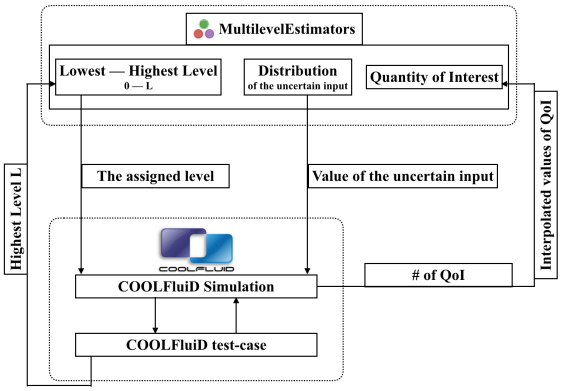

Figure 14: Overview about *MultilevelEstimators* and COOLFluiD coupling

The MLMC needs nested realisations of the QoI, i.e. fixed distribution of the QoI between the different levels. Nevertheless, Gauss-Legendre points distribution is order-dependent and the topology of the solution points changes in function of the polynomial order. To overcome such problems, an interpolation step is needed to evaluate the QoI at nested positions (coordinates) between all levels (i.e. orders). The key idea is to use the solution point distribution at the highest level, to conserve the level of the accuracy at the highest order, and to evaluate the QoI of the lowest orders at the same point distribution of the highest one. Fig.15 shows the interpolated $P1$ heat flux (HF) solution of the Gnoffo test case, evaluated at θ coordinates defined by $P2$ Gauss-Legendre distribution. We can notice that the $P2$ and the interpolated $P1$ heat fluxes are evaluated at the same coordinate θ. Fig.16 shows the evaluation of the interpolated $P2$ heat flux at $P4$ Gauss-Legendre θ coordinates distribution. The following code listing shows how the interpolation is computed in function of the current level (i.e. order of the simulation) and the highest one.

```
orderL : Current Level
orderH : Highest Level
thetaPL : theta coordinates
    of the current level
thetaPH : theta coordinates
    of the highest level

j=1
for i = 0:div((length(thetaPL)-1),
  orderL+1)
  xs = zeros(0); ys = zeros(0)
  for k in orderL:-1:0
   append!( xs, thetaPL[(orderL-k)
            +1+(orderL+1)*i])
   append!( ys, hPL[(orderL-k)
            +1+(orderL+1)*i])
  end
  p=polyfit(xs, ys, orderL)
  counter = 0
  while mod(counter,orderH+1)!=0 ||
    counter==0 && j<=length(thetaPH)
    hPLatPH[j] = polyval(p,thetaPH[j])
    counter = counter+1
    j=j+1
  end
end
```

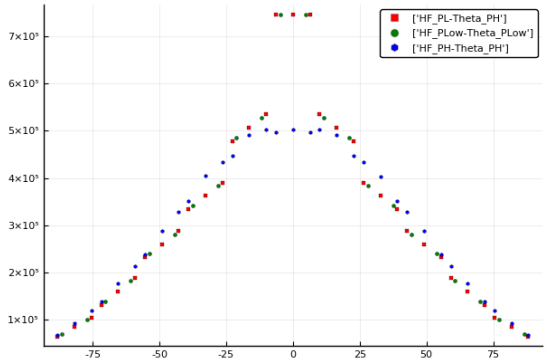

Figure 15: $P1$ HF (circle green) – 1st order interpolation of the $P1$ HF and evaluated at $P2$ θ coordinates (red squares) – $P2$ HF (blue diamonds)

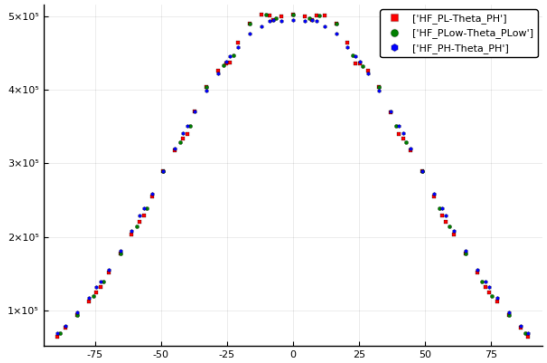

Figure 16: $P2$ HF (circle green) – 2nd order interpolation of the $P2$ HF and evaluated at $P4$ θ coordinates (red squares) – $P4$ HF (blue diamonds)

4.4. Preliminary Results

4.4.1. The Deterministic Gnoffo test case

Preliminary results are obtained for a steady flow over a 2D cylinder with a radius $1m$. The deterministic test case conditions are presented in Tab.4 and Tab.5, while the test case geometry and the corresponding structured mesh is shown in Fig.17.

Table 4: Gnoffo – Flow characteristics

Physical Model	M_{inf}	$\rho\ [kg/m^3]$	$V_{\text{inf}}[m/s]$	$T_{\text{inf}}[K]$	$T_{wall}[K]$
Perfect gas	17.637	0.001	5000	200	500

Table 5: Gnoffo – Mesh characteristics

Dimensions	Type	# Elements	Geometric order
2D	Quadrilateral	297	2 (i.e. curved)
BC 1	BC 2	BC 3	BC 4
Iso-thermal wall	Inlet	Outlet	Outlet

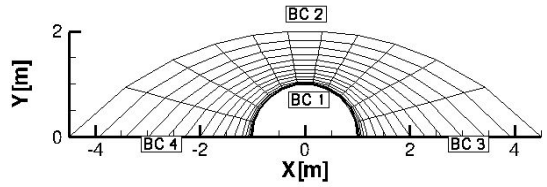

Figure 17: Gnoffo – Mesh Characteristics

4.4.2. MLMC Simulations of the Gnoffo test case

At a first stage, a two-levels MLMC simulations of the Gnoffo test cases are carried out. The effect of the wall temperature, varying uniformly between $[495K, 505K]$, over the stagnation heat flux is studied. The reader should note that the MLMC levels are mapped to the following (cf. Tab.6), ensuring a p-refined MLMC method.

Table 6: Mapped levels between MLMC and FR

MLMC Level	FR Order	# DOF [3]
0	1	1188
1	2	2673

Fig.18 shows the distribution of the total number of samples across all levels for different choices of ϵ (i.e. tolerance). We can indeed show, as expected, that N_l is decreasing in function of level l. More precisely, Tab.7 shows that most samples are taken on the lowest FR-order, while only a limited number of samples are required on the highest order (i.e. P2).

Table 7: Distribution of number of samples in function of ϵ

ϵ	level 0	level 1
285.61	718	202
371.293	463	127
627.485	197	97

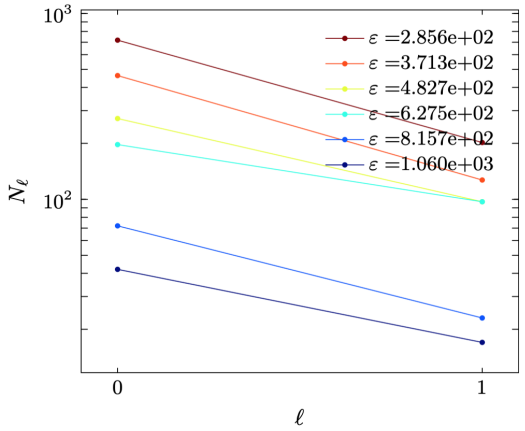

Figure 18: Distribution of number of samples for different tolerances

Note: Tolerance

Two sources of error in the MLMC estimator exist:

1. Approximation error: Introduced by the spatial discretization of the QoI (i.e. Q by Q_l),
2. The stochastic error: Introduced by replacing the expected value by an average of a finite set of samples.

In MultilevelEstimators[16] and in [29], the accuracy of the approximation is controlled via the mean square error (MSE):

$$MSE = \frac{\mathbb{V}[Q_L]}{N} + (\mathbb{E}[Q_L - Q])^2 \qquad (27)$$

The convergence criterion is defined as $MSE = O(\epsilon^2)$. In [30], the authors present an error splitting of the MSE as follows:

[3] DOF: Degrees of freedom

To ensure a MSE of ϵ^2 at most, we need to impose the inequalities present in Inq.28 and Inq.29:

$$\sum_{l=0}^{L} \frac{V_l}{N_l} \leq \theta\epsilon^2, \tag{28}$$

$$(\mathbb{E}[Q_l - Q]))^2 \leq (1-\theta)\epsilon^2. \tag{29}$$

where the splitting parameter $\theta \in [0,1]$. For our simulations, we will choose a constant $\theta = 0.5$.
Tab.8 shows that the stagnation heat flux $HF = 500112 \pm 3922$ over 2 level MLMC simulations for a uniform T_w distribution between $495K$ and $505K$. Fig.19 and Fig.20 show the standard plots for MLMC: the behaviour of the expected value and the variance, respectively.

Table 8: Mean and Standard deviation of the Stagnation HF

Distribution of T_w	Mean HF $[W/m^2]$	Standard deviation $\sigma[W/m^2]$
[495K, 505K]	500112	3922

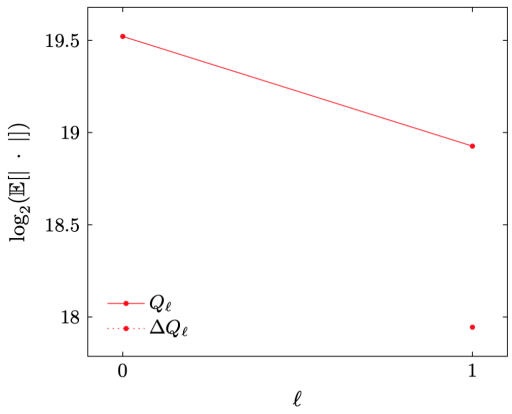

Figure 19: Behaviour of the expected value of the stagnation heat flux and of the correction term ΔQ_l

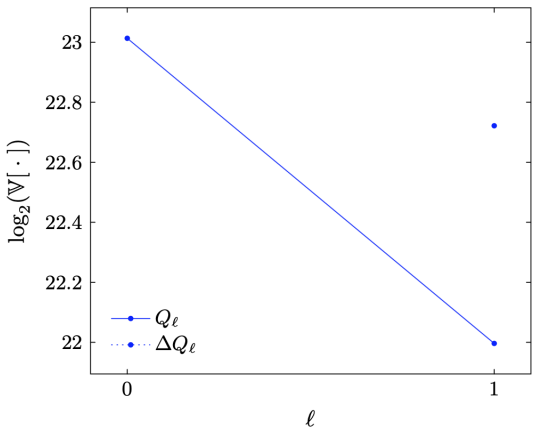

Figure 20: Behaviour of the variance of the stagnation heat flux and of the correction term ΔQ_l

5. Conclusion

5.1. AMR–FR

The novel AMR algorithms are successfully implemented to the FR framework and tested on the wedge test case (first in its kind results, even though still very preliminary). As future work, we will demonstrate the benefits of this coupling by studying the heat flux predictions over benchmark test cases with coarse curved meshes. In fact, high-order solution discretization works best in combination with high-order geometric representation, since it provides a reduced spurious entropy generation by better fitting the real boundary geometry and a better heat flux estimation.

5.2. UQ–FR

The MultilevelEstimators Julia package and COOLFluiD solver are successfully coupled. As additional novelty, the Multi-Level Monte Carlo methods used for UQ constructs levels using p-refinement instead of h-refinement. As future work, we will study the RANS turbulence models by injecting uncertainties over the various parameters of the models (e.g. $k-\omega\ SST$, $\gamma-\alpha$ etc...).

To this end, AMR–FR–UQ simulations will be carried out to limit the numerical errors due to mesh/shock misalignment in order to avoid considering this kind of errors as due to input uncertainties.

Acknowledgments

- The research of Firas Ben Ameur is supported by SB PhD fellowship 1SC3519N of the FWO.

- Many thanks to Ray Vandenhoeck for providing the deterministic FR-Gnoffo test cases.
- Many thanks to Pieterjan Robbe for his assistance on MLMC and Julia language.
- Many thanks to my student Joachim Balis for simulating my AMR_FR codes and generating the wedge results.

References

[1] O. P. L. Matre, Stochastic spectral methods for uncertainty propagation in computational fluid mechanics models, NATO RTO-VKI Lecture Series.

[2] E. M. Sousa, G. Lin, U. Shumlak, Uncertainty quantification of the gem challenge magnetic reconnection problem using the multilevel monte carlo method, International Journal for Uncertainty Quantification 5 (4).

[3] G. Iaccarino, Introduction to uncertainty representation and propagation, NATO RTO-VKI Lecture Series.

[4] M. Pisaroni, Multilevel monte carlo methods for uncertainty quantification and robust design optimization in aerodynamics, Ph.D. thesis, EPFL (2017).

[5] C. S. T. Barth, S. Mishra, Uq methods for nonlinear conservation laws containing discontinuities, NATO RTO-VKI Lecture Series.

[6] P. Gnoffo, Multi-Dimensional Inviscid Flux Reconstruction for Simulation of Hypersonic Heating on Tetrahedral Grids, in: 47th AIAA Aerospace Sciences Meeting, Aerospace Sciences Meetings, American Institute of Aeronautics and Astronautics, 2009.

[7] P. Gnoffo, J. White, Computational Aerothermodynamic Simulation Issues on Unstructured Grids, in: 37th AIAA Thermophysics Conference, Fluid Dynamics and Co-located Conferences, American Institute of Aeronautics and Astronautics, 2004.

[8] K. H. Kim, C. Kim, O.-H. Rho, Methods for the accurate computations of hypersonic flows: I. ausmpw+scheme, Journal of Computational Physics 174 (1) (2001) 38 – 80.

[9] C.-L. Chang, M. Choudhari, Hypersonic Viscous Flow Over Large Roughness Elements, in: Theoretical and Computational Fluid Dynamics, Vol. 25, 2011, pp. 85–104.

[10] K. H. Kim, C. Kim, O.-H. Rho, Methods for the accurate computations of hypersonic flows: Ii. shock-aligned grid technique, Journal of Computational Physics 174 (1) (2001) 81 – 119.

[11] H. Huynh, Z. J. Wang, P. E. Vincent, High-order methods for computational fluid dynamics: a brief review of compact differential formulations on unstructured grids, Computers & Fluids 98 (2014) 209–220.

[12] F. Ben Ameur, A. Lani, Physics-based mesh fitting algorithms for hypersonic flows simulations, in: AIAA Scitech 2019 Forum, San Diego, California, 2019.

[13] R. Vandenhoeck, A. Lani, Implicit high-order flux reconstruction positivity preserving llav scheme for viscous high-speed flows, in: AIAA Scitech 2019 Forum, San Diego, California, 2019.

[14] R. Vandenhoeck, A. Lani, Implicit high-order flux reconstruction solver for high-speed compressible flows, Computer Physics Communications 242 (2019) 1 – 24. doi:https://doi.org/10.1016/j.cpc.2019.04.015.

[15] F. Ben Ameur, R. Vandenhoeck, A. Lani, High-order flux reconstruction scheme for thermo-chemical nonequilibrium high-speed flows, in: AIAA Scitech 2019 Forum, San Diego, California, 2019.

[16] P. Robbe, Multilevel uncertainty quantification methods for robust design of industrial applications, Ph.D. thesis, KU Leuven (2019).

[17] D. Kimpe, A. Lani, T. Quintino, S. Poedts, S. Vandewalle, The coolfluid parallel architecture, in: B. Di Martino, D. Kranzlmüller, J. Dongarra (Eds.), Recent Advances in Parallel Virtual Machine and Message Passing Interface, Springer Berlin Heidelberg, Berlin, Heidelberg, 2005, pp. 520–527.

[18] A. Lani, N. Villedie, K. Bensassi, L. Koloszar, M. Vymazal, S. M. Yalim, M. Panesi, Coolfluid: an open computational platform for multi-physics simulation and research, in: 21st AIAA Computational Fluid Dynamics Conference, 2013, p. 2589.

[19] H. Huynh, A flux reconstruction approach to high-order schemes including discontinuous galerkin methods, AIAA paper 4079 (2007) 2007.

[20] H. Huynh, High-order methods including discontinuous galerkin by reconstructions on triangular meshes, AIAA Paper 44 (2011) 2011.

[21] P. Castonguay, D. M. Williams, P. E. Vincent, M. Lopez, A. Jameson, On the development of a high-order, multi-gpu enabled, compressible viscous flow solver for mixed unstructured grids, AIAA paper 3229 (2011) 2011.

[22] P. Castonguay, P. Vincent, A. Jameson, Application of high-order energy stable flux reconstruction schemes to the euler equations, in: 49th AIAA Aerospace Sciences Meeting, Vol. 686, 2011.

[23] S. Abhyankar, J. Brown, E. M. Constantinescu, D. Ghosh, B. F. Smith, H. Zhang, Petsc/ts: A modern scalable ode/dae solver library, arXiv preprint arXiv:1806.01437.

[24] S. Balay, S. Abhyankar, M. F. Adams, J. Brown, P. Brune, K. Buschelman, L. Dalcin, V. Eijkhout, W. D. Gropp, D. Kaushik, M. G. Knepley, D. A. May, L. C. McInnes, R. T. Mills, T. Munson, K. Rupp, P. Sanan, B. F. Smith, S. Zampini, H. Zhang, H. Zhang, PETSc Web page (2018).

[25] S. Balay, S. Abhyankar, M. F. Adams, J. Brown, P. Brune, K. Buschelman, L. Dalcin, V. Eijkhout, W. D. Gropp, D. Kaushik, M. G. Knepley, D. A. May, L. C. McInnes, R. T. Mills, T. Munson, K. Rupp, P. Sanan, B. F. Smith, S. Zampini, H. Zhang, H. Zhang, PETSc users manual, Tech. Rep. ANL-95/11 - Revision 3.9, Argonne National Laboratory (2018). URL http://www.mcs.anl.gov/petsc

[26] S. Balay, W. D. Gropp, L. C. McInnes, B. F. Smith, Efficient management of parallelism in object oriented numerical software libraries, in: E. Arge, A. M. Bruaset, H. P. Langtangen (Eds.), Modern Software Tools in Scientific Computing, Birkhäuser Press, 1997, pp. 163–202.

[27] B. Frederic, Considerations on the spring analogy, International Journal for Numerical Methods in Fluids 32 (6) (2000) 647–668.

[28] R. Jain, I. Chlamtac., The P2 Algorithm for Dynamic Calculation of Quantities and Histograms Without Storing Observations, Eastern Research Laboratory, Digital Equipment Corporation, 1985.

[29] M. B. Giles, Multilevel monte carlo path simulation, Operations research 56 (3) (2008) 607–617.

[30] N. Collier, A.-L. Haji-Ali, F. Nobile, E. Von Schwerin, R. Tempone, A continuation multilevel monte carlo algorithm, BIT Numerical Mathematics 55 (2) (2015) 399–432.

SHAPE OPTIMIZATION

Aero structural optimisation using adjoint method: treatment of testcases with several bladerows

Tom De Bruyn

Turbomachinery and propulsion Department, von Karman Institute for Fluid Dynamics, Belgium, tom.de.bruyn@vki.ac.be

Supervisor: Tom Verstraete

Professor, Turbomachinery and propulsion Department, von Karman Institute for Fluid Dynamics, Belgium, tom.verstraete@vki.ac.be

Visiting Professor, Department of flow, heat and combustion mechanics, Ghent University, Belgium, tjvrstra.verstraete@ugent.be

Abstract

The flow in turbomachines is inherently unsteady due to the relative motion of bladerows, which shed pitchwise non-uniform flows to downstream rows. With respect to steady computation, unsteady evaluation incurs a computational cost over an order of magnitude higher, especially as typically the entire annulus must be included in the computational domain, compared to single blade passage. This higher computational penalty renders unsteady computations unfeasible for use in an optimisation context, requiring at least several tens of design evaluations. Of the possible approaches to overcome this issue, two are discussed here: the classic mixing plane approach, which is currently implemented in the VKI's adjoint optimisation framework '*CADO*', and harmonic methods, which are under development in this phd project for the same framework.
The former approach is hence discusses first, by an overview of the method and by considering the results of an industrially relevant test case: the 1.5 stage axial 'Aachen' turbine. Just shy of an actual optimisation, sensitivity maps of the design are computed using the adjoint method, demonstrating the capability of the method to provide a gradient-based optimiser with the appropriate derivative information. The harmonic method is only discussed theoretically and contrasted with the current approach.

Keywords: turbomachinery, optimisation, mixing plane, harmonic method

1. Introduction

Real-life turbomachines often conisist of more than a single stage, making the direct optimisation of complete devices with multiple bladerows of great interest. The individual optimisation of each bladerow would indeed necessitate iteratively matching in- and outlet conditions of consecutive domains in order to conserve mass, momentum and energy flux throughout the machine. More importantly, a sequence of individually optimised stages does not guarantee an overall optimal solution. Whereas the optimisation of single components, such as single blade rows, is nowadays well understood, extending such techniques to full components such as multi-blade row machines poses significant challenges. While the flow is inherently unsteady, mostly less expensive steady RANS computations are employed because of the need for multiple evaluations of the design. Gradient-based optimisation methods, which are considered here, are the most efficient in this regard, but still require several tens of evaluations, rendering unsteady RANS too costly.

Hence several approaches exist to enable the use of steady computations or similarly inexpensive methods for multi-bladerow turbomachinery. A straightforward approach is the frozen rotor, maintaining a fixed relative position of consecutive bladerows. Though useful in particular cases, e.g. the interface between impeller and volute in a radial compressor, where averaging would negate the pressure increase over the circumference of the volute, the frozen rotor approach for most applications leads to nonphysical computed flow fields. These can be particularly damaging in an optimisation context, as e.g. the (local) shape of

downstream blades may be greatly influenced if they are positioned in the now no longer moving wake of the upstream blade.

Another rather straightforward approximation is to assume instantaneous, complete and perfect mixing of the flow at bladerow interfaces. This assumption gives rise to the mixing plane approach, which is considered here in more detail.

2. Description of the mixing plane method

The mixing plane method [1] has so far seen quite a few variants [2–5], which are however largely similar. In the most general sense, all variants define an circumferentially averaged state, which is however allowed to vary over the 'height' of the mixing plane interface (corresponding to the span of the blades). In either domain, boundary conditions are implemented based on this averaged condition. As the interface typically cannot be placed similarly far away from the blades as is the case at an in- or outlet - because of the small spacing between bladerows in a real-life machinery - non-reflective boundary conditions following Giles [6] are typically used. These non-reflecting boundary conditions are necessary in those cases, as the flow is strongly non-uniform and flow features (shocks, expansion waves, wakes,...) may be reflected back into the domain if the boundary is not treated properly.

In order to make the boundary non-reflective, the flow field is locally linearised around the average condition and represented by means of a Fourier transform as a set of two-dimensional waves in the meridional-circumferential plane:

$$U'(m,\theta) = \sum e^{i(km+l\theta-\omega t)}\mathbf{u}^R, \tag{1}$$

Where m and θ are the meridional and tangential coordinate respectively, k and l the spatial wave numbers, ω the pulsation frequency and $U'(m,t) = U(m,t) - \bar{U}(m,t)$ the perturbation of the primitive variable vector; $\mathbf{u}^R$ is the (complex) wave amplitude. Entering this description of U' in the linearised (unsteady) Euler equations

$$\frac{\partial U}{\partial t} + A\frac{\partial U}{\partial m} + B\frac{\partial U}{\partial \theta} = 0, \tag{2}$$

and requiring non-trivial solutions to exist, leads to the dispersion relation

$$det(-\omega I + kA + lB) = 0. \tag{3}$$

Matrices A and B, given in appendix, allow to solve for the meridional wave number k as a function of the pulsation frequency ω and the tangential wave number l (u and v are the meridional and tangential velocity components, c the speed of sound):

$$\begin{aligned} k_{1,2,3} &= \frac{\omega - lv}{u}, \\ k_{4,5} &= (lv-\omega)\frac{u \pm \sqrt{1 - \frac{(c^2-u^2)l^2}{(lv-\omega)^2}}}{c^2-u^2}. \end{aligned} \tag{4}$$

The first three solutions are real, and for all ω correspond to solution waves propagating with group velocity $\partial\omega/\partial k = u$ downstream. For the latter two solutions, when taking the limit $\omega \to 0$ to approximate the steady state, the propagation direction becomes dependent on the sign of c - u and thus on the meridional Mach number $M_m = \sqrt{(u^2/c^2)}$. In meridionally supersonic flow, both the last two waves travel downstream, while when the flow is meridionally subsonic, one solution wave travels upstream, while the other still travels downstream. Note that the flow may in the last case still be supersonic if $M^2 = (u^2+v^2)/c^2 = M_m^2 + M_\theta^2 > 1$. It is of interest that while it does have an effect on the implementation of the non-reflective boundary - it dictates whether the criterion depends on the circumferential wave number and thus whether different wave-numbers must be treated separately - the 'total' flow Mach number does not dictate the propagation direction directly.

Having made the distinction between up- and downstream propagating waves, the criterion for non reflectiveness can be set by again entering (1) in the steady formulation of the linearised Euler equations (2) and restructuring:

$$\sum (kI + lA^{-1}B)\mathbf{u}^R = 0, \tag{5}$$

which must be valid for every wave number, so the summation can be dropped. From this equation it is clear that $\mathbf{u}^R$ are the right eigenvectors of $lA^{-1}B$. The left eigenvectors $\mathbf{v^L}$ are orthogonal ($\mathbf{v}_m^L\mathbf{u}_n^R = 0$ for $m \neq n$) and can thus be used to set individual waves to zero by enforcing $\mathbf{v}^L U' = 0$ when m ($\in [1,5]$) corresponds to an incoming wave. For a subsonic inlet for example, the first four waves are in this way set to zero.

Where the various methods in [2–5] do differ slightly is in the update of the circumferentially averaged state

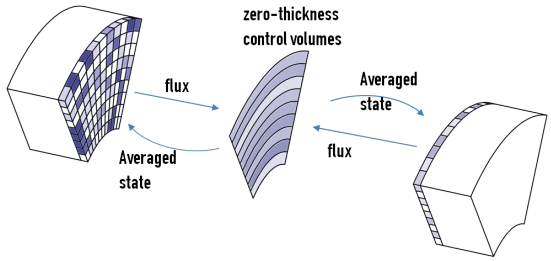

Figure 1: Schematic representation of the mixing plane implementation

at either side of the boundary. 'Earlier' methods would simply invert the flux evaluation routine and apply it to the difference in the fluxes computed on either end, and express the resulting update of the primitive variables $(\rho, u, v, w, P)^T$ in terms of the one-dimensional characteristics. The latter are obtained by using a similar approach as the one followed for the non-reflecting boundary, but neglecting the tangential component, and can be used to compute the eventual update considering only incoming characteristics on either end.

More recently, Wang [5] proposed a modified approach, which is followed in this project. With respect to earlier methods Wang's approach offers superior robustness in low and reverse flow cases. Indeed the transformation from flux to primitive variables used in other methods involves division by the mass flow, becoming increasingly problematic as $\dot{m} \to 0$

In order to overcome this problem, Wang instead defines a set of 1-dimensional 'virtual' control volumes along the span of the mixing plane interface. The conservative variables in these control volumes are updated based on the flux difference between either side:

$$\Delta\rho = \frac{CFL\Delta\bar{F}_1}{v_n + c}, \tag{6a}$$

$$\Delta\rho v_m = \frac{CFL\Delta\bar{F}_2}{v_n + c}, \tag{6b}$$

$$\Delta\rho v_\theta = \frac{CFL\Delta\bar{F}_3}{v_n + c}, \tag{6c}$$

$$\Delta\rho v_s = \frac{CFL\Delta\bar{F}_4}{v_n + c}, \tag{6d}$$

$$\Delta\rho E = \frac{CFL\Delta\bar{F}_5}{v_n + c}, \tag{6e}$$

$$\Delta\rho\phi = \frac{CFL\Delta\bar{F}_6}{v_n + c}, \tag{6f}$$

where $\Delta\bar{F}_1$ to $\Delta\bar{F}_6$ are the net inflow of mass, momentum, energy and of a convected scalar ϕ into the control volume after summation over the pitch on either end. In order not to have to enforce a matching interface during meshing - which, because of the refinement in the tip gap is not desirable - The update (6) is performed on a set of volumes derived from one side's mesh, and the resulting state is interpolated to either side for use in the non-reflective boundary condition. The procedure is visualised in figure 1.

3. 1.5 Stage axial turbine

The 1.5 stage axial 'Aachen' turbine [7] test case is a low-speed subsonic turbine with two 36-blade stators and a single 41 blade rotor. The Turbine, with untwisted prismatic profiles, has been build and tested at the RWTH Aachen. Details of the geometry can be found in [8]. The considered working conditions are summarised in table 1.

Table 1: Working conditions

Rotational Speed	3500 rpm
Static pressure ratio	1.43
Reynoldsnumber (outlet)	~ 750k
Mass flow	~ 8.28 kg/s
Efficiency	~ 86.4 %

The test case is meshed with a multi-block structured mesh of about 3.3 million grid cells. The hub and blade surfaces of the mesh are shown in figure 2.

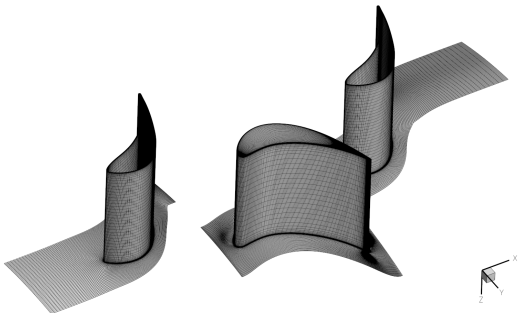

Figure 2: Structured finite volume mesh of the Aachen Turbine

3.1. Convergence of (adjoint) solver

The '*CADO*' framework's CFD solver [9] is used to solve the RANS equations in an absolute frame of reference, using Roe's approximate Riemann solver and MUSCL reconstruction of primitive variables at cell faces for second order spatial accuracy. The viscous flux, for which a central discretisation is used, incorporates the turbulence through the eddy-viscosity hypothesis. The negative Spalart-Allmaras model[10] is used for turbulence modelling. At the mixing plane interface, only the convective flux is considered, corresponding to the above analysis using the Euler equations, and the Spalart-Allmaras transport quantitiy $\tilde{\nu}$ is treated as a passive convected scalar.

To efficiently compute the derivative information required for gradient based optimisation, the discrete adjoint problem of the CFD-evaluation ('primal') is found as follows:
With $\mathbf{U}$ the solution vector $\left(\rho, \rho V_x, \rho V_y, \rho V_z, \rho E, \rho\tilde{\nu}\right)^T$, $\mathbf{X}$ the vector of grid points making the finite volume mesh and J and objective function, the optimisation problem is to find:

$$\min_{\mathbf{X}} \; J(\mathbf{U}, \mathbf{X}) \quad \textit{subject to } \mathbf{R}(\mathbf{U}, \mathbf{X}) = 0, \tag{7}$$

with $\mathbf{R}$ the residual of the CFD computation. Linearising around any solution $(U^*, X^*)^T$ of the CFD leads to the linearised optimisation problem:

$$\begin{aligned} &\min_{\Delta\mathbf{X}} \left(\frac{\partial J}{\partial \mathbf{U}} \frac{\partial J}{\partial \mathbf{X}}\right) \begin{pmatrix} \Delta\mathbf{U} \\ \Delta\mathbf{X} \end{pmatrix} \\ &\textit{subject to } \left(\frac{\partial \mathbf{R}}{\partial \mathbf{U}} \frac{\partial \mathbf{R}}{\partial \mathbf{X}}\right) \begin{pmatrix} \Delta\mathbf{U} \\ \Delta\mathbf{X} \end{pmatrix} = 0, \end{aligned} \tag{8}$$

where $\Delta\mathbf{U}$ and $\Delta\mathbf{X}$ are the difference with the current solution and current mesh vector respectively. Due to the linearisation, the above problem's solution is only bounded in case $(U^*, X^*)^T$ corresponds to the optimum, otherwise ΔJ goes to minus infinity. In the terminology of (economical) linear optimisation problems, this linear problem is called the "resource allocation problem", and can indeed be thought of as looking for the optimal mesh movement, constrained by the requirement that the RANS equations must still hold. For any linear constrained optimisation problem, a dual problem can be constructed, with the same solution - provided a solution exist - and in which variables and constraints have exchanged roles[11]. Applying this procedure to (8) leads to an equivalent linear optimisation problem:

$$\begin{aligned} &\max_{\psi} 0 \\ &\textit{subject to } \begin{pmatrix} \frac{\partial \mathbf{R}}{\partial \mathbf{U}}^T \\ \frac{\partial \mathbf{R}}{\partial \mathbf{X}}^T \end{pmatrix} \psi = \begin{pmatrix} \frac{\partial J}{\partial \mathbf{U}}^T \\ \frac{\partial J}{\partial \mathbf{X}}^T \end{pmatrix}. \end{aligned} \tag{9}$$

The resulting problem leads to two set of equations: namely the adjoint equations:

$$\frac{\partial \mathbf{R}}{\partial \mathbf{U}}^T \psi = \frac{\partial J}{\partial \mathbf{U}}^T, \tag{10}$$

and zero gradient:

$$\frac{\partial J}{\partial \mathbf{X}} - \psi^T \frac{\partial \mathbf{R}}{\partial \mathbf{X}} = \frac{dJ}{d\mathbf{X}} = 0. \tag{11}$$

When the primal problem is unbounded, the system (9) cannot be solved as (11) cannot be made to hold together with 10, but in the optimal solution it can as gradient of constraint and objective co-align. The dual problem than indeed yields the same optimal value as the primal, as the gradient becomes zero there. Combining both problems, finding the optimum becomes equivalent to requiring the constraint in (7) and equations (10) and (11) to simultaneously hold, which can be solved iteratively.

In the terminology of (economical) constrained optimisation problems, this is the "resource validation problem", where the adjoint variable ψ represents the "shadow cost" of the constraint: "the change, per infinitesimal unit of the constraint, in the optimal value of the objective function of an optimisation problem obtained by relaxing the constraint"[12]. Indeed this is the correct physical interpretation of the adjoint: taking the mass flow residual (constraint) as an example, the corresponding variable in the dual problem, the adjoint mass flow, represents the change in objective function if a unit mass flow is added in a particular location (e.g. domain cell).

Although the adjoint equations are a linear system, solving it directly is usually unfeasible as the system is rather stiff. Therefore the same iterative approach

used for the primal problem (JT-KIRK scheme[13]) is used. An interesting property resulting from this is that convergence rate of primal and adjoint solver is identical, provided the derivation of the Jacobian in the left hand side of the adjoint is done correctly and the primal (CFD) is converged to sufficient accuracy. Figure 3 demonstrates this for the AachenTurbine test case. Note that the slope of the adjoint convergence corresponds well to the slope of the CFD in the last iterations of the latter. Unlike for the primal solver, multigrid initialisation is not used in the adjoint solver. Though the adjoint solver could be allowed to continue further, a reduction of seven orders of magnitude in the residual was considered sufficient.

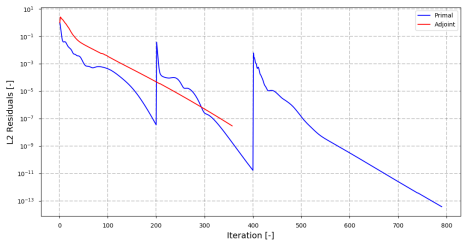

Figure 3: Convergence of the CFD (blue) and adjoint (red) solver

3.2. *Discussion of mixing plane results*

Figure 4 visualises the pressure distribution obtained for the AachenTurbine test case.

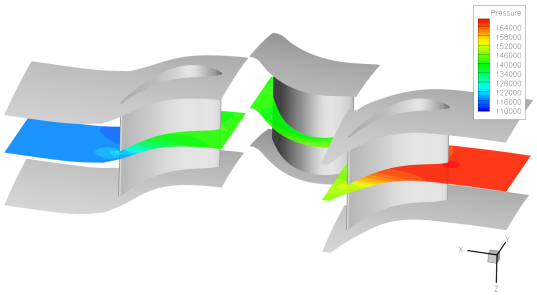

Figure 4: Pressure distribution around mid-span, flow is from right to left

As the pressure is not directly proportional to any of the characteristic variables, it is not averaged on either side of the interface. Indeed the pressure is related to both the fourth and fifth characteristic, and thus (in anything but the rare axially supersonic case) contains both up- and downstream travelling information.

The averaging can however be seen very clearly in the turbulent quantities, which at the interface are convected downstream by the mean flow. Figure 5 shows this. The quantity shown here is μ_T/μ_L, the ratio between eddy and laminar viscosity and as such a direct measure for the local turbulent intensity.

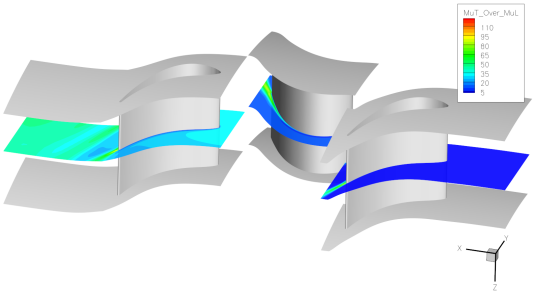

Figure 5: Ratio between turbulent and laminar viscosity

An interesting property of the adjoint, visualised in figure 6, is the inversion of propagation direction with respect to the CFD solver. From the physical interpretation of the adjoint variables this can be understood rather intuitively: As the adjoint corresponds to the change in the objective function resulting from an 'injection' of mass, momentum or energy, the effect of an upstream injection must be at least similar, hence upstream propagation of the adjoint variable must be expected.

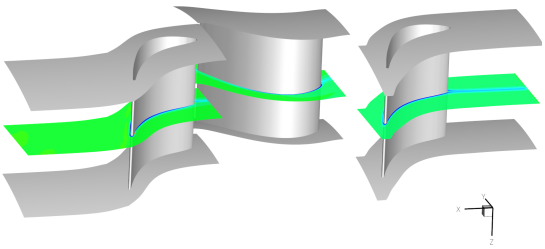

Figure 6: Adjoint turbulent variable (entropy generation adjoint)

3.3. *Sensitivity maps*

A step up to an actual optimisation, for which the geometry should first be parameterised, surface sensitivity maps are presented here for two objective functions: entropy generation and mass flow. These form a indication of the mesh movement required to obtain a higher objective function value.

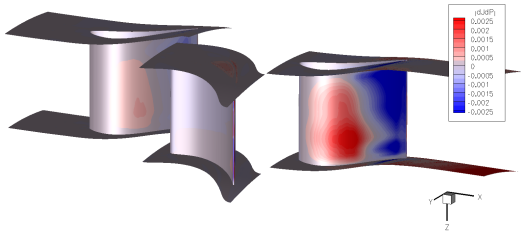

Figure 7: Surface sensitivity for mass flow adjoint, red is outward, flow from left ro right

In both figure 7 and 8 red areas indicates 'outward' movement (into the fluid domain), while blue areas indicate 'inward' movement, enlarging the fluid domain. Both figures assume a grid converged CFD solution. Figure 7 is obtained specifying the outlet mass flow as the objective function, showing the direction of mesh movement which would result in higher mass flow through the machine. Especially noteworthy is the area near the trailing edge on the last stator's suction side, indicated in blue. The inward (away from the observer in figure 7) movement of this array opens up the blade passage at and directly downstream of it's narrowest point, indeed increasing the mass flow. The effect of movement of the pressure side is comparatively lower, as is the (similar) change of the upstream stator, indicating the downstream stator is more restrictive on the massflow.

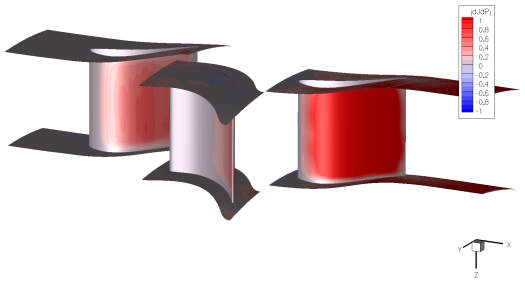

Figure 8: Surface sensitivity for entropy adjoint, red is outward

Figure 8 shows the same type of surface sensitivity map for the entropy generation between in- and outlet. As the change corresponds to an increase of the objective function, the displayed colours and corresponding movement represent an increase of the generated entropy. As one might expect, an increase of the blade's and vane's curvature and thus loading leads to higher entropy generation. Note again that, as expected, the movement of the pressure side has a far smaller effect.

In an optimisation context, surface sensitivities like the ones presented above must typically in some way be weighed with respect to one another to obtain a combined mesh movement, which is used to obtain the next iteration of the design. An optimisation of the 1.5 stage AachenTurbine is however not considered within the current scope.

4. Harmonic solver

While the mixing plane approach is adequate for the optimisation of turbomachinery like the AachenTurbine in design conditions and considering e.g. efficiency in steady state conditions, it fundamentally suppresses the bladerow interaction and possible resulting vibrations which may in fact be a quantity of interest in their own right. One may envisage to optimise for a maximal stable operating range (which additionally necessitates computations in close-to-stall conditions where unsteady effects may be more pronounced) or to impose stability-based constraints.

In order to incorporate unsteadiness without suffering the computational penalty of an unsteady RANS (URANS) computation, an harmonic or frequency-domain method is used to capture most of the unsteadiness at reasonable expense. In order to do so, the solution of the URANS equations for a periodic flow is decomposed into it's - temporal, as opposed to the mixing plane method's spatial - Fourier components:

$$U(t,\mathbf{x}) = Re\left[\sum_{k=0}^{\inf} \hat{U}_k(\mathbf{x}) e^{\mathbf{i}k\omega t}\right], \tag{12}$$

where $\omega = 2\pi f$ is the base frequency. Doing so the unsteady equations can be formulated in the frequency domain:

$$\mathbf{i}k\omega\hat{U}_k(\mathbf{x}) + \hat{R}_k(U) = 0, \tag{13}$$

with $\hat{R}_k$ the k-th harmonic of the Residual R, which depend on all harmonics of the solution U. Writing (13) for all k, one obtains a set of balance equations, leading to the name 'harmonic balance' technique[14].

Where the different harmonic balance approaches in literature differ, is in the choice which terms in these

equations are neglected or modelled, or implicitly included. Writing the residual first as a Taylor series around the steady solution $\hat{U}_0$ and applying the Fourier transform afterwards leads to the following expressions for the harmonics of the Residual in (13), with K total harmonics considered:

$$\begin{aligned} \hat{R}_0 &= R(\hat{U}_0) + D_0(\hat{U}_0, ...\hat{U}_K) \\ \hat{R}_k &= R(\hat{U}_0) + \left.\frac{\partial R}{\partial U}\right|_{\hat{U}_0} + D_k(\hat{U}_0, ...\hat{U}_K) \quad k \neq 0. \end{aligned} \tag{14}$$

The coupling terms D_k are called the deterministic stresses and contain the interaction between the higher harmonics. As the Taylor series expansion introduces polynomials of degree higher than one, these terms are non-linear. Linear harmonic (also called time-linearised) methods neglect all deterministic stress terms in (14), retaining only the first, linear term for the higher harmonics [15].

Non-linear harmonic methods [16; 17] include at least the D_0 term modelling the influence of the unsteadiness on the mean flow field. An attractive alternative approach is not to model the deterministic stresses directly, but rather implicitly incorporate these terms by using the discrete Fourier Transform of the non-linear residual. To do so, the solution U is sampled at$2K + 1$ sample points (K the index of the highest considered harmonic), for which the Residual is evaluated, resulting in a set of equations:

$$\mathbf{i}k\omega\hat{U}_k(\mathbf{x}) + \mathscr{F}_k(R(\mathscr{F}^{-1}(\hat{U}))) = 0, \tag{15}$$

where $\mathscr{F}_k$ is the k-th component of the discrete Fourier transform and $\hat{U}$ is (12) truncated at K, the approximate reconstruction of the flow field [18; 19]. Particular care is needed for these methods to avoid aliasing in the forward and inverse transforms. Often (15) is cast back into the time-domain, corresponding to a pseudo-spectral discretisation of the time-dependent term in the URANS equations.

4.1. Treatment of the bladerow interface

One aspect making the use of frequency domain methods particularly appealing for the considered case of multi-bladerow simulations and as method to include bladerow interaction, is that, unlike when using the same approach for isolated bladerow flutter effects - the base excitation frequency or frequencies are known beforehand. Indeed, the unsteadiness is dominated by the passing frequencies of neighbouring bladerows.

At the interface, spatial and temporal modes of the solution are made to reflect the relative velocity. Using the meridional, tangential and spanwise coordinate system like before, a spatial decomposition of each temporal harmonic k can be written as:

$$\hat{U}_k(m, \theta, s) = \sum_{l \in \mathscr{L}} \hat{U}_{k,l}(m, s) e^{\mathbf{i}l\theta}, \tag{16}$$

where $\mathscr{L}$ is the set of modes with inter-blade phase angle corresponding to the harmonic. In a neighbouring bladerow with relative rotational speed $\Omega' - \Omega$ (prime indicates a quantity for the neighbouring row), a corresponding mode has pulsation $(k\omega)' = k\omega + l(\Omega' - \Omega)$ and for positive or zero $(k\omega)'$ the same spatial wave number l and complex amplitude $\hat{U}_{k,l}$. For negative resulting $(k\omega)'$, $l' = -l$ and $\hat{U}'_{k,l}$ is the complex conjugate of $\hat{U}_{k,l}$.

Implementation of an harmonic solver is a planned future addition to the '*CADO*' optimisation framework in this PhD project.

5. Conclusion

Two methods tackling the inherit unsteadiness in multi-bladerow turbomachinery CFD simulations at limited computational expense are discussed: the mixing plane approach and frequency domain methods. While the former is effectively suppressing the unsteadiness, it's feasibility for use in an adjoint optimisation framework is demonstrated by applying the method to a 1.5 stage subsonic axial turbine. The latter method is presented theoretically, as a future implementation within this PhD project.

Appendix

The matrices A and B of the linearised Euler equations (2) are given below:

$$A = \begin{pmatrix} u & \rho & 0 & 0 & 0 \\ 0 & u & 0 & 0 & \frac{1}{\rho} \\ 0 & 0 & u & 0 & 0 \\ 0 & 0 & 0 & u & 0 \\ 0 & \gamma P & 0 & 0 & u \end{pmatrix}$$

$$B = \begin{pmatrix} v & 0 & \rho & 0 & 0 \\ 0 & v & 0 & 0 & 0 \\ 0 & 0 & v & 0 & \frac{1}{\rho} \\ 0 & 0 & 0 & v & 0 \\ 0 & 0 & \gamma P & 0 & v \end{pmatrix}$$

Acknowledgments

The author's PhD research is supported by a fellowship of the Flanders Scientific Research Fund (FWO)

References

[1] J. D. Denton, The Calculation of Three-Dimensional Viscous Flow Through Multistage Turbomachines, Journal of Turbomachinery 114 (1) (1992) 18–26. arXiv:https://asmedigitalcollection.asme.org/turbomachinery/article-pdf/114/1/18/5604229/18_1.pdf, doi:10.1115/1.2927983.
URL https://doi.org/10.1115/1.2927983

[2] Saxer, Andre P. and Giles, Michael B., Quasi-Three-Dimensional Nonreflecting Boundary Conditions for Euler Equation Calculations, Journal of Propulsion and Power 9 (2) (1993) 263–271.

[3] Calculation of multistage turbomachinery using steady characteristic boundary conditions, Vol. 36th AIAA Aerospace Sciences Meeting and Exhibit of Turbo Expo: Power for Land, Sea, and Air. doi:10.2514/6.1998-968.
URL https://doi.org/10.2514/6.1998-968

[4] Mixing Planes Revisited: A Steady Mixing Plane Approach Designed to Combine High Levels of Conservation and Robustness, Vol. Volume 6: Turbomachinery, Parts A, B, and C of Turbo Expo: Power for Land, Sea, and Air. arXiv:https://asmedigitalcollection.asme.org/GT/proceedings-pdf/GT2008/43161/2649/4578680/2649_1.pdf, doi:10.1115/GT2008-51296.
URL https://doi.org/10.1115/GT2008-51296

[5] D. X. Wang, An Improved Mixing-Plane Method for Analyzing Steady Flow Through Multiple-Blade-Row Turbomachines, Journal of Turbomachinery 136 (8), 081003. arXiv:https://asmedigitalcollection.asme.org/turbomachinery/article-pdf/136/8/081003/6299389/turbo_136_08_081003.pdf, doi:10.1115/1.4026170.
URL https://doi.org/10.1115/1.4026170

[6] Giles, Michael B., Nonreflecting boundary conditions for euler calculations, Vol. 28, 1989. doi:10.2514/6.1989-1942.

[7] R. Walraevens, H. Gallus, Testcase 6: 1-1/2 stage axial flow turbine (1997).

[8] R. E. Walraevens, H. E. Gallus, Three-dimensional structure of unsteady flow downstream the rotor in a 1-1/2 stage turbine, in: 7. Int. Sympos. on Unsteady Aerodyn. and Aeroelasticity of Turbomach. Fukuoka, Japan 1994, 1994.
URL https://publications.rwth-aachen.de/record/123010

[9] L. Mueller, T. Verstraete, Cad integrated multipoint adjoint-based optimization of a turbocharger radial turbine, International Journal of Turbomachinery, Propulsion and Power 2 (3).

[10] S. R. Allmaras, F. T. Johnson, P. R. Spalart, Modifications and clarifications for the implementation of the spalart-allmaras turbulence model, 2011.

[11] J. Matouek, B. Gärtner, Understading and using linear programming, Springer, Berlin, 2006.

[12] Wikipedia contributors, Shadow price — Wikipedia, the free encyclopedia, [Online; accessed 23-April-2020] (2020).
URL https://en.wikipedia.org/w/index.php?title=Shadow_price&oldid=950815073

[13] S. Xu, D. Radford, M. Meyer, J.-D. Mller, Stabilisation of discrete steady adjoint solvers, Journal of Computational Physics 299 (2015) 175 – 195. doi:https://doi.org/10.1016/j.jcp.2015.06.036.
URL http://www.sciencedirect.com/science/article/pii/S0021999115004349

[14] C. Frey, G. Ashcroft, H.-P. Kersken, C. Voigt, A harmonic balance technique for multistage turbomachinery applications, 2014. doi:10.1115/GT2014-25230.

[15] G. Dufour, F. Sicot, G. Puigt, C. Liauzun, A. Dugeai, Contrasting the harmonic balance and linearized methods for oscillating-flap simulations, Aiaa Journal - AIAA J 48 (2010) 788–797. doi:10.2514/1.43401.

[16] S. Vilmin, E. Lorrain, C. Hirsch, M. Swoboda, Unsteady flow modeling across the rotor/stator interface using the nonlinear harmonic method, Vol. 6, 2006. doi:10.1115/GT2006-90210.

[17] L. He, W. Ning, Efficient approach for analysis of unsteady viscous flows in turbomachines, Aiaa Journal - AIAA J 36 (1998) 2005–2012. doi:10.2514/2.328.

[18] K. C. Hall, J.P. Thomas and W. Clark, Computation of Unsteady Nonlinear flows in Cascades Using a Harmonic Balance Technique, AIAA Journal 40 (5) (2002) 879–886.

[19] McMullen, Matthew Scott and Jameson, Anthony and Alonso, Juan J., The Application of Non-Linear Frequency Domain Methods to the Euler and Navier-Stokes Equations, Ph.D. thesis, Stanford University, Stanford, CA (3 2003).

One-shot and multigrid acceleration for industrial shape optimization

Luca Zampini

Turbomachinery Department, von Karman Institute for Fluid Dynamics, Belgium, luca.zampini@vki.ac.be

Supervisors: Tom Verstraete and Sergio Lavagnoli

Professor, Turbomachinery Department, von Karman Institute for Fluid Dynamics, Belgium, tom.verstraete@vki.ac.be

Associate professor, Turbomachinery Department, von Karman Institute for Fluid Dynamics, Belgium, sergio.lavagnoli@vki.ac.be

University Supervisor: Grégory Coussement

Head of department, Deparment of fluid machines, Belgium, gregory.coussement@umons.ac.be

Abstract

Environmental awareness and regulations are accelerating innovation in companies to deliver better products more rapidly to the market. Rapid prototyping and additive manufacturing, e.g., enable a faster introduction in the market and the possibility to explore bold designs. Simulation-driven techniques go in the same direction, predicting the performance of products without building expensive prototypes. The pursuit of optimal performances, however, requires many simulations before the release of a new product. This significant increase in the time-to-market calls for new tools to accelerate the design process. Engineers nowadays still use an iterative practice: they design, evaluate, redesign and re-evaluate. Optimization techniques alleviates this process through an automatic procedure. However, they are mainly focused on a single discipline and a single component. Also, the exploration of the large design space made available by modern production techniques is computationally prohibitive. This leaves a large potential for improvement unexplored. Engineering simulations, indeed, require the solution of partial differential equations that absorb a huge computational effort. A typical evaluation takes a few hours of CPU time on a parallel High Performance Computing machine for example. There is a high need need to reduce the number of such simulations to the minimum. The goal of this proposal is to reduce the cost of optimization algorithms by several orders of magnitude so that overnight optimizations will be possible. The key ingredients are: 1) the gradient information for the design improvement and 2) the gradual convergence of the partial differential equations while the design improves 3) the multigrid acceleration. This project spans over optimal control, computational fluid dynamics and structural mechanics. Success will be measured reducing the design time of turbomachinery components, an extraordinary showcase for a complex, multidisciplinary design.

Keywords: Shape optimization, one-shot acceleration, multigrid acceleration, 3D grid generation, adjoint

COMPRESSOR AERODYNAMICS &

HEAT TRANSFER

Numerical characterization of a HP compressor stage equipped with a closed shrouded stator cavity

Cedric Babin

Turbomachinery and Propulsion Department, von Karman Institute for Fluid Dynamics, Belgium, cedric.babin@vki.ac.be

Supervisor: Fabrizio Fontaneto

Associate Professor, Turbomachinery and Propulsion Department , von Karman Institute for Fluid Dynamics, Belgium, fontaneto@vki.ac.be

University Supervisor: Xavier Ottavy

Head of Turbomachinery Department - LMFA , Ecole Centrale Lyon, France

Abstract

In axial compressors, shrouded stator cavity flows are responsible for performance degradation due to their interaction with the power stream. The present paper aims at exploring the possibility of employing a single stage high pressure axial compressor as a test vehicle for cavity flows investigations. In a first step, the robustness of the adopted RANS approach is tested against experimental data on the closed-cavity baseline configuration (i.e. no downstream-to-upstream recirculation). In a second phase, the effect of different hub cavities layouts of different levels of realism is numerically investigated. The focus is set on the representativeness of a closed cavity configuration with injection. The cavity flow topology and impact on the overall performance are considered in the analysis. At its final extent, this paper provides numerical and experimental guidelines for the robust assessment of cavity flows topology and performance effects.

Keywords: leakage flows, cavity flow, axial compressors, technological effects, shrouded stator.

1. Introduction

In classical turbomachinery components, performance degradation arises from the leakage flow generated at the interface between stationary and rotating parts. This effect is generally avoided by preserving a minimum operational clearance between them. In the case of stator rows, designers have the option of either cantilevered or shrouded blades [1], [2]. With shrouded stators, clearance is preserved under the hub platform, at the interface with the rotor shaft through labyrinth seals, as illustrated in the Figure 1. Since axial clearance must also be ensured, the static pressure increase generated by the stator row drives a flow recirculation from the trailing edge region towards the leading edge. The so called leakage flow or cavity flow is proportional to the seal tooth clearance [3].

Cavity flow was the object of several investigations in the literature. It can be simplified through three quantities that are (1) the leakage fraction (Lf) that is the ratio of mass flow recirculating to the main channel one; (2) the swirl ratio that represents its tangential velocity component over the disc speed at same radius; (3) the increase of cavity flow total temperature due to viscous effects, so called windage heating. As far as topology is concerned Wellborn [5] highlighted that the upstream and downstream cavity trenches are characterized by similar flow structures. In these areas, a trench vortex is normally generated and drives the viscous interaction with the main stream flow.

The proximity of the blade row to the axial clearance trench is responsible for the generation in that region of ingress and egress regions in the pitch-wise direction [5], [6], [7]. In particular, Demargne and Longley [6] highlighted the pitch-wise modulation of the upstream trench flow structures as a consequence of the stator potential effect at multiple leakage fraction levels. It was found that for small recirculating mass flows, a localized ingestion of main stream takes place at mid-pitch.

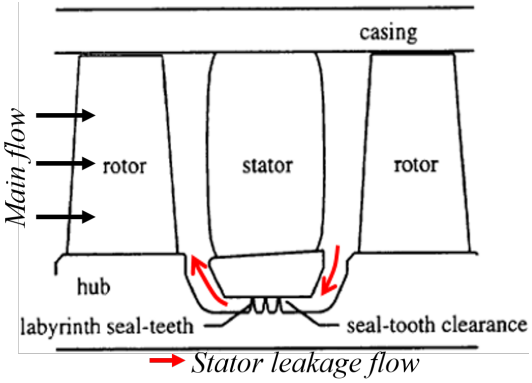

Figure 1: Shrouded stator configuration (adapted from [4]).

Wellborn and Okiishi [4] and Mahmood and Turner [8] confirmed the linear dependency of the leakage fraction with respect to the rim seal gap value. Heidegger et al. [9] and Demargne et al. [6] discussed that, at fixed wheel speed, a higher leakage fraction leads to a lower total temperature increase through the seals and to a reduction of the tangential velocity in the cavity, providing a higher trench exit radial velocity. On the contrary, a higher wheel speed would lead to a more homogeneous tangential velocity distribution at the trench exit section, at the expense of a higher windage heating generation in the rim seals region.

At the trench exit section, the cavity flow is injected into the main stream with a radial and a tangential velocity component. Demargne and Longley [6] concluded that both velocity components directly affect the inlet boundary layer skewness through axial and tangential boundary layer momentum thicknesses. In that extent, the radial velocity is responsible for a reduction of the main channel axial velocity magnitude in the proximity of the trench exit. In particular, the results of Heidegger et al. [9] suggest that, depending on the value of the ratio of the cavity flow radial momentum to the main stream axial one, the cavity flow can either be diverted towards the hub or further penetrate into the power stream. This leads to a localized stator incidence variation as high as 20 []. Generally speaking, all the authors agree in limiting the radial extension of these phenomena to the bottom 20% of the blade span.

The impact of cavity flows on the stage performance was found to be proportional to the leakage fraction. Wellborn and Okiishi [4] first and Mahmood and Turner [8] after, computed a 3% pressure rise penalty and a 1% stage efficiency drop for every 1% increase in rim seals clearance, meaning that shrouded stator cavities effects are as important as tip clearance effects on the overall performance of a compressor stage [2]. Cavity flow directly affects the downstream blade secondary flow system. Aerodynamic losses due to the shroud cavity are generated by the entrainment of the cavity low momentum flow into the hub corner vortex, as a consequence of the end-wall cross-flow [4], [10], [11]. Ozturk et al. [12] and Wellborn [5] discovered how then a fraction of the cavity flow can be re-ingested in the downstream trench, leading to multi-passage windage heating losses that count for 30% of the overall stage loss [13].

The majority of the aforementioned publications rely on specifically designed test sections allowing for experimental access to the flow region of concern. The present paper, on the contrary, aims at investigating at which extent, an existing single stage high pressure axial compressor equipped with closed cavities (i.e. no downstream-to-upstream recirculation), can be efficiently employed to assess the effect of cavity flows on both, stage performance and cavity-to-main stream interactions. The investigation relies on RANS simulations. In a first step, a detailed grid sensitivity analysis is carried out together with a precise validation on experimental data, ensuring the effectiveness of the methodology in properly assessing the cavity flow topology and its impact on the stage performance. In a second phase, a study is performed on the effect of different cavity layouts, featuring a realistic recirculating cavity and a closed cavity configuration with injection at the rims location. The outcome of this analysis will directly drive the design modification of the test section and the definition of the instrumentation to be commissioned. In the end, further conclusions will be drawn on the effectiveness of RANS in capturing cavity flow features, also at small leakage fraction levels.

2. Test section and experimental setup

All the tests were performed in the VKI high speed axial compressor rig R4 (Figure 2). It is equipped with a speed-controlled DC motor delivering a maximum power of 650 [kW] at a rotational speed of 1000 [RPM]. The drivetrain consists of a 12:1 gearbox and of a precision torque meter also providing the measurement of the rotational speed by means of a phonic wheel. The test section discharges the flow into a large collector (B) connected to the inlet plenum (D) by means of the return duct (C). The inlet plenum hosts the precision throttle valve (E) and the exchanger (F).

The former is actuated by a position-controlled stepper motor ensuring a resolution of about 0.1 [mm] and it is equipped with a fast-opening anti-surge valve. The latter consist in two multi passage tube heat exchangers connected in series in a countercurrent arrangement and delivering controlled temperature conditions at the test section inlet, with an accuracy of +/- 1[K]. Eventually, a smooth convergent bell-mouth (A) gently guides the flow from the reservoir to the test section. The performance of the stage (H25) was measured by continuously adjusting the throttle valve (E) from choked to near-stall operating conditions.

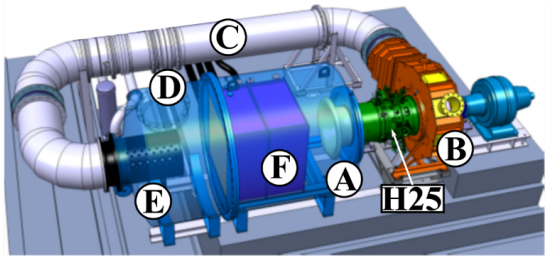

Figure 2: The VKI closed-loop high speed compressor facility R4.

The LEMCOTEC H25 test section is a single stage axial compressor representative of the last stage high pressure compressor for a high overall pressure ratio engine. The main design parameters are reported in Table 1. The shrouded stator vanes hub and tip fillet radii are equal to 10% of the span.

Table 1: Main design parameters of the LEMCOTEC H25 stage

Design Parameter	Value
Blade height [mm]	25
Hub to tip ratio	0.90
Blade count Rotor/Stator	65/80
Average tip gap in rotation	<2% span

Figure 3 reports a cross-section of the H25 stage. Marker C1 and C2 identify the stage inlet and rotor-to-stator hub cavities respectively. As visible, a rim seal labyrinth isolates C1 from the volume A while a second rim seal labyrinth seals C2 with respect to the downstream cavity B. The upstream and downstream volumes are isolated from the exterior and, during operation, they are pressurized / depressurized directly through the rim seals. When an even pressure is reached between the hub cavity and the related volume, mass flow nulls and the hub cavity fully operates

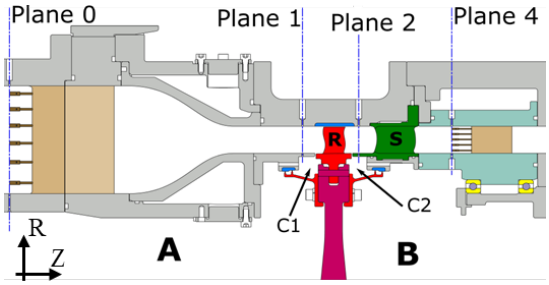

Figure 3: Cross-section of the LEMCOTEC H25 test section.

in closed conditions. In the end, it is worth to mention that the fastening bolts for the metallic lips generating C1 and C2 are placed in volume A and B respectively. In that extent, they do not affect the flow field generated in the hub stator cavities.

Five 6-heads Kiel rakes are placed at the test section inlet (Plane 0), featuring combined total pressure and total temperature measurements. At the exit plane (Plane 4), five 5-heads Kiel total pressure rakes and five 5-heads Kiel total temperature rakes are present. Radial probe traversing is made possible in Plane 0 to Plane 2 (see Figure 3) by means of casing access points at several azimuthal positions. The Plane 4 traversing system does provide both radial and azimuthal traversing capabilities over a 1.5 stator pitch. Ten hub and casing static pressure taps are present in each measurement plane. In Plane 1 to Plane 4, they are azimuthally distributed to cover an entire stator pitch. Probe traversing was always performed at constant throttle and initiated after several minutes of stabilization. In-house miniaturized 3-hole pneumatic pressure probes have been employed to retrieve the span-wise distribution of total pressure and blade-to-blade flow angle. The spatial resolution of the probes coincides with the pressure taps diameter and is equal to 0.3 [mm] while, when fully immersed, the blockage induced by one single probe corresponds to 0.6% of the overall flow cross section in the worst case scenario (Plane 4). All the employed 3-hole probes have been angularly calibrated between 26 [] with an angular step of 1[], the Mach number range was spanned form 0.08 up to 0.5. The holes re-phasing correction was taken into account to maximize the measurements accuracy within steep gradients [14]. The total temperature span-wise distribution was obtained by a traversing an in-house 1 [mm] in external diameter Kiel total temperature probe. The probe recovery factor dependency on the Mach number and the angular insensitivity range were measured through an adi-

abatic calibration in the VKI C4 facility [15]. As for the 3-hole probe, the maximum immersion blockage is equal to 0.6% of Plane 4 cross section. All the measurement devices were sampled at 2 [Hz], forcing to limit the range of the investigation to conditions far enough from the stall-inception point. The fully propagated total and static pressure uncertainties are, in the worst case scenario (Plane 0), equal to 3.2% and 3% of the dynamic pressure respectively, leading to an uncertainty of 1.0 [] on the evaluation of the flow angle. The total temperature uncertainty was computed to be equal 2.5% of the total temperature ratio. The total-to-total pressure ratio related uncertainty budget was estimated to be lower than 1% while the mass flow and the isentropic efficiency uncertainties are equal to 2.1% and 4% for a near-stall operating condition.

Tests have been performed at controlled ambient inlet conditions. The overall performance was investigated from choking conditions up to near stall operation for the design rotational speed (100Nn). The latter was defined on the base of numerical simulations performed by Safran Aicraft Engines. Detailed flow surveys were carried out at two relevant operative points: the LL (low loading) point is an intermediate operating point between choked and design conditions, while the DL (design loading) operating point corresponds and the actual stage design point.

3. Numerical setup

The numerical setup presented hereafter was designed to provide as high as possible geometrical fidelity with respect to the real stage. The numerical domain shown in Figure 4 extends between the experimental Plane 0 and two rotor mid-span chords downstream of Plane 4. In the simulations, the hot geometries (i.e. in rotation) of the blades are used and the associated rotor tip gap is set to the averaged measured value. Hub and tip fillets have been preserved in the numerical domain because of their crucial role on the flow field definition in the area of interest for cavity leakage flows. The previously introduced C1 and C2 cavities are considered in the baseline domain. One blade passage per row is computed. The connection between the rotor and stator row is ensured by a mixing plane approach. The patches are linked with conservative coupling by the pitch-wise row method. The mixing plane is located between the rotor trailing edge and the C2 connection with the main channel. Matching connections are used between cavities and main channel to allow better characterization of the flow exchange at their interface and to detect pitch-wise non uniformities.

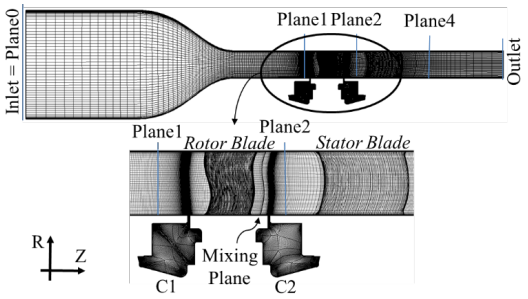

Figure 4: Meridional view of the finest grid for the baseline numerical domain.

The mesh is made with Autogrid5 and IGG software. A multi-block structured mesh approach could be chosen given the geometrical simplicity of the test section cavities. An O-4H mesh topology is used for both blade rows. The rotor tip gap region is meshed with O-H topology and contains 22% of the rotor row stream wise number of points. The blade fillets are generated using a B2B section offset method. With this method, a 50 [] minimal angle rule allows a good balance between skewness level and number of cells consumption in these regions of the mesh. In order to perform multigrid computations, three grid levels are built (Fine grid, Medium grid, Coarse grid) with respectively around 28 million, 3.6 million, and 0.5 million surface cells for the whole domain. The grid point balance (ratio between number of points in the cavity over the one of the associated row) is 0.75 in the rotor row and 0.87 in the stator row. When considering C1 and C2, a non-dimensional wall distance (y+) in the order of 1 must be targeted to ensure a correct evaluation of the wall shear stress and its associated effects on the total temperature field. Average y^+ values are summarized in Table 2.

Figure 5 illustrates the different variations of the baseline numerical domain employed within the present study. The closed cavities configuration (CC - Figure 5a) coincides with the previously described baseline case and represents the ideal condition where the mass flow recirculation falls into the numerical mass flow conservation uncertainty (e.g. high sealing performances). The opposite condition corresponds to the natural cavity case (NC - Figure 5b) which was specifically designed to provide the H25 stator with the worst sealing performances. The natural recirculation cavity is built from the C2 cavity with a symmetry around stator stacking axis and it features a one

rim seal configuration with a 0.8% gap to span ratio (cold R4 facility seal gap). In the end, the no cavity case (NOC - Figure 5c) helps in assessing the relevance of the other domains. Main channel refinement is independent from the cavity layout selected.

Table 2: Non-dimensional wall distance for the fine and medium grid.

y^+	Fine Grid	Medium Grid
Full domain average	0.391	1.005
Average in C1	0.331	0.490
Average in C2	0.850	1.240

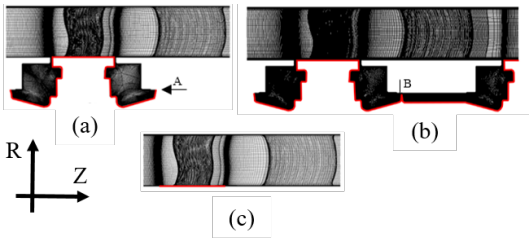

Figure 5: (a) Closed cavities configuration (b) Stator natural recirculation (c) No cavities configuration - (rotating surfaces in red).

Numecas Fine/Turbo steady compressible RANS solver is used to run fully turbulent computations. The closure problem is solved using the two equation k-w SST turbulence model of Menter [16]. This model was chosen as the best compromise for complex flow and free shear flow prediction as for example illustrated in Bardina et al. [17].

Experimental boundary conditions have been employed. At the inlet (Plane 0), the measured azimuthally averaged total temperature and total pressure profiles are imposed while, at the outlet plane, a radial equilibrium condition is used which was set on the mid-span static pressure value. The value of the static pressure at the outlet is set so that numerical and experimental results can be compared for the same static to total pressure ratio (Π_{ST}_04). This condition has been selected as the cavity flow is driven by the static pressure increase in the stator row. The walls in the simulation are considered as adiabatic.

4. Grid sensitivity

Given the crucial role that numerical simulations have in the accomplishment of the papers objectives, care has been taken in precisely assessing the capability of the aforementioned numerical setup in predicting the cavity flow effects on flow field and overall performances. In that extent, a grid sensitivity analysis must be performed to evaluate the impact of the domain spatial discretization on the computed quantities. This becomes even more justified when considering that the cavity region calls for high cell counts. The grid convergence index (GCI), introduced by Roache ([18], [19]) and recently standardized in Celik et al. [20], was adopted at such extent. The method targets the conservative evaluation of the spatial discretization related uncertainty of computations, so that the impact of the selected mesh could be automatically damped in the final result.

The GCI approach requires at least three different grid levels to be generated and gives the relative difference between the CFD computed quantities and their asymptotic numerical value from the Richardson extrapolation. The GCI evaluation is more accurate with grids that are matching in terms of structure and with a homogeneous coarsening between them. In that extent, the three grid levels introduced previously suit well the required conditions. The grids are generated by an isotropic coarsening from the finest mesh in the 3 directions (i.e. 1/8th size ratio between each grid level). In conclusion, the solutions obtained must be in the asymptotic range of convergence to guarantee a correct evaluation of the GCI.

In the present study, the mesh sensitivity on quantities such as the isentropic efficiency (η_s_04), corrected mass flow (W_R) and total-to-total pressure ratio (Π_{TT}_04) have been considered. Table 3 presents the GCI values for the aforementioned quantities for both the fine and the medium grids. It also shows that the isentropic efficiency is the most sensitive quantity to the grid refinement, with an increase from 1% to 4.55% in GCI between the finest grid and the medium grid. It is important to note that the isentropic efficiency evaluation is more precise between the Plane 1 and Plane 4 rather than between the Plane 0 and Plane 4. This can be inferred to the presence of the convergent between the Plane 0 and Plane 1 (as showed on Figure 4) which, by common practice, corresponds also the coarsest mesh region. From the rotor inlet (Plane 1) and downstream, the mesh quality allows to reduce the discretisation error by a factor 2 for the aforementioned quantity.

The grid effects on the azimuthal mass averaged isentropic efficiency profile are shown on Figure 6. By doing so the most sensitive quantity, the areas of the mesh mainly affected by the grid density are directly

highlighted. Beside the poor result of the coarse grid, the medium and the finest grid are in good agreement far from the endwalls. This suggests that the overall mass averaged performance will be well captured by both grid levels, still exhibiting a strong spatial discretization dependency in the flow field region of interest to the present analysis (hub region). As a consequence, the finest grid will be employed in the following sections.

Table 3: Grid Convergence Index for the fine grid (GCI_{fine}) and for the middle grid (GCI_{medium}).

	GCI_{fine} %	GCI_{medium} %
η_s_04	1.00	4.55
η_s_14	0.50	2.47
Π_{ST}_04	0.01	0.02
Π_{TT}_04	0.04	0.24
W_R	0.30	2.24

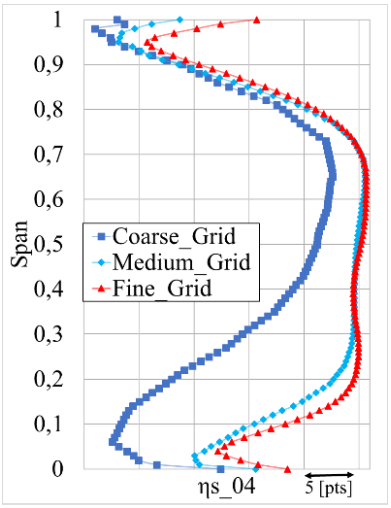

Figure 6: η_s_04 Azimuthal averaged profile for the three grid levels.

5. Numerical results validation

The comparison between the experimental and numerical setup is made at first on global performance. Figure 7 shows that the RANS approach is capable to properly capture the static-to-total compression ratio evolution over the selected operating range while overestimating by 1% to 2% the value of the isentropic efficiency. In order to provide a more detailed validation, a plane-by-plane approach is used in the following section. The comparison in each plane between the experimental and numerical data at DL operating conditions serves multiple purpose:

- In Plane 1, the ability of the simulation to generate the correct boundary layer profile at the rotor inlet is assessed;
- In Plane 2, measurements help validating the stator row inlet conditions;
- In Plane 4, thanks to the more complete experimental setup, the ability of the numerical setup in correctly identifying the flow field detailed features is checked.

Figure 8 shows the total pressure profile in the Plane 1 (rotor inlet). The main difference between the two approaches is a thicker boundary layer at the hub for the CFD case.

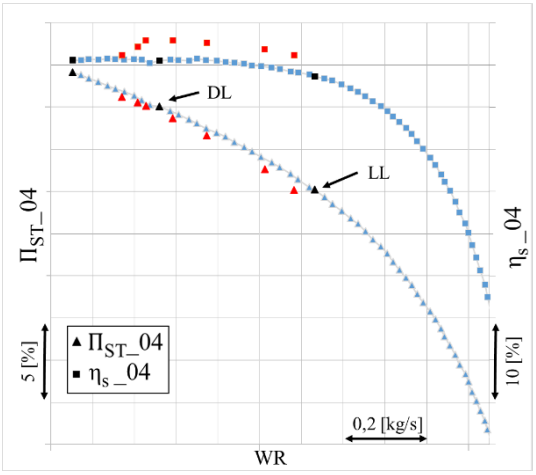

Figure 7: Experimental (Blue) vs CFD (Red) Performances at nominal speed.

The total pressure and absolute flow angle radial distributions in Plane 2 are plotted in Figure 9a and Figure 9b respectively. In particular, the experimental results there presented correspond to the average of two different measurements performed in as many azimuthal locations while the numerical data are pitchwise averaged. As a matter of fact, part of the discrepancies are therefore related to the poor spatial sampling of the experimental data. As previously mentioned, simulations have been run by imposing the average tip gap size measured by means of rubbing gauges. Given the small size of the H25 stage, this

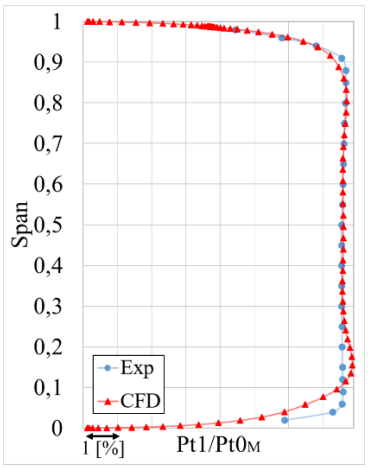

Figure 8: Stage inlet (Plane 1) - Absolute total Pressure (DL).

parameter is thought to provide an important impact on the solution, partially justifying the mismatch between numerical and experimental data in the upper part of the blade span (h > 0.7). Moreover, that the adoption of a mixing plane at the rotor exit acts as an interruption of the stream-wise mixing taking place upstream of the rotor-stator interface (see Figure 4). As a consequence, further downstream at the measurement plane location, higher losses are expected in the measurements rather than for the numerical results, as indeed shown in Figure 9a close to the endwall regions. In general terms, the average total pressure ratio matches within 1% in the freestream conditions while, in the low span region, the flow angle shows an even higher validation rate, providing confidence on the prediction as far as the stator row inlet conditions are concerned.

The traversing system of Plane 4 featured both, radial and tangential traversing capabilities, allowing to treat the data in terms of mass averaged radial distributions. The total temperature distribution on Figure 10a demonstrates that, in the freestream region, CFD results are within the experimental uncertainty. In the endwall region, the best agreement comes in the low span region where CFD results fall beyond the experimental uncertainty range by less than 1 [K]. Still, discrepancies can also arise as a consequence of the choice of an adiabatic boundary condition. As an example, the evident mismatch in the tip region can be justified by the aforementioned consideration: through the outer casing of the facility, heat is transferred to the laboratory environment, leading to the generation of a gentler temperature radial gradient, directly impacting on the predicted efficiency value. Still, the very high agreement in the low span region (T < 1%) supports the choice of the aforementioned boundary condition for the hub and gives confidence on the capability of the present numerical setup in predicting relative performance variations due to different cavity conditions. The flow angle measurements in Figure 10b has the highest relative uncertainty, implying that numerical predictions tend to fall within the confidence interval. Nevertheless, the agreement with the experimental data in the region of interest (lower span) is high. While at casing the flow angle magnitude is well captured by numerical simulations, the radial organization of the flow is not properly predicted, with more than 10% discrepancy between corresponding features (e.g. overturning peak around 0.75 and 0.90 in Figure 10b). The poor prediction close to the endwalls has also to be put in perspective to the variation of the stator inlet conditions induced by the presence of the mixing plane as rotor-stator interface.

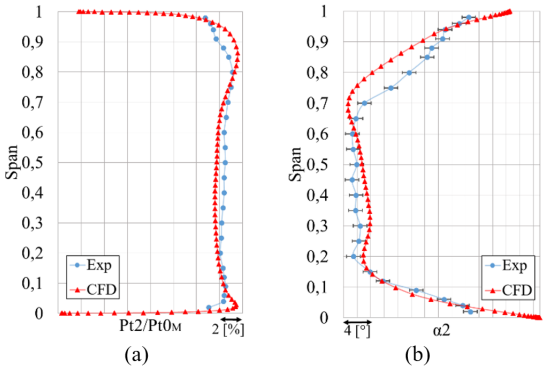

Figure 9: Stator Inlet conditions (Plane 2) - (a) Normalized total Pressure - (b) Absolute flow angle.

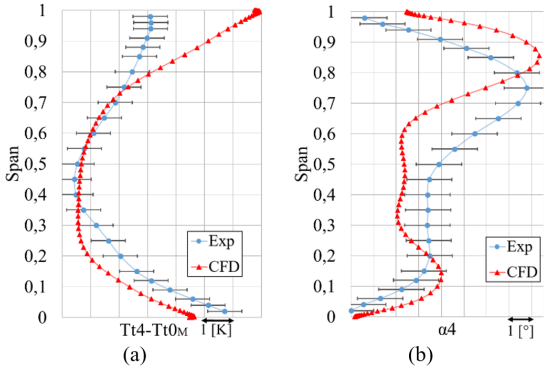

Figure 10: Stator outlet conditions (Plane 4) - (a) Total Temperature - (b) Absolute flow angle.

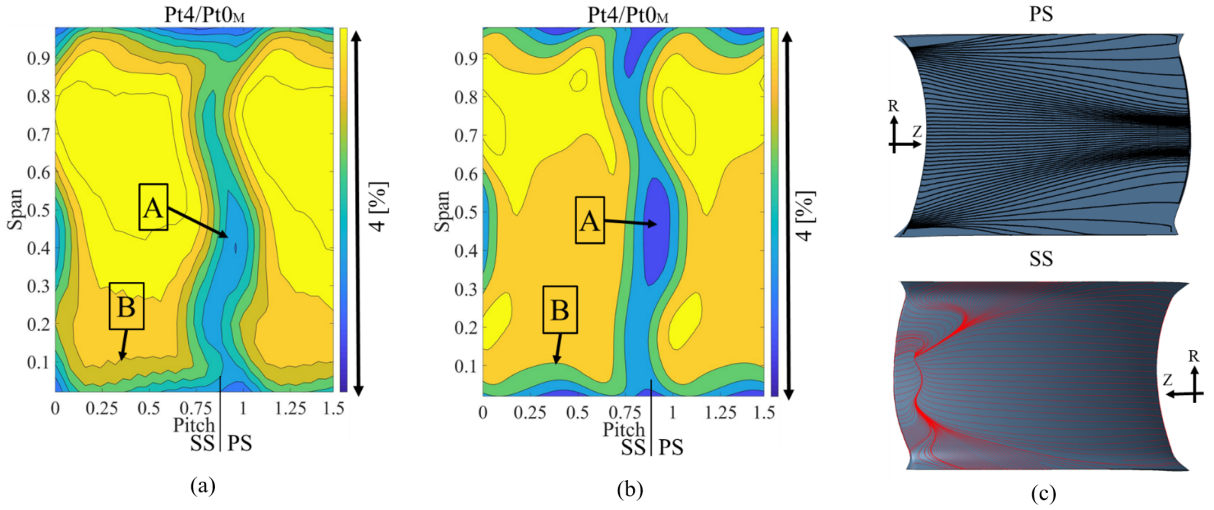

Figure 11: Normalized total Pressure map at design operating conditions - (a) Experimental data - (b) CFD - (c) Numerical friction lines on blade Pressure side Suction side (profile not to scale).

On Figure 11, the normalized total pressure map of both experimental (a) and CFD (b) data are presented. The magnitude of the total pressure difference at stator outlet remains under 0.8% of the pitch-wise averaged values (not shown here). The width of the wake (A) is correctly detected by the CFD. However, the RANS approach over-predicts the wake depth. In this position, the numerical data also show a radial thickening of the wake which results from the strong streamline contraction on the stator pressure side (cf. Figure 11c - PS). In the end-wall region, the wake signature is well described by both numerical and experimental data. Because of the presence of large blade fillets and of the forward-swept design of the H25 stator, no clear corner flow structure can be identified [21], while the suction side shear lines (cf. Figure 11c - SS) describe the accumulation of low momentum fluid at the trailing edge location. The Lei criterion [22] diffusion parameter for the design operating condition was computed to be equal to 0.17, a value in complete agreement with both the computed and measured flow topologies. The passage vortex is clearly identified in the middle of the blade passage on the CFD RANS data (marker B in Figure 11b) but no clear signature of its presence can be evinced in the corresponding experimental data.

6. Cavity flow detection

Kato et al. [13] showed that cavity windage heating is responsible for up to one third of the stage efficiency drop. Given its crucial role in the determination of the overall stage performance, the adopted numerical approach must therefore ensure its correct evaluation. As shown in Figure 12 , the cavity flows total temperature distribution experiences up to 30 [K] increase with respect to the local main stream level, the latter being a consequence of the shear work generated by the cavity rotating surfaces. Even though numerical results are in agreement with literature [8], [9], field and wall temperature measurements are not available to conclude on the CFD approach ability in correctly predicting shear work within cavities.

Leakage flow impact on the stage performance is at a large extent dependent on the flow field generated in the last part of the trench. The main driver is the trench vortex generated at the cavity/main channel connection as it defines the local leakage flow angle in both the axial and the tangential directions, being its span-wise and azimuthal position dependent upon downstream blade potential effects and local leakage fraction (i.e. the local mass flow crossing the trench inlet section). In Figure 13, the averaged azimuthal streamlines in C1 and C2 trenches show that the trench vortex (1) occurs also in the closed cavity condition, rotating accordingly to the main flow direction. Even if both cavities share the same geometry, the flow topology in the deep cavity region differs between C1 and C2. In particular, C1 is characterised by the generation of an intermediate vortex between the trench (1) and deep cavity (2) vortex, while C2 only exhibits a two counter-rotating vortices structure.

The root cause of the aforementioned differences is

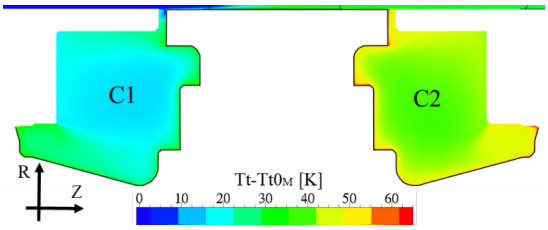

Figure 12: Total temperature distribution in C1 and C2 - Design operating point - (rotating surfaces in black).

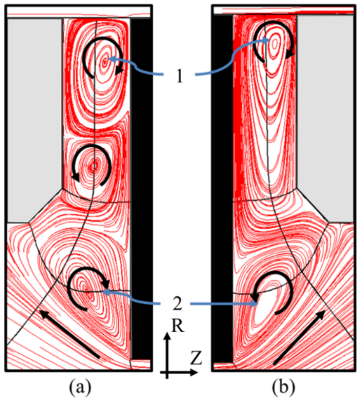

Figure 13: Cavity/main channel interaction vortices - Azimuthally averaged streamlines - (a) C1 trench; (b) C2 trench (rotating platform in black).

linked to the proximity of the rotor row and stator row to C1 and C2 respectively. Figure 14 shows the radial velocity profile at the exit of each trench (0% span). As visible, the rotor row is located right downstream the C1 trench, generating a strong potential effect that drives the generation of ingress / egress regions as large as half of the rotor pitch. The results of Demagne et al. [6] for the 0% leakage fraction case confirm this finding. The stator leading edge plane is located one axial chord downstream the rotor row. As a consequence, no potential effect linked to the stator leading edge reaches the C2 trench, leading to an azimuthally homogeneous radial velocity distribution: ingress and egress regions are axially aligned. The latter analysis highlights the crucial role of the blade blockage effect on the generation of the cavity pattern, but it also suggests that C2 is a good candidate when the role of the cavity geometry only on the leakage flows topology and on the performance impact is of concern. In the end, from a numerical point of view, the latter analysis indicates that C2 data can be properly identified through azimuthal averages, at least when RANS results are considered.

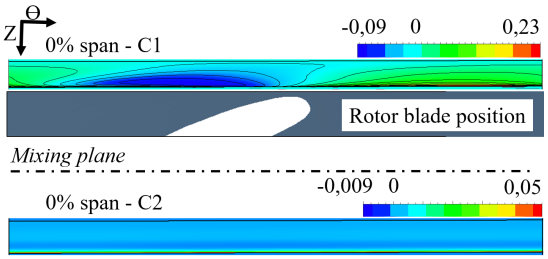

Figure 14: Normalized radial velocity profile (V_r/U_{hub}) at cavity/main flow interface (0% span) Streamwise proportions are not respected for compacity purposes.

7. Performance impact of closed cavities

The representativeness of the closed cavity (CC) configuration is checked against the more realistic case of a natural cavity layout (NC), with the final aim of defining realistic reference leakage conditions to compare with the CC case with injection at the rims location. By means of this analysis, guidelines for forthcoming experiments and facility modifications can be outlined. This study is carried out for two operating points, LL and DL. The no cavity (NOC) configuration serves as reference.

Table 4 summarizes the effects of the cavity layout on the isentropic efficiency and the entropy generation of the stage. Two conclusions can be made. The first one is that closed cavities have an effect on the performance of the stage. The efficiency drop from the NOC case corresponds already to 10% of the value for the NC case, being the latter the worst case scenario. The second is that the closed cavity configuration does not exhibit any variation with the stage loading, contrary to what observed for the natural cavity layout as well as in literature [4]. To put into context the data presented here, Wellborn and Okiishi [4] predicts an efficiency drop of 0.9% at design condition and for the same gap to span ratio than the NC case. The presence of closed cavities has been found to induce a constant offset in efficiency for all the investigated operating conditions at constant rotational speed.

The radial profiles of isentropic efficiency on Figure 15 help understanding the contribution of the C1 cavity on the stage performance degradation for the closed cavity layout. In particular, $\eta_s 1$ only considers the effect of C1 on the rotor row by computing the isentropic efficiency between the rotor inlet and a plane before the mixing plane (so before C2 trench). The $\eta_s 2$ evaluation in Figure 15 takes into account the effect of both cavities, being the second plane located downstream the C2 trench. The reader must be aware

Table 4: Performance impact of cavity.

Config.	η_s-14 LL	η_s-14 DL	Δ_s-14 LL	Δ_s-14 DL
NOC	*Ref*	*Ref*	*Ref*	+2.89%
CC	-0.10%	-0.11%	+1.51%	+4.04%
NC	-0.83%	-0.71%	+8.18%	+9.33%

that the comparison between the η_s1 and η_s2 profiles is biased by the presence of the mixing plane between the rotor trailing edge and the C2 trench. All the distributions confirm that cavity flows are localized in the bottom part of the span, with identical span-wise evolutions from 30% on. A 2% penalty between the CC and the NOC layouts is visible in correspondence of the 5% to 10% of the blade span for the η_s1 case and it represent the impact of C1 on the rotor row performance. The same trend is visible also for the η_s2 case where the presence of C2 appears to be the responsible for a radial migration of the efficiency peak (from h=15% for η_s1 to h=20% for η_s2) and, in general, lower efficiency values in the low span region.

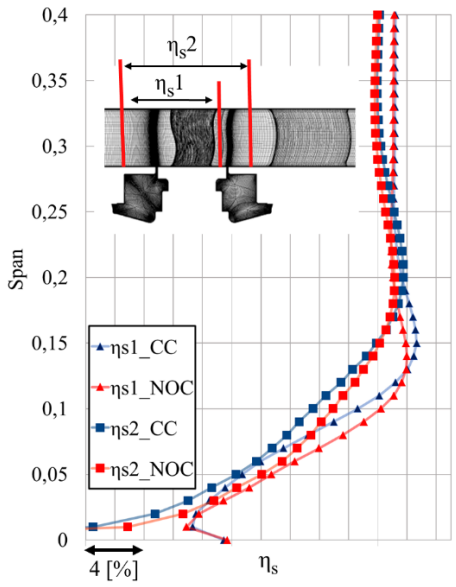

Figure 15: Azimuthal averaged Isentropic efficiency - closed cavities vs no cavities at DL operating conditions - (η_s1) Rotor blade row with C1 only - (η_s2) Rotor blade row with C1 C2.

Due to the presence of the cavity, local incidence variations are generated at the stator inlet. As presented in Figure 16a, an increased incidence condition develops for both the closed cavity and the natural cavity layouts in the bottom 15% of the blade span, with the NC case providing a monotonously increasing stator inlet flow angle towards the end-wall. The latter is mainly related by the blockage induced by the cavity flow, as shown by the axial velocity profiles in Figure 16b in the low span region. As a consequence, flow is accelerated away from the endwall (¿15% span), which explained the local decrease in stator incidence. Small freestream incidence variations are attributed to shifts in operating point from the mass flow not being imposed in the CFD computations. The swirl ratio in Plane 2 is shown Figure 16c. Its definition is given in Equation 1, where V_t is the tangential velocity, r is the radius at which it is computed and ω is the rotational speed of the wheel.

$$\phi = V_t/\omega \qquad (1)$$

The cavity leakage flow generates blockage in the tangential direction. In the bottom 4% of the span in Figure 16c, the NC case is characterized by lower tangential velocity component than the close cavity configuration. As for the axial velocity profile, this trend is inverted at higher span-wise locations (4% < r < 20%), with the peak swirl ratio migrating towards mid-span for a higher leakage mass flow. For the NOC case, the stator platform is elongated over the trench region thus locally imposing no leakage flow so no radial component and a 0% trench exit swirl ratio. As a comparison, the CC case shows an average trench exit swirl ratio of 68%. That is why, at the measurement location for Figure 16c, the NOC swirl ratio is lower than in the CC case. The total temperature radial distribution shown Figure 16d well highlights the shear work generated within the cavity region. The effect of the hot leakage flow ejected from the cavity is visible up to 20% of the span for both CC and NC cases. The higher total temperature levels computed for the natural cavity layout are not only justified by the extra shear work generated in stator downstream cavity (see Figure 5b), but also due to multi windage effect of recirculating hot streaks (i.e. multiple passes in the NC) that RANS is nevertheless able to capture (not shown here).

With the local incidence variations at stator inlet, the cavity flow has an impact on the secondary flow system in the blade passage. The core of the passage vortex is highlighted in red on both Figure 17a and Figure 17b for the CC and the NC layouts respectively. The generally higher tangential velocity level

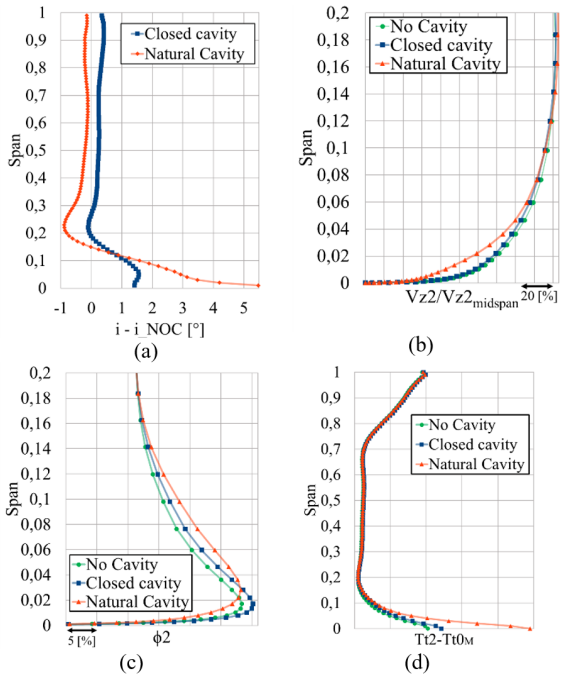

Figure 16: Stator inlet conditions at DL (Plane 2) - (a) Relative incidence to no cavity case - (b) Normalized axial velocity - (c) Swirl ratio (d) Total temperature ratio.

suggests a growth of the passage vortex with the leakage flow. Furthermore, from the entropy increase in the end-wall region (marker A), it is possible to locate the leakage flow that has been diffused within the stator passage, directly contributing to the secondary loss item where the cavity flows effect is lumped.

8. Leakage flow effect on C2 flow and H25 stage performance

In this section, the effect of different leakage flow conditions in C2 are investigated in order to understand their impact on the C2 flow topology as well as on the H25 stage performance. The choice of the leakage fraction as first order parameter comes after the study of Heidegger et al. [9] who identified in this parameter the most affecting cavity flow quantity for the stage performance at fixed wheel speed. The following results are obtained by performing controlled injection at the station A in Figure 5a for both LL and DL operating points. The reference conditions for the injections are taken from the natural cavity case at the outlet of the seal (station B on Figure 5b). The reference leakage is representative of the NC case as far as leakage conditions are concerned.

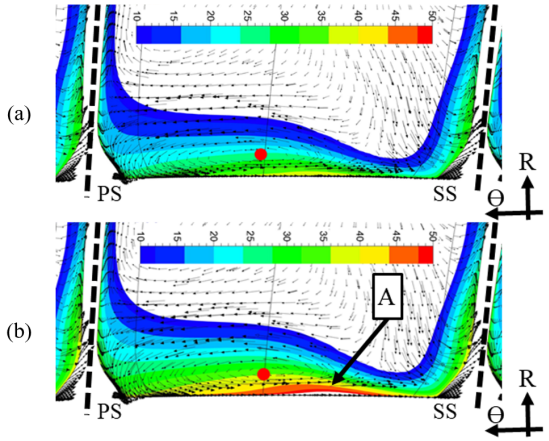

Figure 17: H25 Stator trailing edge 0.77 $Cax_{midspan}$ - Vector field of normalized tangential velocity, contours of entropy - (a) Closed cavity - (b) Natural cavity.

The C2 flow features tracked within the present analysis are defined as in Figure 18 and consist in the C2 main and secondary core vortices. The main core tracking point is fixed at -42% of the span, while the second core is tracked along its evolution with the leakage fraction. The cavity outlet conditions are also considered in the present study.

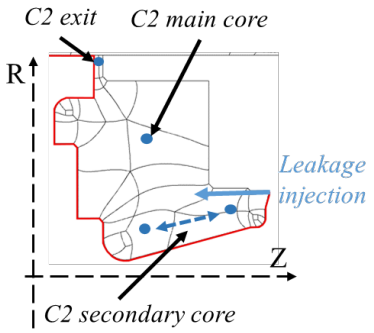

Figure 18: Points of interest in C2 cavity (rotating surfaces in red).

Figure 19a shows the evolution of the swirl ratio for the main core vortex and the secondary core vortex associated to the flow patterns on Figure 19b. The swirl ratio provides an information on the intensity of the tangential speed with respect to the disc speed. The secondary vortex swirl evolution presents a maximum for both operating conditions after $Lf3$. Even though a complete explanation for such behaviour is still to be found, it is clear the presence of an inflection point in the distribution depends on the position of the secondary core as well as on the leakage jet spillage:

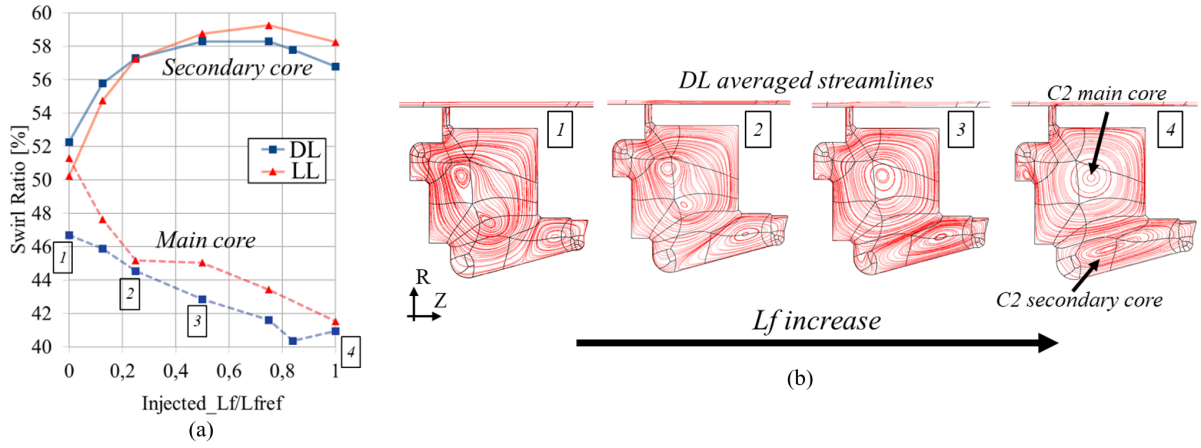

Figure 19: C2 flow topology - Azimuthal averaged quantities - (a) Swirl ratio - (b) C2 azimuthal averaged streamlines.

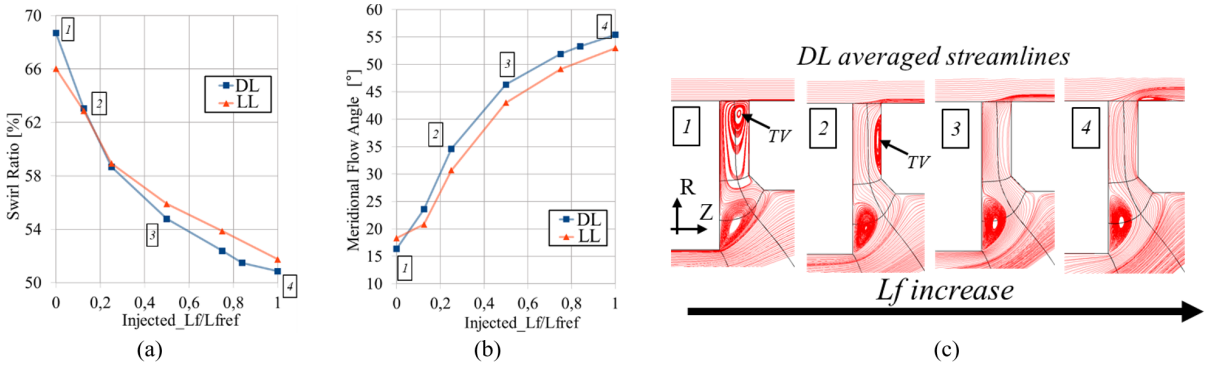

Figure 20: C2 flow exit - Azimuthal averaged quantities (a) Swirl ratio (b) Meridional flow angle (c) Streamlines at DL.

from $Lf1$ to $Lf3$ the secondary core is progressively pushed out from the injection region by the leakage jet coming from the labyrinth; between $Lf3$ and $Lf4$, the core reaches the maximum extension allowed by the local cavity geometry while the leakage jet directly spills towards the rotating surface of the main cavity volume. In both operating conditions, the tangential velocity of the main vortex decreases linearly as more mass flow is injected. At DL, a 30% increase in $Lf/Lfref$ shows a 2% decrease in swirl ratio. It is interesting to notice that on both Figure 19a and Figure 19b data, the closed cavity case ($Lf1$) remains a good extrapolation from the flow topology computed in C2 at zero leakage fraction.

Figure 20a and Figure 20b provide the evolution of the azimuthally averaged swirl ratio and meridional flow angles with the leakage fraction. Data are taken at 0% span, at the cavity-main channel junction. Swirl ratio and meridional angle have an opposite trend with respect to the leakage fraction. Indeed, for larger Lf values, the trench vortex (TV) is progressively pushed out from the cavity, in favour of a more radial flow at the exit section.

This new configuration of the trench flow is the responsible for an increased end-wall blockage, which directly implies larger meridional injection angles within the main stream. This trend, in agreement with the existing literature, is shown in Figure 20c where azimuthally averaged streamlines are employed to highlight the flow topology. Demargne et al. [6] demonstrated that high swirl ratios (as close as possible to 100%), actually reduce the performance degradation of the downstream row as cavity flow acts against blade passage cross flow. On the other hand, the increased blockage induced by a more radial ejection in the mainstream is responsible for the thickening of the end-wall boundary layer which, in turns, enhances the local incidence.

The following blade row will then exhibit stronger secondary flow, as more low momentum fluid is en-

trained in the passage vortex as a consequence of the stronger cross flow. This behaviour is thought to become even more evident with cavities under stronger potential effects (i.e. downstream blade leading edge plane closer to trench) as azimuthal non-uniformities would be reinforced by higher leakage fractions. Again, it is remarkable that at low leakage fractions, results tend toward the closed cavity case ($Lf1$). On both curves, the effect of the operating point is small in terms of quantities evolution with the leakage fraction.

Finally, the effect of the leakage flow injection in C2 on the stage isentropic efficiency is given in Figure 21. For the design operating condition and over the considered leakage fraction range, the isentropic efficiency drops with a linear trend up to 1.1%. This result is in complete agreement with the work of Wellborn and Okiishi [4]. As mentioned earlier, their study also stresses the fact that cavity flows effects are more important at higher loading operating points which is the case between the LL and DL conditions for all leakages considered in the present study. Finally, an extrapolation of the efficiency drop to zero leakage flow is coherent with the result provided by the closed cavity case.

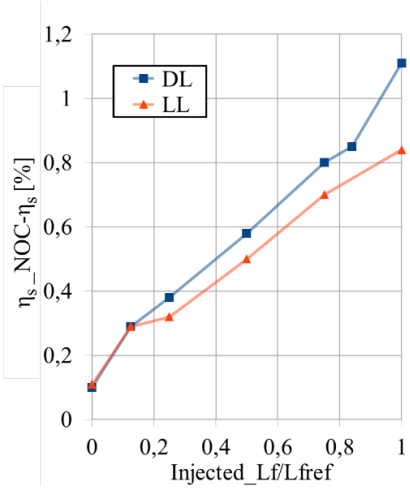

Figure 21: H25 stage isentropic efficiency drop with respect to no cavity case.

9. Conclusions

The present paper explored, under which circumstances, a single stage closed-cavities axial compressor could be employed for the assessment of the cavity flow effects on flow field and overall stage performance. The obtained numerical results demonstrated that realistic cavity flow topologies can be obtained by injecting at the rim seals location (marker A in Figure 5a). In the particular case of the present test section, an effective experimental setup can be commissioned where the injection flow is delivered to cavity C2 through the rims by pressurizing volume B (Figure 3). Still, the temperature level of the injected mass flow must be precisely controlled as a consequence of the absence of the stator downstream cavity. As a matter of fact, this conclusion enables the adoption of the single stage LEMCOTEC H25 stage for the meaningful study of cavity flow effects.

The parametric analysis on the leakage fraction effect suggests moreover that the no-cavity case (i.e. no downstream-to-upstream recirculation) can be considered as the degeneration of a natural recirculation configuration towards negligible leakage mass flow levels. On the other hand, the closed-cavities configuration was shown to be responsible for a loss increase up to 0.1% with respect to the no-cavity case. On the base of these considerations, different conclusions of general interest to the cavity design process can be readily drawn:

- Closed cavities, if present, should always be considered in the numerical domain as their effect is generally measurable and non-negligible.
- When tight seals designs are of concern, an approximated estimation of the related performance impact can be numerically retrieved by employing numerical domains featuring closed cavities. On the other hand, a more precisely evaluation can be achieved by systematically increase the leakage fraction for an injection case, allowing to extrapolate the performance to the condition of interest.
- A robust RANS approach provides enough resolution to detect cavity flow features (such as ingress and egress regions on the trench, flow topology in the deep cavity, etc.) also when the leakage mass flow tends to zero.

In the end, the present analysis shows that the effect of cavity flows for the present configuration is limited to the lower 20% of the blade span, suggesting that any experimental investigation in the main channel should make use of fine measurement meshes close to the hub end-wall. The focus should be set on the measurement of the blade-to-blade flow angle, velocity and temperature distributions towards the hub as

these parameters are the main drivers for entropy generation and secondary flow system topology changes on the downstream blade row to the cavity.

Acknowledgments

The authors would like to acknowledge Safran Aircraft Engines for supporting the investigation.

Nomenclature

Acronyms	
$C1$	*Inlet hub cavity*
$C2$	*Rotor-to-stator hub cavity*
$Cax_{midspan}$	*Mid-span axial chord*
CC	*Closed cavity layout*
CFD	*Computational Fluid Dynamics*
DL	*Design loading operating point*
GCI	*Grid Convergence Index*
h	*Blade height*
Lf	*Leakage fraction*
LL	*Low loading operating point*
	Mass flow
NC	*Natural cavity layout*
NOC	*No-cavity layout*
NR	*Thermodynamic speed*
r	*Radius*
R	*Radial direction*
Re	*Reynolds number*
TV	*Trench vortex*
W_R	*Corrected mass flow*
y^+	*Non-dimensional wall distance*
Z	*Machine axial direction / Flow direction*
Greekletters	
α	*Absolute flow angle*
η	*Efficiency*
Π	*Compression ratio*
ϕ	*Swirl ratio*
Θ	*Azimuthal direction*
ω	*Rotor wheel speed [rad/s]*
Subscripts	
M	*Quantity average*
S	*Isentropic*
TT	*Total-to-total*
ST	*Static-to-total*
i in [0, 4]	*Plane index*

References

[1] M. Swoboda, P. C. Ivey, U. Wenger and V. Gmmer, An Experimental Examination of Cantilevered and Shrouded Stators in a Multistage Axial Compressor, *ASME Turbo Expo 98-GT-282*.

[2] S. Yoon, R. Selmeier, P. Cargill and P. Wood, Effect of the Stator Hub Confguration and Stage Design Parameters on Aerodynamic Loss in Axial Compressor, *ASME Turbo Expo GT2014-26095*.

[3] R. N. Childs, Mechanical Design Engineering Handbook - Chapter 14 - Seals, Butterworth-Heinemann, 2014.

[4] S. R. Wellborn, T. H. Okiishi, Effects of Shrouded Stator Cavity Flows on Multistge Axial Compressors Aerodynamic Performance, Tech. Rep. NASA CR 135391, NASA Lewis Research Center (1996).

[5] S. R. Wellborn, Details of Axial Compressor Shrouded Stator Cavity Flows, *ASME Turbo Expo* $2001_G T_0$495.

[6] A. A. J. Demargne and J. P. Longley, The Aerodynamic Interaction of Stator Shroud Leakage and Mainstream Flows in Compressors, *ASME Turbo Expo* $2000_G T_5$70.

[7] D. R. Flores Galindo, Influence of Labyrinth Seals in Cavities on the Flow of an Axial Compressor, Ph.D. thesis, Institut fr Turbomaschinen und Fluid-Dynamik, Hannover (2018).

[8] A. A. J. Demargne and J. P. Longley, Modeling Capability for Cavity Flows in an Axial Compressor, *ASME Turbo Expo GT2017-64040*.

[9] E. J. H. N. J. Heidegger, R. A. Delaney, Stator Seal Cavity Flow Investigation, Tech. Rep. NASA CR 198504, NASA Lewis Research Center (1996).

[10] S. R. Wellborn and T. H. Okiishi, The Influence of Shrouded Stator Cavity Flows on Multistage Compressor Performance, *ASME Turbo Expo 98-GT-012*.

[11] D. W. Sohn, T. Kim and S. J. Song, Influence of the Leakage Tangential Velocity on the Loss Generation and Leakage Flow Kinematics in Shrouded Axial Compressor Cascades, *ASME Turbo Expo GT2006-90979*.

[12] H. K. Ozturk, P. R. N. Childs , A. B. Turner, J. M. Hannis and J. R. Turner, A Three Dimensional Computational Study of Windage Heating Within an Axial Compressor Stator Well, *ASME Turbo Expo 98-GT-119*.

[13] D. Kato, M. Yamagami, N. Tsuchiya and H. Kodama, The Influence of Shrouded Stator Cavity Flows on the Aerodynamic Performace of a High Speed Multistage Axial Flow Compressor, *ASME Turbo Expo GT2011-46300*.

[14] P. M. Ligrani, B. A. Singer and L. R. Baun, Spatial Resolution and Downwash Velocity Corrections for Multiple-hole Pressure Probes in Complex Flows, Experiments in Fluids 7 (6) (1989) 424–426.

[15] F. Fontaneto and A. Lahalle, Highly Reliable Aerodynamic Calibration for Ground and Flight Testing Total Temperature Probes, *XXIII Biannual Symposium on Measuring Techniques in Turbomachinery Transonic and Supersonic Flow in Cascades and Turbomachines, Stuttgart, 09-2016*.

[16] F. R. Menter, Two-Equation Eddy-Viscosity Turbulence Models for Engineering Applications, AIAA Journal 32 (8) (1994) 1598–1605.

[17] P. G. H. J. E. Bardina, T. J. Coakley, Turbulence Modeling Validation, Testing, and Development, Tech. Rep. NASA Technical Memorandum 110446, NASA Ames Research Center (1997).

[18] P. J. Roache, Perspective : A Method for Uniform Reporting of Grid Refinement Studies, Journal of Fluids Engineering 116 (3) (1994) 405–413.

[19] P. J. Roache, Quantification of Uncertainty in Computational Fluid Dynamics, Annual Review of Fluid Mechanics.
[20] I. B. Celik, U. Ghia, P. J. Roache, C. J. Freitas, H. Coleman and P. E. Raad, Procedure for Estimation and Reporting of Uncertainty Due to Discretisation in CFD Applications, Journal of Fluids Engineering 130 (7) (2008) 078001–1–078001–4.
[21] J. V. Taylor and R. J. Miller, Competing Three-Dimensional Mechanisms in Compressor Flows, Journal of Turbomachinery 139 (2) (2017) 021009–1–021009–10.
[22] V.-M. Lei, Z. S. Spakovsky and E. M. Greitzer, A Criterion for Axial Compressor Hub-Corner Stall, Journal of Turbomachinery 130 (3) (2008) 031006–1–031006–10.

Performance and stability analysis of a highly-loaded low-pressure compressor under distorted inflow conditions

Riccardo Toracchio

Turbomachinery and Propulsion Department, von Karman Institute for Fluid Dynamics, Belgium, riccardo.toracchio@vki.ac.be

Supervisor: Fabrizio Fontaneto

Associate Professor, Turbomachinery and Propulsion Department, von Karman Institute for Fluid Dynamics, Belgium, fontaneto@vki.ac.be

University Supervisor: Koen Hillewaert

Associate Professor, Aerospace and Mechanical Engineering Department, University of Liège, Belgium, koen.hillewaert@uliege.be

Abstract

Advanced aircraft technologies are currently in the focus of research to address the environmental goal of reducing aircraft emissions within the next decade and beyond. Short-nacelle geared high-bypass turbofans and Boundary Layer Ingestion (BLI) engines are among the most promising technologies to improve fuel and propulsive efficiency in the short and long term respectively, forcing nevertheless the engine to operate with a highly distorted inlet flow.

Although operability and performance deterioration of fans under distorted conditions has been the primary focus of research in last decades, almost no information is currently available on the low-pressure compressor (booster), despite its crucial role in the forthcoming generation of engines. The complex flow distortion pattern observed behind the fan will indeed influence the underlying physical mechanisms taking place within the compressor stage, possibly jeopardizing performance and stability of the whole engine.

Due to the impossibility of extending the results obtained for fans to the low-pressure compressor as a consequence of the marked aerodynamic and structural design differences, this research project aims at providing a complete characterization of the physical phenomena driving loss generation and stability deterioration in modern low-pressure compressors when distorted flow conditions set up. An axial compressor representative of the first stage of a modern geared turbofan booster will be experimentally tested with a distorted inlet flow field, while high-resolution CFD simulations will drive the design of experiments.

The assessment of global performance, stall inception and post-stall behavior will be carried out, along with detailed flow surveys to ensure a thorough understanding of the involved physical phenomena. Such extensive set of data will support the development and design of boosters for the forthcoming generation of aircraft engines.

Keywords: distorted inflow, low-pressure compressor, high-bypass turbofan, boundary layer ingestion

TURBINE AERODYNAMICS &

HEAT TRANSFER

Purge and leakage flow effects on the aerodynamics of a high-speed low-pressure turbine cascade

Gustavo Lopes

Turbomachinery and Propulsion Department, von Karman Institute for Fluid Dynamics, Belgium, gustavo.lopes@vki.ac.be

Supervisor: Sergio Lavagnoli

Associate Professor, Turbomachinery and Propulsion Department, von Karman Institute for Fluid Dynamics, Belgium, lavagnoli@vki.ac.be

University Supervisor: Koen Hillewaert

Associate Professor, Department of Aerospace and Mechanics, Université de Liège, Belgium, koen.hillewaert@uliege.be

Abstract

The ultra-high bypass ratio geared turbofan has been identified as a key engine concept to reduce emissions and noise footprint of the next aviation generation. However, the higher pressure ratio promoted by the geared engine architecture implies that the low pressure turbine (LPT) operates at transonic Mach numbers, in combination with low Reynolds number. Within this range of operating conditions, there is a short supply of detailed aerodynamic and performance measurements in high-speed LPTs operating at engine representative conditions. This shortage of relevant experimental data also concerns the impact of leakage and purge flows on the secondary flow structures development, and consequently on the high-speed LPTs loss mechanisms.

This PhD research focuses on the experimental characterization of the combined effect of endwall secondary flows, cavity purge and leakage flows and the unsteady wakes on the aerodynamics and performance of high-speed LPTs tested at engine-scaled conditions.

The three-dimensional flow effects are investigated in the VKI S-1/C high-speed linear cascade, operating at engine representative Mach and Reynolds numbers, and inflow conditions (free-stream turbulence and periodic wakes). Three cavity-airfoil arrangements are studied, representative of the purge flow emerging from the stator-rotor hub cavity and of leakage flows established between the casing and the tip of a shrouded rotor. The secondary air flow rates are also varied to understand the impact of the purge intensity on the LPT performance and three-dimensional flow structures.

The inlet and outlet 3D and unsteady flows are characterized by velocity, pressure and angle measurements by means of pitch and spanwise probe traverses. High-resolution instrumentation will measure time-average and time-resolved blade and endwall static pressure as well as quasi-shear stress by means of pressure taps, fast response piezo-resistive pressure sensors and surface mounted hot-films. This work introduces a novel technique for traversing an instrumented blade along its span, hence allowing to map with high resolution the unsteady pressure and shear stress over the blade span.

This research envisages the output of a high-fidelity database that will aid the development, tuning and validation of analytical and numerical prediction models used in the early design stages of future high efficiency high-speed LPTs.

Keywords: Geared turbofan, Low-pressure turbine, High-speed linear cascade, Purge flow, Leakage flow, Secondary flows, Unsteady wakes, High-resolution instrumentation.

Implicit Large Eddy Simulation of the high-pressure turbine vane LS89

Tânia Sofia Cação Ferreira

Turbomachinery and Propulsion Department, von Karman Institute for Fluid Dynamics, Belgium, tania.sofia.cacao.ferreira@vki.ac.be
Applied Mechanics and Mathematics, Université Catholique de Louvain, Belgium, tania.cacao@uclouvain.be

Supervisor and University Supervisor: Tony Arts

Professor and Head, Turbomachinery and Propulsion Department, von Karman Institute for Fluid Dynamics, Belgium, arts@vki.ac.be
Professor, Institute of Mechanics, Materials and Civil Engineering, Université Catholique de Louvain, Belgium, tony.arts@uclouvain.be

University Supervisor: Vincent Legat

Professor and Head, Applied Mechanics and Mathematics, Université Catholique de Louvain, Belgium, vincent.legat@uclouvain.be

Collaborators: Thomas Toulorge and Michel Rasquin

Senior Research Engineer, Computational Multi-physics Software Development team, Cenaero, Belgium, thomas.toulorge@cenaero.be
Senior Research Engineer, Computational Multi-physics Software Development team, Cenaero, Belgium, michel.rasquin@cenaero.be

Abstract

The design of more efficient gas turbines drives the demand for more engine-representative experimental databases and reliable performance prediction methods. Yet, complex flow phenomena such as boundary layer transition and combustion-representative turbulence levels are seldom well captured, specially with Reynolds-Averaged Navier-Stokes approaches, potentially leading to wrong estimations of heat transfer rates and losses.

The goal of this work is to investigate, with a highly-resolved numerical simulation, relevant high-pressure turbine test cases from an academic database that has been extensively used for numerical code validation and flow physics studies. We initiate this study by simulating the complex flow in a turbine configuration that has not yet been fully well predicted, test case MUR235 ($Re_{is,out}$ = 1.15x10^6, $M_{is,out}$ = 0.93, $Tu_{\infty,in}$ = 6%) of the VKI LS89 cascade. To achieve this, we perform an Implicit Large Eddy Simulation study through Cenaero's in-house code Argo with a discontinuous Galerkin implementation.

Preliminary numerical results for a relatively coarse mesh show a good agreement with experiments, except for the suction side region after s = 20 mm. This region requires a higher mesh resolution and a more accurate artificial viscosity implementation to handle the complex turbulence, acoustic waves, shock and boundary layer flow interaction. These improvements should allow to capture better the turbulent spot production starting from s = 20 mm as well as the shock-boundary layer interaction at $s \approx 60$ mm that renders a fully turbulent boundary layer that is not captured in this simulation.

The following step is to simulate a novel test case at similar flow conditions but at a higher turbulence intensity level ($Tu_{\infty,in} \approx 22\%$). This freestream turbulence level is closer to the one found at the outlet of the combustion chamber, and therefore, at the inlet of the high-pressure turbine stator, thus contributing to numerical studies of more engine-representative flows.

Keywords: boundary layer transition, turbulence, high-pressure turbine (HPT), Implicit Large Eddy Simulation (ILES), Discontinuous Galerkin Method (DGM)

1. Introduction

The large number of operational airplanes together with the problematic of pollution and climate change call for more and more efficient gas turbines.

The increase of the overall efficiency of such engines relies on the optimization of the Brayton cycle;

thus depending on the compressor pressure ratio and turbine inlet temperature. Concerning the latter, not only it is limited by the material proprieties and highly dependent on cooling technology, but it also has an impact on the turbine's lifetime. Excessive and transient heat loads can even lead to the catastrophic mechanical failure of turbine blades [1].

It is therefore of the utmost importance to perform accurate predictions of heat transfer rates and to have a complete understanding of the flow physics occurring in each turbine/blade configuration (under study or design).

Nowadays, even if reasonable results are available for laminar and turbulent boundary layers, the issue remains the accurate prediction of the in-between transition. Wrong estimations of transition onset and/or length can render an erroneous heat transfer profile over a large portion of a vane or blade surface. The prediction of heat transfer rates on the stagnation region is also rendered difficult under high levels of turbulence. This is most critical at the exit of the combustion chamber, where experiments characterize turbulence to be up to 30% in intensity and 3 cm in integral length scale [2; 3].

Gas turbine representative experimental databases and reliable numerical tools can help the design of more efficient blades, vanes and cooling systems that comply with their mechanical safety limits.

One example of such a database is the academic test case of a highly loaded turbine inlet nozzle guide vane, the VKI LS89 [4]. This aero-thermal experimental investigation led to the publication of vane convective heat transfer and velocity distributions for relevant high-pressure turbine (HPT) flow conditions [5]. This database remains to this day widely used in turbomachinery research [6–13], not only for numerical code validation but also, as we go towards high-fidelity numerical methods, for the underlying complex physics present in some test cases. Even if the freestream turbulence level ($Tu_{\infty,in} = 1 - 6\%$) is in the lower range at the inlet of a high-pressure turbine (HPT), some transition phenomena occurring in these experiments are intrinsically hard to simulate numerically. This test case has therefore become a challenge in the improvement of numerical prediction methods.

A recent experimental effort on the same test case provided new heat transfer results for the vane's suction side [14]. Generated freestream turbulence was closer to typical HPT levels: intensities ranged between $10 - 20\%$ with integral length scales of the order of $1 - 2$ cm. The inability of Reynolds-Average Navier-Stokes (RANS) in predicting these flows at such high turbulence levels was also highlighted, boosting the need for a high-fidelity numerical approach.

The main objective of the present work is therefore to perform highly-resolved simulations to gain insight into the experimental flows described above that represent the ones typically found in an HPT. This will allow to understand more deeply the flow physics and their effect on the heat profiles and also potential limitations in their numerical simulation.

In this paper, Implicit Large Eddy Simulations (ILES) are carried out through the Discontinuous Galerkin Method (DGM) implemented in Cenaero's in-house code Argo [15]. From the available test cases in [5], we have selected MUR235, not only due to its inherently complex flow physics, but also to serve as a starting point for a future comparison with a new test case with similar flow conditions but at a higher freestream turbulence intensity $Tu_{\infty,in} \approx 22\%$ [14].

This paper is organized as follows: first, we describe the set-up of the VKI LS89 cascade experiments and test case MUR235 flow physics. Following this, we detail on the current numerical methods, set-up and parameters. In the last section, we analyse and compare our results with the experimental data and reliable simulation results from literature.

2. Experimental test case – VKI LS89

The turbine vane model LS89 is a well-known academic test case of a highly-loaded turbine inlet nozzle guide vane. In the 90's, the flow along this vane was studied for a large range of flow conditions in the Isentropic Light-Piston Compression Tube facility (CT-2), illustrated in Fig. 1, at the von Karman Institute (VKI) [4]. The concept and operation principle of this type of facility are described in [16; 17].

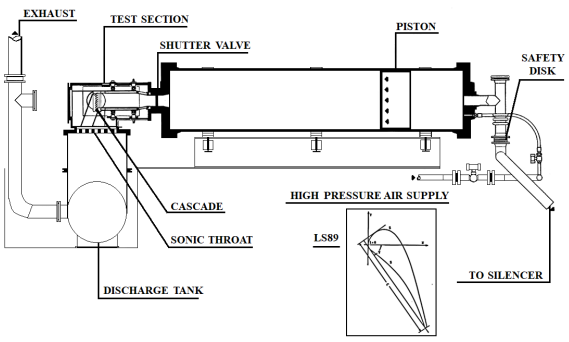

Figure 1: Illustration of CT-2 facility and LS89 vane (edited [4]).

The vane was specifically designed for these experiments and was optimized for an exit isentropic Mach number of 0.9, typical for a first stage stator of an HPT. The vane model consists of a 2D extruded profile, as sketched in Fig. 1, with a chord c of 67.647 mm and a span of 100 mm. The experiments were designed for a 5-vane linear cascade configuration; for a pitch g of 57.5 mm, it results in a test section of 230 x 100 mm^2. The main vane geometrical parameters are summarized in Tab. 1: o is the throat, γ is the stagger angle, α_{in} and α_{out} are the inlet and outlet mechanical flow angles, r_{le} and r_{te} are the leading and trailing edge radii, respectively.

Table 1: LS89 vane main geometrical characteristics [4].

Vane	LS89
c	67.647 mm
g/c	0.850
o/c	0.2207
γ	55°
α_{in}	0°
α_{out}	75°
r_{le}/c	0.061
r_{te}/c	0.0105

Only the central vane was instrumented; the remaining four vanes ensured flow passage periodicity. The former was either covered with static pressure taps for velocity measurements or with thin films for heat flux measurements.

The isentropic Mach number vane distribution is calculated based on the cascade inlet total pressure and vane static pressure; κ is the specific heat ratio of air, equal to 1.4 for the tested flow temperatures range:

$$M_{is} = \sqrt{\left(\frac{P_s}{P_{0,in}}^{\frac{1-\kappa}{\kappa}} - 1\right)\frac{2}{\kappa - 1}} \tag{1}$$

Heat fluxes are obtained from the coupling of wall temperature measuring thin films with electrical circuits. Through the electrical analogy of the heat conduction in a semi-infinite body as a long series of resistances and capacitors, one can derive the wall heat fluxes [18; 19].

The convective heat transfer coefficient h can then be defined as the ratio between the wall heat flux $\dot{q}_{wall}$ and the difference between the total inlet temperature $T_{0,in}$ and the vane wall temperature $T_{s,wall}$:

$$h = \frac{\dot{q}_{wall}}{T_{0,in} - T_{s,wall}} \tag{2}$$

2.1. Experimental flow field analysis – MUR235

From the available test cases in [5], we have selected MUR235, not only due to its inherently complex flow physics, but also to serve as a starting point for a following comparison with a new test case at a higher freestream turbulence intensity.

In this section, we analyse the boundary layer evolution based on the experimental heat transfer measurements, illustrated in Fig. 2.

The flow along the passage is transonic with a relatively high Reynolds and freestream turbulence intensity. The operating flow conditions for this test case are written in Tab. 2.

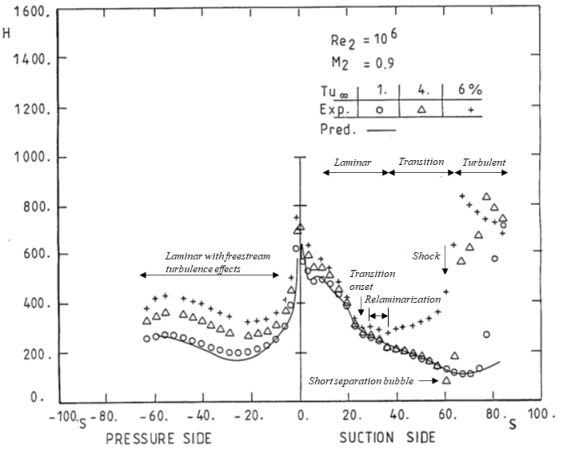

Figure 2: Heat transfer coefficient h for MUR235 (symbol +, edited [5]). Suction side: laminar boundary layer up to s = 20 mm; transition is triggered but soon suppressed by a short relaminarization (due to acceleration) region. Transition resumes due to acoustic waves impact at s = 40 mm. A shock at s = 60 mm drives a fully turbulent boundary layer. Pressure side: laminar boundary layer with freestream turbulence effects.

Table 2: Flow conditions for test case MUR235 [4].

Test case	MUR235
$M_{is,out}$	0.93
$Re_{is,out}$	$1.15{\cdot}10^6$
$P_{0,in}$	1.828 bar
$P_{s,out}$	1.049 bar
$T_{0,in}$	413.30 K
$T_{s,wall}$	301.15 K
$Tu_{\infty,in}$	6.0%

We can describe this case starting by the high heat transfer at the leading edge/stagnation point s = 0 mm. The growth of the ensuing laminar boundary layer reduces the heat transfer due to its thermal insulating

proprieties. The further change in this trend occurs due to other flow phenomena taking place.

In the case of the suction side, a short velocity plateau at $s = 20$ mm is enough to destabilize the boundary layer. Transition is thus triggered; however, it is not sustained due to a following steep acceleration. This results in a short relaminarization region. Further oscillations in the velocity distribution along with the impact of acoustic waves generated from the upper vane's trailing edge flow separation at $s = 40$ mm lead to the effective onset of bypass transition. Before the transition reaches its final stages, a shock at about $s \approx 60$ mm, coherent with Schlieren visualizations at similar flow conditions, shortly renders a fully turbulent boundary layer up to the trailing edge. Although the shock can be seen in numerical results [6–8; 12], the related transition process is rarely well captured by CFD.

As for the pressure side, a laminar boundary layer with freestream turbulence effects remains up to the trailing edge.

The present numerical effort to correctly simulate this test case and get further insight into the flow field is described in the following section.

3. Numerical simulations – ILES on Argo

The governing equations are the unsteady 3D compressible Navier-Stokes equations written in the conservative form as a set of generic convection-diffusion equation for the state vector $\tilde{u}$ containing the conservative variables $\tilde{u} = [\rho\ \rho\mathbf{u}\ \rho E]$ defined on a domain Ω; $\mathcal{F}$ and $\mathcal{D}$ are respectively the convective and diffusive fluxes and s is the source term:

$$\frac{\partial \tilde{u}}{\partial t} + \frac{\partial}{\partial x^k}\mathcal{F}^k(\tilde{u}) + \frac{\partial}{\partial x^k}\mathcal{D}^k(\tilde{u}, \nabla\tilde{u}) + s = 0 \qquad (3)$$

whereby appropriate Dirichlet and Neumann boundary conditions are defined on the boundary $\partial\Omega$.

The used constitutive equations are the ideal gas law ($p = \rho RT$, air specific gas constant $R = 287.1$ J/kg·K), Sutherland's law for the viscosity ($\mu = 1.458 \cdot 10^{-6} T^{3/2}/(T + 110.4)$) and Fourier Law's is used to calculate the heat flux ($\dot{q} = k\nabla T$, for the thermal conductivity k).

3.1. Turbulence modelling - ILES

Implicit LES (ILES) is an alternative approach to subgrid-scale (SGS) models in which there is neither explicit turbulence modelling nor filtering [20]. In this approach, the subgrid-scale dissipation resulting from the numerical scheme is assumed to constitute an appropriate LES model [21]. This is particularly the case with the high-order numerical schemes employed in Argo (see Section 3.2.1). The main advantage of this method is that, without explicit filtering, the numerical grid resolution can be fully exploited.

The present ILES method, combined with DGM, was able to generate as accurate results as state of the art SGS models for homogeneous isotropic turbulence (HIT) and a turbulent channel flow [22].

3.2. Numerical solver – Argo

Cenaero's in-house code Argo is used for the ILES of the LS89 vane. Argo, more specifically Argo DGM, is a multi-physics platform which has been developed for more than 10 years at Cenaero [15]. The present work uses the module *DGFluid* which solves compressible and incompressible Navier-Stokes flow problems.

The numerical code allows for the combined use of shared and distributed memory parallelism through open multi-processing (OpenMP) and message passing interface (MPI). It is particularly adapted to High Performance Computing (HPC), with a particular attention paid to arithmetic efficiency and massively parallel scalability. Moreover, Argo has many features specifically designed for the study of turbulent flows in turbomachines, such as extensive visualization capabilities and embedded statistical treatment of field and probe data (averages, standard deviations, correlations). The code also benefits from the high-order accuracy of the discontinuous Galerkin method on hybrid grids, which is briefly described in the next section.

3.2.1. Spatial discretization – DGM

The spatial discretization is achieved through a high-order discontinuous Galerkin method (DGM) with Symmetric Interior Penalty (SIP) treatment of the diffusive terms.

The DGM is a discontinuous finite element method in the sense that it is formulated as a finite element method but uses a piecewise polynomial representation of the solution which is discontinuous between elements, as illustrated in Fig. 3. The coupling between elements is achieved through the use of numerical fluxes, as in the finite volume method. The advantages of Discontinuous Galerkin schemes for the study of turbulent flows on realistic geometries are the ability to obtain an arbitrarily high order of convergence on unstructured and hybrid meshes, that is particularly

interesting for ILES, and the compact stencil that is amenable to massive parallelization. Compared to finite volume methods, this class of schemes is also less sensitive to the quality of the mesh.

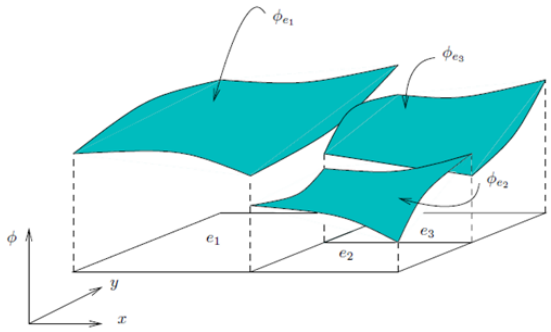

Figure 3: Schematic of the discontinuous Galerkin finite element interpolation space [15]. The basis functions ϕ are defined per element e and allowed to by discontinuous across their boundaries.

3.3. Computational domain and mesh – Gmsh

The computational domain for the LS89 simulations is illustrated in Fig. 4.

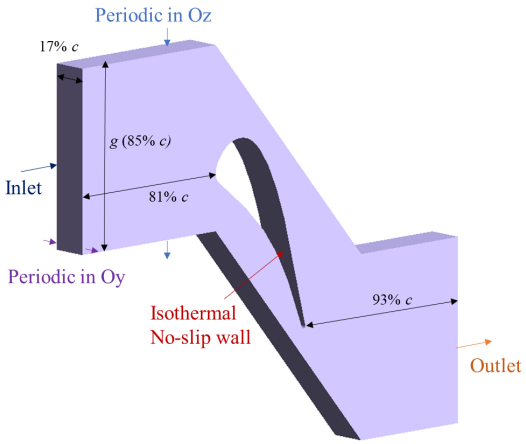

Figure 4: Computational domain and boundary conditions.

The inlet domain length is approximately the same distance from the cascade's leading edge (x = -55 mm, x/c = -0.81) as the inlet total pressure and temperature measurements in the experiments (x = -59 mm). The determination of the inlet length is constrained only by the influence of the inlet boundary condition on the global equilibrium. Unlike numerical studies employing synthetic turbulence generation [12; 7], the present modeling of the turbulence generated upstream of the domain does not require an additional length for establishing a physical turbulence spectrum (see Section 3.5).

The outlet length is x = 63 mm (x/c = 0.93): reflecting waves are inhibited by decreasing the interpolation order of the spatial discretization downstream of the wake.

The span of the domain is 11.5 mm (z/c = 0.17, z/g = 1/5), more than half the spanwise length of the experimental thin films (z = 20 mm).

A periodic condition is defined through the mesh in the pitch- and spanwise directions. The latter implies neglecting end-wall effects on the passage flow and boundary layer. The flow was indeed reported to be essentially 2D [5].

The mesh was generated with *Gmsh* [23] and is shown in Fig. 5. It consists of 747080 elements of mixed type: most are hexahedra and 480 are prisms. The region encompassing the boundary layer is made of "structured" hexahedra elements and the wake and inlet regions facing the vane are further refined to capture well the fine turbulent structures. The use of a high-order spatial discretization method requires the mesh to be curvilinear (2nd order) in order to represent the geometry with sufficient accuracy.

The current vane geometry has been slightly adapted by Cenaero, as the original geometry provided in [5] is known to lack smoothness, which makes it unsuitable for high order numerical simulations [9; 12].

3.4. Numerical and physical set-up

The numerical simulation uses a 3rd order Discontinuous Galerkin spatial discretization and a 2nd order backward differentiation formula (BDF) temporal discretization. Artificial diffusion is added locally in order to stabilize the numerical method in regions where shocks are detected [24].

The boundary conditions are defined according to the experiments: inlet total pressure ($P_{0,in}$ = 1.828 bar) and temperature ($T_{0,in}$ = 413.30 K) and outlet static pressure ($P_{s,out}$ = 1.049 bar) allow to define the operating Mach and Reynolds number levels. The vane wall has no-slip and isothermal conditions ($T_{s,wall}$ = 301.15 K).

Turbulence is injected at the inlet with an intensity of 6% and an integral length scale of 2 mm; the

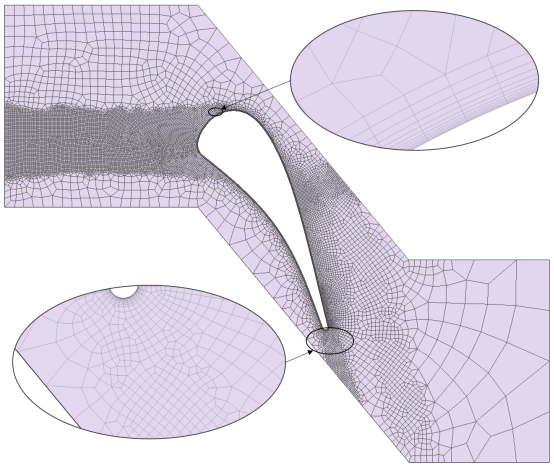

Figure 5: Computational mesh with focus on the near wall and wake region.

method used to add turbulence is described in the next section.

3.5. Inlet turbulence – precursor simulation of HIT

Test case MUR235 is particularly difficult to simulate due to the freestream turbulence generated by a passive grid in the experiments. Even though the turbulence intensity is not especially high ($Tu_\infty = 6\%$), the transition onset and development to a turbulent boundary layer is hardly well captured. Numerical studies with higher turbulence intensities from the experiments can even come close to their heat transfer rates [9; 11; 12]. This indicates that a very high spatial and temporal resolution is required, and that a particular attention should be paid to the physical representativeness of the turbulence injection method and spectrum.

The integral length scales Λ_x also influence the turbulence decay and the interaction with the boundary layer. Computationally, the integral length scale introduces a restriction on the smallest dimension of the inlet domain: for two eddies to be able to interact, one must ensure that this dimension is at least two times the size of the biggest eddies, i.e. the integral length scale. Before a recent experimental work, which for a similar configuration to MUR235 led to $\Lambda_x = 7.6$ mm [25], the integral length scales were an unknown in the LS89 simulations. Still, an LES study found an almost negligible difference in heat transfer results using the experimental length scale of 7.6 mm and a more computationally-friendly one of 3.5 mm (this was not however verified for the most refined mesh that gave the best heat transfer CFD estimation of MUR235 so far) [26].

In this work, we use a precursor simulation approach to add freestream turbulence to the main simulation. In this way, a pre-computed turbulent flow is combined with the main flow and injected to the LS89 computational domain as an inlet boundary condition. This turbulent field is generated by means of the same method and code and has already developed a physical behaviour, thus avoiding the need for a long inlet length for flow establishing.

This turbulence represents the decay of homogeneous isotropic turbulence (HIT), which is statistically invariant under both translations and rotations, and similar to turbulence generated by passive grids [27], as in the experiments. We use Rogallo's method [28] with a Passot-Pouquet spectrum [29], which controls the initial turbulent kinetic energy and integral length scale.

First, in the precursor simulation, the flow is computed in a tri-periodic box where the kinetic energy is integrated over the whole domain. Once the flow reaches a physical solution with the correct kinetic energy decay, it is possible to extract the solution for the intended turbulence intensity and integral length scale. Using Taylor's hypothesis, turbulent fluctuations from the precursor simulation's solution are then superimposed to the mean field at the inlet of the main simulation. To do so, the precursor field is interpolated on a plane sweeping through the precursor domain with the mean inlet velocity of the main simulation. Unfortunately, the time needed by the inlet plane to sweep through the HIT box is typically small compared to the total time of the main simulation. In order to avoid injecting the same turbulent fluctuations with a high frequency, we resort to a post-processing of the precursor simulation that consists in concatenating and blending different pseudo-realization of the precursor field obtained by rotating the original precursor solution [30]. Compared to injecting directly the original precursor solution, this treatment decreases dramatically the spurious spatial and temporal correlations in the injected turbulent field, without increasing the computational cost linked to the precursor simulations.

4. Results

The simulation of MUR235 is still ongoing; initial results are presented here for a relatively coarse mesh.

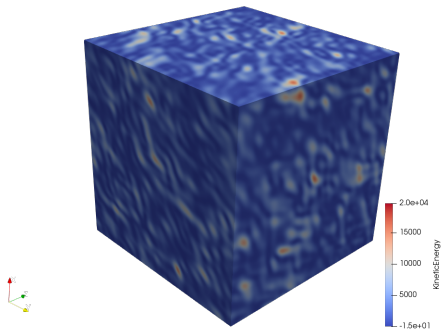

Figure 6: Kinetic energy field of precursor simulation of HIT

4.1. Flow field analysis

We can see the representation of the instantaneous density gradient over the density, which is similar to an experimental Schlieren visualization, in Fig. 7. Trailing edge acoustic waves impact on the suction side of the lower vane and are reflected upstream. As expected, there is a shock at about s = 60 mm. Finer inlet turbulence is captured at the inlet on the region facing the leading edge due to the mesh refinement.

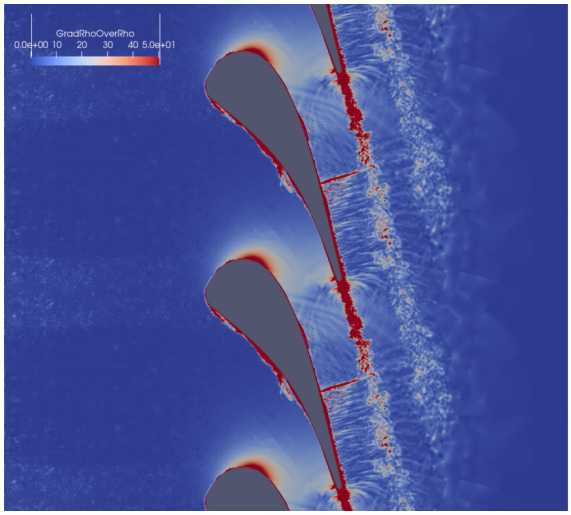

Figure 7: Instantaneous density gradient field $\Delta\rho/\rho$ highlights: inlet turbulence structures, finer facing the leading edge; wake structures; trailing edge acoustic waves impact on the suction side of a lower vane and are reflected.

4.2. Isentropic Mach number analysis

The vane isentropic Mach number distribution is shown in Fig. 8. It is additionally compared with experimental results at distinct but similar exit isentropic Mach numbers (MUR45 at $M_{is,out}$ = 0.875 and MUR47 at $M_{is,out}$ = 1.02 [5]).

The velocity profile on the suction side starts with a steep and steady acceleration up to s = 20 mm, followed but a short velocity plateau. This is ensued by varying accelerations up to s = 60 mm, where a diffusion peak leads to a steady deceleration.

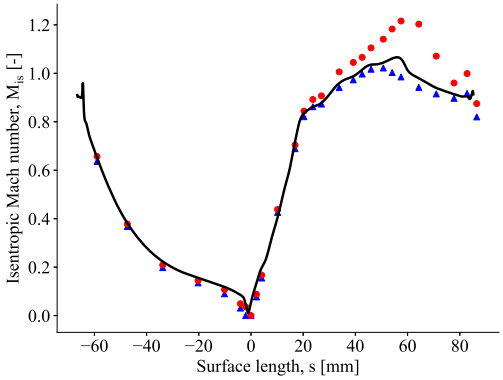

Figure 8: Isentropic Mach number M_{is} prediction ($M_{is,out}$ = 0.93, —) is compared with experimental data MUR45 ($M_{is,out}$ = 0.875, ●) and MUR47 ($M_{is,out}$ = 1.02, ▲) [5]. Results diverge on the suction side from s = 20 mm due to the difference in $M_{is,out}$: velocity peak moves downstream with increasing exit velocity.

The current result follows quite well the trend but starts to diverge from MUR45 at s = 50 mm and from MUR47 at s = 20 mm. This is due to the difference in $M_{is,out}$ and it shows coherence: the velocity peak moves downstream with the increase of the exit velocity. The difference with MUR45 is due to the shock: whereas MUR45 ($M_{is,out}$ = 0.875) presents a fully subsonic Mach profile, MUR235 ($M_{is,out}$ = 0.93) is transonic and has a shock at about 60 mm, which explains the difference. As for MUR47, velocity is higher and the shock moves downstream.

4.3. Convective heat transfer analysis

Current results are compared with test case MUR235 and, additionally, with a similar, but fully subsonic and without turbulence grid, test case MUR129 ($M_{is,out}$ = 0.84, $Tu_{\infty,in}$ = 1%) [5]; their heat transfer coefficient distribution is shown in Fig. 9. We can see a fully well predicted pressure side.

On the other hand, the suction side is more difficult to predict and, in fact, the computation is not matching most of it. Numerical results follow quite well the stagnation and laminar heat transfer up to s = 20

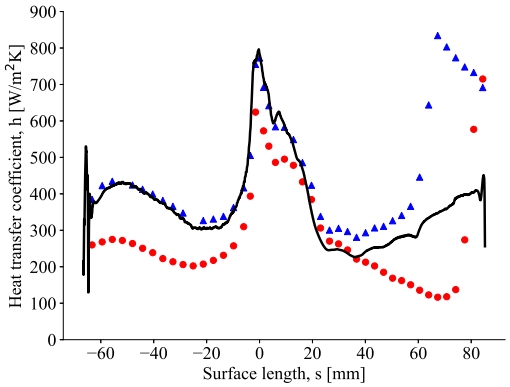

Figure 9: Heat transfer coefficient h prediction ($Tu_{\infty,in}$ = 5.9%, —) is compared with experimental data MUR129 (no turbulence grid, $Tu_{\infty,in}$ = 1.0%, ●) and MUR235 ($Tu_{\infty,in}$ = 6.0%, ▲) [5]. Accurate for the complete pressure side and suction side up to s = 20 mm: prediction follows low turbulence curve instead. Bypass transition onset is triggered at s = 40 mm but the shock-boundary layer interaction at $s \approx 60$ mm is not well captured. The turbulent boundary layer is not reached.

mm. From there, the simulation follows the trend of MUR129 instead. This indicates that the freestream turbulence interaction with the boundary layer may not be well captured and, hence, the destabilizing effect of the velocity plateau at s = 20 mm is not enough to trigger transition to turbulence. As in the experiments, there is also the following strong stabilizing effect of the favourable pressure gradient, suppressing the start of transition.

From s = 40 mm, we have the onset of bypass transition. The development of transition, expected to be 'faster' for bypass transition, is however prolonged: this is also due to the steep acceleration in this region. What changes transition in the experiments is a shock at about s = 60 mm which renders the boundary layer turbulent. This is not captured in the current simulation and therefore we do not reach the fully turbulent boundary layer even towards the trailing edge. The shock is most likely not well resolved yet and the boundary layer resolution may not yet be fine enough. We should also take into account that the upstream failure to capture the turbulence interaction/boundary layer development may have an effect on the downstream boundary layer evolution.

This is work under development: mesh refinement and artificial viscosity. Currently, artificial viscosity is also present in the boundary layer and it may be dissipating the heat from the turbulent spots, attenuating their potential to grow and coalesce into a turbulent boundary layer. The reason for this is due to the artificial viscosity sensor: it acts as a under resolution sensor and so it is hard in this case to decouple the shock and the under resolution of the boundary layer (since the mesh is still being refined). A zonal artificial viscosity is under development to allow to confine the addition of artificial viscosity only to the shock region.

Mesh refinement will improve the resolution, specially important for ILES, where the grid fully [ask] dissipates the unresolved scales and there is no modelling.

5. Conclusion

In this work, we have conducted a preliminary ILES investigation of the LS89 cascade for an HPT-relevant test case, MUR235 ($Re_{is,out}$ = 1.15x10^6, $M_{is,out}$ = 0.93, $Tu_{\infty,in}$ = 6%).

Numerical outcomes for a relatively coarse mesh have been presented and compared with the available experimental data (isentropic Mach number and convective heat transfer vane distributions).

The heat transfer prediction agrees well with the experiments for the full pressure side and for the suction side up to s = 20 mm. From here, complex boundary layer flow interactions, acoustic waves and shocks, require a finer meshing and a more accurate artificial viscosity implementation that will be soon applied. It is expected that these improvements will allow to capture better the turbulent spot production starting from s = 20 mm as well as the shock-boundary layer interaction at $s \approx 60$ mm that renders a fully turbulent boundary layer in the experiments.

As future work, we intend to simulate a similar experimental test case at higher turbulence intensity ($Tu_{\infty,in} \approx 22\%$), closer to the outlet of the combustion chamber, for more engine representative numerical studies.

Acknowledgements

The present research benefited from computational resources made available on the Tier-1 supercomputer of the Fédération Wallonie-Bruxelles, infrastructure funded by the Walloon Region under the grant agreement no. 1117545.

The authors also thank and acknowledge the role of Prof. Koen Hillewaert in forming this collaboration and starting this project.

References

[1] J.-C. Chang, Y.-H. Yun, C. Choi, J.-C. Kim, Failure analysis of gas turbine buckets, Engineering failure analysis 10 (5) (2003) 559–567.

[2] R. J. Goldstein, K. Y. Lau, C. C. Leung, Velocity and turbulence measurements in combustion systems, Exp. Fluids 1 (2) (1983) 93–99. doi:10.1007/BF00266261.

[3] G. J. Van Fossen, R. S. Bunker, Augmentation of stagnation region heat transfer due to turbulence from a DLN can combustor, J. Turbomach. 123 (1) (2000) 140–146. doi:10.1115/1.1330270.

[4] T. Arts, M. Lambert de Rouvroit, Aero-thermal investigation of a highly loaded transonic linear turbine guide vane cascade. A test case for inviscid and viscous flow computations, J. Turbomach. 114 (1) (1992) 147–154. doi:10.1115/1.2927978.

[5] T. Arts, M. Lambert de Rouvroit, A. W. Rutherford, Aero-thermal investigation of a highly loaded transonic linear turbine guide vane cascade. A test case for inviscid and viscous flow computations, Tech. Rep. Technical Note 174, von Karman Institute for Fluid Dynamics (1990).

[6] R. Fransen, E. Collado, F. Duchaine, N. Gourdain, L. Gicquel, L. Vial, G. Bonneau, Comparison of RANS and LES in high pressure turbines, in: 3ème Colloque INCA, ONERA, Toulouse, France, Nov, 2011, pp. 17–18.

[7] N. Gourdain, L. Y. M. Gicquel, E. Collado, Comparison of RANS and LES for prediction of wall heat transfer in a highly loaded turbine guide vane, J. Propuls. Power 28 (2) (2012) 423–433. doi:10.2514/1.B34314.

[8] E. C. Morata, N. Gourdain, F. Duchaine, L. Y. M. Gicquel, Effects of free-stream turbulence on high pressure turbine blade heat transfer predicted by structured and unstructured LES, Int. J. Heat Mass Transf. 55 (21-22) (2012) 5754–5768. doi:10.1016/j.ijheatmasstransfer.2012.05.072.

[9] A. P. S. Wheeler, R. D. Sandberg, N. D. Sandham, R. Pichler, V. Michelassi, G. Laskowski, Direct numerical simulations of a high-pressure turbine vane, J. Turbomach. 138 (7) (2016) 071003. doi:10.1115/1.4032435.

[10] R. Pichler, J. Kopriva, G. Laskowski, V. Michelassi, R. Sandberg, Highly Resolved LES of a Linear HPT Vane Cascade Using Structured and Unstructured Codes, Vol. Volume 2C: Turbomachinery of Turbo Expo: Power for Land, Sea, and Air, 2016, v02CT39A041. doi:10.1115/GT2016-57189.

[11] R. Pichler, R. D. Sandberg, G. Laskowski, V. Michelassi, High-Fidelity Simulations of a Linear HPT Vane Cascade Subject to Varying Inlet Turbulence, Vol. Volume 2A: Turbomachinery of Turbo Expo: Power for Land, Sea, and Air, 2017, v02AT40A001. doi:10.1115/GT2017-63079.

[12] L. M. Troth, L. Y. M. Gicquel, F. Duchaine, J. de Laborderie, LES of the LS89 cascade: influence of inflow turbulence on the flow predictions, in: Proceedings of 12th European Conference on Turbomachinery Fluid dynamics and Thermodynamics ETC12. Stockholm, Sweden, 2017, pp. 3–7. doi:10.29008/ETC2017-159.

[13] L. M. Seguí, L. Y. M. Gicquel, F. Duchaine, J. de Laborderie, Importance of boundary layer transition in a high-pressure turbine cascade using LES, in: Volume 2C: Turbomachinery, American Society of Mechanical Engineers, 2018. doi:10.1115/gt2018-75711.

[14] T. S. Cação Ferreira, T. Arts, E. Croner, On the influence of high turbulence on the convective heat flux on the high-pressure turbine vane LS89, International Journal of Turbomachinery, Propulsion and Power 4 (4) (2019) 37. doi:10.3390/ijtpp4040037.

[15] K. Hillewaert, Development of the discontinuous Galerkin method for high-resolution, large scale CFD and acoustics in industrial geometries, Ph.D. thesis, Université catholique de Louvain (2013).

[16] D. L. Schultz, T. V. Jones, M. L. G. Oldfield, L. C. Daniels, A new transient cascade facility for the measurement of heat transfer rates, in: High Temperature Problems in Gas Turbine Engines, Vol. AGARD CP 229, North Atlantic Treaty Organization, Advisory Group for Aerospace Research and Development, 1978, pp. 1–27.

[17] T. V. Jones, D. L. Schultz, A. D. Hendley, On the flow in an isentropic light piston tunnel, Citeseer, 1973.

[18] D. L. Schultz, T. V. Jones, Heat-transfer measurements in short-duration hypersonic facilities, Tech. rep., North Atlantic Treaty Organization, Paris, France (1973).

[19] M. L. G. Oldfield, T. V. Jones, D. L. Schultz, Online computer for transient turbine cascade instrumentation, IEEE Trans. Aerosp. Electron. Syst. 14 (5) (1978) 738–749. doi:10.1109/TAES.1978.308624.

[20] F. F. Grinstein, L. G. Margolin, W. J. Rider, Implicit Large Eddy Simulation: Computing Turbulent Fluid Dynamics, Cambridge University Press, 2007.

[21] S. Hickel, N. A. Adams, J. A. Domaradzki, An adaptive local deconvolution method for implicit les, J. of Computational Physics 213 (1) (2006) 413–436.

[22] C. C. de Wiart, K. Hillewaert, P. Geuzaine, R. Luccioni, L. Bricteux, G. Coussement, G. Winckelmans, Assessment of les modeling within a high order discontinuous galerkin solver, Proceedings of ETMM9, Thessaloniki, Greece.

[23] gmsh: A 3-d finite element mesh generator with built-in pre- and post-processing facilities.

[24] P.-O. Persson, J. Peraire, Sub-Cell Shock Capturing for Discontinuous Galerkin Methods, in: 44th AIAA Aerospace Sciences Meeting and Exhibit, American Institute of Aeronautics and Astronautics, 2006. doi:10.2514/6.2006-112.

[25] F. Fontaneto, Aero-thermal performance of a film-cooled high pressure turbine blade/vane: a test case for numerical codes validation, Ph.D. thesis, von Karman Institute for Fluid Dynamics/Universitá degli Studi di Bergamo, Rhode-Saint-Genèse, Belgium (2014).

[26] L. M. Seguí Troth, Multiphysics coupled simulations of gas turbines, Ph.D. thesis, PhD thesis, INP Toulouse, France (2017).

[27] S. B. Pope, Turbulent flows, Cambridge University Press, 2000.

[28] R. S. Rogallo, Numerical experiments in homogeneous turbulence, Tech. Rep. NASA-TM-81315, NASA (1981).

[29] T. Passot, A. Pouquet, Numerical simulation of compressible homogeneous flows in the turbulent regime, J. of Fluid Mech. 181 (1987) 441–466.

[30] Z. Xiong, S. Nagarajan, S. K. Lele, Simple method for generating inflow turbulence, AIAA Journal 42 (10) (2004) 2164–2166. doi:10.2514/1.6157.

Roman symbols

c	chord	mm
g	pitch	mm
h	heat transfer coefficient	W/m^2K
k	thermal conductivity	W/mK
M	Mach number	$-$
P	pressure	bar
$\dot{q}$	heat flux	W/m^2
r	radius	mm
R	specific gas constant (air = 287.1)	J/kgK
Re	Reynolds number	$-$
s	vane surface length	mm
T	temperature	K
Tu	turbulence intensity	$\%$

Greek symbols

α	vane flow angle	$^\circ$
Λ	integral length scale	m
ρ	density	kg/m^3
γ	vane stagger angle	$^\circ$
κ	specific heat ratio (air = 1.4)	$-$
Λ	integral length scale	mm
μ	dynamic viscosity	kg/ms
ν	kinematic viscosity	m^2/s
o	throat	mm

Subscripts

0	total quantity
in	cascade inlet plane
is	isentropic quantity
le	vane leading edge
out	cascade outlet plane
s	static quantity
te	vane trailing edge
x	streamwise component
$wall$	wall quantity
∞	freestream quantity

Acronyms

BDF	backward differentiation formula
CT-2	Isentropic Light-Piston Compression Tube
DGM	discontinuous Galerkin method
HIT	homogeneous isotropic turbulence
HPC	High Performance Computing
HPT	high-pressure turbine
ILES	Implicit Large Eddy Simulation
MPI	Message Passing Interface
RANS	Reynolds-Averaged Navier-Stokes
SGS	sub-grid scale
SIP	Symmetric Interior Penalty
OpenMP	Open Multi-Processing

Advanced PIV measurement in high-speed turbomachinery flows

Mizuki Okada

Turbomachinery and Propulsion Department, von Karman Institute for Fluid Dynamics, Belgium, mizuki.okada@vki.ac.be

Supervisor: Sergio Lavagnoli

Associate Professor, Turbomachinery and Propulsion Department, von Karman Institute for Fluid Dynamics, Belgium, lavagnoli@vki.ac.be

University Supervisor: Alessandro Parente

Associate Professor, Ecole polytechnique de Bruxelles, Universit libre de Bruxelles, Belgium, Alessandro.Parente@ulb.ac.be

Abstract

Recent interests in the development of advanced turbines include both the efficient use of purge flow and the reduction of energy loss attributed to leakage flows across the gas path. This study focuses on the implementation of advanced Particle Image Velocimetry (PIV) techniques to evaluate the effect of purge flow emerging from the stator-rotor rim seal gap and shroud leakage flows, as well as the impact of optimized endwall contouring.

The high speed short-duration rotational turbine and the high-speed continuous linear cascade test facilities of the von Karman Institute will host new designed high-pressure and low-pressure turbine geometries on which PIV will be performed. The measurements will generate an extensive experimental database for optimized rotor endwall and various cavity designs. Instantaneous spatial data acquisition with low-intrusiveness and the possibility to analyse the complex three-dimensional flow structures present in turbine stages make PIV a powerful tool for turbomachinery investigations. The available open literature is very scarce about PIV measurements of unsteady flow structures related to endwall contouring, purge flow rates, rim seal and cavity geometries in high speed turbine wind tunnels.

Installation of a PIV equipment into the high-speed rig is challenging due to the packed hardware geometry with multiple design features and the transient operation of the rig itself. In order to get optical access through the turbine casing, endoscopes will be used for both camera sight and laser sheet introduction. The reliable data acquisition in short-duration facilities, for which the blow down test lasts only 0.5 seconds, is challenging due to reduced number of images and repeatability of tests, and limited period for in-situation system set up and tuning. The particle seeding will be carefully designed in order to guarantee the flow traceability and to enhance signal-to-noise ratio. The postprocessing algorithm must be adapted for computation of large velocity gradient present in high speed turbine flow.

The outcome of this research is not only the generation of experimental databases in a particular turbine stage, but also to provide further practical guidelines for the implementation of PIV into high-speed turbomachinery.

Keywords: PIV, turbomachinery, high-speed flow, transient test, endwall contouring, purge flow

Experimental aerodynamics of a high-speed low-pressure turbine

Antonino Federico Maria Torre

Turbomachinery and Propulsion Department, von Karman Institute for Fluid Dynamics, Belgium, antonino.torre@vki.ac.be

Supervisor: Sergio Lavagnoli

Associate Professor, Turbomachinery and Propulsion Department, von Karman Institute for Fluid Dynamics, Belgium, lavagnoli@vki.ac.be

University Supervisor: Koen Hillewaert

Associate Professor, Département d'aérospatiale et mécanique, University of Liège, Belgium, koen.hillewaert@uliege.be

Abstract

Developing a more efficient mobility is prerogative for today aviation growth. Ultra-high bypass ratio Geared Turbofans (GTF) represent one of the most effective evolutions in the propulsion field. The Low-Pressure Turbines (LPT) rotational speed in GTF engines is considerably increased. This allows improvements on performances and weight saving, although will require the turbine to work at transonic exit conditions and low Reynolds numbers. The interest in High-Speed LPT aerodynamics is now rising although a relevant lack of experimental data is found. Its experimental investigations on a multi-row rotating environment at engine-realistic condition is needed, focusing on endwall flows interaction with cavity purge and leakage flows.

Framed within an investigation granted by the Clean Sky 2 research program, this PhD has the objective to experimentally investigate the unsteady aerodynamics of high-speed LP turbines of geared-fan propulsion systems testing in the CT-3 annular rotating axial turbine rig. Tests at engine-realistic conditions will allow characterizing the interactions between mainstream and cavity flows. The impact of different the cavity shapes for both hub cavity and rotor shroud will be quantified. Different purge mass flow rates and rotor clearance will be also tested.

Preliminary Computational Fluid Dynamics will be used to design the experiment including the aerothermodynamic scaling of the rig and to optimize the instrumentation location, range and bandwidth. The test section of the rotating turbine rig will be heavily instrumented to measure the time-averaged and time-resolved aerodynamics of the turbine. Detailed characterization of the inlet total quantities and freestream conditions will be performed. Quasi-shear stress measurements are envisaged to measure the time-resolved behavior of the boundary layer on the airfoil profiles. Aerodynamic and performance measurements will be carried out traversing rakes of fast-response pressure sensors within the turbine stages. Endwalls unsteady aerodynamics will be quantified by means of piezo-resistive pressure sensors and pressure taps. Quasi-shear stress measurements on the shroud and rotor-stator cavity will quantify the impact of cavities geometry variation.

This investigation will contribute to the progress of high-speed low-pressure turbines, characterizing the impact of cavity-purge and leakage flows unsteady aerodynamics and generating a highly space and time-resolved open-access database.

Keywords: Low-pressure turbine, high-speed, geared turbofan, turbine stage, leakage flows, cavity flows, secondary flows, testing

INSTRUMENTATION AND MEASUREMENT TECHNIQUES

Aero-thermal investigation of roughened circular channels

Muhsin Can Akkurt

Environmental Applied Fluid Dynamics Department, von Karman Institute for Fluid Dynamics, Belgium, muhsin.can.akkurt@vki.ac.be

Supervisor: Delphine Laboureur

Assistant Professor, Environmental Applied Fluid Dynamics, von Karman Institute for Fluid Dynamics, Belgium, delphine.laboureur@vki.ac.be

University Supervisor: Kevin Van Geem

Professor, Department of Chemical Engineering and Technical Chemistry, Ghent University, Belgium, Kevin.VanGeem@UGent.be

Abstract

Enhanced roughened tubes are recently used as heat exchangers in various fields such as turbomachinery and chemical reactors. By using them, the heat transfer rates are improved in gas turbine internal cooling passages in order to maximize the thermodynamic efficiency by increasing the turbine inlet temperature. Alternatively, the augmentation of heat transfer provides coke reduction during the production of light olefins by decreasing the wall temperature in steam cracking reactors. Several heat transfer augmentation techniques such as rib turbulators, pin fins, and dimpled surfaces have been introduced in these enhanced tubes to improve heat transfer rates by increasing the heat transfer surface and promoting the flow turbulence. However, the use of these techniques also contributes to the increase of the pressure drop across the channel, which has a negative impact on the corresponding application. Therefore, it is essential to keep the pressure drop or skin friction coefficient at a minimum level while increasing the turbulence intensity and the local heat transfer.

The objective of the present study, which is done in collaboration with the Department of Chemical Engineering and Technical Chemistry of Ghent University (UGent), is to improve the efficiency of steam cracking reactors by investigating different roughened circular channel designs. The majority of the work will be experimental. The flow field in these channels will be measured by using stereo-PIV, whereas the Liquid Crystals Thermography (TLCs) technique will be carried out to measure heat transfer through the corresponding channel. Besides, numerical studies on the geometries chosen with UGent might be examined as well. The geometry with a specific shape of dimples, which is called HeART, has been obtained by an optimization study carried out by UGent. However, during the flow field measurements, it is clear that distortions on the taken PIV images occur due to the complexity of the HeArt shaped dimples. Since the PIV technique measures the velocity through the displacement of tracer particles and therefore requires optical access, the effects of these distortions on the PIV image processing should be removed. For that reason, as the second objective of the present work, the ray tracing-based correction method will be developed to be able to measure the flow field through the complex shaped channels. The method includes three steps: rendering the 3-D experimental facility using open-source software (pbrt), defining the correction matrix during the rendering process, applying the correction to all PIV images for the particles to be properly investigated. The methodology developed during these studies might also be applied to characterize the aero-thermal performance of an alternative enhanced pipe defined by Ghent University.

Keywords: Enhanced tubes, dimples, PIV, image distortions, image correction, TLCs

Monitoring of flow mechanics in cohesive sediment layers

Bart Brouwers

Flanders Hydraulics Research (FHR), Belgium, bart.brouwers@mow.vlaanderen.be

Supervisor: Jeroen van Beeck

Professor, Environmental and Applied Fluid Dynamics Department, von Karman Institute for Fluid Dynamics, Belgium, vanbeeck@vki.ac.be

University Supervisor: Evert Lataire

Professor, Department of Civil Engineering, Maritime Technology Division, Ghent University, Belgium, Evert.Lataire@UGent.be

Abstract

To assess the critical draft of ships in navigation areas, the definition of nautical bottom was introduced in the nautical community. However, when cohesive sediment (mud) layers form on the bottom of navigation areas, there is no clear physical limit which determines the applicable nautical bottom level. Furthermore, the presence of such muddy layers greatly influences the manoeuvrability and controllability of ships, even when the draft of the ship doesn't exceed the initial depth of the mud layer.

Research on the link between the presence of a mud layer and ship's manoeuvring behaviour has therefore been performed intensively by several institutions (FHR, Marin, Sogreah and BAW Hamburg) by means of scale model experiments. Although they have proven their use by defining safety regulations for specific situations which are applied today, these experiments were always based on simplifications of the actual situation.

Due to the complex interactions between ship, mud and water layers, the use of CFD models is preferred in the nautical community to facilitate the research on this topic. Such a model will require validation data derived from physical laboratory tests, in this case using real natural mud. The bottleneck here is the availability of techniques capable of visualizing flow mechanics and measuring velocities within the relevant range (0 - 2m/s), in real natural mud layers. Furthermore, due to the changing properties in depth and time (thixotropy), the use of real natural mud, even in controlled conditions of laboratory tests, has proven to be a challenge with regard to reproducibility and thus reliability of the tests.

With a literature survey, state-of-the-art measurement techniques applied in other fields of application will be evaluated with regards to their potential use in real natural mud. Subsequently, promising techniques will be tested, fine-tuned and calibrated for use in the nautical research experiments by means of small scale experiments. So far, ultrasound imaging shows great potential, while radiography seems less suited for scale model testing.

Additional experimental research and literature survey will be performed to develop specific procedures to condition real natural mud for use in experimental tests, and to monitor relevant characteristics of mud.

Keywords: nautical bottom, ship manoeuvring, cohesive sediment, mud, flow visualization, flow velocity, scale model testing, thixoptropy.